Transactions of the ASME®

Journal of Heat Transfer

Published Quarterly by The American Society of Mechanical Engineers

VOLUME 123 • NUMBER 1 • FEBRUARY 2001

TECHNICAL PAPERS

Conduction Heat Transfer

Forced Convection

Natural and Mixed Convection

Radiative Transfer

(Contents continued on inside back cover)

Transactions of the ASME, Journal of Heat Transfer (ISSN 0022-1481) is published bi-monthly (Feb., Apr., June, Aug., Oct., Dec.) by The American Society of Mechanical Engineers, Three Park Avenue, New York, NY 10016. Periodicals postage paid at New York, NY and additional mailing offices. POSTMASTER: Send address changes to Transactions of the ASME, Journal of Heat Transfer, c/o THE AMERICAN SOCIETY OF MECHANICAL ENGINEERS, 22 Law Drive, Box 2300, Fairfield, NJ 07007-2300. **CHANGES OF ADDRESS** must be received at Society headquarters seven weeks before they are to be effective. Please send old label and new address. **STATEMENT from By-Laws.** The Society shall not be responsible for statements or opinions advanced in papers or ... printed in its publications (B7.1, Para. 3), **COPYRIGHT © 2001** by The American Society of Mechanical Engineers. For authorization to photocopy material for internal or personal use under those circumstances not falling within the fair use provisions of the Copyright Act, contact the Copyright Clearance Center (CCC), 222 Rosewood Drive, Danvers, MA 01923, tel: 978-750-8400, *www.copyright.com*. Request for special permission or bulk copying should be addressed to Reprints/Permission Department. **INDEXED** by Applied Mechanics Reviews and Engineering Information, Inc. Canadian Goods & Services Tax Registration #126148048.

This journal is printed on acid-free paper, which exceeds the ANSI Z39.48-1992 specification for permanence of paper and library materials. ♾™
♲ 85% recycled content, including 10% post-consumer fibers.

(**Contents continued**)

Journal of Heat Transfer **Volume 123, Number 1** **FEBRUARY 2001**

Heat Pipes

Microscale Heat Transfer

Porous Media, Particles, and Droplets

Heat Transfer in Manufacturing

ANNOUNCEMENTS

SPECIAL RECOGNITION

Sensitivity Analysis for Nonlinear Heat Conduction

Kevin J. Dowding
e-mail: kjdowdi@sandia.gov

Bennie F. Blackwell
e-mail: bfblack@sandia.gov

Sandia National Laboratories,
P.O. box 5800, Mail Stop 0828,
Albuquerque, NM 87185-0828

Parameters in the heat conduction equation are frequently modeled as temperature dependent. Thermal conductivity, volumetric heat capacity, convection coefficients, emissivity, and volumetric source terms are parameters that may depend on temperature. Many applications, such as parameter estimation, optimal experimental design, optimization, and uncertainty analysis, require sensitivity to the parameters describing temperature-dependent properties. A general procedure to compute the sensitivity of the temperature field to model parameters for nonlinear heat conduction is studied. Parameters are modeled as arbitrary functions of temperature. Sensitivity equations are implemented in an unstructured grid, element-based numerical solver. The objectives of this study are to describe the methodology to derive sensitivity equations for the temperature-dependent parameters and present demonstration calculations. In addition to a verification problem, the design of an experiment to estimate temperature variable thermal properties is discussed. [DOI: 10.1115/1.1332780]

Keywords: *Conduction, Parameter Estimation, Heat Transfer*

Introduction

Temperature dependence of parameters in the heat conduction equation must be accounted for in many problems. For example, thermal conductivity, volumetric heat capacity, convection coefficients, emissivity, contact conductance, and source terms may demonstrate a dependence on temperature. Except for relatively simple situations where closed form analytical solution can be derived, obtaining a solution when parameters depend on temperature requires a numerical method. A common numerical method is to approximate the temperature dependence via basis functions, such as piecewise-linear. Parameters in the functions that describe the temperature dependence may be known with varied levels of accuracy. In many instances, data are only available at discrete temperatures and the analyst must use engineering judgment to approximate the behavior between data points. Knowing the sensitivity of the solution to parameters that describe the temperature dependence would be valuable to the thermal analyst. Sensitivity analysis for nonlinear heat conduction owing to temperature-dependent properties is the focus of this paper.

Sensitivity analysis determines the partial derivative of the state variable (temperature for thermal problems) with respect to model parameters (thermal conductivity, volumetric heat capacity, convection coefficient, emissivity, etc.). This partial derivative is called a sensitivity coefficient. Although valuable insight may be gleaned from sensitivity coefficients in their own regard, there are many other applications as well. They are used in parameter estimation ([1–3]); optimal experimental design ([4–7]); and uncertainty or error analysis ([8–10]).

Previous formulations for sensitivity analysis are closely related to perturbation based methods. Probabilistic finite elements of structural dynamics are studied for linear ([11]) and nonlinear ([12]) cases. Emergy and Fadale [13] present a formulation for nonlinear heat conduction, which extends their prior work for the linear problem ([10]). Thermal properties are treated as random field parameters in Nicolai and De Baerdermaeker [14,15].

There are several approaches to calculate sensitivities ([16]). The method used here is to differentiate the describing equations with respect to parameters to derive sensitivity equations that are numerically solved. All previously cited references use a similar approach, with one difference. In this paper continuum equations, instead of discrete equations, are used to derive the sensitivity equations. Previous investigations ([11–15]) have derived the sensitivity equations from discrete describing equations. While the two approaches may result in the same numerical value for sensitivity, we believe there is additional insight available from the sensitivity equations as derived in this paper, which is not available from previous approaches.

Temperature dependence of parameters is discussed next. Sensitivity equations for nonlinear heat conduction are derived and discussed in the following section. Then numerical examples are shown including a verification problem and model of an experiment being designed to estimate temperature-dependent thermal properties of a low thermal conductivity material (polyurethane foam).

Temperature-Dependent Parameters

Temperature dependence of parameters can be represented in various ways. For generality, temperature dependence of parameter $g(T)$ is assumed to have an arbitrary functional form

$$g(T)=\sum_{j=1}^{N_g} g_j \theta_j^g(T). \qquad (1)$$

Eq. (1) could, for example, be piecewise linear or a spline function, where g_j are constants, and $\theta_j^g(T)$ is the j^{th} basis function describing parameter $g(T)$; there are N_g terms to describe $g(T)$. It is possible that different temperature-dependent parameters will use different approximations. Representing the temperature dependence, as shown in Eq. (1), allows for generality and flexibility. Furthermore, temperature-dependent functions are parametrized—i.e., represented with a series of constant parameters. Consequently, standard calculus can be used to compute sensitivity (derivatives). Another approach is to consider the temperature-dependent parameters as functions, i.e., infinite-dimensional. In this case variational methods are needed to calculate the derivatives. This approach is not considered further in this paper but may be a more efficient way to get sensitivity to temperature-dependent functions.

Using Eq. (1) temperature-dependent parameters are represented as a collection of constant parameters. The number of parameters that represent the temperature dependence (and associated basis functions) can vary by parameter. We have solved problems that require nominally 5–10 parameters to describe the temperature dependence of a thermal property and/or boundary

---

Contributed by the Heat Transfer Division for publication in the JOURNAL OF HEAT TRANSFER. Manuscript received by the Heat Transfer Division October 5, 1999; revision received August 23, 2000. Associate Editor: S. Sadhal.

coefficient. Hence when multiple materials with temperature-dependent properties are present, the total number of parameters can become quite large; hundreds of sensitivity coefficients may be required. In this study only first-order sensitivity is discussed. Computational requirements for second-order analysis are significantly greater ([16]).

Sensitivity analysis, as will be shown later, requires the derivative of the function $g(T)$ with respect to temperature. The derivative can be related to the original description as

$$\frac{dg(T)}{dT}=\sum_{j=1}^{N_g} g_j \phi_j^g(T), \tag{2}$$

where

$$\phi_j^g(T) \equiv \frac{d\theta_j^g(T)}{dT}. \tag{3}$$

The derivative $dg(T)/dT$ in Eq. (2) will have the same coefficients, g_j, as the function $g(T)$ in Eq. (1). Basis functions for $dg(T)/dT$, however, are the derivative (with respect to temperature) of the basis functions for $g(T)$; see Eq. (3). We note that it is possible that the derivative of the basis function will be discontinuous. An example is a piecewise linear function, which would have a discontinuous derivative at points joining linear segments with different slopes.

Equation for Nonlinear Heat Conduction

Sensitivity equations for general nonlinear heat conduction are derived in this section. Equations are implemented in an unstructured grid, control-volume finite-element code. Hence, an integral equation description is presented. An analogy to the differential formulation of the equations is straightforward ([17]). Sensitivity equations in this paper extend the work in ([16]), which considered linear heat conduction with constant parameters. Prior to discussing sensitivity equations, a formulation for the temperature field is presented.

Temperature Equations. The integral energy equation for a multidimensional body with temperature-dependent thermal properties and source term is

$$\int\int\int_{V} C(T)\frac{\partial T}{\partial t}d\mathcal{V}+\int\int_{\mathcal{A}} \vec{q}\cdot d\vec{\mathcal{A}}=\int\int\int_{\mathcal{V}} \dot{e}'''(T)d\mathcal{V}. \tag{4}$$

The heat flux is represented with Fourier's Law

$$\vec{q}=-\tilde{\mathbf{k}}(T)\cdot\nabla T, \tag{5}$$

where $\tilde{\mathbf{k}}(T)$ can be, in general, a full thermal conductivity tensor. In this work $\tilde{\mathbf{k}}(T)$ only has diagonal entries that represent an orthotropic material

$$\tilde{\mathbf{k}}(T)=\begin{bmatrix} k_{11}(T) & 0 & 0 \\ 0 & k_{22}(T) & 0 \\ 0 & 0 & k_{33}(T) \end{bmatrix}. \tag{6}$$

Flux conditions are prescribed on part of the boundary ($\mathcal{A}_b$) with the three types of prescribed heat flux (constant, convection, and radiation) written in a single equation of the form

$$\int\int_{\mathcal{A}_b} \vec{q}\cdot d\vec{\mathcal{A}}=\int\int_{\mathcal{A}_b} -(\tilde{\mathbf{k}}(T)\cdot\nabla T)_{\vec{x}_b}\cdot d\vec{\mathcal{A}}=\int\int_{\mathcal{A}_b} \dot{q}_b''\hat{n}\cdot d\vec{\mathcal{A}}, \tag{7}$$

where

$$\dot{q}_b''=\left(\begin{array}{ll} \dot{q}_0'' & \text{along } \vec{x}_{b_1} \\ \dot{q}_c''=h(T)(T-T_\infty) & \text{along } \vec{x}_{b_2}. \\ \dot{q}_r''=\varepsilon(T)\sigma(T^4-T_r^4) & \text{along } \vec{x}_{b_3} \end{array}\right. \tag{8}$$

Convection coefficient and emissivity are assumed to be temperature-dependent. A temperature condition is prescribed along the remaining boundary

$$T(\vec{x}_{b_4})=T_b. \tag{9}$$

The initial condition is

$$T|_{t=0}=T_0. \tag{10}$$

Sensitivity Equations

Definition. Although there are other dependent variables for which sensitivity is important, sensitivity coefficients related to temperature are studied in this paper. The sensitivity coefficient is the partial derivative of temperature with respect to a parameter, which is $\partial T/\partial p_i$ for a parameter p_i. Scaling allows sensitivity coefficients for different parameters to be directly compared. A scaled sensitivity coefficient is

$$T_{p_i}\equiv p_i\frac{\partial T}{\partial p_i}. \tag{11}$$

Scaled sensitivity coefficients have units of temperature, allowing magnitudes for different parameters to be directly compared to temperature scales — e.g., magnitude of the transient temperature rise—within the problem.

Describing equations. To derive scaled sensitivity equations, the energy equation in Eq. (4) is differentiated with respect to an arbitrary parameter, p_i, which represents the i^{th} parameter describing $p(T)$, and multiplied by that parameter. (While sensitivity is being computed for parameter $p(T)$, the equations have other temperature-dependent parameters, which are arbitrarily referred to in the coming discussion as $g(T)$. Only one parameter satisfies $p(T)=g(T)$). Note that the parameter p_i is assumed to be independent of time and space so that it can be moved inside the integral sign. Differentiating Eq. (4), multiplying by the parameter, and interchanging the order of differentiation and integration results in

$$\int\int\int_{\mathcal{V}} p_i\frac{\partial C(T)}{\partial p_i}\frac{\partial T}{\partial t}d\mathcal{V}+\int\int\int_{\mathcal{V}} C(T)\frac{\partial T_{p_i}}{\partial t}d\mathcal{V} + \int\int_{\mathcal{A}}\left(p_i\frac{\partial\vec{q}}{\partial p_i}\right)\cdot d\vec{\mathcal{A}}=\int\int\int_{\mathcal{V}} p_i\frac{\partial\dot{e}'''(T)}{\partial p_i}d\mathcal{V}. \tag{12}$$

The dependent variable in Eq. (12) is T_{p_i}. The partial derivative with respect to the heat flux is addressed first. Expanding the third term of Eq. (12), after substituting from Fourier's law, gives

$$p_i\frac{\partial\vec{q}}{\partial p_i}=p_i\frac{\partial}{\partial p_i}[-\tilde{\mathbf{k}}(T)\cdot\nabla T]=-\tilde{\mathbf{k}}(T)\cdot\nabla T_{p_i}-p_i\frac{\partial\tilde{\mathbf{k}}(T)}{\partial p_i}\cdot\nabla T. \tag{13}$$

The differentiation process results in partial derivatives of temperature-dependent parameters—for example $p_i\partial\tilde{\mathbf{k}}(T)/\partial p_i$ in Eq. (13). First, we write these partial derivatives for an arbitrary parameter, $g(T)$. By taking the partial derivative of Eq. (1), the derivative of an arbitrary temperature-dependent parameter is obtained

$$p_i \frac{\partial g(T)}{\partial p_i} = \sum_{j=1}^{N_g} g_j p_i \frac{\partial \theta_j^g(T)}{\partial p_i} + \left\{ \begin{array}{ll} g_i \theta_i^g(T) & p=g \\ 0 & \text{otherwise} \end{array} \right\}. \quad (14)$$

Using the chain rule, the first term on the right side of Eq. (14) can be related to the derivative of $g(T)$

$$\sum_{j=1}^{N_g} g_j p_i \frac{\partial \theta_j^g(T)}{\partial p_i} = \sum_{j=1}^{N_g} g_j \frac{d\theta_j^g(T)}{dT} p_i \frac{\partial T}{\partial p_i} = \frac{dg(T)}{dT} T_{p_i}. \quad (15)$$

The final expression in Eq. (15) follows from the derivative defined in Eqs. (2) and (3). Equation (14) can be rewritten with the result of Eq. (15) as

$$p_i \frac{\partial g(T)}{\partial p_i} = \frac{d_g(T)}{dT} T_{p_i} + \left\{ \begin{array}{ll} g_i \theta_i^g(T) & p=g \\ 0 & \text{otherwise} \end{array} \right\}. \quad (16)$$

The partial derivative of a temperature-dependent parameter has two contributions. The first term on the right side of Eq. (16) arises for all temperature-dependent parameters, regardless of p_i. It is the derivative of the parameter, with respect to temperature, multiplied by the scaled sensitivity coefficient. The second term in Eq. (16) is only nonzero when the parameter p_i is a coefficient describing the function—i.e., $p=g$.

The derivative of the thermal conductivity tensor, with respect to the parameter p_i in Eq. (13), can be written as

$$p_i \frac{\partial \tilde{\mathbf{k}}(T)}{\partial p_i} = \frac{d\tilde{\mathbf{k}}(T)}{dT} T_{p_i} + \left\{ \begin{array}{ll} k_{ll,i} \theta_i^{k_{ll}}(T) & p=k_{ll} \\ 0 & \text{otherwise} \end{array} \right\}. \quad (17)$$

The final term on the right side of Eq. (17) is only nonzero when we are computing sensitivity to k_{ll}.

Substituting Eq. (17) into Eq. (13) allows the partial derivative of the heat flux, with respect to parameter p_i, to be arranged as

$$p_i \frac{\partial \vec{q}}{\partial p_i} = -\tilde{\mathbf{k}}(T) \cdot \nabla T_{p_i} - \left(\frac{d\tilde{\mathbf{k}}(T)}{dT} \cdot \nabla T \right) T_{p_i} - \left\{ \begin{array}{ll} k_{ll,i} \theta_i^{k_{ll}}(T) \dfrac{\partial T}{\partial x_l} \hat{e}_l & p=k_{ll} \\ 0 & \text{otherwise} \end{array} \right\}. \quad (18)$$

The scalar T_{p_i} has been moved outside the product in the second term on the right side of Eq. (18). The first term on the right side of Eq. (18) is present even for constant conductivity; the second term only appears for temperature dependent properties.

The remaining partial derivatives of temperature-dependent parameters in Eq. (12) are written by inspection from Eq. (16)

$$p_i \frac{\partial C(T)}{\partial p_i} = \frac{dC(T)}{dT} T_{p_i} + \left\{ \begin{array}{ll} C_i \theta_i^C & p=C \\ 0 & \text{otherwise} \end{array} \right\} \quad (19)$$

$$p_i \frac{\partial \dot{e}'''(T)}{\partial p_i} = \frac{d\dot{e}'''(T)}{dT} T_{p_i} + \left\{ \begin{array}{ll} \dot{e}_i''' \theta_i^{\dot{e}} & p=\dot{e}''' \\ 0 & \text{otherwise} \end{array} \right\}. \quad (20)$$

Substituting the partial derivatives from Eq. (18) through Eq. (20) into Eq. (12), the integral sensitivity equation for nonlinear heat conduction for an arbitrary parameter p_i can be arranged as follows:

$$\begin{aligned} &\int\int\int_{\mathcal{V}} C(T) \frac{\partial T_{p_i}}{\partial t} d\mathcal{V} - \int\int\int_{\mathcal{A}} [\tilde{\mathbf{k}}(T) \cdot \nabla T_{p_i}] \cdot d\vec{\mathcal{A}} + \int\int\int_{\mathcal{V}} \left[\frac{dC(T)}{dT} \frac{\partial T}{\partial t} \right] T_{p_i} d\mathcal{V} \\ &- \int\int_{\mathcal{A}} \left[\frac{d\tilde{\mathbf{k}}(T)}{dT} \cdot \nabla T \right] T_{p_i} \cdot d\vec{\mathcal{A}} - \int\int\int_{\mathcal{V}} \left(\frac{d\dot{e}'''(T)}{dT} T_{p_i} \right) d\mathcal{V} \\ &= - \left\{ \begin{array}{ll} \displaystyle\int\int\int_{\mathcal{V}} C_i \theta_i^C(T) \frac{\partial T}{\partial t} d\mathcal{V} & p=C \\ 0 & \text{otherwise} \end{array} \right\} + \left\{ \begin{array}{ll} \displaystyle\int\int_{\mathcal{A}} \left[k_{ll,i} \theta_i^{k_{ll}}(T) \frac{\partial T}{\partial x_l} \hat{e}_l \right] \cdot d\vec{\mathcal{A}} & p=k_{ll} \\ 0 & \text{otherwise} \end{array} \right\} \\ &+ \left\{ \begin{array}{ll} \left(\displaystyle\int\int\int_{\mathcal{V}} \dot{e}_i''' \theta_i^{\dot{e}}(T) d\mathcal{V} \right) & p=\dot{e}''' \\ 0 & \text{otherwise} \end{array} \right\}. \end{aligned} \quad (21)$$

Terms on the left side of Eq. (21) depend on the sensitivity coefficient and are present regardless of p_i. Right side contributions do not depend on the sensitivity coefficient (T_{p_i}) and are nonzero when p_i is certain parameters—i.e., those appearing in the energy equation.

Boundary conditions for the sensitivity equation are obtained by performing the same differentiation procedure on the boundary conditions in Eq. (7) through Eq. (9). Prescribed flux boundary conditions for sensitivity are

$$p_i \frac{\partial}{\partial p_i}\int\int_{\mathcal{A}_b} \vec{q}\cdot d\vec{\mathcal{A}} = \int\int_{A_b} -\left[\tilde{\mathbf{k}}(T)\cdot\nabla T_{p_i} + \left(\frac{d\tilde{\mathbf{k}}(T)}{dT}\cdot\nabla T\right)T_{p_i}\right]\Bigg|_{\vec{x}_b}\cdot d\vec{A} + \int\int_{\mathcal{A}_b} p_i \frac{\partial \dot{q}_b''}{\partial p_i}\hat{n}\cdot d\vec{\mathcal{A}}, \tag{22}$$

where

$$p_i\frac{\partial \dot{q}_b''}{\partial p_i} = \left\{\begin{matrix} \dot{q}_0'' & p=\dot{q}_0'' \\ 0 & \text{otherwise} \end{matrix}\right\} \text{along } \vec{x}_{b_1} \tag{23a}$$

$$p_i\frac{\partial \dot{q}_b''}{\partial p_i} = p_i\frac{\partial \dot{q}_c''}{\partial p_i} = h(T)T_{p_i} + \frac{dh(T)}{dT}(T-T_\infty)T_{p_i} + \left\{\begin{matrix} h_i\theta_i^h(T)(T-T_\infty) & p=h \\ 0 & \text{otherwise} \end{matrix}\right\} \text{along } \vec{x}_{b_2} \tag{23b}$$

$$p_i\frac{\partial \dot{q}_b''}{\partial p_i} = p_i\frac{\partial \dot{q}_r''}{\partial p_i} = 4\varepsilon(T)\sigma T^3 T_{p_i} + \frac{d\varepsilon(T)}{dT}\sigma(T^4-T_r^4)T_{p_i} + \left\{\begin{matrix} \varepsilon_i\theta_i^\varepsilon(T)\sigma(T^4-T_r^4) & p=\varepsilon \\ 0 & \text{otherwise} \end{matrix}\right\} \text{along } \vec{x}_{b_3} \tag{23c}$$

The sensitivity boundary condition for a prescribed boundary temperature is

$$T_{p_i}(\vec{x}_{b_4}) = \left\{\begin{matrix} T_b & p=T_b \\ 0 & \text{otherwise} \end{matrix}\right\}. \tag{24}$$

The sensitivity initial condition is

$$T_{p_i}\big|_{t=0} = \left\{\begin{matrix} T_0 & p=T_0 \\ 0 & \text{otherwise} \end{matrix}\right\}. \tag{25}$$

Discussion. Sensitivity to an arbitrary parameter p_i for nonlinear heat conduction is described by Eq. (21) through Eq. (25). Parameter p_i can represent any parameter in the model. All parameters that can depend on temperature have been included. Table 1 summarizes the form of the right side of the sensitivity equation, boundary conditions, and initial condition for the possible parameters that p_i represents. The left side of the equation is as given in Eq. (21), where RHS refers to the right side of this equation. This table parallels Table 4 presented in ([16]) for constant thermal properties.

The approach taken in this paper differentiates the describing equations to derive the sensitivity equation. Previous investigators ([11–15]) have differentiated the discretized equations. Although the two approaches should give the same numerical sensitivity, we believe there is additional insight available from the equation in this paper. The equations can be studied like conservation equations to provide physical insight to the sensitivity. The sensitivity equations are discussed next.

The first two terms in the sensitivity equation, Eq. (21), are identical in form to the first two terms in the describing equation for temperature, which represent the capacitance and diffusion effects in Eq. (4); an analogous term for the volumetric source in the temperature equation is not seen in the sensitivity equation. The third through the fifth terms on the left side of Eq. (21) are the result of parameters being temperature-dependent. All three terms contain the derivative of a parameter with respect to temperature and the scaled sensitivity coefficient; these terms are zero if those parameters are constant. The fourth term is similar to the convection term as it involves a surface integral. However, ''velocity'' is equal to a heat flux like term calculated using the derivative of the conductivity $(d\tilde{\mathbf{k}}(T)/dT\cdot\nabla T)$. The third and fifth terms on the left side are volumetric source-like terms, but are multiplied by the sensitivity coefficient.

When the parameter of interest is in the describing equation there is a right side contribution for the sensitivity equation in Eq. (21). (At most, one of these terms is nonzero for a particular parameter p_i.) The right side terms are completely known, assuming the temperature has been previously calculated. The form of these terms is analogous to those terms appearing in the temperature equation that contain the same parameters. However, the temperature-dependent parameter is represented with a single term from the approximation in Eq. (1)—i.e., we take only the i^{th} term from the summation in Eq. (1).

Flux boundary conditions for the sensitivity equations in Eq. (23*a*) through Eq. (23*c*) have additional terms as well, with the exception of a specified constant flux in Eq. (23*a*). A term that contains temperature, and the derivative of the parameter with respect to temperature, is added for prescribed convection and radiation conditions. Similarly, an additional term is added if the sensitivity parameter, p_i, appears in the boundary condition. The term looks like the applied (convective or radiative) flux, except only a single term from the approximation of the temperature dependent parameter is included.

An important result is that even though the describing equations for temperature are *nonlinear*, the resulting equations for sensitivity are *linear*. It appears to be the rule that nonlinear field equations produce linear sensitivity equations; the authors are not aware of any exception published in the literature. An explanation for this outcome is that the process of differentiation only operates on one piece of the nonlinear term in the field equation at a time. Hence, by definition we will only have linear multiples for the derivative (sensitivity) when we differentiate. For example, consider a term that is nonlinear in T

$$g(T)T^2\nabla T. \tag{26}$$

The corresponding terms for sensitivity of T to parameter k are

$$\frac{dg(T)}{dT}\frac{\partial T}{\partial k}T^2\nabla T + g(T)2T\frac{\partial T}{\partial k}\nabla T + g(T)T^2\nabla\left(\frac{\partial T}{\partial k}\right). \tag{27}$$

Each term in Eq. (27) has a linear dependence on the derivative, $\partial T/\partial k$, regardless of the form of $g(T)$. We note that Eq. (27) is nonlinear in terms of T, but since we tacitly assume we will solve the field equation first this nonlinearity does not complicate matters. Finally, there is a difference between a nonlinear differential equation, which contains nonlinear multiples of the dependent variable (solution nonlinearity), and a field variable (temperature) which is a nonlinear function of the parameter (parameter nonlinearity). Parametric nonlinearity exists when the unscaled sensitivity equation is a function of the parameter. Parametric nonlinearity can exist, and often does, even though the solution is linear; most sensitivities for constant properties demonstrate this outcome ([16]). Solution nonlinearity, on the other hand, insures parametric nonlinearity due to the inherent dependence of the unscaled sensitivity equations on the field variable (temperature), and hence the parameter.

Linear sensitivity equations may allow for computational savings compared to a finite difference approximation of the sensitivity coefficient, where two nonlinear solutions are required to numerically approximate a sensitivity coefficient. At most, solving sensitivity equations will require the same computational effort as a finite difference approximation. Only when the temperature is obtained with a linear solution will computational efforts be similar.

Table 1 Definition of various right-hand side and initial/boundary condition terms for the sensitivity coefficient equations. RHS refers to the right-hand side of Eq. (21).

T_{p_i}	RHS	$p_i \frac{\partial \dot{q}_b''}{\partial p_i}\Big\vert_{\vec{x}_{b_1}}$	$p_i \frac{\partial \dot{q}_b''}{\partial p_i}\Big\vert_{\vec{x}_{b_2}}$	$p_i \frac{\partial \dot{q}_b''}{\partial p_i}\Big\vert_{\vec{x}_{b_3}}$	$T_{p_i}\big\vert_{\vec{x}_4}$
$T_{k_{ll,i}}$	$\iint_{\mathcal{A}} k_{ll,i}\theta_i^{k_{ll}}(T)\frac{\partial T}{\partial x_l}\hat{e}_l \cdot d\vec{\mathcal{A}}$	0	$\left[h(T)T_{k_{ll,i}} + \frac{dh(T)}{dT}(T-T_\infty)T_{k_{ll,i}}\right]\Big\vert_{\vec{x}_2}$	$\left[4\varepsilon(T)\sigma T^3 T_{k_{ll,i}} + \frac{d\varepsilon(T)}{dT}\sigma(T^4-T_r^4)T_{k_{ll,i}}\right]\Big\vert_{\vec{x}_3}$	0
T_{k_i}	$\iint_{\mathcal{A}}(k_i\theta_i^k(T)\nabla T \cdot d\vec{\mathcal{A}})$	0	$\left[h(T)T_{k_i} + \frac{dh(T)}{dT}(T-T_\infty)T_{k_i}\right]\Big\vert_{\vec{x}_2}$	$\left[4\varepsilon(T)\sigma T^3 T_{k_i} + \frac{d\varepsilon(T)}{dT}\sigma(T^4-T_r^4)T_{k_i}\right]\Big\vert_{\vec{x}_3}$	0
T_{C_i}	$-\iiint C_i\theta_i^C(T)\frac{\partial T}{\partial t}d\mathcal{V}$	0	$\left[h(T)T_{C_i} + \frac{dh(T)}{dT}(T-T_\infty)T_{C_i}\right]\Big\vert_{\vec{x}_2}$	$\left[4\varepsilon(T)\sigma T^3 T_{C_i} + \frac{d\varepsilon(T)}{dT}\sigma(T^4-T_r^4)T_{C_i}\right]\Big\vert_{\vec{x}_3}$	0
$T_{\dot{e}_i'''}$	$\iiint_{\mathcal{V}}\dot{e}_i'''\theta_i^{\dot{e}}(T)d\mathcal{V}$	0	$\left[h(T)T_{\dot{e}_i'''} + \frac{dh(T)}{dT}(T-T_\infty)T_{\dot{e}_i'''}\right]\Big\vert_{\vec{x}_2}$	$\left[4\varepsilon(T)\sigma T^3 T_{\dot{e}_i'''} + \frac{d\varepsilon(T)}{dT}\sigma(T^4-T_r^4)T_{\dot{e}_i'''}\right]\Big\vert_{\vec{x}_3}$	0
$T_{\dot{q}_o''}$	0	$\dot{q}_o''$	$\left[h(T)T_{\dot{q}_o''} + \frac{dh(T)}{dT}(T-T_\infty)T_{\dot{q}_o''}\right]\Big\vert_{\vec{x}_2}$	$\left[4\varepsilon(T)\sigma T^3 T_{\dot{q}_o''} + \frac{d\varepsilon(T)}{dT}\sigma(T^4-T_r^4)T_{\dot{q}_o''}\right]\Big\vert_{\vec{x}_3}$	0
T_{h_i}	0	0	$h(T)T_{h_i} + \frac{dh(T)}{dT}(T-T_\infty)T_{h_i}\Big\vert_{\vec{x}_2} +$ $[h_i\theta_i^h(T)(T-T_\infty)]\Big\vert_{\vec{x}_2}$	$\left[4\varepsilon(T)\sigma T^3 T_{h_i} + \frac{d\varepsilon(T)}{dT}\sigma(T^4-T_r^4)T_{h_i}\right]\Big\vert_{\vec{x}_3}$	0
T_{ε_i}	0	0	$\left[h(T)T_{\varepsilon_i} + \frac{dh(T)}{dT}(T-T_\infty)T_{\varepsilon_i}\right]\Big\vert_{\vec{x}_2}$	$\left[4\varepsilon(T)\sigma T^3 T_{\varepsilon_i} + \frac{d\varepsilon(T)}{dT}\sigma(T^4-T_r^4)T_{\varepsilon_i}\right]\Big\vert_{\vec{x}_3}$ $[\varepsilon_i\theta_i^\varepsilon(T)\sigma(T^4-T_r^4)]\Big\vert_{\vec{x}_3}$	0
T_{T_∞}	0	0	$\left[h(T)T_{T_\infty} + \frac{dh(T)}{dT}(T-T_\infty)T_{T_\infty}\right]\Big\vert_{\vec{x}_2}$ $-h(T)T_\infty$	$\left[4\varepsilon(T)\sigma T^3 T_{T_\infty} + \frac{d\varepsilon(T)}{dT}\sigma(T^4-T_r^4)T_{T_\infty}\right]\Big\vert_{\vec{x}_3}$	0
T_{T_r}	0	0	$\left[h(T)T_{T_r} + \frac{dh(T)}{dT}(T-T_\infty)T_{T_r}\right]\Big\vert_{\vec{x}_2}$	$\left[4\varepsilon(T)\sigma T^3 T_{T_r} + \frac{d\varepsilon(T)}{dT}\sigma(T^4-T_r^4)T_{T_r}\right]\Big\vert_{\vec{x}_3}$ $-4\varepsilon(T)\sigma T_r^4\Big\vert_{\vec{x}_3}$	0
T_{T_b}	0	0	$\left[h(T)T_{T_b} + \frac{dh(T)}{dT}(T-T_\infty)T_{T_b}\right]\Big\vert_{\vec{x}_2}$	$\left[4\varepsilon(T)\sigma T^3 T_{T_b} + \frac{d\varepsilon(T)}{dT}\sigma(T^4-T_r^4)T_{T_b}\right]\Big\vert_{\vec{x}_3}$	T_b
T_{T_o}	0	0	$\left[h(T)T_{T_o} + \frac{dh(T)}{dT}(T-T_\infty)T_{T_o}\right]\Big\vert_{\vec{x}_2}$	$\left[4\varepsilon(T)\sigma T^3 T_{T_o} + \frac{d\varepsilon(T)}{dT}\sigma(T^4-T_r^4)T_{T_o}\right]\Big\vert_{\vec{x}_3}$	T_o

Sensitivity equations for *nonlinear* heat conduction have several additional left side terms compared to the temperature equation. In contrast, sensitivity equations for linear problems do not contain additional left side terms compared to the temperature equation. Sensitivity equations for the linear case are identical to the temperature equations, except for known right side contributions ([16]). This outcome for the linear case allows for potential computational savings by storing the global matrices after they are assembled for the temperature. Subsequent sensitivity problems can use the stored global matrices, and only a right side contribution needs to be calculated. If one can afford the storage for an LU decomposition algorithm, the decomposition can be used for efficiently solving for multiple sensitivities that only vary by their right-hand sides.

Emergy and Fadale [13] suggest solving the (linear) sensitivity equations for nonlinear heat conduction in an iterative procedure to avoid altering the structure of their finite element code. Global matrices are formulated and stored to calculate temperature. Subsequent sensitivity calculations use the same global matrices. The additional left side terms in the sensitivity equations, compared to the temperature equations are moved to the right side, and the equations are solved iteratively. This procedure saves recomputing the global matrices, but requires an iterative solution. Efficiency may be improved by adding the contributions from the additional terms to the stored global matrices that arise in the sensitivity equations. Then sensitivity can be solved in a linear manner. We do not reuse any of the assembled global matrices since we want to address very large problems for which storage of the global matrix is not practical.

Numerical Solution. The details of the numerical methods to solve the temperature and sensitivity equations are described in ([18]). An unstructured grid numerical solver based on a control volume finite element formulation for spatial discretization and implicit time discretization is used. The code architecture has been designed such that multiple equations can be solved. With this design, solving sensitivity equations requires writing additional element assembly routines for the desired sensitivity equations.

Numerical Examples

Verification Problem. A one-dimensional slab of thickness, L, with temperature-dependent thermal conductivity is studied. The boundaries are isothermal. A mathematical description of the problem can be written as

$$\frac{d}{dx}\left(k(T)\frac{dT}{dx}\right)=0 \tag{28}$$

$$T|_{x=0}=T_L \tag{29a}$$

$$T|_{x=L}=T_R. \tag{29b}$$

Thermal conductivity is represented with two piecewise-linear segments

$$k(T)=\left\{\begin{array}{ll} k_1\left(1-\dfrac{T-T_1}{T_2-T_1}\right)+k_2\left(\dfrac{T-T_1}{T_2-T_1}\right), & (T_1\leqslant T\leqslant T_2)\\ k_2\left(1-\dfrac{T-T_2}{T_3-T_2}\right)+k_3\left(\dfrac{T-T_2}{T_3-T_2}\right), & (T_2< T\leqslant T_3)\end{array}\right\}. \tag{30}$$

An analytical solution can be obtained by integrating Eq. (28). Performing the integration over the two temperature segments that conductivity is defined and applying continuity between the two segments, gives quadratic equations to calculate temperature

$$\left\{\begin{array}{ll}\dfrac{\beta_1}{2}T^2+(k_1-\beta_1T_1)T+C_1 & (T_1\leqslant T\leqslant T_2)\\ \dfrac{\beta_2}{2}T^2+(k_2-\beta_2T_2)T+C_2 & (T_2< T\leqslant T_3)\end{array}\right\}=0. \tag{31}$$

In Eq. (31) the slopes of the linear conductivity segments are

$$\beta_i=\left(\frac{k_{i+1}-k_i}{T_{i+1}-T_i}\right),\quad i=1,2 \tag{32}$$

and the constant terms (with regard to the unknown temperature) are

$$\begin{aligned}C_1=&-\left[\frac{\beta_1}{2}T_L^2+(k_1-\beta_1T_1)T_L\right]\left(1-\frac{x}{L}\right)\\ &+\left\{\frac{(\beta_2-\beta_1)}{2}T_2^2+[(k_2-\beta_2T_2)-(k_1-\beta_1T_1)]T_2\right\}\frac{x}{L}\\ &-\left[\frac{\beta_2}{2}T_R^2+(k_2-\beta_2T_2)T_R\right]\frac{x}{L}\end{aligned} \tag{33}$$

$$\begin{aligned}C_2=&-\left[\frac{\beta_1}{2}T_L^2+(k_1-\beta_1T_1)T_L\right]\left(1-\frac{x}{L}\right)\\ &+\left\{\frac{(\beta_2-\beta_1)}{2}T_2^2+[(k_2-\beta_2T_2)-(k_1-\beta_1T_1)]T_2\right\}\left(\frac{x}{L}-1\right)\\ &-\left[\frac{\beta_2}{2}T_R^2+(k_2-\beta_2T_2)T_R\right]\frac{x}{L}.\end{aligned} \tag{34}$$

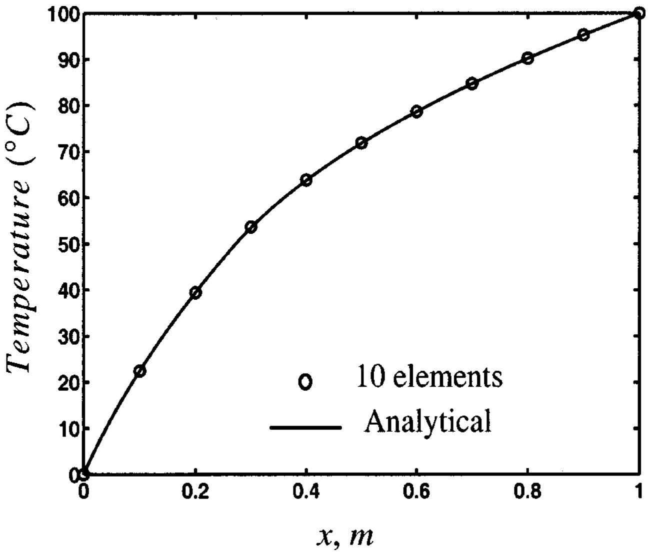

Fig. 1 Temperature of a one-dimensional body with isothermal boundaries and temperature-dependent thermal conductivity represented with two piecewise linear segments

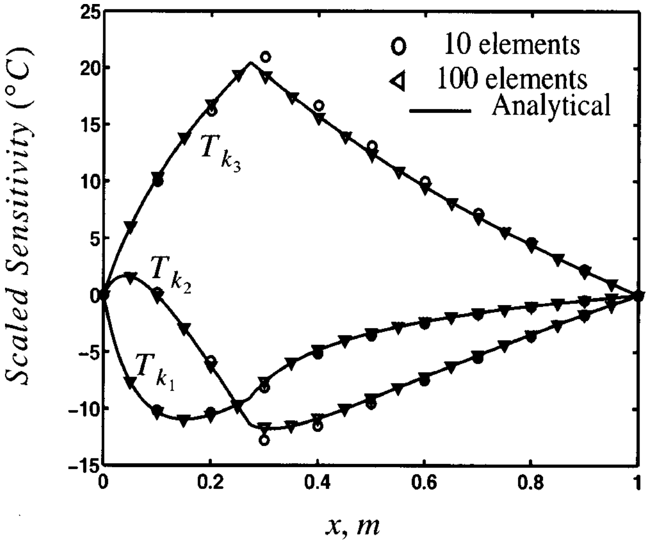

Fig. 2 Sensitivity coefficients for parameters describing two piecewise linear segments representing temperature-dependent thermal conductivity for a one-dimensional body with isothermal boundaries

To obtain temperature from Eq. (31), the physically meaningful root of the quadratic equations is taken. Analytical expressions for the sensitivity to k_1, k_2, and k_3 can be obtained by differentiating Eq. (31) with respect to these parameters.

Temperature is computed for a region of unit length ($L=1$ m). Boundary temperatures are maintained at $T_L=0\ °C$ and $T_R=100\ °C$. Conductivity is represented with two piecewise linear segments interpolating between conductivity values at three temperature: $k_1=1.0\ W/m\ °C$ at $T_1=0\ °C$, $k_2=2.0\ W/m\ °C$ at $T_2=50\ °C$, and $k_3=6.0\ W/m\ °C$ at $T_3=100\ °C$. The variation in this example represents a 4-to-1 change in the slope of the two piecewise linear segments representing $k(T)$. Figure 1 compares the numerically computed temperature with the analytical solution. Note that the temperature profile would be a straight line between the boundary temperatures for constant thermal conductivity. Agreement within 1.2 percent of the maximum temperature

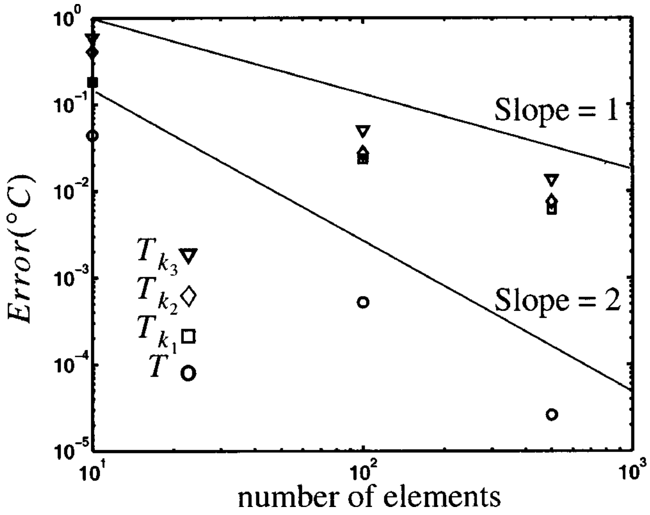

Fig. 3 Grid convergence study at x=0.2 m for verification problem with temperature-dependent thermal conductivity

is demonstrated with only 10 uniformly spaced elements. A comparison for sensitivity to the three components of thermal conductivity is shown in Fig. 2. Near the location where the piecewise linear segments join ($T(x\approx 0.27\ m)=50\ °C$), all three sensitivity coefficients have a sudden change in shape; the slope (derivative) of sensitivities to k_2 and k_3 changes sign at this location. With only ten elements the numerical and analytical results have the largest deviation near this region ($x\approx 0.27\ m$); the error is 4 to 8 percent of the maximum sensitivity value. This outcome demonstrates that a grid that results in small error for the temperature is not necessarily adequate for the sensitivity coefficients. It is expected that the largest errors are near the location joining the linear segments. Terms in the sensitivity equations in Eq. (21) to Eq. (25) contain the derivative of the conductivity with respect to temperature. For a piecewise linear representation, this derivative is discontinuous. Further refining the mesh to 100 uniformly spaced elements produces agreement within 1 percent of the analytical results for all sensitivity coefficients; see Fig. 2. Notice that the sensitivity to conductivity is zero on boundaries where temperature is specified.

A grid convergence study for the verification problem is shown in Fig. 3. Error is defined as the absolute difference between the numerical and analytical solutions. Results at location $x=0.2\ m$ are shown in the figure. Temperature demonstrates a second-order accuracy—that is, the error decreases with a slope of two as the spatial discretization is refined. Sensitivity, however, appears first-order accurate. Grid convergence at other spatial locations demonstrates the same order. For constant thermal properties the discretization schemes used to solve the temperature and sensitivity equations have been verified as second-order accurate ([16]). A possible explanation for the sensitivity solutions only achieving first-order accuracy could be the discontinuity in the derivative of piecewise-linear conductivity. This point is being studied further.

Experimental Design. An experimental configuration proposed to estimate thermal properties of a polyurethane foam is shown schematically in Fig. 4. Two nominally identical foam specimens are sandwiched about an electric heater. On the foam surface opposite the heater is an aluminum block. All components have cross-sectional dimensions of $w\times d$, whereas the thicknesses are L_h for the heater, L_f for the foam, and L_a for the aluminum. The symmetry of the configuration permits quantifying the input flux by measuring the electrical power to the heater. By knowing the input flux and measuring temperatures elsewhere in the configuration, thermal properties of the foam can be estimated. In most cases a known input heat flux permits conductivity and volumetric heat capacity to be simultaneously estimated from a single experiment. The aluminum block maintains a nearly constant temperature on the backside of the foam. In the calculations that follow we assume the proposed apparatus can be modeled as symmetric one dimensional heat flow with a known applied heat flux $\dot{q}_0''$. The apparatus must be carefully designed to satisfy this assumption, but details associated with this design process are not considered further in this paper.

Optimal experimental conditions to estimate constant thermal properties for similar configurations are well known ([3–4]). The thickness of the foam and duration of the experiment should be selected such that the foam responds like a finite body heated by a constant flux on one surface and isothermal on the other surface. These conditions can readily be achieved in the laboratory for low conductivity materials. Based on D-optimally ([3]) the finite case is superior to the case where the foam responds thermally as a semi-infinite body. (These conclusions were reached while neglecting thermal effects of the heater and aluminum block.)

Optimum conditions to estimate temperature-dependent properties are less clear. A sequential method can be used to combine experiments at different temperature ranges ([1,19]). There are other approaches for estimating temperature dependent properties as well ([1]). In this paper the situation of estimating linearly varying temperature-dependent properties from a single experi-

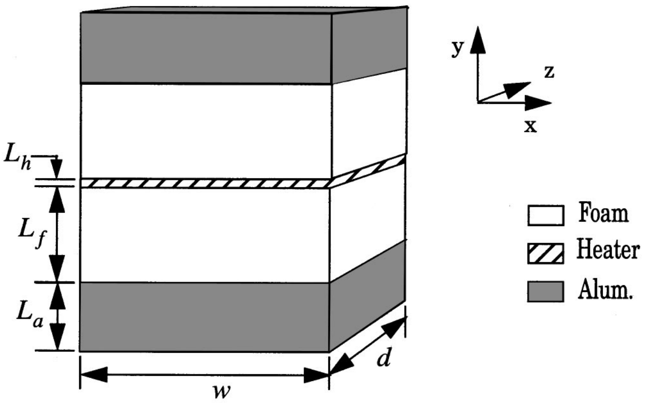

Fig. 4 Experiment to estimate thermal properties of polyurethane foam

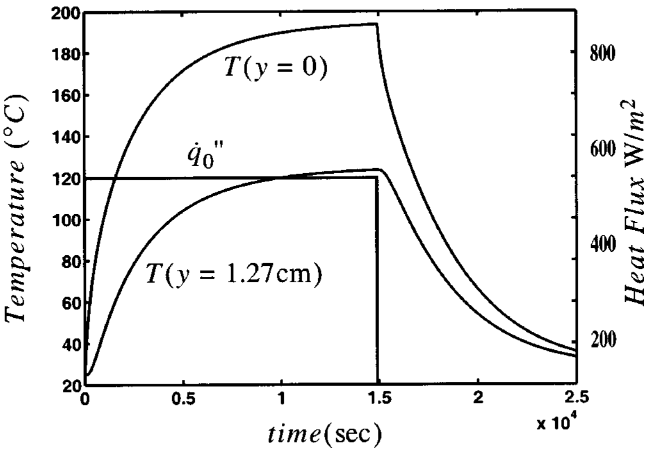

Fig. 5 Temperature response for a foam thickness of 2.54 cm and linearly varying temperature-dependent properties (finite case)

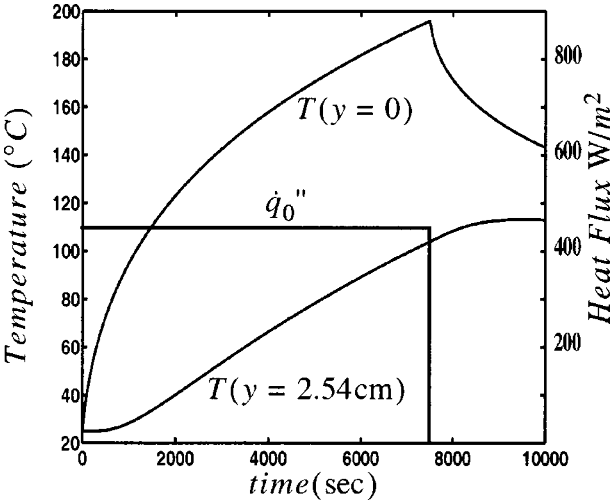

Fig. 6 Temperature response for a foam thickness of 34.3 cm and linearly varying temperature-dependent properties (semi-infinite case)

ment is addressed. Experimental design to estimate temperature-dependent properties is not, to our knowledge, available in the literature.

The case where properties (conductivity and volumetric heat capacity) vary linearly with temperature is considered. Foam thicknesses of 2.54 cm and 34.3 cm are used to compare experiments where the foam responds thermally as a finite and semi-infinite body, respectively. Although the foam specimens are obviously finite in size, if the thickness is large enough, thermal effects do not extend across its thickness. This case is referred to as semi-infinite. For low conductivity materials, like foam, the thermal response can be modeled as semi-infinite for appropriate time and length scales.

Temperature variable thermal properties for a foam density of 374 kg/m^3 are taken from ([20]); $k_f = 0.05$ W/m $°C$ and $C_f = 0.433E+0.6$ J/m^3 $°C$ at 25 °C and $k_f = 0.102$ W/m $°C$ and $C_f = 1.19E+06$ J/m^3 $°C$ at 200 $°C$. A thermal model of the heater assumes a thickness of 0.63 mm and constant properties of $k_h = 0.1$ W/m $°C$ and $C_h = 2.3E+06$ J/m^3 $°C$. These properties are equivalent to the effective properties estimated for a mica heater including contact resistance ([21]). Thermal properties of the aluminum are temperature-dependent, 2024 aluminum ([22]); the aluminum is not included in the model for the semi-infinite case. Simulated temperature responses assuming one dimensional symmetric heat flow in the configuration of Fig. 4 for a foam thickness of 2.54 cm (finite case) and 34.3 (semi-infinite case) are shown in Fig. 5 and Fig. 6, respectively. Two measurement locations are simulated for both cases: one at the heated surface ($y=0$) and the second within the foam. The finite case has the second location at the midplane of the foam thickness ($y=1.27$ cm). The semi-infinite case selects a second location 2.54 cm below the heated surface ($y=2.54$ cm). The applied heat flux is plotted with the temperature responses in Fig. 5 and Fig. 6.

The sensitivity coefficients for four parameters representing temperature-dependent properties in a finite body ($L_f = 2.54$ cm) are shown in Fig. 7. Sensitivities are shown at the surface of the foam ($y=0$) in the top figure and at the midplane of the thickness ($y=1.27$ cm) in the bottom figure. Sensitivity coefficients are normalized by the maximum temperature rise. Results for a semi-infinite body ($L_f = 34.3$ cm) are shown in Fig. 8 for locations at the surface of the foam (top figure) and 2.54 cm below the surface (bottom figure). As will be discussed later, the heating conditions and experimental duration for each case are selected because they maximize the D-optimality criteria to estimate the four parameters.

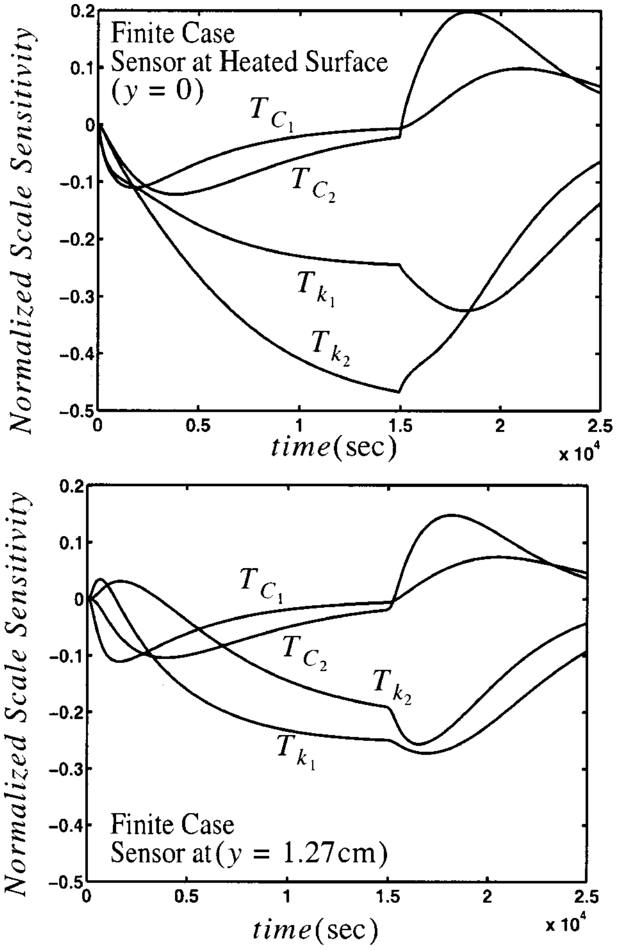

Fig. 7 Sensitivity normalized by the maximum temperature rise for estimating linearly varying, temperature-dependent properties and a foam thickness of 2.54 cm (finite case)

Sensitivity coefficients tend to be larger for the finite case in Fig. 7 than they are for the semi-infinite case in Fig. 8. The finite case has maximum values over 0.4, whereas the semi-infinite case has maximum less than 0.3. A second notable trend in the sensitivity plots is that the shapes for different parameters are more similar for the semi-infinite case than for the finite case, particularly for the sensor on the heated surface ($y=0$). Sensitivity for k_2 and C_2 and k_1 and C_1 have similar shapes in Fig. 8. (If thermal properties are constant, sensitivities for k and C have identical shapes at ($y=0$) and are perfectly correlated.) Finally, notice how dramatically the shape of the sensitivity coefficients change when the heat flux ends for the finite case. Sensitivity to C_1 and C_2 actually change sign after the heat flux ends. Such changes in the shape of the sensitivity coefficients improves the information available in an experiment. Sensitivity coefficients for the semi-infinite case have only a slight change in shape when the heating ends.

In the design of experiments to estimate thermal properties, we want the (scaled) sensitivity coefficients to be large and uncorrelated or have different shapes. However, drawing conclusions from sensitivity plots for multiple parameters and several locations can be difficult. It is further complicated in this case because different experimental conditions are compared. Normalizing the sensitivity coefficients by the maximum temperature rise provides some consistency; both experiments then have the same temperature range. Even with normalization it may be difficult to distinguish correlation between the sensitivity coefficients for different parameters. A criteria may be needed to gauge which experiment

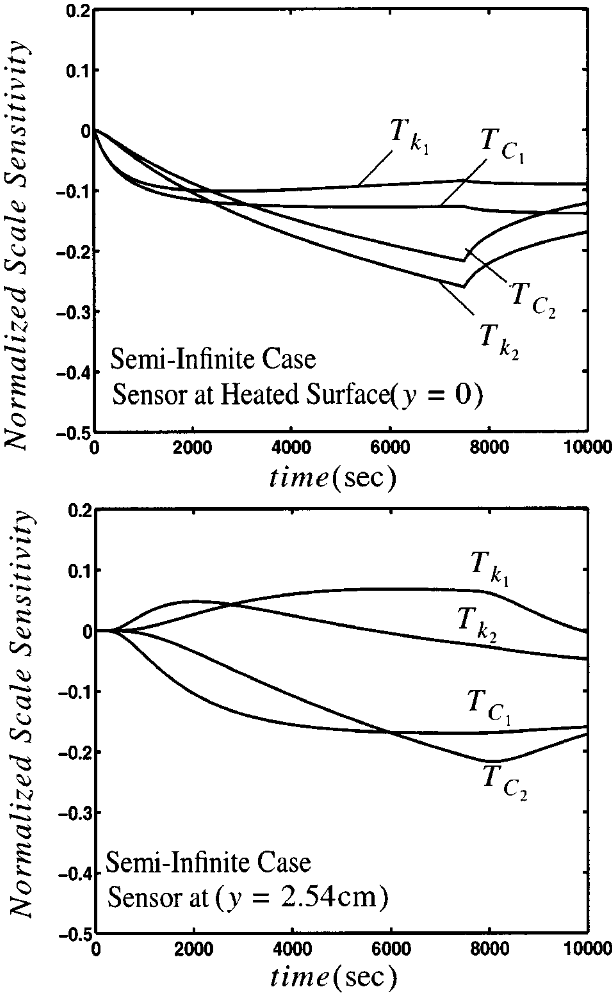

Fig. 8 Sensitivity normalized by the maximum temperature rise for estimating linearly varying, temperature-dependent properties and a foam thickness of 34.3 cm (semi-infinite)

is better. *D*-optimality ([3]) has been used to discriminate the optimal experiment. Emergy and Fadale [6] discuss several other criteria.

Sensitivity plots appear to indicate that the finite case is superior to the semi-infinite; sensitivities for the finite case are larger and have more varied shapes for the different parameters. To investigate which experiment is better, the *D*-optimality criteria is evaluated. The *D*-optimality criteria maximizes the determinant of the sensitivity matrix

$$\Delta \equiv |\mathbf{X}^T\mathbf{X}|. \tag{35a}$$

X is the sensitivity matrix;

$$\mathbf{X}^T = \left[\frac{\partial \mathbf{T}}{\partial p_1}, \frac{\partial \mathbf{T}}{\partial p_2}, \ldots, \frac{\partial \mathbf{T}}{\partial p_{N_p}}\right], \tag{36}$$

where **T** is a vector (length N_sN_t) of temperatures for each time and sensor location. Assuming there are N_t discrete measurements in time, N_s measurement locations, and N_p parameters, the dimensions of **X** are $N_sN_t \times N_p$. The basis for this criteria is that it minimizes the volume of a confidence region. To provide a fair comparison for possibly different experimental conditions, constraints are introduced to the criteria. Measurements at the N_s locations are assumed to be equally spaced in time at intervals Δt up to time t_f. The maximum temperature rise of the experiment is T_{max}, and scaled sensitivity is used. To introduce these constraints, the optimality criteria is modified as

$$\Delta^+ \equiv \frac{|\mathbf{T}_{p_i}^T \mathbf{T}_{p_i}|}{(T_{max}^2 N_t N_s)^{N_p}}, \tag{37}$$

where $\mathbf{T}_{p_i}$ is the scaled sensitivity matrix.

The values of Δ^+ are 4.0E-09 and 2.95E-10 for the finite and semi-infinite cases, respectively. The ratio is 13.6, meaning the volume of the confidence region is an order of magnitude smaller for the finite case. A finite body is superior for the experimental conditions and thermal properties selected. A range of the applied heat flux magnitude, heat flux duration, and experimental duration were investigated to identify the optimal experimental conditions for both cases. The sensitivity plots in Fig. 7 and Fig. 8 are for the conditions that gave the largest magnitude of Δ^+. Superiority of the finite body case is consistent with the outcome for constant properties ([4]). However, for constant properties measurements at the heated surface alone are optimal.

Conclusions

A general methodology to derive sensitivity equations for nonlinear heat conduction has been presented. Sensitivity equations were obtained by differentiating the continuum equations. These sensitivity equations were examined to provide insight to the factors that influence sensitivity coefficients. An important outcome was that the sensitivity equations are linear, even for the nonlinear temperature problems.

A verification problem demonstrated that while the numerical temperature was spatial second-order accurate, sensitivity calculations for temperature-dependent properties were only first-order accurate. Previous calculations for constant thermal properties have shown that the sensitivity calculations were second-order accurate. Sensitivity analysis was applied to design an experiment for estimating thermal properties varying linearly with temperature. Using the criteria *D*-optimality a finite geometry was demonstrated to be better than semi-infinite for estimating temperature-dependent properties.

Acknowledgments

The authors would like to acknowledge comments concerning this work from Robert Cochran, Dean Dobranich, Shawn Burns, and Steve Kempka of Sandia National Laboratories. Sandia is a multiprogram laboratory operated by Sandia Corporation, a Lockheed Martin Company, for the United States Department of Energy under Contract DE-AC04-94AL85000.

Nomenclature

$\mathcal{A}$ = area, m^2
C = volumetric heat capacity, J/m^3-$°C$
$\dot{e}'''$ = energy source, W/m^3
g = general temperature-dependent parameter
h = convective heat transfer coefficient, W/m^2-$°C$
k = thermal conductivity, W/m-$°C$
k_{ll} = diagonal component of thermal conductivity tensor, $W/m°C$
$\tilde{\mathbf{k}}$ = thermal conductivity tensor, W/m-$°C$
L = thickness, m
N_g = number of parameters describing temperature dependence, g
N_s = number of sensor locations
N_t = number of discrete time measurements
N_p = number of parameters
p = arbitrary parameter
$\dot{q}''$ = heat flux, W/m^2
$\dot{q}_c''$ = convective heat flux, W/m^2
$\dot{q}_0''$ = constant value of heat flux, W/m^2
$\dot{q}_r''$ = radiative heat flux, W/m^2
$T, \mathbf{T}$ = temperature, temperature vector, $°C$

T_b = boundary temperature, °C
T_0 = initial temperature, °C
T_{p_i} = scaled temperature sensitivity coefficient for parameter p_i, °C
T_r = radiation temperature, °C
T_∞ = convection temperature, °C
$\mathbf{X}$ = sensitivity matrix
$\vec{x}_{b_1}$ = boundary with constant heat flux, m
$\vec{x}_{b_2}$ = boundary with convective heat flux, m
$\vec{x}_{b_3}$ = boundary with radiative heat flux, m
$\vec{x}_{b_4}$ = boundary with isothermal temperature, m
$\mathcal{V}$ = volume, m^3

Greek

β = conductivity ratio, Eq. (32)
Δ, Δ^+ = optimality criteria
$\theta_j^g(T)$ = basis function for component j of parameter g
$\phi_j^g(T)$ = derivative of basis function for component j of parameter g
σ = Stefan-Boltzmann constant.

References

[1] Dowding, K. J., Beck, J. V., and Blackwell, B. F., 1999, ''Estimating Temperature-Dependent Thermal Properties of Carbon-Carbon Composite,'' J. Thermophys. Heat Transfer, **13**, No. 3, pp. 328–336.

[2] Dowding, K. J., Blackwell, B. F., and Cochran, R. J., 1999, ''Application of Sensitivity Coefficients for Heat Conduction Problems,'' Numer. Heat Transfer, Part B, **36**, No. 1, pp. 33–55.

[3] Beck, J. V., and Arnold, K., 1977, *Parameter Estimation in Engineering and Science* Wiley, New York.

[4] Taktak, R., Beck, J. V., and Scott, E., 1993, ''Optimal Experimental Design for Estimating Thermal Properties of Composite Materials,'' Int. J. Heat Mass Transf., **36**, No. 12, p. 2977.

[5] Taktak, R., 1992, ''Design and Validation of Optimal Experiments for Estimating Thermal Properties of Composite Materials,'' Ph.D thesis, Michigan State University, East Lansing, MI.

[6] Emery, A. F., and Fadale, T. D., 1996, ''Design of Experiments Using Uncertainty Information,'' ASME J. Heat Transfer, **118**, pp. 532–538.

[7] Fadale, T. D., Nenarokomov, A. V., and Emery, A. F., 1995, ''Two Approaches to Optimal Sensor Locations,'' ASME J. Heat Transfer, **117**, pp. 373–379.

[8] Coleman, H. W., and Stern, F., 1997, ''Uncertainties and CFD Code Validation,'' J. Fluids Eng., **119**, pp. 795–803.

[9] Coleman, H. W., and Steele, W. G., 1995, ''Engineering Applications of Experimental Uncertainty Analysis,'' AIAA J., **33**, No. 10, pp. 1888–1896.

[10] Fadale, T. D., and Emery, A. F., 1994, ''Transient Effects of Uncertainties on the Sensitivities of Temperatures and Heat Fluxes Using Stochastic Finite Elements,'' ASME J. Heat Transfer, **116**, pp. 808–814.

[11] Liu, W. K., Besterfield, G., and Belytschko, T., 1988, ''Transient Probabilistic Systems,'' Comput. Methods Appl. Mech. Eng., **67**, pp. 27–54.

[12] Liu, W. K., Belytschko, T., and Mani, A., 1986, ''Probabilistic Finite Elements for Nonlinear Structural Dynamics,'' Comput. Methods Appl. Mech. Eng., **56**, pp. 61–81.

[13] Emery, A. F., and Fadale, T. D., 1997, ''Handling Temperature Dependent Properties and Boundary Conditions in Stochastic Finite Element Analysis,'' Numer. Heat Transfer, Part A, **31**, pp. 37–51.

[14] Nicolai, B. M., and De Baerdemaeker, J., 1997, ''Finite Element Perturbation Analysis of Non-Linear Heat Conduction Problems with Random Field Parameters,'' Int. J. Numer. Methods Heat Fluid Flow, **7**, No. 5, pp. 525–544.

[15] Nicolai, B. M., and De Baerdemaeker, J., 1993, ''Computation of Heat Conduction in Materials with Random Variable Thermophysical Properties,'' Int. J. Numer. Methods Eng., **36**, pp. 523–536.

[16] Blackwell, B. F., Dowding, K. J., and Cochran, R. J., 1999, ''Development and Implementation of Sensitivity Coefficient Equations For Heat Conduction Problems,'' Numer. Heat Transfer, Part B, **36**, No. 1, pp. 15–32.

[17] Blackwell, B. F., and Dowding, K. J., 1999, ''Sensitivity Analysis and Uncertainty Propagation in a General Purpose Thermal Analysis Code,'' *Proceedings of the 3rd ASME/JSME Joint Fluids Engineering Conference*, July 18–23, 1999, San Francisco, CA.

[18] Blackwell, B. F., Cochran, R. J., and Dowding, K. J., 1998, ''Development and Implementation of Sensitivity Coefficient Equations for Heat Conduction Problems,'' *ASME Proceedings of the 7th AIAA/ASME Joint Thermophysics and Heat Transfer Conference*, ASME-HTD-Vol. **357-2**, pp. 303–316.

[19] Beck. J. V., and Osman, A. M, 1991, ''Sequential Estimation of Temperature-Dependent Thermal Properties,'' High Temperature-High Pressure **23**, pp. 255–266.

[20] Jin, G., Venkatesan, G., Chyu, M.-C., and Zheng, J.-X., 1998, ''Measurement of Thermal Conductivity and Heat Capacity of Foam Insulation During Transient Heating,'' AV-7569, Final Report, Department of Mechanical Engineering, Texas Tech. University, May 20, 1998.

[21] Dowding, K., Beck, J., Ulbrich, A., Blackwell, B., and Hayes, J., 1995, ''Estimation of Thermal Properties and Surface Heat Flux in a Carbon-Carbon Composite Material,'' J. Thermophys. Heat Transfer, **9**, No. 2, pp. 345–351.

[22] Incropera, F. P., and Dewitt, D. P., 1990, *Introduction to Heat Transfer*, 2nd Edition, Wiley, New York.

Thermal Contact Resistance Modeling of Non-Flat, Roughened Surfaces With Non-Metallic Coatings

E. E. Marotta
Assistant Professor,
Mem. ASME
Mechanical Engineering Department,
Clemson University,
Clemson, SC 29634-0921

L. S. Fletcher

Thomas A. Dietz
Professor,
Fellow ASME
Mechanical Engineering Department,
Texas A&M University,
College Station, TX 77843-3123

Essentially all models for prediction of thermal contact conductance or thermal contact resistance have assumed optically flat surfaces for simplification. A few thermal constriction models have been developed which incorporate uncoated, optically non-flat surfaces based on the bulk mechanical properties of the material. Investigations have also been conducted which incorporate the thermophysical properties of metallic coatings and their effective surface microhardness to predict the overall thermal contact conductance. However, these studies and subsequent models have also assumed optically flat surfaces; thus, the application of these models to optically non-flat, coated surface conditions is not feasible without modifications. The present investigation develops a thermomechanical model that combines both microscopic and macroscopic thermal resistances for non-flat, roughened, surfaces with non-metallic coatings. The thermomechanical model developed as a result of this study predicts the thermal contact resistance of several non-metallic coatings deposited on metallic aluminum substrates quite well.

[DOI: 10.1115/1.1338135]

Keywords: *Conduction, Contact Resistance, Heat Transfer, Modeling, Thermophysical*

Introduction

To predict thermal contact conductance at an interface formed by two non-conforming, roughened surfaces with non-metallic coatings, a theoretical model must be based on the knowledge of surface geometry, coating properties, and the mode of asperity deformation. The development of the present model was derived from numerous experimental and theoretical models for nominally flat, metallic coated surfaces in contact. The following review highlights the important experimental and theoretical developments, which led to the development of the present model.

Mikic and Carnasciali [1] investigated the effect of the thermal conductivity of plating material for a fixed geometry and fixed base substrate, both theoretically and experimentally. The total constriction resistance for the plated substrate was divided into the thermal constriction resistance of the plating material and the underlying thermal constriction resistance of the base substrate. They concluded that for nominally flat surfaces, where microscopic thermal constriction predominates, the effect of the plating material on the thermal constriction resistance could reduce the thermal constriction resistance by as much as one order of magnitude.

Khan et al. [2] developed expressions for both the oxide film thermal resistance and the oxide film to foreign metal interface resistance as a function of interface pressure. The constants for their expression were obtained from a correlation of the experimental thermal contact resistance data measured. They were able to derive from the resulting equation an expression for the oxide film thermal conductance. The equation was only valid for oxide films produced on SAE 1020 wrought steel with 0.20 percent carbon at an interface temperature of 65.5°C (150°F), for oxide film thicknesses from 254 to 2032 μm (0.010 to 0.080 in.), and for a pressure range below the yield point of the base metal. In addition, Khan et al. [2] concluded from their data that the fracture of the oxide film would lead to lower contact resistance only after sufficient plastic flow of the base metal through the cracks in the oxide film.

Yip [3] derived analytically the thermal contact resistance for contact between oxidized metals (*i.e.*, aluminum alloy) with nominally flat and rough surfaces, which can be characterized by a random height distribution. He considered only heat conduction at the points of contact, assuming the transfer of heat through radiation and convection mechanisms to be negligible.

Veziroglu et al. [4] conducted an analytical study for the prediction of thermal contact conductance with interstitial plates, and an expression was developed in terms of known properties and parameters. The model assumed that both macroscopic and microscopic contact regions exist with two cylindrical solids having a circular contact at the center with a gap filled with a material of uniform conductance.

Antonetti and Yovanovich [5] developed a thermo-mechanical model for the prediction of the thermal contact conductance of nominally flat, rough surfaces (*i.e.*, nickel substrate) enhanced with a soft metallic coating (*i.e.*, vapor deposited silver) and verified their model with experimental measurements. The correlation included tribological parameters, such as coating microhardness, and thermal parameters, such as coating and substrate thermal conductivity. A correlation for bare joints, developed by Yovanovich [6], was employed as the basis for their coated contact model.

Antonetti and Yovanovich [5] presented their thermal contact conductance predictions in dimensionless form, which includes such parameters as surface roughness and asperity slope, effective microhardness of the layer-substrate combination, apparent pressure, and the effective thermal conductivity of the joint. They presented two expressions for the dimensionless thermal contact conductance of coated surfaces. Experiments were conducted for silver coated nickel specimens in contact with bare nickel specimens to verify their model. They concluded that the thermomechanical model predicted the thermal contact conductance of the experimental data quite well, and analytically the model for the coated joint could be reduced to an equivalent bare joint by

---

Contributed by the Heat Transfer Division for publication in the JOURNAL OF HEAT TRANSFER. Manuscript received by the Heat Transfer Division November 25, 1997; revision received, July 10, 2000. Associate Editor: A. S. Lavine.

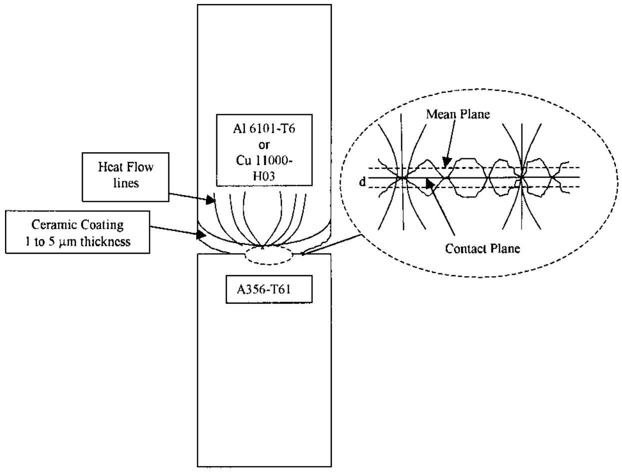

Fig. 1 Constriction of the heat flow through the macroscopic contact area and microscopic contact areas

using the concepts of effective microhardness and effective thermal conductivity. They further concluded that a silver layer could enhance the thermal contact conductance of nominally flat, rough, contacting nickel specimens by as much as one order of magnitude. However, they noted that their study applied only to nominally flat surfaces and was not applicable to non-flat contacting surfaces.

Previous thermophysical models or correlations, which predict thermal contact conductance or resistance for both bare and coated surfaces (*e.g.*, Cooper et al. [7], Mikic [8], Yip [3], Al-Astrabadi et al. [9], Antonetti and Yovanovich [5]) have assumed optically or nominally flat surfaces. Other models (*e.g.*, Clausing and Chao [10], Veziroglu and Chandra [11], Kitscha and Yovanovich [12], Jones et al. [13], Burde and Yovanovich [14], Majumdar and Tien [15], and Lambert and Fletcher [16]) have developed thermal constriction models which incorporated optically non-flat, bare surfaces with bulk thermophysical properties.

Therefore, of practical value would be a model that incorporates the influence of the coating material properties such as Young's modulus and Poisson's ratio, and geometric parameters such as profile radius of curvature and surface roughness to calculate the macroscopic contact resistance. This would extend the prediction of the thermal contact resistance for non-flat, coated surfaces in contact. The model should also be able to predict thermal contact resistance for both crown and convex surface profiles with either metallic or non-metallic coatings; however, this investigation only dealt with non-metallic coatings.

Problem Statement

When two surfaces are brought into contact with each other, the resulting area of contact is incomplete and the real area of contact for heat transfer to occur is a fraction of the apparent cross-sectional area. The real contact spots that occur are only at a few discrete spots or asperity heights, which are dependent on contact pressure. This may not hold true if either of the contacting surfaces is a soft metal or elastomeric polymer where the actual contact area may be greater than the apparent area. The number of real contact spots is further reduced if either of the surface profiles is wavy (*i.e.*, profile flatness deviations other than nominally flat). If there are no interstitial fluids or materials between the surfaces in contact, the heat flow lines initially converge at the macroscopic contact area and then converge further at the microscopic contacting spots. If a hard, non-metallic coating is deposited on one or both contacting surfaces this will further influence the convergence of the heat flow lines at the interface as shown in Fig. 1. The convergence of the heat flux lines is a direct result of the surface roughness and wavy profile of the joint interface. Therefore, the development of a predictive model should encompass (1) microscopic parameters such as surface roughness, and (2) macroscopic parameters such as surface profile radius of curvature. The development of a predictive model for heat transfer across an uncoated, wavy joint is very complex and this complexity is further increased when a nonmetallic coating is added to the interface. Therefore, the predictive model for nonmetallic coatings on metal substrates should also encompass (3) the dependence of the microscopic and macroscopic contact resistance on the mechanical and thermophysical properties of the nonmetallic coating.

What has heretofore not been available is a predictive model for non-metallic coated materials that takes into account several of the important parameters: mechanical and thermophysical properties of the substrate and coating, surface topography, and the component geometry for relatively soft metallic substrates. In addition, the effect of surface roughness on the macroscopic contact area for the macroscopic contact resistance is also required. Therefore, a model that incorporates these parameters will be developed in this section. The present experimental investigation involved the study of refractory ceramic coatings deposited on both aluminum and copper alloys. The experimental data gathered for model verification involved a refractory ceramic coating deposited on a wavy metallic surface, which was in contact with a nominally flat metallic surface.

Assumptions of Present Model

For the present model, it is presumed that the following assumptions hold to be true:

1 The microscopic contacts are uniformly distributed over the entire macroscopic area (contour area)

2 The determination of the macroscopic contour area between two bodies of different radii of curvature can be solved by Hertzian contact theory

3 The harmonic mean may be employed for both the Young's modulus and Poisson ratio for the coating/substrate combination. The harmonic mean was employed for the thermal conductivity of the two metallic substrates in contact while the effective thermal conductivity was employed for the coating/substrate combination

4 Modified Hertzian contact theory for surface roughness can be employed to determine the microscopic contact area and

5 The real effective contour area of radius α is placed on the origin of a circular apparent area of radius B.

Total Joint Resistance for Non-Flat, Coated Surfaces

When two non-flat solid surfaces in contact are considered, the resulting real area of contact is further reduced due to the formation of a macroscopic contact area. Within this macroscopic region, the density of microcontacts is very high while, beyond its boundary the density of the microcontacts becomes quite small with only very high asperities coming into contact. As a consequence, both macroscopic and microscopic thermal resistances occur in series, which may be combined to obtain the total joint thermal contact resistance:

$$R_{\text{total}}=R_{\text{microscopic}}+R_{\text{macroscopic}} \tag{1}$$

If the microscopic contact spots are all assumed identical, and are all to be found within a single circular macroscopic contact spot that is centrally located on a nominally flat surface, the expression for the total joint thermal contact resistance may be written in the following form for n contact spots (Yovanovich [6]):

$$R_{\text{total}}=\frac{\varphi(a_e/b_i)}{4K'na_e}+\frac{\varphi(\alpha/B)}{4K_m\alpha}, \tag{2}$$

where the constriction factor φ was first obtained by Roess [17] for the constriction resistance due to an isothermal circular spot of radius a_e, which feeds heat into a coaxial right circular cylinder of radius b:

$$\varphi(a_e/b_i)=1-1.4093(a_e/b_i)+0.2959(a_e/b_i)^3+0.0525(a_e/b_i)^5 \tag{3}$$

Clausing and Chao [18] also employed the approximate solution developed by Roess [17] for their proposed macroscopic constriction resistance model with similar coefficients but modified to include the macroscopic contact radius. The present model also employs this same expression but incorporates a different constriction ratio which takes into account the real effective contour radius and the radius of the apparent area:

$$\varphi(\alpha/B)=1-1.4093(\alpha/B)+0.2959(\alpha/B)^3+0.0525(\alpha/B)^5 \tag{4}$$

The expressions for the modified elastic contact radius a_e, modified effective thermal conductivity K', harmonic thermal conductivity K_m, constriction parameter correction factor for surface two (2) C_2, which contains the non-metallic coating, and real effective contour radius α were formulated for nonmetallic coated contacts deposited on relatively soft metals.

$$K'=\frac{2K_1K_2}{C_2K_1+K_2} \tag{5}$$

$$K_m=\frac{2K_1K_2}{K_1+K_2}. \tag{6}$$

Such parameters as the surface roughness (σ) and absolute asperity slope (m_{abs}), the Young's modulus (E) of the coating material, and the bulk material properties of the underlying soft substrate were included to predict these values.

Refinement of the Expression for the Elastic Contact Radius

If two surfaces are brought together until their reference planes and contact plane are separated by a distance d, there will be contact at any asperity whose height is initially greater than the separation as shown in Fig. 2. Therefore, the probability of making contact at any given asperity, with height z, becomes:

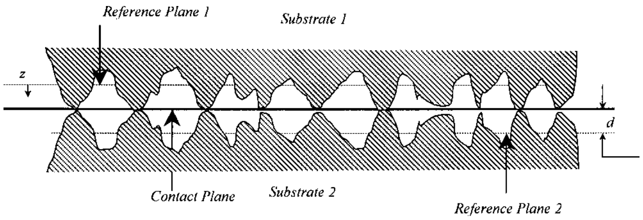

Fig. 2 Contact of rough surfaces

$$prob(z\geqslant d)=\int_d^{\infty}\Theta(z)dz. \tag{7}$$

The expected number of contact spots n can be calculated from the following:

$$n=N\int_d^{\infty}\Theta(z)dz, \tag{8}$$

where N is the total number of asperities and $\Theta(z)$ is the Gaussian probability density function. The modified elastic contact radius a_e can be obtained from the analysis of Hertz [19]. The equation for n can be simplified with the introduction of the standard deviation σ to describe the height distribution of the asperities and the apparent contact area A_a (Mikic [8]):

$$n=\frac{1}{16}\left(\frac{m_{abs}}{\sigma}\right)^2 A_a\frac{\exp(-h^2)}{erfc\left(\frac{h}{\sqrt{2}}\right)} \tag{9}$$

$$a_e=\frac{4}{\sqrt{\pi}}\frac{\sigma}{m_{abs}}\exp\left(\frac{h^2}{2}\right)\Psi_0\left(\frac{h}{\sqrt{2}}\right) \tag{10}$$

$$\Psi_0\left(\frac{h}{\sqrt{2}}\right)=\frac{1}{2}erfc(X), \tag{11}$$

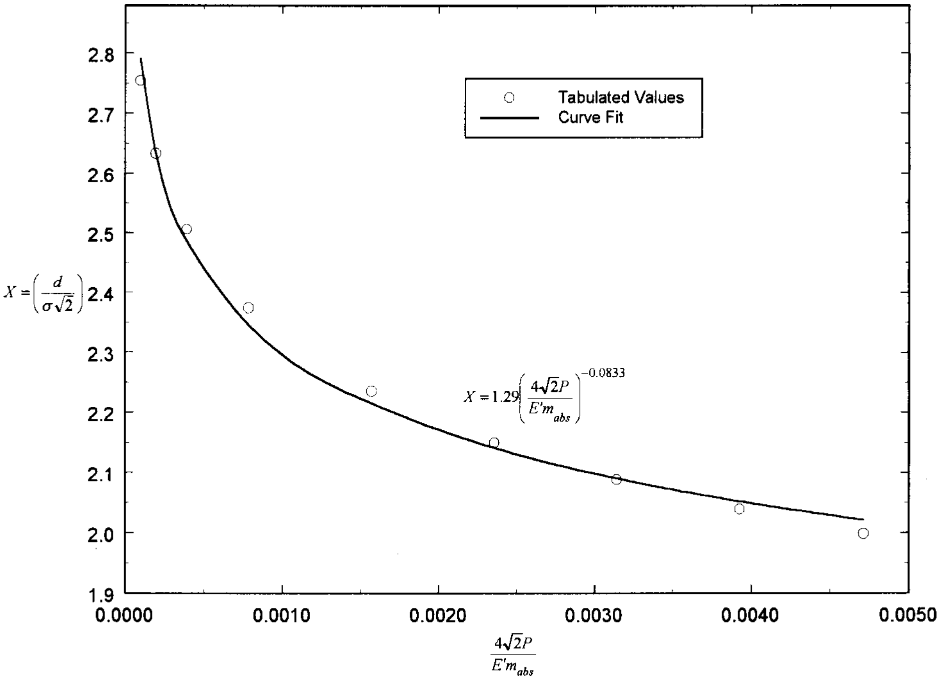

Fig. 3 Dimensionless separation as a function of dimensionless interface pressure

where h is the standardized separation which is equal to d/σ.

If the elastic contact radius expression, Eq. (10), is multiplied by the dimensionless plane separation X (Mikic [8]), a simple expression for the elastic contact radius in terms of dimensionless interface pressure can be obtained:

$$X=\frac{d}{\sigma\sqrt{2}}=\frac{h}{\sqrt{2}}=erfc^{-1}\left(\frac{4\sqrt{2}P}{E' m_{abs}}\right) \tag{12}$$

$$a_e X=\frac{2}{\sqrt{\pi}}\frac{\sigma}{m_{abs}}\exp(X^2)erfc(X)X. \tag{13}$$

A plot of Eq. (12) for the range of parameters (P, E', and m_{abs}) considered in the present investigation is shown in Fig. 3, and a curve fit of the tabulated values resulted in a simple expression for X:

$$X=1.29\left(\frac{4\sqrt{2}P}{E' m_{abs}}\right)^{-0.0833}. \tag{14}$$

The constant and exponent for Eq. (14) are a direct result of the material properties of the nonmetallic coatings and underlying substrate used in this investigation. In addition, Eq. (14) for the dimensionless plane separation X is applicable only for the portion of the macroscopic contour area that provides the microscopic contact spots.

As a result of the material properties of the nonmetallic coatings and substrate employed in this study, the product of the exponential, complementary error function, and dimensionless plane separation X term of Eq. (13) becomes:

$$\exp(X^2)erfc(X)X=0.530 \tag{15}$$

Substitution of Eq. (15) and Eq. (14) into Eq. (13), then solving for the contact radius a_e, gave a simple expression that can be easily computed from known surface and material parameters:

$$a_e=0.464\frac{\sigma}{m_{abs}}\left(\frac{4\sqrt{2}P}{E' m_{abs}}\right)^{0.0833}. \tag{16}$$

Refinement to the Effective Thermal Conductivity

Antonetti and Yovanovich [5] first introduced the effective thermal conductivity for coated surfaces that were composed of silver layers of various thicknesses deposited on a hard metallic substrate such as nickel. One underlying assumption that Antonetti and Yovanovich [5] made, which is not explicitly stated, is that the thermal conductivity of the deposited silver coating is equal to the bulk material property. While this may be a good assumption for metallic layers, which are vapor deposited onto metallic substrates, there is strong evidence to suggest that this assumption may not be valid for nonmetallic coatings.

The expression developed by Antonetti and Yovanovich [5] for the constriction parameter correction factor for coated surfaces was employed but modified to include the expression developed for the modified elastic contact radius (where η accounts for the influence of the coating layer and ρ accounts for the heat flux distribution assumed):

$$\varphi\left(\frac{a_e}{b_i},\eta_i\right)=\frac{16}{\pi\frac{a_e}{b_i}}\sum_{i=1}^{\infty}\frac{J_1^2\left(\zeta_i b\frac{a_e}{b_i}\right)}{(\zeta_i b)^3 J_0^2(\zeta_i b)}\cdot\eta_i\cdot\rho_i \tag{17}$$

$$\eta_i=K^*\left(\frac{(1+K^*)+(1-K^*)e^{-2\zeta_i a_e \tau}}{(1+K^*)-(1-K^*)e^{-2\zeta_i a_e \tau}}\right)\quad\text{where}\quad K^*=\frac{K_s}{K_c} \tag{18}$$

$$\rho_i=\frac{\sin\left(\zeta_i b\frac{a_e}{b_i}\right)}{2J_1\left(\zeta_i b\frac{a_e}{b_i}\right)} \tag{19}$$

$$C_2=\varphi\left(\frac{a_e}{b_i},\eta_i\right)\Big/\varphi\left(\frac{a_e}{b_i}\right). \tag{20}$$

An expression for the thermal conductivity of the thin film coating K_c as a function of film thickness has been developed for the determination of the correct constriction parameter correction factor (Marotta [20]). Substitution of Eq. (20) into Eq. (5) enabled the evaluation of the effective thermal conductivity K' for a surface which contains a deposited nonmetallic coating.

This expression, Eq. (5), for the effective thermal conductivity was initially employed by Antonetti and Yovanovich [5] for soft, metallic coatings, which takes into account the effect of the coating thermal conductivity on the thermal constriction factor. For this study the above expression was employed for nonmetallic coatings deposited onto a metallic substrate.

Refinement to the Macroscopic Resistance for Rough, Coated Spherical Surfaces

An analysis developed by Greenwood and Tripp [21] for rough surfaces in contact will be the foundation for the development of the macroscopic area (contour area) for solid bodies. While they considered only the physical model of an uncoated sphere in contact with an uncoated plane since it was easier to visualize, their basic concepts have been extended in the present analysis to a physical model for coated surfaces.

Greenwood and Tripp [21] defined a dimensionless effective radius α^* for bodies that are brought together into contact with surfaces that possess roughness. The dimensionless effective radius is a function of the dimensionless load L^*, convergence value χ which Greenwood and Tripp [21] conveniently chose to be 2.36, and dimensionless bulk compliance $\omega^*(0)$:

$$\alpha^*=\frac{\chi L^*}{2\pi\omega^*(0)}\Rightarrow\alpha^*=\frac{0.375L^*}{\omega^*(0)}, \tag{21}$$

and the real effective contour radius can be defined as:

$$\alpha=\alpha^*\sqrt{2\beta\sigma}, \tag{22}$$

where the values for β are calculated from the averaged orthogonal radii of curvature measured for each contacting surface as:

$$\beta=\frac{RC_1+RC_2}{2RC_1RC_2}. \tag{23}$$

For the present analysis the Poisson ratio and Young's modulus are modified for the coating/substrate composite. They are assumed as the harmonic mean of the two materials, the nonmetallic coating and the metallic substrate; thus, the influence of the coating on E_1 and v_1 was taken into account:

$$E_1=E_{s-c}=\frac{2E_cE_s}{E_c+E_s} \tag{24}$$

$$\nu_1=\nu_{s-c}=\frac{2\nu_c\nu_s}{\nu_c+\nu_s}. \tag{25}$$

The harmonic value for each component, E_{s-c} and v_{s-c}, was calculated from the individual known values for the nonmetallic coating and underlying substrate. The effective Young's modulus employed in the determination of the dimensionless load and the bulk compliance incorporates the influence of the coating/substrate composite and the opposite substrate material in contact (Greenwood and Tripp [21]):

$$L^{*}=\frac{2L}{\sigma E'\sqrt{2\beta\sigma}} \tag{26}$$

$$\omega^{*}(0)=\frac{\omega(0)}{\sigma} \tag{27}$$

$$\omega(0)=\sqrt[3]{\frac{9\pi^{2}L^{2}(E_{s-c}+E_{2})(RC_{1}+RC_{2})}{16RC_{1}RC_{2}}} \tag{28}$$

$$E'=\left(\frac{1-\nu_{s-c}^{2}}{E_{s-c}}+\frac{1-\nu_{2}^{2}}{E_{2}}\right)^{-1}. \tag{29}$$

Present Model

The substitution of Eqs. (9) and (16) into the expression for the total joint thermal contact resistance, Eq. (2), results in the following expression which has been multiplied by the apparent area A_a:

$$R''_{\text{total}}=7.68\,\frac{\varphi(a_e/b_i)\operatorname{erfc}(X)\exp(2X^{2})}{K'\dfrac{m_{\text{abs}}}{\sigma}\left(\dfrac{\sqrt{2}P}{E'm_{\text{abs}}}\right)^{0.0833}}+\frac{\sqrt{\pi}\varphi(\alpha/B)}{4K_m}\,\frac{A_a}{\sqrt{\pi\alpha^{2}}}, \tag{30}$$

where the exponential term for the expected number of contact spots n, Eq. (9), incorporates the dimensionless plane separation X:

$$h^{2}=\left(\frac{d}{\sigma}\right)^{2}=2X^{2}. \tag{31}$$

The model does not encompass microscopic asperity contacts that deform plastically or may behave elastoplastically. The first term in Eq. (30) would have to be modified to reflect this mode of deformation in conjunction with an expression for the composite microhardness. A surface that has been coated with a soft metallic coating may still incorporate the second term (*i.e.*, macroscopic resistance) but the first term would need to incorporate the analysis of Antonetti and Yovanovich [5]. The macroscopic resistance term (*i.e.*, second term) assumes that only one macroscopic contact spot exists (*i.e.*, $n=1$) and its contact radius was defined by α. Therefore, the microscopic elastic radius a_e was replaced with the macroscopic radius α in the second term of Eq. (30).

Marotta and Fletcher [22] has provided the justification for the use of an elastic model rather than a plastic model (*i.e.*, first term) to describe the microscopic contact resistance for aluminum alloys. The main difference between the two microscopic models lies in the fact that elastic asperities return to their initial configuration upon removal of the applied load while plastic asperities are permanently set. This effect leads to the contact radius and resulting area for plastic deformation being greater than elastic deformation of the contacting spots.

Results and Discussion

An experimental investigation was conducted to obtain data for both uncoated and non-metallic coated surfaces over a broad range of test parameters (Marotta [20]). These data involved the measurement of thermal contact conductance in a vacuum environment for a coated, convex profile on an uncoated, nominally flat plane. The thermal contact conductance values were then compared to the present model which accounts for both microscopic and macroscopic thermal contact resistances of non-flat, roughened surfaces coated with non-metallic coatings.

To investigate the interrelationship between macroscopic contact resistance and microscopic contact resistance with a non-metallic coating (aluminum nitride, 3 μm thickness), a parametric study of Eq. (30) was conducted. This analysis was carried out for variations in geometric profiles (*i.e.*, radii of curvature *RC*), surface roughness (*i.e.*, σ), and coating thermal conductivity (*i.e.*, K_c). The latter parameter was included since microscale effects will affect the value of the coating's thermal conductivity as dimensional features achieve very small scales. Figure 4 shows these plots. The ratio of macroscopic profile radius of curvature to microscopic surface roughness RC/σ was varied from 0.01 (*i.e.*, spherical contact) up to 100 (*i.e.*, nominally flat conditions). These values were chosen to encompass the range of experimental parameters employed in the investigation for both uncoated and coated aluminum substrates and explore the limits where each contact resistance regime will dominate.

The joint contact resistance increases dramatically to infinity at very low RC/σ ratios while the joint contact resistance converges to a finite value for high RC/σ ratios. That is, at low RC/σ ratios (*i.e.*, values less than 0.1) the macroscopic contact resistance shows predominance and further dominates, as the ratio becomes smaller. On the other hand, when the RC/σ ratio is greater than one, the microscopic contact resistance begins to dominate, which is illustrated by the asymptotic convergence of the plots as they approach a ratio of 100. These trends hold true for Figs. 4(*b*) and 4(*c*) where the film conductivity is relatively high, however, at the lower film conductivity and higher RC/σ ratios the dimensionless joint contact resistance begins to increase with increasing surface roughness as indicated by the increasing dimensionless roughness ratio σ/t. Convergence to a finite value was not achieved for this case as shown in Fig. 4(*a*). This trend is in line with archival studies that have shown an increasing contact resistance with increasing surface roughness for nominally flat surfaces.

The plots in Fig. 4 also show the effect that an increased surface roughness (*i.e.*, σ/t from 0.033 to 2.66) has on the dimensionless joint contact resistance and the transition to microscopic contact resistance. The higher surface roughnesses tend to subdue the influence of the lower radius of curvature and cause the microscopic contact resistance to show more dominance. The applied load L was arbitrarily set to 500 N for the purpose of this analysis. One would tend to believe, if the present results were extrapolated, that as the applied load is further increased from the present value of 500 N that the curves would begin to compress. They would quickly approach the regime where the microscopic contact resistance would control the joint contact resistance. The same may be true if the applied load was decreased from the present value and the macroscopic contact resistance would control the joint contact resistance. It must be noted that the variation of the computed dimensionless resistance in Fig. 4 at low radius of curvature and the higher surface roughnesses approaches a single curve.

Figures 5–7 present the dimensionless thermal contact resistance as a function of dimensionless contact pressure for beryllium oxide, boron nitride, and aluminum nitride coatings, respectively, for several coating thicknesses and interface contact temperatures. The parameters employed for the dimensionless parameters are effective thermal conductivity, contour radius, effective Young's modulus, and absolute asperity slope. Both the radius of curvature and absolute asperity slope were measured by stylus profilometry. The influence on the dimensionless thermal contact resistance of the profile radius of curvature can be clearly observed as the radius is decreased for the beryllium oxide coatings. An increase in contact resistance as the profile radius of curvature is decreased from approximately 10 to 1 meters becomes obvious. At this lower value, the macroscopic contact resistance dominates with very little influence by the microscopic contact resistance. The profile radius of curvature for each specimen was measured by stylus profilometry and not computed from flatness deviation, thus, surface waviness effects were minimized. The measured radii of curvature shown for each coated specimen were measured orthogonally to each other, giving an indication of the hemispherical profile that existed prior to contact with the uncoated surface. Boron nitride and aluminum nitride coatings were deposited by RF magnetron sputtering under similar gas mixture and substrate voltage bias conditions; thus, each coating possessed similar film microstructure. The deposition of the be-

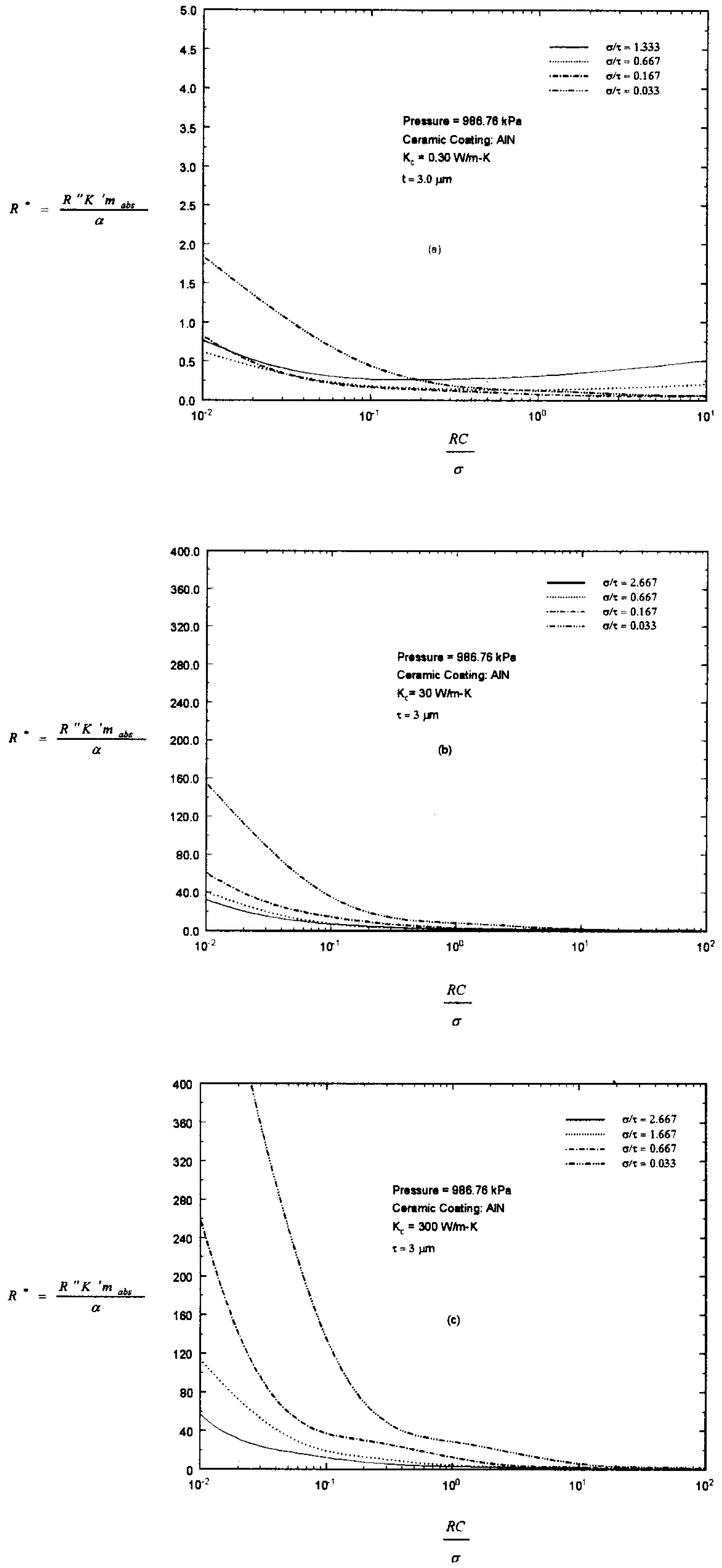

Fig. 4 Dimensionless joint contact resistance as a function of dimensionless radii of curvature for varying surface roughness and coating thermal conductivity

ryllium oxide coatings involved the sputtering of a solid BeO compound target onto the negatively biased substrate set between 100–2000 V and substrate temperatures between 200–500°C; therefore, the film microstrucRF magnetron sputtering under similar gas mixture and substrate voltage bias conditions; thus, each coating possessed similar film ture was different than the BN and AlN coatings (e.g., greater film porosity). These coatings represent some of the highest achievable thermal conductivity values when measured in bulk form (with diamond having the highest value).

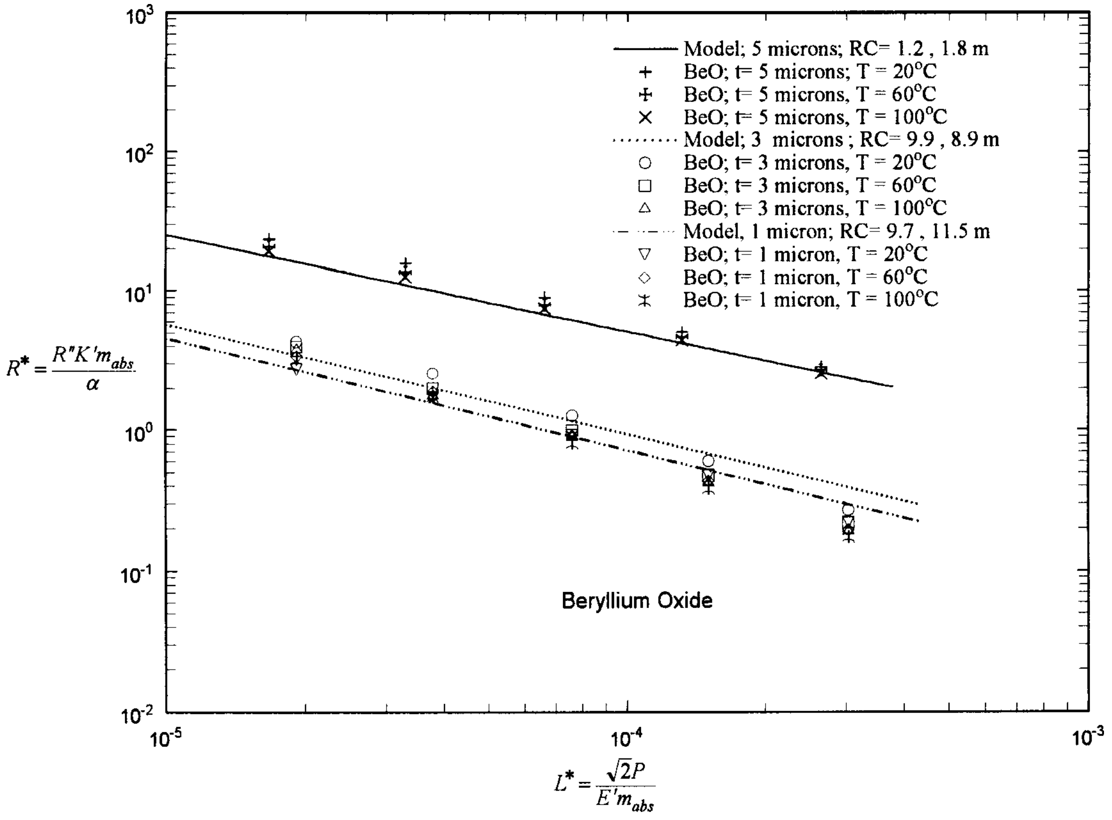

Fig. 5 Dimensionless thermal contact resistance as a function of dimensionless pressure for beryllium oxide coatings

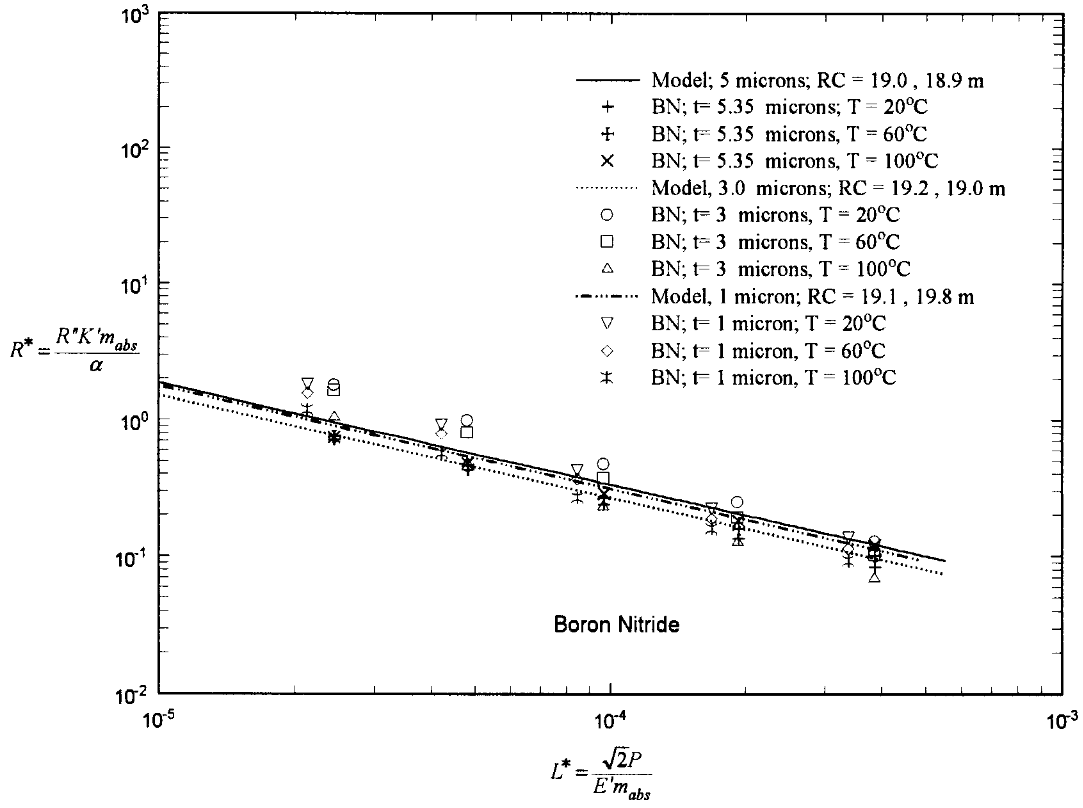

Fig. 6 Dimensionless thermal contact resistance as a function of dimensionless pressure for boron nitride coatings

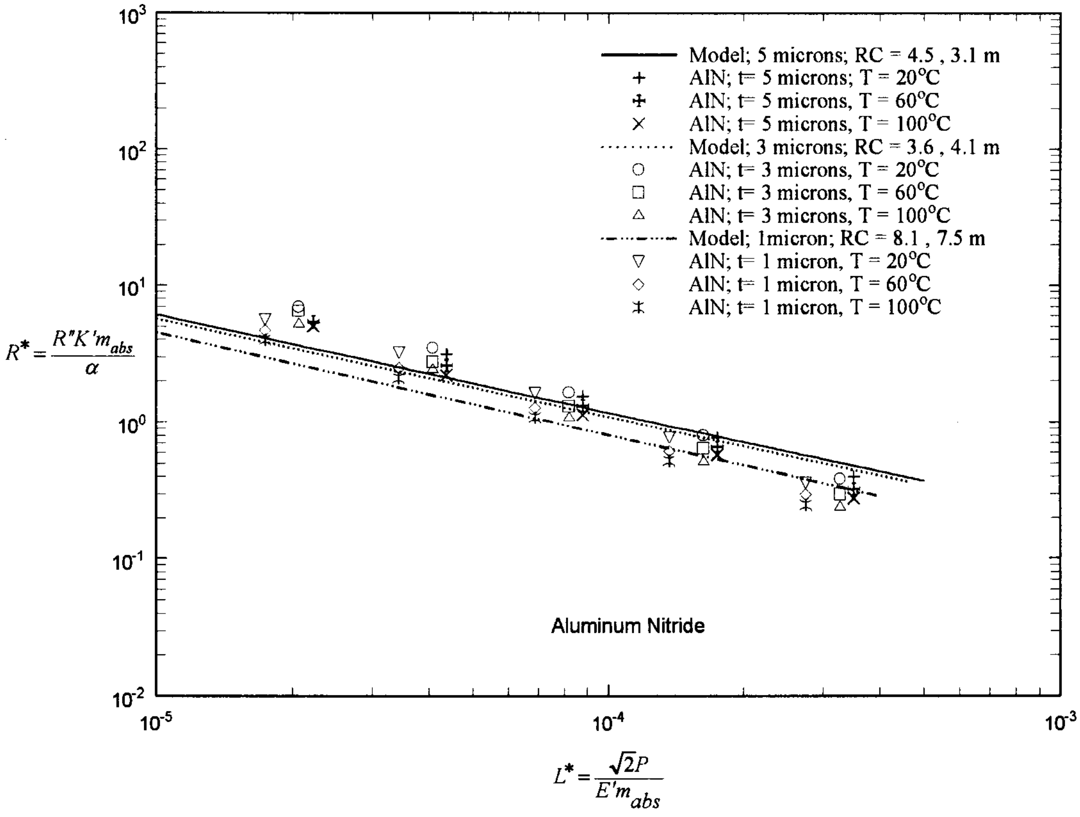

Fig. 7 Dimensionless thermal contact resistance as a function of dimensionless pressure for aluminum nitride coatings

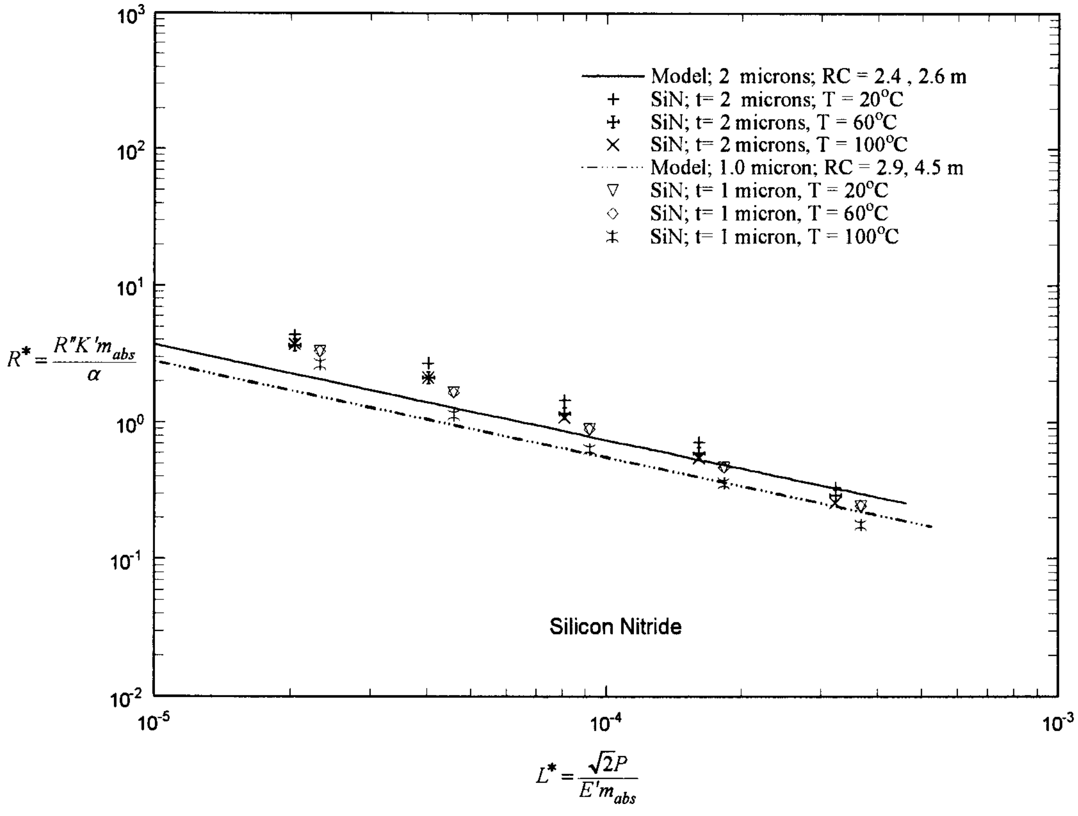

Fig. 8 Dimensionless thermal contact resistance as a function of dimensionless pressure for silicon nitride coatings

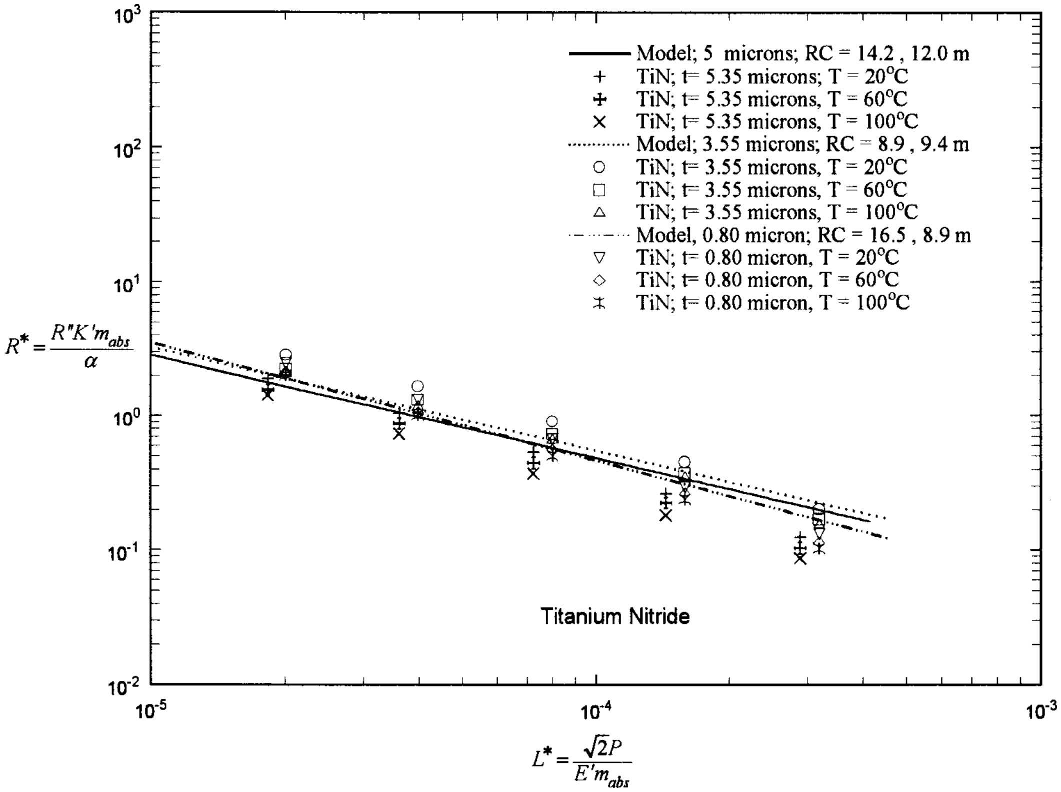

Fig. 9 Dimensionless thermal contact resistance as a function of dimensionless pressure for titanium nitride coatings on aluminum 6101-T6

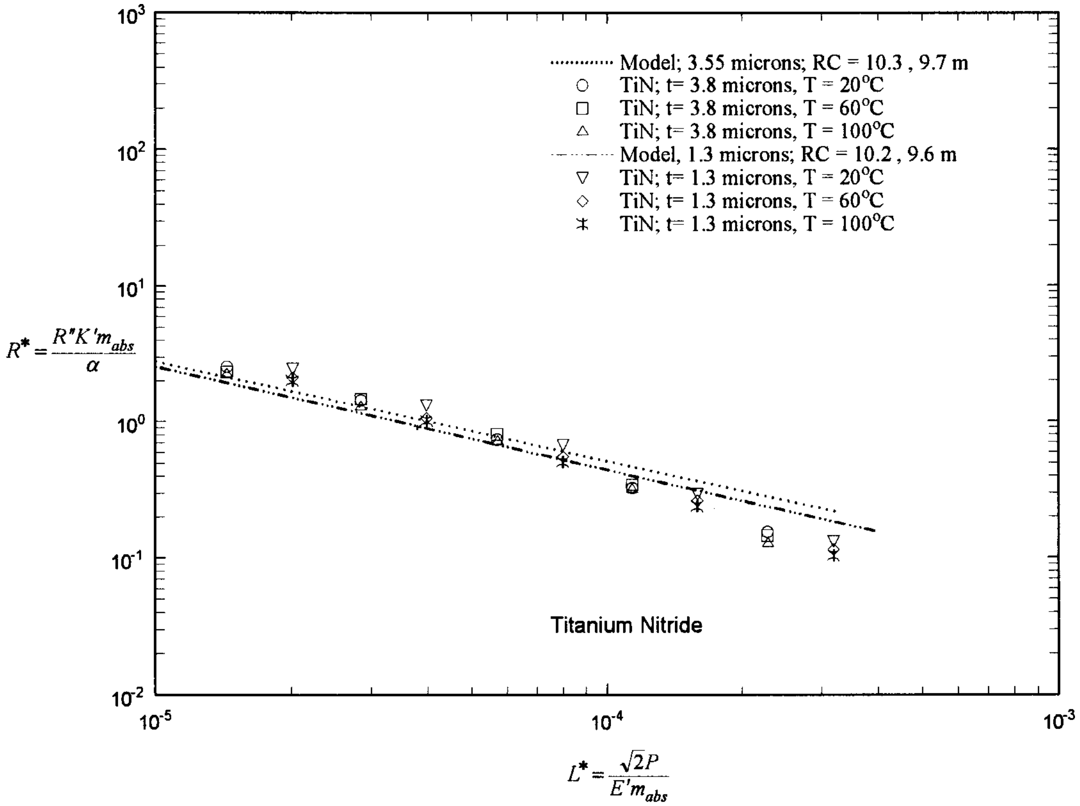

Fig. 10 Dimensionless thermal contact resistance as a function of dimensionless pressure for titanium nitride on copper C11000-H03

The effect of increasing coating thickness tends to increase the thermal contact resistance while among the individual ceramic materials the thermal contact resistance either increases or decreases with the material's thermal conductivity. A comparison between the measurements and the model predictions for thermal contact resistance for all three coating materials and thicknesses shows good agreement throughout the range of conditions examined.

Figures 8 and 9 present the dimensionless thermal contact resistance as a function of dimensionless contact pressure for silicon nitride and titanium nitride coatings deposited on aluminum 6101-T6. Figure 9 shows an inflection in the prediction for the 0.8 μm coating that would be physically difficult to explain at first; however, the measured orthogonal radii of curvature of the coated specimen indicate a surface profile that is not truly hemispherical. A non-hemispheric profile would result in a higher thermal contact resistance prediction at low loads (*i.e.*, higher than the other two thicknesses) due to a smaller contour area but a lower predicted thermal contact resistance at the higher loads because of the flatter surface profile and thinner coating thickness. The two extreme points would cause the predicted curve to cross the other two predicted curves for the 3 and 5 μm coating thicknesses. Figure 10 presents a similar plot for the titanium nitride coatings that were deposited on copper C11000-H03. The interesting aspect of these results, in comparison to Fig. 9, is that the underlying copper substrate has no influence on the interface contact resistance. It appears that the coating material, present at the interface with its mechanical and thermal properties, has the dominating influence on the thermal contact resistance.

The dimensionless thermal contact resistance for measured data is compared to model predictions for each ceramic coating material and each coating thickness. The radii of curvature for the coated test specimens ranged from a low value of 2.4 meters for the silicon nitride coatings to a value of approximately 16.5 meters for the titanium nitride coatings. With this range of radii of curvature, the comparison between measured data and model predictions again shows good agreement. The largest deviation between experimental data and model predictions occurs at low contact pressures; however, good agreement does exist at high contact pressures except for titanium nitride coatings deposited on copper. For titanium nitride coatings deposited on copper C11000–H03, two data points had significant deviation from the model predictions. These data points occurred at the high contact pressures.

Table 2 RMS and T-test values for the experimental data and model predictions

Ceramic Coatings	Coating Thickness (μm)	Overall % RMS Difference (10^2)	Means (Exp.; Model)	T-test on Means
Si_3N_4	1	0.42	1.109 ; 0.748	0.523
	2	0.37	1.558 ; 1.089	0.523
BeO	1	0.21	1.359 ; 1.256	0.892
	3	0.27	1.360 ; 1.603	0.924
	5.5	0.15	9.937 ; 8.511	0.747
AlN	1	0.31	1.876 ; 1.419	0.639
	3	0.46	2.295 ; 1.619	0.607
	5	0.31	2.063 ; 1.651	0.713
BN	1	0.28	0.607 ; 0.478	0.693
	3	0.58	0.608 ; 0.369	0.443
	5	0.24	0.348 ; 0.459	0.581
TiN	1	0.14	0.821 ; 0.726	0.840
	3	0.31	0.822 ; 0.705	0.582
	5	0.25	0.644 ; 0.701	0.877

An analysis of the uncertainty for thermal contact resistance for beryllium oxide, boron nitride, aluminum nitride, silicon nitride, titanium nitride on aluminum, and titanium nitride on copper using the Kline and McClintock [23] method yielded experimental average uncertainties of 7.8, 4.3, 5.4, 4.6, 8.3, and 8.0 percent, respectively. A more detailed analysis for uncertainty values may be found in Marotta [20].

Comparison of Model Predictions with Experimental Results

A comparison between computed joint conductance values with experimentally gathered data for beryllium oxide deposited on aluminum 6101-T6 for one (1) coating thickness is shown in Table 1. The table includes measured joint conductance data along with its corresponding interface temperature, apparent contact pressure, material properties, geometric data such as surface roughness, asperity slope, and radii of curvature, and percent difference. A statistical analysis was conducted to determine the Root Mean Square (rms) percent difference between the experimental data and model predictions, as shown in Table 2. In addition, a significance test for the difference between the two means was conducted to determine whether the values were significant or

Table 1 Beryllium oxide coating on A6101-T6 (1.0 μm); experimental data and model predictions

BeO											
t (μm)	1	$H_{a356\,(VHS)}$	85		% Diff.	$H_{6101\,(VHS)}$	48	σ (μm)$_{a356}$	0.83	m (rad)$_{a356}$	0.155
P_{app}(Pa)	h_c(W/m^2-K)	N*	R*(Exp.)	R*(Model)		$E_{a356\text{-}T61}$ (GPa)	82.825	σ (μm)$_{6101}$	0.80	m (rad)$_{6101}$	0.142
172400	620.54	3.04e-4	.222	.289	+31.4	$E_{6101\text{-}T6}$ (GPa)	64.825	σ (μm)$_{coat}$	0.97	m (rad)$_{coat}$	0.204
344800	982.75	1.51e-4	.479	.562	+17.3	k_{a356} (W/m-K)	151.15	σ_{rms} (μm)$_{s\text{-}c}$	1.27	m_{rms} (rad)$_{s\text{-}c}$	0.256
689600	1682.61	7.61e-5	.923	.994	+7.7	k_{6101} (W/m-K)	208.44	T_{avg} (K)	293.0		
1379200	2869.46	3.79e-5	1.715	1.689	−1.5	RC_1 (m)	9.7				
2758400	4801.05	1.92e-5	2.738	2.764	+0.9	RC'_1 (m)	11.5				
t (μm)	1					RC'_2 (m)	22	σ (μm)$_{a356}$	0.83	m (rad)$_{a356}$	0.155
P_{app}(Pa)	h_c(W/m^2-K)	N*				RC_2 (m)	20	σ (μm)$_{6101}$	0.80	m (rad)$_{6101}$	0.142
172400	717.77	3.04e-4	.195	.289	+48.2	$\nu_{a356\text{-}T61}$	0.33	σ (μm)$_{coat}$	0.97	m (rad)$_{coat}$	0.204
344800	1146.62	1.51e-4	.431	.560	+29.9	$\nu_{6101\text{-}T6}$	0.33	σ_{rms} (μm)$_{s\text{-}c}$	1.27	m_{rms} (rad)$_{s\text{-}c}$	0.256
689600	1982.72	7.61e-5	.903	.991	+9.7	ν_{BeO}	0.25	T_{avg} (K)	332.7		
1379200	3405.27	3.79e-5	1.883	1.684	-6.3	TIR_b (μm)	11.83				
2758400	5799.62	1.92e-5	3.383	2.757	-16.3	TIR_c (μm)	18.91				
t (μm)	1							σ (μm)$_{a356}$	0.83	m (rad)$_{a356}$	0.155
P_{app}(Pa)	h_c(W/m^2-K)	N*						σ (μm)$_{6101}$	0.80	m (rad)$_{6101}$	0.142
172400	842.01	3.04e-4	.173	.289	+67.0			σ (μm)$_{coat}$	0.97	m (rad)$_{coat}$	0.204
344800	1404.85	1.51e-4	.380	.560	+47.4			σ_{rms} (μm)$_{s\text{-}c}$	1.27	m_{rms} (rad)$_{s\text{-}c}$	0.256
689600	2395.63	7.61e-5	.795	.991	+24.6			T_{avg} (K)	372.5		
1379200	4061.49	3.79e-5	1.740	1.684	-3.2						
2758400	7112.11	1.92e-5	3.206	2.755	-14.1						

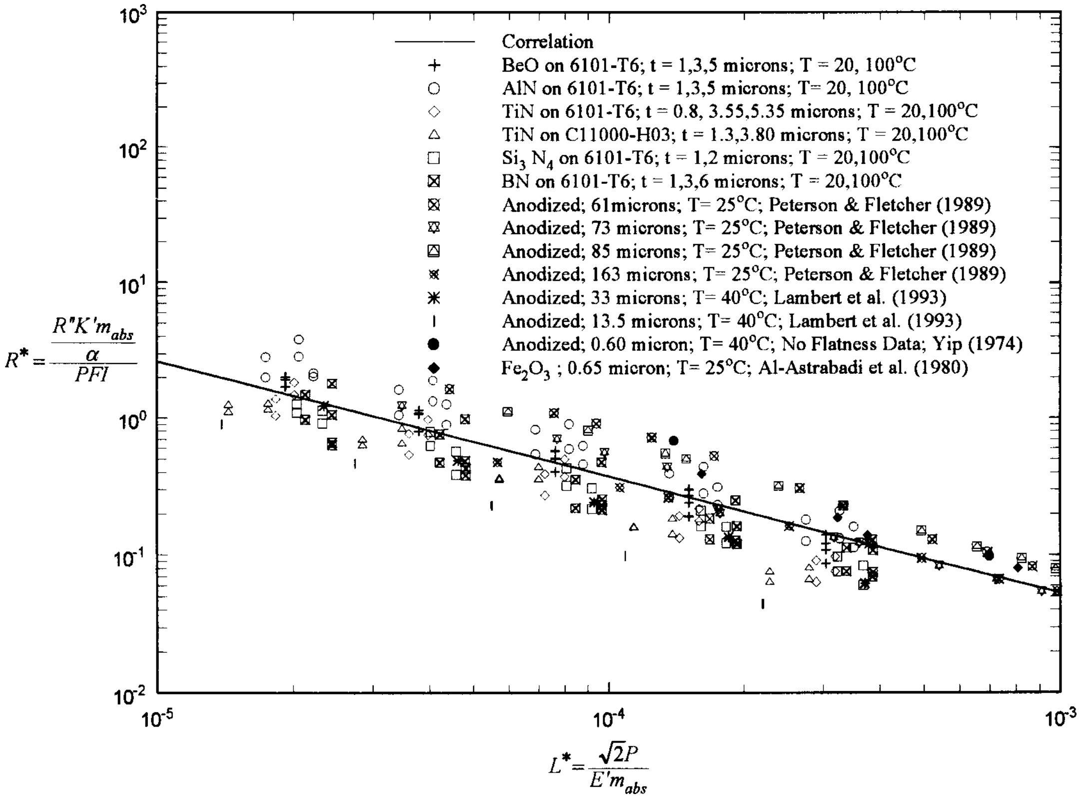

Fig. 11 A correlation for dimensionless thermal contact resistance as a function of dimensionless pressure for non-metallic coatings

not. At a 95 percent confidence level and 4 degrees of freedom, if the tabulated *t*-test values exceed a value of 2.571 there would exist a significant difference between the experimental data and model predictions. In addition, Table 2 summarizes the tabulated rms percent differences and the *t*-test values for each coating employed in the investigation at a representative interface temperature of 60°C. Each computed *t*-test value on the means was substantially lower than 2.571, which indicated no significant difference between the two mean values.

Correlation of Experimental Data

A correlation was developed to predict the total thermal contact resistance for all the refractory ceramic coatings employed in this investigation. Figure 11 presents a curve fit that uses dimensionless variables for all refractory ceramic coatings investigated. The correlation equation was obtained from a curve fit (graphically) to a functional form, which incorporates the parameters of the present model. The correlation incorporates a profile geometric parameter, called the Profile Flatness Index (*PFI*), defined as:

$$\mathrm{PFI}=\mathrm{TIR}_{\mathrm{act}}/\mathrm{TIR}_{\mathrm{nom}} \tag{32}$$

that takes into account the influence of the macroscopic resistance. The *PFI* is the ratio of the flatness profile deviation (*TIR*) measured post processing TIR_{act} to that for a nominally flat surface TIR_{nom}. The index is an indicator of the contribution to the flatness profile deviation caused by either the addition of the coating or the deformation of the profile surface during the deposition process from a nominally flat surface. The high deposition temperatures present in the gas reaction chamber can cause these profile distortions. Its origin arose from experimental observations of the measured values of the specimen's profile flatness prior and subsequently after the coating's deposition onto the metallic substrate.

As the value of the *PFI* ratio approaches unity, the contacting surface approaches nominally flat conditions, the first term in Eq. (30) dominates and the macroscopic term becomes negligible. In turn, as the *PFI* ratio deviates from unity in the positive direction, the contacting surface approaches non-flat conditions, the second term dominates and the microscopic term becomes negligible. Therefore, the *PFI* ratio can be a rough indicator, of which term, microscopic or macroscopic, in Eq. (30) that will dominate.

As the microscopic resistance dominates (the first term in Eq. (30)), a downward shift occurs for the total contact resistance, which implies that the *PFI* ratio will decrease towards unity. When the macroscopic resistance dominates (the second term in Eq. (30)), an upward shift occurs for the total contact resistance, which implies that the *PFI* ratio increases. This is clearly exhibited by the experimental results for beryllium oxide, as shown in Fig. 5, where the total contact resistance decreases as the orthogonal radii of curvature approach nominally flat surfaces.

If one considers the wide range of material properties, coating thicknesses, and geometric parameters used in this investigation a relatively simple parameter such as the *PFI* correlates well all the experimental data for thermal contact resistance. The *PFI* ratio ranged from approximately 1.3 for titanium nitride coatings to approximately 10.7 for beryllium oxide coatings deposited on aluminum 6101-T6 substrates. This range in *PFI* ratios translates to a range of radii of curvature, which vary from 1.2 to 19.0 meters. It must be noted that the *PFI* ratio can be easily obtained from most modern surface analyzers, which determine surface roughness and absolute asperity slope along with surface profile deviation or flatness.

If the dimensionless contact resistance R^* and the dimensionless contact pressure L^* are defined as:

$$R^*=R''K'm_{\mathrm{abs}}/\alpha \tag{33}$$

$$L^*(\sqrt{2}P/E' m_{\mathrm{abs}}) \quad (34)$$

the correlation equation groups the Profile Flatness Index with the dimensionless contact resistance R^* as:

$$\left(\frac{\dfrac{R''K' m_{\mathrm{abs}}}{\alpha}}{\mathrm{PFI}}\right) = 1.4x10^{-4}(\sqrt{2}P/E' m_{\mathrm{abs}})^{-0.848}. \quad (35)$$

To assess the applicability of the present correlation for predicting experimentally measured data originating from other investigators, thermal contact conductance values for non-metallic coatings either grown or deposited on aluminum alloys were obtained from the literature. Experimental anodized coating data from Peterson and Fletcher [24], Lambert et al. [25], and Yip [3] were compared to the present correlation in Fig. 11. The experimental investigation by Peterson and Fletcher [24] involved the measurement of thermal contact conductance of several anodized coating thicknesses grown on aluminum 6061-T6 substrates in contact with a common uncoated aluminum 6061-T6 substrate. The anodized coating thicknesses ranged from 61.0 to 163.0 μm while the contact pressure was varied from approximately 290 to 12,300 kPa (42 to 1784 psi).

To further assess the applicability of the present correlation to predict experimentally measured data from other studies, experimental data obtained by Al-Astrabadi et al. [9] for a thin iron oxide film grown on EM3B mild steel in contact with an uncoated steel substrate were also compared in Fig. 11. The iron oxide film consisted mainly of hematite Fe_2O_3, which was grown in an oxidizing environment of 70°C (158°F) temperature and 80 percent humidity. The experimental data from Al-Astrabadi et al. [9] and the present correlation compared favorably, as shown in Fig. 11. The surface roughness and absolute asperity slope for the oxide film (2.28 μm and 0.210 radian, respectively) were similar to values encountered in the present study for ceramic coatings. Again, the experimental study did not include surface profile flatness deviation prior to film growth or post processing; therefore, a value of one was assumed for the PFI. The other experimental studies by Peterson and Fletcher [24] and Lambert et al. [25] provided flatness deviation pre and post-processing; therefore, the PFI ratio was easily calculated. The thermal conductivity values for the anodized coatings were obtained from data published by Ogden et al. [26].

Conclusions and Recommendations

The total contact resistance for non-flat, metallic surfaces with a non-metallic coating was obtained by superposition of the microscopic (contact spots) resistance and the macroscopic (contour) resistance. Prior to this investigation, liquid analog and non-flat surfaces in contact with an optically flat, uncoated surface had been investigated. An experimental and analytical investigation to study the effect on total thermal contact resistance for non-flat, metallic surfaces coated with non-metallic material (*i.e.*, ceramic materials) was conducted.

The development of the macroscopic thermal contact resistance expression using Hertzian contact theory was employed with modifications for roughened surfaces. The reduction in thermal conductivity in dielectric ceramic materials when applied as a thin film was also taken into account.

A comparison of the present model for total thermal contact resistance was made with several refractory ceramic coatings deposited on a single metallic substrate while the opposite contacting substrate remained uncoated. Experimental data from several investigations were also included for comparison. Both the present data and those gathered from other experimental studies compared favorably with the model and correlation.

A total thermal contact resistance, which includes both the microscopic and macroscopic resistance, was computed from the thermophysical and mechanical properties of both the substrate and coating material. Geometric and profile parameters such as surface roughness, absolute asperity slope, and profile flatness were also employed. The correlation equation, Eq. (35), contains terms that account for the macroscopic resistance and the microscopic resistance with the importance of each term inferred from the *PFI* ratio. As the value of the *PFI* ratio approaches unity, the contacting surface approaches nominally flat conditions, the first term dominates and the macroscopic term becomes negligible. In turn, as the *PFI* ratio deviates from unity in the positive direction, the contacting surface approaches non-flat conditions, the second term dominates and the microscopic term becomes negligible. Therefore, the *PFI* ratio can be a rough indicator, of which term, microscopic or macroscopic, in Eq. (30) that will dominate.

In conclusion, a total thermal contact resistance that includes both the microscopic and macroscopic resistance was computed form the thermophysical and mechanical properties of both the underlying substrate and coating material. Geometric parameters, such as surface roughness, absolute asperity slope, and profile flatness deviation, were also instrumental in its computation.

Acknowledgments

Partial support for this investigation was provided by ONR Grant N00014-95-1-0842, and the Texas Engineering Experiment Station Center for Space Power.

Nomenclature

A_a = apparent area (m^2)
a = microscopic contact spot radius (m)
B = radius of apparent area (m)
b = flux tube radius (m)
C = constriction parameter correction factor
d = plane separation (m)
E = Young's Modulus (N/m^2)
E' = equivalent Young's Modulus (N/m^2) $[(1-\upsilon_1{}^2/E_1 + (1-\upsilon_2{}^2)/E_2{}^{-1}$
h = standardized separation (d/σ)
K = thermal conductivity (W/m K)
L = load (N)
m_{abs} = combined absolute asperity slope, $m_{\mathrm{abs}}=(m_{\mathrm{abs1}}{}^2 + m_{\mathrm{abs2}}{}^2)^{1/2}$ (rad)
N = total number of asperities
n = expected number of contact spots
P = apparent contact pressure (N/m^2)
Q = heat transfer rate (W)
q = heat flux (W/m^2)
R = thermal resistance (K/W)
R'' = thermal resistance per unit area (m^2 K/W)
RC = profile radius of curvature (m)
s = dimensionless distance from mean reference plane (z/σ)
T = temperature (°C)
TIR = total profile flatness deviation (m); $\mathrm{TIR}=\mathrm{TIR}_1+\mathrm{TIR}_2$
t = coating thickness (μm)
X = defined by Eq. 14
z = height above mean plane of surface (m)

Greek Letters

α = real effective contour radius (m)
β = defined by Eq. 23
ΔT_c = effective temperature drop across interface (K)
ζ_i = roots of Bessel function $J_1(\zeta_i)$
η = defined by Eq. 18
λ = eigenvalues
ν = Poisson ratio
ρ = defined by Eq. 19
σ = rms surface roughness (m)
τ = dimensionless coating thickness (t/a_e)
Θ = probability density function of peak heights
χ = convergence value

φ = macroscopic and microscopic thermal constriction factor
ω = bulk compliance (m)

Superscripts

$*$ = non-dimensional parameter
$'$ = effective

Subscripts

1 = substrate 1
2 = substrate 2
a = apparent
act = actual parameter
b = bare or uncoated surface
c = coating
e = elastic
Hz = Hertzian
i = index of summation
J = joint
m = harmonic
nom = nominally flat or non-wavy parameter
s = substrate
$s\text{-}c$ = substrate-coating

References

[1] Mikic, B. B., and Carnasciali, G., 1970, ''The Effect of Thermal Conductivity of Plating Material on Thermal Contact Resistance,'' ASME J. Heat Transfer, **92**, No. 3, pp. 475–482.

[2] Khan, E. U., Dix, R. C., and Kalpakjian, S., 1969, ''Thermal Contact Resistance of Thick Oxide Layers on Steel,'' J. Iron Steel Inst., London, pp.457–460.

[3] Yip, F. C., 1974, ''Effect of Oxide Films on Thermal Contact Resistance,'' AIAA Paper No. 74-693.

[4] Veziroglu, T. N., Yuncu, H., and Kakac, S., 1975, ''Analysis of Thermal Conductance of Contacts with Interstitial Plates,'' Int. J. Heat Mass Transf., **19**, pp. 959–966.

[5] Antonetti, V. W., and Yovanovich, M. M., 1985, ''Enhancement of Thermal Contact Conductance by Metallic Coatings: Theory and Experiment,'' ASME J. Heat Transfer, **107**, No. 3, pp. 513–519.

[6] Yovanovich, M. M., 1971, Thermal Contact Resistance: Theory and Applications, a short course presented at the University of Tennessee Space Institute, April 26–28.

[7] Cooper, M. G., Mikic, B. B., and Yovanovich, M. M., 1969, ''Thermal Contact Conductance,'' Int. J. Heat Mass Transf., **12**, January, pp. 279–300.

[8] B. B. Mikic, 1974, ''Thermal Contact Conductance; Theoretical Considerations,'' Int. J. Heat Mass Transf. **17**, No. 3, pp. 205–214.

[9] Al-Astrabadi, F. R., O'Callaghan, P. W., and Probert, S. D., 1980, ''Thermal Resistance of Contacts: Influence of Oxide Film,'' AIAA Paper No. 80-1467.

[10] Clausing, A. M., 1966, ''Some Influences of Macroscopic Constrictions on the Thermal Contact Conductance,'' NASA Report No. ME-TN-242-2.

[11] Veziroglu, T. N., and Chandra, S., 1970, ''Direction Effect in Thermal Contact Conductance,'' Proceedings of the Fourth International Heat Transfer Conference, U. Grigull and E. Hahne, eds., **1**, Paris-Versailles, France, Elsevier, Amsterdam, pp. 1–11.

[12] Kitscha, W. W., and Yovanovich, M. M., ''Experimental Investigation of the Thermal Resistance of Sphere-Flat Contacts,'' Paper No. AIAA 74-113.

[13] Jones, A. M., O'Callaghan, P. W., and Probert, S. D., 1974, ''Effect of Interfacial Distortions on the Thermal Contact Resistance of Coaxial Cylinder,'' AIAA Progress in Astronautics and Aeronautics, **39**, Heat Transfer with Thermal Control Applications, M. M. Yovanovich, ed., MIT Press, pp. 21–44.

[14] Burde, S. S., and Yovanovich, M. M., 1978, ''Thermal Resistance at Smooth-Sphere/Rough-Flat Contacts: Theoretical Analysis,'' AIAA Paper 78-871.

[15] Majumdar, A., and Tien, C. L., 1991, ''Fractal Network Model for Contact Conductance,'' Int. J. Heat Mass Transf., **113**, August, pp. 516–525.

[16] Lambert, M. A., and Fletcher, L. S., 1995, ''Thermal Contact Conductance of Spherical, Rough Metals: Theory and Comparison to Experiment,'' *4th ASME/JSME Thermal Engineering Joint Conference*, Honolulu, HI, March 19–24.

[17] Roess, L. C., 1948, ''Theory of Spreading Conductance,'' Appendix of N. D. Weills and E. A. Ryder, *Thermal Resistance Measurements on Joints Formed Between Stationary Metal Surfaces*, Semi-Annual ASME Heat Transfer Division Meeting, Milwaukee, WI.

[18] Clausing, A. M., and Chao, B. T., 1965, ''Thermal Contact Resistance in a Vacuum Environment,'' ASME J. Heat Transfer, **87**, No. 3, pp. 243–251.

[19] Hertz, H., 1881, ''On the Contact of Elastic Bodies,'' J. Reine Angew. Math., **92**, pp. 156–171.

[20] Marotta, E. E., 1997, ''Thermal Contact Conductance of Non-Flat, Non-Metallic, Isotropic Roughened Coated Surfaces: Analytical and Experimental Investigation,'' Ph.D. dissertation, Texas A&M University, College Station, TX.

[21] Greenwood, J. A., and Tripp, J. H., 1967, ''The Elastic Contact of Rough Spheres,'' ASME J. Appl. Mech., March, pp. 153–159.

[22] Marotta, E. E., and Fletcher, L. S., 1998, ''Thermal Contact Conductance for Aluminum and Stainless Steel Contacts: Analytical and Experimental Comparison,'' J. Thermophys. Heat Transfer, **12**, No. 3, pp. 374–381.

[23] Kline, S. J., and McClintock, F. A., 1953, ''Describing Uncertainties in Single-Sample Experiments,'' Mechanical Engineering, **75**, No. 1, pp. 3–8.

[24] Peterson, G. P., and Fletcher, L. S., 1989, ''Measurement of the Thermal Contact Conductance and Thermal Conductivity of Anodized Aluminum Coatings,'' ASME J. Heat Transfer, **112**, pp. 579–585.

[25] Lambert, M. A., Marotta, E. E., and Fletcher, L. S., 1995, ''The Thermal Contact Conductance of Hard and Soft Coat Anodized Aluminum,'' ASME J. Heat Transfer, **117**, No. 2, pp. 270–275.

[26] Ogden, T. R., Rathsam, A. D., and Gilchrist, J. T., 1987, ''Thermal Conductivity of Thick Anodic Oxide Coatings on Aluminum,'' Mater. Lett., **5**, No. 3, Elsevier Science, New York, pp. 84–87.

C. Aviles-Ramos

A. Haji-Sheikh

Department of Mechanical and
Aerospace Engineering,
The University of Texas at Arlington,
Arlington, TX 76019-0023

J. V. Beck

Department of Mechanical Engineering,
Michigan State University,
East Lansing, MI 48824-1226

K. J. Dowding

Thermal Sciences Department,
Sandia National Laboratory,
Albuquerque, NM 87185-0835

Estimation of Thermophysical Properties by the Spectral Method—Development and Evaluation

This paper reports the evaluation of a spectral technique for estimating thermophysical properties. It demonstrates that one can construct a virtual quasi-steady periodic experiment from a limited but properly selected set of transient non-periodic data. In the spectral domain, the phase angles of the responses at different locations relative to a periodic input signal depend on the thermophysical properties. For the purpose of this evaluation, the transient temperature responses to a surface heat flux input are analytically obtained at pre-selected sensor locations. The transient data are converted to periodic data, phase angles are computed, and thermophysical properties are estimated. All deviations from known property values due to numerical errors are reported.
[DOI: 10.1115/1.1336507]

Keywords: *Conduction, Heat Transfer, Inverse, Properties, Thermophysical*

Introduction

The estimation of thermophysical properties for a complex system needs accurately measured transient temperature at pre-selected sites. In these applications, various inverse techniques have emerged in the literature. They permit the estimation of thermophysical properties from measured temperature data. Parker et al. [1] developed the Flash method for the estimation of thermal diffusivity in slab specimens. Taylor [2] extended Parker's flash method to high temperatures utilizing a laser pulse. Mottram et al. [3] reported thermal diffusivity measurements in fiber-phenolic resin composites. Donaldson et al. [4] used a laser pulse for thermal diffusivity measurement by a radial heat flow method. Dowding et al. [5,6] used electric heaters to conduct one and two-dimensional experiments to estimate orthotropic thermal properties of a carbon-carbon composite.

This theoretical inverse study uses phase angles and amplitudes instead of local temperature to estimate the thermophysical properties. Among earlier work, Hensel [7] has described use of the Fast Fourier Transform (FFT) and frequency domain adjoint analysis in parameter estimation with applications to heat transfer. According to the sensitivity analysis for sinusoidal heat input, Haji-Sheikh et al. [8], it is possible to accurately estimate the thermal diffusivity if phase angles are experimentally obtained. Often, the acquisition of the phase angle requires only the functional variation of temperature; therefore, one can measure a temperature-dependent effect and calculate the phase angle without knowing the exact value of temperature or heat flux. Among the candidates whose magnitudes can be affected by temperature are electrical resistivity, voltage output from a bimetallic junction, change of surface reflectance for polished metals, and emitted surface radiation. In some applications, e.g., laser heating, it is difficult, if not impossible, to supply a well-defined harmonic heat flux to a surface. However, it is possible to have a heat flux pulse at a surface and gather a well-defined set of experimental response data. This paper demonstrates that response data due to a non-periodic heat flux pulse can be used to generate multi-frequency data, referred to as virtual periodic data or virtual data herein. The virtual periodic data is used to develop a virtual experiment primarily to predict the phase angles and to estimate the selected thermophysical properties.

The technique presented here is a conceptual method of using an inverse analysis in the spectral domain to determine the thermophysical properties. This method can provide accurate results when it is not possible to obtain periodic data. Accordingly, one can use virtual periodic data instead of hard-to-get real periodic data for determining the thermophysical properties. A method of obtaining a set of virtual periodic data is discussed in the next section. To provide a critical evaluation, a quasi-steady-state virtual experiment is carried out using analytically calculated temperature.

Construction of Virtual Periodic Data

Preliminary to any analysis, it is necessary to discuss a method of constructing a set of quasi-steady periodic data. The following analysis applies to a linear system where the thermophysical properties within a narrow temperature range are assumed constant about a mean temperature; potential applications include high temperature and thin film studies. The development of this concept is related to the behavior of the Fourier series. Consider a solid that is subject to a typical non-periodic heat input $q(t)$ during time 0 to t_s as shown in Fig. 1(a). Assume the experimental response data, e.g., temperature data are acquired during the heating period t_s and the data acquisition is continued after heating stops and until any change in the response is negligible. The step-by-step procedures to obtain virtual periodic data are described below:

Step 1. The first step is to acquire response data such as temperature at every (x_l, y_l) location and the data shall be designated as $R_0(x_l, y_l, t)$ in the following steps. For the sake of brevity and without loss of any generalization, it is assumed the conduction of heat is two-dimensional.

Step 2. This step describes the procedure to construct a set of quasi-steady periodic data. One can arbitrarily select a time t_1, preferably $t_1 \geqslant t_s$, and expand the input heat flux $q(t)$ in the Fourier series within $0 < t < \tau_0$ using equation

---

Contributed by the Heat Transfer Division for publication in the JOURNAL OF HEAT TRANSFER. Manuscript received by the Heat Transfer Division June 18, 1999; revision received, July 10, 2000. Associate Editor: A. Majumdar.

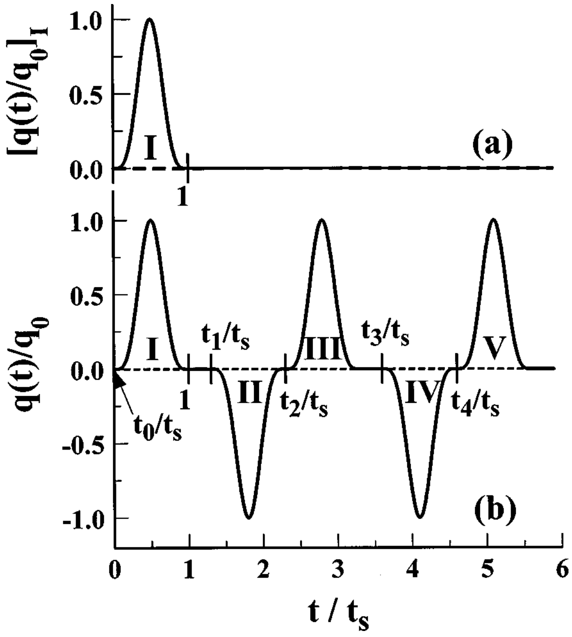

Fig. 1 A typical dimensionless heat flux: (*a*) the original heat pulse; and (*b*) the constructed periodic heat flux

$$q(t)/q_0=\sum_{n=1}^{\infty} a_n \sin(n\pi t/\tau_0), \tag{1a}$$

where $\tau_0=(t_s+t_1)/2$. The left side of this equation represents a surface heat flux pulse during $0\leq t\leq t_s$ and it is plotted in Fig. 1(*a*). When using a Fourier sine series, Eq. (1*a*), one assumes a periodic form for $q(t)/q_0$ as plotted versus the dimensionless time t/t_s in Fig. 1(*b*) for $0<t/t_s<6$. Figure 1(*b*) contains a series of positive and negative inputs. Figure 1(*b*) shows a period equal to t_s+t_1 that corresponds to a frequency $\nu=\pi/\tau_0$. Once the frequency ν is determined by arbitrary selection of t_1, Eq. (1*a*) expresses the data as a Fourier series of $\sin(n\pi t/\tau_0)=\sin(n\nu t)$ that represent a set of harmonic functions with pre-assigned frequencies. The time domain within each period now includes a positive pulse and a negative pulse, see Fig. 1(*b*). Therefore, one can arbitrarily select t_1, compute $\tau_0=(t_s+t_1)/2$ and $\nu=\pi/\tau_0$, and then use the frequencies $n\nu$, for $n=1,2,\cdots$, to analyze the multi-frequency signals.

Step 3. The task within this step is to use superposition and account for the effect of individual heat pulses shown in Fig. 1(*b*). The first pulse designated by I starts at $t_0=0$ and produces a response equal to $R_0(x_l,y_l,t)$ at a location (x_l,y_l) for $t>0$. The next pulse, Pulse II, is the same as Pulse I except it has a negative magnitude and begins at time t_1; this pulse provides a response equal to $-R_0(x_l,y_l,t-t_1)$ at (x_l,y_l) for $t>t_1$. This process can be continued for the third pulse, fourth pulse, and so on. Therefore, for a linear system, one can use superposition to construct a periodic response $R(x_l,y_l,t)$ from a non-periodic response $R_0(x_l,y_l,t)$. The superposition using the relation

$$R(x_l,y_l,t)=\sum_{j=0}^{N_j}(-1)^j R_0(x_l,y_l,t-t_j), \tag{1b}$$

where $t_j=j\tau_0+(\tau_0-t_s)[1-(-1)^j]/2$ and $R_0(x_l,y_l,t-t_j)=0$ when $t<t_j$, yields quasi-steady periodic response to a periodic input signal when N_j is sufficiently large. The values of t_0,t_1,t_2, etc. are designated in Fig. 1(*b*).

Step 4. Once the virtual periodic data $R(x_l,y_l,t)$ at all pre-selected sensor locations are available, the fourth step is finding the phase angles and amplitudes for predetermined frequencies ν, 2ν, 3ν, etc. One can apply Discrete Fourier Transform (DFT) or Fast Fourier Transform (FFT) ([9]) to the input and response signals to obtain phase angles and amplitudes for all relevant frequency signals at all (x_l,y_l) locations. Both DFT and FFT are readily available packages to perform Fourier analysis.

Step 5. At any given frequency, it is necessary to select a suitable computation method and compute the response $R(x_l,y_l,t)$ for a given sinusoidal heat input. Therefore, in this study, the fifth step is the analytical or numerical prediction of a steady periodic temperature response for comparison with the signal processing results.

Step 6. The sixth and final step is to compare experimentally determined phase angles and amplitudes with those computed analytically and to estimate the thermophysical properties by minimizing the differences. Before attempting to perform this inverse procedure, it is necessary to select a geometrical configuration and perform analytical studies mainly to gain insight into the problem.

Direct Analysis

As a test case, a two-region system, as shown in Fig. 2, is selected. Region 1 is orthotropic with thermal conductivities k_{1x} and k_{1y} in x and y directions, density ρ_2, and specific heat c_{p1}. Region 2 is homogeneous with thermal conductivity k_2, density ρ_2, and specific heat c_{p2}. The relevant dimensions *a*, *b*, *c*, and *d* are shown in Fig. 2. All surfaces are adiabatic except at $y=c$ where there is a heat flux over $0<x\leq d$.

The analytical temperature solution for prescribed heat flux over all surfaces is in Aviles-Ramos et al. [10]. The conduction of heat in the two-layer body depicted in Fig. 2 is described by the diffusion equation in region 1 as

$$k_{1x}\frac{\partial^2 T_1}{\partial x^2}+k_{1y}\frac{\partial^2 T_1}{\partial y^2}=\rho_1 c_{p1}\frac{\partial T_1}{\partial t} \tag{2a}$$

and the diffusion equation in region 2,

$$k_2\frac{\partial^2 T_2}{\partial x^2}+k_2\frac{\partial^2 T_2}{\partial y^2}+g_2(x,y,t)=\rho_2 c_{p2}\frac{\partial T_2}{\partial t}, \tag{2b}$$

where $g_2(x,y,t)$ is a volumetric heat source function that could include the surface heat flux. The solutions of Eqs. (2*a*) and (2*b*) are available in Aviles-Ramos et al. [10] for the following boundary and initial conditions:

$$\frac{\partial T_1}{\partial x}=0 \text{ and } \frac{\partial T_2}{\partial x}=0 \text{ at } x=0 \text{ and } x=a \tag{3}$$

$$\frac{\partial T_1}{\partial y}=0 \text{ at } y=0 \tag{4}$$

$$T_1(x,y,t)=T_2(x,y,t) \text{ at } y=b \tag{5}$$

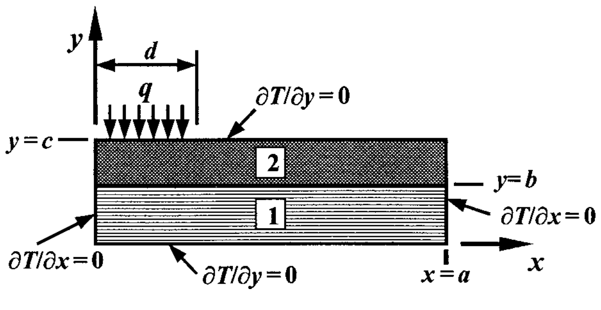

Fig. 2 Schematic of a two-layer body and boundary conditions

$$k_{1x}\frac{\partial T_1}{\partial x}=k_2\frac{\partial T_2}{\partial y} \quad \text{at } y=b \tag{6}$$

$$k_2\frac{\partial T_2}{\partial y}=0 \quad \text{at } y=c \tag{7}$$

$$T_1(x,y,t)=0 \quad \text{and} \quad T_2(x,y,t)=0 \quad \text{at } t=0. \tag{8}$$

A solution to the problem stated by Eqs. (2*a*) through (8) is ([10])

$$T_i(x,y,t)=\sum_{n=0}^{\infty}\sum_{m=0}^{\infty}\frac{F_{i,mn}(x,y)}{N_{mn}}\int_{\tau=0}^{t}\exp[-\lambda_{mn}^2(t-\tau)]\times\left[\int_0^a\int_b^c g_2(x',y',\tau)F_{2,mn}(x',y')dy'dx'\right]d\tau;$$

$$\text{for } i=1 \text{ or } 2, \tag{9}$$

where $F_{i,mn}(x,y)$ are the eigenfunctions given as

$$F_{1,mn}(x,y)=\cos(n\pi x/a)\cos(\gamma_{mn}k_r y) \tag{10}$$

$$F_{2,mn}(x,y)=\cos(n\pi x/a)[B_{mn}\sin(\eta_{mn}y)+C_{mn}\cos(\eta_{mn}y)] \tag{11}$$

$$N_{mn}=\int_0^a\int_0^b\rho_1c_{p1}[F_{1,mn}(x',y')]^2dy'dx'+\int_0^a\int_b^c\rho_2c_{p2}[F_{2,mn}(x',y')]^2dy'dx' \tag{12}$$

$k_\gamma=\sqrt{k_{1x}/k_{1y}}$, γ_{mn} and η_{mn} are related to the eigenvalues λ_{mn} by the equation

$$\gamma_{mn}=\sqrt{\gamma_{mn}^2/\alpha_{1x}-(n\pi/a)^2} \tag{13}$$

$$\eta_{mn}=\sqrt{\lambda_{mn}^2/\alpha_2-(n\pi/a)^2}, \tag{14}$$

where $\alpha_{1x}=k_{1x}/\rho_1c_{p1}$ and $\alpha_2=k_2/\rho_2c_{p2}$. The contact conditions, Eqs. (5) and (6), yield B_{mn} and C_{mn},

$$B_{mn}=\cos(\gamma_{mn}k_rb)\sin(\eta_{mn}b)-(\gamma_{mn}/\eta_{mn})(\sqrt{k_{1x}k_{1y}}/k_2)\sin(\gamma_{mn}k_rb)\cos(\eta_{mn}b) \tag{15}$$

$$C_{mn}=\cos(\gamma_{mn}k_rb)\cos(\eta_{mn}b)+(\gamma_{mn}/\eta_{mn})(\sqrt{k_{1x}k_{1y}}/k_2)\sin(\gamma_{mn}k_rb)\sin(\eta_{mn}b). \tag{16}$$

Equation (9) can account for the effect of a surface heat flux $q(x,t)$ at $y=c$, see Fig. 2, by setting $g_2(x,y,t)$ equal to

$$g_2(x,y,t)=q(x,t)\,\delta(y-c), \tag{17}$$

where $\delta(y-c)$ is the Dirac delta function. A heat flux surface function $q(x,t)$ at $y=c$ is chosen, to conform to the Dowding et al. [6] experiments, as

$$q(x,t)=q_0[H(x)-H(x-d)][H(t)-H(t-t_s)], \tag{18}$$

where q_0 is a constant, the step function $H(\cdot)$ is the Heaviside function, and t_s is the time when the heat flux goes to zero. Equation (18) contains a square wave function expressed by two step functions $H(t)-H(t-t_s)$; it is expanded in Fourier sine series for $0\leqslant t\leqslant\tau_0$ to produce

$$q(x,t)=\frac{4q_0}{\pi}[H(x)-H(x-d)]\times\sum_{k=1}^{\infty}\frac{1}{k}\sin^2(k\nu t_s/2)\sin(k\nu t); \quad t\leqslant\tau_0, \tag{19}$$

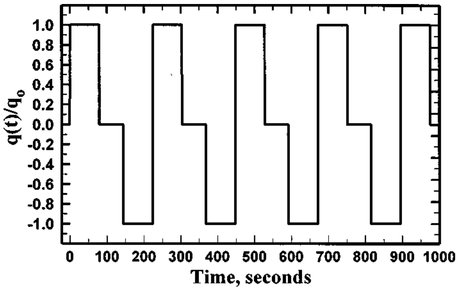

Fig. 3 Heat flux input to produce virtual temperature responses, $t_s=80$ sec. and $\tau_o=112$ sec.

where ν is the angular frequency. It is defined as

$$\nu=\pi/\tau_0 \tag{20}$$

and τ_0 is selected arbitrarily so that $\tau_0>t_s$. When analyzing actual experimental data, the time range of available data influences the selection of τ_0.

Temperature Response to a Periodic Heat Flux. Equation (19) contains sinusoidal components of heat flux. Figure 3 shows the effect of the right side of Eq. (19) as q/q_0 is plotted for $0<t<1000$. This figure shows a periodic heat flux with a period of $2\tau_0$. It is of current interest to study the form of temperature at selected locations if the surface heat flux has the form depicted in Fig. 3. The temperature at any location should change periodically and should attain a quasi-steady periodic form as time becomes large. In an actual experiment, a quasi-steady condition may not be attainable; therefore, the goal is to acquire a set of virtual periodic data. Notice that the diffusion equation is linear; hence, all sinusoidal components of temperature at a given site will have the same angular frequencies, $k\nu$, as those of the input heat flux, Eq. (17), shown by Eq. (19). However, for each *k*-component of the surface heat flux in Eq. (19), the periodic component of temperature will have a phase shift depending on the location, signal angular frequency, and thermophysical properties.

The final form of the volumetric heat generation function $g_2(x,y,t)$ is obtained by substituting Eq. (19) into Eq. (17),

$$g_2(x,y,t)=\frac{4q_0}{\pi}\delta(y-c)[H(x)-H(x-d)]\times\sum_{k=1}^{\infty}\frac{1}{k}\sin^2(k\nu t_s/2)\sin(k\nu t). \tag{21}$$

The analytical solution is obtained substituting Eq. (21) into Eq. (9). Then, the temperature solution is cast in a convenient form for obtaining the phase angles and amplitudes, that is

$$T_i(x,y,t)=\sum_{k=1}^{\infty}\Psi_{i,k}(x,y)\sin[k\nu t-\varphi_{i,k}(x,y)]+\sum_{k=1}^{\infty}D_{i,k}(x,y)+\sum_{k=1}^{\infty}C_{i,k}(x,y,t) \tag{22}$$

for $i=1$ or 2. The amplitude, $\Psi_{i,k}(x,y)$, in Eq. (22) is

$$\Psi_{i,k}(x,y)=\sqrt{A_{i,k}^2(x,y)+B_{i,k}^2(x,y)} \tag{23}$$

and the corresponding phase angle, $\varphi_{i,k}(x,y)$, is

$$\varphi_{i,k}(x,y)=\tan^{-1}\left[\frac{-A_{i,k}(x,y)}{B_{i,k}(x,y)}\right]. \tag{24}$$

Other functions and parameters in Eqs. (22–24) are

$$
\begin{aligned}
A_{i,k}(x,y) = {} & -\frac{4q_0 d}{\pi}\,\frac{F_{i,00}(x,y)}{N_{00}}\,\frac{\sin^2(k\nu t_s/2)}{k^2\nu} - \frac{4q_0 a\nu}{\pi^2} \\
& \times \sum_{m=1}^{\infty}\sum_{n=1}^{\infty} \frac{F_{i,mn}(x,y)}{nN_{mn}} \\
& \times \frac{\Phi_{mn}(c)\sin(n\pi d/a)\sin^2(k\nu t_s/2)}{\lambda_{mn}^4+(k\nu)^2} \\
& - \frac{4q_0 d\nu}{\pi}\sum_{m=1}^{\infty} \frac{F_{i,m0}(x,y)}{N_{m0}}\,\frac{\Phi_{m0}(c)\sin^2(k\nu t_s/2)}{\lambda_{m0}^4+(k\nu)^2}
\end{aligned}
\tag{25}
$$

$$
\begin{aligned}
B_{i,k}(x,y) = {} & \frac{4q_0 a}{\pi^2}\sum_{m=1}^{\infty}\sum_{n=1}^{\infty} \frac{\lambda_{mn}^2 F_{i,mn}(x,y)}{nkN_{mn}} \\
& \times \frac{\Phi_{mn}(c)\sin(n\pi d/a)\sin^2(k\nu t_s/2)}{\lambda_{mn}^4+(k\nu)^2} \\
& + \frac{4q_0 d}{\pi}\sum_{m=1}^{\infty} \frac{\lambda_{m0}^2 F_{i,m0}(x,y)}{kN_{m0}}\,\frac{\Phi_{m0}(c)\sin^2(k\nu t_s/2)}{\lambda_{m0}^4+(k\nu)^2}
\end{aligned}
\tag{26}
$$

$$
\begin{aligned}
C_{i,k}(x,y,t) = {} & \frac{4q_0 a\nu}{\pi^2}\sum_{m=1}^{\infty}\sum_{n=1}^{\infty} \frac{F_{i,mn}(x,y)}{nN_{mn}} \\
& \times \frac{\Phi_{mn}(c)\sin(n\pi d/a)\sin^2(k\nu t_s/2)}{\lambda_{mn}^4+(k\nu)^2}\exp(-\lambda_{mn}^2 t) \\
& + \frac{4q_0 d\nu}{\pi}\sum_{m=1}^{\infty} \frac{F_{i,m0}(x,y)}{N_{m0}} \\
& \times \frac{\Phi_{m0}(c)\sin^2(k\nu t_s/2)}{\lambda_{m0}^4+(k\nu)^2}\exp(-\lambda_{m0}^2 t)
\end{aligned}
\tag{27}
$$

$$
D_{i,k}(x,y) = \frac{4q_0 d}{\pi}\left(\frac{F_{i,00}(x,y)}{N_{00}}\right)\frac{\sin^2(k\nu t_s/2)}{k^2\nu} \tag{28}
$$

$$
\Phi_{mn}(c) = B_{mn}\sin(\eta_{mn}c) + C_{mn}\cos(\eta_{mn}c). \tag{29}
$$

Equation (22) may be used to generate a set of analytically produced data. Equations (23) and (24) provide amplitudes and phase angles for property estimation.

Spectral Analysis and Property Estimation

Spectral Analysis for Amplitudes and Phase Angles Estimation. Equation (22) represents the direct solution for temperature distribution in a composite region due to the heat flux shown in Fig. 3. It provides the temperature as a function of time at any given spatial location if thermophysical properties of the materials are prescribed. In an inverse analysis, the thermophysical properties may be the unknowns to be determined. For this reason, it is desirable to place sensors at pre-selected locations and use the transient response of the sensors to estimate the thermophysical properties.

A periodic input heat flux induces a periodic temperature at the sensor locations with an angular frequency of the input signal. For example, if the input signal has components $\sin(k\nu t)$ with $k = 1,2,\cdots$, as identified by Eq. (19), then the temperature at any location will have components with exactly the same angular frequencies. Theoretically, it is possible to decompose such a temperature response into its harmonic components with the aforementioned frequencies. A spectral analysis is employed in order to extract the amplitudes and phase angles of the harmonic components.

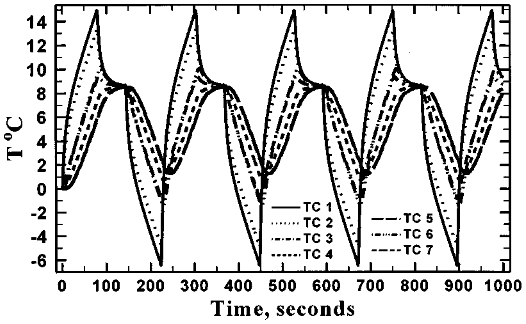

Fig. 4 Temperature data at seven locations generated using Eq. (22) for heat flux input as shown in Fig. 3

In general, a periodic function can be expressed in terms of the sine and cosine components using the Fourier series

$$
h(t) = \frac{1}{2}a_0 + \sum_{n=1}^{\infty}\left[a_n\cos(n\nu t) + b_n\sin(n\nu t)\right] \tag{30}
$$

over one period. When $h(t)$ is any periodic function such as temperature at a sensor location, the coefficients a_n and b_n are obtainable by numerical integration or by using a fast Fourier transform. Therefore, it is necessary to test the accuracy and efficiency of numerical techniques to compute a_n and b_n coefficients and then the phase angles and amplitudes.

Before addressing an experimental case, it is essential to validate this inverse analysis method by simulating temperature data analytically. A set of seven temperature responses is generated to investigate the accuracy of numerical computations. The sensor locations for simulated temperature sensors (x_l, y_l) are selected the same as those in Dowding et al. [11]. The coordinates of (x_l, y_l) for $l = 1$ through 7, using (x,y) axes shown in Fig. 2, are: (0.889, 0.9144), (1.905, 0.9144), (3.175, 0.9144), (4.290, 0.9144), (6.731, 0.9144) (1.270, 0), (6.35, 0), respectively; all units are in centimeters. Equation (22) is used to generate these signals for a virtual experiment assuming $q_0 = 0.5276\ \mathrm{W/cm^2}$ during $t_s = 80s$ of heating, then data are generated during a period of 448 sec. To obtain simulated data, Eqs. (1*b*) and (9) yield the same results as those from Eq. (22). A sensitivity analysis in Dowding et al. [11] discusses the selection of the heating time t_s for adequate response in the *x* and *y*-directions. Figure 4 shows these computed temperature responses. The analytically generated data in Fig. 4 show that the temperature solution becomes quasi-steady and periodic for times greater than $2\tau_0 = 224$ sec. The geometrical dimensions as shown in Fig. 2 are $a = 7.62$ cm, $b = 0.914$ cm, $c = 0.958$ cm, and $d = 2.36$ cm. The thermophysical properties used to produce simulated input data are for carbon-carbon composite in Region 1 and mica in Region 2. The property values for Region 1 are $k_{1x} = 0.608\ \mathrm{W/cm\cdot K}$, $k_{1y} = 0.039\ \mathrm{W/cm\cdot K}$, $\rho_1 c_{p1} = 1.56\ \mathrm{J/cm^3\cdot K}$ obtained from Dowding et al. ([6], Eqs. (2–4)) at a mean temperature of 72.5°C. The effective property values for Region 2 are $k_2 = 0.001\ \mathrm{W/cm\cdot K}$, $\rho_2 c_{p2} = 2.0\ \mathrm{J/cm^3\cdot K}$ Dowding et al. [5]. For a surface heat flux shown in Fig. 3, Eq. (22) produces periodic temperature responses at all thermocouple sites when $t \geqslant 2\tau_0 = 224s$. Indeed, the temperature responses are quasi-steady and periodic when $t > 224s$ with a period of 224 and Eq. (20) yields a frequency of 0.028 rad/s.

In general, Eq. (30) can be used to compute the phase angles and amplitudes of temperature at any location. The sensitivity analysis for temperature response by Dowding et al. [11], as mentioned earlier, shows that the temperature measurements at the corners of the specimen are the most sensitive. Note that the coordinates for $l = 1$, 2, 5, 6 and 7 are located near the corners of the specimen (see Fig. 2). The sensitivity coefficients for the phase angles defined by Eq. (24) were calculated at the locations (x_l, y_l) for $l = 1$ through $l = 7$. The results show that the sensitivity coef-

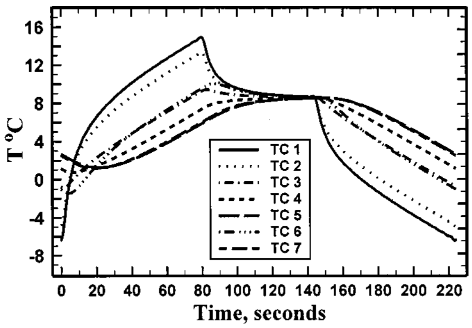

Fig. 5 Temperature responses for application of the FFT; a window within 224≤*t*≤448*s* is shifted to 0≤*t*≤224*s*

Table 2 Estimated thermophysical properties from the phase angles given in Table 1

N	k_{1x} $W/cm \cdot K$	k_{1y} $W/cm \cdot K$	$\rho_1 c_{p1}$ $J/cm^3 \cdot K$	k_2 $W/cm \cdot K$
2^8	0.6360 +4.7%	0.0411 +5.1%	1.628 +4.2%	0.00125 +25%
2^{12}	0.6140 +1.1%	0.0396 +1.1%	1.579 +1.1%	0.00101 +0.9%
2^{16}	0.6080 +0.065%	0.0392 +0.069%	1.563 +0.066%	0.00100 +0.1%
2^{19}	0.6077 +0.013%	0.0391 +0.015%	1.563 +0.013%	0.00100 +0%
Input data	0.6076	0.0391	1.562	0.00100

ficients for k_{1x}, k_{1y}, $\rho_1 c_{p1}$, and k_2 are linearly independent in the interval $0.028\,\text{rad/s} \leq kv \leq 0.7\,\text{rad/s}$. The sensitivity results showed tendencies similar to those for temperature in Dowding et al. [11].

There are established numerical schemes available in the literature to accomplish the task of computing the phase angles and amplitudes. The accuracy of these numerical techniques depends on the number of available data points within a computation window that is equal to one period. It is important to investigate the accuracy of widely used numerical schemes by analyzing the simulated temperature data within the second period of those data shown in Fig. 4, after a quasi-steady response has been attained. Here, Eqs. (23) and (24) can analytically provide the exact values of amplitudes and phase angles. Also, they can be computed from temperature data by using the Discrete Fourier Transform (DFT), see Press et al. [9]. The DFT can be computed with greater numerical efficiency using an algorithm called the Fast Fourier Transform (FFT) ([9]). The data within a window used for calculating the phase angles are shown in Fig. 5. The phase angles calculated from the temperature responses in Fig. 5 using the FFT are listed in Table 1. Results for different numbers of discrete points, *N*, within the window are shown in Table 1.

For comparison, Table 1 also provides the exact value of $\varphi_{1,1}$ in column 2. When $N = 2^8 = 256$, the deviation from the exact values is less than 1 percent. This deviation decreases as *N* increases. A value with 5 accurate significant figures is obtained when $N = 2^{19} = 524288$. These results show that the finite-duration numerical sequences obtained from the temperature response displayed in Fig. 5 are the typical sampled points that should be used when applying the FFT to temperature responses. The phase angles are also calculated using the Fourier coefficients in Eq. (30). They agree to 6 decimal figures with entries in column 2 of Table 1; 512 equally spaced time increments are used in the numerical integration.

Estimation of Thermophysical Properties. Once the phase angle is computed, the next task is the estimation of thermophysical properties from a set of nonlinear equations. Since the exact value of the phase angle is known a priori, the data reveals the effect of a finite sample size in the FFT window on estimated thermophysical properties. The computed phase angles in Table 1 are used to compute the thermophysical properties. Further details concerning the method of computing the thermophysical properties from given phase angles and estimation of error is in Aviles-Ramos [12]. Table 2 shows the estimated values of thermophysical properties for the number of data points $N = 2^8, 2^{12}, 2^{16}, 2^{19}$ used in the FFT. For comparison, the final row in the table is the true property values described earlier in this paper. Table 1 shows the effect of numerical integration that is an integral part of FFT.

There are four thermophysical properties that can be estimated because the sensitivity coefficients of the phase angles for k_2 and $\rho_2 c_{p2}$ are linearly dependent. For this reason, it is assumed that $\rho_2 c_{p2} = 2.0\,\text{J/cm}^3 \cdot \text{K}$ is known a priori. Next, the sum of squares of differences between calculated phase angles and phase angles from the simulated data

$$S = \sum_{l=1}^{7} \{[\varphi_{1,1}(x_l, y_l)]_{\text{calc.}} - [\varphi_{1,1}(x_l, y_l)]_{\text{FFT}}\}^2 \tag{31}$$

is minimized. Only a single frequency, $k = 1$, is used in this minimization. Brent's [13] method is used in the minimization leading to the computation of the thermophysical properties. Table 2 includes the error values when computing the thermophysical properties with different numbers of discrete points. In general, when *N* is large, the error is small. The error in estimated thermophysical properties is larger than the error in phase angles shown in Table 1.

To determine the effect of random noise on the numerical sequences fed to the FFT, a uniformly distributed random noise is added to these sequences. The added random noise is equal to ±3 percent of the maximum temperature rise at thermocouple No. 1; approximately ±0.5°C. Accordingly, the random numbers are bounded within the limits $-0.03\,T_m \leq \varepsilon \leq 0.03\,T_m$, where $T_m = T(x_1, y_1, t)$ is a near maximum temperature in the data set. Equation (22) is used to generate 513 data points within the computational window; the time between two consecutive data points is 0.4375 sec. Random noise, as defined earlier, is added to the

Table 1 Exact and numerical phase angles, $\varphi_{1,1}(x_l, y_l)$ at seven thermocouple locations, (x_l, y_l), calculated using the FFT

l in (x_l, y_l)	Exact $\varphi_{1,1}$ Eq. (24)	$\varphi_{1,1}$, FFT $N = 2^8$	$\varphi_{1,1}$, FFT $N = 2^{12}$	$\varphi_{1,1}$, FFT $N = 2^{16}$	$\varphi_{1,1}$, FFT $N = 2^{19}$
1	0.76278	0.75604	0.76236	0.76275	0.76278
2	0.86149	0.85417	0.86103	0.86146	0.86149
3	1.44307	1.43174	1.44237	1.44303	1.44307
4	1.86533	1.85193	1.86449	1.86527	1.86532
5	2.25908	2.24537	2.25823	2.25903	2.25908
6	1.45698	1.44582	1.45628	1.45693	1.45697
7	2.21997	2.20626	2.21911	2.21991	2.21996

Table 3 Exact and numerical phase angles, $\varphi_{1,1}(x_l, y_l)$ at seven thermocouple locations with 3 percent random error added

l in (x_l, y_l)	Exact $\varphi_{1,1}$ Eq. (24)	$\varphi_{1,1}$, FFT $N = 2^8$	$\varphi_{1,1}$, FFT $N = 2^{12}$	$\varphi_{1,1}$, FFT $N = 2^{16}$	$\varphi_{1,1}$, FFT $N = 2^{19}$
1	0.76278	0.75651	0.76108	0.76147	0.76150
2	0.86149	0.85495	0.86248	0.86291	0.86294
3	1.44307	1.43235	1.44320	1.44386	1.44390
4	1.86533	1.84555	1.85895	1.85972	1.85977
5	2.25908	2.24367	2.25342	2.25423	2.25428
6	1.45698	1.43791	1.44881	1.44946	1.44949
7	2.21997	2.20480	2.21955	2.22037	2.22041

Table 4 Estimated thermophysical properties from the phase angles with random error in Table 3

N	k_{1x} W/cm·K	k_{1y} W/cm·K	$\rho_1 c_{p1}$ J/cm^3·K	k_2 W/cm·K
2^8	0.6347 +4.5%	0.0418 +6.7%	1.628 +4.2%	0.00135 +35%
2^{12}	0.6312 +3.9%	0.0413 +5.7%	1.627 +4.2%	0.00107 +6.8%
2^{16}	0.6310 +3.8%	0.0414 +5.7%	1.627 +4.2%	0.00105 +5.4%
2^{19}	0.6309 +3.8%	0.0413 +5.6%	1.627 +4.1%	0.00105 +5.3%
Input data	0.6076	0.0391	1.562	0.00100

temperature data. The same set of data is used for each of the N values depicted in Table 1. The interpolation between data points is used to generate the input to the FFT. Then, the resultant sequences are fed to the FFT and the computed phase angles are shown in Table 3. The data show that the departure from the exact values of the phase angle is small, about 0.5 percent; for a random noise of ±3 percent, especially when N is large. This is due to the noise filtering capability of the FFT. Alternatively, instead of using FFT, the phase angles are obtained by calculating the Fourier series coefficients in Eq. (30). The calculated phase angles agree with data in column 5 to four decimal places.

The computed phase angles in Table 3 are used to estimate the thermophysical properties. This estimation shows the effect of the random error in the virtual data on the estimated thermophysical properties. These computed properties are shown in Table 4. The error in the computed phase angles, for $N=2^{19}$, in Table 3 is very small, less than 0.2 percent. However, the errors in the estimated properties, Table 4, are much larger but they remain at the same order as the input noise; 3.82 percent, 5.59 percent, and 4.13 percent for k_{1x}, k_{1y}, and $\rho_1 c_{p1}$, respectively.

Table 2 shows that, in the absence of the random noise, the error in the estimated property values decreases and becomes negligible as N increases. In contrast, for data in Table 4, the errors remain nearly constant for N larger than 2^8 that is less than the number of data (513) per thermocouple. It is likely that the random noise in temperature data produces this anomaly as it increases the phase angle error in the high frequency components of the response data. As shown in Haji-Sheikh et al. [10], for a harmonic component $\Delta\varphi = \Delta T/\Psi$, that is, an error ΔT in the harmonic data produces an error $\Delta\varphi$ while Ψ is the amplitude. Since the amplitude in high frequency data is small then the noise in temperature data can amplify the error in the phase angle.

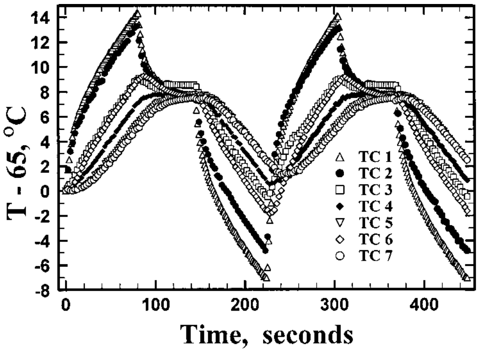

Fig. 6 Experimental temperature data for $t<112s$ from Dowding et al. [6] and virtual data generated for $t>112s$

Table 5 Thermophysical properties for the carbon-carbon composite sample, initial temperature 65°C

Source	k_{1x} W/cm·K	k_{1y} W/cm·K	$\rho_1 c_{p1}$ J/cm^3·K
Dowding et al. (1996)	0.584	0.0389	1.52
Spectral method	0.602	0.0367	1.61
Dowding et al. (1996), row 1, perfect insulation	0.604	0.0358	1.67

The simulated temperature data generated earlier to study the newly proposed method closely approximates the experimental data from Dowding et al. [6]. To assist the efficiency of this new method, experimental data are studied. Properties estimated using the measured temperature response are then compared with those estimated using the proposed method. Experimental data from Dowding et al. [6] are shown in Fig. 6 for $t<112s$. They are acquired from an experiment that can be represented as shown in Fig. 2 when $q_0=0.5276\,\text{W/cm}^2$ over $y=c$ and $0<x<a$ surface for a heating duration of 80 seconds. The data for $t>112s$ are produced using Eq. (1*b*). To generate data when $t>112s$ for inclusion in R_0, Eq. (1*b*), it is necessary to extrapolate the experimental data. Clearly, the experimental data from Dowding et al. [6] should approach a constant value as $t\to\infty$ if the surfaces are perfectly insulated. However, finding this limit is not a critical step since it only provides a small temperature offset and it has a negligible effect on the phase angles and amplitudes. To obtain virtual periodic data from acquired experimental data, Eq. (1*b*) is used and the results for $t>112$ are given in Fig. 6. The estimated thermophysical properties of carbon-carbon, Region 1, using measured temperature data, as reported in Dowding et al. [6], are in the first row of Table 5. The second row in Table 5 contains the corresponding virtual data analyzed by this spectral method. The calculation of Dowding et al. [6] included the effect of heat loss through the insulation at $y=0$ whereas the data in the second row assume perfect insulation. The data in the third row, Table 5, are computed in the same manner as those in the first row except assuming perfect insulation at $y=0$. Although the differences between data in the first and second rows is within the error bounds reported in Dowding et al. ([6] see Fig. 4), the difference between data in the second and third rows is further reduced.

Remarks and Conclusions

The technique for the computation of the phase angle presented here is purely analytical. When it is not possible to obtain an analytical temperature solution for a given set of thermophysical properties, a numerical solution becomes necessary. In general, one can consider a solid subject to a harmonic (sinusoidal) input, such as heat flux, temperature, or volumetric heat source; e.g., $q=q_0\sin(\nu t)$. As time becomes large, the temperature at any point within the solid assumes a periodic form described by the relation $T(x,y,t)=A(x,y)\cos(\nu t)+B(x,y)\sin(\nu t)$. Substituting $T(x,y,t)$ in the diffusion equation yields two simultaneous relations

$$\nabla\cdot[k(x,y)\nabla A(x,y)]+\rho(x,y)c_p(x,y)\nu B(x,y)=0 \quad (33a)$$

$$\nabla\cdot[k(x,y)\nabla B(x,y)]-\rho(x,y)c_p(x,y)\nu A(x,y)=0 \quad (33b)$$

with appropriate boundary conditions. Equations (33*a*,*b*) may be solved by a numerical scheme, see Hensel [7].

This procedure is mathematically based and the initial emphasis is directed toward Fourier conduction. The results, using simulated temperature data show that an accurate estimation of thermophysical properties is possible. In some applications, it may be impossible to provide accurate temperature data; instead one can use any other temperature-dependent property to determine the phase angle and estimate the unknown thermophysical properties without knowing the temperature magnitude.

Figure 4 shows steady periodic temperature values beyond the first period. There is a constant temperature offset because $F_{i,00}(x,y)$ in Eq. (28) is a constant that makes $D_{i,k}(x,y)$ a constant. Therefore, a Fourier series of sine and cosine can adequately describe the temperature distribution. Since the dominant frequencies are known in advance, the numerical integration to compute the Fourier coefficients is computationally faster than the FFT.

The potential applications include conduction in materials with non-Fourier behavior. However, since this proposed methodology is new, the computation window and consequently the period of the virtual data are selected to analyze the experimental data Fig. 6. Indeed, the sensitivity of the phase angle to a specific property depends on the location of the sensor and the specific frequency in the Fourier analysis. The sensitivity to a single parameter is discussed in Haji-Sheikh et al. [10]. The study of sensitivity coefficients for multi-parameter estimation is a subject for future studies.

Acknowledgments

The first two authors wish to acknowledge the support of the National Science Foundation through a supplemental fund, Grant No. CTS-9400647.

Nomenclature

a, b, c, d = dimensions in Fig. 2, cm
$A_{i,k}(x,y)$ = function, Eq. (25)
$B_{i,k}(x,y)$ = function, Eq. (26)
B_{mn} = coefficients, Eq. (15)
C_{mn} = coefficients, Eq. (16)
$C_{i,k}(x,y)$ = function, Eq. (27)
c_{p1} = specific heat, region 1, J/kg·K
c_{p2} = specific heat, region 2, J/kg·K
$D_{i,k}(x,y)$ = function, Eq. (28)
$F_{1,mn}(x,y)$ = eigenfunction for two-dimensional solution, Eq. (10)
$F_{2,mn}(x,y)$ = eigenfunction for two-dimensional solution, Eq. (11)
$g_i(x,y,t)$ = volumetric heat source, W/cm^3
$H(t)$ = Heaviside function
i = index for material domain
k = index in the Fourier series expansion
k_{1x} = thermal conductivity in region 1 along x, W/cm·K
k_{1y} = thermal conductivity in region 1 along y, W/cm·K
k_2 = thermal conductivity in region 2, W/cm·K
k_r = $(k_{1x}/k_{1y})^{1/2}$
m, n = indices in eigenfunctions
N = number of sampled points in discrete Fourier transform
N_{mn} = norm of two-dimensional solution, Eq. (12)
q = heat flux function, Eq. (18), W/cm^2
q_0 = constant heat flux, W/cm^2
R = response function
t = time, s
t_s = duration of heating, s
$T_i(x,y,t)$ = temperature in regions 1 or 2, Eqs. (22), °C
TC = thermocouple
x, y = coordinates, cm

Greek Symbols

α_{1x} = thermal diffusivity, $k_{1x}/\rho_1 c_{p1}$, cm^2/s
α_2 = thermal diffusivity $k_2/\rho_2 c_{p2}$, cm^2/s
γ_{mn} = eigenvalues, Eq. (13), cm^{-1}
δ = Dirac delta function
ε = random error, °C
η_{mn} = eigenvalues, Eq. (14), cm^{-1}
λ_{mn} = eigenvalues for time, s^{-1}
ν = frequency, rad/s
ρ_1, ρ_2 = density of regions 1 and 2, kg/cm^3
τ_0 = final experimental measurement time, s
$\varphi_{i,k}(x,y)$ = phase angles, Eq. (24), rad
$\Phi_{mn}(c)$ = functions, Eq. (29)
$\Psi_{i,k}(x,y)$ = amplitudes, Eq. (23)

References

[1] Parker, W. J., Jenkins, R. J., Butler, C. P., and Abbott, G. L., 1961, ''Flash Method of Determining Thermal Diffusivity, Heat Capacity, and Thermal Conductivity,'' J. Appl. Phys., **32**, pp. 1679–1684.
[2] Taylor, R., 1980, ''Construction of an Apparatus for Heat Pulse Thermal Diffusivity Measurements From 300K–3000K,'' J. Phys. E, **3**, pp. 1193–1199.
[3] Mottram, J. T., and Taylor, R., 1987, ''Thermal Conductivity of Fiber-Phenolic Resin Composites: Part I—Thermal Diffusivity Measurements,'' Compos. Sci. Technol., **29**, pp. 189–210.
[4] Donaldson, A. B., and Taylor, R. E., 1975, ''Thermal Diffusivity Measurements by a Radial Heat Flow Method,'' J. Appl. Phys., **10**, pp. 4584–4589.
[5] Dowding, K. J., Beck, J. V., Urlich, A., Blackwell, B., and Hayes, J., 1995, ''Estimation of Thermophysical Properties and Surface Heat Flux in Carbon-Carbon Composite,'' J. Thermophys. Heat Transfer, **9**, No. 2, pp. 345–361.
[6] Dowding, K. J., Beck, J. V., and Blackwell, B., 1996, ''Estimation of Directional-Dependent Thermal Properties in a Carbon-Carbon Composite,'' Int. J. Heat Mass Transf., **39**, No. 15, pp. 3157–3164.
[7] Hensel, E., 1991, *Inverse Theory and Applications for Engineers*, Prentice-Hall, Englewood Cliffs, NJ.
[8] Haji-Sheikh, A., Hong, Y. S., You, S. M., and Beck, J. V., 1998, ''Sensitivity Analysis for Thermophysical Property Measurements Using Phase Delay,'' ASME J. Heat Transfer, **120**, pp. 568–576.
[9] Press, W. H., Teukolsky, S. A., Vetterling, W. T., and Flannery, B. P., 1992, *Numerical Recipes in FORTRAN: The Art of Scientific Computing*, Cambridge University Press, London, UK.
[10] Aviles-Ramos, C., Haji-Sheikh, A., and Beck, J. V., 1998, ''Exact Solution of Heat Conduction in Composites and Application to Inverse Problems,'' ASME J. Heat Transfer, **120**, No. 3, pp. 592–599.
[11] Dowding, K. J., Blackwell, B. F., and Cochran, J., 1998, ''Application of Sensitivity Coefficients for Heat Conduction Problems,'' Sandia National Laboratories, SAND098-0543C.
[12] Aviles-Ramos, C., 2000, ''Estimation of Thermophysical Properties of an Orthotropic Solid in a Two-Layer Body,'' Ph.D. dissertation, The University of Texas at Arlington, Arlington, TX.
[13] Brent R. P., 1973, *Algorithms for Minimization Without Derivatives*, Prentice-Hall, Inc., Englewood Cliffs, NJ.

Modified Hazen-Dupuit-Darcy Model for Forced Convection of a Fluid With Temperature-Dependent Viscosity

Arunn Narasimhan

José L. Lage

Laboratory for Porous Materials Applications,
Mechanical Engineering Department,
Southern Methodist University,
Dallas, TX 75275 0337

We investigate numerically the global pressure-drop of fluids with temperature dependent viscosity, flowing through a porous medium channel bounded by two parallel isoflux surfaces. By reviewing the development of the Hazen-Dupuit-Darcy (HDD) equation we bring to light the inappropriateness of the model in estimating the global pressure-drop of fluids with temperature dependent viscosity. Albeit this observation, we tested the accuracy of the HDD model in comparison with numerical results by using three alternatives, namely (1) fluid viscosity determined at the average bulk temperature, (2) fluid viscosity determined at the log-mean bulk temperature and (3) fluid viscosity replaced by a channel-length averaged fluid viscosity. The HDD model is inadequate because the temperature dependent fluid viscosity surprisingly affects both, viscous and form, global drag terms. We propose and validate a new global model, which accounts for the effects of temperature dependent viscosity in both drag terms of the original HDD model. Based on our new model, two regimes are discovered as the surface heat flux increases. In the first regime both drag terms are affected, while in the second regime only the form drag term is affected, prior to the model reaching an inviscid limit. Predictive empirical relations correcting the viscous and form drag terms, complementing the new model, are obtained as functions of the surface heat flux. [DOI: 10.1115/1.1332778]

Keywords: *Channel Flow, Forced Convection, Heat Transfer, Porous Media*

Introduction

Darcy [1] described his empirical studies on steady-state filtration demonstrating that the water volume passing through a sand layer is proportional to the pressure-drop across the length of the layer, leading to the equation

$$\alpha = \frac{U^*}{\left(\frac{\Delta P^*}{L^*}\right)}, \tag{1}$$

where α is the *hydraulic conductivity* of the porous medium, U^* is the channel cross-section averaged fluid speed, also known as the *seepage speed*, and ΔP^* is the hydrostatic pressure difference (inlet minus outlet) across the layer of length L^*.

Three observations regarding Eq. (1) are fundamentally important and pertinent to our study. The first is that the fluid used by Darcy (liquid water) was not heated/cooled along the sand layer. Therefore, we can consider his experiment isothermal. A second observation is that Eq. (1), as is, involves no fluid material property, a direct consequence of Darcy using the same incompressible fluid, and not heating/cooling the fluid throughout his experiments. Hence, Eq. (1) is valid, essentially, for incompressible fluid in isothermal flow through a porous medium. The third and final observation is that Darcy's equation, as proposed, is an algebraic equation involving cross-section average quantities, which we call *global* quantities.

Several steps have been taken to generalize Eq. (1). Hazen [2] unveiled the fluid viscosity effect on the original flow equation proposed by Darcy, Eq. (1). By altering the temperature of the fluid (liquid water) before entering the porous medium, he observed the influence of temperature on the hydraulic conductivity calculated using Eq. (1). He proposed a modification to the original equation in the form

$$U^* = \left(\frac{T^* + 10}{60}\right)\alpha_{50}\frac{\Delta P^*}{L^*}, \tag{2}$$

where T^* is the water temperature, measured in degrees Fahrenheit, and α_{50} is the reference hydraulic conductivity value measured when the water is at 50°F.

A quick inspection reveals that the correction $60/(T^* + 10)$, called the *Fahrenheit-factor*, mimics the water viscosity dependence on temperature, namely $\mu(T^*)/\mu(50°\mathrm{F})$, to less than one percent for $40°\mathrm{F} \leqslant T^* \leqslant 90°\mathrm{F}$. One can then rewrite Eq. (2) to read

$$U^* = \frac{K}{\mu(T^*)}\frac{\Delta P^*}{L^*}, \tag{3}$$

where $K = [\mu(50°\mathrm{F})\alpha_{50}]$, known as *specific permeabaility*, is a parameter supposedly independent of fluid properties. Keep in mind that Hazen's experiment was performed under isothermal conditions as well, that is, invariant fluid temperature from inlet to outlet of the porous medium. We refer to Eq. (3) as the Hazen-Darcy equation.

Dupuit [3] was the first scientist to use theoretical principles to interpret Darcy's equation [4]. A consequence of Dupuit's study is the inclusion of a quadratic velocity term added to Eq. (3) modeling the resistive form drag imposed on the fluid by the solid permeable medium

$$\frac{\Delta P^*}{L^*} = \frac{\mu(T^*)}{K}U^* + C\rho U^{*2}, \tag{4}$$

where the coefficient C is the form coefficient of the porous layer. We refer to Eq. (4) as the Hazen-Dupuit-Darcy equation [4], or simply, the HDD model equation.

Contributed by the Heat Transfer Division for publication in the JOURNAL OF HEAT TRANSFER. Manuscript received by the Heat Transfer Division May 2, 2000; revision received, August 20, 2000. Associate Editor: A. Bejan.

Another step towards the generalization of Darcy's equation is the ad-hoc extension to differential form, i.e.,

$$-\nabla^* p^* = \frac{\mu(T^*)}{K}\mathbf{u}^* + C\rho|\mathbf{u}^*|\mathbf{u}^*, \tag{5}$$

where $\mathbf{u}^*$ is the local (macroscopic, or representative elementary volume) seepage fluid velocity and $\nabla^* p^*$ is the local (macroscopic) pressure gradient. The two terms in the RHS of Eq. (5) represent the lumped viscous and lumped form effects (forces) within the macroscopic permeable medium and are usually designated as viscous drag and form drag respectively, as they *impede* the flow. (The absence of the convective inertia and Brinkman terms in Eq. (5) is valid for low permeability media, as treated in the present work.)

Noteworthy is the widespread use of the uniform viscosity assumption when applying Eq. (5) to model convection through a porous medium (see for instance Kaviany [5] and Nield and Bejan [6] for general reviews of the subject and Lauriat and Vafai [7] and Lage and Narasimhan [8] for reviews specific to forced convection), even though most fluids have viscosity strongly dependent on temperature.

Ling and Dybbs [9] presented a very interesting theoretical investigation of the temperature-dependent fluid viscosity influence on the forced convection through a semi-infinite porous medium bounded by an isothermal flat plate. The fluid viscosity was modeled as an inverse linear function of the fluid temperature, which is a very good model for many liquids, including water and crude oil. Their study showed a very strong influence of temperature dependent viscosity on the heat transfer from the flat plate. However, they did not consider the effects of temperature dependent viscosity on the global pressure-drop across the porous medium. Also important, in their analysis they have considered the fluid flow as governed by the Darcy equation, i.e., Eq. (5) with $C=0$. In this case, the pressure-drop goes to zero when the fluid temperature tends to infinite (because the fluid viscosity goes to zero). This is not the case when $C\neq 0$.

Equations (4) and (5) are commonly referred to as the *Forchheimer-extended Darcy* equation in the literature. This is not only historically incorrect, as ascertained by Lage [4], but it also conceals the true significance of the viscosity in the linear velocity term by ignoring Hazen's experiments, which were isothermal. One can, for instance, question the validity of Eq. (4) for predicting the pressure-drop of a fluid, with viscosity dependent on temperature, being heated/cooled as it flows through a porous medium.

Our study addresses precisely this aspect. We consider the effects on the global pressure-drop of a fluid with temperature-dependent viscosity flowing through an isoflux porous channel, in which case the fluid viscosity varies continuously along the channel. We use Eq. (5) as our model equation to obtain, through numerical simulations, the global pressure-drop (inlet minus outlet cross-section averaged pressure) along the channel for several configurations.

Our main objective is to address the appropriateness and validity of Eq. (4) under these circumstances. Those unaware of the historical events leading to Eq. (4) would expect that the viscosity variation affect only the linear term in Eq. (4) (the only term dependent on fluid viscosity). Observe, however, that Eq. (4) does not state how this variation affects the pressure-drop, for it does not specify at what temperature the fluid viscosity should be evaluated. That is, one can immediately question the appropriateness of Eq. (4). This and other fundamental issues are treated in detail in the following sections.

Physical Model

Consider the forced convection of a fluid with temperature-dependent viscosity $\mu(T^*)$ through a porous medium sandwiched between two parallel isoflux surfaces, spaced by a distance $2H^*$, as shown in Fig. 1. The channel has length L^*, and the fluid enters the channel with uniform temperature T_0^* and uniform longitudinal speed U_0^*. The mass, momentum, and energy transport equations in non-dimensional form are, respectively,

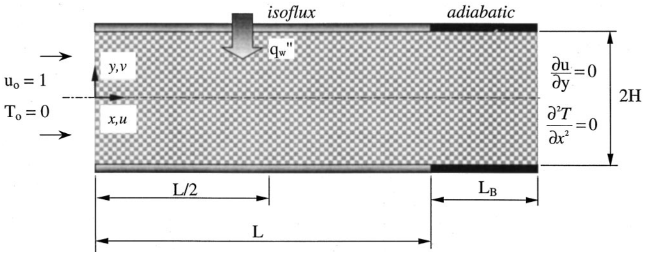

Fig. 1 Schematic of the flow channel considered for investigation

$$\nabla\cdot\mathbf{u} = 0 \tag{6a}$$

$$0 = -\nabla p - \left[\frac{\eta(T)}{\lambda+1}\right]\mathbf{u} - \left(\frac{\lambda}{\lambda+1}\right)\mathbf{u}|\mathbf{u}| \tag{6b}$$

$$\mathbf{u}\cdot\nabla T = \left(\frac{1}{\lambda\,\mathrm{Pr}_e}\right)\nabla^2 T, \tag{6c}$$

where λ is the ratio of global form drag ($D_C=\rho C U_0^{*2}$) to global viscous drag ($D_\mu=\mu_0 U_0^*/K$), and η is the ratio of $\mu(T^*)$ to $\mu(T_0^*)$, respectively,

$$\lambda = \left(\frac{\rho C K}{\mu_0}\right)U_0^* \quad \text{and} \quad \eta = \frac{\mu(T^*)}{\mu_0}, \tag{7}$$

where $\mu_0=\mu(T_0^*)$. The other respective non-dimensional variables are

$$(x,y) = \frac{(x^*,y^*)}{KC} \quad (u,v) = \frac{(u^*,v^*)}{U_0^*} \quad p = \frac{p^*}{(D_C+D_\mu)KC}$$
$$T = \frac{(T^*-T_0^*)}{\mu_0}\left|\frac{d\mu}{dT^*}\right|_{T_0^*} \quad \mathrm{Pr}_e = \frac{\mu_0 c_p}{k_e} \quad q'' = \frac{q^{*\prime\prime}}{\left(\frac{k_e}{KC}\right)\mu_0}\left|\frac{d\mu}{dT^*}\right|_{T_0^*}. \tag{8}$$

Here, k_e is the effective thermal conductivity of the medium, assumed equal to $\phi k_f + (1-\phi)k_s$, with k_f and k_s being the fluid and solid thermal conductivities, respectively, and ϕ is the porosity of the porous medium. All other quantities are defined in the nomenclature.

Boundary conditions are shown in Fig. 1. Inlet dimensionless boundary conditions, at $x=0$, are $u=u_0=1$ and $T=T_0=0$. To reduce the computational effort of solving Eqs. (6*a*)–(6*c*), we restricted the computational domain to the region $0\leqslant y\leqslant H$, imposing symmetry conditions at $y=0$ for both temperature and fluid longitudinal velocity ($\partial T/\partial y=\partial u/\partial y=0$). The upper boundary, at $y=H$, is impermeable and isoflux ($v=0, \partial T/\partial y=-q_w''$).

We imposed the velocity condition $\partial u/\partial y=0$, and zero longitudinal heat diffusion, $\partial^2 T/\partial x^2=0$, at the outlet $x=L^*/KC$. To make sure these conditions would not interfere with the numerical results, we added a buffer zone of length L_B beyond the heating zone (see Fig. 1), along which the channel surfaces are modeled as adiabatic. This buffer zone allows the flow to reach thermal equilibrium along the transverse *y*-direction before reaching the end of the channel, recovering uniform temperature and velocity profiles, matching the imposed outlet boundary conditions. The length of the buffer zone, not known *a priori*, is determined numerically by increasing L_B until the numerical results were no longer affected within the accuracy of our calculations.

Observe that by using the nondimensional parameters listed in Eqs. (7) and (8), the HDD equation, Eq. (4), can be written as

$$\frac{\Delta P}{L}=\left[\frac{\eta(T)}{\lambda+1}\right]+\left(\frac{\lambda}{\lambda+1}\right). \tag{9}$$

Specific Parameter Values

We take Poly-α-olefins (PAOs) as specimen fluids that suit well our purpose. These are low molecular weight, branched, synthetically produced, saturated hydrocarbons that have lubrication properties superior to that of naturally occurring mineral oil. This had led to the widespread use of PAOs in a variety of applications, ranging from industrial lubrication to high grade synthetic motor oil basestock to cooling military avionics (Kioupis and Maginn [10], Maginn [11], Lage et al. [12], Lage et al. [13], Nield et al. [14]).

The wide applicabaility of PAOs has merited the study of their viscosity with renewed interest in chemical engineering and applied chemistry (Kioupis and Maginn [10]). Fluids (like PAOs, motor-oils, synthetic lubricants, etc.) whose viscosities are dependent on temperature are modeled using different relations (White [15], Darby [16]) involving power, logarithmic (Kioupis and Maginn [10]) or exponential functions (Maginn [11]), yielding better accuracy over different temperature ranges. The dynamic viscosity (Chevron [17]) of PAOs can be modeled as

$$\mu(T^*)=0.1628T^{*-1.0868},\quad 5°\mathrm{C}\leqslant T^*\leqslant 170°\mathrm{C}. \tag{10}$$

Within the same temperature range, the variations of density, specific heat and thermal conductivity of PAO are negligible.

Obviously, neither the theory proposed nor the fundamental results of the present work are restricted by this fluid selection as they can be extended with reasonable validity to other fluids with similar temperature dependent viscosity.

In order to focus on the validity of Eq. (9), we designed our numerical experiments with specific parameter values. We assume the distance between the plates $2H^*=0.10$ m, and the length of the heated section $L^*=1$ m. The adiabatic buffer zone length was determined to be $L_B^*=22.5$ cm. The inlet temperature T_0^* of the PAO is chosen as 21°C, yielding $\mu_0=5.95\times10^{-3}$ kg/ms, $\rho=768.5$ kg/m^3, $c_p=1971.35$ J/kg°C, and $k_f=0.1424$ W/m°C. Our hypothetical porous matrix has $\phi=0.58$, $K=4.4\times10^{-10}$ m^2, and $C=1.2\times10^5$ m^{-1}. These values are representative of values obtained from isothermal (non-heating) experiments utilizing an aluminum foam having $k_s=170$ W/m°C, as reported by Lage et al. [12]. The dimensional inlet fluid velocity U_0^* and the dimensional heat flux $q_w^{*\prime\prime}$ are chosen to highlight the effect of temperature-dependent viscosity on the pressure-drop, varying from 10^{-2} m/s to 10^{-1} m/s and from 0.01 to 1.0 MW/m^2, respectively.

The corresponding nondimensional quantities are $2H=2\times10^3$, $L=2\times10^4$, $L_B=440$, $\mathrm{Pr}_e=0.164$, λ varying from 0.065 to 0.65, and q_w'' from 0.38×10^{-3} to 38×10^{-3}.

Numerical Scheme

Adopting a control volume formulation, the balance equations are discretized by a fully implicit scheme and solved through a line-by-line relaxation method (Thomas Algorithm). A modified version of the general-purpose algorithm SAINTS (Software for Arbitrary Integration of Navier-Stokes Equation with Turbulence and Porous Media Simulator), proposed by Nakayama [18] as an enhanced adoption of SIMPLE explained in detail in Patankar [19], is used in this study.

For each heat flux (no heating being a special case of zero heat flux), the governing equations are solved numerically for various flow velocities to obtain the corresponding pressure-drop and temperature distribution along the channel. The convergence criterion employed is

$$\mathrm{MAX}\left|\frac{\delta^{i+1}-\delta^{i}}{\delta_i}\right|<10^{-7}, \tag{11}$$

where i and $i+1$ are two consecutive iterations, and δ can be either $|\Delta P|$, i.e., the difference of the cross-section averaged pressures at $x=0$ and $x=L+L_B$, in the case of momentum equation, or $|\overline{T}|$, the volume averaged temperature within the entire channel, in the case of the energy equation.

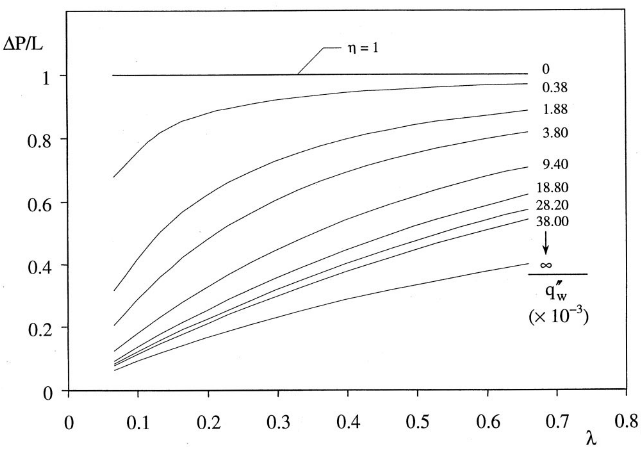

Fig. 2 Longitudinal nondimensional pressure-drop versus drag-ratio parameter λ for several heat fluxes

Grid accuracy tests were performed with a uniform grid, the coarsest being 20×23 and the finest 40×49. The maximum relative errors for $|\Delta P|$ and $|\overline{T}|$ are less than two percent, respectively, when going from 30×36 to 40×49 grid. Results are then presented for a 40×49 grid. Observe that this grid includes the buffer zone (with length $L_B\approx0.2\,L$).

Results and Discussion

The results of our numerical experiments are presented in Fig. 2 in terms of the nondimensional global (cross-section averaged) pressure-drop ΔP versus the nondimensional parameter λ. Three important observations are made (1) for a fixed λ, as the heat flux increases the global pressure-drop across the channel decreases, as expected because of the decrease in fluid viscosity; (2) the pressure-drop is progressively less affected by the heat flux as the heat flux increases; and (3) the curvature of the pressure-drop versus fluid-speed curve changes as the heat flux increases, indicating that the heat flux effect is not uniform as the fluid speed varies. This last observation is predominant at the lowest heat flux, i.e., $q_w''=0.38\times10^{-3}$.

To verify the appropriateness of the original HDD equation, written as Eq. (9), we consider three possibilities. The first, and simplest one, is to set $\eta=\eta(T_{\mathrm{ave}})$, where T_{ave} represents the arithmetic average of the inlet and outlet fluid bulk-temperatures, at $x=0$ and $x=L$, with the bulk temperature $T_b(x)$ defined as

$$T_b(x)=\frac{1}{H}\int_0^H (uT)|_x\,dy. \tag{12}$$

Observe that the outlet bulk temperature can be obtained from the first law of thermodynamics (neglecting longitudinal diffusion) as

$$T_b(L)-T_b(0)=\frac{1}{\lambda\,\mathrm{Pr}_e}\left(\frac{q''L}{H}\right). \tag{13}$$

The second possibility is to use $\eta=\eta_{\mathrm{LMD}}=\eta(\mu(T_{\mathrm{LMD}}^*)/\mu_0)$, where T_{LMD}^* is the dimensional log-mean bulk temperature, defined as

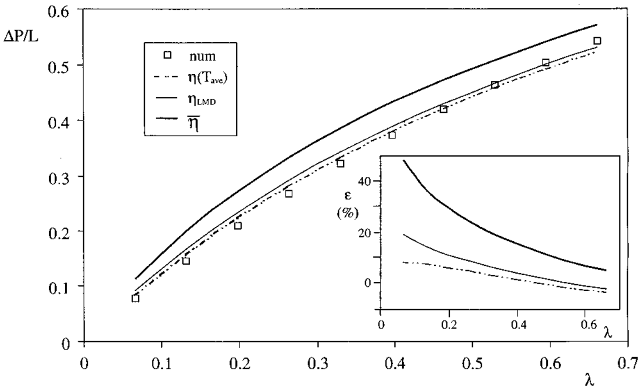

Fig. 3 Comparison of three HDD alternatives with numerical results for $q''_w=38\times10^{-3}$. Insert: relative pressure-drop error ε for the three HDD alternatives.

$$T^*_{\mathrm{LMD}}=\frac{T^*_b(L^*)-T^*_b(0)}{\ln\left[\frac{T^*_b(L^*)}{T^*_b(0)}\right]}. \tag{14}$$

And, the third, and final possibility considered here, is to calculate a length averaged viscosity along the entire channel, using the known temperature dependency $\mu(T^*)$ in terms of the bulk temperature, i.e., $\mu(T^*_b)$. Hence, in dimensionless form, we have

$$\bar{\eta}=\frac{1}{L}\int_0^L \eta[T_b(x)]dx. \tag{15}$$

Observe that the three alternatives, with $\eta=\eta(T_{\mathrm{ave}})$, $\eta=\eta_{\mathrm{LMD}}$, and $\eta=\bar{\eta}$, are all implemented in Eq. (9), which assumes that the viscosity effect on the global pressure-drop is restricted to the linear velocity term.

The predicted results from these three alternatives are compared in Fig. 3 against the numerical results for the case $q''_w=38\times10^{-3}$. Observe that the length averaged viscosity approach, $\eta=\bar{\eta}$, yields a curve with curvature similar to the numerical results curve but with a consistent deviation. The arithmetic mean bulk temperature approach, $\eta=\eta(T_{\mathrm{ave}})$, and the log-mean bulk temperature approach, $\eta=\eta_{\mathrm{LMD}}$, yield similar results, and smaller deviation from the numerical results than the length averaged viscosity approach. However, their curvature is different from the curvature of the curve obtained from the numerical results.

The insert graph in Fig. 3 shows the relative error ε

$$\varepsilon=\left|\frac{\Delta P_{\mathrm{Eq.\,(9)}}-\Delta P_{\mathrm{num}}}{\Delta P_{\mathrm{num}}}\right| \tag{16}$$

between each one of the three alternatives for computing the global pressure-drop $\Delta P_{\mathrm{Eq.\,(9)}}$ from the HDD model, Eq. (9), and the global pressure-drop predicted numerically ΔP_{num}. It is clear that the HDD model, even when adapted by any of the three alternatives considered here, does not capture correctly the temperature-dependent viscosity effect on the pressure-drop.

To understand why Eq. (9) is inappropriate, we consider the local (at mid-channel, i.e., $x=L/2$) profiles of longitudinal macroscopic fluid speed u and temperature T in Figs. 4 and 5, respectively. These figures show the heat flux effect when $\lambda=0.67$.

For a nonheating configuration $q''_w=0$ (equivalent to $\eta=1$ throughout the entire channel), the velocity profile in Fig. 4 is flat, as expected. As the wall heat flux increases, the fluid temperature next to the wall increases (Fig. 5), decreasing the fluid viscosity, which in turn increases the local fluid speed. Mass conservation requires this increase in fluid speed near the heated surface to be compensated by a reduction in fluid speed elsewhere along the cross section of the channel. This happens as we approach the axis $(y=0)$ of the channel, Fig. 4.

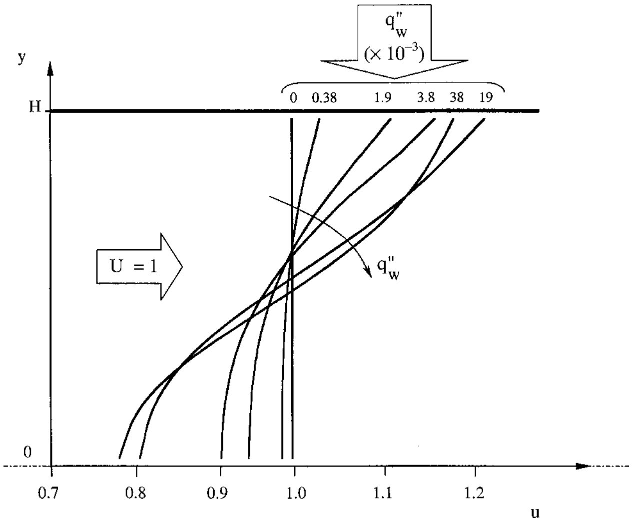

Fig. 4 Longitudinal velocity profiles at mid-plane $(x=L/2)$ for increasing heat flux

Hence, heating the channel makes the fluid viscosity become a spatially (in x and y) varying parameter, distorting the uniform inlet velocity profile. Observe that the velocity variation in y is caused entirely by thermal effects via viscosity variation.

Another interesting observation is the shape variation of the velocity profile as q''_w is increased beyond 3.8×10^{-3}. In fact, observe a decrease in the fluid speed adjacent to the heated wall as q''_w is increased from 19×10^{-3} to 38×10^{-3}.

On the other hand, Fig. 5 shows that the shape of the fluid temperature profiles at mid-channel are preserved as the heat flux increases. The temperature dependency of the viscosity induces a decrease in the fluid temperature, the decrease being sharper near the heated wall where the fluid speed is greater. Worth noting is the increase in the difference between nonheating and heating temperatures, for increasing heat flux.

When the fluid is heated (or cooled) along the channel, the spatial variation of fluid viscosity distorts the velocity profile, thus

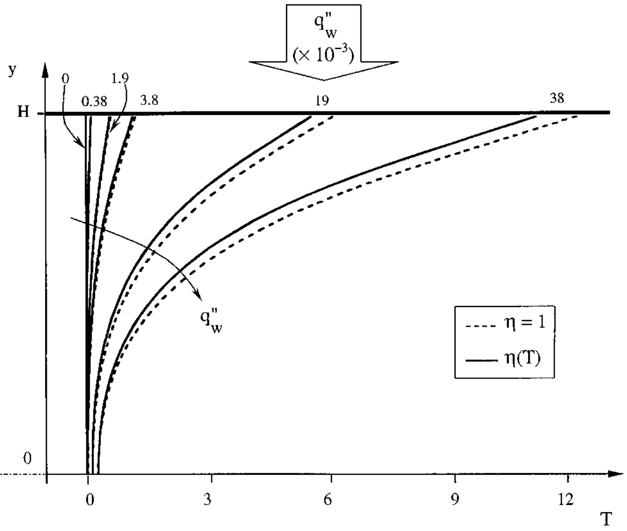

Fig. 5 Variation of the temperature profile at mid-plane $(x=L/2)$ for increasing heat flux

affecting the energy transport equation. The resulting altered temperature profile affects the local fluid viscosity, which in turn affects the fluid speed owing to the coupling between energy and momentum transport equations.

Obviously, the local viscous drag and form drag terms of Eq. (5) vary when the fluid is heated because the local velocity u changes. More specifically, when u is function of y, the unidirectional differential Eq. (5) in non-dimensional form becomes

$$-\frac{\partial p(y)}{\partial x}=\eta(T)\left(\frac{1}{\lambda+1}\right)u(y)+\left(\frac{\lambda}{\lambda+1}\right)u(y)^2. \tag{17}$$

The algebraic representation of Eq. (17) is obtained by cross-section averaging, i.e.,

$$\left(\frac{1}{H}\int_0^H-\frac{\partial p(y)}{\partial x}dy\right)=\left(\frac{1}{\lambda+1}\right)\left(\frac{1}{H}\int_0^H\eta(T)u(y)dy\right)+\left(\frac{\lambda}{\lambda+1}\right)\left(\frac{1}{H}\int_0^H u(y)^2\,dy\right) \tag{18}$$

The first term of Eq. (18) can be replaced by the cross-section averaged quantity $\partial P/\partial x$. Similar replacement is not possible for the second term, as $\eta(T)$ also is function of y. The replacement also does not work for the third term, because the y-integral of $u(y)^2$ does not equal HU^2 when u is function of y! This last observation is interesting for highlighting the indirect dependency of the quadratic term on the fluid viscosity, something not anticipated by the original HDD model, Eq. (5).

We progress with our objective to obtain an algebraic representation of Eq. (17) by averaging Eq. (18), now along the channel length L

$$\frac{1}{L}\int_0^L-\frac{\partial P}{\partial x}dx=\left(\frac{1}{\lambda+1}\right)\frac{1}{L}\int_0^L\left(\frac{1}{H}\int_0^H\eta(T)u(y)dy\right)dx+\left(\frac{\lambda}{\lambda+1}\right)\frac{1}{L}\int_0^L\left(\frac{1}{H}\int_0^H u(y)^2\,dy\right)dx. \tag{19}$$

The first term of Eq. (19) is again trivial, with the integral leading to $\Delta P/L$. The second and third integrals cannot be resolved because the integrands are functions of x as well, and we cannot resolve the integrals unless we know the temperature and velocity variations in x and y.

The question is how to alter Eq. (19) to fulfill the experimental need for an algebraic representation of the pressure-drop versus fluid speed in terms of global, cross-section averaged quantities (quantities that are easily measured in experiments). We propose the introduction of two new coefficients, ζ_μ and ζ_C, defined as

$$\zeta_\mu=\frac{1}{L}\int_0^L\left(\frac{1}{H}\int_0^H\eta(T)u(y)dy\right)dx$$

and

$$\zeta_C=\frac{1}{L}\int_0^L\left(\frac{1}{H}\int_0^H u(y)^2dy\right)dx \tag{20}$$

allowing us to rewrite Eq. (19) as

$$\frac{\Delta P}{L}=\zeta_\mu\left(\frac{1}{\lambda+1}\right)+\zeta_C\left(\frac{\lambda}{\lambda+1}\right). \tag{21}$$

This new algebraic model, Eq. (21), when dimensionalized, *retains* the same form of Eq. (4). The coefficients ζ_μ and ζ_C represent, respectively, the correction for viscous and form drag terms due to the global effect of temperature on viscosity and on the fluid velocity profile (via viscosity). Obviously, for no heating (uniform viscosity), $\zeta_\mu=\zeta_C=1$ and Eq. (21) becomes identical to Eq. (4) upon dimensionalization.

Model Eq. (21) is tested using the numerical results for various heat flux values. Observe that with the available numerical results we could calculate from Eq. (20) values of ζ_μ and ζ_C for Eq. (21). This is preposterous because testing model Eq. (21) by determining ζ_μ and ζ_C from the numerical resuls is redundant. What we must verify is the correctness of Eq. (21) from an experimentalist point-of-view. That is, an experimentalist having obtained $\Delta P/L$ and λ would desire to find an appropriate analytic correlation between these two quantities. In this regard, we use the numerical results of $\Delta P/L$ and λ as if they were experimental results. For validation, model Eq. (21) then would require the determination of suitable values for ζ_μ and ζ_C that best correlate $\Delta P/L$ and λ. The deviation of $\Delta P/L$ predicted by the correlation from the experimentally (numerically in our case) obtained $\Delta P/L$ is then a measure of the appropriateness of our proposed model, Eq. (21).

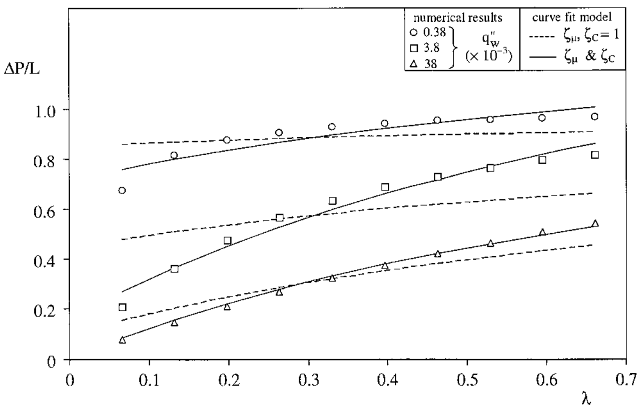

Fig. 6 Verification of one ($\zeta_\mu,\zeta_C=1$) and two (ζ_μ,ζ_C) coefficients model, Eq. (21)

Therefore, we curve-fit the numerical results using Eq. (21) allowing both ζ_μ and ζ_C to vary. This is shown in Fig. 6 as the continuous-line curves, where the numerical results are marked with symbols. It is evident from Fig. 6 that model Eq. (21) satisfactorily correlates the numerical results.

A simpler situation in which the form drag correcting-factor ζ_C of Eq. (21) equals unity yields a poor curve-fitting result (dashed curves in Fig. 6). Nevertheless this is done to isolate the temperature effect on the fluid velocity profile (the effect responsible for ζ_C). Setting $\zeta_C=1$ does reveal where the temperature effect on the velocity profile is strongest, i.e., when $q''_w\sim3.8\times10^{-3}$.

Figure 7 shows the corresponding average deviation σ between curve-fit model results and numerical results for several heat flux values. The maximum deviation can be as high as 20 percent when using the model with $\zeta_C=1$, but only 3.8 percent when using ζ_μ and ζ_C. Model Eq. (21), using ζ_μ and ζ_C, predicts $\Delta P/L$ with superior accuracy than the previous HDD model.

Figure 8 presents in graphical form the values of ζ_μ and ζ_C leading to the best curve fit results of Fig. 6, for several heat flux values. For increasing heat flux, by following the circles, we observe that ζ_μ becomes negative beyond $q''_w=19\times10^{-3}$ (white circles). This is physically inconsistent. Therefore, when $\zeta_\mu<0$ the curve fitting is redone with $\zeta_\mu=0$ (black circles beyond $q''_w=19\times10^{-3}$). Consequently, the previous ζ_C values (white triangles beyond $q''_w=19\times10^{-3}$) are replaced by new ζ_C values (black triangles) from the best curve fitting. The region in which ζ_μ is set to zero is referred as the *null global viscous drag regime*, as shown in Fig. 8.

It is difficult to precisely identify the switch by ζ_μ, from nonzero (positive) to zero value, hence we prefer to present a transition region, shown as a shaded rectangle in Fig. 8. The corrected values of ζ_μ and ζ_C, valid beyond the transition zone, are indicated by black circles and black triangles, respectively. Based on these results we propose two empirical correlations, namely,

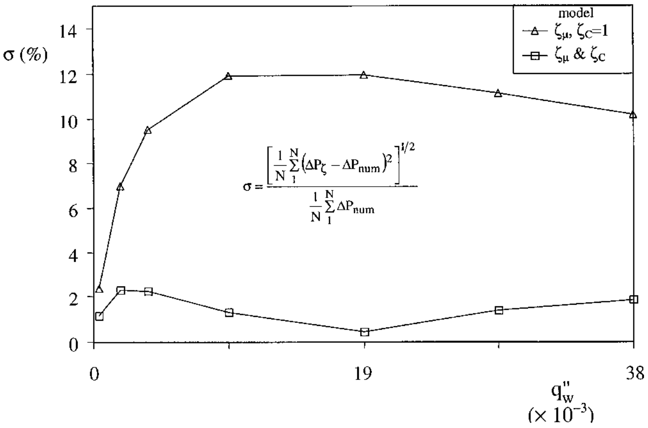

Fig. 7 Average deviation between curve-fit model results and numerical results

$$\zeta_{\mu}=\left[1-\left(\frac{q''_w}{1+q''_w}\right)^{0.325}\right]\left(\frac{1}{1+q''_w}\right)^{18.2} \tag{22}$$

$$\zeta_C=2+q''^{0.11}_w-\zeta_{\mu}^{-0.06} \tag{23}$$

as best curve fits with average deviation (similar to σ, defined in Fig. 7) for ζ_μ and ζ_C of 7 percent and 8 percent, respectively.

Now reconsider the observation made earlier regarding the velocity profiles when discussing Fig. 4. We noticed a switch on the curvature of the velocity profile from $q''_w=3.8\times10^{-3}$ to $q''_w=38\times10^{-3}$. As q''_w increased beyond 19×10^{-3}, the fluid velocity adjacent to the heated surface decreased with the velocity profile tending to flatten again. This phenomenon can now be explained by the reduction of viscous effect as the heat flux increases. As the fluid temperature in the region adjacent to the heated surface increases, the viscosity progressively is reduced allowing the form drag to predominate. For a certain heat flux (in our case, $q''_w\sim19\times10^{-3}$), the viscous drag effect on the global longitudinal pressure drop becomes insignificant because the local viscosity value becomes very small.

More interestingly however, the effect of viscosity *does not* disappear! It is still felt by the global pressure-drop through ζ_C, the correcting form drag coefficient. Although the *global* ζ_μ is zero beyond the transition region, the fluid still feels the viscous effect locally along the channel because of the distorted velocity profile. Indeed, we notice a continuous decrease in ζ_C for increasing heat flux, even when ζ_μ is set to zero (Fig. 8). As the heat flux increases further, the viscosity effect on ζ_C will eventually subside throughout the channel, making ζ_C equal to one, a constant value independent of the heat flux. At this stage, the velocity profile would become flat again—similar to the slug flow profile.

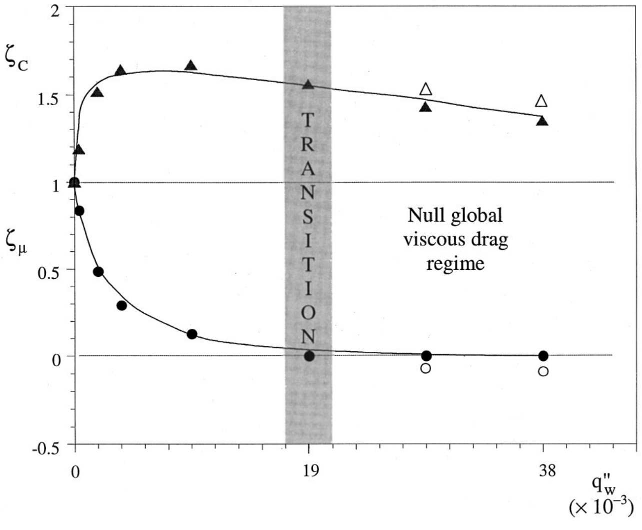

Fig. 8 ζ_μ and ζ_C versus heat flux

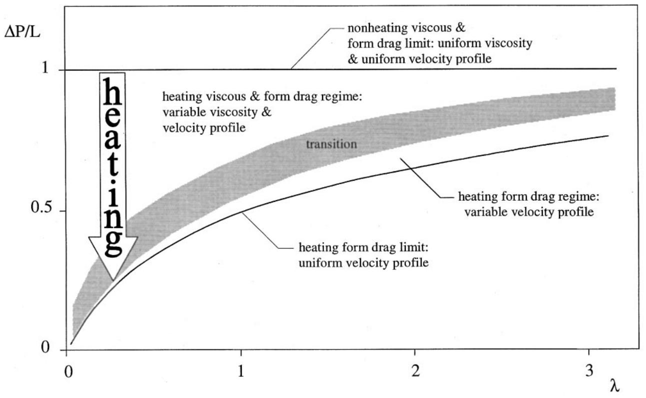

Fig. 9 Summary of hydrodynamic regimes for forced convection of fluid with temperature-dependent viscosity through a heated porous medium channel

Further heating will have no significant hydrodynamic effect through viscosity, and this limit (at which $\zeta_C=1$ and $\zeta_\mu=0$) is termed the *heating form drag limit*, as the global form drag becomes independent of the viscosity effect. Consequently, for this limiting case, the longitudinal pressure-drop will be equal to the form drag when the channel is not heated. In other words, this limit can be predicted by the simple equation

$$\frac{\Delta P}{L}=\frac{\lambda}{\lambda+1}. \tag{24}$$

This result, already shown as the curve $q''_w\rightarrow\infty$ in Fig. 2, is fundamental in nature—true for all fluids with viscosity inversely dependent on temperature—and of great practical importance, as it sets an upper bound for the magnitude of the reduction in the global pressure-drop achievable by heating a fluid with temperature dependent viscosity.

A summary of our findings is presented in Fig. 9. Start from the upper curve, valid for a nonheating configuration (uniform viscosity), when $\Delta P/L=1$. When the heat flux is progressively increased (following the arrow) we immediately get into a viscous and form drag regime in which both viscous and form drag terms of the global pressure-drop equation are affected by the viscosity dependency on temperature. This regime is then followed by a transition beyond which a form drag regime is achieved where only the form drag term is affected by the viscosity variation. Finally, when the heat flux is large enough, the viscosity effect becomes negligible, the fluid velocity profile becomes uniform again, and the global pressure-drop is predicted by Eq. (24). This is called the *heating form drag limit*.

One of the reviewers questioned the use of KC in Eq. (8), instead of H^*, as the length scale. Notice, firstly, that the choice of length scale is irrelevant to the momentum equation. One can simple substitute KC by H^* in the nondimensional length and pressure expressions and Eq. (6*b*) will remain exactly the same. This is not true, however, when the energy equation is nondimensionalized. Using H^* as a length scale will result in λ being substituted in Eq. (6*c*) by $(\rho H^* U_0)/\mu_0$, which can be defined as a Reynolds number, leading to known misconceptions (e.g., the use of Re∼1 as the criterion for the transition from linear to quadratic flow regime, [4]).

Moreover, choosing KC as length scale for nondimensionalizing the heat-flux in Eq. (8) has another advantage. Observe in Eqs. (22) and (23), that choosing H^* as length scale leads to the ζ's being independent of the porous medium characteristics (KC). This, for an experimentalist interested in calculating ζ's using Eqs. (22) and (23), wrongly indicates the apparent independence of ζ's on the porous medium characteristics.

The same reviewer criticized our choice of including a buffer zone for the numerical simulations and questioned also the use of the boundary condition $\partial u/\partial y = 0$ at the outlet of the channel, instead of the condition $\partial u/\partial x = 0$.

We must recognize that the problem under consideration is much more complex than when the fluid viscosity is uniform and constant. When the viscosity is dependent on temperature, the velocity profile continuously changes until a fully developed velocity profile of *slug flow* is achieved. We do not know *a priori* how long the channel must be for the flow to achieve this profile. Therefore, the boundary condition imposed at the end of the channel would affect the solution whenever the chosen channel length happens to be short.

Now, along the buffer zone, where the fluid is not heated, the temperature profile tends to become uniform much quicker and by consequence does the viscosity, and so does the fluid velocity. Hence, with a relatively short buffer zone the flow can achieve a fully developed (slug flow) profile before the fluid reaches the outlet. In this way, the boundary condition $\partial u/\partial y = 0$ (or $\partial u/\partial x = 0$) is satisfied before the fluid reaches the outlet boundary (no effect on the solution).

Finally, the outlet condition $\partial u/\partial y = 0$ is less restrictive than $\partial u/\partial x = 0$. Observe that the latter yields (from the continuity equation) the condition $\partial v/\partial y = 0$. Together with the impermeable condition $v = 0$ at the top and bottom surfaces of the channel, we conclude that $v = 0$ at the outlet, which restricts the possible solutions.

Summary and Conclusions

By investigating three alternatives, namely (1) fluid viscosity determined at the algebraic average of inlet and outlet bulk temperature, (2) fluid viscosity determined at the log-mean of inlet and outlet bulk temperature, and (3) fluid viscosity function of the bulk temperature averaged along the entire channel, we have assessed, by comparison with numerical results, the accuracy of the Hazen-Dupuit-Darcy (HDD) model in estimating the global pressure-drop of a fluid flowing through a heated porous channel.

The best estimate, obtained with alternative (1), although leading to a discrepancy within 10 percent, did not yield the correct curvature of the pressure-drop versus fluid-speed curve. Therefore, this alternative is likely to diverge further when a wider λ-range is utilized.

The heating of the fluid as it flows along the channel results in a non-uniform fluid temperature in the transverse (perpendicular to the heated plates) and longitudinal directions. This causes the viscosity of the fluid to vary in y, resulting in a non-uniform velocity profile (in y) as well. As the velocity is non-uniform along y, the local viscous and form drags, dependent on u and u^2 respectively, are no longer uniform in y. Therefore, the cross-section averaged viscous and form drags are altered leading to different global coefficients. This observation highlights the inappropriateness of the HDD model, which does not account for these effects.

We proposed a modification to the original HDD model to account for the effects of temperature dependent viscosity and the effect of viscosity variation on the transverse velocity profile. The modification is done by including two new parameters, namely ζ_μ and ζ_C, to correct the viscous and form drag coefficients, respectively. Our analysis of this new model indicates that both ζ_μ and ζ_C are necessary, apart from physical grounds, for an accurate curve-fitting of the numerical results.

For higher heat fluxes (in our case, $q''_w \sim 19 \times 10^{-3}$), the effect of ζ_μ becomes negligible because the fluid temperature gets so high that the viscous effect becomes negligible making the flow form drag effect dominant. Nevertheless, the effect of the viscosity variation is still *felt* by the form drag term via ζ_C. This null global viscous drag regime is characterized by a modified ζ_C obtained after setting $\zeta_\mu = 0$.

Moreover, the correcting form drag coefficient ζ_C decreases for further increase in heat flux eventually reaching the lower bound value of unity. At this limit, the flow becomes essentially independent of viscosity effects, the fluid velocity profile becomes uniform, the plot of global pressure-drop versus average fluid-speed reaches a minimum, and the pressure-drop becomes dependent only on the square of the fluid speed, as if the channel was not heated.

We identified the heat flux influence on the value of ζ_μ and ζ_C by proposing two empirical correlations.

A final interesting observation: the analogy between Hagen-Poiseuille flow ([20]) and ([21]) through capillary beds and flow through porous media is also limited when considering flow of fluids with temperature dependent viscosity. In Hagen-Poiseuille flow, the pressure-drop decreases without limit, with an increase in the heat flux. In porous medium flow, the decrease in pressure-drop by increasing the heat flux is limited by the pressure-drop caused by the form drag, which is always present at high enough fluid speed.

Nomenclature

C = form coefficient, m^{-1}
D = global drag, $\mathrm{Pa\,m}^{-1}$
H^* = half-channel spacing, m
K = permeability, m^2
L^* = channel length, heated section, m
p^* = macroscopic pressure, Pa
P^* = global (cross-section averaged) pressure, Pa
Pr_e = effective Prandtl number, Eq. (8)
$q^{*\prime\prime}$ = heat flux, $\mathrm{W\,m}^{-2}$
T^* = temperature, °C
u^* = x-component, seepage macroscopic velocity, $\mathrm{m\,s}^{-1}$
U^* = global (cross-section averaged) longitudinal velocity, $\mathrm{m\,s}^{-1}$
$\mathbf{u}^*$ = seepage macroscopic velocity vector
v^* = y-component, seepage macroscopic velocity, $\mathrm{m\,s}^{-1}$

Greek Symbols

α = hydraulic conductivity, $\mathrm{kg}^{-1}\,\mathrm{m}^3\,\mathrm{s}$
ε = relative pressure-drop error
ϕ = porosity
η = viscosity ratio $[=\mu(T^*)/\mu(T_0^*)]$
λ = form and viscous drag ratio, Eq. (7)
ζ = drag correction factor

Superscripts

$*$ = dimensional variable

Subscripts

ave = arithmetic-mean
b = bulk
B = buffer zone
C = form
e = effective
f = fluid
LMD = log-mean
s = solid
w = wall
0 = inlet
μ = viscous

References

[1] Darcy, H. P. G., 1856, *Les Fontaines Publiques de la Ville de Dijon*, Victor Dalmont, Paris.

[2] Hazen, A., 1893., ''Some Physical Properties of Sand and Gravels with Special Reference to Their Use in Filtration,'' *Twenty-Fourth Annual Report*, Massachusetts State Board of Health, p. 541.

[3] Dupuit, A. J. E. J., 1863, *Études Théoriques et Pratiques sur le Mouvement des aux dans les Canaux Découverts et a Travers les Terrains Perméables*, Victor Dalmont, Paris.

[4] Lage, J. L., 1998, ''The Fundamental Theory of Flow through Permeable Media; From Darcy to Turbulence,'' *Transport Phenomena in Porous Media*, D. B. Ingham and I. Pop, eds., Pergamon, New York, pp. 1–30.

[5] Kaviany, M., 1991, *Principles of Heat Transfer in Porous Media*, Springer-Verlag, New York.

[6] Nield, D. A., and Bejan, A., 1999, *Convection in Porous Media*, 2nd ed. Springer-Verlag, New York.

[7] Lauriat, G., and Vafai, K., 1991, ''Forced Convective Flow and Heat Transfer Through a Porous Medium Exposed to a Flat Plate or a Channel,'' *Convective Heat and Mass Transfer in Porous Media*, S. Kakaç et al., eds., Kluwer, Dordrecht, pp. 289–327.

[8] Lage, J. L., and Narasimhan, A., 2000, ''Porous Media Enhanced Forced Convection: Fundamentals and Applications,'' *Handbook of Porous Media*, K. Vafai, ed., Marcel Dekker, New York, **8**, pp. 357–394.

[9] Ling, J. X., and Dybbs, A., 1992, ''The Effect of Variable Viscosity on Forced Convection over a Flat Plate Submersed in a Porous Medium,'' ASME J. Heat Transfer, **114**, pp. 1063–1065.

[10] Kioupis, L. I., and Maginn, E. J., 1999, ''Molecular Simulation of Poly-α-olefin Synthetic Lubricants: Impact of Molecular Architecture on Performance Properties,'' J. Phys. Chem. B, **103**, pp. 10781–10790.

[11] Maginn, E., J., 2000, private communication.

[12] Lage, J. L., Antohe, B. V., and Nield, D. A., 1997, ''Two Types of Nonlinear Pressure-Drop Versus Flow-Rate Relation Observed for Saturated Porous Media,'' ASME J. Fluids Eng., **119**, pp. 700–706.

[13] Lage, J. L., Price, D. C., Weber, R. M., Schwartz, G. J., and McDaniel, J., 1999, ''Improved Cold Plate Design for Thermal Management of Phased Array Radar Systems,'' US Patent Office Patent #5960861.

[14] Nield, D. A., Porneala, D. C., and Lage, J. L., 1999, ''A Theoretical Study, With Experimental Verification of the Viscosity Effect on the Forced Convection through a Porous Medium Channel,'' ASME J. Heat Transfer, **121**, pp. 500–503.

[15] White, F. M., 1991, *Viscosity Fluid Flow*, 2nd ed., McGraw-Hill, New York.

[16] Darby, R., 1996, *Chemical Engineering Fluid Mechanics*, Marcel-Dekker, New York.

[17] Chevron, 1981, *Synfluid Synthetic Fluids*, Physical Property Data.

[18] Nakayama, A., 1995, *PC-aided Numerical Heat Transfer and Convective Flow*, CRC Press, Boca Raton.

[19] Patankar, S. V., 1980, *Numerical Heat Transfer and Fluid Flow*, Taylor & Francis, Washington, DC.

[20] Hagen, G., 1839, ''Ueber [Über] die Bewegung des Wassers in engen c[z]ylindrischen Röhren,'' Poggendorfs Annalen der Physik und Chemis, **16**, p. 423.

[21] Poiseuille, J. L. M., 1840, ''Récherches Expérimentales sur le Mouvement des Liquides dans les Tubes de Très Petits Diamètres,'' C. R. Acad. Sci. (Paris), **11**, pp. 961–967, 1041–1048.

G. J. Hwang
Professor, Fellow ASME

S. C. Tzeng

C. P. Mao

Department of Power Mechanical Engineering,
National Tsing Hua University,
Hsinchu, Taiwan 30043,
Republic of China

C. Y. Soong
Professor, Mem. ASME
Department of Aeronautical Engineering,
Chung Cheng Institute of Technology,
Tahsi, Taoyuan, Taiwan 33509,
Republic of China

Heat Transfer in a Radially Rotating Four-Pass Serpentine Channel With Staggered Half-V Rib Turbulators

The present work is concerned with experimental investigation of the convective heat transfer in a radially rotating four-pass serpentine channel. Two types of staggered half-V rib turbulators are considered to examine their effects on heat transfer enhancement. The coolant air is pressurized and pre-cooled to compensate for the low rotating rate and low temperature or density difference in key parameters of thermal and flow characteristics. The geometric dimensions are fixed, whereas the ranges of the thermal and flow parameters in the present measurements are $20{,}000 \leqslant Re \leqslant 40{,}000$, $0 \leqslant Ro \leqslant 0.21$, *and* $Gr/Re^2 \sim O(10^{-2})$. *The present results disclose the effects of the pressurized flow, rib arrangement, channel rotation, and centrifugal buoyancy on the local heat transfer in each passage of the channel. Finally, the present data are fitted on correlation equations for evaluation of local heat transfer in the rotating four-pass ribbed channel configurations considered.* [DOI: 10.1115/1.1338130]

Keywords: *Cooling, Heat Transfer, Rotating, Roughness, Turbines*

1 Introduction

Most power machinery such as turbo-engines convert energy by rotation. In gas turbines, the thermal efficiency can be improved by increasing the turbine inlet temperature. High operating temperature may cause material degradation, thereby shorten the life of the turbine blade. Under a high turbine-inlet temperature, the cooling design must be subject to the limits of turbine blade materials. For cooling and maintaining the structural integrity of blades and vanes in gas turbine engines, the cooling system requires complex airflow passage incorporated inside the rotating airfoil section.

Problems associated with applying the cooling technique on the turbine blade are well known in design and operation of turbomachines. Understanding of the heat transfer mechanisms is significant and useful in design of the cooling devices of the turbine blades. Because of its effectiveness in removing locally concentrated heat, the internal cooling has been widely studied for cooling elements exposed to high temperature and high heat flux environments. In addition to the main flow effects on the hydrodynamic and thermal behaviors, the Coriolis-induced secondary flow and centrifugal-buoyancy radial flow are also the influential factors inside a heated rotating channel. Since the rotation-induced effects vary locally over each wall of the flow passages, this fact leads to a significant difference in heat transfer rates on the leading edge, trailing edge, and sidewalls. Moreover, accurately predicting the rotational effects on heat transfer remains a challenging task because of the complexities of flow mechanisms involved. Due to its variety of flow phenomena and significance in applications, the gas turbine quickly became the most highly researched engine in history. Many investigations of the rotational effects and geometry effects on flow and heat transfer characteristics in turbomachinery, especially turbine blade, have been reported for decades.

In general, gas turbine blades are cooled externally and internally. External cooling is also referred to as film cooling. Internal cooling is achieved by passing the coolant through several serpentine passages inside the blades and, then, extracting the heat from outside. Owing to increased secondary flow and turbulent mixing, angle ribs in the rotating channel enhance the heat transfer for internal cooling. Table 1 lists the dimensional and dimensionless parameters of some recent experiments in radially rotating serpentine channels with a rib-roughed surface.

Zhang et al. [1] assessed the local heat transfer performance in a rotating serpentine passage with rib-roughened surfaces. According to their results, the heat transfer is significantly enhanced in the stationary and rotating cases, as attributed to an installation of the ribs. Also, their results revealed that both the Rotation and Rayleigh numbers profoundly influence the heat transfer performance of the trailing and leading walls. Besides, Reynolds number is also an influential factor to the Nusselt numbers in the rib-roughed passage at the stationary and rotating conditions.

Johnson et al. [2] elucidated the heat transfer in multi-pass passages with both radially rotating inward and outward flows. Trip strips, skewed at 45 deg to the flow direction, were machined on the leading and trailing surfaces. The heat transfer coefficients on surfaces decreased to as low as 40 percent of the value without rotation. However, the maximum values of heat transfer coefficients with high rotation were only slightly above that obtained previously with the smooth wall model. The investigation concluded that: (1) both Coriolis and buoyancy effects should be considered in designs of turbine blade cooling with trip strips; (2) the rotational effects markedly differ from each other, depending on the flow direction; and (3) the heat transfer with skewed trip strips is relatively less sensitive to buoyancy than that in models with smooth walls or normal trips.

Fann et al. [3] studied the heat transfer in a rotating rib-roughened serpentine passage with uniform wall heat flux. The investigation also compared results obtained for heat transfer distributions with those having smooth surfaces. The channel rotation, wall roughness, and angle-of-attack of ribs significantly influence the heat transfer performance in both stationary and rotating cases.

Parsons et al. [4] investigated how channel orientation and wall heating condition affect the local surface heat transfer coefficient

---

Contributed by the Heat Transfer Division for publication in the JOURNAL OF HEAT TRANSFER. Manuscript received by the Heat Transfer Division March 20, 1999; revision received, July 21, 2000. Associate Editor: J. Han.

Table 1 Some recent experimental investigations on heat transfer in radially rotating serpentine channels with rib turbulators

AUTHOR S	COMPRESSED AIR FLOW (MPa)	PASS OF CHANNEL	RIB MODE	B. C.	MAX. RPM	D(mm)	L/D	$\bar{R}/D$	Re $\times 10^{-3}$	$Re\,Re_\Omega$ $\times 10^{-6}$ $(Re \times 10^{-3})$*	$\overline{Gr_\Omega}$ $\times 10^{-6}$	e/D	P/e
Zhang et al. (1993)	No (0.1)	2	90 deg	UHF	327	25.4	8.86	-----	23 - 70	291.06 (70)	-----	0.0787	11.3
Johnson et al. (1994)	Yes (1)	4	Skew-ribs	UWT	875	12.7	14	49	12.5 - 75	218.75 (25)	229.32	0.1	10
Fann et al. (1994)	No (0.1)	4	45, 60 90 deg	UHF UWT	332	25.4	8.86	-----	10.2-31.3	14.56 (10.2)	-----	0.0787	11.3
Parsons et al. (1995)	No (0.1)	2	60, 90 deg	UHF	800	12.7	12	30	2.5 - 25	22 (25)	2.56	0.125	10
Dutta & Han (1996)	No (0.1)	2	Half-V 60 deg	UHF	800	11.7	26	55	2.5 - 25	18.75 (25)	4.02	0.125	10
Present study	Yes (0.5)	4	Half-V 60 deg	UHF	1250	10	10	53	20 - 40	160 (40)	214.4	0.125	10

* The values of Reynolds number are used to define the Rotation number

in a rotating, two-pass, square channel with 60 deg and 90 deg ribs on the leading and trailing walls at Reynolds number ranging from 2500 to 25,000 and rotation number ranging from 0 to 0.352. The Nusselt number ratios for the channel with 60 deg ribs are up to 30 percent above the corresponding Nusselt number ratios for that with 90 deg ribs.

Dutta and Han [5], and Ekkad and Han [6] examined the heat transfer in two-pass square channels with smooth and ribbed surfaces. In their investigations, the ribs were placed in a half-V fashion. The channel orientation was varied with respect to the rotation plane. In addition, altering the channel orientation with respect to the rotating frame changes the secondary flow structure and the related flow and turbulence distributions. Consequently, a change appeared in the heat transfer rate from the individual surfaces. According to their data, half-V ribs generally resulted in higher heat transfer coefficients than those with 90 and 60 deg continuous ribs.

In the light of previous investigations of heat transfer in rotating channels, the present work is planned to study the rotational effects on the local heat transfer in a radially rotating four-pass

Table 2 Parameters for aircraft engine and present test rig

Parameters	Aircraft engine*	Present study**
Coolant passage diameter D (mm)	~4	10
Coolant passage length L (mm)	48 ~ 70	100
Mean rotational radius $\bar{R}$ (mm)	200~360	530
Mean rotational radius/diameter ratio $\bar{R}/D$	50~90	53
Rib height/hydraulic diameter ratio e/D	0.01~0.15	0.125
Pitch/rib height ratio P/e	7~13	10
Maximum passage wall temperature T_w (K)	1256 (1800°F)	356.3
Inlet coolant bulk temperature $T_{b,i}$ (K)	867 (1100°F)	283
Density ratio $(\Delta\rho/\rho)_i = (\rho_{b,i} - \rho_w)/\rho_{b,i} = (T_w - T_{b,i})/T_w$	0.366	0.229
Rotational speed Ω (rpm)	0~15000	0~1250
Mean coolant velocity W_o (m/s)	34.5 ~ 69.0	6.17 ~ 12.34
Flow Reynolds number Re	$2.0 \sim 4.0 \times 10^4$	$2.0 \sim 4.0 \times 10^4$
Rotation number $Ro = Re_\Omega / Re$	0.091 ~ 0.182	0.1~ 0.2
Mean rotational Buoyancy parameter $\overline{Gr^*} = \overline{Gr_\Omega}/Re^2$	0.152 ~ 0.608	0.134~0.536

* The thermophysical properties for an aircraft engine are valued at P = 17 atm , $\rho = 6.002$ kg/m^3, T=1000 K and $\bar{R}/D = 50$

** The thermophysical properties for the present test rig are valued at P = 5 atm , $\rho = 5.94$ kg/m^3, T=300 K and $\bar{R}/D = 53$

serpentine square-sectioned flow passages with 60 deg staggered half-V rib. The coolant flowrate, rotational speed and wall heating power input are controlled to vary the experimental conditions. The pressurized and pre-cooled coolant air is used to obtain the values of parameters approximately the same as those of a real turbo-engine. The main flow directions are two radially outward flows and two radially inward flows in the flow passages. The rotational effects in these multi-pass serpentine channels may differ from each other for the different main flow directions and the presence of 180 deg bends. Two rib arrangements of different rib angle in the second and fourth passages are studied. Finally, one attempt of this work is to correlate the measured data for heat transfer in a radially rotating four-pass serpentine channel with staggered half-V rib turbulators.

2 Parametric Analysis

The flow in a heated, rotating four-pass serpentine channel is three-dimensional and extremely complex in nature. The combined effects of the Coriolis induced cross-stream secondary flow and centrifugal-buoyancy radial flows influence the flow and heat transfer characteristics in rotating channels. Refer to the previous parametric analysis by Soong et al. [7], with fixed geometric parameters, heat transfer rate can be expressed as a function of through-flow Reynolds number, $\mathrm{Re}=\rho W_o D/\mu$; rotation number, $\mathrm{Ro}=\Omega D/W_o$, and rotation-induced buoyancy parameter, $\mathrm{Ra}_\Omega^* = \mathrm{Ra}_\Omega/\mathrm{Re}^2$ or $\mathrm{Gr}_\Omega^* = \mathrm{Gr}_\Omega/\mathrm{Re}^2$. Accordingly, in the present work, Nusselt number is expressed as a function of the key parameters, viz.

$$\mathrm{Nu}_\Omega = f(\mathrm{Re},\mathrm{Ro},\mathrm{Gr}_\Omega^*) \qquad (1)$$

in which Prandtl number is not included for its constant value, $\mathrm{Pr}=0.72$

To simulate the real operating conditions, this study attempts to keep the parameters in the test rig as close to those in a real engine as possible. Table 2 reveals the geometry of the present test rig, including coolant passage diameter D, length L, and mean rotating radius $\bar{R}$ are similar to that in a real engine. On the other hand, the temperature and rotational speed of the test rig are significantly lower than those of an aircraft engine. Notably, the low rotational speed yields a low rotation number and a low rotational Grashof number. In the present study, strategically, the pressurized airflow is employed to compensate for the low rotational speed in the experiment. By using the pressurized air, a lower velocity of main flow is needed to keep the same value of a Reynolds number. Therefore, the low axial velocity yields a high rotation number. The coolant airflow was also pre-cooled to obtain a high-density ratio before entering the rotating duct. This high-density ratio yields Grashof numbers of the same order-of-magnitude as that in a real engine. Table 2 lists the ranges of parameters in an aircraft engine and the present test rig. Due to the limitation of electrical power input to the wall heaters, the values of some parameters in this study are slightly lower than those in the designed test rig.

3 Experimental Apparatus and Test Section

The experimental apparatus, as shown in Fig. 1 consists of five major parts: (1) a coolant air supply system; (2) heater and power control system; (3) speed controller; (4) test section; and (5) data acquisition system. The coolant air was supplied from a storage tank with a 0.7 MPa air compressor. A by-pass valve at the exit of the storage tank and a flowrate control valve at the exit of the piping system were used to maintain the required flowrate and pressure. Two electric digital flowmeters with the ranges of 0 ~670 and 0~1700 liter/min were mounted on the piping system. Also, two electrical digital pressure gauges with the range of 0 ~1.0 MPa were installed. Therefore, the pressures and flowrates of the coolant air at both ends of the test section can be detected. The average values were used to evaluate the parameters in this study. The differences of the two-end pressures and flowrates are the pressure drop and the flow leakage, respectively. A chiller was used to decrease the coolant temperature to around −2 °C before entering the rotating shaft. A condenser is installed on the upstream pipeline system of the coolant air inlet to collect the water condensed from the vapor contained in the air. The rotating shaft had two co-axial cylinders: an annular passage for the coolant inlet and an inner passage for the coolant outlet. A high-speed rotating joint and four sets of mechanical seals were used in the rotating shaft to prevent airflow leakage. The flow leakage was kept within 3 percent for minimum flowrate. Next, the pressure

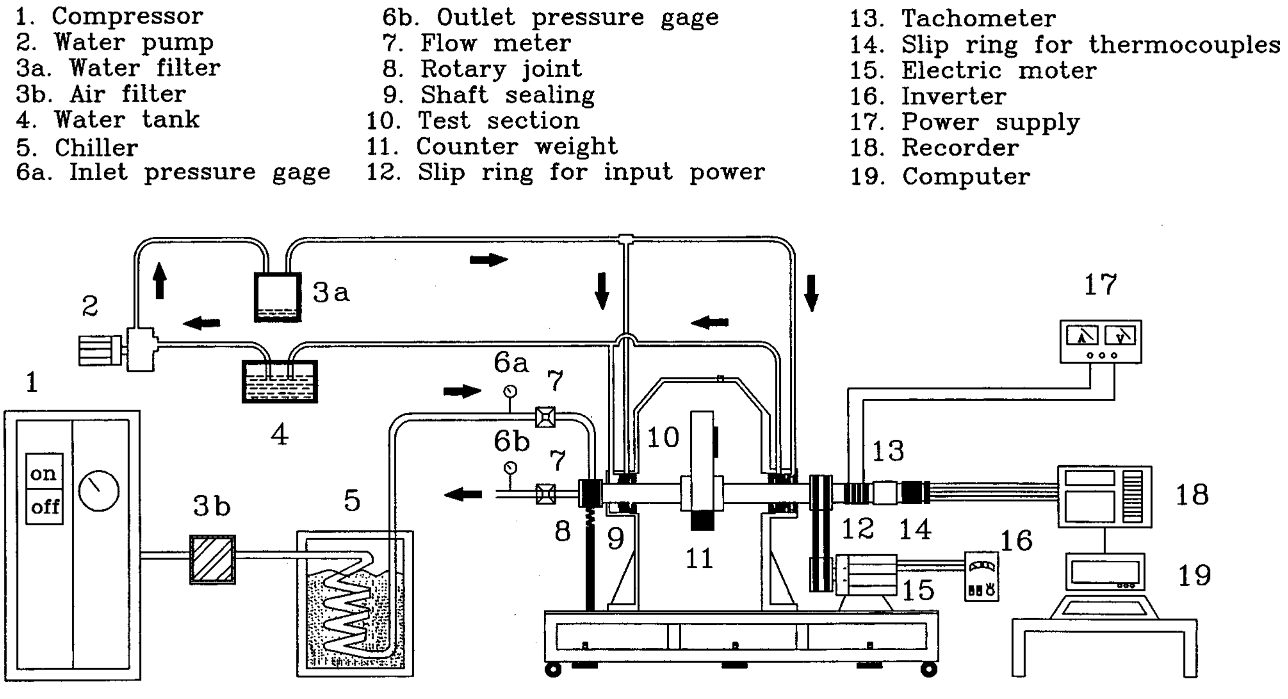

Fig. 1 Schematic diagram of experimental apparatus

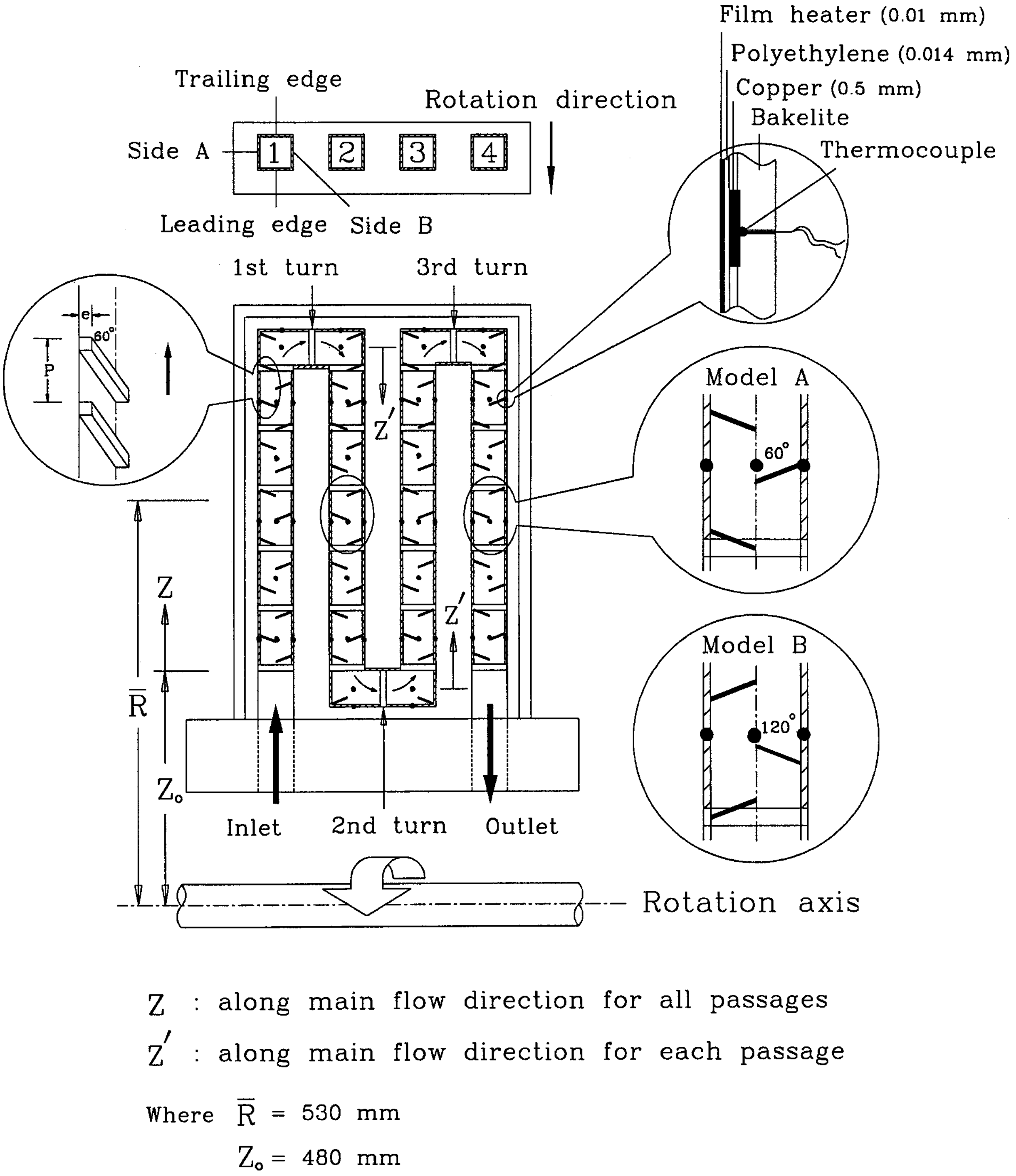

Fig. 2 Heat transfer test section of the four-pass channel model with staggered half-V ribs

was measured 0.51 MPa at the inlet and 0.49 MPa at the outlet. A water cooling-cycle system was used to cool the mechanical seals.

A 3.73 kW AC induction motor impelled the rotating hollow shaft with a belt-pulley system. The rotational speed can be adjusted continuously by an inverter to a maximum rotating speed of 1250 rpm. The rotational speed was detected by a photoelectric tachometer. The shaft rotating direction could be in a clockwise or counter-clockwise direction to measure the leading and trailing wall temperature distributions with only one wall thermocouple installation.

Along the flow passage, T-type thermocouples for measuring the wall temperature were embedded under the interior wall surface of the flow passage. Two T-type thermocouples were positioned at the duct inlet and outlet for measuring the inlet and exit coolant bulk temperatures. Finally, a 20 contact point slip ring was used to transfer outputs of fifty-eight thermocouples to a 60-point hybrid recorder by a switching device.

To reduce the measurement errors in the experimental data and the signal of temperature from slip ring, the eccentric bearing in the rotating part was used to minimize the vibration of the machine. Also, a pump was installed to cycle the extra coolant water, thereby alleviating the temperature rise coming from the rotating shaft. The measurement process was tested in a closed space (1200×400×1200 mm) to reduce the heat loss. Further, the air

Table 3 The values of local Nusselt number for $\Omega=0$ in four-pass staggered half-v rib serpentine channels

Position	Z/D	Re=20000		Re=30000		Re=40000	
		Model A	Model B	Model A	Model B	Model A	Model B
1st Passage	1.0	113.01	146.01	132.72	163.57	148.87	184.17
	2.5	147.41	156.21	168.88	176.30	194.43	201.82
	4.0	175.58	170.27	196.05	190.46	223.31	219.83
	5.5	194.61	187.14	214.69	212.71	239.10	236.64
	7.0	211.43	206.98	226.98	247.81	251.22	267.11
1st Turn	8.5	202.08	258.64	211.86	277.83	230.72	290.80
	10.5	178.52	277.65	190.97	293.46	210.18	304.26
2nd Passage	12.0	174.49	201.55	186.82	228.18	209.68	257.36
	13.5	158.34	163.87	171.35	200.05	190.37	230.78
	15.0	139.61	155.48	152.22	193.80	168.57	224.34
	16.5	128.51	161.63	141.31	190.89	154.30	218.15
	18.0	131.83	179.59	144.20	200.39	159.02	225.79
2nd Turn	19.5	148.25	236.67	165.99	245.36	182.40	264.04
	21.5	177.33	224.76	201.72	238.29	226.64	255.02
3rd Passage	23.0	168.01	162.31	191.15	188.15	212.81	215.11
	24.5	157.63	145.17	177.92	170.61	198.26	195.82
	26.0	172.38	145.87	197.54	170.90	219.79	194.27
	27.5	191.79	145.88	216.72	172.04	246.05	197.17
	29.0	210.97	172.22	240.26	198.83	275.96	212.47
3rd Turn	30.5	236.50	251.38	275.78	260.01	300.24	271.62
	32.5	250.58	279.83	290.64	290.03	325.58	301.92
4th Passage	34.0	192.83	213.14	219.22	224.03	250.96	257.66
	35.5	175.71	185.25	197.59	208.47	225.64	232.35
	37.0	167.64	170.88	189.24	192.43	212.76	213.71
	38.5	152.31	153.09	170.33	175.24	191.58	199.42
	40.0	102.35	149.58	112.25	169.92	122.79	189.81

flow inlet and outlet was clogged up and the varying power was input. The electric power was supplied to the film heater until the every wall temperature readings reached the steady state. The steady-state wall temperature was measured for several power levels to establish the relationship between wall to ambient temperature difference.

3.1 Test Section. The rotation number in the test process was increased by compressing the inlet airflow to 5 atm to subsequently increase the density of the coolant airflow. Therefore, the entire test section was uniquely designed, in which the material of the test section, including the base and cover was made of Bakelite. The base part had *U* groove for installation of the O-rings to prevent the compressed air flow from leaking. The thermocouple was embedded into the copper block. To prevent the air leakage, the back of the copper having the two level spaces filled with seal glue to mount the Bakelite. Also, the O-ring was inserted between the test section and the support section, and between the support and the rotating shaft. Two sets of mechanical seals were installed into the front and back of the bearing in the rotating shaft. Therefore, the entire test section was not affected by the room environment temperature.

The test section of the serpentine channel had two outward flow passages, and two inward flow passages, along with three 180 deg turn sections as shown Fig. 2. The test section was of a hydraulic diameter of 10 mm and a mean rotational radius of 530 mm. To compare our experimental data with that of Han et al. [8] at 1 atm, a 180 deg turn section was designed by consisting of two 90 deg bends with 10 mm apart. The main flow direction of the passage was perpendicular to the centerline of the rotating shaft. The ribs were mounted correspondingly on both the leading and trailing walls. In Model A, the ribs were oriented 60 deg to the bulk flow for each passage, which is the same as that of Dutta and Han [5]. In Model B, the ribs were oriented 60 deg to the bulk flow for first and third passages and the ribs were oriented 120 deg to the bulk flow for second and fourth passage. The staggered half-V ribs mostly generated higher turbulence due to orientation of the ribs against bulk flow in second and fourth passage. Copper ribs of square cross section are glued to the heater surfaces. The rib height-to-hydraulic diameter ratio is 0.125, and the pitch-to-height ratio is 10. The ribs on the opposing surfaces were aligned with each other rather than staggered. To characterize the heat transfer rate on each wall, the circumferential wall heat conduction was deliberately suppressed by using material of a low thermal conductivity. The heaters started at $Z_o=480$ mm and attached on the walls including straight sections and sections of 180 deg bends.

A thermocouple was positioned at the duct inlet for measuring the bulk temperature of inlet coolant air. A mixing chamber with staggered rod bundles was attached on the exit plane to provide a well-mixed condition. The outlet bulk temperature was read by a thermocouple located behind the mixing chamber. Twenty-six thermocouples were installed on the trailing wall. The thermocouples were arranged along the centerline on the trailing wall at position Z/D as indicated in Table 3. Sixteen thermocouples on the sidewall A and fourteen thermocouples on the sidewall B were mounted at the same axial distance as that of the trailing wall. The temperature on the leading wall was measured by merely changing the rotation direction. In the present study, the thermocouples were embedded in a copper block having a thickness 1.5 mm. The copper blocks were electrically insulated from the heater by a polyethylene film of thickness 0.014 mm. The installation of thermocouples resembled that of Dutta and Han [5]; only the leading and trailing walls were fitted with T-type thermocouples. Further constructional details of the test section are shown in Fig. 2. In the present study, the channel walls were uniformly heated by a constant heating power but with the presence of heat loss. Strictly speaking, it is neither exactly uniform heat flux nor uniform wall temperature. However, the heat transfer surface is made of extremely thin stainless-steel sheet of 0.01 mm in thickness, the thermal boundary condition is very close to uniform heat flux. A detailed discussion on the heat transfer condition of this design of rotating channel can be found in Hwang and Kuo [9].

An adapter of 42 cm in length was made of Bakelite and placed between the test section and the rotating shaft to increase the radial length of the test section. The data of heater power input and the wall temperature distributions were recorded and analyzed to obtain the heater transfer coefficients. Dynamical balance was examined and achieved for the assembly of a rotating shaft and test section.

3.2 Data Reduction. The local heat transfer coefficient h_Z was evaluated as the ratio of the net wall heat flux q_{net} to the temperature difference between the wall temperature $T_{W,Z}$ and the coolant bulk temperature $T_{b,Z}$, i.e., $h_Z = q_{\mathrm{net}}/(T_{W,Z} - T_{b,Z})$. The net heat flux from the duct walls to the airflow was obtained by subtracting the external heat loss from the electrical power supplied by the film heaters. The heat loss tests were performed not only at stationary but also at various rotating rates, i.e., $\Omega = 0$, 250, 500, 750, 1000, and 1250 rpm. Thermocouples were installed on the outer surfaces of four walls. The measured electrical power input and steady state temperature determine the amount of heat loss at the measured temperature. By varying the electrical power input, the relationship between the heat loss and temperature can be obtained. The external heat loss including the axial conduction and convection is attributed to both conduction from the heated test section to the model support structure and convection to the ambient air in the test cell. The value is about 445.12 watt/m^2 for the extreme cases. The heat loss of 7.3 percent heat loss of the total input power was estimated. For airflow across each heating element of copper block, The local bulk temperature $T_{b,Z}$ can be determined by considering a local energy balance of input heat, estimated heat loss and the fluid enthalpy change. The bulk temperature at downstream station of the previous heating element is used as the upstream $T_{b,Z}$ for the next station. The local Nusselt number was calculated from the local heat transfer coefficient, hydraulic diameter and thermal conductivity of air as

$$\mathrm{Nu}_{\Omega} = h_z D / k_{\mathrm{air}}. \tag{2}$$

The value of the thermal conductivity K_{air} was evaluated at the local bulk temperature.

3.3 Uncertainty Analysis. The errors in the temperature reading were obtained in a preliminary calibration of the thermocouples. The uncertainty was ±0.1°C from the readout of data recorder. The difference between wall temperature and bulk temperature was greater than 15°C. The flow rate was calibrated by using compressed air at 5 atmospheric pressure. The maximum error in the flow rate was about 3 percent at 7.17×10^{-4} m^3/s. The rotational speed was detected by a tachometer with only a little of oscillation, and the maximum error of the rotational speed was 2 percent at 250 rpm. The analysis also included uncertainties of air thermophysical properties and the probable error from each junction. Uncertainties in parameters were estimated by using the root-sum-square method of Kline and McClintock [10]. The measured quantity and its uncertainty can be expressed as $R = R \pm \delta R$. The uncertainties of cross-sectional area, power, volume flowrate, pressure, temperature, Reynolds number, Nusselt number, rotation number, and Rayleigh number were estimated within ±1.41 percent, ±4.04 percent, ±2.33 percent, ±2 percent, ±9.9 percent, ±2.73 percent, ±10.88 percent, ±3.24 percent, and ±13.14 percent, respectively.

4 Results and Discussion

Distribution of the local Nusselt number was determined along the four-pass walls for the ranges of Reynolds number (Re $=20{,}000$, 30,000, and 40,000), rotational speed (0, 250, 500, 750, 1000, and 1250 rpm), and outlet-to-inlet temperature differences ($T_{b,o} - T_{b,i} = 20$, 30, and 40 °C). Data presented herein were obtained in the first, second, third and fourth passages with radially outward, inward, outward and inward flows, respectively.

4.1 Heat Transfer in Stationary Channels. Figure 3 gives the wall and coolant bulk temperatures at Re=20,000, 30,000, and 40,000 for $\Omega = 0$. The temperature differences among those of leading (trailing) and side walls are not significant. As the Reynolds number increases, the gradient of the coolant bulk temperature decreases. The average slope of the wall temperature distribution is the same as the slope of the coolant bulk temperature distribution at the selected Reynolds numbers. The temperature difference in the regions of two 90 deg bends drops due to a large heat transfer rate in this region. As the Reynolds number increases, the effect of bends on the wall temperature is less pronounced.

The Dittus-Boelter correlation [11] for the stationary condition is

$$\mathrm{Nu}_{\infty} = 0.023\,\mathrm{Re}^{0.8}\,\mathrm{Pr}^{0.4}. \tag{3}$$

For Pr=0.72 (air) in the this study, Eq. (3) is reduced to

$$\mathrm{Nu}_{\infty} = 0.0202\,\mathrm{Re}^{0.8} \tag{4}$$

for the fully developed turbulent flow in a smooth circular duct with a uniform wall temperature. As generally assumed, the Nusselt numbers in Eqs. (3) and (4) are roughly the same as those in a square duct with uniform wall heat flux [12]. On the first, second and third turns, the Nusselt numbers are higher than those in the passages due to the secondary flow induced by the two 90 deg bends. The Nusselt number achieves its highest value at the second 90 deg bend.

Figure 4 illustrates the heat transfer rates in stationary channels at selected Reynolds numbers. Measured data indicate that the values of Nusselt of these passages increase with an increase in

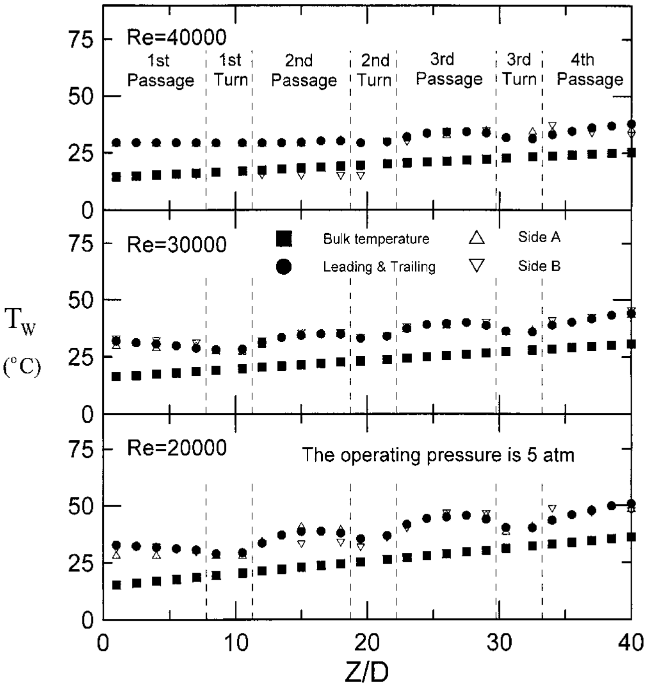

Fig. 3 Local distribution of wall and fluid bulk temperature at Re=20,000 and $\Omega = 0$ (the operating pressure is 5 atm)

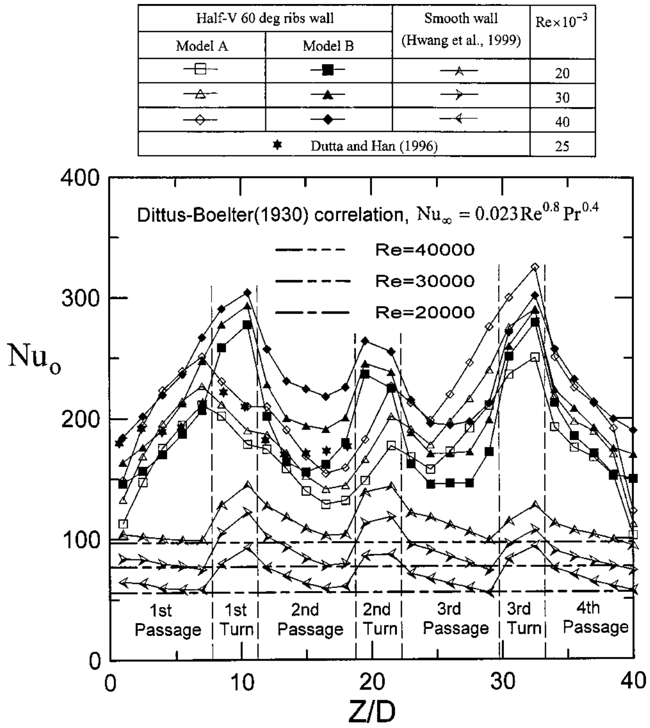

Fig. 4 Reynolds number effects on the local Nusselt numbers in both smooth channel and ribbed channel at $\Omega=0$ (the operating pressure is 5 atm)

Re for each passage and bending region. Depending on the rib geometry, heat transfer is enhanced by up to threefold more than a smooth wall circular tube ([11]) at zero rotation. Also, the largest difference of the heat transfer rates occurs from the smooth wall [13] and with a staggered half-V angle rib. It is attributed to the turbulent mixing from the staggered half-V angle rib. The Nusselt number in the half-V ribbed passage is nearly two to three times higher than for the smooth wall, which is close to that observed by Dutta and Han [5]. Since the orientation of the ribs in the second and fourth passage against bulk flow, Model B can generate a higher level of turbulence than Model A. The local Nusselt number of Model B is higher than that of Model A in the second passage. In the first and second turns, the local heat transfer rates in Model B are still higher than that in Model A. It is possibly attributed to the higher turbulence generated by the ribs in the second passage of Model B. In the fourth passage, there is only little difference between heat transfer rates.

4.2 Comparison of Heat Transfer in Smooth and Ribbed Channels. Figure 5 compares the rib effects on the heat transfer at non-rotating condition at Re=20,000. Obviously, the Nusselt number for ribbed walls are higher than the smooth wall. It is speculated that this behavior is due to the increase of the development of the secondary flow with ribbed wall effect and interacts with the separate flow, destabilized near-wall flow field. The complex flow interaction results in the different heat transfer characteristics of Model A and Model B. It could be conjectured that separation flow at inter-rib space has a profound impact on the heat transfer results. In both the second and fourth passages, heat transfer in Model B are higher than that in the Model A. This is attributed to the different rib arrangement in the second and fourth passages of Model B. The ribs in these two passages are placed at an angle-of-attack 120 deg with respect to the main flow direction. This arrangement is just like to sweep the ribs against the main flow and, therefore, results in better turbulent mixing and heat transfer performance.

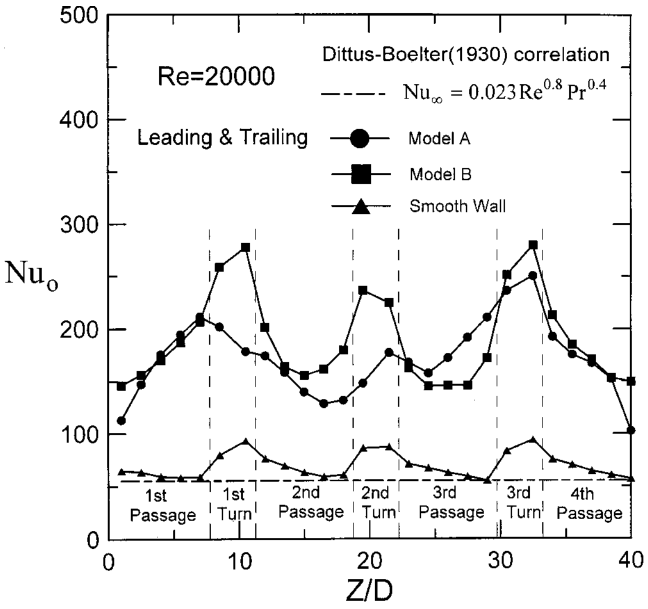

Fig. 5 Rib effects on the local heat transfer at Re=20,000 and $\Omega=0$ (the operating pressure is 5 atm)

To highlight the rib effects, typical results of heat transfer ratios (Nu_r/Nu_s) for Model A at Re=20,000 and Ro=0.042, 0.127, and 0.210 are shown in Fig. 6. For a rotating channel, heat transfer from the rib surfaces themselves varies significantly between the different rib surfaces. This indicates that heat transfer enhancement by the ribs is about 2~3 times than that on smooth walls. Heat transfer from ribbed trailing wall increase for small rotation number and then decreases at higher rotation number as opposed to decrease in trailing smooth wall. Interaction of rotation with secondary flow from ribs and flow separation near ribs are the cause of this beneficial increase in heat transfer rate from the trailing walls at small rotation number. Heat transfer from the leading wall with ribs behaves similar to that for the smooth walls.

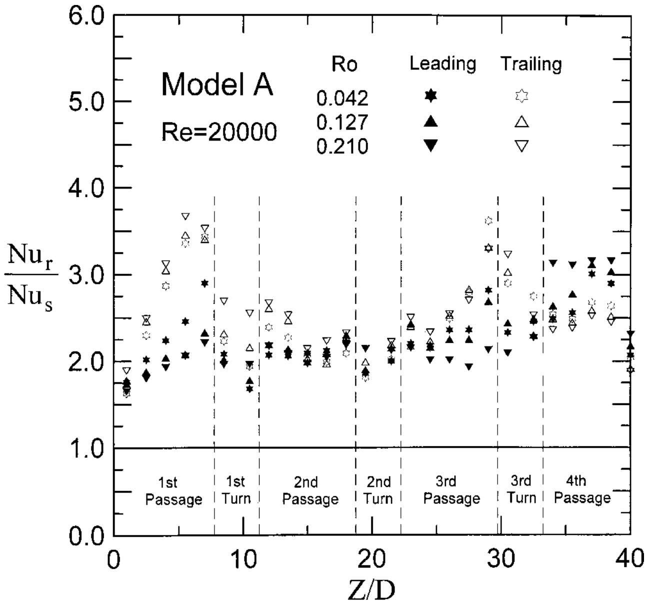

Fig. 6 Heat transfer ratios Nu_r/Nu_s at Re=20,000 in rotating channel model *A* with Ro=0.042, 0.127, and 0.210 (the operating pressure is 5 atm)

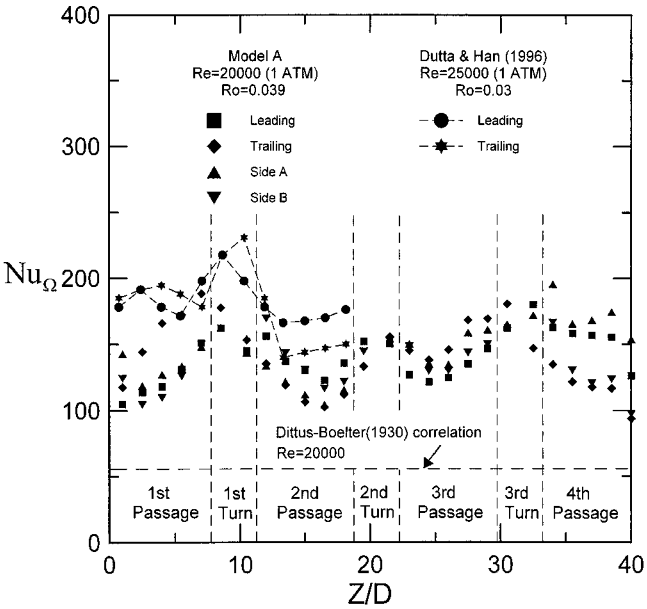

Fig. 7 Local heat transfer rates at Re=20,000 on the leading wall, trailing wall, and two side-walls of rotating channel model A (the operating pressure is 1 atm)

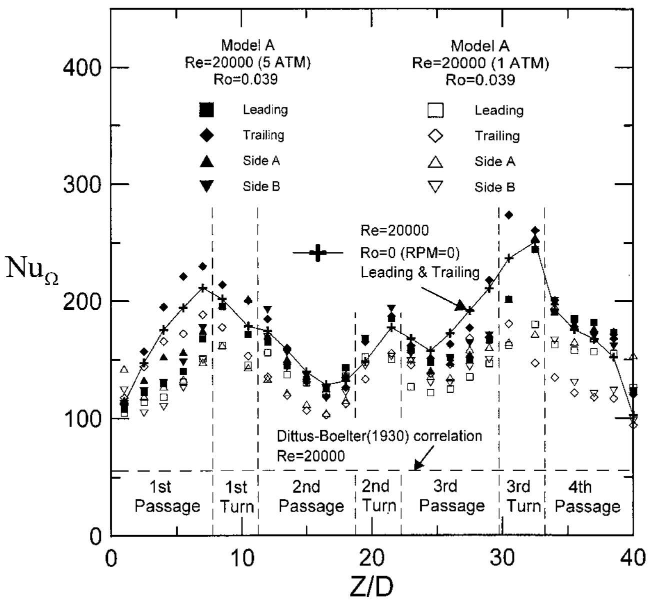

Fig. 8 Heat transfer performance of pressurized (5 atm) and atmospheric (1 atm) airflows in rotating ribbed channel Model A

In the first and third passages, heat transfer enhancement by rib effect on trailing wall is obviously larger than that on leading wall. In the second and fourth passage, the superior changes. In the first and third flow passages, the rib effects on heat transfer enhancement of the leading wall reduce with increasing rotation number, whereas the situation inverses in the second and fourth passages. Considering the outward and inward mail flow and the change in Coriolis-induced cross-stream in these flow passages, the above mentioned phenomena are reasonably attributed to a combined effect of the Coriolis-induced secondary flow and the presence of the ribs.

4.3 Effects of Operating Pressure. In Fig. 7, the present measurements of the local heat transfer with staggered half-V 60 deg ribs on the leading and trailing walls are compared with the experimental data of Dutta and Han [5]. Basically, two sets of Nu_Ω at 1 atm have the same order. The deviation in the entrance region is caused by the different design of the model inlet. Our model has an extension of long pipe upstream the inlet. Also, Dutta and Han's data in the second passage increase along the channel for the exit effect.

Figure 8 shows the local heat transfer performance of pressurized (5 atm) and atmospheric (1 atm) airflow in Model A at $Re = 20{,}000$ and $Ro = 0.039$. The pressurized flow results in a stationary channel, $Ro = 0$, are also plotted for comparison. Generally speaking, the pressurized coolant airflow performs better heat transfer performance than the atmospheric flow.

4.4 Effects of Rib Arrangement on Heat Transfer. Figure 9 compares the heat transfer in channels of smooth walls [13], Model A and Model B at Re=20,000 and Ro=0.2. Notably, the arrangement of the ribs in Model A is oriented 60 deg to the bulk flow for each passage. Also, in Model B, the ribs were oriented 60 deg to the bulk flow for first and third passage. While the ribs were oriented 120 deg to the bulk flow in the second and fourth passages. Refer to the inner wall of the 180 deg-turn, the ribs in the second and fourth passages are swept upstream against the main flow. These staggered half-V ribs in Model B mostly generated a higher turbulence due to the orientation of the ribs against bulk flow in the second and fourth passages.

In Fig. 9, it is observed that the rib-effects on heat transfer of leading walls are higher than that of trailing walls in the first and third passages (radially outward flow), but lower in the second and fourth passages (radially inward flow). It is a consequence of Coriolis force effect. As to the differences in results of Models A and B, the leading wall heat transfer rates in the portion including the first turn, the second passage and second turn of Model B are noticeably higher than that in model A. The different arrangement of the rib is responsible for this deviation. In the downstream part, i.e., the third and fourth passages, the fluid turbulence might become sufficiently high. The differences between flow characteris-

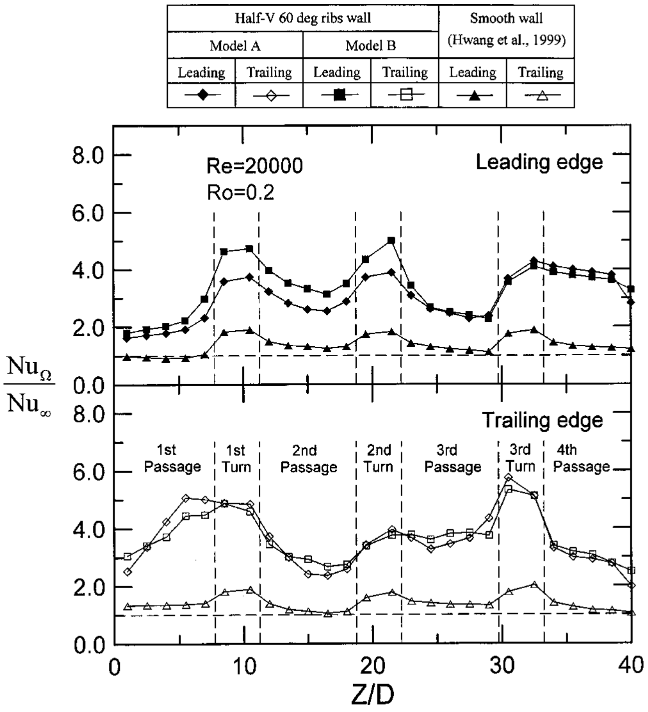

Fig. 9 Comparison of local Nusselt number ratios in smooth channel, ribbed channels Model A and Model B at Re=20,000 and Ro=0.2 (the operating pressure is 5 atm)

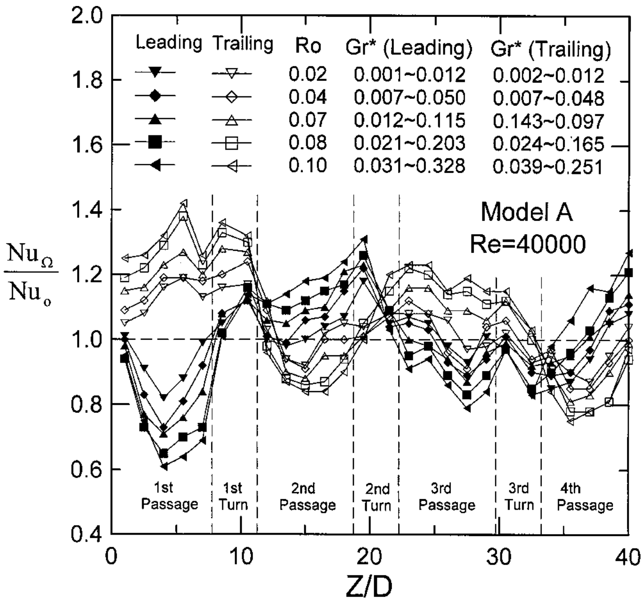

Fig. 10 Effect of rotation number on the local Nusselt number ratio at Re=40,000 for Model A (the operating pressure is 5 atm)

tics and, therefore, the deviations between heat transfer rates in two models reduce. On the trailing walls, the differences in heat transfer of Models A and B are relatively small. It is speculated that the turbulence levels induced by the two rib arrangements are not too much different on these pressure sides.

4.5 Rotational Effects on Heat Transfer. Figure 10 displays the effect of rotation number on the local heat transfer ratio, $\mathrm{Nu}_\Omega/\mathrm{Nu}_o$ at Re=40,000 in Model A. The notation Nu_o denotes Nusselt number under stationary condition. The rotation numbers are 0.02, 0.04, 0.07, 0.8, and 0.1. Since the strength of the Coriolis-induced cross-stream secondary flow is increasingly intensified with an increase of the rotation number, the local Nusselt number ratios on the trailing wall for the outward flow and on the leading wall for the inward flow increase as well. This tendency becomes more apparent at a higher rotation number than that at a lower one. On the trailing wall for the outward flow (e.g., the first and third passages) and on the leading wall for the inward flow (e.g., the second and fourth passages), the heat transfer rates are increased. Notably, the effects of rotation number on heat transfer are most pronounced in the first passage. In the second, third and fourth passages, the effects of rotation number become attenuated. This is largely attributed to that the effect on turning geometry in those passages dominates the heat transfer

Figure 11 shows the local values of $\mathrm{Nu}_\Omega/\mathrm{Nu}_o$ with variations of rotation number on the selected sections of flow passages at Re=20,000 and $T_{b,o}-T_{b,i}=20$ in Model A and Model B. With increasing Ro, the deviations between values of $\mathrm{Nu}_\Omega/\mathrm{Nu}_o$ for leading and trailing walls are enlarged. By examining the data at Ro=0.2, it is found that the rotational effect is most remarkably in the first and third passages, e.g., $Z/D=4.0$ and 26.0. In these two passages, the main flow is radially outward and the heat transfer performance can be benefited from the Coriolis-induced secondary flow and the centrifugal buoyancy effect. In the second and fourth passages, e.g., $Z/D=15.0$ and 37.0, the reverse effect of Coriolis force changes the roles of leading and trailing walls and also shortens the deviation between the rotational effects on the heat transfer of two walls. In the bend regions, although the flow physics could be very complicated with the presence of turbulence, separation and recirculation, the rotational effects are still noticeable. The above observations are valid for both Models A and B.

4.6 Rotational Buoyancy Effect on Heat Transfer Rate. Figure 12 depicts the centrifugal buoyancy effect on the mean heat transfer rate at each passage in Model A at Re =20,000. The inlet-to-outlet bulk temperature was maintained at $T_{b,o}-T_{b,i}=20$, 30, and 40 °C. In a rotational flow field like this, centrifugal force exerts in the mail flow by producing radial pressure gradient. With density variation in the non-isothermal flow, additionally, the thermal buoyancy stemmed from centrifugal force emerges, alters flow and heat transfer characteristics signifi-

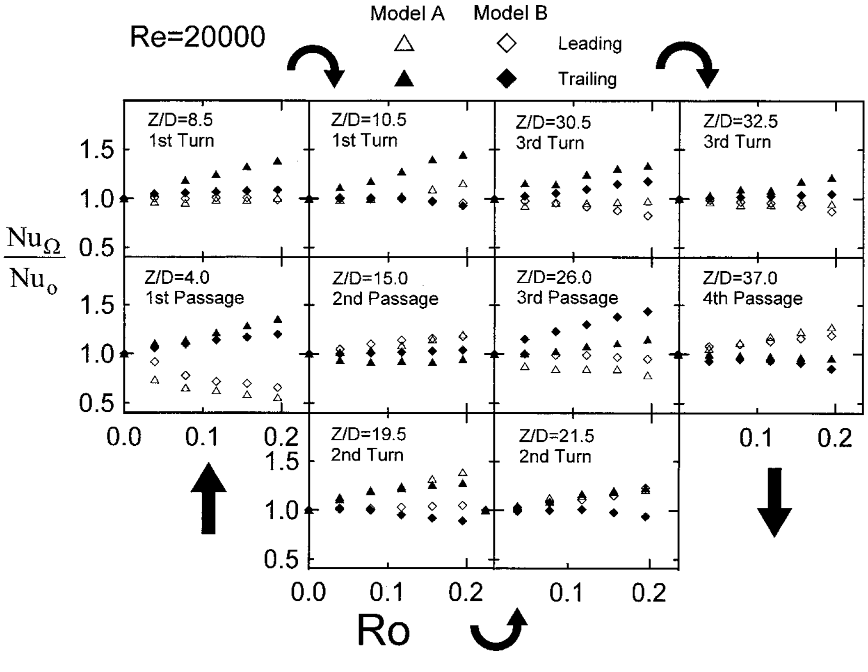

Fig. 11 Local heat transfer performance at Re=20,000 in both ribbed channels A and B with variation of rotation number on the selected cross section of flow passages (the operating pressure is 5 atm)

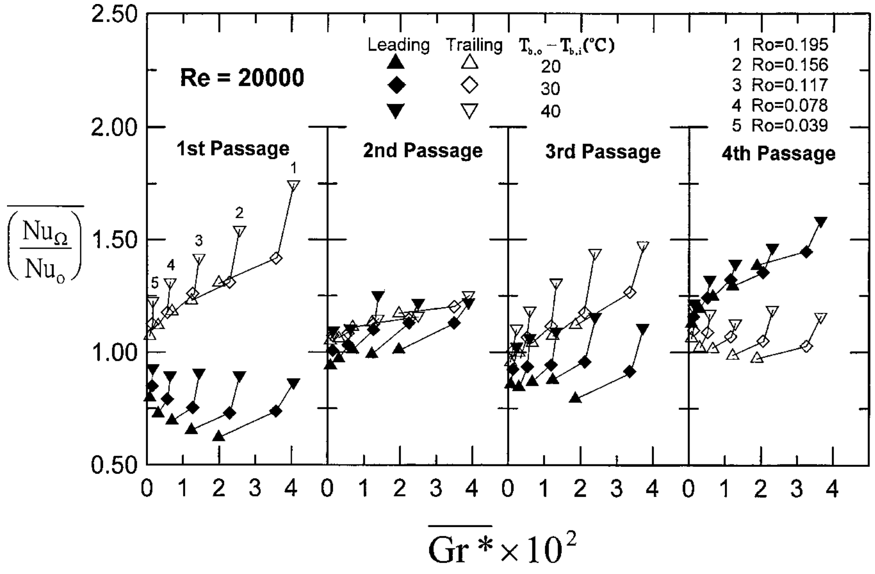

Fig. 12 The centrifugal buoyancy effects on the mean heat transfer rate at Re =20,000 in each passage of ribbed channel A (the operating pressure is 5 atm)

cantly. In the extreme case of the present study, the ratio of thermal centrifugal force to hydrodynamic centrifugal force is $\beta\Delta T$. In addition, the heat transfer is enhanced for a higher temperature difference. The direction of main flow and buoyancy flow is attributed to the difference of the results. In the outward-flow passage, the direction of forced flow is in contrast to the buoyancy flow (opposing flow). In the inward-flow passage, these two forces are in the same direction (aiding flow). The Nusselt number ratio increases with an increase in the Grashof number in all passages. This observation differs from that of Hwang and Kuo [14] at Re=5000 in the transitional flow regime. In laminar and transitional flow regimes, centrifugal buoyancy effects usually decreases the Nusselt number ratio, Nu_Ω/Nu_o, [7,14,15]. However, in a turbulent mixed convection, increasing buoyancy parameter in a buoyancy opposing flow may result in an increasing velocity fluctuation [16], therefore, the heat transfer can be enhanced. These phenomena can be observed when analyzing the mixed convection of buoyancy-induced opposing and aiding flows in a vertical heated tube [17–19]. In the present results, the growing trend of $\overline{Nu_\Omega/Nu_o}$ with $\overline{Gr^*}$ is most pronounced for the buoyancy opposing flow in the first and third passages. When increasing the

Leading edge	rms (%)				$Re \times 10^{-3}$
	1st	2nd	3rd	4th	
◆ Model A	9.52	7.85	7.70	8.76	20, 30, 40
◇ Model B	10.12	10.46	8.43	9.28	20, 30, 40
✸ Dutta and Han (1996)	5.59	5.16	----	----	25

Trailing edge	rms (%)				$Re \times 10^{-3}$
	1st	2nd	3rd	4th	
◆ Model A	9.90	8.58	10.21	8.20	20, 30, 40
◇ Model B	9.67	9.85	10.04	8.48	20, 30, 40
✸ Dutta and Han (1996)	8.08	11.67	----	----	25

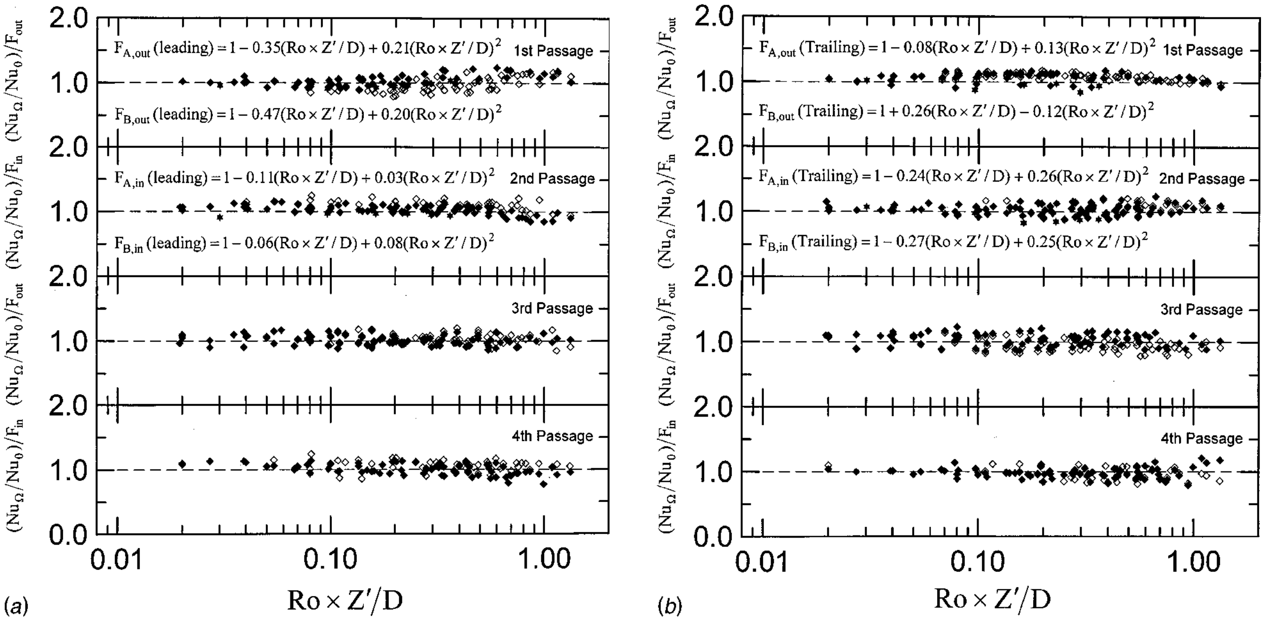

Fig. 13 The correlation of heat transfer data for the four passages of serpentine channels with staggered half-V rib turbulators: (*a*) leading wall; (*b*) trailing wall (the operating pressure is 5 atm)

rotational buoyancy parameters in the outward flow passage, Wagner et al. [20,21], Morris and Ghavami-Nasr [22], and Han and Zhang [23] observed the increasing tendency on heat transfer, either. Generally, the present data in Fig. 12 are quite reasonable in qualitative sense. However, the rapid change of the data at $T_{b,o}-T_{b,i}=40$ seems to need further study.

4.7 Heat Transfer Correlation. Figures 13(*a*) and 13(*b*) show the correlation of the present heat transfer data for the four-pass serpentine flow passage with staggered half-V rib turbulators on the leading and trailing walls. The correlation is for the outlet and inlet temperature difference $T_{b,o}-T_{b,i}=20\,^{\circ}\mathrm{C}$ and Reynolds number $=20{,}000$, $30{,}000$, and $40{,}000$. By using the relation of $\mathrm{Nu}_{\Omega}/\mathrm{Nu}_{o}=F(\mathrm{Ro},Z'/D)$, the data of the outward and inward flows on the leading and trailing walls can be fitted. According to the results for $\mathrm{Ro}=0\sim0.2$, they are correlated by the following expressions: For Model A (the ribs were oriented 60 deg to the bulk flow for each passage), it is given by

$$F_{A,\mathrm{out}}(\text{leading})=1-0.35(\mathrm{Ro}\times Z'/D)+0.21(\mathrm{Ro}\times Z'/D)^{2} \tag{5}$$

$$F_{A,\mathrm{in}}(\text{leading})=1-0.11(\mathrm{Ro}\times Z'/D)+0.03(\mathrm{Ro}\times Z'/D)^{2} \tag{6}$$

$$F_{A,\mathrm{out}}(\text{Trailing})=1-0.08(\mathrm{Ro}\times Z'/D)+0.13(\mathrm{Ro}\times Z'/D)^{2} \tag{7}$$

$$F_{A,\mathrm{in}}(\text{Trailing})=1-0.24(\mathrm{Ro}\times Z'/D)+0.26(\mathrm{Ro}\times Z'/D)^{2}. \tag{8}$$

For Model B (the ribs were oriented 60 deg to the bulk flow for first and third passage and the ribs were oriented 120 deg to the bulk flow for second and forth passage), it is given by

$$F_{B,\mathrm{out}}(\text{leading})=1-0.47(\mathrm{Ro}\times Z'/D)+0.20(\mathrm{Ro}\times Z'/D)^{2} \tag{9}$$

$$F_{B,\mathrm{in}}(\text{leading})=1-0.06(\mathrm{Ro}\times Z'/D)+0.08(\mathrm{Ro}\times Z'/D)^{2} \tag{10}$$

$$F_{B,\mathrm{out}}(\text{Trailing})=1+0.26(\mathrm{Ro}\times Z'/D)-0.12(\mathrm{Ro}\times Z'/D)^{2} \tag{11}$$

$$F_{B,\mathrm{in}}(\text{Trailing})=1-0.27(\mathrm{Ro}\times Z'/D)+0.25(\mathrm{Ro}\times Z'/D)^{2}. \tag{12}$$

The correlation is curve fitted independently to correlate the data of the radially rotating four-pass serpentine channel with staggered half-V ribbed turbulators on each passage. In Model A, for the leading wall, root-mean-square deviations of 9.52 percent and 7.70 percent are found in the first and third passages, 7.85 percent and 8.76 percent are in the second and fourth passages. Also for the trailing wall root-mean-square deviations of 9.90 percent and 10.21 percent are in the first and third passages, 8.58 percent and 8.20 percent are in the second and fourth passage. In Model B, for the leading wall, root-mean-square deviations of 10.12 percent and 8.43 percent are found in the first and third passages, 10.46 percent and 9.28 percent are in the second and fourth passages. Also for the trailing edge root-mean-square deviations of 9.67 percent and 10.04 percent are in the first and third passages, 9.85 percent and 8.48 percent are in the second and fourth passage. The maximum error of root-mean-square deviations in the correlation Eq. (10) for Nusselt number ratio is 10.46 percent.

The experimental data of Dutta and Han [5] for uniform wall heat flux at Reynolds number $=25{,}000$ are also presented. In general, those data correlate well with the present correlation on both the trailing and leading edges. The error of root-mean-square deviations is about 5 percent for the leading wall. It increases to 11.67 percent in the second passage for trailing wall, which is possibly attributed to the difference in the arrangement of the ribs in second passage.

Concluding Remarks

The present study thoroughly elucidates the rotational heat transfer in a serpentine four-pass channel with staggered half-V rib turbulators. The intake coolant is pressurized and pre-cooled in the present experiments, therefore, the ranges of Reynolds number, rotation number and Grashof number closely resemble those of a real turbine engine.

1 From the experimental results of the present two models of ribbed four-pass channels, it is found that the rib effects on the local heat transfer are significant through the whole channels.

2 In a rotating channel, for example model A, the rib effects on local heat transfer enhancement $\mathrm{Nu}_{r}/\mathrm{Nu}_{s}$ can be coupled with the rotational effects. In radially outward flow in the first and third passages, the influences of rotation are relatively remarkable.

3 In the present results, it is found that the pressurized coolant airflow shows better heat transfer performance.

4 From the comparison of the measured data on Models A and B, it is observed that Model B with ribs placed 120 deg against the main flow in the second and fourth passages has beneficial effects in local heat transfer, especially in the region of the first turn, the second passage and the second turn. It implies that the rib arrangement is one of significant factors in design of ribbed coolant channel.

5 With increasing characteristic temperature difference, the Nusselt number ratio increases with buoyancy parameters in this turbulent mixed convection with the presence of rotation-induced buoyancy effects.

6 The empirical correlations for local heat transfer data in the present parameter ranges are proposed. The previous data of Dutta and Han [5] are also well correlected with the present correlations. It is believed that the correlations are useful reference in design of the multi-pass ribbed coolant channel.

Acknowledgment

The authors would like to thank the National Science Council, Taiwan, ROC for financially supporting this research under Grant No. NSC-87-2212-E-007-048.

Nomenclature

A = cross sectional area of the flow passage, mm^2
Cp = specific heat, J/(Kg·K)
D = hydraulic diameter $=2ab/(a+b)$, mm
e = rib height
F_{in} = correlation function for inlet passage
F_{out} = correlation function for outlet passage
Gr_{Ω} = local rotational Grashof number
= $\beta(T_{W,Z}-T_{b,Z})(\varepsilon+Z'/D)\mathrm{Re}^{2}\,\mathrm{Ro}^{2}$
$\overline{\mathrm{Gr}_{\Omega}}$ = mean rotational Grashof number
= $\beta(T_{b,o}-T_{b,i})(\varepsilon+Z'/D)\mathrm{Re}^{2}\,\mathrm{Ro}^{2}$
Gr^{*} = local rotational Buoyancy parameter $=\mathrm{Gr}_{\Omega}/\mathrm{Re}^{2}$
$\overline{\mathrm{Gr}^{*}}$ = mean rotational Buoyancy parameter $=\overline{\mathrm{Gr}_{\Omega}}/\mathrm{Re}^{2}$
h_{Z} = heat transfer coefficient $=q_{\mathrm{net},Z}/(T_{W,Z}-T_{b,z})$, W/(m^2·°C)
k_{air} = thermal conductivity of air, W/(m·K)
L = coolant passage length, mm
Nu = Nusselt number $=h_{Z}D/k_{\mathrm{air}}$
Nu_{r} = Nusselt number for ribbed wall
Nu_{s} = Nusselt number for smooth wall
Nu_{o} = Nusselt number for non-rotating condition
Nu_{Ω} = Nusselt number for rotating condition
Nu_{∞} = Nusselt number for fully developed turbulent flow in a non-rotating circular tube
P = rib pitch or streamwise spacing
Pr = Prandtl number $=Cp\cdot\mu/k_{\mathrm{air}}$
q_{net} = net wall heat flux, W/m^2
$\overline{R}$ = mean rotational radius $=Z_{o}+L/2$, mm
Re = through-flow Reynolds number $=\rho W_{o}D/\mu$

Re_Ω = Rotational Reynolds number$=\rho\Omega D^2/\mu$
Ro = rotation number$=\mathrm{Re}_\Omega/\mathrm{Re}=\Omega D/W_o$
$T_{b,i}$ = inlet coolant bulk temperature, K
$T_{b,o}$ = outlet coolant bulk temperature, K
$T_{b,Z}$ = local coolant bulk temperature, K
$T_{W,Z}$ = local wall temperature, K
U, V, W = velocity component, m/s
W_o = mean coolant velocity, m/s
Z = distance along main flow direction for all passages, mm
Z_o = distance between rotating axis and heater, mm
Z' = distance along main flow direction for each passage, mm

Greek Symbols

β = volume expansion coefficient, $1/K$
ε = eccentricity$=Z_o/D$
ρ = coolant density, kg/m^3
Ω = rotational speed, rad/s

Subscripts

$\overline{(\quad)}$ = mean quantity

References

[1] Zhang, N., Chiou, J., Fann, S., and Yang, W. J., 1993, ''Local Heat Transfer Distribution in a Rotating Serpentine Rib-Roughened Flow Passage,'' ASME J. Heat Transfer, **115**, pp. 560–567.

[2] Johnson, B. V., Wagner, J. H., Steuber, G. D., and Yeh, F. C., 1994, ''Heat Transfer in Rotating Serpentine Passages With Trips Skewed to the Flow,'' ASME J. Turbomach., **116**, pp. 113–122.

[3] Fann, S., Yang, W. J., and Zhang, N., 1994, ''Local Heat Transfer in a Rotating Serpentine Passage with Rib-Roughened Surface,'' Int. J. Heat Mass Transf., **37**, No. 2 pp. 217–228.

[4] Parsons, J. A., Han, J. C., and Zhang, Y., 1995, ''Effect of Model Orientation and Wall Heating Condition on Local Heat Transfer in a Rotating Two-Pass Square Channel with Rib Turbulators,'' Int. J. Heat Mass Transf., **38**, No. 7, pp. 1151–1159.

[5] Dutta, S., and Han, J. C., 1996, ''Local Heat Transfer in Rotating Smooth and Ribbed Two-Pass Square Channels With Three Channel Orientations,'' ASME J. Heat Transfer, **118**, pp. 578–584.

[6] Ekkad, S. V., and Han, J. C., 1997, ''Detailed Heat Transfer Distributions in Two-Pass Square Channels with Rib Turbulators,'' Int. J. Heat Mass Transf., **40**, No. 11, pp. 2525–2537.

[7] Soong, C. Y., Lin, S. T., and Hwang, G. J., 1991, ''An Experimental Study of Convective Heat Transfer in Radially Rotating Rectangular Ducts,'' ASME J. Heat Transfer, **113**, pp. 604–611.

[8] Han, J. C., Zhang, Y. M., and Kalkuohler, K., 1993, ''Uneven Wall Temperature Effect on Local Heat Transfer in a Rotating Two-Pass Square Channel with Smooth Walls,'' ASME J. Heat Transfer, **115**, pp. 919–920.

[9] Hwang, G. J., and Kuo, C. R., 1996, ''Experimental Studies and Correlations of Radially Outward and Inward Air-Flow Heat Transfer in a Rotating Square Duct,'' ASME J. Heat Transfer, **118**, pp. 23–30.

[10] Kline, S. J., and McClintock, F. A., 1953, ''Describing Uncertainties in Single Sample Experiments,'' Mech. Eng. (Am. Soc. Mech. Eng.), Jan., pp. 3–8.

[11] Dittus, F. W., and Boelter, L. M. K., 1930, ''Heat Transfer in Automobile Radiators of the Tubular Type,'' University of California Publications in Engineering, **2**, No. 13, pp. 443–461; reprinted in Int. Commun. Heat Mass Transfer, **12**, 1985, pp. 3–22

[12] Holman, J. P., 1989, *Heat Transfer*, McGraw-Hill, New York.

[13] Hwang, G. J., Tzeng, S. C., and Mao, C. P., 1999, ''Experimental Study of Convective Heat Transfer of Compressed Air Flow in a Radially Rotating Duct,''*Proceedings of the 5th ASME/JSME Thermal Engineering Joint Conference*, San Diego, California.

[14] Hwang, G. J., and Kuo, C. R., 1997, ''Experimental Study and Correlations of Convective Heat Transfer in a Radially Rotating Serpentine Passage,'' ASME J. Heat Transfer, **119**, pp. 460–466.

[15] Morris, W. D., and Ayhan, T., 1979, ''Observation on the Influence of Rotation on Heat Transfer in the Coolant Channel of Gas Turbine Rotor Blade,'' Proc. Inst. Mech. Eng., **193**, pp. 303–311.

[16] Swanson, L. W., and Catton, I., 1987, ''Enhancement Heat Transfer Due to Secondary Flows in Mixed Turbulent Convection,'' ASME J. Heat Transfer, **109**, pp. 943–946.

[17] Buhr, H. O., Horsten, E. A., and Carr, A. D., 1974, ''The Distortion of Turbulent Velocity and Temperature Profiles on Heating for Mercury in a Vertical Pipe,'' ASME J. Heat Transfer, **96**, pp. 152–158.

[18] Abdelmeguid, A. M., and Spalding, D. B., 1979, ''Turbulent Flow and Heat Transfer in Pipes with Buoyancy Effects,'' J. Fluid Mech., **94**, pp. 383–400.

[19] Cotton, M. A., and Jackson, J. D., 1987, ''Calculation of Turbulent Mixed Convection in a Vertical Tube Using a Low-Reynolds-Numerical κ-ε Turbulence Model,'' presented at *the 6th Symposium on Turbulent Shear Flows*, Toulouse, Trance.

[20] Wagner, J. H., Johnson, B. V., and Hajek, T. J., 1991, ''Heat Transfer in Rotating Passages with Smooth Walls and Radial Outward Flow,'' ASME J. Turbomach., **113**, pp. 42–51.

[21] Wagner, J. H., Johnson, B. V., and Kopper, F. C., 1991, ''Heat Transfer in Rotating Serpentine Passage with Smooth Walls,'' ASME J. Turbomach., **113**, pp. 321–330.

[22] Morris, W. D., and Ghavami-Nasr, G., 1991, ''Heat Transfer in Rectangular Channel With Orthogonal Mode Rotation,'' ASME J. Turbomach., **113**, pp. 339–345.

[23] Han, J. C., and Zhang, Y., 1992, ''Effect of Uneven Wall Temperature on Local Heat Transfer in a Rotating Square Channel with Smooth Walls and Radial Outward Flow,'' ASME J. Heat Transfer, **114**, pp. 850–858.

Experimental Study of Heat Convection From Stationary and Oscillating Circular Cylinder in Cross Flow

H. G. Park
Jet Propulsion Laboratory,
California Institute of Technology
Pasadena, CA 91109

Morteza Gharib
Graduate Aeronautical Laboratories,
California Institute of Technology,
Pasadena, CA 91125

An experimental study is made on the processes of heat transfer from the surface of a forced oscillating cylinder in a crossflow. A range of oscillation amplitude ($A/D = 0.1, 0.2$), forced oscillation frequency ($0 < St_c < 1$), and Reynolds number ($Re = 550, 1100, 3500$) is covered in water ($Pr = 6$). Besides the increase at the natural vortex shedding frequency, large increases in the heat transfer are found at certain superharmonics. By using Digital Particle Image Velocimetry/Thermometry (DPIV/T), the increase in the heat transfer rate is found to correlate inversely with the distance at which vortices roll-up behind the cylinder, i.e., the distance decreases when the heat transfer increases. The cause of the increase is found to be the removal of the stagnant and low heat convecting fluid at the base of the cylinder during the roll-up of the vortices.

[DOI: 10.1115/1.1338137]

Keywords: Convection, Cooling, Cylinder, Enhancement, Entrainment, Experimental, Fluids, Forced Convection, Heat Transfer, Heat Exchangers, Image Processing, Nonintrusive Diagnostics, Recirculating, Separated, Surface, Temperature, Thermal, Unsteady, Vibrating, Vortex, Wakes

Introduction

The process of heat transfer from the surface of a body to the surrounding fluid is of great interest in the field of thermo-fluid mechanics. This process is of technological importance in the design of heat exchanger devices such as cooling or heating systems. One body shape of particular importance is a bluff body, and the most commonly studied is the circular cylinder. Despite its simple shape, a circular cylinder generates a wake which is dynamically complex. The most essential parameter which characterizes the wake of a smooth circular cylinder is the Reynolds number, $Re = U_\infty D/\nu$, where U_∞ is the freestream velocity, D is the diameter, and ν is the kinematic viscosity. Below $Re \approx 5$, the wake is steady and the boundary layer remains attached. Above $Re \approx 5$, the boundary layers on top and bottom separate (Taneda [22]) which gives rise to a pair of steady symmetric vortices in the wake. The vortices become elongated as the Reynolds number is increased until the symmetry is broken at $Re \approx 40$, where the wake becomes unsteady, and the Karman vortices appear downstream. Above $Re \approx 90$, the wake is characterized by alternate shedding of vortices at the top and bottom of the cylinder with opposite signs of vorticity; a process termed ‘‘vortex shedding.’’ While unsteady, the flow remains laminar and two-dimensional until $Re \approx 180$ (Williamson [24]), above which the wake becomes three-dimensional and ‘‘turbulent.’’ At above $Re \approx 1000$, the separated shear layers, which roll-up to form the vortices, become turbulent, and the wake progressively grows more turbulent. Finally, above $Re \approx 200{,}000$, or the ‘‘critical’’ Reynolds number, the boundary layer on the cylinder surface becomes turbulent, and the wake narrows to produce a large reduction in drag. A review of this Reynolds number region is given by Bearman [1]. Beyond this Reynolds number, little is known about the structure of the wake of a circular cylinder.

Thus by varying the Reynolds number, a rich set of flow patterns is observed, but even more wake patterns are observed by forced oscillation of the cylinder. Under forced transverse oscillations, various vortex shedding patterns are possible by varying the oscillation frequency and amplitude. An extensive review of the wake patterns is given by Williamson and Roshko [24], and some possible patterns are shown in Fig. 3(*a–b*) in their paper. At oscillation frequencies below the vortex shedding frequency of a stationary cylinder, the vortices may be shed and paired in various different ways. At oscillation frequencies above the vortex shedding frequency of a stationary cylinder, the cylinder may shed small vortices which then coalesce into large vortices. For small amplitudes ($A/D < 0.5$), the large vortices may recover to the Karman vortex street farther downstream. The wake patterns at high oscillation frequencies have been studied by Ongoren and Rockwell [17] who reported that the large vortices, which form in the near wake ($x/D < 5$) by the coalescence of smaller vortices, shed at or near the vortex shedding frequency of a stationary cylinder. At the super-harmonic frequencies, i.e., multiples of the vortex shedding frequency of a stationary cylinder, they observed organized vortex shedding patterns where a pair of small vortices are shed for each cycle of cylinder oscillation and coalesce with nearby vortices to form the large vortices.

It is intuitive to believe that oscillating a cylinder in a fluid will increase its heat transfer from its surface. Martinelli and Boelter [12] measured that the heat transfer from the surface of a cylinder is increased up to 500 percent compared to that of free convection by oscillating it in water. Surprisingly, for the case of forced convection over a circular cylinder ($5000 < Re < 25{,}000$), Sreenivasan and Ramachandran [21] found no appreciable increase in heat transfer for large forced transverse oscillation amplitudes of $A/D = 0.43$ and 3.7 as compared to that of a stationary cylinder. However, the oscillation frequencies they concentrated on were well below the vortex shedding frequency of a stationary cylinder. A different study by Kezios and Prasanna [11] ($5500 < Re < 14{,}000$) focused on oscillation frequency corresponding to the vortex shedding frequency of a stationary cylinder. The study found that the surface heat transfer increased by approximately 20 percent, even for small amplitudes ($0.02 < A/D < 0.075$) when the oscillation frequency matched the vortex shedding frequency. It

---

Contributed by the Heat Transfer Division for publication in the JOURNAL OF HEAT TRANSFER. Manuscript received by the Heat Transfer Division January 3, 2000; revision received, May 17, 2000. Associate Editor: Bau.

was noted that the increase in heat transfer could not be accounted for by the relative increase in the freestream velocity due to the transverse motion of the cylinder. Saxena and Laird [20] found that a large increase (40 percent to 60 percent) in heat transfer occurs in water as the forced oscillation frequency approached the vortex shedding frequency of a stationary cylinder for large oscillation amplitudes ($0.89<A/D<1.99$) at Re=3,500. The maximum frequency reached was 0.8 times the shedding frequency. More recently, Karanth et al. [9] conducted a computational study at Re=200 where increases of 1.2 percent and 3 percent in the surface heat transfer were observed for forced transverse oscillations amplitudes of $A/D=0.25$ and 0.5, respectively. Cheng and Hong [5], in another computational study at Re=200, observed that the heat transfer increased 1.6 percent, 3.9 percent, 7.5 percent, and 12.5 percent for $A/D=0.14$, 0.3, 0.5, and 0.7, respectively. Following their computational study, Cheng et al. [4] measured increases in the surface heat transfer from 3 percent to 30 percent for $A/D=0.138$, 0.314, 0.628 at Re=200, 500, and 1000 when the cylinder was forced to oscillate at the vortex shedding frequency of a stationary cylinder. A new study by Gau et al. [8] found increase in the heat transfer up to 50 percent for $A/D=0.064$ at Re=1600 in air for an oscillating cylinder. The study covered small amplitudes, $A/D=0.016$, 0.032, and 0.064 and Re range of 1600, 3200, and 4800. For Re=1600, the cylinder was oscillated to three times the natural vortex shedding frequency, and they found even higher increase (70 percent) in the heat transfer rate.

The previous authors have cited the phenomenon of ''lock-in'' or the synchronization of the vortex shedding with the mechanical oscillation of the cylinder as the reason for the increase in the surface heat transfer. When the vortex shedding becomes synchronized with the mechanical oscillation, a pair of vortices is always shed for each cycle of cylinder oscillation. However, it has never been fully explained why this synchronization leads to higher surface heat transfer. In addition, Cheng et al. [4] noticed that past the synchronization frequency, the heat transfer continued to increase for large amplitudes ($A/D=0.626$), decreased then increased for medium amplitudes ($A/D=0.314$), or returned too close to the value of the stationary cylinder for small amplitudes ($A/D=0.138$). (See Fig. 6 of Cheng et al. [4]) The study stopped at 1.5 times the synchronization frequency, and the increase in the heat transfer for larger oscillation amplitudes at higher frequencies was attributed to the ''turbulence'' effect. The ''turbulence'' effect was left unclear and is presumed to be connected to some unsteadiness in the wake or boundary layer of the cylinder.

Recent flow visualization study of Gau et al. [8] showed that the vortices roll-up close to the cylinder when the oscillation frequencies are one and three times that of the natural vortex shedding frequency for $0.016<A/D<0.064$. This result hints that perhaps coherent motions the vortices, i.e., organized structure of the wake, is responsible for the rise in the heat transfer rate at certain oscillation frequencies. Thus a comprehensive set of experiments is carried out to study the relationship between the heat transfer and the wake behind the cylinder. First, a study is made of the overall heat transfer of a forced oscillating heated cylinder near the natural vortex shedding frequency, similar to previous studies. In addition, the heat transfer characteristics of a forced heated cylinder is examined all the way up to five times the natural shedding frequency where new findings are uncovered. Second, a study is made of the wake structure at selected frequencies and amplitudes to address the primary cause of the increased heat transfer near the natural shedding and other frequencies.

Experimental Setup and Procedure

Experimental Setup. A schematic of the water tunnel facility where the experiments were conducted is shown in Fig. 1. The cross-sectional dimensions of the test section were 15.2 cm wide and 15.2 cm high. The tunnel was operated by a pair of pumps and had a speed range of 3 to 50 cm/s. The temperature of the flow through the test section could be raised by a bank of staggered heating rods in the inlet pipe to the diffuser section of the tunnel and could be lowered by a re-circulating chiller (Neslab RTE-110) at the downstream section of the tunnel. Using a closed-loop temperature controller (Tronac PTC-41), the mean freestream temperature could be maintained to within ±0.02°C at a flow speed of 5 cm/s or within ±0.01°C at a flow speed of 40 cm/s.

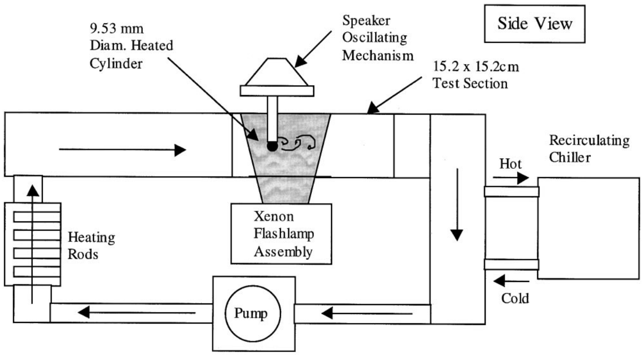

Fig. 1 Schematic of water tunnel facility

The test cylinder was an electrically heated rod of diameter 9.53 mm (Watlow Firerod). The electric heating element was protected by an outer sheath made from Incoloy alloy. A J-type thermocouple, which gave an estimate of the cylinder temperature, was embedded in the core of the cylinder at mid-span. The cylinder was heated by a constant DC voltage power supply (Kepco BOP 50-4M), and its temperature was measured by a thermocouple thermometer (Omega HH21) which had a resolution of ±0.1°C. The cylinder had a thermal boundary condition of constant integrated heat flux over the surface. The cylinder was mounted horizontally to a transverse oscillating mechanism by two vertical hollow supports at the ends of the cylinder. The electrical and thermocouple leads were passed through the hollow supports from the cylinder to the power supply and thermocouple thermometer, respectively. The supports were thermally insulated from the cylinder by a layer of silicone. The disturbance to the flow was minimized by placing the supports outside of two flat end plates that had rounded leading edges. The distance between the two end plates was 12.1 cm, and thus the effective aspect ratio (L/D) of the cylinder was 13.

The oscillating mechanism was a 15 cm cone speaker in which the cone was stiffened by a circular thin-aluminum plate. The plate provided torsional stiffness to the cone and kept the cylinder level with respect to the bottom of the tunnel. The speaker was driven by a feedback amplifier that was fed a sinusoidal signal from a multi-wave generator (HP 3314A). With the cylinder mass, the speaker was capable of generating sinusoidal motion amplitude of 4 mm peak-to-peak from 0 to 10 Hz. The actual displacement of the cylinder was measured by an optical transducer (photo-detector grid) which generated a voltage proportional to the displacement of the laser diode mounted on the cylinder oscillating mechanism.

Velocity and Temperature Measurements

The freestream velocity measurements were made using a single component Laser Doppler Anemometer (LDA) placed several diameters upstream of the test cylinder. The velocity and temperature measurements in the wake were made using Digital Particle Image Velocimetry/Thermometry (DPIV/T). The details of DPIV/T are found in Park [18], Dabiri and Gharib [6], and Willert and Gharib [23]. The flow was seeded with encapsulated TLC particles and was illuminated by a reflector assembly which produced a sheet of light at the center of the test section. The light reflector assembly was a mirror surfaced elliptical cylinder with a thin slit on top. The light, which was produced by two 25 cm long xenon flashtubes located at the foci of the ellipse, escaped through the slit and was collimated by two lenses to form a light sheet of 2–3 mm thickness. Each flashtube was fired at 15 Hz with a flash duration of 150 μs and had an energy release of 8 J. Alternate firing of the flashtubes synchronized with the 30 Hz frame rate of the video camera.

The flow was imaged from the side of the water tunnel using a 3-CCD color camera (Sony DXC-9000) which has a standard set of NTSC R, G, and B color filters. The camera, which was placed approximately 2 m from the test section, imaged an area of 60 mm wide by 50 mm high at the mid-span of the test section. The flow was seeded with 40 μm diameter thin-walled encapsulated TLC particles (Hallcrest BM40C26W20) which had thermal response time of 4 ms (Dabiri and Gharib [6]). The response time was much smaller than the expected time scale of the vortex shedding ($\approx$600 ms). The flow was illuminated from the bottom of the test section by a xenon white light sheet of 2–3 mm thickness, and the images were digitized to a real-time digital video recorder with 8-bit resolution per RGB channel (24-bit total).

The velocity distribution was measured using standard DPIV technique. While temperature distribution of the wake was obtained using DPIV/T, only the velocity measurements are presented for the purposes of this paper. The heat transfer rate was not derived from the temperature distribution of the wake. Instead, the rate was measured directly from the thermocouple and heat input measurements as described in a later section.

Phase Averaging Methodology

For each of the frequency and amplitude, the structure of the wake was studied by phase averaging the DPIV/T velocity data. The phase averaged statistics were generated from 1000 pairs of image, corresponding to 1000 instantaneous velocity fields. This number represents roughly 95 vortex shedding cycles. For the forced oscillating cases, there was no ambiguity in phase since the phase averaging was synchronized with the mechanical motion of the cylinder. Depending on the case, the displacement signal was divided into either 6 or 12 evenly spaced phases. However, an ambiguity was encountered in the phase for the stationary cylinder since the period of the shedding varied slightly for each cycle. This ambiguity has been encountered by both Cantwell and Coles [3] and Matsumura and Antonia [13] who had to adjust slightly the period of each vortex shedding cycle to compute the phase average correctly. Similarly, the period of each vortex shedding cycle was adjusted in computing the phase average quantities.

For the stationary cylinder or a case in which the vortex shedding is not synchronized with the mechanical oscillation of the cylinder, a reference signal from which the phase of the vortex shedding can be determined is needed. Cantwell and Coles [3] used the signal from a static pressure tap on the surface of the cylinder 65 deg from the forward stagnation point of the cylinder, while Matsumura and Antonia [13] used the signal from a hot-wire just outside of the wake. Others have used the lift signal as the reference signal (Karniadakis [10]), but any clean signal generated by the vortex shedding process is sufficient. For this study, the vertical velocity (u_y) at the location of maximum fluctuation level on the centerline of the wake was used as the reference signal. The maximum u_y fluctuation level occurs just downstream the region where the vortices roll-up, and the signal there is both clear and large in magnitude. The period of each shedding cycle was determined by measuring the time between consecutive zero crossings of the u_y signal, and each period was divided into 12 evenly spaced phases.

Nusselt Number Versus Oscillation Frequency

Experimental Conditions. The average heat transfer from the surface of a cylinder undergoing forced oscillation was measured for three different Reynolds numbers of 550, 1100, and 3,500 based on a freestream temperature of 25.8°C. The Prandtl number, Pr, of water at this temperature is 6. The cylinder was heated with constant power inputs of 45.5, 58.4, and 90.9 W for Re=550, 1100, and 3500, respectively. The ratio between the Grashof number and the square of the Reynolds number, $\mathrm{Gr}/\mathrm{Re}^2$, which is a measure of the buoyancy effect, was low enough (0.01) to not affect the wake structure.

The measurements were made at two amplitudes, $A/D=0.1$ and 0.2. The range of Strouhal frequency of the cylinder, St_c, was from 0 to 0.95 for Re=550 and 1,100. The Strouhal number of the cylinder is defined as $f_cD/U\infty$ where f_c is the cylinder oscillation frequency. The ranges in physical frequency unit were from 0 to 5.6 Hz for Re=550 and from 0 to 11.4 Hz for Re=1,100. For Re=3500, the range of St_c was from 0 to 0.35, corresponding to a range in physical frequency from 0 to 13.4 Hz. The maximum frequency at this Reynolds number was limited by the mechanical driving mechanism which could not exceed 14 Hz.

Nusselt Number Calculations

The Nusselt number, defined as

$$\mathrm{Nu}=\frac{hD}{k},$$

where h is the average convection heat transfer coefficient, and k is the thermal conductivity of the fluid medium, is computed from the estimate of the average surface temperature of the cylinder and the input power. Because the Biot number, defined as

$$\mathrm{Bi}=\frac{hD}{k_c},$$

where k_c is thermal conductivity of the cylinder, is of the order unity, the approximation that the temperature at the surface, T_c, is the same as the temperature at the core, T_{tc}, cannot be made. Therefore, a first order approximation is made to estimate the surface temperature from the core temperature as measured by the embedded thermocouple (T_{tc}).

The procedure is as follows. We assume that the temperature varies only in the radial direction and that the cylinder is composed of a uniformly heated inner shell and an unheated outer shell (Fig. 2). If we assume uniform material properties, the steady-state temperature distribution in the inner shell is then given by the heat equation in radial coordinates:

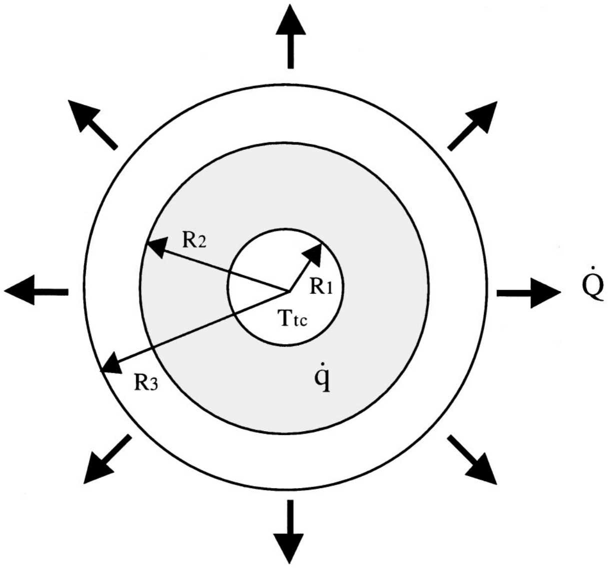

Fig. 2 Layout of the cylinder

$$\frac{\partial^2 T}{\partial r^2}+\frac{1}{r}\frac{\partial T}{\partial r}+\frac{\dot{q}}{k}=0 \quad (R_1\leqslant r\leqslant R_2), \tag{1}$$

where $\dot{q}$ is the power input per unit volume, or:

$$\dot{q}=\frac{\dot{Q}}{\pi(R_2^2-R_1^2)L}, \tag{2}$$

where $\dot{Q}$ is the total power input, L is the length of the cylinder, R_1 is the radius at which the thermocouple is located, and R_2 is the outer radius of the inner shell. The steady-state temperature distribution in the outer shell is given simply by

$$\frac{\partial^2 T}{\partial r^2}+\frac{1}{r}\frac{\partial T}{\partial r}=0, \quad (R_2\leqslant r\leqslant R_3). \tag{3}$$

The boundary conditions for these equations are:

$$T(R_1)=T_{tc}, \tag{4}$$

$$-k_{CO}\left.\frac{\partial T}{\partial r}\right|_{r=R3}=h(T_c-T_\infty)=\frac{\dot{Q}}{2\pi R_3 L}, \tag{5}$$

where k_{CO} is the thermal conductivity of the outer shell, and R_3 is the outer radius of the cylinder. The matching condition is at R_2 where the temperatures of the outer and inner shells must be equal. Solving Eqs. (1) and (3) with the appropriate boundary conditions, the temperature at the surface, T_c, is given by

$$T_c=T_{tc}-\frac{\dot{Q}}{2\pi L}\left[\frac{1}{k_{CO}}\ln\left(\frac{R_3}{R_2}\right)+\frac{1}{k_{CI}}\left(\frac{1}{2}-\frac{R_2^2}{R_2^2-R_1^2}\ln\left(\frac{R_2}{R_1}\right)\right)\right], \tag{6}$$

where k_{CI} is the thermal conductivity of the inner shell. From Eqs. (5) and (6), we can compute the convection heat coefficient, where

$$h=\frac{\dfrac{\dot{Q}}{2\pi R_3 L}}{\left\{\begin{array}{c}(T_{tc}-T_\infty)\\ -\dfrac{\dot{Q}}{2\pi L}\left[\dfrac{1}{k_{CO}}\ln\left(\dfrac{R_3}{R_2}\right)+\dfrac{1}{k_{CI}}\left(\dfrac{1}{2}-\dfrac{R_2^2}{R_2^2-R_1^2}\ln\left(\dfrac{R_2}{R_1}\right)\right)\right]\end{array}\right\}}. \tag{7}$$

From h, we can then compute the Nusselt number.

The computed Nusselt number inherently has a level of uncertainty because the surface temperature of the cylinder is not truly uniform. The temperature at the base of the cylinder is typically higher than at the forward stagnation point. This was confirmed by intrusive measurements using a thermocouple at various circumferential locations around the cylinder. The temperature gradients in the radial direction were found to be roughly three times higher than the circumferential direction. To quantify this error, a detailed two-dimensional finite element simulation was carried out using circumferential distribution of Nusselt number from Gau et al. [8]. The results show that the bias error in Nusselt number using the one-dimensional approximation instead of two-dimensional is roughly 25 percent. However, the relative uncertainty, i.e., uncertainty between two measurements, is smaller at 10 percent and is the quantity of interest in this paper. This is discussed further in the error analysis section.

Results

The plots of normalized Nusselt number versus oscillation frequency are shown in Figs. 3 and 4 for $A/D=0.1$ and 0.2, respectively. The Nusselt number is normalized by the respective stationary values at each Reynolds number. The stationary Nusselt number values for Reynolds number 550, 1100, and 3500 are 19.5, 24.8, and 56.0, respectively. For each Reynolds number and oscillation amplitude, a peak near $\mathrm{St}_c\approx 0.21$ is observed. These peaks are associated with the synchronization of the vortex shedding with the mechanical oscillations. This phenomenon has been well documented by many previous researchers starting from Kezios and Prasanna [11]. For each Reynolds number, higher oscillation amplitudes results in higher Nusselt number at this frequency as noted by previous researchers (Kezios and Prasanna [11]; Cheng et al. [4]).

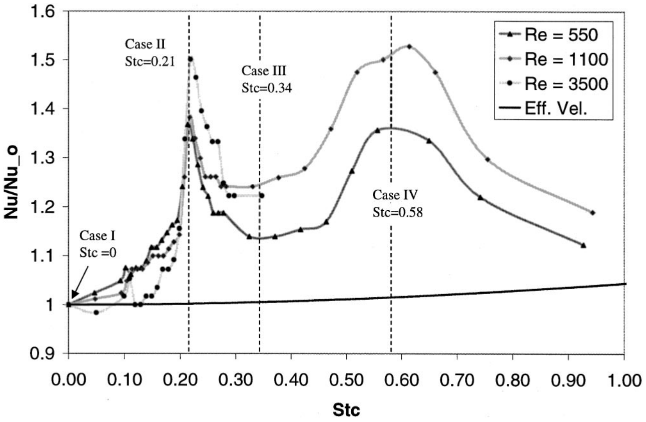

Fig. 3 Normalized surface heat transfer as function of oscillation frequency for *A/D*=0.1

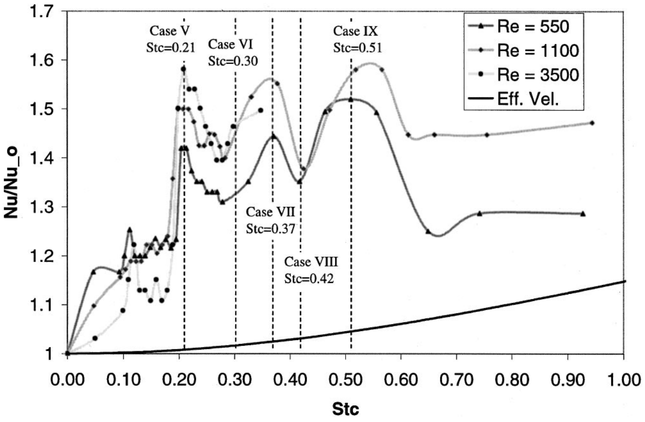

Fig. 4 Normalized surface heat transfer as function of oscillation frequency for *A/D*=0.2

The locations of all of the peaks appear to be correlated with the amplitude of oscillation. The figures show that the locations of the peaks and valleys are nearly coincident for given amplitude, irrespective of the Reynolds number. For $A/D=0.1$, there is a broad valley from $\mathrm{St}_c\approx 0.3$ to ≈ 0.45, and a broad peak at $\mathrm{St}_c\approx 0.6$ with roughly the same height as the peak at $\mathrm{St}_c=0.21$. For $A/D=0.2$, there are valleys at $\mathrm{St}_c\approx 0.3$ and 0.4, and two peaks at $\mathrm{St}_c\approx 0.35$ and ≈ 0.55.

Discussion

While it has been well documented that there is an increase in the Nusselt number at the synchronization frequency ($\mathrm{St}_c\approx 0.2$), the increases in the Nusselt number at other frequencies have not been well documented. The results of this study show that the Nusselt number does not increase or decrease monotonically past the synchronization frequency ($\mathrm{St}_c\approx 0.2$) but has definite peaks and valleys. As will be seen in the following sections, the peaks are associated with certain modes of the wake. The increase at $\mathrm{St}_c\approx 0.6$ for $A/D=0.1$ is associated with a mode at three times the natural shedding frequency, whereas the increases seen at $\mathrm{St}_c\approx 0.35$ and 0.55 for $A/D=0.2$ are associated with modes at twice and three times the natural vortex shedding frequency, respectively. At the higher amplitude ($A/D = 0.2$), the mode frequencies appear to have shifted slightly away from exact multiples of the fundamental synchronization frequency.

The increase in the Nusselt number cannot be simply accounted for by the ''effective'' velocity of the cylinder due to added velocity from the oscillatory motion of the cylinder. Following Sreenivasan and Ramachandran [21], the effective velocity, V_e, is defined as:

$$V_e = \sqrt{U_\infty^2 + V_v^2}, \tag{8}$$

where

$$V_v = \frac{2\pi f A}{\sqrt{2}}, \tag{9}$$

is the RMS velocity of the oscillation. For a stationary cylinder, the MacAdams relation (MacAdams [14]) predicts the Nusselt number as function of the Reynolds number ($100 < \mathrm{Re} < 4000$) or the freestream velocity as:

$$\mathrm{Nu} \propto \mathrm{Re}^{0.475} \propto U_\infty^{0.475}. \tag{10}$$

Substituting V_e into Eq. (7), the Nusselt number as function of oscillation frequency and freestream velocity becomes:

$$\mathrm{Nu}(A, f_c, U_\infty) \propto (U_\infty^2 + 2\pi^2 f_c^2 A^2)^{0.475}. \tag{11}$$

This relationship is plotted as the solid curves in Fig. 3 and 4. As noted by previous researchers (Cheng et al. [4]), the relation in Eq. (11) cannot account for the increase in the Nusselt number for the oscillation frequencies of interest.

The trends in Figs. 3 and 4 are actually consistent with those observed by Cheng et al. [4] and Gau et al. [8]. Chen et al. [4] observed that for $A/D = 0.138$, the Nusselt number decreased and remained low past $\mathrm{St}_c \approx 0.2$, while at $A/D = 0.314$, the Nusselt number first decreased then began to increase again. Since they did not measure the Nusselt number beyond 1.5 times the shedding frequency ($\mathrm{St}_c \approx 0.30$), they were likely observing a decrease associated with a valley from $\mathrm{St}_c \approx 0.3$ to ≈ 0.45 for $A/D = 0.134$, and an increase associated with a peak at $\mathrm{St}_c \approx 0.35$ for $A/D = 0.314$. They attributed the rise at $A/D = 0.314$ past St ≈ 0.3 to the ''turbulence'' effect. They did not precisely define what the ''turbulence'' effect was, although it is inferred from their paper that it is associated with some unsteady (incoherent) motion of the wake or the boundary layer.

Further information about the wake comes from Gau et al.[8] who found a rise in the heat transfer for $\mathrm{St}_c \approx 0.6$ or 3 times the shedding frequency for $A/D = 0.064$. Their flow visualization results gave an impression that organized structures in the wake may be responsible for the increase in the heat transfer. Therefore, a detailed DPIV/T study of the wake is presented to clarify the connection between the wake structure and the rate of heat transfer.

DPIV/T Study

Experimental Conditions. A detailed DPIV/T study of wake was carried out at Reynolds number of 610. The freestream temperature was 25.8°C, and the cylinder was heated with a constant power input of 63.8 W. The wake velocity-temperature field measurements were made for two different amplitudes ($A/D = 0.1$ and 0.2) at frequencies corresponding to peaks and valleys of the heat transfer versus oscillation frequency curve in Figs. 3 and 4. A total of nine cases, denoted by Roman numerals I through IX, are presented at frequencies and amplitudes shown in Figs. 3 and 4.

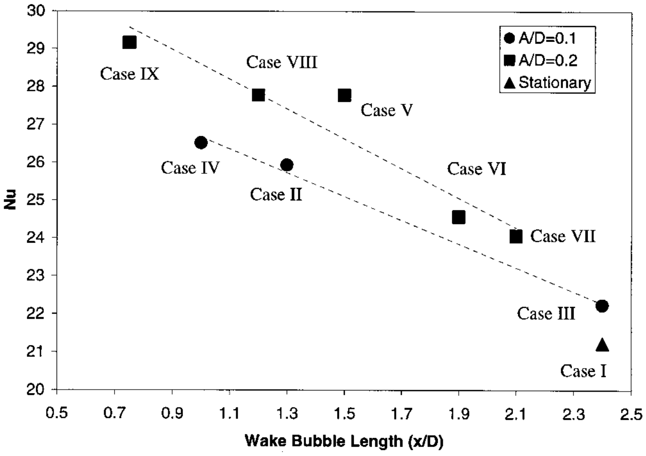

Fig. 5 Nusselt number versus length of the mean wake bubble (formation length)

Roll-up Distance Versus Heat Transfer. The most important result from the DPIV/T study is the connection between the length of the mean wake bubble, i.e., length of the recirculation bubble, and the surface heat transfer. Figure 5 shows that there is a strong correlation between the wake bubble length and the overall Nusselt number. There is, however, a dependence on oscillation amplitude. The wake bubble length is computed by averaging the velocity field and locating the closure point of the recirculation bubble. For example, the wake bubble length is much shorter for the forced oscillated cylinder, Case II, ($x/D = 1.3$) than for the stationary cylinder, Case I, ($x/D = 2.5$) which has much lower heat transfer rate. For all of the high heat transfer cases, Case II, IV, V, VII, and IX, the wake bubble lengths are short, $x/D < 1.5$, while for all of the low heat transfer cases, Case I, III, VI, and VIII, the lengths are long, $x/D > 1.9$ (Fig. 5).

The length of the wake bubble is a quantitative measure of the downstream distance at which the wake vortices roll-up. Thus the reason behind the increased heat transfer when the vortices roll-up close to the cylinder is that the vortices are able to scrub away the hot fluid at the base of the cylinder. For Case I (stationary cylinder), there is a region of stagnant fluid just behind the cylinder which does not convect any heat away from the base of the cylinder. Figure 6 shows the closest approach that a vortex makes during its roll-up. The vortex is sufficiently far away that the fluid near the base of the cylinder remains stagnant and does not carry away any heat. In the high heat transfer cases, this region of stagnant fluid is non-existent. As an example, Fig. 6 shows the closest approach that a vortex makes during its roll-up in Case II. The vortex is close enough to induce flow around the base of the cylinder and carry away heat from the base. While the local Nusselt number was not measured in this study, and thus the increase in the heat transfer at the base of the cylinder could not be directly verified, it is strongly believed that the heat transfer increases at the base when the vortices scrub away the normally stagnant and non-heat convecting fluid away from the cylinder at the base. The overall heat transfer thus increases when the heat transfer rate at the normally low region (Eckert and Soehngen [7]) is increased.

Intuitively it is interesting to correlate the length of the wake bubble with the rate of surface heat transfer. However, the heat transfer cannot be a simple function of the wake bubble length because the length can grow or shrink as function of only the Reynolds number. It has been observed that the length of the wake bubble, or the ''formation length'' of the vortices, increases for roughly $200 < \mathrm{Re} < 1500$ (Bloor [2]). For a cylinder with ''high'' aspect ratio ($L/D > 50$), the length of the wake bubble increases from $x/D = 1.6$ to 2.2 (≈ 40 percent increase) from Reynolds number 500 to 1000 for a stationary cylinder (Noca et al. [15]). The Nusselt number may also increase in this span of Reynolds number by ≈ 40 percent (MacAdams [14]). Since the trends are opposite to those of the forced oscillating cylinder (increase in wake bubble length results in decreased heat transfer), the Reynolds number, not the wake bubble length, must be the essential parameter in determining the heat transfer from a stationary cylinder.

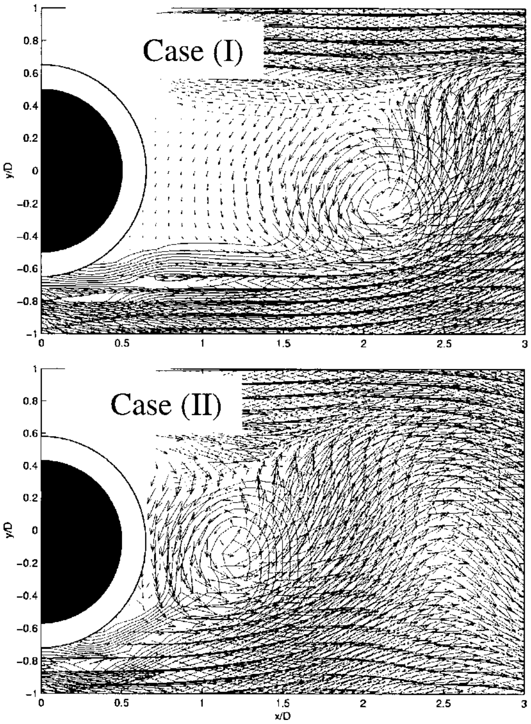

Fig. 6 Stagnant and non-heat convecting fluid near the base of the cylinder for Case (I), and vortices scrubbing away fluid near the base of the cylinder for Case (II). Note the close roll-up of the vortex and large velocity near the base of the cylinder in Case (II) as compared to Case (I). Note: the contours are lines of constant vorticity.

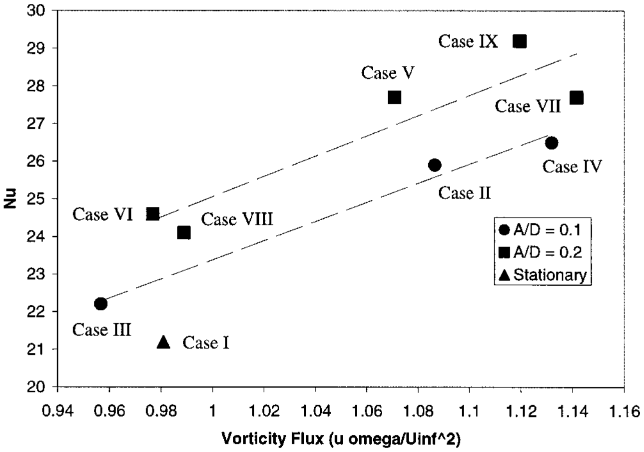

Fig. 7 Nusselt number versus mean total vorticity flux of the lower shear layer at $x/d=0.8$

When the cylinder is in forced oscillation, the wake bubble length, not the ''effective'' Reynolds number or freestream velocity (Eq. 11), appears to be the essential parameter in correlating the heat transfer. These effects must be kept in mind when examining the trend between the wake bubble length and Nusselt number as shown in Fig. 5.

The increase in the heat transfer may be also correlated with the increase in the vorticity flux through a surface normal to the wake centerline as shown in Fig. 7. The measured vorticity flux is the amount of surface normal vorticity (ω_z) passing in the streamwise direction through a surface below the wake centerline at $x/D=0.8$, i.e., the location of the lower shear layer. The most likely reason why the Nusselt number correlates so well with the vorticity flux is that the amount of vorticity a shear layer contains may have direct influence the formation length, i.e., length of the mean wake bubble. It is observed that the larger the amount of vorticity flux, the shorter the length of the bubble. This is consistent with the ''free-streamline'' or ''cavity'' theory (Roskho [19]) which predicts that the bubble length will decrease if the vorticity flux is increased. Hence, a shorter bubble length implies more closely rolled-up vortices which are more effective in transporting away the non-heat convecting fluid at the base of the cylinder. The correlation between the vorticity flux and the length of the mean wake bubble is shown in Fig. 8.

Structure of the Wake. The observation of a short wake bubble length, or a roll-up of the vortices close to the cylinder, always coincides with the synchronization of the wake with some integer fraction ($1/n$, $n=1,2,3$) of the mechanical oscillation frequency. Regardless of the oscillation frequency, the frequency of the large-scale vortex shedding remains near $\mathrm{St}=0.2$ (Ongoren and Rockwell [17]). When the frequency of oscillation approaches some multiples of the large-scale vortex shedding frequency, the wake pattern becomes synchronized with the cylinder oscillation, and this may result in the roll-up of the vortices very close to the cylinder. In Cases II and V, the wake is synchronized with the mechanical oscillation frequency since the wake and oscillation frequencies match. For other frequencies that are multiples or close to multiples of the large-scale vortex shedding frequencies, period doubling (case VII) and period tripling (cases IV and IX) are observed with respect to the cylinder oscillation period. This phenomenon of period doubling and tripling has been observed by Ongoren and Rockwell [17] through flow visualization in water (hydrogen bubble technique) for cylinders of various shapes. For a wedge shaped cylinder, they observed the formation of one small vortex per side (top and bottom) for each oscillation of the cylinder when the oscillation frequency was an integer multiple, *n*, of the large-scale vortex shedding frequency. The *n* distinct vortices merged downstream to form the large-scale vortices which then shed at a much lower frequency ($1/n$ of the oscillation frequency). The merging process is shown in Fig. 11 of Ongoren and Rockwell [17]. Similar observations are made in this study, except that merging appears to occur much closer for the case of the circular cylinder, especially for Case IV and IX (i.e., $n=3$). Figure 9 shows the sequence of phase averaged vorticity fields for Case IV. Ongoren and Rockwell [17] observed that oscillating the cylinder three times the natural shedding frequency generated three distinct vortices per side, of which the first two merged some distance ($x/D\approx 2.5$, where D is the side length of a 60 deg wedge) downstream followed by a merger of the third vortex with the first two at $x/D\approx 4$. In this study (circular cylinder as opposed to a wedge), three distinct vortices are not observed. Instead, one large vortex

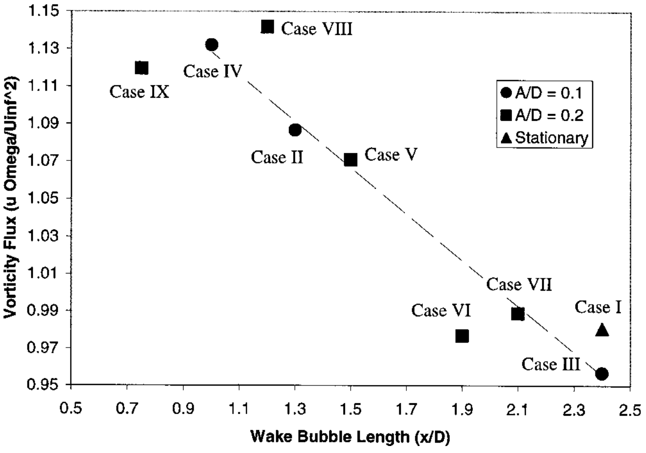

Fig. 8 Vorticity flux versus the length of the mean wake bubble

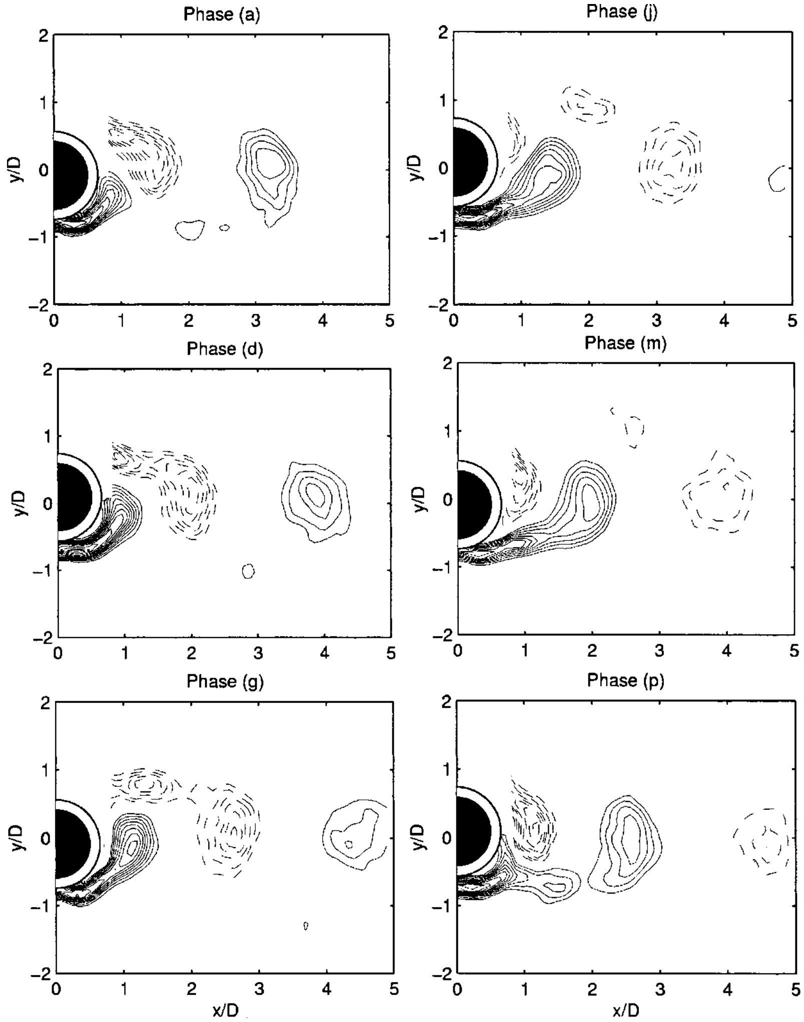

Fig. 9 Sequence of phase averaged vorticity fields for forced oscillating cylinder at $St_c=0.58$, $A/D=0.1$ (Case IV). ($|\langle \omega_z \rangle D/U_\infty| \rangle 1.0$, contour increment 0.5). See Fig. 13(*D*) for phase corresponding to each letter.

is generated in two cylinder oscillation, and a second smaller vortex is generated which does not appear to merge with the larger vortex in the near wake (Fig. 9).

In this study, a lack of synchronization of the wake with the cylinder oscillation is associated with roll-up of the vortices far downstream of the cylinder. For Case III and VI, the wake is not synchronized with the motion of the cylinder. The PSD of Case III, computed from the time-trace of u_y (transverse velocity) at the location of maximum fluctuations on the wake centerline, shows that the dominant frequency in the wake is at $St=0.20$ (Fig. 10). The Strouhal number, St, is defined as $St=fD/U_\infty$, where f is the wake frequency. The cylinder is oscillated at $St_c=0.34$, but there is little sign of wake excitation at the frequency of oscillation ($St_c=0.34$) in the PSD. This suggests that the shedding of the large-scale vortices is unaffected by the cylinder oscillation and remains near the frequency of the stationary cylinder at $St \approx 0.20$. A sequence of the phase averaged vorticity field locked to the mechanical oscillation of the cylinder shows that the vorticity field at each phase looks remarkably like the mean vorticity field (Fig. 11(*A*)). This further confirms that the large-scale vortex shedding is unaffected by the cylinder oscillation at this oscillation frequency. By phase averaging with respect to u_y as described in the phase averaging section, the large-scale vortex shedding cycle can be recovered as shown in Fig. 11(*B*). The same behavior is observed for Case VI which has higher amplitude of $A/D=0.2$.

While a lack of synchronization of the wake with the mechanical oscillation of the cylinder results in vortices rolling-up far from the cylinder, a simple synchronization of the wake is *not* a sufficient condition to cause the vortices to roll-up close to the cylinder, i.e., high heat transfer. Figures 12(*A*) and (*B*) show the

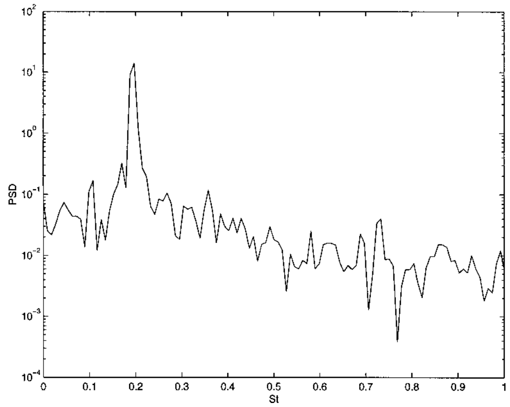

Fig. 10 PSD of u_y at location of maximum u_y fluctuations on the wake centerline for forced oscillating cylinder at $St_c=0.34$, $A/D=0.1$ (Case III)

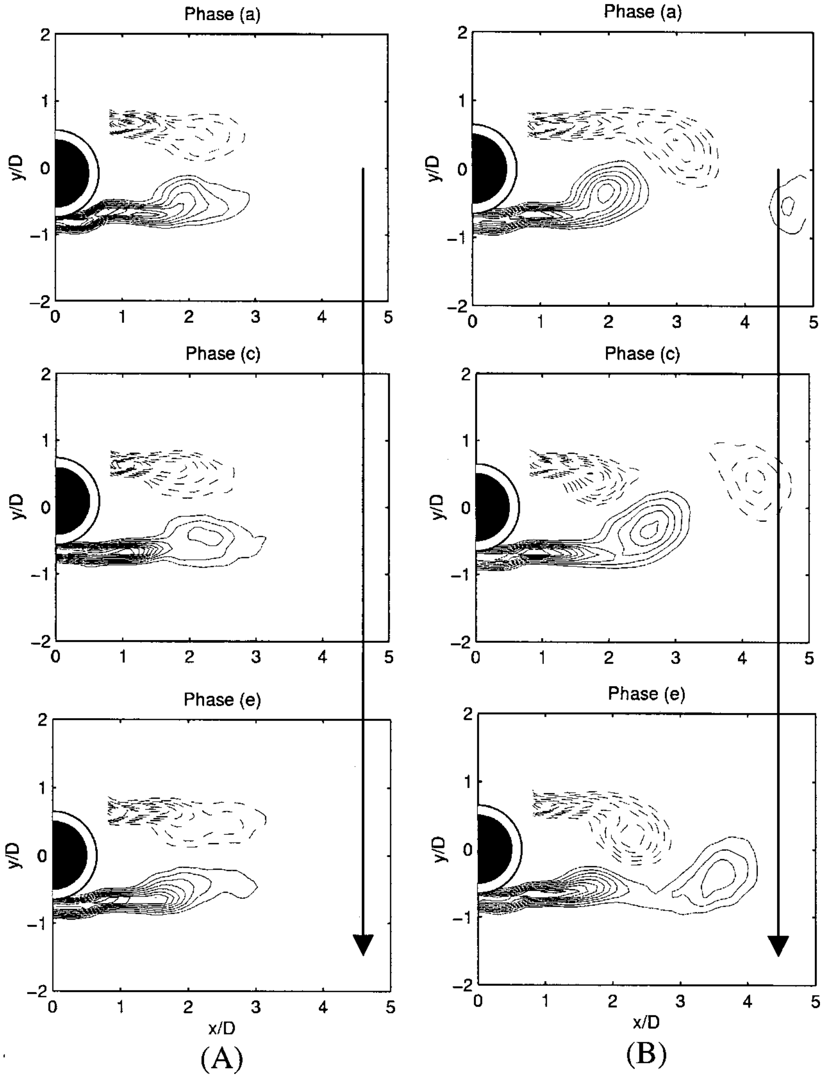

Fig. 11 Sequence of phase averaged vorticity fields for forced oscillating cylinder at $\mathrm{St}_c=0.34$, $A/D=0.1$ (Case III). ($|\langle\omega_z\rangle D/U_\infty|$)1.0, contour increment 0.5). The phase averaging is done with respect to the cylinder oscillation frequency in (*A*) and u_y at location of maximum u_y fluctuations on the wake centerline in (*B*). See Fig. 13(*A*) and (*B*) for phase corresponding to each letter.

wake patterns are synchronized with the one-half the cylinder oscillation frequency for both Cases VII and VIII, respectively. However, in Case VIII, which is of only slightly higher frequency, the vortices roll-up farther downstream as compared to Case VII, and this case has a low effective heat transfer rate.

Finally, the oscillation frequencies corresponding to the peaks in the heat transfer rate seem to shift slightly as function of oscillation amplitude. For $A/D=0.2$, the oscillation frequencies corresponding to the maximum heat transfer rates seem to shift lower than the multiples of the vortex shedding frequency of the unforced cylinder (Fig. 4). For smaller amplitude ($A/D=0.1$), the maximum heat transfer rate seem to nearly coincide with the multiples of the vortex shedding frequency of the unforced cylinder. Oddly, no peak in the heat transfer rate is observed for $A/D=0.1$ at twice the large-scale vortex shedding frequency. This is consistent with the results of Gau et al. [8] which also showed an increase at *only* three times the shedding frequency for $A/D<0.064$. While the results from Case III do not show any synchronization of the wake pattern with the oscillation frequency, the oscillation frequency may be too low ($\mathrm{St}_c=0.34$). It is likely that the wake achieves synchronization at $\mathrm{St}_c\approx 0.4$ but probably fails to generate a pattern where the vortices roll-up close to the cylinder. Analogously, the heat transfer does not increase for oscillations frequencies corresponding to four or five times the large-scale vortex shedding frequency. The reason for why the wake has certain preferred frequencies at which the vortices roll-up close to the cylinder is unknown at this time.

''Turbulence'' Effect

From the results, we attempt to address the ''turbulence'' effect as described by Cheng et al. [4] who attributed it to the rise in heat transfer at $A/D=0.314$ past $\mathrm{St}_c\approx 0.3$. The ''turbulence'' effect, as it turns out, appears to be an organized pattern in the wake associated with the synchronization of the wake with the cylinder oscillation through processes of period doubling and tripling. For $A/D>0.2$, the increase in the heat transfer just above the natural vortex shedding frequency is associated with period doubling and is the result of vortices rolling-up closer to the cylinder and scrubbing away the stagnant fluid at the base of the cylinder for selected oscillation frequencies. At the lower amplitudes $A/D<0.1$, the heat transfer decreases because the vortices roll-up

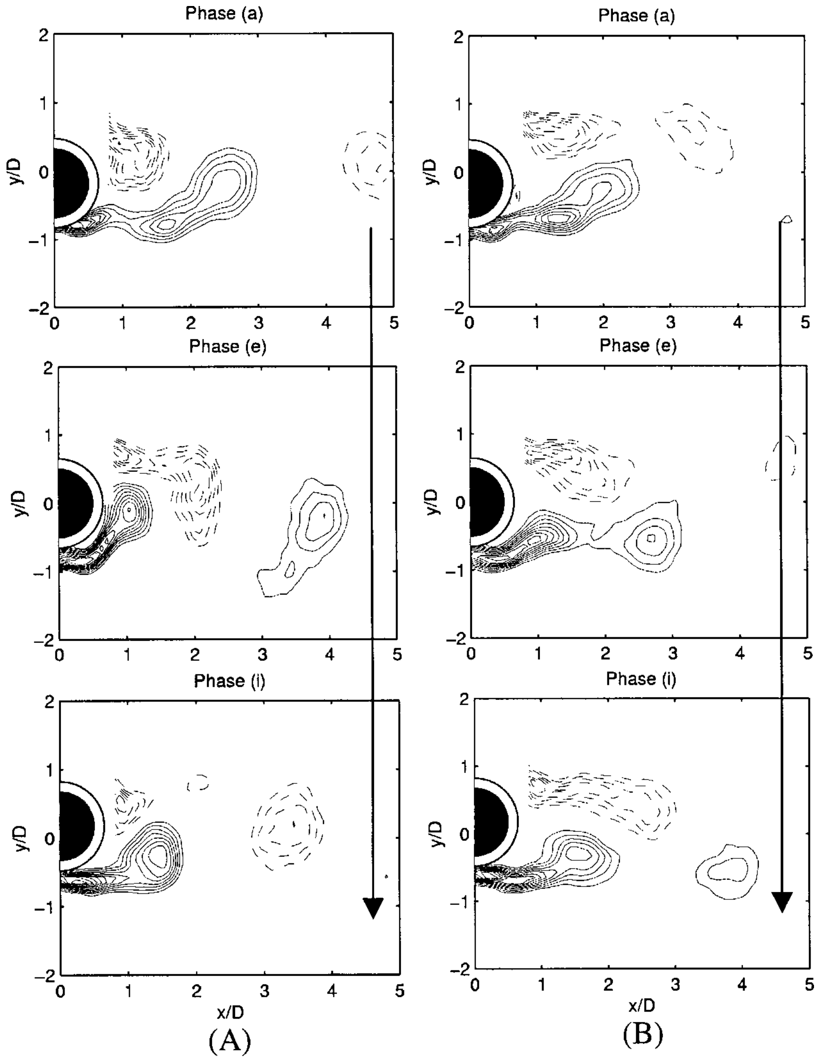

Fig. 12 Sequence of phase averaged vorticity fields for forced oscillating cylinder at $\mathrm{St}_c=0.37$, $A/D=0.2$ (Case VII) (*A*), and $\mathrm{St}_c=0.42$, $A/D=0.2$ (Case VIII) (*B*). ($|\langle\omega_z\rangle D/U_\infty|$)1.0, contour increment 0.5). See Fig. 13(*C*) for phase corresponding to each letter.

close to the cylinder only for three times the vortex shedding frequency. This result is confirmed by measurements by Gau et al. [8] for $A/D<0.064$. There may be indeed an effect from incoherent or ''turbulent'' motions in the wake as suggested by the result of Nusselt number never quite returning to the value of the stationary cylinder (Figs. 3 and 4, and Gau et al. [8]). However, the large increases observed at particular frequencies are the result of coherent or synchronized motion of the wake with respect to the cylinder oscillation.

Error Analysis

The relative uncertainty in the Nusselt number is given by:

$$\frac{\delta\mathrm{Nu}}{\mathrm{Nu}}=\left(\begin{array}{l}\left[\frac{\delta(T_{tc}-T_\infty)}{(T_{tc}-T_\infty)}\right]^2+\left(\frac{\delta\dot{Q}}{\dot{Q}}\right)^2+\left(\frac{\delta D}{D}\right)^2+\left(\frac{\delta L}{L}\right)^2+\\ \sum_{i=1}^{2}\left(\frac{\delta R_i}{R_i}\right)^2+\left(\frac{\delta k}{k}\right)^2+\left(\frac{\delta k_{CO}}{k_{CO}}\right)^2+\left(\frac{\delta k_{CI}}{T_{CI}}\right)^2\end{array}\right)^{1/2}. \tag{12}$$

The relative uncertainty in the Nusselt number is on the order of 10 percent. The absolute uncertainty is roughly 25 percent. The large absolute uncertainty in Nusselt number comes using one-dimensional approximation of the surface temperature. A two-dimensional simulation shows that one-dimensional approximation produces a somewhat large bias error, i.e., absolute uncertainty, but the relative error is less sensitive. In other words, Nu_o may be off, but $\mathrm{Nu}/\mathrm{Nu}_o$ is accurate. Irrespective of our results, there is a large scatter in the Nusselt number found in literature. Again, one cause of the scatter might be the cylinder aspect ratio (L/D). It has been observed that decreasing the aspect ratio increases the wake bubble length; hence, the distance at which the vortices roll-up (Norberg [16]; Noca et al. [15]). Since the distance at which vortices roll-up plays an important role in the surface heat transfer when the cylinder is oscillated, the aspect ratio may be an important parameter in determining the relative increase in the heat transfer between a stationary and oscillated cylinder. Review of the aspect ratios used in previous studies show a range of rather low values, from $L/D=3$ of Saxena and Laird [20], $L/D=10.7$ of Kezios and Prasanna [11], $L/D=16$ of Cheng et al. [4], $L/D=17$ of Gau et al. [4], to $L/D=17.5$ for Sreenivasan and Ramachandran [21]. The end boundary conditions of these experiments have not been well documented. Therefore, the measurements from these studies, as well as the present study, may not be truly representative of heat transfer from an ''infinitely long'' circular cylinder which may be achieved only

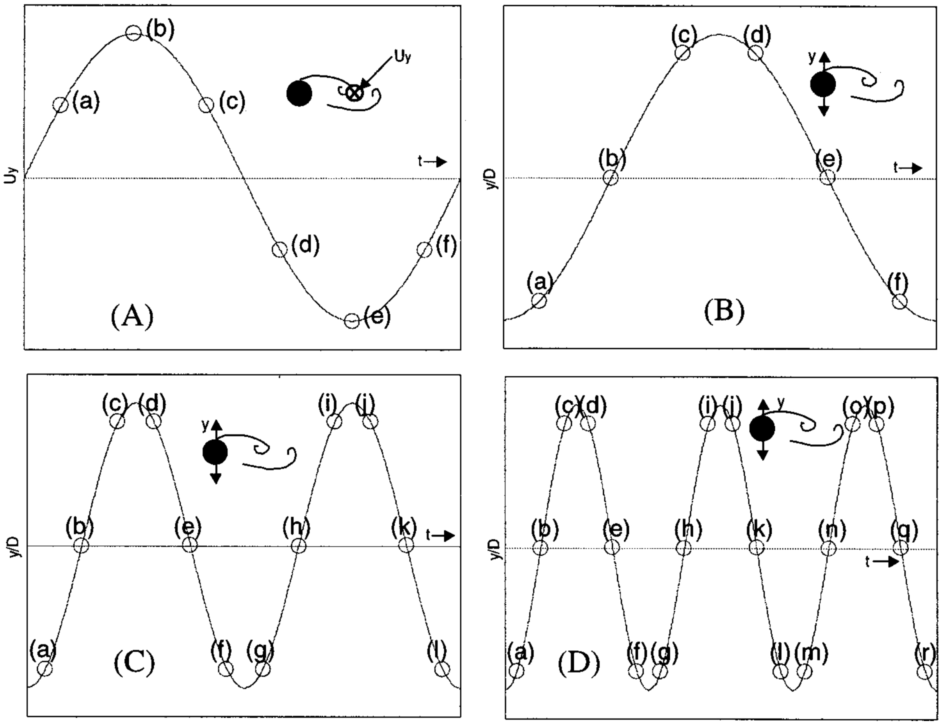

Fig. 13 Reference velocity and displacement of the cylinder corresponding to each letter of phase average

Table 1 Parameters from different studies

Authors	Re	Medium	A/D	Max. Nu/Nu$_o$	Nu$_o$/ Re$^{0.5}$Pr$^{0.33}$	T$_c$-T$_\infty$	L/D
Sreenivasan and Ramachandran (1961)	5,000-25,000	Air	0.43-3.7	≈1.0	≈0.5-0.7	≈75 °C	18
Kezios and Prasanna (1966)	5,500-14,000	Air	0.02-0.075	≈1.2	???	≈85 °C	11
Saxena and Laird (1978)	3,500	Water	0.89-1.99	≈1.6	???	≈9 °C	3
Cheng et al. (1997)	200-1000	Air	0.14-0.63	≈1.3	≈0.55	≈65 °C	16
Gau et al. (1999)	1600-4800	Air	0.064-0.016	≈1.4	≈0.55	???	17
Present Study	550-3500	Water	0.1-0.2	≈1.6	≈0.4-0.5	≈10 °C	13

when $L/D > 50 (200 < \mathrm{Re} < 1000)$ and $L/D > 200$ for $\mathrm{Re} > 1000$ (Norberg [16]). Thus there may not be a ''universal'' Nusselt number for a given Reynolds number. The parameters and results of each study are shown in Table 1.

A review of the previous measurements shows that there is a wide scatter in the measured heat transfer increase at the wake synchronization frequency ($\mathrm{St}_c \approx 0.2$). Experimentally, Kezios and Prasanna [11] measured increase of 20 percent for $A/D = 0.075$ at $\mathrm{Re} = 5500$, while Cheng et al. [4] measured increase of 10 percent for $A/D = 0.138$ at $\mathrm{Re} = 1000$ Gau et al. [8] has found increase up to 40 percent for $A/D = 0.064$ at $\mathrm{Re} = 1600$. There are some possible reasons for these discrepancies. First, some experiments were conducted in water and others in air, thus there may be Prandtl number effects. Second, each study used a different technique of computing the Nusselt number. Kezios and Prasanna [11] used thermocouples on the surface of a cylinder which was heated continuously, and the Nusselt number was estimated from the continuous power input and the average surface temperature. Gau et al. [8] made measurements similar to Kezios and Prasanna [11] except the heater strips were used to measure local Nusselt number. Cheng et al. [4] used thermocouples embedded within a cylinder which was first heated then allowed to cool by convection. The Nusselt number was computed indirectly by measuring the cooling rate of the cylinder. In this study, the cylinder is continuously heated, but the Nusselt number is computed using an *estimate* of the surface temperature from a thermocouple embedded in the cylinder core and the power input. It can be argued that the methods of Kezios and Prasanna [11] and Gau et al. [8] are the most accurate since they are the most direct measures of the Nusselt number. The results of this study are closer to those of Gau et al. [8] than those of Kezio and Prasanna [11] and Cheng et al. [4], but the issue is far from resolved. Since the cylinder used in this study was primarily designed for DPIV/T measurements, the computed Nusselt numbers in this study is not precise enough to address this question. However, the observed trends in the heat transfer rate as function of oscillation frequency and amplitude in this study are believed to be completely accurate.

Conclusion

In this study, we examine the effect of forced transverse oscillations on the heat transfer from the surface of a circular cylinder for $\mathrm{Re} = 550$, 1100, 3500. A map is made of the heat transfer versus forced oscillation frequency for oscillation amplitudes, $A/D = 0.1$ and 0.2. It is found that besides the increase in heat transfer at the oscillation frequency corresponding to the unforced vortex shedding frequency, there are other higher frequencies, namely super-harmonics, at which there is a large increase in the heat transfer. In particular, there is a large increase in heat transfer at approximately three times the unforced vortex shedding frequency for $A/D = 0.1$, and there are large increases at approximately two and three times the frequency for $A/D = 0.2$. A close inspection of the flow field using DPIV/T reveals that the increase in the heat transfer from a forced oscillating cylinder is linked with the distance at which vortices roll-up behind the cylinder. When the vortices roll-up close to the cylinder, the heat transfer is increased as the result of the removal of the stagnant and low heat convecting fluid at the base of the cylinder when the vortices approach close to the cylinder. The close roll-up of the vortices coincides with the synchronization of the wake with the mechanical oscillation of the cylinder through period doubling and/or tripling of the wake pattern with respect to the cylinder oscillation period. However, the synchronization of the wake with the mechanical oscillation is not found to be a sufficient condition to cause a large increase in the surface heat transfer. Only when the wake is synchronized and the vortices roll-up close to the cylinder, is a large increase in the surface heat transfer observed. Finally, the large increases in the heat transfer appear to be the result of coherent motions of the wake, not ''turbulent'' or incoherent motions.

Acknowledgments

We thank David Jeon and Dr. Flavio Noca for their generous help. This research was supported by NSF Grant CTS-9418973.

Nomenclature

A = amplitude of oscillation
Bi = Biot number (hD/k)
C_p = heat capacity
D = diameter of cylinder
f = frequency
f_c = frequency of cylinder oscillation
Gr = Grashof number ($g\beta(T_c - T_\infty)D^3/\nu^2$)
g = acceleration of gravity
h = convection heat transfer coefficient
k = thermal conductivity
k_{CO} = thermal conductivity of outer shell of cylinder
k_{CI} = thermal conductivity of heat coil inside cylinder
L = span of cylinder
Nu = Nusselt number (hD/k)
Nu_o = Nusselt number of stationary cylinder
Pr = Prandtl number (ν/α)
$\dot{Q}$ = heat input
$\dot{q}$ = heat input per unit mass
R_1 = inner radius of heating coil inside cylinder
R_2 = outer radius of heating coil inside cylinder
R_3 = outer radius of cylinder
Re = Reynolds number ($U_\infty D/\nu$)
St = Strouhal frequency (fD/U_∞)
St_c = Strouhal frequency of cylinder ($f_c D/U_\infty$)
T = temperature
T_∞ = freestream temperature
T_c = surface temperature of cylinder
T_{tc} = temperature of thermocouple inside cylinder
t = time
U_∞ = freestream velocity
$\vec{u}$ = velocity vector
u_i = i^{th} velocity component
V_e = effective velocity of cylinder
V_v = RMS of transverse velocity of oscillating cylinder

Greek

α = heat diffusion coefficient ($k/\rho C_p$)
β = coefficient of thermal expansion
ρ = density
ν = kinematic viscosity
ω = vorticity

References

[1] Bearman, P. W., 1969, ''On Vortex Shedding From a Circular Cylinder in the Critical Reynolds Number Regime,'' J. Fluid Mech., **37**, pp. 577–586.
[2] Bloor, S., 1964, ''The Transition to Turbulence in the Wake of a Circular Cylinder,'' J. Fluid Mech., **19**, pp. 290–304.
[3] Cantwell, B., and Coles, D., 1983, ''An Experimental Study of Entrainment and Transport in the Turbulent Near Wake of a Circular Cylinder,'' J. Fluid Mech., **136**, pp. 321–374.
[4] Cheng, C. H., Chen, H. N., and Aung, W., 1997, ''Experimental Study of the Effect of Transverse Oscillation on Convection Heat Transfer From a Circular Cylinder,'' Journal of Heat Transfer, **119**, pp. 474–482.
[5] Cheng, C. H., and Hong, J. L., 1997, ''Numerical Prediction of Lock-On Effect on Convective Heat Transfer From a Transversely Oscillating Circular Cylinder,'' Int. J. Heat Mass Transf., **40**, pp. 1825–1834.
[6] Dabiri, D., and Gharib, M., 1991, ''Digital Particle Image Thermometry: The Method and Implementation,'' Exp. Fluids, **11**, pp. 77–86.
[7] Eckert, E. R. G., and Soehngen, E., 1952, ''Distribution of Heat Transfer Coefficients Around Circular Cylinder in Crossflow at Reynolds Numbers From 20 to 500,'' Trans. ASME, **74**, pp. 343–347.
[8] Gau, C., Wu, J. M., and Liang, C. Y., 1999, ''Heat Transfer Enhancement and Vortex Flow Structure Over a Heated Cylinder Oscillating in the Crossflow Direction,'' ASME Journal of Heat Transfer, **121**, pp. 789–795.
[9] Karanth, D., Rankin, G. W., and Sridhar, K., 1994, ''A Finite Difference

Calculation of Forced Convective Heat Transfer From an Oscillating Cylinder,'' Int. J. Heat Mass Transf., **37**, pp. 1619–1630.

[10] Karniadakis, G. E., 1997, private communication, Brown University, Providence, RI.

[11] Kezios, S. P., and Prasanna, K. V., 1966, ''Effect of Vibration on Heat Transfer From a Cylinder in Normal Flow,'' ASME Paper 66-WA/HT-43.

[12] Martinelli, R. C., and Boelter, L. M. K., 1938, ''The Effect of Vibration on Heat Transfer by Free Convection From a Horizontal Cylinder,'' *Proceedings of 5th International Congress of Applied Mechanics*, p. 578.

[13] Matsumura, M., and Antonia, R. A., 1993, ''Momentum and Heat Transport in the Turbulent Intermediate Wake of a Circular Cylinder,'' J. Fluid Mech., **250**, pp. 651–668.

[14] McAdams, W. H., 1954, *Heat Transmission*, McGraw-Hill, New York, p. 260.

[15] Noca, F., Park, H. G., and Gharib, M., 1998, ''Vortex Formation Length of a Circular Cylinder ($300<\mathrm{Re}<4{,}000$) Using DPIV,'' *Proceedings of ASME Fluids Engineering Division Summer Meeting*, Paper FEDSM 98-5149.

[16] Norberg, C., 1994, ''An Experimental Investigation of the Flow Around a Circular Cylinder: Influence of Aspect Ratio,'' J. Fluid Mech., **275**, pp. 258–287.

[17] Ongoren, A., and Rockwell, D., 1988, ''Flow Structure From an Oscillating Cylinder Part 1. Mechanisms of Phase Shift and Recovery in the Near Wake,'' J. Fluid Mech., **191**, pp. 197–223.

[18] Park, H. G., 1998, ''A Study of Heat Transport Processes in the Wake of a Stationary and Oscillating Circular Cylinder Using Digital Particle Image Velocimetry/Thermometry,'' Ph.D. thesis, California Institute of Technology, Pasadena, CA.

[19] Roshko, A., 1993, ''Perspectives on Bluff Body Aerodynamics,'' J. Wind. Eng. Ind. Aerodyn., **49**, pp. 79–100.

[20] Saxena, U. C., and Laird, A. D. K., 1978, ''Heat Transfer From a Cylinder Oscillating in a Cross-Flow,'' ASME J. Heat Transfer, **100**, pp. 684–689.

[21] Sreenivasan, K., and Ramachandran, A., 1961, ''Effect of Vibration on Heat Transfer From a Horizontal Cylinder to a Normal Air Stream,'' Int. J. Heat Mass Transf., **3**, pp. 60–67.

[22] Taneda, S., 1956, ''Experimental Investigation of the Wakes Behind Cylinders and Plates at Low Reynolds Numbers,'' J. Phys. Soc. Jpn., **11**, p. 302.

[23] Willert, C. E., and Gharib, M., 1991, ''Digital Particle Image Velocimetry,'' Exp. Fluids, **10**, pp. 181–193.

[24] Williamson, C. H. K., and Roshko, A., 1988, ''Vortex Formation in the Wake of an Oscillating Cylinder,'' J. Fluids Struct., **2**, pp. 355–381.

S. S. Sazhin
School of Engineering,
Faculty of Science and Engineering,
The University of Brighton,
Brighton BN2 4GH, UK
e-mail: S.Sazhin@brighton.ac.uk

V. A. Gol'dshtein
Department of Mathematics
and Computer Sciences,
Ben-Gurion University of The Negev,
P.O.B. 653,
Beer Sheva 84105, Israel

M. R. Heikal
School of Engineering,
Faculty of Science and Engineering,
The University of Brighton,
Brighton BN2 4GH, UK

A Transient Formulation of Newton's Cooling Law for Spherical Bodies

Newton's law of cooling is shown to underestimate the heat flux between a spherical body (droplet) and a homogeneous gas after this body is suddenly immersed into the gas. This problem is rectified by replacing the gas thermal conductivity by the effective thermal conductivity. The latter reduces to the gas thermal conductivity in the limit of $t\to\infty$, but can be substantially higher in the limit of $t\to 0$. In the case of fuel droplet heating in a medium duty truck Diesel engine the gas thermal conductivity may need to be increased by more than 100 percent at the initial stage of calculations to account for transient effects during the process of droplet heating. [DOI: 10.1115/1.1337650]

Keywords: *Droplet, Heating, Heat Transfer, Spheres, Sprays, Thermal*

1 Introduction

Newton's law of cooling gives the expression for convective heat flux leaving a solid surface in the form ([1]):

$$\dot{q}=h(T_s-T_{g0}), \tag{1}$$

where h is the convective heat transfer coefficient, T_s is the temperature of the surface of the body, T_{g0} is gas temperature at sufficiently large distances from the body. Although the expression (1) is traditionally called the cooling law, it can be equally applied to the problem of heating of the body.

The value of h can be estimated as ([1]): $h=\mathrm{Nu}k/L$, where Nu is the Nusselt number, k is the gas thermal conductivity, L is the characteristic size. This expression can be considerably simplified in the case of spherical bodies (e.g., droplets, particles), assuming that both Reynolds and Prandtl numbers are small. In this case we can assume that $\mathrm{Nu}=2$ and simplify the expression for h to

$$h=k/r_s, \tag{2}$$

where $r_s=L/2$ is the radius of the sphere.

Strictly speaking, this form of the expression for h is valid in stationary cases only. However, it has been widely used for modeling not only stationary but also transient processes, including the combustion of fuel droplets (e.g., [2–6]). This assumption allows the analysis to be considerably simplified, but its applicability has never been rigorously justified to the best of our knowledge.

The objective of this paper is to investigate the transient heat transfer between a spherical body and surrounding gas in order to clarify the range of applicability of Eqs. (1) and (2). The aim of this paper is to generalize these equations so that they can be applied to both stationary and transient processes. The effects of evaporation and combustion will be ignored. This enables the results to be applied to a heat-up period of fuel droplets—a problem complementary to the unsteady effects in droplet evaporation and combustion discussed by Crespo and Liñan [7].

Basic equations will be derived and discussed in Section 2. In Section 3 our results will be applied to the modeling of a typical problem of heating fuel droplets in a Diesel engine. The main conclusions of the paper are summarized in Section 4.

2 Basic Equations

Let us assume that a sphere of radius r_s and temperature T_s is immersed into an infinite homogeneous gas at temperature T_{g0}. The temperature of sphere remains constant, but the changes in gas temperature are described by the heat conduction equation in the form ([8]):

$$\frac{\partial T}{\partial t}=\kappa\left(\frac{\partial^2 T}{\partial r^2}+\frac{2}{r}\frac{\partial T}{\partial r}\right), \tag{3}$$

where $\kappa=k/(c_{pg}\rho_g)$, c_{pg} is the gas specific heat capacity, ρ_g is the gas density, r is the distance from the center of the sphere, t is time, $T(r_s)=T_s$.

The assumption $T_s=\text{const}$ made to simplify the mathematical formulation of the problem has a number important physical implications. For example, in the case of fuel droplets, their heating by heat transfer from the hot gas can be compensated by their cooling through evaporation (cf. [9,10]).

Equation (3) can be reformulated in terms of new variables

$$V=rT-r_sT_s \quad R=r-r_s$$

and written as

$$\frac{\partial V}{\partial t}=\kappa\frac{\partial^2 V}{\partial R^2}. \tag{4}$$

The boundary and initial conditions for this equation are presented as

$$V(0,t)=0 \quad V(R,0)=f(R), \tag{5}$$

where

$$f(R)=\begin{cases} RT_{g0}+r_s(T_{g0}-T_s) & \text{when } R>0\\ 0 \quad \text{when } R=0.\end{cases}$$

The solution of Eq. (4) subject to conditions (5) can be written as ([11]):

$$V(R,t)=\frac{1}{2\sqrt{\pi\kappa t}}\int_0^\infty f(\xi)\left\{\exp\left[-\frac{(R-\xi)^2}{4\kappa t}\right]-\exp\left[-\frac{(R+\xi)^2}{4\kappa t}\right]\right\}d\xi. \tag{6}$$

Having substituted the explicit expression for $f(\xi)$ into (6) and returning to variables T and r we obtain:

Contributed by the Heat Transfer Division for publication in the JOURNAL OF HEAT TRANSFER. Manuscript received by the Heat Transfer Division September 23, 1999; revision received June 21, 2000. Associate Editor: J. P. Gore.

$$T=T_{g0}+\frac{r_s}{r}(T_s-T_{g0})\left[1-\operatorname{erf}\left(\frac{r-r_s}{2\sqrt{\kappa t}}\right)\right], \tag{7}$$

where

$$\operatorname{erf}(x)=\frac{2}{\sqrt{\pi}}\int_0^x \exp(-t^2)\,\mathrm{d}t.$$

In the limit $r=r_s$ Eq. (7) gives $T=T_s$. In the limit $t\to 0$, but $r\neq r_s$, this equation gives $T=T_{g0}$ in agreement with conditions (5).

Equation (7) gives the radius of the effective cooling zone around the cold body (droplet) in a hot gas as a function of time. If, for example, we assume that time is large and define the cooling zone as the one where $T=0.8T_{g0}$ then the radius of this zone (r_{cz}) can be obtained as

$$r_{cz}=5r_s(T_{g0}-T_s)/T_{g0}.$$

If $T_{g0}\approx 3T_s$ (realistic situation in Diesel engines: see [12]) then $r_{cz}\approx 10r_s$. This condition needs to be accounted for in computer modeling of heat exchange between droplets and gas in order to avoid grid dependence when coupling Lagrangian droplet tracking with the Eulerian gas phase in CFD calculations. It is usually satisfied in realistic Diesel spray calculations where the drop sizes are of the order of 10 μm and the grid sizes are of the order of 250 μm, although this effect can be important in the case of larger droplets.

Based on (7) the heat flux from the surface of the sphere ($r=r_s$) can be estimated as:

$$\dot{q}=-k\frac{\partial T}{\partial r}=\frac{k(T_s-T_{g0})}{r_s}\left(1+\frac{r_s}{\sqrt{\pi\kappa t}}\right). \tag{8}$$

Comparing Eqs. (1), (2), and (8), it can be seen that the Newton's law of cooling can be used to describe the transient process discussed above, if the gas thermal conductivity k is replaced by the ''effective'' thermal conductivity k_{eff} defined as

$$k_{\mathrm{eff}}=k(1+\zeta), \tag{9}$$

where

$$\zeta=r_s\sqrt{\frac{c_{pg}\rho_g}{\pi k t}}. \tag{10}$$

In the limit $t\to\infty$, $k_{\mathrm{eff}}\to k$ as expected. On the other hand, k_{eff} can be infinitely large when $t\to 0$.

The average value of k_{eff} over the period from $t=t_0$ to $t=t_0+\Delta t$ can be estimated as

$$\overline{k_{\mathrm{eff}}}=k(1+\overline{\zeta}), \tag{11}$$

where

$$\overline{\zeta}=\frac{1}{\Delta t}\int_{t_0}^{t_0+\Delta t}\zeta\,\mathrm{d}t=\frac{2}{\Delta t}r_s\sqrt{\frac{c_{pg}\rho_g}{\pi k}}(\sqrt{t_0+\Delta t}-\sqrt{t_0}). \tag{12}$$

In the case when $t_0=0$ Eq. (12) is simplified to

$$\overline{\zeta}=2r_s\sqrt{\frac{c_{pg}\rho_g}{\pi k\Delta t}}. \tag{13}$$

On the other hand when $\Delta t\ll t_0$ Eq. (12) is simplified to

$$\overline{\zeta}=r_s\sqrt{\frac{c_{pg}\rho_g}{\pi k t_0}}. \tag{14}$$

3 Discussion

Equation (9) is applied to a typical situation of gas cooling around a fuel droplet in a medium truck Diesel engine where droplets are injected at room temperature into air at $T_{g0}=880$ K and pressure 60 bar. Under these conditions $\rho_g=23.8$ kg/m^3, $k=0.061$ W/m·K, $c_{pg}=1120$ J/kg·K. For a typical timestep used in CFD calculations ($\Delta t=10^{-5}$ s) we obtain from Eq. (13) that at the start of calculations $\zeta\approx 1.4$. This means that the thermal conductivity of gas used for the estimate of the rate of the initial droplet heating can be significantly higher (more than 100 percent) than commonly believed. This time scale is much less than a typical droplet evaporation time (10^{-3} s). Moreover, the change of droplet temperature over $\Delta t=10^{-5}$ s can be safely ignored. Hence the assumptions of our model regarding the absence of evaporation and the condition that T_s=const are satisfied in this particular case.

4 Conclusions

It is pointed out that the Newton's law of cooling can be applied to the problem of transient cooling or heating of a spherical body (droplet) in a homogeneous gas if one replaces gas thermal conductivity by the effective thermal conductivity. The latter reduces to the gas thermal conductivity in the limit of $t\to\infty$, but can be substantially larger than the gas thermal conductivity in the limit of $t\to 0$. In the case of fuel droplet heating in a medium duty truck Diesel engine gas thermal conductivity may need to be increased by more than 100 percent for the initial stages of calculations to account for transient effects during the process of heating of these droplets.

References

[1] Incroperra, F. P., and DeWitt, D. P., 1996, *Fundamentals of Heat and Mass Transfer*, Wiley, New York.

[2] Kuo, K. K., 1986, *Principles of Combustion*, Wiley, New York.

[3] Griffiths, J. F., and Bernard, J. A., 1995, *Flame and Combustion*, Blackie Academic & Professional, United Kingdom.

[4] Goldfarb, I., Gol'dshtein, V., Kuzmenko, G., and Greenberg, J. B., 1997, ''Monodisperse Spray Effects on Thermal Explosion in a Gas,'' *Proceedings of ASME Heat Transfer Division (1997)*, HTD-352, **2**, pp. 199–206, ASME International Congress and Exposition, Dallas (USA).

[5] Goldfarb, I., Gol'dshtein, V., Kuzmenko, G., and Greenberg, J. B., 1998, ''On Thermal Explosion of a Cool Spray in a Hot Gas,'' *Proceedings of the 27th International Symposium on Combustion* (Colorado, USA), **2**, pp. 2367–2374.

[6] Goldfarb, I., Gol'dshtein, V., Kuzmenko, G., and Sazhin, S. S., 1999, ''Thermal Radiation Effect on Thermal Explosion in Gas Containing Fuel Droplets,'' Combust. Theory Modell., **3**, pp. 769–787.

[7] Crespo, A., and Liñan, A., 1975, ''Unsteady Effects in Droplet Evaporation and Combustion,'' Combust. Sci. Technol., **11**, pp. 9–18.

[8] Carslaw, H. S., and Jaeger, J. C., 1986, *Conduction of Heat in Solids*, Clarendon Press, Oxford.

[9] Lefebvre, A. H., 1989, *Atomization and Sprays*, Taylor & Francis, Hemisphere Publishing Corporation, New York.

[10] Williams, A., 1990, *Combustion of Liquid Fuel Sprays*, London, Butterworths.

[11] Budak, B. M., Samarsky, A. A., and Tikhonov, A. N., 1972, *Problems on Mathematical Physics*, Nauka Publishing House (in Russian).

[12] Flynn, P. F., Durrett, R. P., Hunter, G. L., zur Loye, A. O. Akinyemi, O. C., Dec, J. E., and Westbrook, C. K., 1999, ''Diesel Combustion: An Integral View Combining Laser Diagnostics, Chemical Kinetics, and Empirical Validation,'' SAE Paper 1999-01-0509.

U. Goldberg
Senior Scientist,
Metacomp Technologies, Inc.,
650 Hampshire Road, No. 200,
Westlake Village, CA 91361
e-mail: ucg@metacomptech.com

Hypersonic Flow Heat Transfer Prediction Using Single Equation Turbulence Models

Three single equation turbulence models were applied to a test case of a Mach 9 flow over a 38 deg ramp. None of the models have been optimized to high-speed flows. Results indicate that the R_t closure outperforms both the Spalart-Allmaras and Menter's models in predicting this flow. Since the R_t model's formulation is also topography-parameter-free, it seems to be the best choice for use in hypersonic heat transfer prediction within the single equation closure family. [DOI: 10.1115/1.1337653]

Keywords: Boundary Layer, Computational, Flow, Heat Transfer, Modeling, Turbulent

1 Introduction

There has recently been renewed interest in hypersonic flight vehicles. Projects such as Sandia laboratories' Hypersoar and NASA's Hyper-X are current examples. The engine inlets of these vehicles typically involve compression ramps which, through a series of shocks, reduce the engine inflow Mach number to supersonic levels to enable supersonic combustion. Such a shock system imposes, however, a severe penalty in terms of surface heating, requiring careful attention to the choice of materials and/or cooling devices to avoid the possibility of local melting of the vehicle's skin. It is important, therefore, to be able to predict hypersonic flow over ramp configurations, including surface heating characteristics, with the aim of using this capability for analysis and design purposes of vehicle components such as engine inlets. The ability to predict turbulent hypersonic flows with high level of confidence carries much broader benefits, namely entire vehicle external/internal flow prediction capability for preliminary design and, later, for various analysis purposes.

Since k-ϵ models are known to severely overpredict heat transfer levels in flows involving adverse pressure gradient ([1]), it is desirable to evaluate the performance of single equation closures under such flow conditions. This paper aims, therefore, at testing the performance of three single equation turbulence models in predicting hypersonic flow heat transfer: the R_t model ([2]), the Spalart-Allmaras model ([3]) (henceforth denoted as ''S-A''), and Menter's one-equation model ([4]). To this end, the Mach 9 flow over a 38 deg cooled ramp, with experimental data by Coleman and Stollery [5], was chosen. The formulations of the latter two models are given in detail in Refs. ([3]) and ([4]), respectively. The R_t model is described in the Appendix.

2 Highlights of the Numerical Approach

A Navier-Stokes solver for either compressible or incompressible fluid flows was used in the present work. The solver features a second order Total Variation Diminishing (TVD) discretization based on a multi-dimensional interpolation framework which is utilized also for the viscous terms. An HLLC (Harten, Lax, van Leer, with Contact wave) nonlinear Riemann solver is used to define the (limited) upwind fluxes. This Riemann solver is particularly suitable for hypersonic flow applications since, unlike classical linear solvers such as Roe's scheme, it automatically enforces entropy and positivity conditions. Further details regarding the numerical methodology can be found in Refs. ([6–9]).

3 Results

Before testing the models under hypersonic conditions, a transonic flow test case is examined. In all calculations presented here the boundary layer was allowed to develop and transition naturally, starting from a freestream inflow. All models were initialized with eddy viscosity equal to the molecular one.

3.1 Transonic Flow Over an Axisymmetric Bump. A Mach 0.875 flow over an axisymmetric bump at $\mathrm{Re}_\infty = 13.6 \times 10^6/\mathrm{m}$ was computed. Experimental data are by Bachalo and Johnson [10]. Here a normal shock, impinging on the bump, causes flow detachment from the surface with subsequent reattachment further downstream on the cylindrical portion of the model. The computations were performed on a 151×81 grid with $y^+ \leqslant 1$ at the first centroid away from the wall. Streamwise clustering was also imposed, centered at $x/c = 0.7$ where the shock impinges on the wall according to the experiment. A second calculation on a 214×115 mesh (twice the previous grid) confirmed grid independence of the results as seen in Fig. 2. A sketch of the geometry and main flow features is included in Fig. 1. Figures 2 and 3 present surface pressure coefficient (C_p) and skin friction (C_f) profiles, respectively. In the figures the origin of the axial coordinate, *x*, is at the bump leading edge; the radial coordinate, *y*, originates at the axis. All lengths are scaled by the bump cord, *c*. The R_t model predictions on the two grids coincide. Figure 4 shows velocity profiles at two streamwise locations; one within the reversed flow region, the other downstream of reattachment. Finally, Fig. 5 shows convergence history.

The R_t and Menter models predict the pressure best, whereas the S-A closure predicts the shock further downstream than indicated by the data. The post-reattachment pressure level is correspondingly overpredicted by this model. On the other hand, the

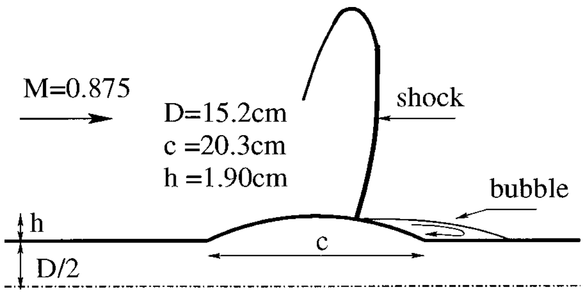

Fig. 1 Axisymmetric bump: geometry and flow features

Contributed by the Heat Transfer Division for publication in the JOURNAL OF HEAT TRANSFER. Manuscript received by the Heat Transfer Division August 4, 1999; revision received, September 5, 2000. Associate Editor: J. Gore.

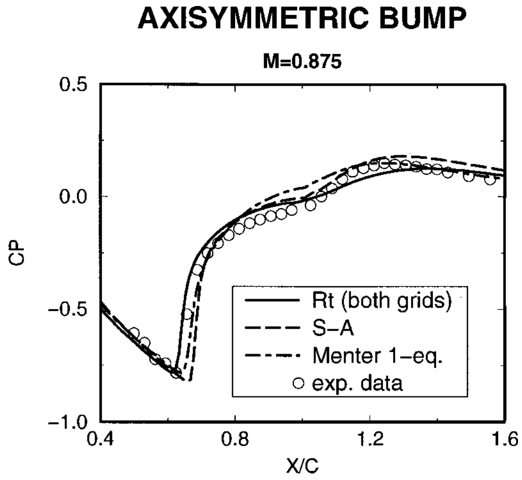

Fig. 2 Axisymmetric bump: wall pressure distribution

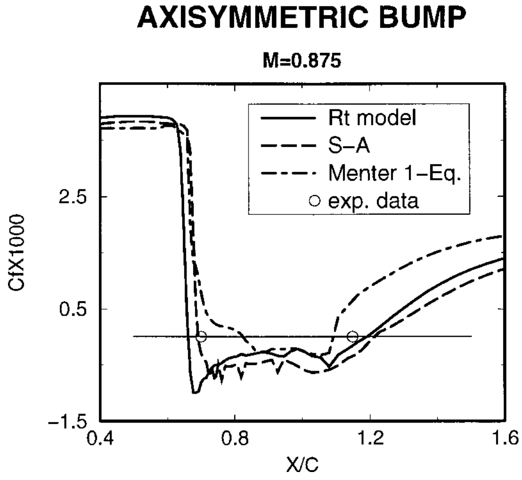

Fig. 3 Axisymmetric bump: skin friction distribution

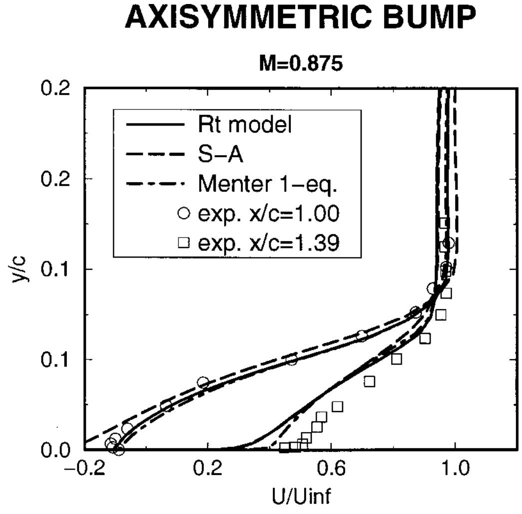

Fig. 4 Axisymmetric bump: velocity profiles

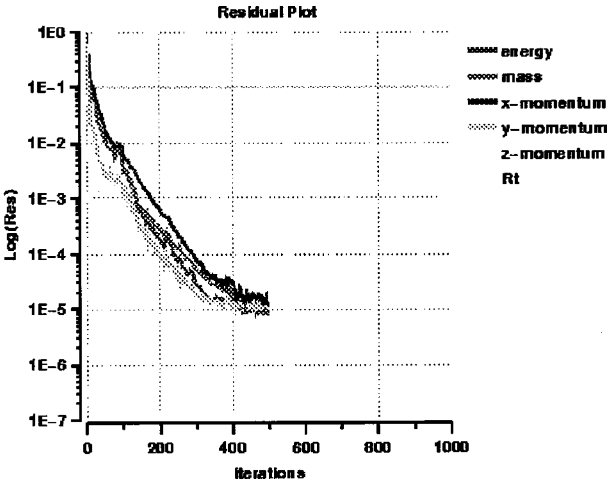

Fig. 5 Axisymmetric bump: convergence history

S-A and R_t models capture the skin friction well, whereas Menter's closure underpredicts the extent of the separation bubble by about 40 percent, reminiscent of some linear k-ϵ models' performance. This aspect of Menter's model is evident also in the next flow case and stems from the fact that it was largely derived from the standard k-ϵ closure. Turning to the velocity profiles, the S-A model overpredicts the extent of the reversed flow while the R_t and Menter's model capture the reversed flow profile quite well. All models predict a sluggish boundary layer post-reattachment recovery, but Menter's model is slightly better in the near-wall region, again, typical of k-ϵ models which tend to underpredict the extent of flow separation. The R_t model yields the best overall prediction of this flow case.

3.2 Hypersonic Flow Over a Compression Ramp. This case is a two-dimensional Mach 9 flow over a 38 deg cooled ramp, with experimental data reported in Ref. ([5]). An oblique shock, impinging on the boundary layer downstream of the ramp corner, induces flow detachment with subsequent reattachment onto the ramp surface, where a large heat transfer peak occurs. Figure 6 shows the geometry and main flow features. The flow conditions are as follows: inflow Mach number is 9.22, $\mathrm{Re}_\infty = 0.47\times 10^6/\mathrm{cm}$, total temperature is 1070 K, $T_\infty = 64.5$ K and the wall temperature is 295 K.

The computation was done on a 250×200 grid with at least 20 cells inside the viscous sublayer, first centroidal point away from the wall being at $y^+ \approx 0.1$. The grid was clustered in the x direction too, centered at the ramp corner. A 200×150 grid was also used to ascertain grid independence of the reported fine mesh results.

Figure 7 shows wall pressure distribution as predicted by the single equation models and Fig. 8 shows the corresponding wall heat transfer. Comparison with the experimental data indicates that the R_t model predicts this flow better than the other two models. It captures the extent of the separation region; hence, it also captures correctly the shock location and the peak pressure level. The S-A model predicts less than half the size of the experimentally observed bubble, and Menter's model predicts an even smaller reversed flow, thus both models place the shock too

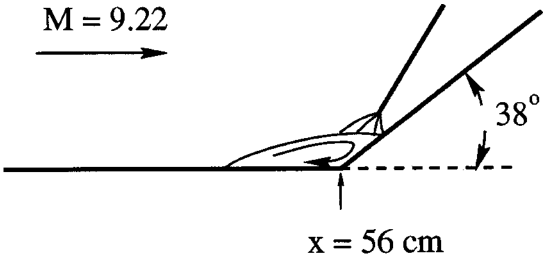

Fig. 6 Hypersonic ramp flow: geometry and flow features

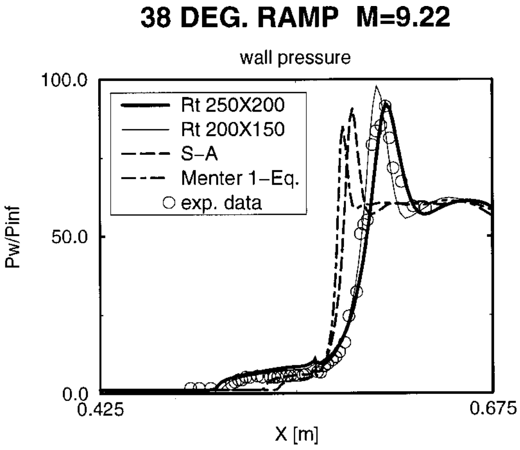

Fig. 7 Hypersonic ramp flow: wall pressure distribution

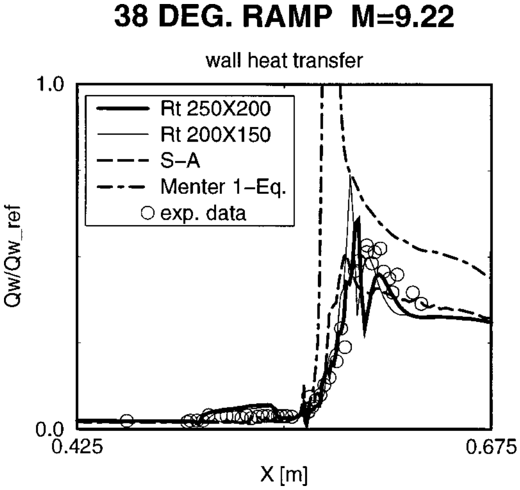

Fig. 8 Hypersonic ramp flow: heat transfer distribution

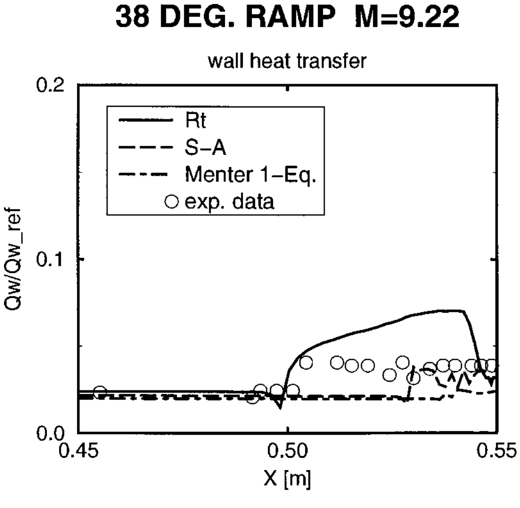

Fig. 9 Hypersonic ramp flow: heat transfer distribution detail

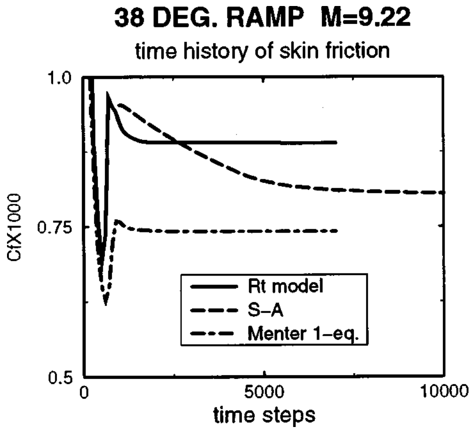

Fig. 10 Hypersonic ramp flow: convergence history

far upstream and underpredict the peak level. The heat transfer is, again, best predicted by the R_t model, but the S-A closure also performs quite well. Menter's model, however, yields a peak heat transfer some four times the observed level, much like the performance of k-ϵ models. The oscillatory behavior exhibited by the R_t model in the peak heat transfer region is observed in the experimental data as well (albeit to a lesser extent) and may stem from a local structure in the reattachment zone. Predictions on the two grids exhibit relatively minor differences. Figure 9 depicts the heat transfer distribution in the reversed flow region upstream of the shock, showing that the R_t model captures the start of increase in heat transfer above the flat plate level, associated with the leading edge of the separation bubble. The other two models do not capture this flow region correctly, resulting in inferior performance further downstream.

Figure 10 is a convergence history plot, based on skin friction. It shows that the R_t and Menter's model converge about four times faster than the S-A model.

4 Summary and Conclusions

The performance of three single equation turbulence models was evaluated under transonic and hypersonic flow conditions, both involving adverse pressure gradients strong enough to impose a large reversed flow region. In the former case all models performed well, but Menter's model underpredicted the extent of flow separation. In the latter case neither the S-A nor Menter's model was able to capture the pressure profile correctly due to underpredicting the bubble size. The S-A model nevertheless predicted the heat transfer distribution quite well, whereas Menter's closure yielded about four times the observed peak level. In contrast, the R_t model predicted this flow very well, even though it has not been optimized to high-speed flows. It was also observed that Menter's model behaved similar to a typical k-ϵ closure under adverse pressure gradient conditions.

It is concluded that the topography-parameter-free R_t model may be the best choice, within single equation closures, for reliable prediction of hypersonic wall-bounded flows.

5 Appendix: R_t Model Formulation

The R_t model consists of solving the following transport equation for the undamped eddy viscosity *(R)*:

$$\rho\frac{DR}{Dt}=\frac{\partial}{\partial x_j}\left[\left(\mu+\frac{\mu_t}{\sigma_R}\right)\frac{\partial R}{\partial x_j}\right]+C_1\rho(RP_k)^{1/2}-(C_3f_3-C_2)\rho\mathcal{D}, \tag{1}$$

where the turbulence production is expressed in terms of the Boussinesq approximation

$$P_k=\nu_t\left[\left(\frac{\partial U_i}{\partial x_j}+\frac{\partial U_j}{\partial x_i}\right)\frac{\partial U_i}{\partial x_j}-\frac{2}{3}\left(\frac{\partial U_k}{\partial x_k}\right)^2\right], \tag{2}$$

and the destruction term is

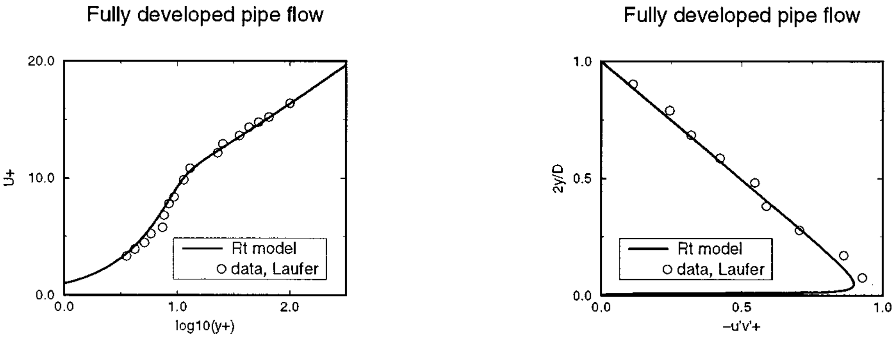

Fig. 11 Pipe flow: law-of-the-wall and shear stress profiles

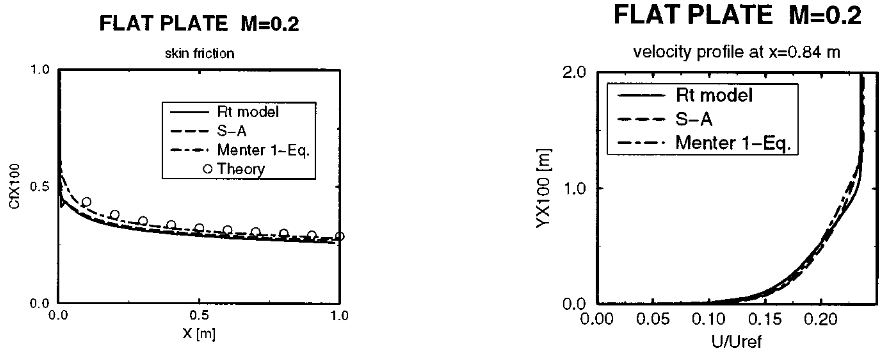

Fig. 12 Flat plate flow: skin friction and velocity profiles

$$\mathcal{D}=\begin{cases}\dfrac{\partial R}{\partial x_j}\dfrac{\partial R}{\partial x_j}, & \varphi>0\\ 0, & \text{otherwise}\end{cases}, \tag{3}$$

where

$$\varphi=\frac{\partial Q}{\partial x_j}\frac{\partial R}{\partial x_j}, \tag{4}$$

and

$$Q=[(U-U_0)^2+(V-V_0)^2+(W-W_0)^2]^{1/2}. \tag{5}$$

Here $\{U_0,V_0,W_0\}$ is the velocity vector of the frame of reference (often 0); $U_i=(U,V,W)$ are the cartesian velocity components; $x_i=(x,y,z)$ are the corresponding coordinates; μ and μ_t are the dynamic molecular and eddy viscosities, respectively; ρ is density; and ν_t is the kinematic eddy viscosity μ_t/ρ. The conditional application of the sink term avoids sharp turbulent/nonturbulent interfaces at shear layer edges since the term is used only in the lower portion of the boundary layer, where $\varphi>0$. It is noted that this term vanishes naturally at the location of maximum R, since $\nabla R=0$ there. The formulation retains $\mathcal{D}=0$ from that point toward the boundary layer edge.

The eddy viscosity field is given by

$$\mu_t=f_\mu \rho R, \tag{6}$$

where

$$f_\mu=[\tanh(\alpha\chi^2)]/[\tanh(\beta\chi^2)], \tag{7}$$

and

$$\chi\equiv\rho R/\mu. \tag{8}$$

The model constants and the damping function f_3 are derived from asymptotic arguments at walls and limit flow regions such as pipe centerline and the logarithmic overlaps of flat plate, pipe and channel flows. No additional calibration or optimization to specific flows was done. Figures 11 and 12 show grid-independent results for fully developed pipe flow and flat plate flow. All models predict the same flat plate boundary layer thickness (Fig. 12). The R_t and S-A closures are in close agreement regarding the skin friction distribution and slightly underpredict the theoretical curve.

Further details about the model are given in Ref. ([2]). Final results for the closure parameters are as follows:

$$f_3=1+2\alpha/(3\beta C_3\chi), \tag{9}$$

$$C_1=\kappa^2(C_3-C_2-\sigma_R^{-1}), \tag{10}$$

$$C_2=-5\alpha/(3\beta\sigma_R), \tag{11}$$

and

$$C_3-C_2=3/(2\sigma_R), \tag{12}$$

where $\sigma_R=0.8$, $\alpha=0.07$, and $\beta=0.2$.

Equation (1) is subject to the following boundary conditions:

1 Solid Walls

$$R=0, \tag{13}$$

2 Freestream Inflow and Initial Conditions

$$R_\infty\leqslant\nu_\infty \tag{14}$$

The model has been validated for numerous two-dimensional and three-dimensional wall-bounded internal and external flow cases across the Mach number range ([2,11]). While its formulation is general, it has not been validated for free-shear flows.

References

[1] Launder, B. E., 1988, ''On the Computation of Convective Heat Transfer in Complex Turbulent Flows,'' ASME J. Heat Transfer, **110**, pp. 1112–1128.

[2] Goldberg, U., 1999, ''Turbulence Closure with a New Topology-Free Single Equation Model,'' submitted to Computer Methods in Applied Mechanics and Engineering.

[3] Spalart, P. R., and Allmaras, S. R., 1992, ''A One-Equation Turbulence Model for Aerodynamic Flows,'' AIAA Paper No. 92-0439.
[4] Menter, F. R., 1997, ''Eddy Viscosity Transport Equations and Their Relation to the k-ϵ Model,'' ASME J. Fluids Eng., **119**, pp. 876–884.
[5] Coleman, G. T., and Stollery, J. L., 1972, ''Heat Transfer from Hypersonic Turbulent Flow at a Wedge Compression Corner,'' J. Fluid Mech., **56**, No. IV, pp. 741–752.
[6] Chakravarthy, S., Peroomian, O., and Sekar, B., 1996, ''Some Internal Flow Applications of a Unified-Grid CFD Methodology,'' AIAA Paper No. 96-2926.
[7] Peroomian, O., Chakravarthy, S., and Goldberg, U., 1997, ''A 'Grid-Transparent' Methodology for CFD,'' AIAA Paper No. 97-07245.
[8] Peroomian, O., Chakravarthy, S., Palaniswamy, S., and Goldberg, U., 1998, ''Convergence Acceleration for Unified-Grid Formulation Using Preconditioned Implicit Relaxation,'' AIAA Paper No. 98-0116.
[9] Batten, P., Leschziner, M. A., and Goldberg, U. C., 1997, ''Average-State Jacobians and Implicit Methods for Compressible Viscous and Turbulent Flows,'' J. Comput. Phys., **137**, pp. 38–78.
[10] Bachalo, W. D., and Johnson, D. A., 1979, ''An Investigation of Transonic Turbulent Boundary Layer Separation Generated on an Axisymmetric Flow Model,'' AIAA Paper No. 79-1479.
[11] Goldberg, U., Batten, P., Palaniswamy, S., Chakravarthy, S., and Peroomian, O., 2000, ''Hypersonic Flow Predictions Using Linear and Nonlinear Turbulence Closures,'' AIAA Journal of Aircraft, **37**, No. 4, pp. 671–675.

Practical Experience With the Discrete Green's Function Approach to Convective Heat Transfer

Keith A. Batchelder
e-mail: kito@genemachines.com
Genomic Instrumentation Services, Inc.,
935 Washington Street,
San Carlos, CA 94070

John K. Eaton
e-mail: eaton@vonkarman.stanford.edu
Department of Mechanical Engineering,
Thermosciences Division,
Stanford University,
Stanford, CA 94305-3030

The heat transfer from a short uniform heat flux strip beneath a turbulent boundary layer with and without freestream turbulence was measured using a liquid crystal imaging technique. Freestream turbulence intensities were on the order of 12 percent. Data were taken at momentum thickness Reynolds numbers on the order of 1000 and 2000 for the turbulent and steady freestreams, respectively. Heat transfer enhancement due to the presence of freestream turbulence was quantified in terms of the ratio of the average St's on the strip: turbulent freestream divided by steady freestream. Compared to the baseline case of a uniformly heated surface upstream of the strip, the heat transfer enhancement decreased by 20 percent. The temperature distribution measured on and downstream of the heated strip represented one column of a discrete Greens function that was used to predict the heat transfer for any arbitrarily specified thermal boundary condition given the same flowfield. Predictions are compared against correlations and numerical predictions as well as data from the literature. The details and practical applications of this approach to handling heat transfer with non-uniform thermal boundary conditions are presented. [DOI: 10.1115/1.1336509]

Keywords: *Conjugate, Experimental, Forced Convection, Heat Transfer, Turbulent*

Introduction

Usually convective heat transfer takes place over surfaces with non-uniform temperature and heat flux distributions. Analysis of the heat transfer is important to insure that maximum temperatures stay below material limits, and to calculate thermal stresses. Prediction of average component temperatures or bulk heat loads is not sufficient in many applications. Analytical or computational methods also must be able to yield local temperature distributions often requiring conjugate solutions of the conduction and convection problems.

The majority of convective heat transfer data are given in terms of the conventional definition of the heat transfer coefficient, h, which has the shortcoming that it does not incorporate any consideration for variations in thermal boundary condition (TBC). A measured or calculated distribution of h can only be used to predict heat transfer in situations with the same TBC. For a conjugate solution, the distribution of h must be recalculated at each iteration, or worse yet, re-measured if experimental data are used. Little regard is given in most experiments to matching the TBC expected in an application. Typically, data are obtained in simplified laboratory experiments where the hydrodynamics are matched, while the TBC is dictated by the measurement technique.

What is needed is a description of the heat transfer that is independent of the TBC and can be measured with reasonable effort and accuracy. This paper presents a discrete Green's function descriptor for the convective heat transfer that is independent of the TBC as long as the thermal energy equation can be assumed to be linear. We show that the discrete Green's function offers a convenient formulation of heat transfer problems and is applicable to arbitrarily complex flows. Once the Green's function has been determined for a given flow, it can be used to calculate the heat transfer for any distribution of wall temperature or heat flux using simple matrix-vector multiplication. Contrast this to using a modern CFD code which requires the user to set up the boundary conditions and re-solve at least one differential equation for each new thermal boundary condition.

The Green's function description suggests appropriate experiments for measuring heat transfer. One technique to measure the Green's function is described and its accuracy is assessed relative to computed and conventionally measured results. This technique is demonstrated for a simple flat plate flow here. The same technique is also applicable to more complex flows, although a more time consuming set of experiments is required.

Existing Methods for Describing Heat Transfer Independent of the TBC

The idea of using superposition to calculate heat transfer rates is not a new one. Rubesin [1] showed that the heat transfer for any arbitrary distribution of surface temperature could be calculated by representing the surface temperature as a series of finite temperature steps. Sellers et al. [2] developed a superposition solution for the case of laminar flow in a tube. Reynolds [3] derived an approximate integral analysis for calculating the heat transfer from a step change in wall temperature after an unheated starting length for a flat plate turbulent boundary layer. He used this solution as a basis for calculating the heat transfer from any arbitrarily specified distribution of surface temperature. These techniques are now incorporated in many textbooks, but they are not applicable to complex flows.

Arvizu and Moffat [4] showed that superposition could be used to describe the heat transfer in more complex electronics cooling flows. Heat transfer was measured on an array of heated rectangular elements. In order to account for upstream heating effects on local element heat transfer they used the concept of the adiabatic temperature rise, T_{ad}, defined as the temperature rise which would occur on a local adiabatic element due only to the effects of

---

Contributed by the Heat Transfer Division for publication in the JOURNAL OF HEAT TRANSFER. Manuscript received by the Heat Transfer Division February 9, 2000; revision received, May 26, 2000. Associate Editor: B. Chung.

upstream heating. Anderson and Moffat [5] extended the concept of T_{ad} by introducing an adiabatic heat transfer coefficient, h_{ad}, defined as

$$h_{ad}=\frac{\dot{q}''_{\text{element}}}{T_{\text{element}}-T_{ad}} \tag{1}$$

They demonstrated that h_{ad} is independent of TBC's. This description is well suited to electronic cooling flows and other cases where isolated elements are heated.

Vick et al. [6] analytically determined Green's functions for laminar and slug flow in tubes and used them for numerical evaluation of the heat transfer with arbitrarily varying boundary conditions. Ramanathan and Ortega [7] used approximate Green's functions, determined by assuming uniform flow velocity, to solve conjugate heat transfer problems in simplified electronics cooling situations. They showed that such a representation allowed noniterative solutions to conjugate problems.

Hacker and Eaton [8,9] introduced the discrete Green's function (DGF) as a generalization of Anderson and Moffat's work to the case of a continuous heated surface. They developed a transient technique to measure the heat flux for a large number of different surface temperature distributions in a separated flow field. They then inferred the discrete Green's function from the set of experiments. They were able to demonstrate the validity of the DGF method by using it to predict heat transfer in separated flows with a wide variety of TBC's. The complexity of this approach led to relatively large uncertainties that will be partially remedied by the more direct measurement technique described below.

The Discrete Green's Function Formulation DGF

The general Green's function approach is applicable to linear differential equations where superposition can be applied. In the case of convective heat transfer, the energy equation is linear when the fluid velocity field and the fluid properties are independent of the temperature field. This limits the applicability to relatively small temperature differences. However, once a description of the convective heat transfer has been quantified for the constant properties case, it should be possible to correct it for variable property effects as is commonly done using conventional descriptions of the heat transfer. We introduce the DGF for the simple case of an external flow with a constant free stream temperature. Again, generalization of the technique should be possible although we have not done a full analysis.

The DGF method is illustrated for a one-dimensional heat transfer surface with an unheated starting length. Heating begins at a distance x_0 downstream of the start of the hydrodynamic boundary layer and ends some distance x_0+L downstream. This region is discretized into n strips, each of length $\ell=L/n$ in the streamwise direction. The value of ℓ is chosen short enough to adequately resolve the temperature distribution. The specified temperature rise distribution is discretized in terms of a series of square pulses in temperature, where the term pulse refers to spatial rather than temporal extent. Each square pulse represents the average temperature rise over each strip as shown in Fig. 1. The resulting heat flux distribution is integrated over each strip to obtain the discretized heat rate distribution, $\dot{q}_i$ (power/unit width).

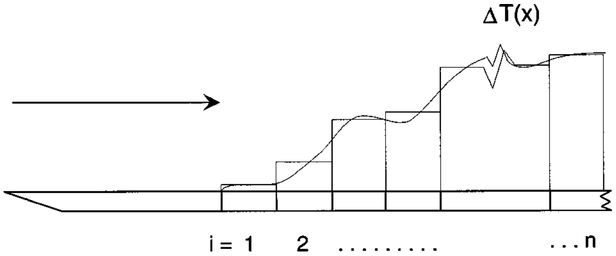

Fig. 1 Discretization of the heat transfer surface

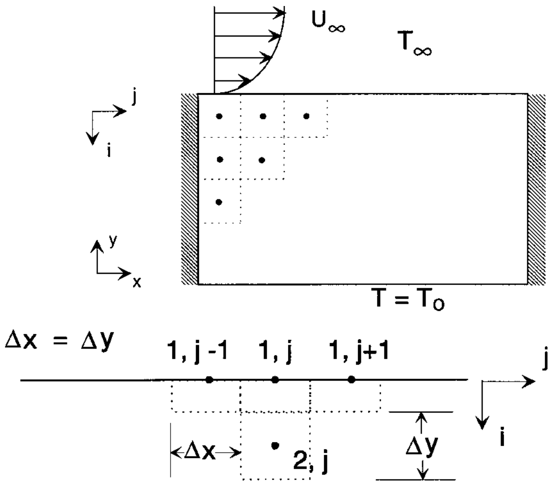

Fig. 2 Two-dimensional finite difference domain with discrete Green's function thermal boundary condition

The Discrete Green's Function, G, relates a specified discrete temperature rise distribution to a resulting discrete heat rate distribution. It is defined as an array of elements for which the following relation may be written:

$$\dot{q}_{ij}=g_{ij}\Delta T_j, \tag{2}$$

where g_{ij} is the element of G which relates the average temperature rise on strip j to the resulting heat rate on strip i. In SI notation g_{ij} will have units of W/(m-K).

The method of superposition allows the effect of each of the n square pulses in temperature rise to be considered individually. The net effect on element i is found by summing the contributions from all n elements

$$\dot{q}_i=\sum_{j=1}^{n} g_{ij}\Delta T_j. \tag{3}$$

The net effect of all the square pulses in temperature rise on the total heat rate distribution can be written in terms of a matrix multiplication

$$\dot{q}=G\Delta T, \tag{4}$$

where ΔT is a vector containing the discrete temperature rise at each location and $\dot{q}$ is a vector containing the resulting heat rates at each location. In the most general case, each square pulse in temperature rise will contribute to the resulting heat rate at all n locations. Therefore, G will be an $n\times n$ array. For attached flows where upstream heating effects can be considered negligible, a square pulse in temperature rise will have no effect on the heat rate at the upstream locations. In terms of the DGF notation this means that all of the above-diagonal terms of G, where $j<i$, will be zero. The diagonal elements of G relate the local temperature rise to the local heat rate and are thus equivalent to Anderson and Moffat's adiabatic heat transfer coefficient normalized by the length of the strip

$$h_{ad}=\frac{g_{ii}}{\ell}. \tag{5}$$

The inverse Discrete Green's Function, G^{-1}, relates a specified heat rate distribution to a resulting temperature rise distribution. It is an array of elements equal in dimension to G, where each element is defined so that

$$\Delta T_{ij}=g_{ij}^{-1}\dot{q}_j. \tag{6}$$

Using the method of superposition the total temperature rise response can be written in terms of a matrix multiplication

$$\Delta T = G^{-1}\dot{q}. \tag{7}$$

The formulation of the DGF makes it particularly useful for numerical solution of conjugate heat transfer problems. The DGF allows explicit solutions to the coupled problem as illustrated below for a simple second order finite difference scheme. Figure 2 shows a typical discretization of a solid conduction problem with a convective boundary condition on one surface. A DGF is used with elements the same size as the surface elements. The energy balance equation for element 1, j is then

$$\begin{aligned} &-k\frac{\Delta y}{2}\frac{(T_{1,j+1}-T_{1,j})}{\Delta x}-k\frac{\Delta y}{2}\frac{(T_{1,j-1}-T_{1,j})}{\Delta x} \\ &\quad = k\Delta x\frac{(T_{2,j}-T_{1,j})}{\Delta y}+\sum_{p=1}^{j} g_{j,p}(T_{\infty}-T_{1,p})\Delta x. \end{aligned} \tag{8}$$

Writing a similar equation for each element results in a set of linear algebraic equations that can be solved for the temperature of each element.

Calculating G from G^{-1}

In most flows, it is considerably simpler to measure G^{-1} than G. At first glance, it appears possible to obtain G through direct matrix inversion of the known G^{-1} matrix. However, because the Green's function is discretized, this matrix inversion results in non-physical oscillation of the off-diagonal elements of G. To get the correct behavior of G, G^{-1} must be measured at higher resolution, then inverted. The resulting matrix is a high resolution version of G that contains non-physical oscillations. This matrix is averaged in blocks to eliminate the oscillations and reduce the matrix to the desired resolution.

To test this procedure, we used a pseudo data set produced using the STAN7 boundary layer code ([10]) to mimic the experiments. We considered the case of a flat-plate boundary layer with an unheated starting length and the heated section discretized into 15 elements. A 15×15 inverse Green's function (called G_{15}^{-1}) was determined by fifteen separate runs of the code. In each run, one element had a constant heat flux and all other elements were adiabatic. Thus, the resulting temperature distribution (averaged over the elements) represented one column of G^{-1}. A high resolution (90×90) version of G^{-1} was found by averaging the same temperature distributions over elements 1/6 the original size. This gave 15 columns of G_{90}^{-1}. The remaining 75 columns were filled in by interpolation. A reference G against which inverted forms of G^{-1} were compared was determined by 15 separate runs of STAN7 in which a single element was held at an elevated temperature and all other elements were held at the freestream temperature. The resulting heat flux distribution was averaged over the elements to find G.

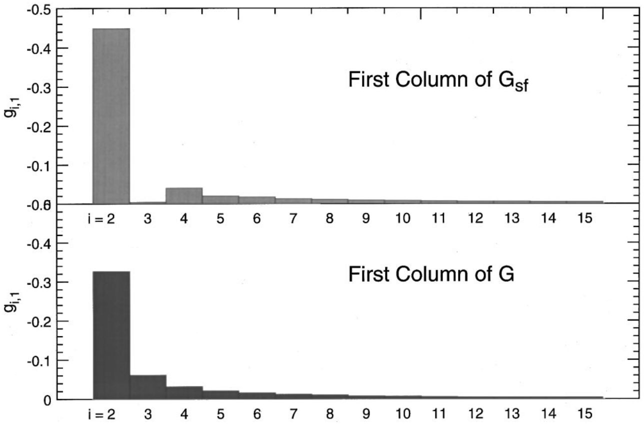

Fig. 3 Elements of first column of non-dimensionalized *G* beginning with second element

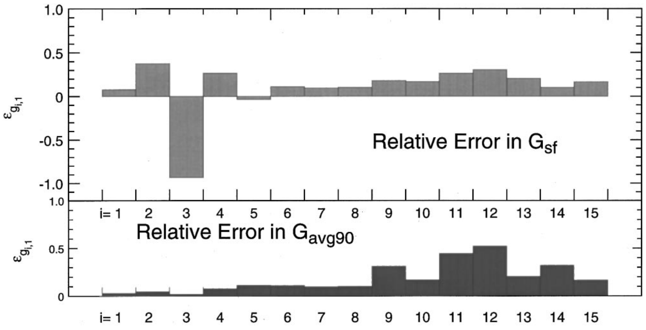

Fig. 4 Relative error in elements of first column of non-dimensionalized *G*

Figure 3 shows the first column of G determined by direct calculations and by inversion of G_{15}^{-1}. The matrix obtained by inversion is called G_{sf}. The first element is omitted because it has the same value in both cases and is much larger than the other elements. The off-diagonals are all negative and decay monotonically as expected for the directly calculated G. However, the version obtained by inverting G_{15}^{-1} shows non-monotonic behavior. The relative error of the elements is plotted in Fig. 4. It is obvious that the direct inversion produces large errors in the most important off-diagonal components. A second estimate of G was found by inverting G_{90}^{-1} then averaging the result over 6×6 blocks to form a 15×15 Green's function. The relative error using this approach is also plotted in Fig. 4 showing much improved results. The relative errors are larger for the far off-diagonals, but these values are very small so have a relatively small effect on heat transfer calculations.

Experimental Apparatus and Technique

Wind Tunnel. All experiments were run in a closed-loop boundary layer wind tunnel with a 500 mm wide by 220 mm high by 2.4 m long test section. The mean flow across the cross section of the tunnel test section was uniform to within 1.4 percent. Freestream turbulence levels were maintained below 0.1 percent through the use of a converging nozzle with an 8:1 area ratio. The top wall of the test section was flexible and was adjusted to accommodate boundary layer growth and maintain a uniform static pressure. A 2 mm high boundary layer trip was placed at the inlet of the test section so that the boundary layer was turbulent from the start of the test section. A complete description of the tunnel can be found in Ames and Moffat [11].

Two flowfields were investigated: a turbulent boundary layer under a steady freestream and a turbulent boundary layer under a turbulent freestream (referred to as steady freestream and high turbulence, respectively). In order to generate freestream turbulence, the wind tunnel was fitted with a removable square-bar grid, having an open area ratio of 69 percent, in series with a jet grid.

For a mean freestream velocity of 10.5 m/s, freestream turbulence intensities were 12 percent at 1.05 m downstream of the boundary layer trip, and 7.5 percent at 1.85 m. Turbulence characteristics and boundary layer parameters were measured using single-wire and cross-wire anemometers. The mean velocity for the high turbulence flowfield was uniform within ±4.0 percent, and the streamwise and vertical RMS velocities were uniform within ±6.0 percent and ±2.0 percent, respectively, at a streamwise location of 1.05 m.

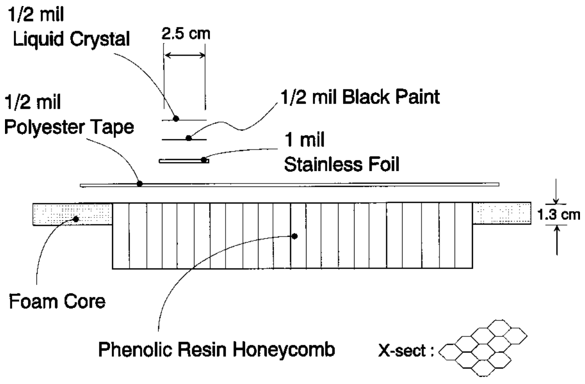

Fig. 5 Apparatus: cross section of short heated strip

Heat Transfer Surfaces

Two different TBC's were employed in this investigation. First, a uniform heat flux condition was used to generate baseline heat transfer results. Second, a square pulse in heat flux on an otherwise adiabatic surface was used to measure the elements of the inverse DGF. A different heat transfer surface was used for each TBC. The uniform heat flux TBC was generated using a guarded constant-heat-flux surface developed by Ames and Moffat [11].

The square pulse in heat flux was generated by passing a current through a 0.0127 mm (half mil) stainless steel foil. This foil was 2.54 cm long in the streamwise direction and 50 cm long in the spanwise direction. The stainless foil was attached to a 0.0127 mm (half mil) polyester film using a 0.0127 mm adhesive film. The polyester film was mounted on top of a phenolic resin honeycomb, which was secured in a foam core frame as shown in Fig. 5. The thermal conductivity of the polyester film was estimated to be on the order of 0.1 W/m-K. The polyester film and phenolic resin honeycomb provided a near adiabatic boundary condition surrounding the heated foil, minimizing the pathway for lateral conduction.

Temperatures were measured on the foil and adiabatic surface using both thermochromic liquid crystals (TLC's), and thermocouples. TLC temperature measurements were obtained using the calibration technique and imaging system described in detail by Farina et al. [12]. TLC's with a nominal activation range of 25°C to 30°C were applied over black paint on a 30 mm wide strip along the centerline of the test surface. The uncertainty in the absolute temperature measurements were estimated to be ± 0.4°C. The emissivity of the TLC and black paint layer was measured to be 0.91 using a Device and Services AE 657 emissometer. The heat transfer surface was also instrumented with AWG 36 chromel-alumel (type K) thermocouples. The thermocouples were placed at streamwise intervals of 2.54 cm. The uncertainty in the thermocouple measurement was estimated at ± 0.1°C. Both the TLC's and the thermocouples were located in the central one-third of the heat transfer surface and were far enough away from the ends of the foil so that there were no end effects.

Experimental Results

Baseline Results. Baseline boundary layer heat transfer data were acquired using the constant heat flux surface and are shown in Fig. 6. Numerical and analytical predictions for the low-turbulence case are represented by the solid and dashed lines, respectively. The data are plotted against momentum thickness Reynolds number in order that a comparison with the high-turbulence case may be made. In both cases heating began at the same x location. For the low-turbulence case, the experimental data were within 3 percent of the correlation of Reynolds and within 7 percent of the STAN7 numerical prediction. The uncertainty in the measurements was estimated to be approximately 5 percent considering the uncertainty in temperature and power measurements and additional uncertainty caused by imperfect corrections for back losses and radiation.

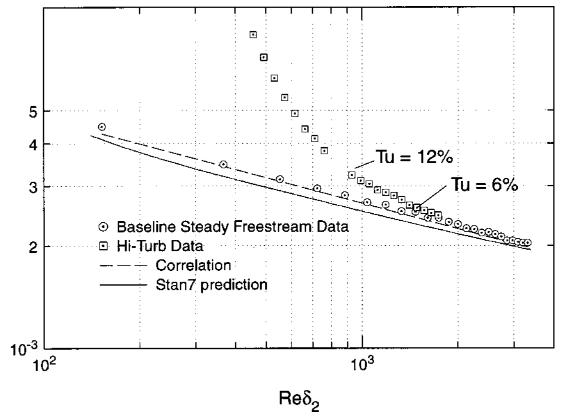

Fig. 6 Stanton number for uniform heat flux, steady freestream and high freestream turbulence

The Stanton number for the high freestream turbulence case was approximately 100 percent higher than the low-turbulence case at the most upstream measurement point, where the freestream turbulence intensity was 35 percent. As the freestream turbulence intensity decayed, the Stanton number relaxed back towards the baseline value. At the downstream end, the freestream turbulence intensity had decayed to 6 percent and the Stanton number was augmented by 4 percent.

Short Heated Strip

Surface temperature data were acquired with the heated strip in two positions, $x = 1.37$ m and $x = 1.73$ m. The strip heat flux was 500 W/m^2 and the remainder of the surface was unheated. All measurements were performed at a freestream velocity of 10.5 m/s. Figure 7 shows the measured surface temperature profiles for the upstream position with both low and high freestream turbulence. Agreement between the thermocouple and TLC measurements was within 0.1 K. Also shown is the temperature distribution computed using the STAN7 code. The predicted temperature profile had a higher peak value possibly due to lateral conduction in the foil. No correction was made for lateral conduction since the data were later averaged over the width of the strip to compute the DGF. Measurements at the downstream position were very similar and are not shown here.

Foil averaged St from the short heated strip and baseline St are tabulated in Table 1. The average Stanton number measured on

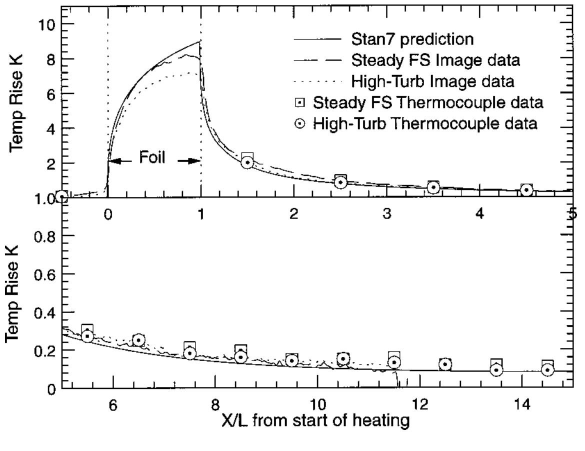

Fig. 7 Temperature rise profile, $x_0 = 1.75$ m, Re$= 1.74 \times 10^4$

Table 1 Stanton number at two X locations for two thermal boundary conditions, steady and turbulent freestreams

TBC	x [m]	Freestream	Re_{δ_θ}	St	$\frac{St_{turb}}{St_{steady}}$
Uniform Heat Flux	1.37	turbulent	989	.0031	1.38
		steady	2127	.0023	
	1.75	turbulent	1258	.0028	1.30
		steady	2617	.0022	
Short Strip	1.37	turbulent	989	.0065	1.12
		steady	2127	.0058	
	1.75	turbulent	1258	.0064	1.13
		steady	2617	.0057	

the short heated strip for the low-turbulence case was 5 percent higher than the STAN7 value. The estimated uncertainty of the experimental data at this streamwise location was ±3 percent. Comparing measurements at the same x-location, the ratio of the high-turbulence St to the low-turbulence St was 1.3 for the baseline data and 1.1 for the short strip data. This indicates that freestream turbulence has a greater effect on the temperature-rise downstream of the heated strip than on the heated strip itself. The distinction between the effect of high-turbulence on local heat transfer and its effect on the influence of the upstream TBC can be more easily understood when the heat transfer from the short heated strip is formulated in terms of an inverse DGF as shown below.

Measurement of the Discrete Green's Function

Measuring the Inverse One-Dimensional DGF. The intent is to formulate a 15×15 inverse discrete Green's function (G^{-1}) with the first element located at $x=1.37$ m and an element length of 25.4 mm. The discrete temperature profile at $x=1.37$ m shown in Fig. 8 represents the first column of G^{-1}. To find the remaining fourteen columns of G^{-1}, it would be necessary, in principle, to measure a complete temperature profile with the heated strip located at each of the fourteen other positions. Instead, a second temperature profile was measured only for the strip located at the fifteenth position ($x=1.73$ m). The temperature rise on the foil strip increased only 2.8 percent for the low turbulence case as compared to 1.4 percent for the high turbulence case. Thus, the intermediate columns of G^{-1} were determined by linear interpolation of the results measured at the first and fifteenth positions. Experimental low and high-turbulence G^{-1} arrays were calculated in this manner. Figure 9 shows the off diagonal terms for $j>3$ plotted on an expanded scale to emphasize the decay of the thermal wake far downstream of the heated element. The temperature rise decays approximately 30 percent faster in the high turbulence case indicating that the thermal energy from the heated element was mixed outward more rapidly. This rapid decay of the thermal wake means that the upstream thermal boundary condition has a smaller region of influence for high freestream turbulence. The large increases in heat transfer coefficient observed in high turbulence experiments on constant temperature or constant heat flux surfaces are due mostly to the fact that the downstream wall is not ''shielded'' as effectively by the thermal wake of the upstream surface. The measured G^{-1} can be used to predict the temperature-rise for any arbitrarily specified distribution of heat flux. Figure 10 shows a comparison between the experimental DGF prediction and STAN7 predictions for the case of a constant heat flux boundary condition with an unheated starting length of 1.37 m. The experimental DGF prediction agrees with the STAN7 prediction within the uncertainty interval over the first half of the heat transfer surface then falls slightly below further downstream. Recall that the baseline experimental data also fell slightly below STAN7 predictions.

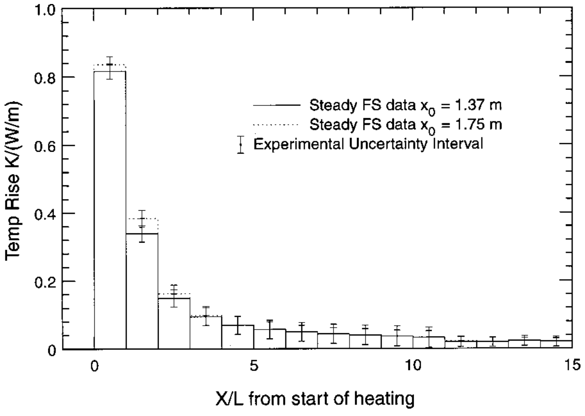

Fig. 8 Comparison of low-turb temp profiles with heated strip at first and last streamwise locations

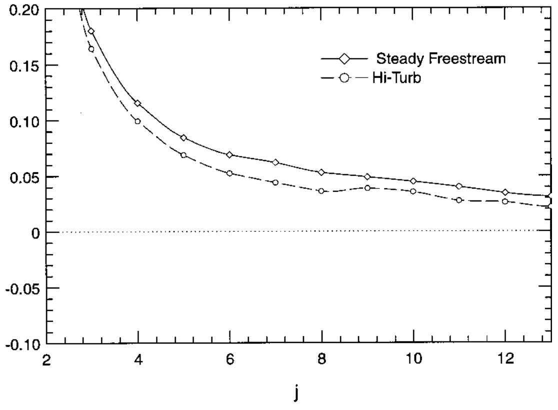

Fig. 9 First column of G^{*-1} normalized by $g_{1,1}$

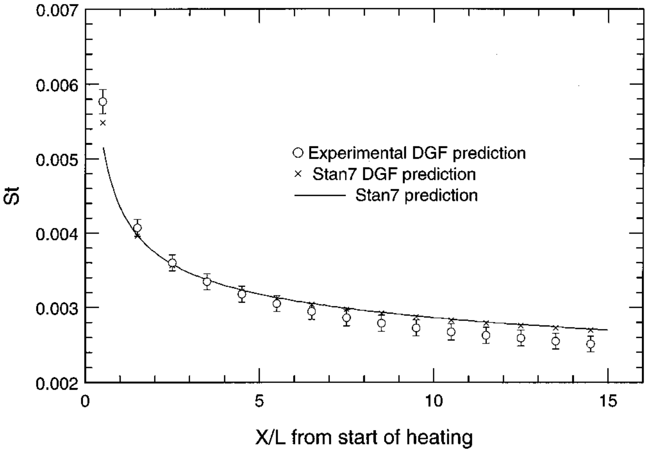

Fig. 10 Unheated starting length followed by a uniform heat flux boundary condition: STAN7 and experimental discrete Green's function predictions

Predicting Temperature With the One-Dimensional DGF

The matrix G was computed from G^{-1}, and then used to predict heat transfer for several specified temperature distributions. Figure 11 shows the comparison between STAN7 and the experi-

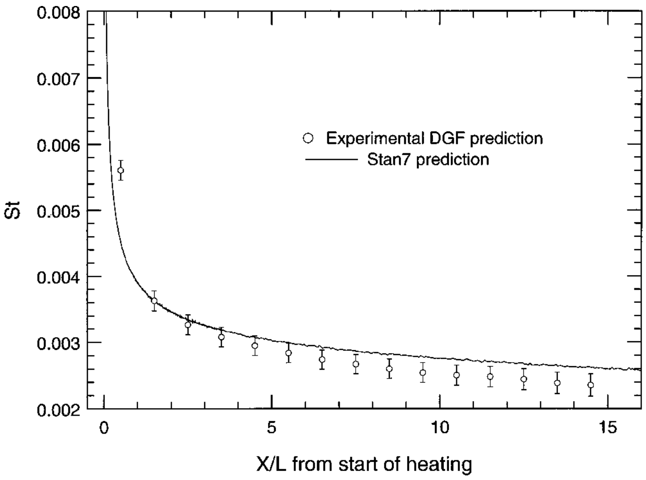

Fig. 11 Unheated starting length followed by a uniform temperature boundary condition

mental DGF prediction for the case of an unheated starting length followed by a uniform temperature boundary condition. Agreement between the different predictions followed the same trends as for the uniform heat flux case. The uncertainty intervals for the unheated starting length prediction made using G were approximately 50 percent larger at the downstream locations than those for the prediction made using G^{-1}. This is a result of the associated uncertainties being amplified by the matrix inversion.

Figure 12 shows a comparison for an unheated starting length followed by a sinusoidal temperature distribution. DGF and STAN7 predictions are compared against the experimental data of Hacker and Eaton. The current experimental DGF predictions have been scaled to match the experimental conditions of Hacker and Eaton. No uncertainty interval was given for their data and it is likely that the uncertainty was relatively large. In view of this, the agreement between the experimental DGF prediction and the data was relatively good, 17 percent at the peak value of heat flux.

The solid line in the plot represents a STAN7 prediction for the exact experimental situation of Hacker and Eaton, where a continuous temperature distribution was used. Agreement between the STAN7 prediction and the experimental DGF prediction was within the uncertainty interval except at the minimum heat flux where the relatively small absolute magnitude of the heat flux resulted in differences which were large on a percentage basis. Also plotted is the predicted heat flux based on the standard unheated-starting-length correlation from Reynolds [3]. This correlation was developed for the case of an unheated starting length followed by a uniform temperature boundary condition. It is included here to illustrate how errors can arise in heat flux prediction when heat transfer correlations developed for uniform boundary conditions are applied in situations where the boundary condition is non-uniform. The correlation compared to the STAN7 prediction underestimated the maximum heat flux by 26 percent while the experimental DGF prediction had only a 4 percent deviation. The correlation also failed to predict the negative heat transfer rate which occurs at the temperature minimum.

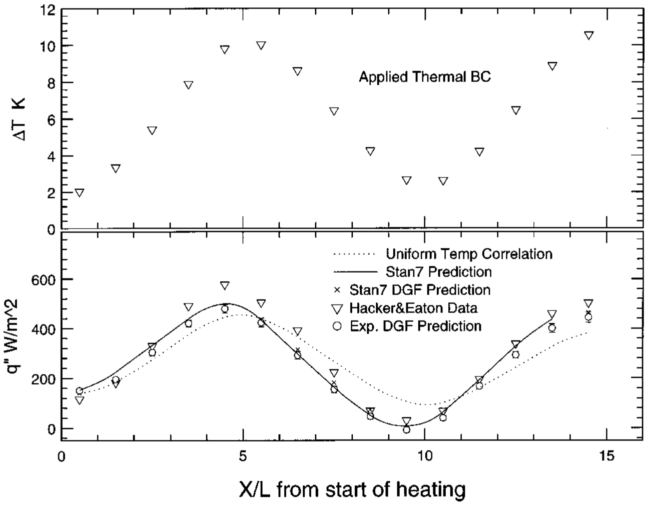

Fig. 12 Heat flux response to an unheated starting length followed by a sinusoidal temperature distribution

Conclusions

The preceding results show that the one-dimensional DGF approach is a practical and effective means for predicting heat transfer in two-dimensional flows. A simple experiment yielded results that were used to predict heat transfer within an uncertainty interval of approximately 10 percent. The DGF predictions showed good agreement with experimental data and the STAN7 boundary layer code.

The DGF array was determined in terms of G^{-1} by measuring temperature profiles with the short heated strip located at the first and last streamwise locations and filling out the entire array by interpolation. This approach worked well for a boundary layer flow with an unheated starting length. However, in situations where the flowfield changes more drastically over the streamwise extent of the surface, such as in the case of a separated flow, it would be necessary to make measurements at more streamwise locations. This would require additional time for experiments but would not cause any additional complexity.

This investigation also provided insight into the effects of high-turbulence on boundary layer heat transfer. It was found that high-turbulence had a more pronounced effect on the thermal wake of the heated strip than on the strip averaged heat transfer. This indicates that in real-world flows, where freestream turbulence is often an important factor, this simplified approximate approach to the DGF may be viable.

Nomenclature

G = discrete Green's function matrix
G^{-1} = inverse discrete Green's function matrix
G_{15}^{-1} = inverse Green's function measured with 15 elements
G_{sf} = Green's function calculated by inversion of G_{15}^{-1}
g_{ij} = element of discrete Green's function matrix
h = heat transfer coefficient
h_{ad} = adiabatic heat transfer coefficient
k = thermal conductivity
ℓ, L = streamwise length of Green's function element
$\dot{q}_i$ = heat transfer out of element i
Re = Reynolds number
St = Stanton number
T_{ij} = temperature of element in finite difference scheme
T_∞ = freestream temperature
x = streamwise coordinate
x_0 = position of start of heating
δ_Θ = enthalpy thickness
ΔT = vector of element temperatures
ΔT_j = temperature of element j

References

[1] Rubesin, M. W., 1951, ''The Effect of an Arbitrary Surface Temperature Variation on the Convective Heat Transfer in an Incompressible Turbulent Boundary Layer,'' NACA TN 2345.

[2] Sellars, J. R., Tribus, M., and Klein, S. J., 1956, ''Heat Transfer to Laminar Flow in a Round Tube or Flat Conduit—the Graetz Problem Extended,'' Trans. ASME, **78**, pp. 441–448.

[3] Reynolds, W. C., Kays, W. M., and Kline, S. J., 1958, ''Heat Transfer in the Turbulent Incompressible Boundary Layer: II—Step Wall Temperature Distribution,'' NASA Memo 12-2-58W, Washington.

[4] Arvizu, D. E., and Moffat, R. J., 1981, ''Experimental Heat Transfer From an Array of Heated Cubical Elements on an Adiabatic Channel Wall,'' Thermosciences Division Report HMT-33, Mechanical Engineering Department, Stanford University, Stanford, CA.

[5] Anderson, A., and Moffat, R. J., 1990, ''Convective Heat Transfer From Arrays of Modules With Non-Uniform Heating: Experiments and Models,'' Thermosciences Division Report HMT-43, Mechanical Engineering Department, Stanford University, Stanford, CA.

[6] Vick, B., Beale, J. H., and Frankel, J. I., 1987, ''Integral Equation Solution for Internal Flow Subjected to a Variable Heat Transfer Coefficient,'' ASME J. Heat Transfer, **109**, No. 4, pp. 856–860.

[7] Ramanathan, S., and Ortega, A., 1996, ''A Uniform Flow Effective Diffusivity Approach for Conjugate Forced Convection From a Discrete Rectangular Source on a Thin Conducting Plate,'' Proceedings of 5th ITHERM Conference, Orlando, FL.

[8] Hacker, J., and Eaton, J. K., 1995, ''Heat Transfer Measurements in a Backward Facing Step Flow With Arbitrary Wall Temperature Variation,'' Thermosciences Division Report MD-71, Mechanical Engineering Department, Stanford University, Stanford, CA.

[9] Hacker, J. M., and Eaton, J. K., 1997, ''Measurements of Heat Transfer in a Separated and Reattaching Flow With Spatially Varying Thermal Boundary Conditions,'' Int. J. Heat Fluid Flow, **18**, No. 1, pp. 131–141.

[10] Kays, W. M., and Crawford, M. E., 1980, *Convective Heat and Mass Transfer*, 2nd ed., McGraw Hill, New York.

[11] Ames, F. A., and Moffat, R. J., 1990, ''Heat Transfer in Turbulent Flow,'' presented at AIAA/ASME Thermophysics and Heat Transfer Conference, Seattle, USA, ASME HTD, **138**, pp. 11–17.

[12] Farina, D. J., Hacker, J., Moffat, R. J., and Eaton, J. K., 1994, ''Illuminant Invariant Calibration of Thermochromic Liquid Crystals,'' Exp. Therm. Fluid Sci., **9**, No. 1, pp. 1–12.

Numerical Study of Three-Dimensional Oscillatory Natural Convection at Low Prandtl Number in Rectangular Enclosures

Shunichi Wakitani
e-mail: wakitani@cit.sangitan.ac.jp
Department of Mechanical Engineering,
College of Industrial Technology,
1-27-1 Nishikoya, Amagasaki 661-0047, Japan

Numerical investigations are presented for three-dimensional natural convection at low Prandtl numbers (Pr) from 0 to 0.027 in rectangular enclosures with differentially heated vertical walls. Computations are carried out for the enclosures with aspect ratios (length/height) 2 and 4, and width ratios (width/height) ranging from 0.5 to 4.2. Dependence of the onset of oscillation on the Prandtl number, the aspect ratio, and the width ratio is investigated. Furthermore, oscillatory, three-dimensional flow structure is clarified. The structure is characterized by some longitudinal vortices (rolls) as well as cellular pattern. [DOI: 10.1115/1.1336508]

Keywords: Crystal Growth, Enclosure Flows, Heat Transfer, Instability, Liquid Metals, Natural Convection, Three-Dimensional

Introduction

Since experiments of Hurle et al. [1], the problem in natural convection in low Prandtl number (Pr) fluids has attracted many investigators, because of growing interest in the transport phenomena in crystal growth processes ([2]). In the processes from a liquid phase, convective flow in the crystal melt affects the homogeneity and purity of crystals. It is well known that under certain condition, convective oscillations appear in such low Prandtl number fluids as the crystal melt. The oscillations frequently cause undesirable structure of a growing crystal called as striations. Hurle et al. [1] observed thermal oscillations in a differentially heated boat of liquid gallium experimentally. Hart [3] analyzed the stability of shallow flows (Hadley circulations) for an infinitely long layer of low Prandtl number fluids. In actual crystal growth processes, aspect ratios $Ar(=\text{length/height})$ are finite, so the oscillatory characteristics are different from those of their stability analyses.

Winters [4] carried out two-dimensional calculations for $\text{Pr}=0$ in an enclosure with finite *Ar*. Since then, extensive two-dimensional numerical studies were performed as a benchmark problem at GAMM Workshop [5] for low Prandtl number. Their studies were mainly focused on an enclosure with $Ar=4$, and fluids of $\text{Pr}=0$ and 0.015. Several two-dimensional calculations have still been tried for low Prandtl number fluids in enclosures with rigid horizontal boundaries, or cavities with rigid lower boundary and stress-free upper boundary (for example, [6–10]). Most of their two-dimensional numerical results show that the flow evolves from unicellular to multicellular steady flow, and to oscillatory convection as the Grashof number is increased. In crystal growth processes or experiments, the width ratio Wr $(=\text{width/height})$ as well as *Ar* are finite. Therefore, these two-dimensional, numerical results may not represent the correct flow configurations and instabilities. In fact, two-dimensional calculations could not predict the unicellular flow observed in experiments ([11]).

Viskanta et al. [12] performed three-dimensional steady calculations for $\text{Pr}=0.02$ in rectangular enclosures with $Ar=1$ and $Wr=1$, and with a few combinations of *Ar* and *Wr*. Their numerical results were preliminary because of using coarse finite-difference meshes. They measured several temperature distributions of liquid gallium in the enclosures experimentally. They show that for low Pr fluids three-dimensional effects develop not only near the walls but also in the core of the enclosure, and multiple longitudinal flows exist. However, they used the parameter range, Grashof number $\text{Gr}>10^7$, in which oscillatory convections have already developed ([13]).

A small number of three-dimensional, time-dependent simulations have been performed for low Pr fluids. Afrid and Zebib [14] have obtained numerical results for a zero Pr fluid in an enclosure with $Ar=4$, and $Wr=1$ or 2. For both a rigid upper boundary and a stress-free upper boundary they found the critical Grashof number Gr_c, at which the onset of oscillation occurs, and the frequency of oscillation. They also found that the steady flow was a unicellular structure, unlike the multicellular flow predicted by two-dimensional simulations. However, three-dimensional structure of oscillatory convection is not clarified for low but finite Pr fluids.

In this paper, we perform three-dimensional, time-dependent numerical simulation of natural convection in enclosures with rigid boundaries. For $Ar=2$ and 4 we investigate the dependence of the onset of oscillation and the flow structure on *Wr* and Pr in details, and compare the results with available experimental results. Then, the unsteady heat transfer characteristics in low Pr fluids are clarified. This paper is the first of a series of papers on such practical applications as heat transfer control for low Pr fluids related to crystal growth.

Numerical Calculations

Governing Equations. Consider three-dimensional natural convection of low Pr fluids in an enclosure of height *H*, length *L*, and width *W* (Fig. 1). The vertical walls at $x=0$ and *L* are maintained at uniform constant temperatures, T_h and $T_c(<T_h)$, respectively. The other sidewalls are adiabatic. We define the coordinate system as shown in Fig. 1. We consider the flow of a Newtonian

---

Contributed by the Heat Transfer Division for publication in the JOURNAL OF HEAT TRANSFER. Manuscript received by the Heat Transfer Division April 12, 2000; revision received, September 27, 2000. Associate Editor: F. Cheung.

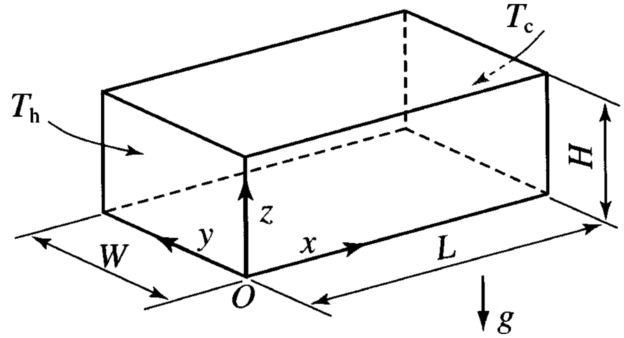

Fig. 1 Geometry of the enclosure and coordinate system

fluid and assume that the fluid satisfies the Boussinesq approximation. According to Ostrach's suggestion [15] for natural convection of $\mathrm{Gr}^{1/2} \geqslant 1$ and $\mathrm{Pr} \leqslant 1$, we introduce $V_r = (g\beta\Delta TH)^{1/2}$ as reference velocity, where Gr is the Grashof number, Pr the Prandtl number, g the acceleration due to gravity, β the coefficient of thermal expansion, and ΔT the temperature difference $(=T_h - T_c)$.

The governing equations are the continuity equation, Navier-Stokes equations, and energy equation. These equations can be put into dimensionless forms by scaling length with the height H, velocity with V_r, pressure with ρV_r^2, temperature with ΔT, and time with $H/V_r = \mathrm{Gr}^{-1/2} H^2/\nu$, where ρ is density, and ν is kinematic viscosity. The dimensionless temperature is defined as $T = (T^* - T_r)/\Delta T$ with $T_r = (T_h + T_c)/2$, where T^* is fluid temperature.

The governing equations can be written in the following dimensionless forms:

$$\nabla \cdot \mathbf{v} = 0, \tag{1}$$

$$\frac{\partial \mathbf{v}}{\partial t} + (\mathbf{v} \cdot \nabla)\mathbf{v} = -\nabla p + T\mathbf{k} + \frac{1}{\mathrm{Gr}^{1/2}} \nabla^2 \mathbf{v}, \tag{2}$$

$$\frac{\partial T}{\partial t} + (\mathbf{v} \cdot \nabla) T = \frac{1}{\mathrm{Pr}\,\mathrm{Gr}^{1/2}} \nabla^2 T, \tag{3}$$

where t is the time, $\mathbf{v} = (u, v, w)$ are the velocity components in the (x,y,z) directions, p is the deviation from the hydrostatic pressure, ∇ is the gradient operator, and $\mathbf{k}$ is a unit vector along the $+z$-axis.

The boundary conditions are

$$\mathbf{v} = 0 \quad \text{at all boundaries}, \tag{4}$$

$$T = 0.5 \quad \text{at} \quad x = 0 \quad \text{and} \quad T = -0.5 \quad \text{at} \quad x = Ar, \tag{5}$$

$$\partial T/\partial y = 0 \quad \text{at} \quad y = 0, Wr, \tag{6}$$

$$\partial T/\partial z = 0 \quad \text{at} \quad z = 0,1. \tag{7}$$

As the initial condition, a motionless and isothermal state is taken

$$\mathbf{v} = T = p = 0 \quad (0 < x < Ar, 0 < y < Wr, 0 < z < 1) \quad \text{at} \quad t = 0. \tag{8}$$

Numerical Algorithm. The numerical technique used in the present study is same as previous papers ([16,17]) based on the finite difference method of Kawamura and Kuwahara [18]. If velocity and temperature fields are known at a time step $n\Delta t$, then the Poisson equation for the pressure, which is derived by taking divergence of Eq. (2), is solved by using the SOR iterative scheme, subject to the appropriate boundary conditions. The Poisson equation is

$$\nabla^2 p = -\nabla \cdot (\mathbf{v} \cdot \nabla)\mathbf{v} + \frac{\partial T}{\partial z} + R, \tag{9}$$

where

$$R = -\frac{\partial D}{\partial t} + \frac{1}{\mathrm{Gr}^{1/2}} \nabla^2 D, \quad D = \nabla \cdot \mathbf{v}. \tag{10}$$

In the same manner as the MAC method, a correction term R is retained to prevent the accumulation of numerical errors and is discretized as

$$R = -\frac{D^{n+1} - D^n}{\Delta t} + \frac{1}{\mathrm{Gr}^{1/2}} \nabla^2 D^{n+1} = \frac{D^n}{\Delta t}, \tag{11}$$

where D^{n+1} is set to zero to satisfy the equation of continuity (1) at each time step.

Then, using the pressure obtained in this manner, the velocity and temperature at the next time step $(n+1)\Delta t$ are computed from discretized ones of Eqs. (2) and (3). The Euler implicit scheme is used for time marching. The nonlinear terms in their equations are linearized and approximated by means of a third-order upwind scheme ([18]). Such a higher order upwind scheme for inertial terms may be required to simulate natural convection of low Pr fluids, even if the Grashof number is not large enough ([19]). The spatial derivatives in the remaining terms are expressed in terms of the second-order central-differences. These finite difference equations are solved by using the SOR method.

An orthogonal, nonuniform, and nonstaggered grid system is used. One-dimensional transformations, $x = x(\xi)$, $y = y(\eta)$, $z = z(\zeta)$, into the generalized coordinate system are introduced to concentrate the grid points near the wall. Equations (2), (3), and (9) have been solved by applying the above transformations. For example, the x-grid points have been determined as a function of the equally divided coordinate $\xi (0 \leqslant \xi \leqslant 1)$ as $x = 0.5Ar\{1 + \tanh a(2\xi - 1)/\tanh a\}$ with a stretching parameter a.

The effects of the grid size and the stretching parameters on the flow characteristics have been examined. According to Wr, the grid of $41 \times 25 \times 41$ to $41 \times 91 \times 41$ points is adopted for $Ar = 2$, and $101 \times 31 \times 41$ to $101 \times 91 \times 41$ points for $Ar = 4$. The stretching parameters, typically (1.4, 1.2, 1.4) in the (x,y,z) grid points, are used so that the finest grid size near the walls is about two times smaller than the one corresponding to a uniform grid. To minimize errors occurring from discretization of time derivative in the Euler scheme, the sufficiently small time increment Δt is re-

Table 1 Comparison of the average Nusselt numbers with those of other studies

Authors	Grid	$\overline{\mathrm{Nu}}$			
		$\mathrm{Ra}=10^4$	$\mathrm{Ra}=10^5$	$\mathrm{Ra}=10^6$	$\mathrm{Ra}=10^7$
Present study	41^3	2.068	4.378	8.742	—
	61^3	—	4.365	8.711	16.54
	81^3	—	4.359	8.694	16.52
Haldenwang and Labrosse [20]	—	—	—	8.61	16.12
Le Peutrec and Lauriat [21]	31^3	—	4.356	8.665	—
	41^3	—	—	8.657	16.40
Fusegi et al. [22]	62^3	2.100	4.361	8.770	—

quired. The time increment has been tested in the range 0.0005–0.002. In consideration of accuracy and computing cost, $\Delta t = 0.001$ is generally used in the present computations.

Accuracy Assessment. The computation based on the above algorithm was first tested for three-dimensional steady convection of air in a square enclosure ($Ar = Wr = 1$, $\mathrm{Pr} = 0.71$) at Rayleigh numbers $\mathrm{Ra}(=\mathrm{Pr}\,\mathrm{Gr}) = 10^5$, 10^6, and 10^7. The average Nusselt numbers $\overline{\mathrm{Nu}}$ were compared with the other results [20–22]. Local Nusselt number is given as

$$\mathrm{Nu} = -Ar \cdot \left.\frac{\partial T}{\partial x}\right|_{x=0} \quad \text{or} \quad -Ar \cdot \left.\frac{\partial T}{\partial x}\right|_{x=Ar} \tag{12}$$

on the hot wall or the cold wall, respectively. Therefore, the average Nusselt number was evaluated from

$$\overline{\mathrm{Nu}} = \frac{1}{Wr}\int_0^1\int_0^{Wr} \mathrm{Nu}\, dy\, dz \tag{13}$$

by numerical integration using Simpson's rule. The first-order approximation to $\partial T/\partial x$ was used at the boundary. Table 1 gives the average Nusselt numbers obtained from steady solutions for some grid points. The difference between the average Nusselt numbers on the hot and the cold wall could not be found. Our results as well as those of ([21]) show the results from stretching parameters, which obtain a reasonable compromise between accuracy and computing cost for each grid. The maximum difference from the result of ([20]) calculated using a spectrum method is 2.5 percent at $\mathrm{Ra} = 10^7$. The present results are in good agreement with those of other authors obtained from finite difference method.

Results and Discussion

Onset of Oscillation. All computations have been conducted by starting with a fluid at rest. Generally, onset of oscillations appears suddenly when Gr is slightly increased from steady flow near the critical state. The value of Gr is taken as a critical one, at which the amplitude of oscillation in dimensionless velocity (u, v, or w) is larger than 0.01 in approximately steady oscillation. The amplitude of temperature oscillation is usually smaller than that of velocity. To check some values of Gr_c, we have also conducted several computations by starting with steady solutions. The results show no differences among them.

Figures 2(*a*) and (*b*) show the dependence of critical Grashof numbers Gr_c on the Prandtl numbers Pr for $Ar = 2$ and 4, respectively. In the case $Ar = 2$, the values of Gr_c for $Wr = 0.5$ and 1 slightly decrease as Pr is increased from zero to 0.005, and those for $Wr = 1$ and 2 largely increase as Pr exceeds about 0.01 and 0.018, respectively. Similarly, as shown in Fig. 2(*b*), in the case $Ar = 4$, Gr_c for $Wr = 1$ largely increases as Pr exceeds about 0.008. In the case $Ar = 4$, we can compare the results for $\mathrm{Pr} = 0$ with those of Afrid and Zebib [14]. Table 2 gives the critical Grashof number and the nondimensional frequency f of oscillations for $Wr = 1$ and 2. The Grashof number and the frequency used by ([14]) are multiplied by Ar and $\mathrm{Gr}^{-1/2}$ to fit with our notation, respectively. For $Ar = 4$ and $Wr = 2$, our results agree with those of ([14]), but for $Ar = 4$ and $Wr = 1$ they do not agree. This discrepancy will be discussed later. The experimental results for $\mathrm{Pr} = 0.026$ ([23,24]) are plotted in Fig. 2(*b*). The experimental results roughly agree with the numerical results.

Figure 3 shows the dependence of Gr_c on width ratios *Wr* for $Ar = 2$ and 4 in cases $\mathrm{Pr} = 0.015$ and 0.025. Some experimental results of Kamotani and Sahraui [13] are plotted in Fig. 3. They conducted experiments using rectangular enclosures filled with mercury of $\mathrm{Pr} = 0.02$. The numerical results are in good agreement with their experimental results. In general, as *Wr* is increased, Gr_c decreases. However, every numerical result shows an existence of a short range, in which values of Gr_c increase and decrease abruptly along with increasing *Wr*. It may be expected that transition of flow structure occurs in the vicinity of such a range of *Wr*.

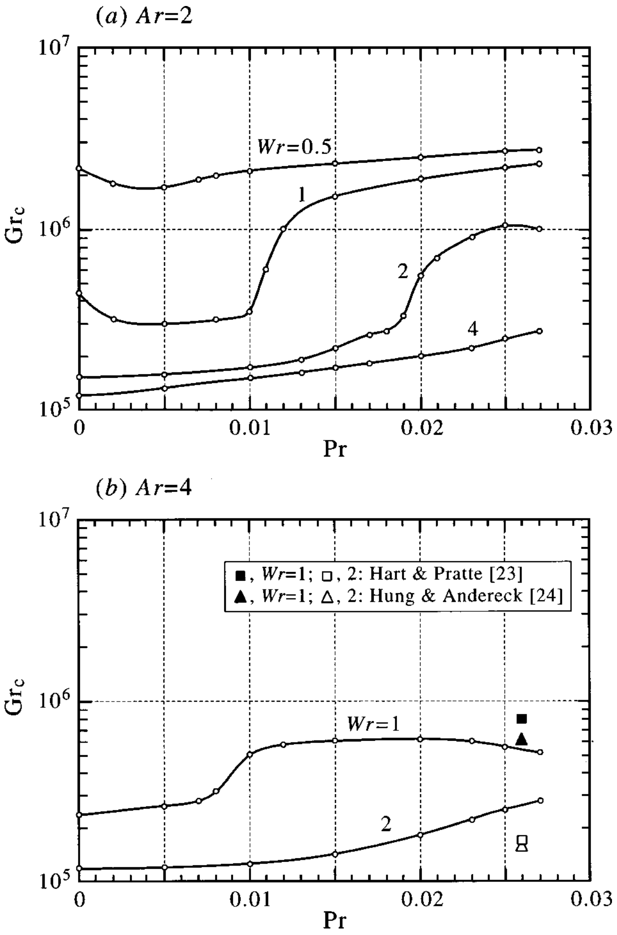

Fig. 2 Critical Grashof number as a function of Prandtl number for (*a*) $Ar = 2$, and (*b*) $Ar = 4$

Structure of Oscillatory Flow. Figure 4 shows unsteady velocity vectors and instantaneous streamlines at Gr_c in the case $\mathrm{Pr} = 0$ and $Ar = 4$. Those for $Wr = 1$ and 2 at a dimensionless time $t = 300$ are displayed in Figs. 4(*a*) and (*b*), respectively. Though the instantaneous streamlines have no obvious physical meaning for three-dimensional flows, they are effective to understand flow state.

The upper in either Fig. 4(*a*) or (*b*) corresponds to the result in the *y*-*z* plane on $x = Ar/2$, and the lower in the *x*-*z* plane on $y = Wr/2$. The arrow with figures outside an enclosure shows reference velocity scale. In general, u and w-velocities are an order of magnitude larger than v-velocity as shown in Figs. 4 and 5. Therefore, the convective structures are roughly unicellular for both $Wr = 1$ and 2, unlike the multicellular flow predicted by two-dimensional studies. These results agree with the steady solutions obtained by Afrid and Zebib [14]. However, they assumed that the flow was symmetric with respect to $y = Wr/2$, and they calculated the half region of the enclosures using second-order central difference scheme for spatial derivatives. The oscillatory flow at Gr_c for $Ar = 4$ and $Wr = 2$ is symmetric, but the one for $Ar = 4$ and $Wr = 1$ is asymmetric with respect to $y = Wr/2$ as shown in Fig. 4. For $Ar = 4$ and $Wr = 1$, the flow structure is characterized by longitudinal vortices (rolls). To demonstrate this point, for $Ar = 4$ and $Wr = 1$, we carried out a few calculations by assuming flow symmetry with respect to $y = Wr/2$ and using a grid $(101 \times 16 \times 41)$. The result ($\mathrm{Gr}_c = 4.8 \times 10^5$, $f = 0.051$) roughly agrees with that of

Table 2 Comparison of the critical Grashof numbers and the frequency of oscillation for Pr=0 with those of Afrid and Zebib [14]

Authors	$Ar=4$, $Wr=1$			$Ar=4$, $Wr=2$		
	Grid	Gr_c	f	Grid	Gr_c	f
Present study	101×31×41	2.35×10^5	0.060	101×51×41	1.18×10^5	0.102
Afrid and Zebib [14]	62×17×32	5.0×10^5	0.055	42×22×32	1.2×10^5	0.106

([14]) as shown in Table 2. Thus, the disagreement in Gr_c for $Wr=1$ may be attributed to this asymmetry. In the case Pr=0, the convective structures for $Ar=2$ are also unicellular except in the vicinities of the corner, $(x,z)=(0,0)$ and $(Ar,1)$, where weak cells appear.

Figure 5 shows velocity vectors and streamlines at several dimensionless times t for $Ar=4$, $Wr=1.5$, $\mathrm{Pr}=0.025$, and $\mathrm{Gr}=5\times10^5$. The value of Gr is slightly higher than Gr_c. At $t=200$ and 300, the convection is a two-cell structure with four rolls but a unicellular flow at $t=400$. The arrangement of rolls is symmetric with respect to $y=Wr/2$ at $t=200$, but asymmetric at $t=300$. At $t=400$, existence of rolls becomes obscure. In the case $Ar=4$, our calculations show that oscillatory flows at Gr slightly higher than Gr_c are two-cell structures for $Wr\leqslant1.4$, but are unicellular for $Wr\geqslant1.6$ at any time. These results are different from those for Pr=0. In the case $Ar=2$, such a two-cell structure could be observed for $\mathrm{Pr}=0.025$ in the range $Wr\leqslant1$. However, the structure is limited to a narrow region around the center of width $(y\approx Wr/2)$. In the case $\mathrm{Pr}=0.015$, convective structures are unicellular for any Wr except in the vicinities of the corner.

Figure 6 shows the time evolutions of the u-velocity and temperature at a point $(x=0.3174,\ y=0.2668,\ z=0.5)$ under the same condition as Fig. 5. As t exceeds 100, small oscillation clearly appears in velocity, but then at $t>300$ it changes into oscillation with double period and larger amplitude. This occurrence corresponds to the change in flow structure of convection. The abrupt change in Gr_c with Wr as shown in Fig. 3 may be attributed to such a change. Time sequence of these oscillatory patterns at $t>400$ is shown in Fig. 7 over roughly half a period. This figure demonstrates that two rolls exist and their senses of rotation reverse in half a period.

Figure 8 shows velocity vectors and instantaneous streamlines in the y-z plane on $x=Ar/2$ at $t=400$ for $Ar=2$, $\mathrm{Pr}=0.025$. Figures 8(*a*)–(*c*) correspond to those for $Wr=2.3$, 2.4, and 2.5, respectively. The value of Gr is slightly higher than each critical value. Obvious four rolls appear in Fig. 8(*a*) and three rolls in Fig. 8(*b*), but no rolls appear in Fig. 8(*c*). For $Wr>2.5$, such obvious rolls have not been found except in the neighborhood of corners of an enclosure. As mentioned above, in the case $Ar=2$, flows for $Wr>1$ are unicellular. Therefore, for $Ar=2$, abrupt changes in Gr_c with Wr may be attributed to behaviors of rolls.

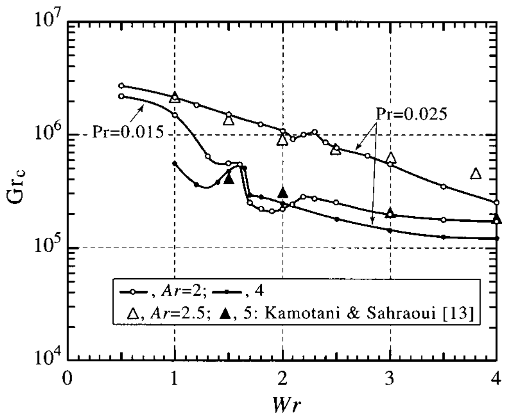

Fig. 3 Critical Grashof number as a function of width ratio *Wr* for Pr=0.015 and 0.025

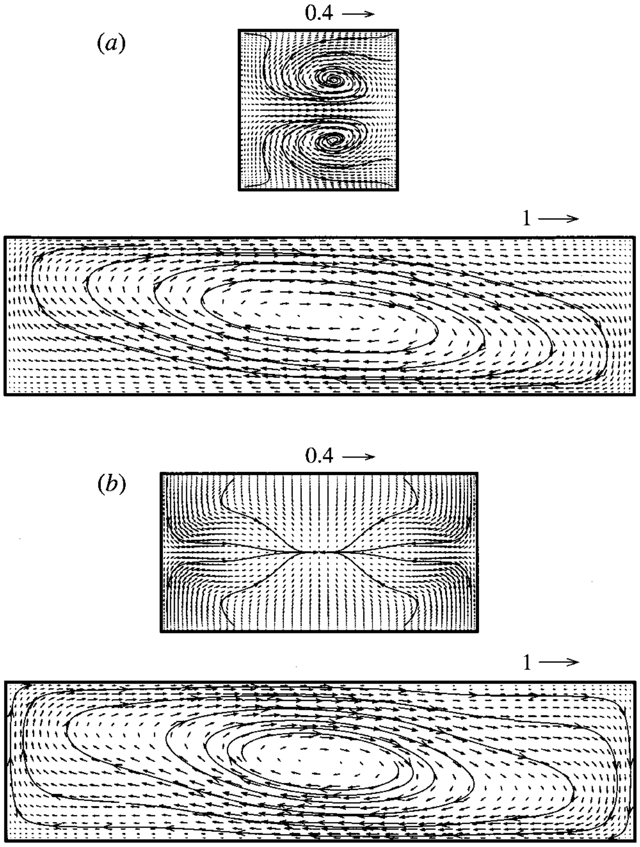

Fig. 4 Velocity vectors and instantaneous streamlines at critical Grashof number for Pr=0 in enclosures with (*a*) $Ar=4$, $Wr=1$, and (*b*) $Ar=4$, $Wr=2$ at $t=300$. The upper is those at $x=2$ in the *y-z* plane, and the lower is at $y=Wr/2$ in the *x-z* plane.

Heat Transfer. It is important in crystal growth processes to understand the effect of oscillatory convection on heat transfer rate. Figure 9 shows an example of local Nusselt numbers Nu on the cold wall for Pr=0.025. A steady profile for $Ar=2$, $Wr=1$, and $\mathrm{Gr}=2\times10^6$ at $t=300$ is displayed in Fig. 9(*a*). The value of Gr is lower than the critical value. It is noted that three peaks appear in the profile. On the other hand, for $Ar=4$, $Wr=2$, and $\mathrm{Gr}=3\times10^5$, the Nusselt numbers are oscillatory as shown in Fig. 9(*b*). Only a peak appears in their profiles (Fig. 9(*a*)), and its position fluctuates in the y-direction, periodically. The phase difference in position of the peak in Nu is about 180 deg between the hot and the cold wall.

Figure 10 shows the average Nusselt numbers $\overline{\mathrm{Nu}}$ as a function of Gr for Pr=0.015 and 0.025. Figures 10(*a*) and (*b*) correspond to time-averaged and root-mean-squared (rms) values of $\overline{\mathrm{Nu}}$, respectively. In the region that Gr exceeds Gr_c, their values are evaluated after approximately steady oscillations in $\overline{\mathrm{Nu}}$ have

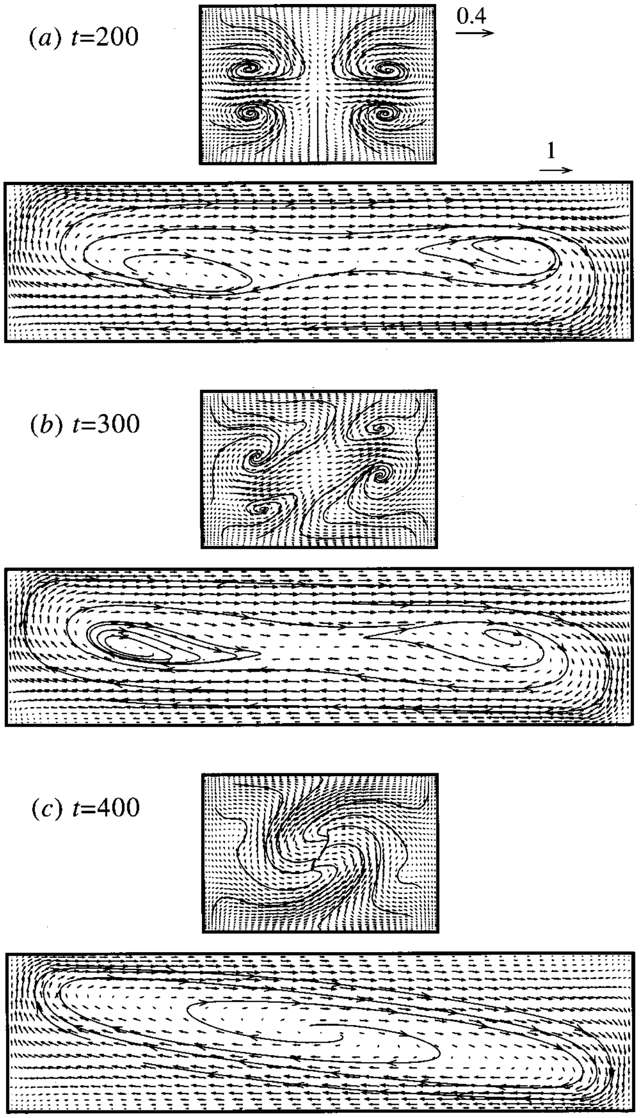

Fig. 5 Velocity vectors and instantaneous streamlines at $Gr=5\times10^5$ for $Pr=0.025$ in an enclosure with $Ar=4$, $Wr=1.5$ at (*a*) $t=200$, (*b*) 300, and (*c*) 400. The upper is those at $x=2$ in the *y-z* plane, and the lower is at $y=Wr/2$ in the *x-z* plane.

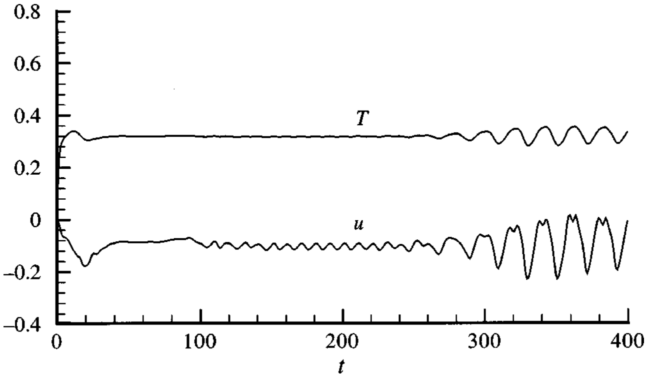

Fig. 6 Time evolutions of the *u*-velocity and temperature at a point $(x,y,z)=(0.3174,0.2668,0.5)$ at $Gr=5\times10^5$ for $Pr=0.025$ in an enclosure with $Ar=4$, $Wr=1.5$

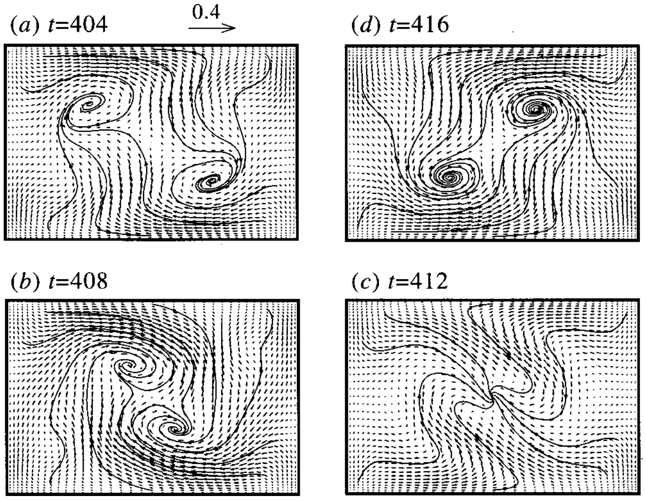

Fig. 7 Time sequence of velocity vectors and instantaneous streamlines at $Gr=5\times10^5$ for $Pr=0.025$ in an enclosure with $Ar=4$, $Wr=1.5$

reached. The results for $Ar=2$ show that the average Nusselt numbers for $Pr=0.025$ are about 30 percent higher than those for $Pr=0.015$ at $Gr\geqslant3\times10^5$ (Fig. 10(*a*)). The ratio of the rms value of $\overline{Nu}$ to the time-averaged value reaches about 3.6 percent at $Gr=2\times10^6$ for $Ar=4$ and $Wr=2$ (Fig. 10(*b*)). There, amplitude of $\overline{Nu}$ is about 5 percent of the time-averaged value. The result for $Pr=0.025$ with $Ar=2$ and $Wr=1$ show that amplitude of oscillations takes the large peak value in a narrow region around

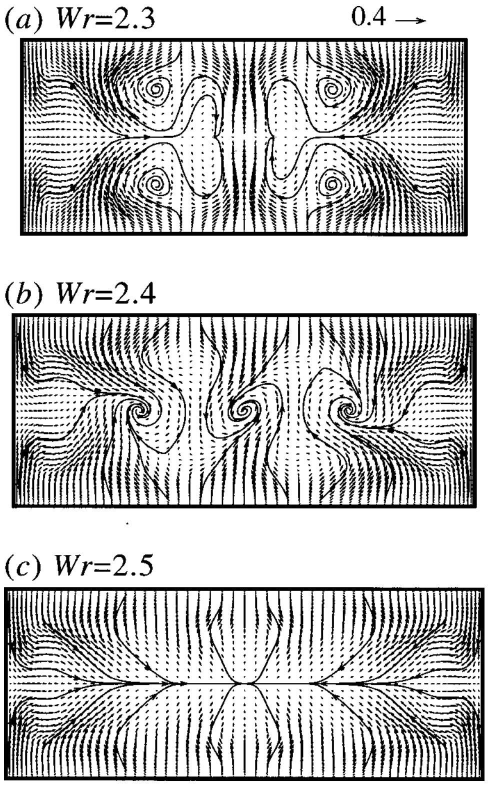

Fig. 8 Velocity vectors and instantaneous streamlines in the *y-z* plane on $x=1$ at $t=400$ for $Ar=2$, $Pr=0.025$. (*a*) $Wr=2.3$; (*b*) 2.4; (*c*) 2.5.

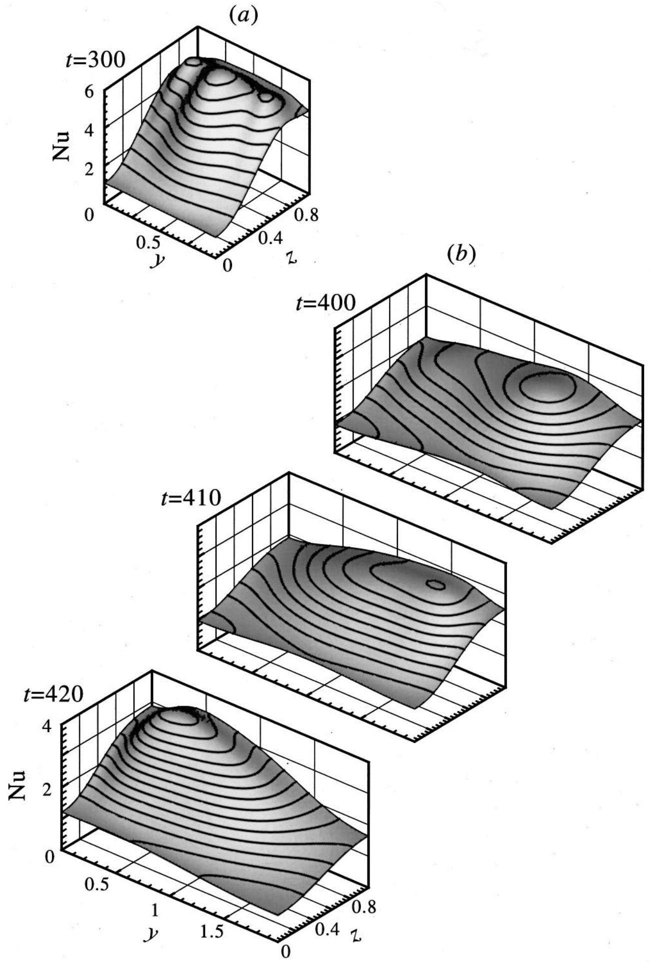

Fig. 9 Local Nusselt number on the cold wall for Pr=0.025 at some times in enclosures with (*a*) *Ar*=2, *Wr*=1, and (*b*) *Ar*=4, *Wr*=2

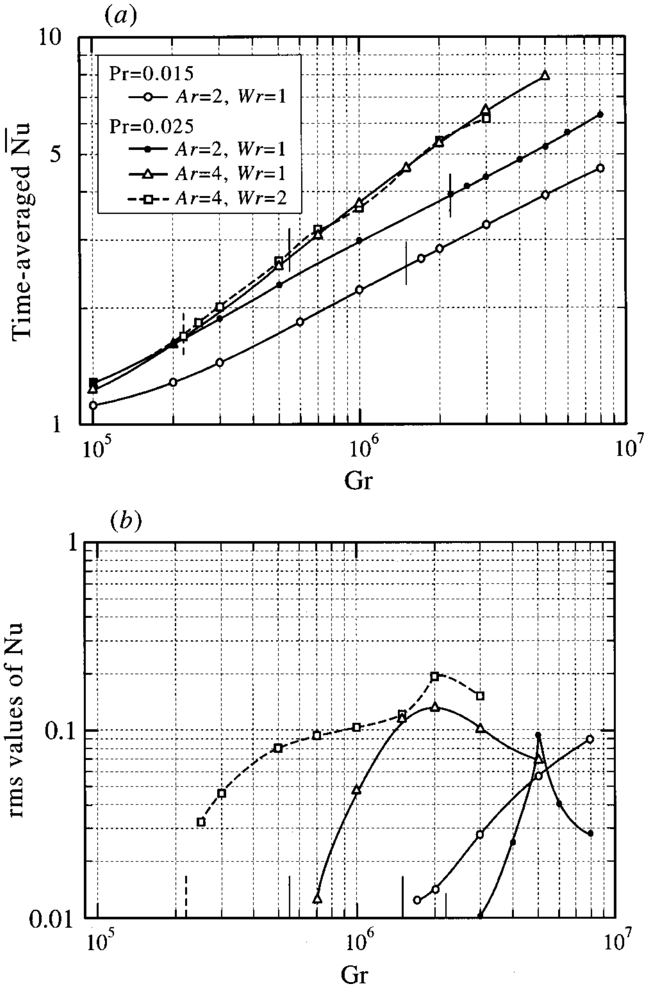

Fig. 10 Average Nusselt number on the cold wall as a function of Grashof number: (*a*) time-averaged value; (*b*) rms value. Each vertical segment indicates the critical Grashof number.

$\mathrm{Gr}=5\times10^6$. A variation in *Wr* has little effect on the average Nusselt number. The average Nusselt number is sensitive to Gr for $Ar=4$ than $Ar=2$.

Summary

In this paper, three-dimensional, time-dependent numerical simulation has been performed on natural convection in rectangular enclosures filled with low Prandtl number (Pr) fluids. Calculations are carried out for the enclosures with aspect ratios (*Ar*) 2 and 4, and width ratios (*Wr*) ranging from 0.5 to 4.2.

In cases $(Ar,Wr)=(2,1)$, (2,2) and (4,1), the critical Grashof number (Gr_c) at which the onset of oscillation occurs largely depends on Pr. The numerical results for Gr_c agree with available experimental results. The flow structure is characterized by cellular pattern and weak longitudinal vortices (rolls). As *Wr* is increased, Gr_c decreases except in a short range of *Wr*. In such a range an abrupt change in Gr_c occurs. This is attributed to such a change of flow structure as transition from two-cell to unicellular pattern, or to variation in the arrangement of rolls. In cases Pr=0 and 0.015, the convective structures at Gr_c are unicellular in general. In the case Pr=0.025, however, oscillatory two-cell patterns are observed in the range $Wr\leqslant 1$ for $Ar=2$, or $Wr\leqslant 1.4$ for $Ar=4$. The flow structures are unicellular for other range of *Wr*.

The oscillatory convection has significant effect on heat transfer rate. The average Nusselt number that is space-averaged is oscillatory. For $Ar=4$, oscillations make an about 10 percent difference among the average Nusselt numbers.

Acknowledgment

This work is partially supported by Grant-in-Aid for Scientific Research No. 11650238 from Japan Society for the Promotion of Science.

Nomenclature

Ar = aspect ratio$=L/H$
H = height of enclosure
L = length of enclosure
$\overline{\mathrm{Nu}}$ = average Nusselt number
Gr = Grashof number$=g\beta H^3\Delta T/\nu^2$
T_c = temperature at cold wall
T_h = temperature at hot wall
W = width of enclosure
Wr = width ratio$=W/H$
β = volumetric expansion coefficient
ΔT = temperature difference$=T_h-T_c$

References

[1] Hurle, D. T. J., Jakeman, E., and Johnson, C. P., 1974, ''Convective Temperature Oscillations in Molten Gallium,'' J. Fluid Mech., **64**, pp. 565–576.
[2] Ostrach, S., 1983, ''Fluid Mechanics in Crystal Growth,'' ASME J. Fluids Eng., **105**, pp. 5–10.
[3] Hart, J. E., 1983, ''A Note on the Stability of Low Prandtl Number Hadley Circulatios,'' J. Fluid Mech., **132**, pp. 271–281.
[4] Winters, K. H., 1988, ''Oscillatory Convection in Liquid Metals in a Horizontal Temperature Gradient,'' Int. J. Numer. Methods Eng., **25**, pp. 401–414.

[5] Roux, B., ed., 1990, *GAMM Workshop: Numerical Simulation of Oscillatory Convection in Low-Pr-Fluids*, Notes on Numerical Fluid Mechanics, **27**, Vieweg.

[6] Ben Hadid, H., and Roux, B., 1992, ''Buoyancy- and Thermocapillary-Driven Flows in Differentially Heated Cavities for Low-Prandtl-Number Fluids,'' J. Fluid Mech., **235**, pp. 1–36.

[7] Okada, K., and Ozoe, H., 1993, ''The Effect of Aspect Ratio on the Critical Grashof Number for Oscillatory Natural Convection of Zero Prandtl Number Fluid: Numerical Approach,'' J. Cryst. Growth, **126**, pp. 330–334.

[8] Gelfgat, A. Y., and Tanasawa, I., 1994, ''Numerical Analysis of Oscillatory Instability of Buoyancy Convection with the Galerkin Spectral Method,'' Numer. Heat Transfer, Part A, **25**, pp. 627–648.

[9] Mundrane, M., and Zebib, A., 1994, ''Oscillatory Buoyant Thermocapillary Flow,'' Phys. Fluids, **6**, pp. 3294–3305.

[10] Braunsfurth, M. G., Skeldon, A. C., Juel, A., Mullin, T., and Rilley, D. S., 1997, ''Free Convection in Liquid Gallium,'' J. Fluid Mech., **342**, pp. 295–314.

[11] Hung, M. C., and Andereck, C. D., 1988, ''Transitions in Convection Driven by a Horizontal Temperature Gradient,'' Phys. Lett. A, **132**, pp. 253–258.

[12] Viskanta, R., Kim, G. M., and Gau, C., 1986, ''Three-Dimensional Convection Heat Transfer of a Liquid Metal in a Cavity,'' Int. J. Heat Mass Transf., **29**, pp. 475–485.

[13] Kamotani, Y., and Sahraoui, T., 1990, ''Oscillatory Natural Convection in Rectangular Enclosures Filled with Mercury,'' ASME J. Heat Transfer, **112**, pp. 253–255.

[14] Afrid, M., and Zebib, A., 1990, ''Oscillatory Three-Dimensional Convection in Rectangular Cavities and Enclosure,'' Phys. Fluids A, **2**, pp. 1318–1327.

[15] Ostrach, S., 1988, ''Natural Convection in Enclosures,'' ASME J. Heat Transfer, **110**, pp. 1175–1190.

[16] Wakitani, S., 1997, ''Development of Multicellular Solutions in Natural Convection in an Air-Filled Vertical Cavity,'' ASME J. Heat Transfer, **119**, pp. 97–101.

[17] Wakitani, S., 1998, ''Flow Patterns of Natural Convection in an Air-Filled Vertical Cavity,'' Phys. Fluids, **10**, pp. 1924–1928.

[18] Kawamura, T., and Kuwahara, K., 1984, ''Computations of High Reynolds Number Flow around a Circular Cylinder with Surface Roughness,'' *AIAA Paper* No. 84-0340.

[19] Tagawa, T., and Ozoe, H., 1996, ''Effect of Prandtl Number and Computational Schemes on the Oscillatory Natural Convection in an Enclosure,'' Numer. Heat Transfer, Part A, **30**, pp. 271–282.

[20] Haldenwang, P., and Labrosse. G., 1986, ''2-D and 3-D Spectral Chebyshev Solutions for Free Convection at High Rayleigh Numbers,'' *Sixth International Symposium on Finite Element Methods in Flow Problems*, pp. 261–266.

[21] Le Peutrec, Y., and Lauriat, G., 1990, ''Effects of the Heat Transfer at the Side Walls on Natural Convection in Cavities,'' ASME J. Heat Transfer **112**, pp. 370–378.

[22] Fusegi, T., Hyun, J. M., Kuwahara, K., and Farouk, B., 1991, ''A Numerical Study of Three-Dimensional Natural Convection in a Differentially Heated Cubical Enclosure,'' Int. J. Heat Mass Transf., **34**, pp. 1543–1557.

[23] Hart, J. E., and Pratte, J. M., 1990, ''A Laboratory Study of Oscillations in Differentially Heated Layers of Mercury,'' *GAMM Workshop: Numerical Simulation of Oscillatory Convection in Low-Pr-Fluids*, B. Roux, ed., Notes on Numerical Fluid Mechanics, **27**, pp. 329–337, Vieweg.

[24] Hung, M. C., and Andereck, C. D., 1990, ''Subharmonic Transitions in Convection in a Moderately Shallow Cavity,'' *GAMM Workshop: Numerical Simulation of Oscillatory Convection in Low-Pr-Fluids*, B. Roux, ed., Notes on Numerical Fluid Mechanics, **27**, pp. 338–343, Vieweg.

Visualization and Prediction of Natural Convection of Water Near Its Density Maximum in a Tall Rectangular Enclosure at High Rayleigh Numbers

C. J. Ho
Professor
Fellow ASME
E-mail: cjho@mail.ncku.edu.tw

F. J. Tu

Department of Mechanical Engineering,
National Cheng Kung University,
Tainan, Taiwan 70101, ROC

An experimental and numerical investigation is presented concerning the natural convection of water near its maximum-density in a differentially heated rectangular enclosure at high Rayleigh numbers, in which an oscillatory convection regime may arise. The water in a tall enclosure of $A_y=8$ is initially at rest and at a uniform temperature below 4°C and then the temperature of the hot vertical wall is suddenly raised and kept at a uniform temperature above 4°C. The cold vertical wall is maintained at a constant uniform temperature equal to that of the initial temperature of the water. The top and bottom walls are insulated. Using thermally sensitive liquid crystal particles as tracers, flow and temperature fields of a temporally oscillatory convection was documented experimentally for $Ra_W=3.454\times10^5$ with the density inversion parameter $\theta_m=0.5$. The oscillatory convection features a cyclic sequence of onset at the lower quarter-height region, growth, and decay of the upward-drifting secondary vortices within counter-rotating bicellular flows in the enclosure. Two and three-dimensional numerical simulations corresponding to the visualization experiments are undertaken. Comparison of experimental with numerical results reveals that two-dimensional numerical simulation captures the main features of the observed convection flow. [DOI: 10.1115/1.1336511]

Keywords: Density Inversion, Enclosure Flows, Heat Transfer, Natural Convection, Unsteady

Introduction

The present study deals with the natural convection of water near its density maximum (cold water) in a vertical rectangular enclosure of high height/width aspect ratio as depicted in Fig. 1. Cold water is characterized by an anomalous density-temperature relationship, the so-called density inversion phenomenon, having its maximum density at about 4°C at sea-level atmospheric pressure. Natural convection of cold water commonly arises in the environment and in technology [1]. The natural convection of cold water is of fundamental interest, as well as having practical relevance in the study of numerous natural systems and in technical applications. Thus, a number of studies have been made of steady-state natural convection of cold water in vertical rectangular enclosures, representative works being given in Refs. [2–6]. However, there are relatively few previous papers [7–11] regarding transient natural convection of cold water in vertical rectangular enclosures.

Among the existing works concerning either steady state or transient natural convection of cold water in enclosures, only a few have considered Rayleigh numbers (Ra_H) above 10^6. Lankford and Bejan [12] studied steady state natural convection of cold water in a vertical rectangular enclosure of a 5.05 height/width ratio with Rayleigh numbers from $10^8\sim10^{11}$. A mixed thermal boundary condition of constant heat flux and isothermal temperature below 4°C was used for the thermally active walls of the enclosure. Ivey and Hamblin [13], on the other hand, presented an experimental study of natural convection in a differentially heated shallow rectangular enclosure with aspect ratios of 0.1 to 0.5, and Rayleigh numbers from 10^5 to 10^8. They demonstrated through dye-injection flow visualization that the interior sinking jet-like flow structure along the maximum density contour of cold water in the shallow enclosures was unstable for $\mathrm{Ra}_H>10^7$. This is similar to the findings reported by Lankford and Bejan [12] for a tall vertical enclosure. In a finite-element simulation, Nishimura et al. [14] attempted to predict the occurrence of unstable natural convection of cold water in a vertical rectangular enclosure of aspect ratio 1.25 at Rayleigh numbers of $10^5\sim10^8$. Their simulations, however, predicted stable buoyant flow and temperature fields, even at the high Rayleigh numbers in which unstable convection may be expected to arise. In a recent experimental study, Nishimura et al. [15] examined the effect of initial temperature on the inception of oscillatory natural convection of cold water in a vertical enclosure of aspect ratio 1.25. The vertical walls of the enclosure were maintained isothermal at 8°C and 0°C, respectively, while the others were insulated. With an initial water temperature at 4°C, an unstable buoyant flow in the enclosure was observed for $\mathrm{Ra}_H>9\times10^6$, featuring an oscillatory sinking jet-like flow structure. At initial temperatures other than 4°C, however, no oscillatory flow was detected experimentally. In their corresponding finite-element simulations, only partial agreement was found in comparison with the experimental results. More recently, motivated by the related problem of natural-convection-dominated melting of ice in a rectangular enclosure, the present authors presented a two-dimensional numerical study [16] concerning the inception of oscillatory natural convection of cold water in a vertical enclosure of high aspect ratio ($A_y=8$). Selection of a tall water-filled enclosure was intended to simulate the early stages of the ice-melting process in a rectangular enclosure,

---

Contributed by the Heat Transfer Division for publication in the JOURNAL OF HEAT TRANSFER. Manuscript received by the Heat Transfer Division December 9, 1999; revision received, July 20, 2000. Associate Editor: C. Beckermann.

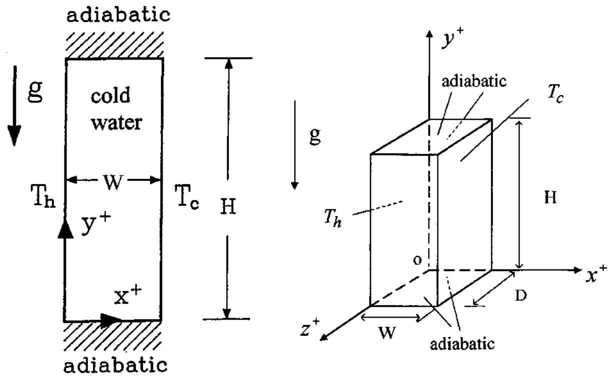

Fig. 1 Schematic diagram of the physical configuration and coordinate systems

during which water occupies a narrow vertical region. With incremental increase in the Rayleigh number, transition to a self-sustained oscillatory convection regime through a *Hopf* bifurcation was predicted, featuring an oscillatory multicellular structure within counter-rotating bicellular flow regions. The maximum water density contour exhibited, accordingly, a traveling wave motion. The transitional instability into oscillatory convection was demonstrated to be buoyancy-driven.

The present study represents our continuing research efforts concerning natural convection of cold water in vertical enclosures. It focuses primarily on experimental documentation of buoyancy-driven flow and temperature fields at the high Rayleigh numbers in which oscillatory convection was predicted in our previous numerical study [16]. To this end, visualization experiments of both temperature and flow fields were conducted to unravel the transient development of buoyancy-driven convection in a cold-water-filled enclosure with a height/width ratio of eight. Supplemental to the experiments, corresponding two and three-dimensional numerical simulations were also undertaken for comparison.

Temperature and Flow Visualization Experiments

The experiments were performed in a rectangular test cell of the same height/width aspect ratio considered in our previous numerical study [16]. The inner dimensions of the test cell are 3 cm in width, 24 cm in height, and 7 cm in depth. The hot and cold vertical walls of the test cell were constructed of aluminum plates, within which a thermally regulated fluid (a mixture of water and ethanol) is circulated through milled channels. The thermally regulated fluid was supplied by constant-temperature bath. The horizontal (top and bottom) walls of the enclosure were constructed of acrylic plates. For optical observation of the flow and temperature fields, a double-pane window made of 5-mm-thick glass plates with a 1-cm gap between the panes was constructed for the front and rear walls of the test cell. The 1-cm gap was filled with nitrogen gas to prevent moisture condensation and to provide good thermal insulation for the test cell. The test cell was covered with 12-cm-thick Styrofoam insulation and housed inside a temperature-controlled cold chamber.

Surface temperature measurements at the hot and cold vertical walls were made by seven copper-constant thermocouples embedded in the aluminum plates. Surface temperature variations on the hot and cold walls were found to be less than 0.2°C both vertically and horizontally. In addition, a thermocouple placed in a stainless tube with an outer diameter of 1.5 mm was inserted from the ceiling of the test cell to monitor the temperature variation at the geometrically central point of the enclosure. The thermocouples were calibrated and the uncertainty in temperature was estimated as 0.1°C. In the temperature range encountered in this study, the uncertainty in estimating the temperature-difference across the enclosure (ΔT) is 7 percent. In the present work, the following density-temperature correlation proposed by Gebhart and Mollendorf [17] was employed for evaluating the density of the cold water

$$\rho=\rho_m(1-rsp|T-T_m|^b), \tag{1}$$

where $\rho_m=999.9720\ \mathrm{kg/m^3}$, $rsp=9.297173\times10^{-6}(^\circ\mathrm{C})^{-b}$, $b=1.894816$, and $T_m=4.029325^\circ\mathrm{C}$. The uncertainties in estimating the Rayleigh number, the Prandtl number, and the dimensionless time-period are 18 percent, 0.1 percent, and 5 percent, respectively.

Distilled water was used in all tests. All experiments were initiated from cold start; namely, water was initially at rest and at a uniform temperature equal to that of the cold wall of the enclosure ($T_i=T_c$). To this end, before the test run the hot and cold walls of the test cell were connected to two constant temperature baths setting at the initial temperature of the water T_i. The water within the test cell was then given sufficient time to reach thermal equilibrium with the temperature of thermally active walls. A test run was initiated by switching the connection of the left vertical (hot) wall of the enclosure to another constant temperature bath, which was already tuned to a selected temperature T_h higher than the initial temperature of the water.

Temporal variation of the water temperature in the test cell was made visible by using encapsulated thermochromic liquid crystal (TCL) particles (type BM/R3C2W/S-33, Hallcrest, Inc., USA) as the temperature tracer. The liquid crystal particles in water have a specific gravity of 1.028. For vivid visualization of the maximum-density temperature range of cold water, the TCL particles were selected to be visible over a temperature range of $3\sim5^\circ\mathrm{C}$. A concentration of 0.02 percent in weight of TCL particles was added into and premixed with the water in the test cell before each test run started. The TCL particles were illuminated, during the test runs, by a pair of fluorescent lamps located symmetrically in front of the test cell. A Nikon F-4 camera using a typical exposure time of 1 sec was used to record photographically the color patterns of temperature field in the test cell.

Flow visualization experiments were performed separately using another type of TCL particle (BM/R0C1W/S-33) as the flow tracer. The cross-sectional view of the transient buoyancy-driven flow structure in the test cell was visualized via a He-Ne laser light sheet and recorded photographically on black and white films with exposure times ranging from 20 to 60 sec.

Numerical Simulations

Numerical simulations were undertaken to predict the transient natural convection of cold water in the physical configuration of Fig. 1 under the cold-start conditions considered in the experiments. Initially, water inside the rectangular enclosure is at rest and at a uniform temperature of T_i. At time $t=0$ the left-hand vertical wall is instantaneously heated and thereafter maintained at a constant isothermal temperature T_h, while the right-hand vertical wall remains isothermal at the initial temperature ($T_c=T_i$). The remaining sidewalls of the enclosure are taken as adiabatic.

The physical properties of water, except for the density in the buoyancy force terms, are assumed constant. The governing equa-

Table 1 Summary of experimental conditions ($A_y=8$, $A_z=2.333$)

Test No.	$T_h(^\circ C)$	$T_c(^\circ C)$	θ_m	Ra_W	Ra_H
1	7	1	0.5	3.454×10^5	1.768×10^8
2	8	0	0.5	5.957×10^5	3.050×10^8
3	7	2	0.4	2.522×10^5	1.291×10^8
4	8.5	1	0.4	5.437×10^5	2.784×10^8

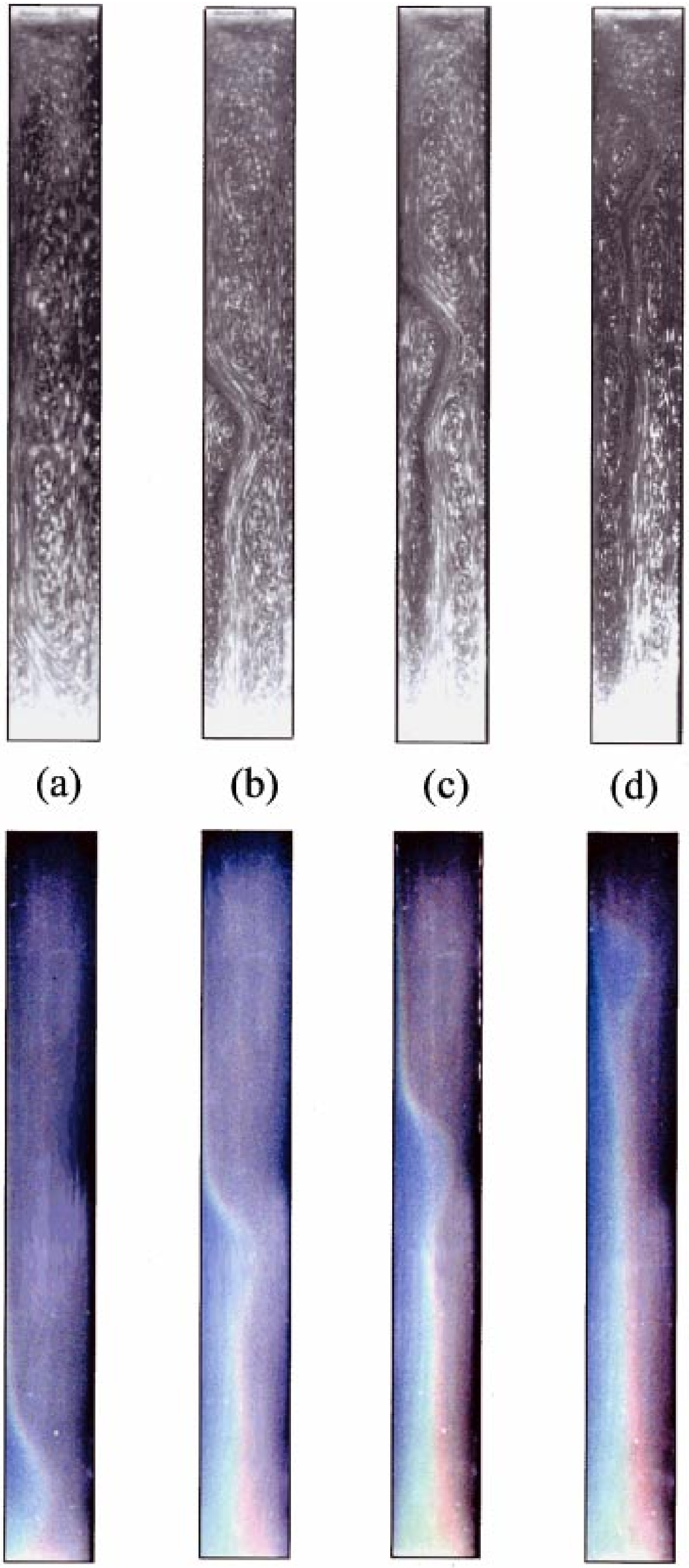

Fig. 2 Photographs of the transient evolution of the flow structre (upper) and temperature field (lower) at (*a*) $Fo=0.023$ ($t=2$ min and 30 sec), (*b*) $Fo=0.054$ ($t=6$ min), (*c*) $Fo=0.077$ ($t=8$ min and 30 sec), and (*d*) $Fo=0.127$ ($t=14$ min) for $\theta_m=0.5$, $Ra_W=3.454\times10^5$

tions for the two- and three-dimensional transient natural convection in the cold-water-filled enclosure are expressed by means of the stream-function-vorticity formulation and the pseudovorticity-velocity formulation [18], respectively. The mathematical formulation as well as the numerical methods adopted for the two-dimensional simulations follows essentially those detailed in our previous work [16]. For the three-dimensional simulations, the normalized governing equations in terms of the pseudovorticity vector $\tilde{\omega}$, velocity vector $\mathbf{V}$ and temperature θ can be expressed as follows:

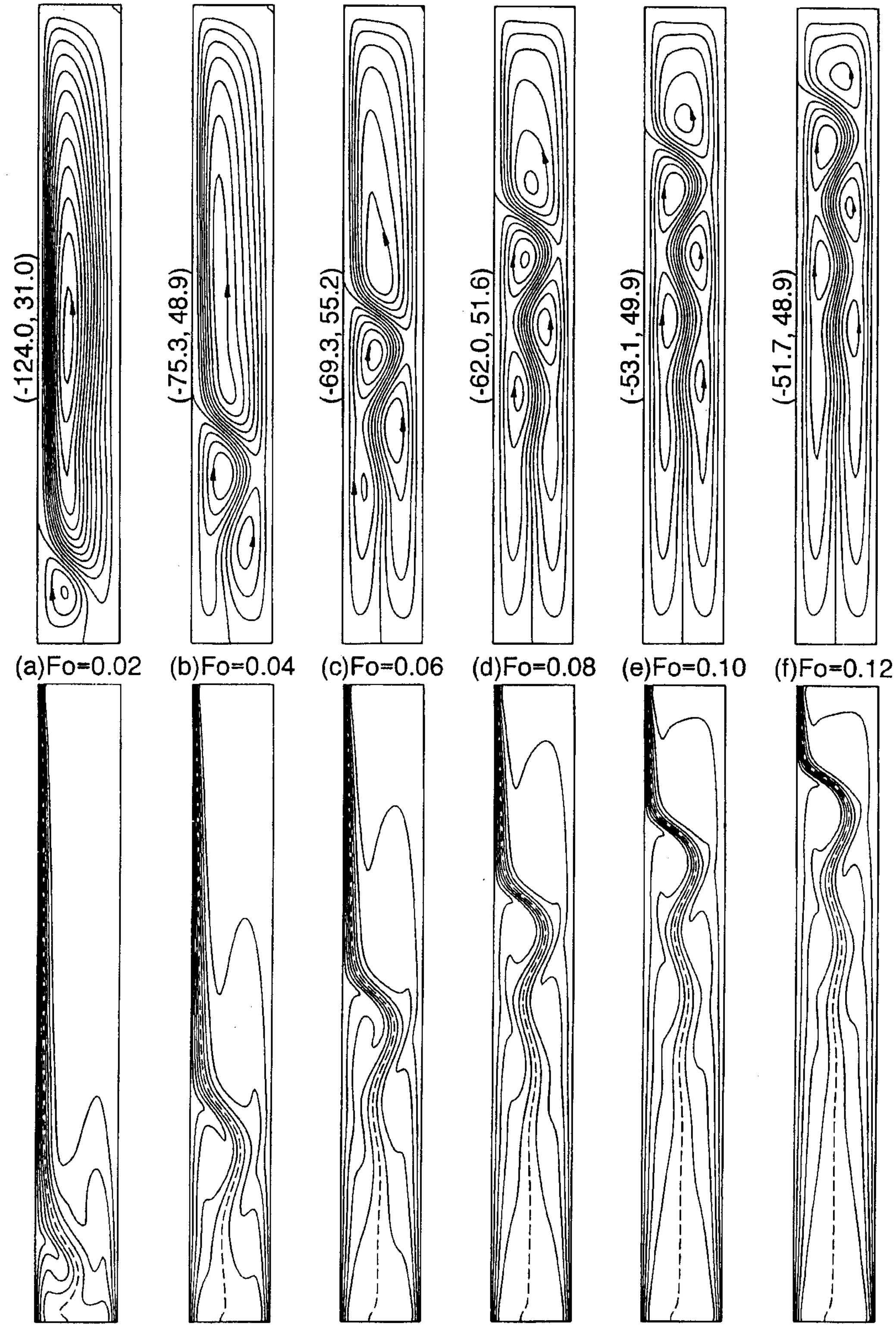

Fig. 3 Two-dimensional prediction of transient streamlines (upper) and isotherms (lower) in the cold-water-filled enclosure for $\theta_m = 0.5$, $\mathrm{Ra}_W = 3.454 \times 10^5$

$$\frac{\partial \mathbf{V}}{\partial Fo} + \nabla \times (\tilde{\omega} + \Pr \nabla \times \mathbf{V}) = \mathbf{0} \tag{2}$$

$$\nabla^2 \tilde{\omega} = \nabla \times [\mathbf{V} \times (\nabla \times \mathbf{V})] + \Pr\ \mathrm{Ra}_W \nabla \times (|\theta - \theta_m|^b \hat{\mathbf{e}}_g) \tag{3}$$

$$\frac{\partial \theta}{\partial Fo} + \mathbf{V} \cdot \nabla \theta = \nabla^2 \theta. \tag{4}$$

The initial and boundary conditions of the present simulation are

$$Fo = 0; \quad \mathbf{V} = \tilde{\omega} = \mathbf{0}, \theta = 0 \tag{5}$$

$Fo > 0$;

$$x = 0; \quad \mathbf{V} = \mathbf{0}, \theta = 1 \tag{6a}$$

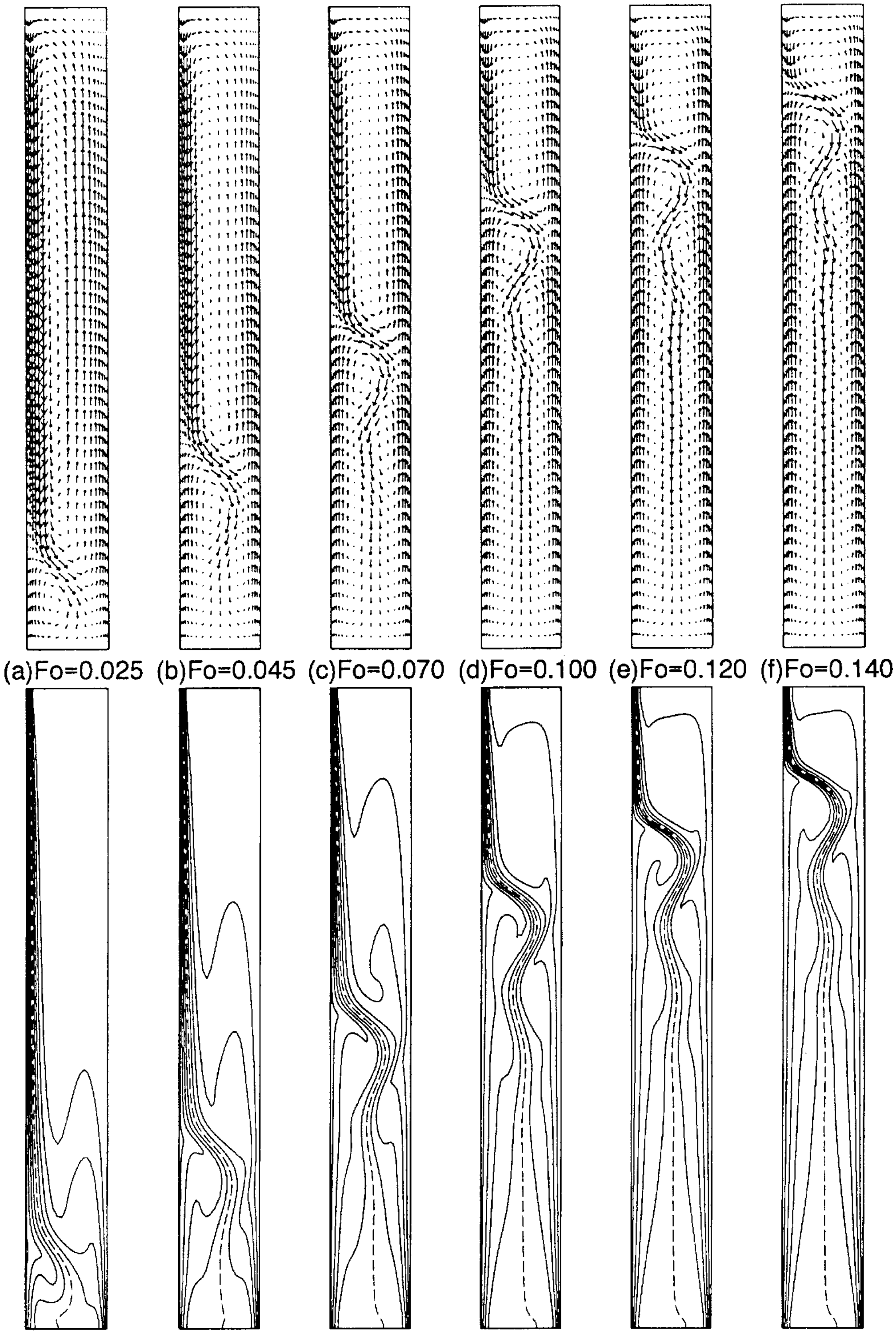

Fig. 4 Three-dimensional prediction of transient cross-sectional (*x-y* midplane) flow (upper) and temperature (lower) fields in the cold-water-filled enclosure for $\theta_m = 0.5$, $Ra_W = 3.454 \times 10^5$ with $A_z = 2$

$$x=1; \quad \mathbf{V}=\mathbf{0}, \theta=0 \tag{6b}$$

$$y=0 \text{ or } A_y; \quad \mathbf{V}=\mathbf{0}, \partial\theta/\partial y=0 \tag{6c}$$

$$z=0 \text{ or } A_z; \quad \mathbf{V}=\mathbf{0}, \partial\theta/\partial z=0 \tag{6d}$$

The boundary conditions for the pseudovorticity on the sidewalls of the enclosure, as shown in Ref. [18], can be evaluated explicitly from the wall vorticity.

The foregoing formulation reveals that the relevant dimensionless parameters for the three-dimensional natural convection in the cold-water-filled enclosure include: the Rayleigh number, Ra_W; the Prandtl number, Pr; the density inversion parameter, θ_m; the height/width ratio, A_y; and the depth/width ratio, A_z. In the present work, the height/width ratio of the enclosure, A_y, was fixed at eight. Due to the constraints on the available computing resources and times, the actual value of the depth/width ratio of the enclosure in the experiment ($A_z = 2.333$) was not considered in the numerical simulations. Instead, two values of the depth/width ratio, $A_z = 1$ and 2, were considered to reflect possible effects of the lateral (front and rear) vertical walls on transient convection in the enclosure. Furthermore, the two-dimensional simulations may be viewed as the three-dimensional simulations with $A_z = \infty$.

The above differential equations along with the initial/boundary conditions were solved by a finite difference method. The differential equations were discretized spatially using a second-order central difference approximation for the diffusion terms and the QUICK scheme [19] for the advection terms. A non-uniform grid in the x-direction was constructed for effectively capturing the steep gradients along the thermally active walls of the enclosure, while uniform grids were used in both y and z-directions. The time-dependent velocity and temperature Eqs. (2) and (4) were integrated in time using an explicit approximation with second-order accuracy.

The explicit simulation used in this study starts with solving Eqs. (2) and (4) for the velocity and temperature fields, respectively, based on the initial condition of stagnant flow and uniform temperature fields in the enclosure. A time step of 5×10^{-6} was found sufficiently small for the present simulations. At each time step, the discretized pseudovorticity Eq. (3) is calculated iteratively by a successive relaxation method until a relative convergence criterion of less than 5×10^{7} is met. The transient solution is considered asymptotically approaching the steady state condition if the relative convergence criteria of 10^{-7} and 5×10^{-7} are, respectively, satisfied for the solutions of temperature and velocity. The relative convergence criterion adopted is of the form:

$$\frac{|\phi^{m+1} - \phi^{m}|_{\max}}{|\phi^{m+1}|_{\max}} < \varepsilon_{\phi}, \tag{7}$$

where m denotes the iteration number or the time level of the field variable of interest ϕ.

Throughout the present simulations, double-precision arithmetic was incorporated to achieve high solution accuracy. Based on a grid-size variation study, a grid of $37 \times 201 \times 31 (x \times y \times z)$ was found sufficiently fine for the three-dimensional simulations. CPU times required for a three-dimensional calculation on an IBM SP2 workstation range from 290 to 400 h, depending on the Rayleigh number and the occurrence of the oscillatory convection.

The accuracy of the present three-dimensional code was validated against the reported solutions for steady state natural convection in an air-filled cubical enclosure [20,21]. The calculated results of isotherms and velocity distributions in the cubical enclosure for $\mathrm{Ra} = 10^4 - 10^6$ were found to agree well with those obtained in Refs. [20–21]. The maximum difference in the surface-averaged Nusselt number was less than one percent.

Results and Comparisons

The conditions for the various visualization experiments performed here are summarized in Table 1. Cold and hot vertical walls of the enclosure were maintained at temperatures, respectively, lower and higher than the maximum-density temperature of water T_m, leading to two values of the density inversion parameter, $\theta_m = 0.4$ and 0.5. The temperature difference across the cold-water-filled enclosure, $\Delta T (= T_h - T_c)$, was purposely selected to yield the Rayleigh numbers in which oscillatory convection was predicted to arise in our previous numerical study [16]. It should be noted that in Ref. [16] the calculations at the higher Rayleigh numbers were initiated from the numerical results of the lower Rayleigh numbers, instead of the initial cold-start condition considered here. For the four test conditions listed in Table 1, the temperature and flow visualization experiments were performed separately. Corresponding to these experimental conditions, two and three-dimensional numerical simulations were conducted for comparison.

Table 2 Summary of buoyancy-driven flow regimes in the cold-water enclosure

Parameters		Flow regimes			
θ_m	Ra_W	Experimental visualization	2-D simulation ($A_z = \infty$)	3-D simulation ($A_z = 2$)	3-D simulation ($A_z = 1$)
0.5	3.454×10^5	Periodic	Periodic	Steady	Steady
0.5	5.957×10^5	Steady	Steady	Steady	Steady
0.4	2.522×10^5	Steady	Steady	Steady	Steady
0.4	5.437×10^5	Steady	Periodic	Steady	Steady

Transient Convection Development. The transient evolution of the buoyancy-driven flow structure and temperature fields observed experimentally in the cold-water-filled enclosure is typified by the sequence of photographs shown in Fig. 2 for $\theta_m = 0.5$, $\mathrm{Ra}_W = 3.454 \times 10^5$. During the early stage, the buoyancy-driven flow in the enclosure is, as can be expected, dominated by a counterclockwise circulation flow. At $Fo = 0.023$ ($t = 2$ min and 30 sec) a secondary clockwise eddy confined roughly by the maximum density contour arises at the bottom left corner of the enclosure as shown in Fig. 2(*a*). As the isothermal heating continues at the hot wall, the sequence of photographs in Figs. 2(*b*)–(*d*) reveals that the clockwise circulation flow structure proceeds to strengthen and to grow with the vortex center moving upward, while the counter-clockwise circulation becomes gradually suppressed. Closer examination of Fig. 2 reveals a vortex-splitting phenomenon occurring within the counter-rotating double-circulation structure in the enclosure. Meanwhile, from the color patterns of the transient temperature field in Fig. 2, it is evident that the maximum density contour of water exhibits an upward traveling wave movement during its transverse penetration process into enclosure core.

For comparison, Figures 3 and 4 present, respectively, the transient development of the flow and temperature fields predicted by the corresponding two- and three-dimensional simulations to the condition of Fig. 2. In the contour plots of the isotherms, the maximum density contour of the water is denoted by a dashed line. The contour plots were drawn with an equal increment between the maximum and minimum values within the entire enclosure. Furthermore, the velocity vector plots were scaled with the maximum velocity in the cross-section of interest. Comparison of the predicted (Figs. 3 and 4) and observed (Fig. 2) results indicates that the predicted transient development of the buoyancy-driven flow and temperature fields in the enclosure by the two and three-dimensional simulations are in good agreement with the experimental visualization. In particular, the predicted traveling wave movement of the maximum density contour of water associated with the vortex-splitting process throughout the development of the clockwise circulation structure agrees well with the experimental observation shown in Fig. 2. Further scrutiny of the predicted flow patterns in Figs. 3 and 4 reveals that in comparison with the two-dimensional results, the transient development of the clockwise circulation structure in the three-dimensional simulation proceeds rather slowly. This may be due to the effects associated with the presence of lateral (front and rear) walls in the three-dimensional configuration. With a lower depth/width ratio of $A_z = 1$, the corresponding three-dimensional simulation (not shown here) reveals a similar transient development to that displayed in Fig. 4 for $A_z = 2$ but at a somewhat slower pace.

Convection Regimes. As summarized in Table 2, the transient flow and temperature fields were observed to approach a steady state for all the test conditions with the exception of $\theta_m = 0.5$ and $\mathrm{Ra}_W = 3.454 \times 10^5$, under which a self-sustained temporally oscillatory convection regime was detected. Figure 5 displays a timed sequence of visualization photographs of the flow and temperature fields taken over one period of the oscillatory

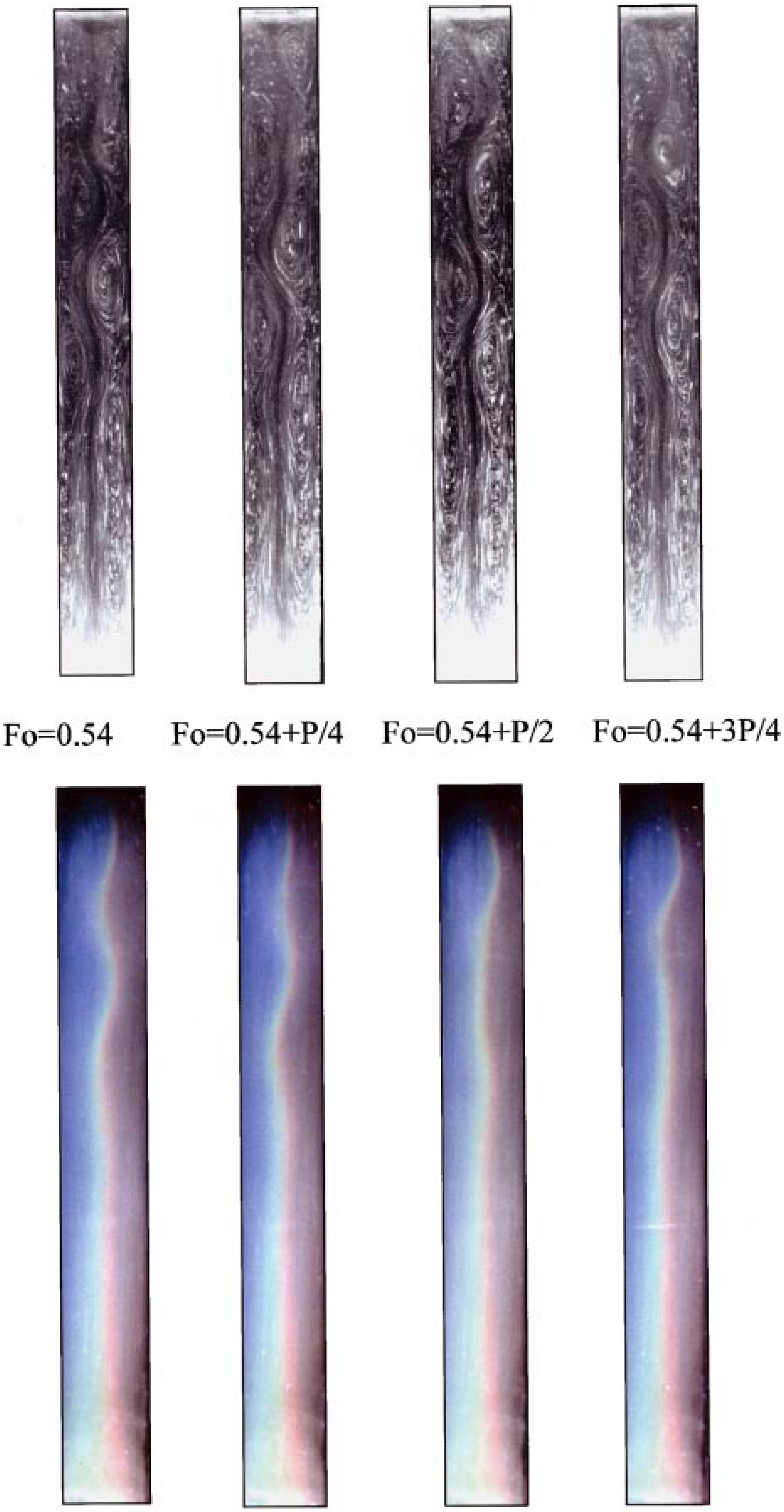

Fig. 5 Photographs of the flow structure (upper) and temperature field (lower) of the oscillatory convection in the cold-water-filled enclosure at $\theta_m = 0.5$, $\mathrm{Ra}_W = 3.454\times10^5$

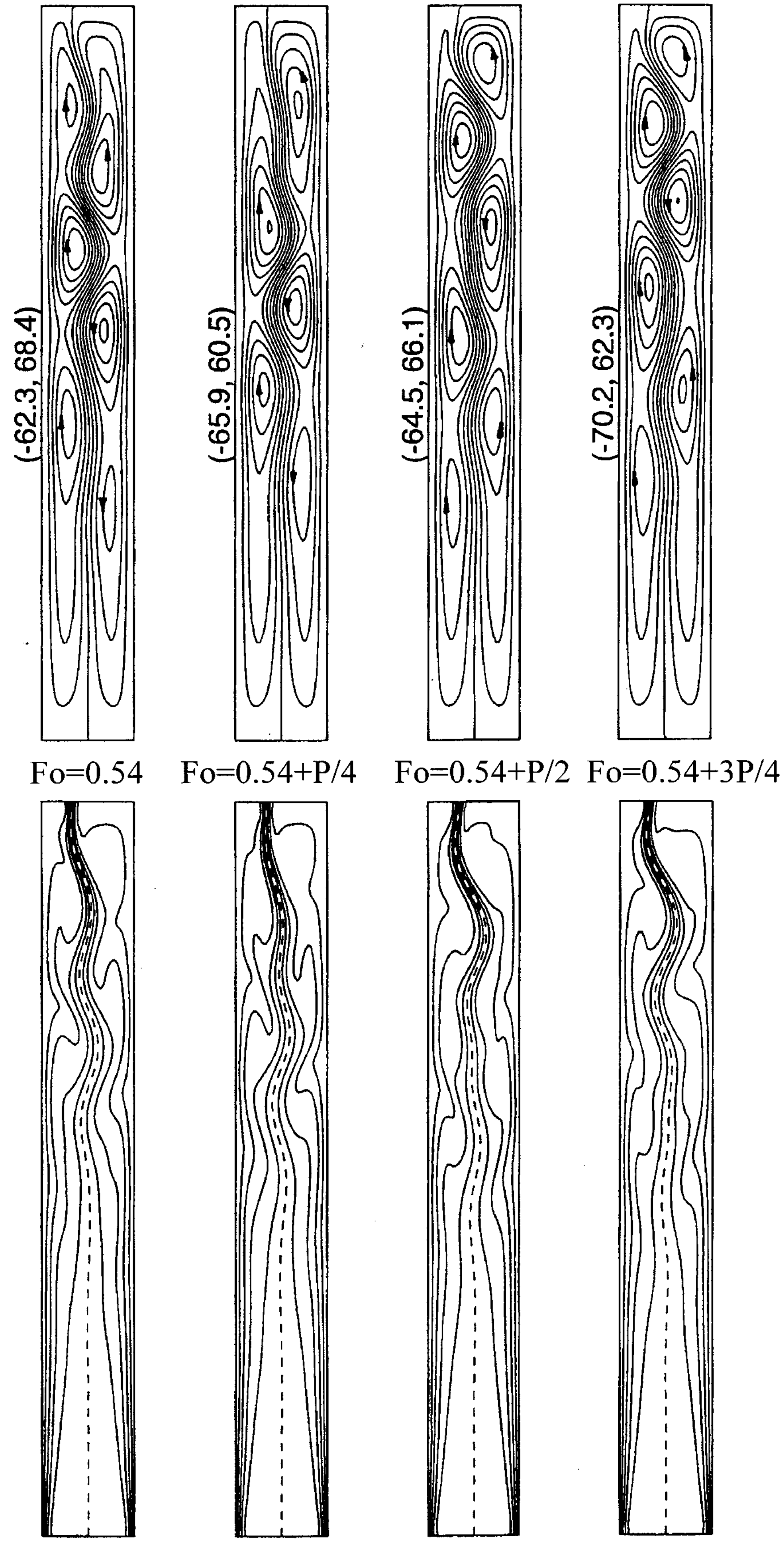

Fig. 6 **Predicted cyclic flow (upper) and temperature (lower) fields of the oscillatory convection in the cold-water-filled enclosure by the two-dimensional numerical simulation at $\theta_m=0.5$, $\mathrm{Ra}_W=3.454\times10^5$**

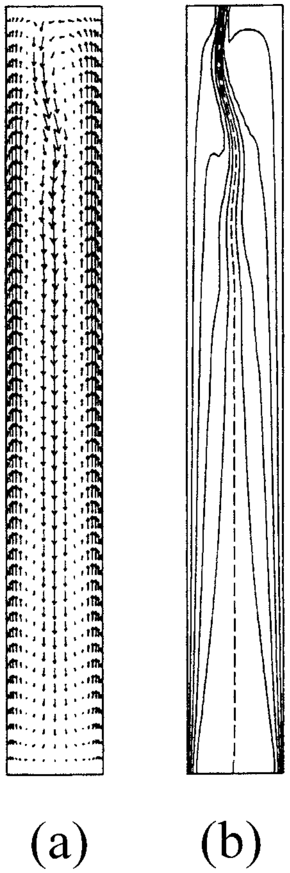

Fig. 7 Steady state cross-sectional (*x-y* midplane) (*a*) flow and (*b*) temperature fields predicted by the three-dimensional numerical simulation at $\theta_m=0.5$, $\mathrm{Ra}_W=3.454\times10^5$ with $A_z=2$

convection at $\theta_m=0.5$ and $\mathrm{Ra}_W=3.454\times10^5$. A cyclic sequence of onset at the lower-quarter-height region, growth, and then decay can be vividly observed for the upward drifting secondary vortices within the counter-rotating double circulation regions. Accordingly, as shown in the temperature-visualization photographs of Fig. 5, an upward-traveling wave movement of the maximum density contour through the core region of the enclosure can be discerned. The upward traveling wave motion of the maximum density contour was observed to sway at a time period of about 60 sec (or a dimensionless period of $P=0.0091$), which is greatly shorter than the oscillation periods observed by Nishimura et al. [15] for an enclosure of height/width aspect ratio 1.25.

Also included in Table 2 are the convection regimes predicted by the corresponding numerical simulations to the visualization experiments. As indicated in Table 2, contradictory results were obtained from the corresponding two and three-dimensional simulations to the case of $\theta_m=0.5$ and $\mathrm{Ra}_W=3.454\times10^5$. By the corresponding two-dimensional numerical simulation, a self-sustained oscillatory convection regime was indeed predicted to arise, as depicted by the cyclic sequence of streamlines and isotherms in Fig. 6. The predicted main features of the upward-drifting multicellular structure along with the wavy maximum density contour agree well with the experimental observations of Fig. 5. Moreover, the predicted period of the swaying motion of the maximum density contour is 59.3 sec, also in excellent agreement with the measured data. In contrast, the corresponding three-dimensional simulations for both values of A_z predicted an asymptotically steady-state convection regime. Figure 7 illustrates the steady-state cross-sectional velocity and temperature fields in the enclosure predicted by the three-dimensional simulation for $A_z=2$. A bicellular flow structure can be seen to prevail in the *x-y*

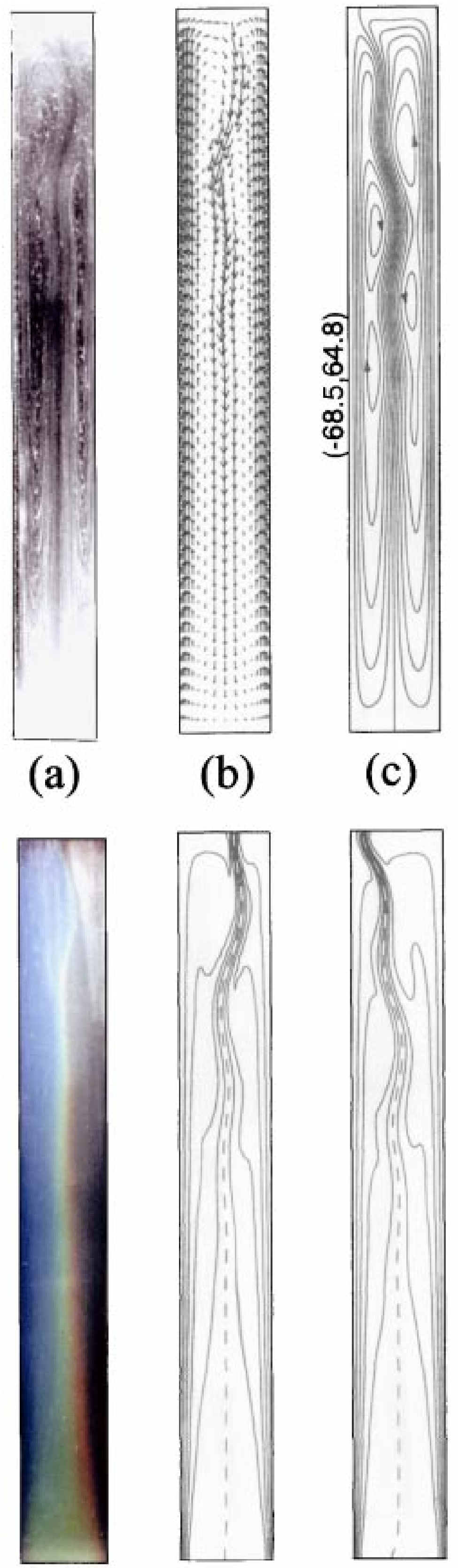

Fig. 8 Comparison of the steady state flow patterns (upper) and temperature fields (lower) among (*a*) visualization experiment, (*b*) three-dimensional ($A_z=2$), and (*c*) two-dimensional simulations at $\theta_m=0.5$, $\mathrm{Ra}_W=5.957\times10^5$

mid-plane of the enclosure, featuring a wavy jet-like maximum-density flow sinking from the mid-ceiling. The waviness of the sinking maximum-density flow gradually diminishes as it descends to the central core of the enclosure. The disparity between the two- and three-dimensional simulations may be attributed primarily to the viscous dissipation effect associated with the presence of the lateral (front and rear) vertical walls in the three-dimensional configuration [22].

With further increase of the Rayleigh number to $\mathrm{Ra}_W = 5.957 \times 10^5$ under $\theta_m = 0.5$, a reverse transition to steady-state convection regime was found both experimentally and numerically. Figure 8 compares experimental and numerical results of the steady state flow and temperature fields for $\mathrm{Ra}_W = 5.957 \times 10^5$ with $\theta_m = 0.5$. The experimental results agree closely with the predicted flow structure and temperature distribution from the three-dimensional simulation, featuring a bicellular flow structure demarcated by a descending maximum-density stream from a point of the ceiling closer to the cold wall. By contrast, the two-dimensional prediction shows a different bicellular flow structure such that the maximum-density stream emerges from a point of the ceiling very close to the hot wall. Such a disparity between the three and two-dimensional simulations further reflects the lateral wall effect of the enclosure on the buoyancy-driven convection of cold water.

Next, at $\theta_m = 0.4$, steady-state convection was found from both experiment and simulations at $\mathrm{Ra}_W = 2.522 \times 10^5$. Comparison of numerical and experimental results of flow and temperature fields, as illustrated in Fig. 9, reveals very good agreement between experiment and predictions from three or two-dimensional simulations. As indicated in the visualization photographs, a counter-rotating bicellular flow dominated by clockwise circulation prevails, with a sinking maximum density jet emanating from the upper part of the cold wall. The clockwise circulation in the top region stretches downward along the hot wall through a narrow region shaped like and referred to hereafter as a bottleneck region. Around the bottleneck region, waviness of the thermal boundary layer along the hot wall can be discerned. Further increase of the Rayleigh number at $\mathrm{Ra}_W = 5.437 \times 10^5$ under $\theta_m = 0.4$, both the visualization experiments and three-dimensional simulation produce steady-state convection flow and temperature fields (not shown) similar to those displayed in Fig. 9 for $\mathrm{Ra}_W = 2.522 \times 10^5$. By contrast, with the absence of the damping effect of the lateral vertical walls, the corresponding two-dimensional simulation at $\mathrm{Ra}_W = 5.437 \times 10^5$ yields a convection regime of self-sustained periodic oscillation, as illustrated in Fig. 10. This appears similar to what was predicted in the earlier study [16]. A cyclic sequence of splitting and merging of the upward-drifting secondary vortices evolves within the counter-rotating bicellular structure. A traveling wave motion of the maximum density jet-like flow arises as it turns through the bottleneck region into the enclosure core.

Additionally, the foregoing disparities among the experimental observations and numerical predictions may be associated with the assumption of constant properties in the mathematical model. In fact, the temperature difference imposed across the enclosure in the experiments has appreciable and differential effects on the thermophysical properties of water, particularly the viscosity.

Finally, in Table 3, comparison is made for the measured results of the steady-state or periodically-mean water temperature, $(T_{\mathrm{center}})_{ss}$ or $(T_{\mathrm{center}})_{\mathrm{mean}}$, at the central point of the enclosure, with the corresponding numerical predictions. It can be seen from the table that the measured and predicted values of the steady-state or periodically mean water temperature at the central point of the enclosure are in good agreement, within experimental uncertainty. Also included in Table 3 is the amplitude of temperature fluctuation, A_T, at the central point of the enclosure when the self-sustained oscillatory convection occurs. The measured fluctuation amplitude of 0.3°C for the case of $\mathrm{Ra}_W = 3.454 \times 10^5$ and $\theta_m = 0.5$ appears to be smaller by half of that predicted by the

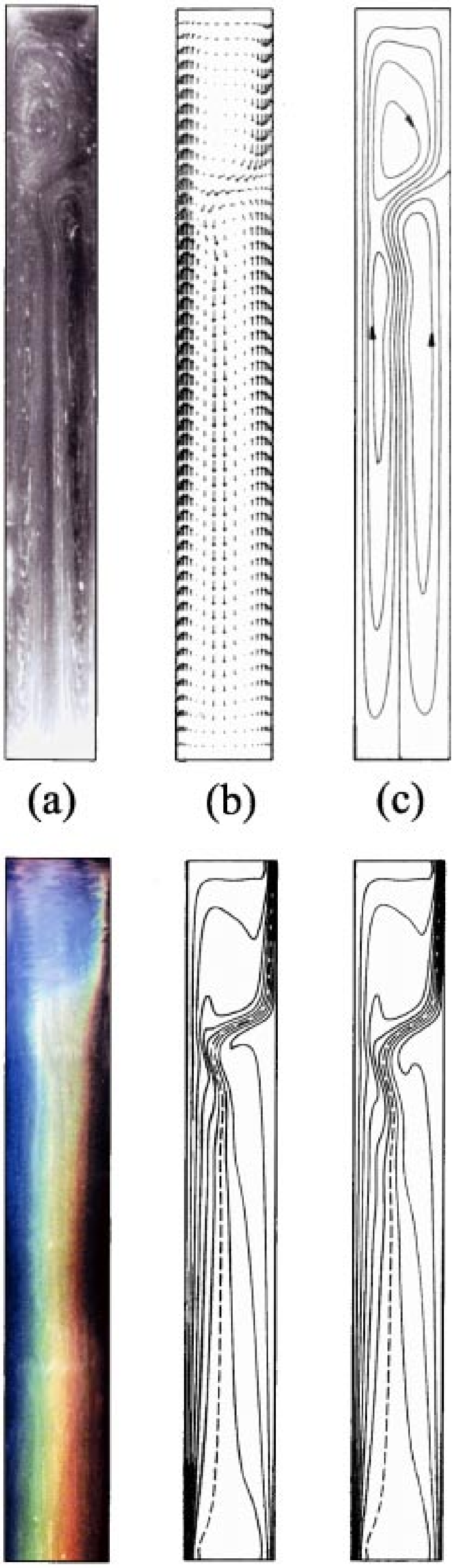

Fig. 9 Comparison of the steady state flow patterns (upper) and temperature fields (lower) among (*a*) visualization experiment, (*b*) three-dimensional ($A_z = 2$), and (*c*) two-dimensional simulations at $\theta_m = 0.4$, $\mathrm{Ra}_W = 2.522 \times 10^5$

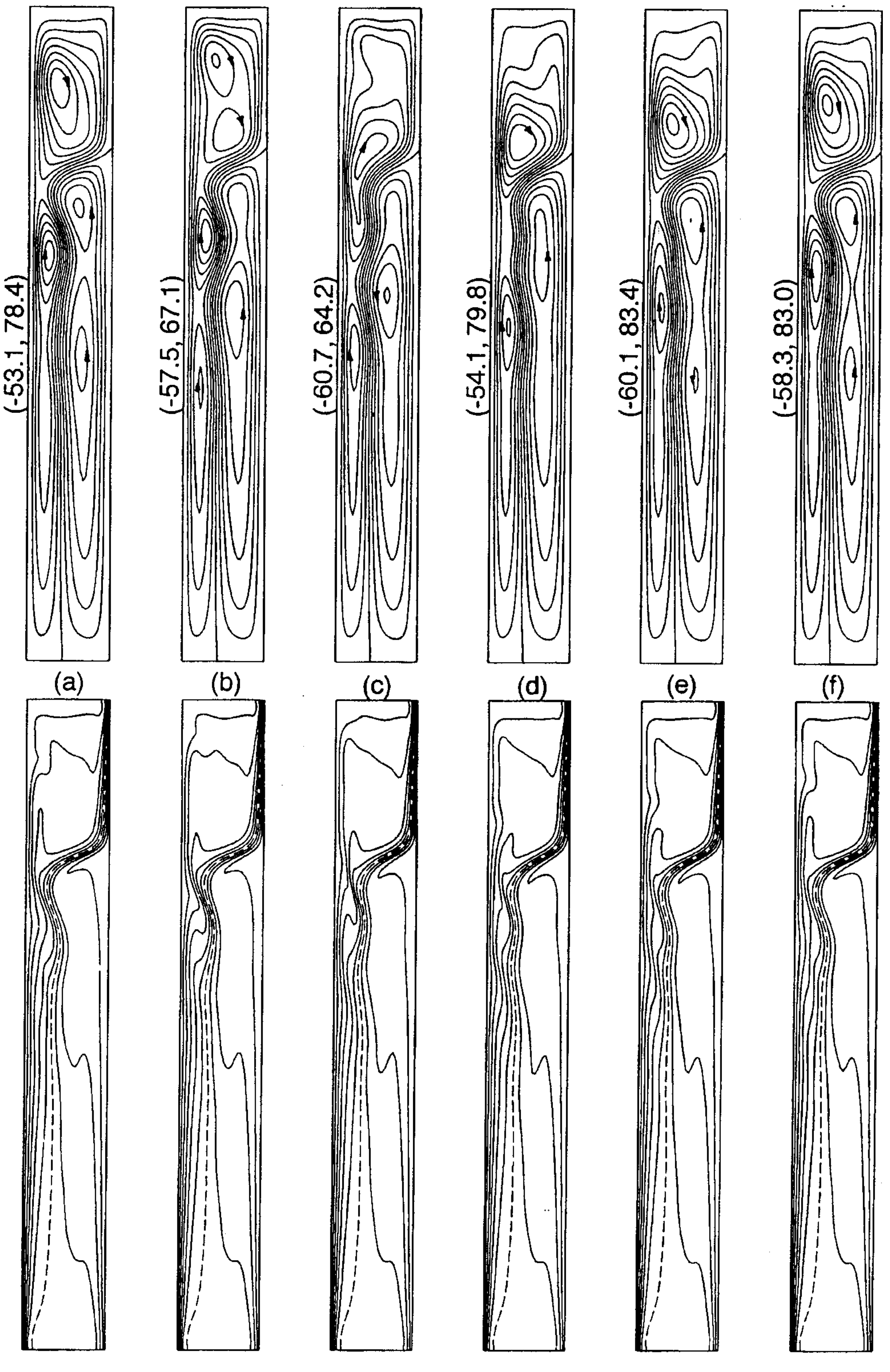

Fig. 10 Periodic variations of the flow structure (upper) and temperature field (lower) predicted by two-dimensional simulation at $\theta_m = 0.4$, $Ra_W = 5.437 \times 10^5$

corresponding two-dimensional simulation. This is a further indication of the dissipation effect associated with the three-dimensionality of the enclosure in experiment.

Concluding Remarks

In the present study, the primary objective has been to document experimentally the features of buoyancy-driven convection, under strong density inversion influence, in a vertical water-filled enclosure of high height/width ratio ($A_y = 8$) at high Rayleigh numbers, in which a temporally oscillatory convection regime may be expected to occur. A convection regime of self-sustained periodic oscillation in time has been confirmed, via temperature and flow visualization experiments, in an enclosure of depth/width ratio $A_z = 2.333$ at $Ra_W = 3.454 \times 10^5$ under $\theta_m = 0.5$. The oscilla-

Table 3 Comparison of measurements and simulations

		$(T_{center})_{ss}$ or $(T_{center})_{mean}$ (°C)				A_T (°C)			
θ_m	Ra_W	Exp.	Num. ($A_z=\infty$)	Num. ($A_z=2$)	Num. ($A_z=1$)	Exp.	Num. ($A_z=\infty$)	Num. ($A_z=2$)	Num. ($A_z=1$)
0.5	3.454×10^5	4.1	4.1	4.0	4.0	0.3	0.8	-	-
0.5	5.957×10^5	4.1	4.0	3.9	4.0	-	-	-	-
0.4	2.522×10^5	3.2	3.5	3.4	3.3	-	-	-	-
0.4	5.437×10^5	2.7	2.5	2.5	2.4	-	0.3	-	-

tory convection has been visualized experimentally, and was found to feature a cyclic sequence of onset at the lower quarter-height region, growth, and decay of the upward drifting secondary vortices within counter-rotating bicellular flows. A periodic traveling wave motion of the maximum density contour of water has also been detected in the temperature visualization experiment. The corresponding two-dimensional numerical simulation is able to capture the main features of the observed oscillatory convection flow and temperature fields in the enclosure and provides a good agreement with the measured time period of the cyclic traveling wave motion of the maximum density contour.

Acknowledgments

The authors wish to thank the National Science Council of Republic of China in Taiwan for providing financial support for the present study through Project Nos. NSC-83-221-E006-110 and NSC-84-2212-E006-013. The necessary computing resources were kindly provided by the National Center for High Performance Computing of NSC. The constructive comments of the reviewers are sincerely appreciated.

Nomenclature

A_T = amplitude of temperature fluctuation
A_y = height/width ratio$=H/W$
A_z = depth/width ratio$=D/W$
b = exponent in the density equation
D = depth
Fo = Fourier number $=\alpha t/W^2$
g = gravitational acceleration
H = height
P^+ = time period
P = dimensionless time period$=P^+\alpha/W^2$
Pr = Prandtl number=v/α
Ra_H = Rayleigh number based on height of enclosure$=g\cdot rsp(\Delta T)^b H^3/(\upsilon\alpha)$
Ra_W = Rayleigh number based on width of enclosure$=g\cdot rsp(\Delta T)^b W^3/(\upsilon\alpha)$
rsp = coefficient in density equation
t = time
T = temperature
ΔT = temperature difference between hot and cold wall$=(T_h-T_c)$
$\mathbf{V}$ = dimensionless velocity vector
W = width
x^+,y^+,z^+ = Cartesian coordinates
x,y,z = dimensionless coordinates$=x^+/W,y^+/W,z^+/W$

Greek Symbols

α = thermal diffusivity
θ = dimensionless temperature $=(T-T_c)/\Delta T$
θ_m = density inversion parameter$=(T_m-T_c)/\Delta T$
υ = kinematic viscosity
ρ = density
$\tilde{\omega}$ = dimensionless pseudovorticity vector

Subscripts

c = cold wall
center = central point of enclosure
cr = critical state
h = hot wall
m = maximum density
max = maximum value
mean = periodically mean value
ss = steady state

Superscripts

m = iteration number or time level

References

[1] Gebhart, B., 1979, ''Buoyancy Induced Motions Characteristics of Applications in Technology,'' ASME J. Fluids Eng., **101**, pp. 5–28.
[2] Watson, A., 1972, ''The Effect of the Inversion Temperature on the Convection of Water in an Enclosed Rectangular Cavity,'' Quarterly J. Mech. Appl. Math., **15**, pp. 423–446.
[3] Seki, N., Fukusako, S., and Inaba, H., 1978, ''Visual Observation of Nature Convective Flow in a Narrow Vertical Cavity,'' J. Fluid Mech., **84**, pp. 695–704.
[4] Inaba, H., and Fukuda, T., 1984, ''Natural Convection in an Inclined Square Cavity in Regions of Density Inversion of Water,'' J. Fluid Mech., **142**, pp. 363–381.
[5] Lin, D. S., and Nansteel, N. W., 1987, ''Natural Convection Heat Transfer in a Square Enclosure Containing Water Near its Density Maximum,'' Int. J. Heat Mass Transf., **30**, pp. 2319–2329.
[6] Tong, W., and Koster, J., 1993, ''Natural Convection of Water in a Rectangular Cavity Including Density Inversion,'' Int. J. FLuid Flow, **14**, pp. 366–375.
[7] Vasseur, P., and Robillard, L., 1980, ''Transient Natural Convection Heat Transfer in a Mass of Water Cooled Through 4°C,'' Int. J. Heat Mass Transf., **23**, pp. 1195–1205.
[8] Robillard, L., and Vasseur, P., 1981, ''Transient Natural Convection Heat Transfer of Water with Maximum Density Effect and Supercooling,'' ASME Journal Heat Transfer **103**, pp. 528–534.
[9] Braga, S. L., and Viskanta, R., 1992, ''Transient Natural Convection of Water Near Its Density Extremum in a Rectangular Cavity,'' Int. J. Heat Mass Transf., **35**, pp. 861–875.
[10] McDonough, M. W., and Faghri, A., 1994, ''Experimental and Numerical Analyses of the Natural Convection of Water Through its Density Maximum in a Rectangular Enclosure,'' Int. J. Heat Mass Transf., **37**, pp. 783–801.
[11] Tong, W., and Koster, J., 1994, ''Density Inversion Effect on Transient Natural Convection in a Rectangular Enclosure,'' Int. J. Heat Mass Transf., **37**, pp. 927–938.
[12] Lankford, K. E., and Bejan, A., 1986, ''Natural Convection in a Vertical Enclosure Filled With Water Near 4°C,'' ASME Journal of Heat Transfer **108**, pp. 755–763.
[13] Ivey, G. N., and Hamblin, P. F., 1989, ''Convection Near the Temperature of Maximum Density for High Rayleigh Number, Low Aspect Ratio, Rectangular Cavities,'' ASME Journal of Heat Transfer **111**, pp. 100–105.
[14] Nishimura, T., Wake, A., and Fukumori, E., 1995, ''Natural Convection of Water Near the Density Extremum for a Wide Range of Rayleigh Numbers,'' Numer. Heat Transfer, Part A, **27**, pp. 433–449.
[15] Nishimura, T., Hayashida, Y., Mineoka, M., and Wake, A., 1997, ''Oscillatory Natural Convection of Water Near the Density Extremum at High Rayleigh Numbers,'' Int. J. Heat Mass Transf., **40**, pp. 3449–3465.
[16] Ho, C. J., and Tu, F. J., 1999, ''Numerical Study on Oscillatory Convection of Cold Water in a Tall Vertical Enclosure,'' Int. J. Numer. Methods Heat Fluid Flow, **9**, pp. 487–508.
[17] Gebhart, B., and Mollendorf, J., 1974, ''A New Density Relation for Pure and Saline Water,'' Deep-Sea Res., **24**, pp. 831–838.
[18] Ho, C. J., and Lin, F. H., 1997, ''Simulation of Natural Convection in a Vertical Enclosure by Using a New Incompressible Flow Formulation—Pseudo Vorticity-Velocity Formulation,'' Numer. Heat Transfer, Part A **31**, pp. 881–896.
[19] Leonard, B. P., 1983, ''A Convectively Stable, Third-Order Accurate Finite Difference Method for Steady Two-Dimensional Flow and Heat Transfer,'' *Numerical Properties and Methodologies in Heat Transfer*, T. M. Shih, ed., Hemisphere Publishing Corp., Washington, D.C., pp. 211–226.
[20] Fusegi, T., Hyun, J. M., Kuwahara, K., and Farouk, B., 1991, ''A Numerical Study of Three-Dimensional Natural Convection in a Differentially Heat Cubical Enclosure,'' Int. J. Heat Mass Transf., **34**, pp. 1543–1557.
[21] Le Peutrec, Y., and Lauriat, G., 1990, ''Effects of the Heat Transfer at the Side Walls on Natural Convection in Cavities,'' ASME Journal of Heat Transfer **112**, pp. 370–378.
[22] Janssen, R. J. A., Henkes, R. A. W. M., and Hoogendoorn, C. J., 1993, ''Transition to Time-Periodicity of a Natural-Convection Flow in a 3-D Differentially Heated Cavity,'' Int. J. Heat Mass Transf., **36**, pp. 2927–2940.

L. Czechowski
Graduate Student

J. M. Floryan
Professor, Fellow ASME
e-mail: mfloryan@eng.uwo.ca

Department of Mechanical
and Materials Engineering,
The University of Western Ontario,
London, Ontario, N6A 5B7, Canada

Marangoni Instability in a Finite Container-Transition Between Short and Long Wavelengths Modes

Marangoni instability in a finite container with a deformable interface in the absence of gravity has been investigated. It is shown that the critical Marangoni number Ma_{cr} is a non-monotonic function of the length of the container. Two different physical mechanisms driving convection are indicated. The advection of heat is essential for the first, advective (''classical'') mechanism that gives rise to short wavelength modes. The interface deformation is essential for the second mechanism that gives rise to long wavelength modes. If the container is sufficiently long, the second mechanism leads to an unconditional instability. The available results suggest that the unconditional instability leads to segmentation of the interface. [DOI: 10.1115/1.1339005]

Keywords: Heat Transfer, Instability, Natural Convection, Surface Tension, Thermocapillary

1 Introduction

Consider a quiescent liquid layer heated from below that is bounded from above by a passive gas. A sufficiently strong heating leads to instability. The instability motion can be a result of either the Marangoni effect associated with the temperature dependent surface tension or the buoyancy effect associated with the temperature dependent density. The Marangoni effect in the absence of gravity is investigated in the present study.

Bénard [1] carried out the first study concerning the origin and development of thermal instabilities in liquids in 1900. He observed convection in a layer of spermaceti just beyond critical conditions and noted that convection cells formed a regular hexagonal pattern and that the upward flow was below the surface depressions and the downward flow was under the surface elevations. Bénard [1] assumed that buoyancy was the main force that drove this convection. Block [2] indicated that in shallow liquid layers, as in Bénard's experiment, the temperature dependent surface tension was more important than density gradient.

Pearson [3] gave a linear theory for the Marangoni instability for an infinite layer of fluid with a nondeformable interface. He found that the critical condition giving rise to the onset of convection was governed by a non-dimensional group consisting of the Marangoni number Ma (Ma measures temperature sensitivity of the surface tension) and the Biot number Bi (Bi measures efficiency of the heat transfer from liquid to gas).

Scriven and Sterling [4], Smith [5], Davis and Homsy [6], and Davis [7,8] discussed the role of the deformability of the interface for infinite layers. The deformability provides an additional ''degree of freedom'' and cannot be neglected even if the actual deformation is infinitesimal (e.g., in the linear stability analysis). The capillary number Ca (Ca measures softness of the interface) must therefore be included as an additional parameter. It has been found that the surface deflection stabilizes the system if buoyancy is dominant and destabilizes the system if the Marangoni effect is dominant ([6]). The system becomes unconditionally unstable with respect to disturbances with a sufficiently long wavelength ([4,7]). Goussis and Kelly [9] identified separate short and long wavelength instability mechanisms. Krishnamoorthy et al. [10] showed that long wavelength disturbances may lead to a spontaneous rupture of the layer. VanHook et al. [11] documented the existence of a long wavelength instability that leads to rupture of the layer.

Marangoni instability in a finite cavity was studied by Winters et al. [12] who determined the critical condition for short cavities with a nondeformable interface. Dijkstra [13] provided a detailed description of the associated bifurcations. Dijkstra [14,15] and Dauby and Lebon [16] extended this analysis to three-dimensional cavities. Because of the presence of a fixed interface, the long wavelength modes were effectively eliminated from the analysis.

The main objective of the present work is the determination of how the finite size of the container (in two-dimensions) and the deformability of the interface affect the critical conditions leading to the onset of convection. In particular, it is of interest to analyze the difference between the instability in finite cavities and in infinite layers, to identify the dominant instability mechanisms and to elucidate the pattern of the most unstable modes. A successful resolution of the last issue should permit critical evaluation of the results based on the analysis of infinite layers, and especially the role played by the long wavelength deformational modes. The analysis is limited to two-dimensional flow configurations only. The problem formulation and the governing equations are presented in Section 2. The methodology used in the analysis is discussed in Section 3. Section 4 presents a discussion of the results. Section 5 gives a short summary of the main conclusions.

2 Problem Formulation

Consider a rectangular cavity of length L and height d, as shown in Fig. 1. The upper surface, described by $y=h(x,t)$, is a free surface bounded by a passive gas of negligible density and viscosity kept at a constant temperature T_{gas}. The free surface is associated with a surface tension σ that decreases linearly with temperature, i.e., $\sigma=\sigma_0-\gamma(T-T_{\mathrm{gas}})$. The liquid is incompressible, Newtonian, has density ρ, thermal conductivity k, specific heat per unit mass c, thermal diffusivity $\kappa=k/\rho c$ kinematic viscosity v and dynamic viscosity μ. The bottom of the cavity is kept at a constant temperature T_{bot} and the sides are kept insulated.

In the absence of gravity, the motion of the liquid is governed by the equations

---

Contributed by the Heat Transfer Division for publication in the JOURNAL OF HEAT TRANSFER. Manuscript received by the Heat Transfer Division October 25, 1999; revision received September 27, 2000. Associate Editor: R. Douglass.

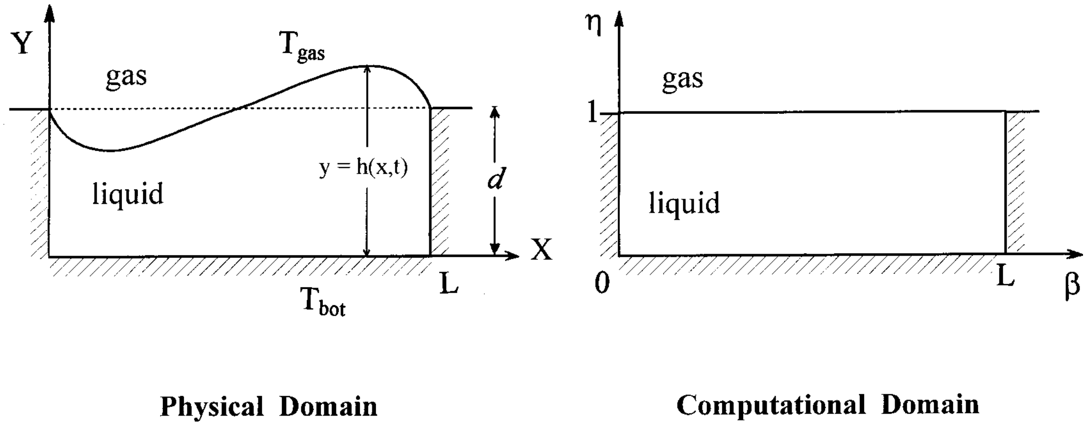

Physical Domain

Computational Domain

Fig. 1 Sketch of the flow configuration and the coordinate system used in the present analysis

$$u_x+v_y=0, \tag{1a}$$

$$\mathrm{Re}(u_t+uu_x+vu_y)=-p_x+u_{xx}+u_{yy}, \tag{1b}$$

$$\mathrm{Re}(v_t+uv_x+vv_y)=-p_y+v_{xx}+v_{yy}, \tag{1c}$$

$$\mathrm{Ma}(T_t+uT_x+vT_y)=T_{xx}+T_{yy}, \tag{1d}$$

where u and v are, respectively, the x and y components of the velocity vector, p is the pressure, T is the temperature of the liquid, t stands for the time, Re and Ma are, respectively, the Reynolds and Marangoni numbers, and subscripts x,y,t stand for $\partial/\partial x$, $\partial/\partial y$, and $\partial/\partial t$, respectively. These equations are subject to the following boundary conditions:

$$x=0:\quad u=0,\quad v=0,\quad T_x=0, \tag{2a}$$

$$x=L:\quad u=0,\quad v=0,\quad T_x=0, \tag{2b}$$

$$y=0:\quad u=0,\quad v=0,\quad T=1, \tag{2c}$$

$$y=h(x,t):\quad v=h_t+uh_x, \tag{2d}$$

$$-p+2[h_x^2u_x+v_y-h_x(v_x+u_y)](1+h_x^2)^{-1} = \mathrm{Ca}^{-1}(1-\mathrm{Ca}T)h_{xx}(1+h_x^2)^{-3/2} \tag{2e}$$

$$2h_x(-u_x+v_y)+(1-h_x^2)(v_x+u_y)=-(T_x+h_xT_y)(1+h_x^2)^{1/2}, \tag{2f}$$

$$(-h_xT_x+T_y)(1+h_x^2)^{-1/2}+\mathrm{Bi}T=0. \tag{2g}$$

In the above, Ca and Bi stand for the capillary and the Biot numbers, respectively. Equation (2*d*) describes the kinematic condition at the interface, (2*e*) and (2*f*) describe the balance of the normal and tangential forces at the interface, respectively, and (2*g*) specifies a general heat transfer condition at the interface. Equation (2*g*) assumes that the Newton's Law of Cooling is valid, which is an idealization ([17]). Detailed derivation of conditions (2*d*)–(2*g*) is given by ([18]). The deforming interface must satisfy the mass conservation constraint and contact conditions

$$\int_0^L h(x,t)dx=V, \tag{3}$$

$$h(0)=h(L)=1. \tag{4}$$

Equation (3) describes conservation of the global volume of the liquid in the cavity. Equation (4) expresses assumption that the contact points between the interface and the side walls remain unchanged during motion of the liquid. The above problem has been scaled with cavity depth d as a length scale, $U_m=\gamma\Delta T/\mu$ as a velocity scale, $d/\mu U_m$ as a pressure scale, σ_0 as a surface tension scale, d/U_m as a time scale and $\Delta T=T_{\mathrm{bot}}-T_{\mathrm{gas}}$ as a temperature scale. The dimensionless parameters are defined as follows:

$$\mathrm{Re}=U_m d\rho/\mu,\quad \mathrm{Ma}=U_m d/\kappa,\quad \mathrm{Ca}=\gamma\Delta T/\sigma_0,\quad \mathrm{Bi}=Hd/k \tag{5}$$

where H stands for the coefficient of heat transfer from the liquid to the gas. The dimensionless temperature was defined as $T=(T^*-T_{\mathrm{gas}})/\Delta T$ where star denotes dimensional temperature.

Pearson [3] used a temperature scale based on the temperature gradient b in the basic state, i.e., $\Delta T=bd$. This scale is equal to the temperature difference between the cavity bottom and the interface, i.e., $\Delta T_p=T_{\mathrm{bot}}-T_{\mathrm{int}}$. Assuming static (no motion) steady state, it is easy to show that

$$T_{\mathrm{int}}=(T_{\mathrm{bot}}+\mathrm{Bi}T_{\mathrm{gas}})/(1+\mathrm{Bi}) \tag{6}$$

For Bi→0, temperature scale $\Delta T_p\to 0$ and this type of scaling becomes singular. As a result, the results in ([3]) for Bi=0 do not correspond to any realistic physical situation (see also [13]). The temperature scale used in this analysis avoids this problem.

The definition of capillary number given in (5) has been used in the analysis of Marangoni instability in short containers ([13]). An alternative definition used in the analysis of stability of infinite liquid layers ([8]) has the form

$$\mathrm{Ca}_D=\mu\kappa/d\sigma_0, \tag{7}$$

$$\mathrm{Ca}=\mathrm{Ca}_D\mathrm{Ma}. \tag{8}$$

3 Numerical Solution

The question of the stability of the liquid is investigated using direct numerical simulation. The required algorithm has to be able to solve the unsteady free-boundary problem. The irregular, time-dependent solution domain (as defined by $h(x,t)$) is mapped onto a fixed rectangular domain in the computational (ξ,η) plane (Fig. 1) using a transformation on the form

$$\xi=x,\qquad \eta=y/h(x,t). \tag{9}$$

The flow problem is expressed in terms of the stream function—vorticity formulation that permits a simple enforcement of the incompressibility condition. The field equations to be solved numerically have the form

$$\Delta^2\psi+\omega=0, \tag{10a}$$

$$\omega_t-\eta h^{-1}h_t\omega_\eta+h^{-1}(\psi_\eta\omega_\xi-\psi_\xi\omega_\eta)=\Delta^2\omega/\mathrm{Re}, \tag{10b}$$

$$T_t-\eta h^{-1}h_tT_\eta+h^{-1}(\psi_\eta T_\xi-\psi_\xi T_\eta)=\Delta^2 T/\mathrm{Ma}, \tag{10c}$$

where

$$u=\psi_y, \quad v=-\psi_x, \quad \omega=v_x-u_y,$$

$$\Delta^2=\frac{\partial^2}{\partial\xi^2}-2\,\eta h_\xi h^{-1}\frac{\partial^2}{\partial\xi\partial\eta}+h^{-2}(\eta^2h_\xi^2+1)\,\frac{\partial^2}{\partial\eta^2}$$

$$+(2h_\xi^2-hh_{\xi\xi})\,\eta h^{-2}\frac{\partial}{\partial\eta}. \tag{10d}$$

The boundary conditions take the form

$$\xi=0: \quad \psi=0, \quad \psi_\xi=0, \quad T_\xi=0, \tag{10e}$$

$$\xi=L: \quad \psi=0, \quad \psi_\xi=0, \quad T_\xi=0, \tag{10f}$$

$$\eta=0: \quad \psi=0, \quad \psi_\xi=0, \quad T=1, \tag{10g}$$

$$\eta=1: \quad h_t+\psi_\xi=0, \tag{10h}$$

$$-p+2\,\frac{(h_\xi\psi_{\xi\xi}-(1+h_\xi^2)h^{-1}\psi_{\xi\eta}+h_\xi h^{-2}(1+h_\xi^2-hh_{\xi\xi})\,\psi_\eta)}{(1+h_\xi^2)}$$

$$=\mathrm{Ca}^{-1}(1-\mathrm{Ca}T)h_{\xi\xi}(1+h_\xi^2)^{-3/2} \tag{10i}$$

$$-(1-h_\xi^2)\,\psi_{\xi\xi}+h^{-2}(1+h_\xi^2)^2\psi_{\eta\eta}-2h_\xi h^{-1}(1+h_\xi^2)\,\psi_{\xi\eta}$$

$$+[(1-h_\xi^2)hh_{\xi\xi}+2h_\xi^2(1+h_\xi^2)]h^{-2}\psi_\eta=-T_\xi(1+h_\xi^2)^{1/2} \tag{10j}$$

$$(1+h_x^2)^{1/2}h^{-1}T_\eta-h_\xi(-1+h_\xi^2)^{-1/2}T_\xi+\mathrm{Bi}T=0. \tag{10k}$$

The above problem is discretized using a second-order finite-difference approximation for the spatial derivatives and a first-order, fully implicit approximation for the temporal derivatives. The method used and its testing are described in ([19]). The cases where steady, saturated states exist were investigated using the steady algorithm described in ([20]).

4 Stability Investigation

The stability investigation relied on the primary meaning of the instability. The basic state was perturbed and the evolution of disturbances was followed in time. The solution was considered to be stable if the disturbance decreased in time. If the disturbance increased then the solution was considered to be unstable. In all unstable cases considered, the growth of disturbances resulted in the appearance of a convective motion.

The basic state considered in this analysis consisted of quiescent liquid, i.e.,

$$\psi=0, \quad \omega=0, \quad T(t,\xi,\eta)=1-\mathrm{Bi}\,\eta/(1+\mathrm{Bi}), \quad h(t,\xi)=1. \tag{11}$$

Several methods have been used for perturbing the liquid, most commonly through perturbing the temperature field. Two shapes of perturbation function were used. In the delta-like perturbation, the temperature at one grid point (close to the side wall) was increased by a value of the order of 10^{-4}–10^{-5}. Such perturbation contains symmetric and asymmetric modes of all wavelengths admissible by the flow system. This is an important property of this form of perturbation because we do not know a priori which of the possible modes (and whether it is symmetric or asymmetric) is the most unstable one. In the second approach, the sum of a few basic (symmetric and asymmetric) modes was used as an initial perturbation. In this case the shape function was represented as $\delta T(t=0,\xi,\eta=0.5)=10^{-5}\Sigma_i\cos(\pi\xi i/L)$ with i typically varying from 1 to 10. This perturbation was added to the static temperature at depth $\eta=0.5$. The reader may note that certain properties of the resulting motion (like, for example, direction of rotation in the cell), may depend on the shape function. The values of the critical Marangoni number, however, are the same for both shape functions within the error of the present analysis, except in some extremal cases.

The amplitude of the perturbation as measured, for example, by maximum values of the stream function $|\psi|_{\max}$ and the vorticity $|\omega|_{\max}$, must fulfill two conditions. The first is that the resulting instantaneous motion must exceed by a few orders of magnitude the ''numerical zero'' level (approximately 10^{-12} for the stream function for the time-dependent algorithm). The second is that the amplitude of the motion must be significantly lower than any steady state solution that may exist for the given values of A, Bi, L, Re and the Marangoni number equal to $\mathrm{Ma}_{cr}+0.5$. Here Ma_{cr} denotes the critical value of the Marangoni number and the value 0.5 stands for the accuracy of determination of Ma_{cr}.

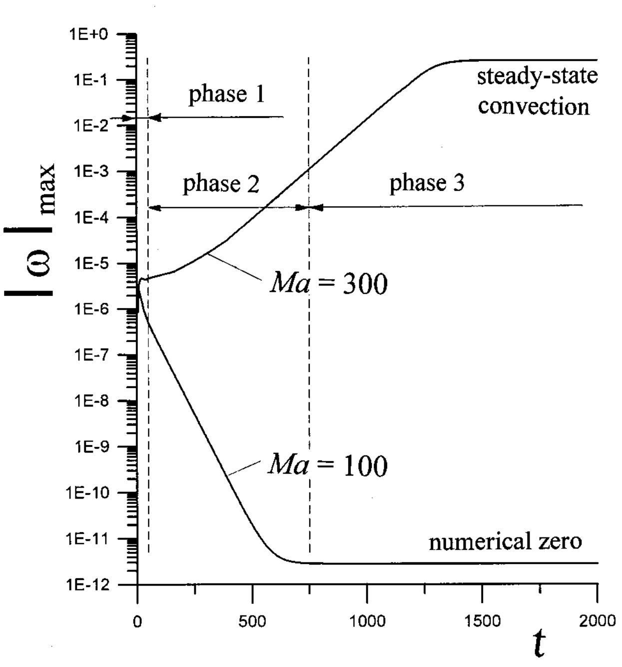

Fig. 2 Evolution of perturbations for a subcritical (Ma=100 — lower line) and supercritical (Ma=300 — upper line) Marangoni numbers for Ca=1.5, Bi=2, Pr=1 and $L=3$. The critical value of the Marangoni number is $\mathrm{Ma}_{cr}=210$. The maximum value of the vorticity $|\omega|_{\max}$ is used as a measure of the magnitude of the perturbation. The classical, short wavelength disturbance pattern dominates, leading to the formation of a saturated supercritical steady convection.

After introducing one of the above perturbations, the evolution of the flow system was followed in time. A typical behavior of the solution is presented in Fig. 2. At the beginning (phase 1) there is no dominant tendency; the disturbances can either decrease or increase depending on the shape of the perturbation used. This is so because this perturbation consists of a number of modes that have their wave numbers close to the wave number of the most unstable mode. These modes decay very slowly and, consequently, it takes a long time to sort out the decreasing and increasing modes.

After the end of phase 1 a distinct tendency can be observed, with both the maximum of the stream function and the maximum of the vorticity either decreasing or increasing (phase 2). The (in/de)crease lasts for a long time (thousands of time units) until either a steady state is reached or the calculations have to be terminated for numerical reasons. Small oscillations of the solution are usually observed around the steady state if it exists (phase 3).

The solution was classified on the basis of its behavior in phase 2. If both $|\psi|_{\max}$ and $|\omega|_{\max}$ changed monotonically for a few hundred time steps, the solution was classified as either stable (perturbation was decreasing) or unstable (perturbation was increasing). After a decision had been made, the calculations were interrupted and repeated with a new value of Marangoni number until Ma_{cr} was found with accuracy of 0.5.

Table 1 Critical values of the Marangoni number Ma_{cr} and the number of cells for different grid resolutions. Calculations were performed for Bi=2, Ca=1.5, i.e., close to the region of transition from the one-cell regime to the two-cell regime (see Fig. 2).

	Grid Size			
	11x11	32x64	64x64	101x101
Length				
2.0	207, 1 cell	225, 1 cell	230, 1 cell	231, 1 cell
2.6	226, 1 cell	221, 2 cells	224, 2 cells	225, 2 cells

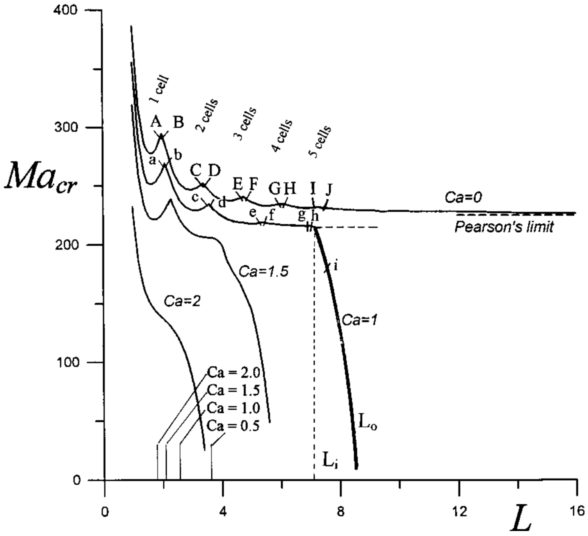

Fig. 3 The critical Marangoni number Ma_{cr} as a function of the cavity length *L* for different values of the Capillary number Ca and for Bi=2. The half-wavelengths of disturbances leading to the unconditional instability, according to the linear stability analysis of an infinite layer ([8]), are marked on the horizontal axis. Transition of flow patterns from one cell to two cells, and then to three, four, five, etc., cells are marked by points A and B, C and D, E and F, G and H, I and J, respectively, for Ca=0, and by points a and b, c and d, e and f, g and h, respectively, for Ca=1. The four and five cells *S*-pattern and the 3 cells *L*-pattern for Ca=1 are shown in Fig. 4. The thick lines indicate critical conditions for the *L*-pattern of response for Ca=1.

The method is very sensitive with respect to Marangoni number; hence, the critical value of Ma could be determined with a good precision. The limit of the precision is imposed by the grid size. In the calculations, the grid with resolution either 1/32 or 1/64 had been used. The corresponding error of Ma_{cr} is 3–5 (for grid 1/32) and 1–2 (for grid 1/64) for flat parts of the neutral stability curves and could be larger close to the region of the unconditional instability—see Table 1 and Figure 3.

5 Results and Discussion

4.1 Cavity With a Nondeformable Interface. Marangoni instability in a two-dimensional cavity with a nondeformable interface has been studied by a number of authors. The initial analyses (see, for example, [3]) were concerned with infinite liquid layers only. More recently, Dijkstra [13] considered (short) finite cavities with length $L \leqslant 4$ and determined the corresponding bifurcation structures. The transition between the finite cavity and an infinite layer has not yet been studied. This problem provides a good starting point as well as a test for our methodology. Thus, we seek Ma_{cr} as a function of Bi and L with $\mathrm{Ca}=0$. For convenience and without loss of generality we set $\mathrm{Pr}=1$ since the Prandtl number Pr (or the Reynolds number Re) do not effect the neutral state.

Figure 3 displays variations of the critical Marangoni number Ma_{cr} as a function of the cavity length L. The curve with $\mathrm{Ca}=0$ corresponds to a nondeformable interface and its part for $L \leqslant 4$ is qualitatively similar to the one obtained in ([13]) (results in ([13]) are for a different value of Bi). The reader may note a nonmonotonic character of variations of Ma_{cr} as L increases and the existence of an asymptotic limit of Ma_{cr} for $L \to \infty$. The local maxima of Ma_{cr} correspond to the change in the number of convection cells found in the liquid (the corresponding flow patterns are not shown), in qualitative agreement with experiments described in ([21]). The very sharp form of these maxima underscores the fact that there are well-defined cavity lengths that separate flow patterns with a different number of cells. These border points are double points since they give rise to two flow patterns, one being symmetric and the other one being asymmetric. These double points correspond to the intersections of the symmetric and asymmetric bifurcation branches ([13]).

When the cavity length increases ($L \to \infty$), the symmetric and asymmetric bifurcation branches approach each other and the local maxima and minima of Ma_{cr} become less and less distinguishable (see Fig. 3). In the limit, $L = \infty$, there is no distinction between both branches. The limiting value of Ma_{cr} is equal to the one determined in ([13]) in the case of an infinite layer. Detailed comparison between the present and Pearson's results is given in Table 2. When L increases, the flow pattern alternates between symmetric (with odd number of cells) and asymmetric (with an

Table 2 Critical values of the Marangoni number Ma_{cr} for the finite container and the rigid interface (i.e., Ca=0) and the Pearson's ([3]) results for the infinite layer

	Length of the cavity *L*					
Bi	4	6	12	16	∞ Pearson's re-scaled	∞ Pearson's original
2	239	229	227	226	225	150
4	277	272	-	271	271	217
6	349	335	331	331	330	283

even number of cells) flow patterns. The cells' configurations approach the common limit consisting of cells characterized by the critical wave number, $\alpha_{cr} \approx 2.4$, ([3]).

5.2 Cavity With a Deformable Interface. The questions to be addressed in this section are (i) how the interface deformability affects the critical stability conditions, (ii) what are the corresponding flow patterns, and (iii) what is the character of transition from the behavior of a finite cavity to the behavior of an infinite layer. In the case of an infinite layer the system is unconditionally unstable with respect to disturbances with the wave number α such that $\alpha^2 < 1.5\,\mathrm{Ca}$ ([4,8]). For convenience, and without loss of generality, we set Pr=1 and carry out calculations for various cavity lengths L and various Capillary number Ca, and for selected values of Bi.

The form of plots of Ma_{cr} as a function of L for different values of Ca (see Fig. 3) suggests the existence of two qualitatively different types of response of the system, depending on the length of the cavity. For L smaller than a certain critical value, $L < L_i$, an increase of deformability of the interface (an increase of Ca) results in a small reduction of the critical Marangoni number Ma_{cr}. The maximum cavity length that supports such response decreases at the same time. The magnitudes of both changes increase with an increase of Ca. The qualitative character of this response is very similar to the case of a nondeformable interface (compare neutral curves for Ca=1 and Ca=0 in Fig. 3). We shall refer to this process as the *S*-pattern of response (*S* stands for short cavity). When cavity length increases above the maximum length that supports the *S*-pattern of response, $L > L_i$, the critical Marangoni number rapidly decreases and the system becomes unconditionally unstable for $L > L_o$. Both L_i and L_o are functions of Ca. We shall refer to this process as the *L*-pattern of response (*L* stands for long cavity). We shall demonstrate, by looking at the form of the most unstable disturbances, that the *S* and *L*-patterns are very distinct and are driven by different physical mechanisms.

The above result is qualitatively consistent with the known results for infinite layers. The results of ([6,7]) indicate that the presence of a deformable interface reduces the critical Marangoni number if the system is dominated by thermocapillary effect. Disturbances of a sufficiently long wavelength λ($\lambda > 2\pi[2/(3\,\mathrm{Ca})]^{1/2}$) become unconditionally unstable ([8]). The cavity sidewalls have, however, a very strong stabilizing effect on such disturbances. If one uses results obtained for an infinite layer as a guideline, the minimum cavity length that permits appearance of the unconditionally unstable disturbances should be no less half the wavelength of the shortest unconditionally unstable disturbance, i.e., $L > \pi[2/(3\,\mathrm{Ca})]^{1/2}$. Results displayed in Fig. 3 show that such disturbances are conditionally stable in a finite cavity, and the length of the cavity has to be significantly larger before the onset of the unconditional instability is possible.

The transition between the *L* and *S*-patterns is illustrated in Figs. 4–5 for Ca=1. The five-cell symmetric flow pattern exists in a very narrow range of cavity lengths (see Fig. 3) and then it is replaced by a three-cell flow pattern illustrated in Fig. 4(*i*). We were unable to find any intermediate state with four cells. This means that the transition from the *S*-pattern to the new state (*L*-pattern) is not continuous and should not be interpreted as a gradual change of the aspect ratio of the *S*-pattern cells. The discontinuous character of this change is well illustrated in Fig. 5 displaying interface deformation. The *L* and *S*-patterns give rise to qualitatively different shapes of the interface, with the *L*-pattern inducing deformation larger by a factor of ten. The new, three-cell flow pattern and the associated deformation pattern, which remain unchanged with any further increase of the cavity length, represent the characteristic features of the *L*-pattern of response. The lengths of the cells are always approximately equal to $L/4$, $L/2$, and $L/4$ in sequence from the left to the right end of the cavity (Fig. 4(*i*)). We investigated this problem in detail and found that even for very large L (equal to several times the critical length L_i) lengths of the cells always remained approximately $L/4$, $L/2$, $L/4$.

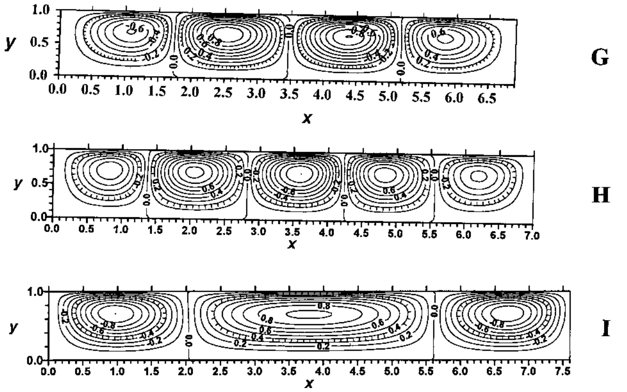

Fig. 4 Flow patterns associated with the most unstable disturbances in the case of a deformable interface for Ca=1, Ma=Ma$_{cr}$, Bi=2. The interface deformation is ignored as too small for plotting purposes. The *S*-pattern of response is illustrated for cavity lengths *L*=6.9 and 7.0 (see Figs. 4(*g–h*), while the *L*-pattern is illustrated for cavity length *L*=7.6 (see Fig. 4(*i*)). The corresponding flow conditions are marked by points *g*, *h*, and *i*, in Fig. 3, respectively. The forms of the interface for *L*=7.0 and 7.6 are shown in Fig. 5. Flow normalization condition used in all cases — $|\psi|_{\max}=1$. The system evolution corresponds to phase 2 in Fig. 2.

The reader should note that the data displayed in Figs. 4–5 has been taken from phase 2 of the instability (see Fig. 2). In order to take time out of considerations, the data has been normalized with condition $|\psi|_{\max}=1$ which corresponds to the selection of an arbitrary constant in the linear stability theory. Figure 4 presents streamlines with the deformation that has not been normalized (deformation is too small to be visible in this plot). Figure 5 presents normalized deformation. All calculations were nonlinear, however, the nonlinear effects played no role due to early stages

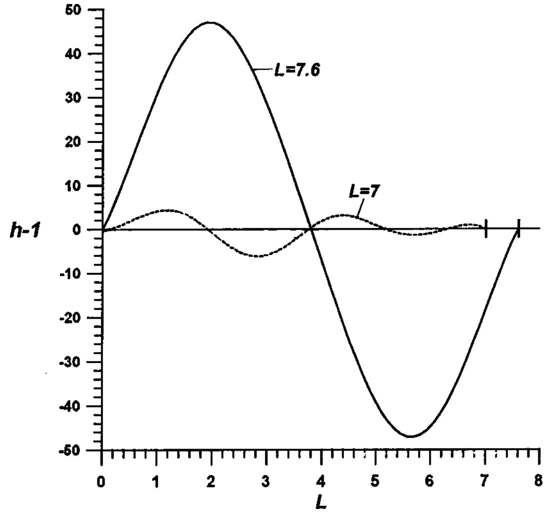

Fig. 5 Deformations of the interface associated with the most unstable disturbances for Ma=Ma$_{cr}$, Ca=1, Bi=2. The *S* and *L*-patterns are illustrated for cavity lengths *L*=7 and 7.6, respectively. The corresponding flow fields are shown in Fig. 4. The magnitude of the deformation shown resulted from the use of the same normalization condition $|\psi|_{\max}=1$ in all cases. Note that the *L*-pattern gives rise to the deformation that is by an order of magnitude bigger than the deformation associated with the *S*-pattern. The system evolution corresponds to phase 2 in Fig. 2.

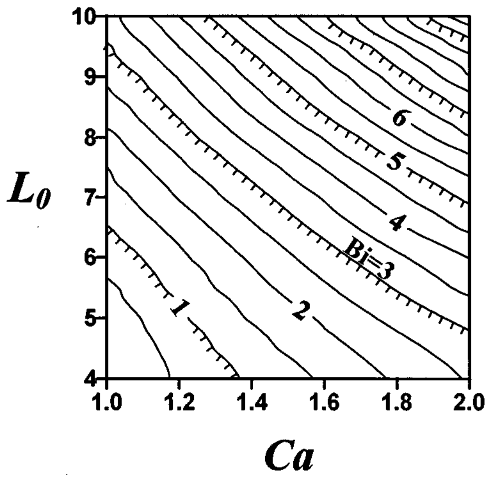

Fig. 6 The critical length L_o for the unconditional instability as a function of the Capillary number Ca and the Biot number Bi

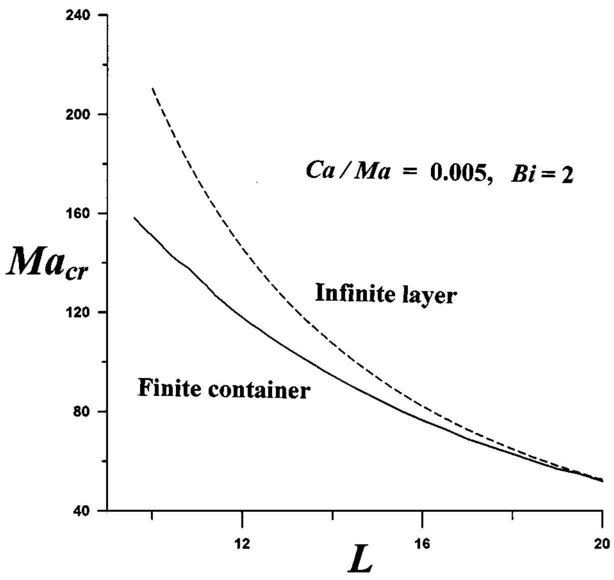

Fig. 7 Comparison of the critical Marangoni numbers Ma_{cr} for a finite container and for an infinite layer with a deformable interface for Bi=2 and for the ratio Ca/Ma=0.005 kept constant. In the case of a finite layer, *L* denotes the length of the container, while in the case of an infinite layer *L* denotes half of the wavelength of the most unstable disturbance. See text for a discussion.

of the instability. This fact had been verified by checking shape of the streamlines, i.e., taking data from different time instances and comparing them under the same normalization.

The above results can be interpreted as shown in Fig. 3 (see curve for Ca=1). There are two branches of the plot of Ma_{cr} as a function of L; one for the S-pattern and another one for the L-pattern. The lower value of Ma_{cr} given by either of these two branches should be treated as the proper critical value for the complete system. At $L = L_i$ both branches intersect and the S-pattern is replaced by the L-pattern. The point of intersection is a double point.

For $L > L_i$, the critical value of the Marangoni number decreases dramatically and reaches zero when the length of the cavity reaches a critical value L_o. For $L > L_o$, the static solution (11) is unconditionally unstable, i.e., it is unstable for any value of Ma. The critical length L_o depends on the capillary Ca and Biot Bi numbers; it decreases with an increasing Ca or a decreasing Bi as illustrated in Fig. 6.

The approach of the system towards the unconditional instability as L increases can be illustrated by using the definition of the capillary number given by Eq. (7). This definition is of interest because it permits direct comparisons of our results with the known results for infinite layers. In particular, it is known ([4,8]) that infinite layers in the large wavelength limit are unconditionally unstable for disturbances with the wavelength λ greater than the critical value, i.e.,

$$\lambda^2 > 8\pi^2/(3\ \mathrm{Ma}\ \mathrm{Ca}_D). \tag{12}$$

A question arises whether this formula can be used for the prediction of the onset of the instability in finite (but very long) cavities. The reader may note that in the case of infinite layers all disturbances have the same wavelength while in the case of finite cavities the flow pattern consists of two types of cells, with one having the lengths $L/2$ and the other one having the length $L/4$. Figure 7 displays the neutral curve for the L-pattern of response for $\mathrm{Ca}_D = \mathrm{Ca}/\mathrm{Ma} = 0.005$ computed directly using the methodology described earlier in this paper. For comparison, the same figure shows critical Marangoni numbers evaluated on the basis of Eq. (12) as

$$\mathrm{Ma}_{cr} = 8\pi^2 (3\ \mathrm{Ca}_D)^{-1} \lambda^{-2}, \tag{13}$$

with λ taken to be $L/2$ (i.e., describing the shorter cell; the reader may note that while the length of the shorter cell is about $L/4$, one has to take two cells to get the equivalent wavelength). The fact that both neutral curves approach each other as L increases suggests that formula (13) provides a meaningful approximation of Ma_{cr} (as long as the shorter cell is considered to be dominant). It should be stressed that this agreement may be fortuitous because the flow patterns in the infinite layer and in the finite cavity are different. One should keep in mind that we have investigated cavities with length $L < 20$ only; it is possible that for longer cavities both curves may separate. One may note that Eq. (13) overpredicts Ma_{cr} (for $L < 20$) which suggests that a cell that is bounded by identical cells on both sides (as in an infinite layer) requires larger heating than a cell that is bounded by a solid wall on one side and a cell twice as big on the other side. Results shown in Fig. 7 suggest that, when the length of the cell increases, the effect of the difference between the forms of the neighboring cells on Ma_{cr} becomes less and less important.

5.3 Physical Mechanisms of Instability. The existence of two neutral branches indicates the existence of two different physical mechanisms of the instability. The ''classical'' mechanism, which we shall refer to as the advective mechanism, can be described as follows. Let us assume that a hot spot appears on the interface as a result of some random temperature perturbation δT. The resultant change of thermocapillary stresses $\delta\sigma$ produces a surface flow δv away from the spot. Conservation of mass is then satisfied by a vertical up-flow, which forms below the spot. Since the temperature of the fluid increases beneath the interface, this up-flow additionally increases the temperature of the spot. If the temperature gradient in the layer is large enough, the convective heating will overcome the cooling effects of conduction and viscous friction leading to an increase in the temperature of the spot and liquid flow, i.e., the system becomes unstable. Deformation of the interface may result from the instability, but is not essential for this mechanism, as demonstrated in ([3]).

The second mechanism, which we shall refer to as the deformational mechanism, can be described by starting with a random deformation of the interface. If the interface moves locally down by δh, its temperature at this location increases by δT due to an increased heat flux from the bottom. This leads to a local decrease of surface tension $\delta\sigma$ that, in turn, produces flow δv away from this point. Conservation of mass is then satisfied by a vertical up-flow, which further increases the temperature of the spot. An

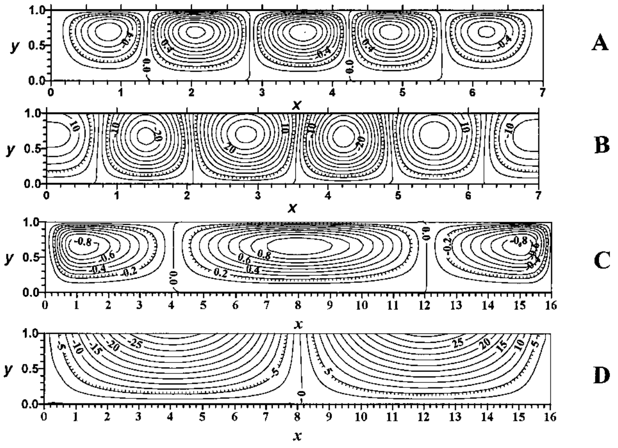

Fig. 8 Comparison of the stream function and temperature disturbance fields for the most unstable (linear) disturbances for Ca=1, Bi=2 for the *S* and *L*-patterns. Figures 8*A*, *B* display stream function and temperature, respectively, for $L=7$ (*S*-pattern) and $\mathrm{Ma}=\mathrm{Ma}_{cr}=215$. Figures 8*C*, *D* display stream function and temperature, respectively, for $L=17$ (*L*-pattern), Ma=10 and Pr=1. The critical Marangoni number for these conditions is $\mathrm{Ma}_{cr}=0$. Data for presentation were taken from the exponential growth period described by the linear theory. Normalization condition used in all cases — $|\psi|_{\max}=1$.

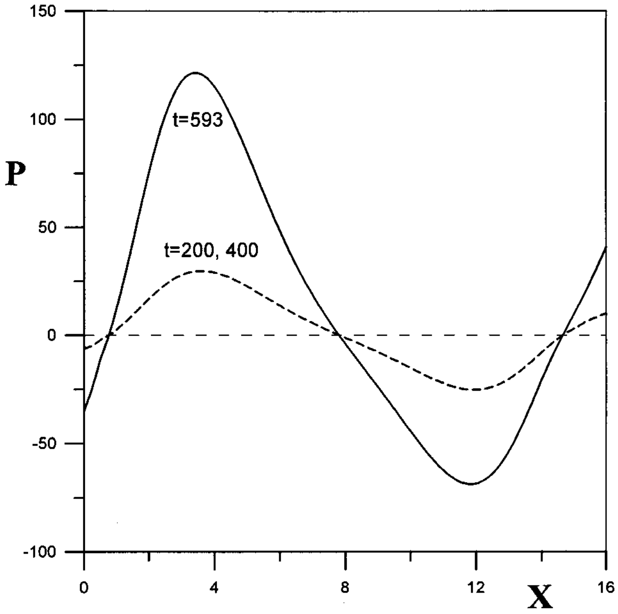

Fig. 9 Surface pressure distribution for the *L*-pattern response for Ca=1.0, Ma=150, Bi=2, Pr=1 and $L=16$ at $t=200$, 400, 593. Calculations had to be terminated at $t=594$. Normalization condition used — $|\psi_{\max}|_{\text{instantaneous}}=1$. Slight asymmetry in the pressure distribution is due to the growth of asymmetric disturbances present in the initial conditions (see text for a discussion).

analogous process can be described for the interface moving locally upwards and thus creating a cold spot. In order to understand when this mechanism may become operative, it is essential to realize that interface perturbations consist of decaying capillary waves. For a nonisothermal system, a restoring surface tension force competes with the pressure field induced by the convection, and the deformation increases when the latter prevails. We shall describe this process in detail later in the text. The instability may occur only if the rate of decay of the interface deformation is slower than the rate at which convection sets in. For a given temperature gradient across the liquid, a cavity of increasing length admits longer and longer, less damped capillary waves and, eventually, if the cavity is made long enough, there will be a capillary wave decaying slowly enough to permit initiation of the convection. Our results show that when this mechanism becomes active, the instability is always initiated by the least damped (i.e., longest) capillary wave permitted in the system. The deformation pattern associated with such a wave is well approximated by a sine function with wavelength L. This deformation gives rise to only one hot spot located approximately either at $L/4$ or at $3L/4$, and one cold spot located approximately at either $3L/4$ or at $L/4$, respectively (initial conditions determine whether the hot spot is at $L/4$ or at $3L/4$). Such a temperature distribution determines the convection pattern, which always consists of one central cell of length $L/2$ and two side cells of length $L/4$ each (see Fig. 4(*i*)). It is the deformational mechanism that is responsible for the *L*-pattern of response and, indeed, this mechanism gives rise to the interface deformation that is much larger than the one created by the advective mechanism (see Fig. 5).

The difference between the way both mechanisms operate is illustrated in Fig. 8 displaying the flow and temperature perturbation patterns. The disturbance temperature field associated with the *S*-pattern (Fig. 8(*B*)) is characterized by closed isotherms, which points to the importance of advection (if the advection was not active, appearance of closed isotherms would imply existence of heat sinks/sources which is clearly not the case). The disturbance temperature field associated with the *L*-pattern (Fig. 8(*D*)) is characterized by open isotherms suggesting negligible effect of heat advection. To confirm this observation, we carried out calculations without the advection term in the energy Eq. (1*d*). Although the advective mechanism cannot work in such situations, the instability did occur and it had the form of the *L*-pattern. The apparent lack of adiabacity of the side walls in Fig. 8(*D*) is the artifact of plotting resulting from omission of isotherms corresponding to temperatures very close to zero.

In real systems both instability mechanisms exist simultaneously. In the case of sufficiently short cavities (i.e., those with the *S*-pattern of response), the deformational mechanism reinforces the advective mechanism resulting in the reduction of Ma_{cr} (see Fig. 3). For sufficiently long cavities (i.e., those with the *L*-pattern of response), the deformational mechanism dominates leading to the unconditional instability. There exists a narrow range of cavity lengths, $L_i<L<L_o$ (Fig. 3), where the deformational mechanism leads to a conditional instability.

The flow configuration in long cavities is very similar to the case of a cavity with differentially heated sidewalls. It has been shown ([22]) that as the length of the cavity increases, the convection cell can be separated into two turning zones attached to the side walls and a core zone where the flow is well approximated by the Couette-Poiseuille solution. For a sufficiently long cavity, the form of the interface deformation is dictated by the flow in the core zone. The pressure gradient in the core zone changes as L^{-1}, the total pressure difference along the cavity remains constant, the magnitude of deformation increases proportionally to L^2 and, as a result, the steady deformed interface cannot exist if the cavity length is larger than a certain critical value. The central cell arising from the instability has a similar structure, i.e., it has two turning zones and a core (see Fig. 4(*i*)) characterized by a constant pressure gradient (see Fig. 9). For a certain range of cavity lengths pressure difference produced by the central cell can be balanced out by the capillary forces. Increase of cavity length rapidly reduces the available restoring capillary force, which reduces the magnitude of pressure required to maintain the deformation. This, in turn, translates into reduction of the amount of heating required to maintain the motion and thus reduction of the critical Marangoni number. For a sufficiently long cavity ($L>L_0$) the restoring capillary force is negligible and any amount of heating results in instability. It will be shown in the

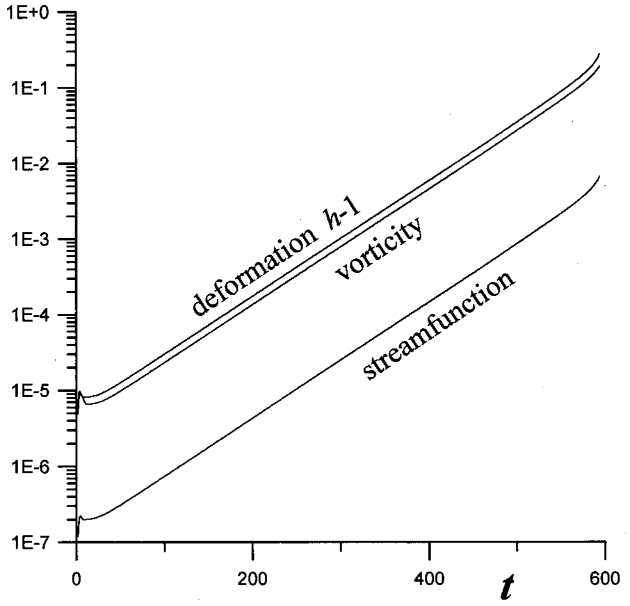

Fig. 10 Maxima of the interface deformation $|h-1|_{\max}$, vorticity $|\omega|_{\max}$ and stream function $|\psi|_{\max}$ as a function of time for the *L*-pattern response for the same conditions as in Fig. 9. A characteristic acceleration of growth of perturbations as a result of nonlinear effects can be easily observed. This behavior is qualitatively different from the one observed in the case of the *S*-pattern, where a nonlinear saturation and a steady final state are observed (see Fig. 2).

next section that under such conditions, i.e., negligible restoring force, the instability leads to large deformations and, possibly, rupture of the interface.

5.4 Finite-Amplitude Convection. Calculations of the finite amplitude convection (i.e. for the Marangoni number exceeding the critical value Ma_{cr}) have been performed in order to explore the differences in the response of the system in the regimes corresponding to the *S* and *L*-patterns of response under critical conditions. The Prandtl number Pr (or the Reynolds number Re) appears now as an additional parameter.

In all cases considered, the *S*-pattern of response was characterized by the existence of a nonlinearly saturated steady state (see Fig. 2) that is analogous to the *S*-pattern found at critical conditions. Detailed analysis of this response will not be presented here.

The *L*-pattern of response is qualitatively different. We considered several cases of supercritical conditions with $L_i<L<L_o$ and observed that, typically, the maximum deformation of the interface increased steadily up to several tens of percent after which the calculations had to be terminated for numerical reasons. In spite of a significant effort we were unable to find any stable, steady-state solution. It may be concluded that the steady-state response either does not exist or the region of its existence is extremely narrow and thus impossible to capture in a numerical experiment of the type attempted in this study.

Figures 9–10 present an example of the evolution of the supercritical convection corresponding to the *L*-pattern of response. The maximum stream function $|\psi|_{\max}$, vorticity $|\omega|_{\max}$, and deformation $|h-1|_{\max}$ increase exponentially in time (Fig. 10). The exponential growth is accelerated when the nonlinear effects set in. This acceleration suggests that the system does not tend to a steady state but that nonlinear effects initiate a process that leads to segmentation of the layer (compare Figs. 2 and 10). The pattern of convection during this acceleration is essentially the same as for the most unstable mode of *L*-pattern at critical conditions, i.e., it consists of three cells.

In order to understand the mechanics of the growth process, the reader should recall that the instability in the *L*-pattern regime is initiated by capillary waves that are amplified by thermocapillary effect (Section 4.3). The essence of the deformational instability mechanism consists of a delicate interplay between the interface-deforming thermocapillarity-induced pressure forces and the restoring surface tension forces. When pressure prevails, interface deformation increases inducing a stronger thermocapillary force and a larger pressure difference that, in turn, further accelerates the growth of the deformation. This process is well illustrated in Fig. 9 displaying time evolution of surface pressure. The simplicity of this closed-loop self-amplification is underscored by the fact that there is no change in the flow pattern during the rapid acceleration of the growth of the instability caused by nonlinear effects.

Results shown in Fig. 9 raise an interesting question regarding pattern formation and suggest the existence of a rich bifurcation structure in this problem. In all our calculations, the initial flowfield disturbances used to trigger the instability contained both symmetric and asymmetric modes that lead to the symmetric 3-cell flow pattern at critical conditions. The symmetric flow pattern leads to asymmetric pressure. Pressure distribution during exponential growth shown in Fig. 9 shows a small departure from asymmetry suggesting presence of asymmetric modes in the flow pattern growing at almost the same rate as the symmetric modes. The same calculation (not shown) with only asymmetric initial disturbances showed initial growth of the instability at a rate similar to the one shown in Fig. 10, and the emerging flow pattern correlating well with the deformation induced by the first symmetric capillary wave. This suggests that the pattern formation could be easily affected by the form of the initial disturbances, especially in very long cavities admitting a number of capillary waves long enough to trigger the deformational mechanism. This issue requires further investigation.

As discussed above, our results indicate that whenever the *L*-pattern of the instability sets in, it initiates a process of continuous increase of deformation leading, most likely, to rupture of the layer. We cannot answer the question whether, in real systems, the interface ruptures or not. When deformation becomes large, new physical effects associated with attraction between the interface and the bottom wall may arise, and they may or may not prevent segmentation of the layer. These effects are not accounted for in our model. The recent experiment of Van-Hook et al. [11] show, however, that long-wavelength deformational instability does lead to rupture of the interface, in qualitative agreement with our results. Simulations of Krishnamoorthy et al. [10] carried out for an infinite layer with long-wavelength periodic disturbances showed interface evolving towards rupture, again in qualitative agreement with our results. Finally, one may note that the form of the central cell in the *L*-pattern is very similar to the convection cell in a cavity with differentially heated sidewalls. Floryan and Chen [22] showed that a continuous interface could not exist in such a cavity if its length is too large. Hamed and Floryan [18] demonstrated that the critical length could be made very small by increasing the value of Ca, which is in qualitative agreement with our results.

It should be stressed that our analysis does not account for the possible presence of hexagonal cells and other three-dimensional effects. While, undoubtedly, such effects will alter the evolution of the instability, their presence does not prevent the liquid from rupturing, as documented by the experiments in ([11]).

6 Summary

Marangoni instability in a finite, two-dimensional container with a deformable interface was investigated using direct numerical simulations as the main methodology. Complete governing equations were solved using an implicit unsteady algorithm. Certain cases, such as steady supercritical convection, were checked using a separately developed steady version of the algorithm.

It has been found that deformability of the interface always destabilizes the system. The magnitude of the destabilization as well as the pattern of response change qualitatively depending on cavity length, from being a contributing factor in short cavities to being a dominant factor in long cavities.

Two different physical mechanisms driving the instability have been indicated. The advection of heat is essential for the first, advective (''classical'') mechanism, which dominates response of the system for short cavities. The resulting flow pattern is referred to as the *S*-pattern because the length of the resulting convection cells is of the order of layer thickness (short cells). This pattern is very similar to the one found in infinitely long layers with a non-deformable interface. The interface deformation is responsible for the second, deformational mechanism. The resulting flow pattern is referred to as the *L*-pattern because the length of the resulting convection cells is of the order of the length of the container (long cells).

The *S*-pattern appears in short cavities when critical conditions, expressed in terms of critical Marangoni number Ma_{cr}, are met. The flow pattern alternates between symmetric forms (odd number of convection cells) and asymmetric forms (even number of convection cells) when the length L of the cavity increases. This corresponds to the symmetric and asymmetric bifurcation branches crossing each other as a function of L. Increase of Ma above its critical value leads to steady supercritical convection whose pattern is analogous to that found at critical conditions.

When cavity length increases above a critical value L_i, there is a rapid (discontinuous) transition from the *S*-pattern to the *L*-pattern of response, the critical Marangoni number decreases dramatically and the liquid becomes unconditionally unstable. The convection pattern always consists of three cells of length $L/4$, $L/2$, and $L/4$, regardless of cavity length (for the range of parameters studied). The form of these cells correlates well with the most unstable capillary wave. When the *L*-pattern sets in, it leads to large interface deformations and, most likely, ruptures of the interface. Nonlinear effects, arising for large enough deformations, accelerate the growth of the instability rather than leading to a nonlinear saturation, which is in contrast to the *S*-pattern of response. This problem requires further investigation. Capillary number Ca_D, which does not include temperature difference in its definition and thus is easier to control experimentally, should be used as a preferable measure of the stiffness of the interface.

Acknowledgments

The Natural Sciences and Engineering Research Council of Canada has supported this work.

Nomenclature

Bi = Biot number ($Bi=Hd/k$)
c = specific heat
Ca = Capillary number ($Ca=\gamma\Delta T/\sigma_0$)
Ca_D = different definition of Capillary number (see Eqs. (7),(8)
d = cavity depth
H = heat transfer coefficient
h = location of the interface
k = thermal conductivity
L = cavity length
$\mathrm{Ma}(\mathrm{Ma}_{cr})$ = Marangoni number (critical Marangoni number) ($Ma=U_m d/\kappa$)
p = pressure
Re = Reynolds number ($\mathrm{Re}=U_m d\rho/\mu$)
$T(T^*)$ = temperature (dimensional temperature)
T_{bot} = temperature of the bottom of the cavity
T_{gas} = temperature of the gas far above the interface
t = time
u,v = velocity components in the (x,y) directions
U_m = velocity scale ($=\gamma\Delta T/\mu$)
V = volume of the liquid
x,y = cartesian reference system
γ = surface tension gradient
κ = thermal diffusivity
λ = wavelength of disturbances
μ = dynamic viscosity
ν = kinematic viscosity
ρ = density
$\sigma(\sigma_0)$ = surface tension (reference surface tension)
ω = vorticity
ψ = stream function
ξ,η = coordinates in the computational plane

References

[1] Bénard, H., 1900, ''Les Tourbillons Cellulaires dans une Nappe Liquide,'' Rev. Gen. Sci. Pures Appl., **11**, pp. 1261–1271; *ibid.* **11**, pp. 1309–1328.
[2] Block, M. J., 1956, ''Surface Tension as the Cause of Benard Cells and Surface Deformation in a Liquid Film,'' Nature (London), **178**, pp. 650–651.
[3] Pearson, J. R. A., 1958, ''On Convection Cells Induced by Surface Tension,'' J. Fluid Mech., **4**, pp. 489–500.
[4] Scriven, L. E., and Sterling, C. V., 1964, ''On Cellular Convection Induced by Surface Tension Gradients: Effect of Mean Surface Tension and Viscosity,'' J. Fluid Mech., **19**, pp. 321–340.
[5] Smith, M. K., 1966, ''On Convective Instability Induced by Surface Tension Gradients,'' J. Fluid Mech., **24**, pp. 401–414.
[6] Davis, S. H., and Homsy, G. M., 1980, ''Energy Stability Theory for Free Surface Problems: Buoyancy-Thermocapillary Layers,'' J. Fluid Mech., **98**, pp. 527–553.
[7] Davis, S. H., 1983, ''Rupture of Thin Liquid Films,'' in *Waves on Fluid Interfaces*, R. E. Meyer, ed., Academic Press, New York, pp. 291–302.
[8] Davis, S. H., 1987, ''Thermocapillary Instabilities,'' Annu. Rev. Fluid Mech., **19**, pp. 403–435.
[9] Goussis, D. A., and Kelly, R. E., 1990, ''On the Thermocapillary Instabilities in a Liquid Layer Heated from Below,'' Int. J. Heat Mass Transf., **33**, pp. 2239–2245.
[10] Krishnammoorthy, S., Ramaswamy, B., and Joo, S. W., 1995, ''Spontaneous Rupture of Thin Liquid Films due to Thermocapillary: A Full Scale Numerical Simulation,'' Phys. Fluids, **7**, pp. 2291–2293.
[11] VanHook, S. J., Schatz, M. F., Swift, J. B., McCormick, W. D., and Swinney, H. L., 1997, ''Long-Wavelength Surface-Tension-Driven Benard Convection: Experiment and Theory,'' J. Fluid Mech., **345**, pp. 45–78.
[12] Winters, K. H., Plesser, Th., and Cliffe, K. A., 1988, ''The Onset of Convection in a Container due to Surface Tension and Buoyancy,'' Physica D, **29**, pp. 387–401.
[13] Dijkstra, H. A., 1992, ''On the Structure of Cellular Solution in Rayleigh-Benard-Marangoni Flows in Small-Aspect-Ration Containers,'' J. Fluid Mech., **243**, pp. 73–102.
[14] Dijkstra, H. A., 1995, ''Surface Tension Driven Cellular Patterns in Three-Dimensional Boxes—Linear Stability,'' Microgravity Sci. Technol., **7**, pp. 307–312.
[15] Dijkstra, H. A., 1995, ''Surface Tension Driven Cellular Patterns in Three-Dimensional Boxes—A Bifurcation Study,'' Microgravity Sci. Technol., **7**, pp. 307–312.
[16] Dauby, P. D., and Lebon, G., 1996, ''Marangoni-Benard Instability in Rigid Rectangular Containers,'' J. Fluid Mech., **329**, pp. 25–64.
[17] Perez-Garcia, C., Echebarria, B., and Bestehorn, M., 1998, ''Thermal Properties in Surface-Tension-Driven Convection,'' Phys. Rev. E, **57**, pp. 475–481.
[18] Hamed, M., and Floryan, J. M., 2000, ''Marangoni Convection: Part 1—Cavity with Differentially Heated Side Walls,'' J. Fluid Mech., **405**, pp. 79–110.
[19] Hamed, M., and Floryan, J. M., 1998, ''Numerical Simulation of Unsteady Nonisothermal Capillary Interfaces,'' J. Comput. Phys., **145**, pp. 110–140.
[20] Chen, C., and Floryan, J. M., 1994, ''Numerical Simulation of Non-isothermal Capillary Interfaces,'' J. Comput. Phys., **111**, pp. 183–193.
[21] Koschmieder, E. L., and Prahl, S. A., 1990, ''Surface-Tension-Driven Benard Convection in Small Containers,'' J. Fluid Mech., **215**, pp. 571–583.
[22] Floryan, J. M., and Chen, C., 1994, ''Thermocapillary Convection and Existence of Continuous Layer in the Absence of Gravity,'' J. Fluid Mech., **277**, pp. 303–329.

A Scattering-Mediated Acoustic Mismatch Model for the Prediction of Thermal Boundary Resistance

Ravi S. Prasher
Assembly Technology and Development,
Intel Corporation, CH5-157,
5000 W. Chandler Blvd.,
Chandler, AZ 85226-3699

Patrick E. Phelan
E-mail: phelan@asu.edu
Department of Mechanical & Aerospace Engineering,
Arizona State University,
Tempe, AZ 85287-6106

Solid-solid thermal boundary resistance (R_b) plays an important role in determining heat flow, both in cryogenic and room-temperature applications, such as very large scale integrated circuitry, superlattices, and superconductors. The acoustic mismatch model (AMM) and the related diffuse mismatch model (DMM) describe the thermal transport at a solid-solid interface below a few Kelvin quite accurately. At moderate cryogenic temperatures and above, R_b is dominated by scattering caused by various sources, such as damage in the dielectric substrates and formation of an imperfect boundary layer near the interface, making R_b larger than that predicted by AMM and DMM. From a careful review of the literature on R_b, it seems that scattering near the interface plays a far more dominant role than any other mechanism. Though scattering near the interface has been considered in the past, these models are either far too complicated or are too simple (i.e., inaccurate) for engineering use. A new model, called the scattering-mediated acoustic mismatch model (SMAMM), is developed here that exploits the analogy between phonon and radiative transport by developing a damped wave equation to describe the phonon transport. Incorporating scattering into this equation and finding appropriate solutions for a solid-solid interface enable an accurate description of R_b at high temperatures, while still reducing to the AMM at low temperatures, where the AMM is relatively successful in predicting R_b. [DOI: 10.1115/1.1338138]

Keywords: *Conduction, Contact Resistance, Heat Transfer, Packaging, Scattering*

1 Introduction

Solid-solid thermal boundary resistance plays an important role in determining heat flow, both in cryogenic and room-temperature applications, such as very large scale integrated circuitry, superlattices, and superconductors [1–3]. The acoustic mismatch model (AMM) describes the thermal transport at a solid-solid interface below a few degrees Kelvin quite accurately. Another model, known as the diffuse mismatch model (DMM), though seemingly more suitable for interfacial transport above a few Kelvin, is no better than AMM for predicting R_b at a solid-solid interface [1]. According to Cahill [2], no experiment has yet been able to distinguish between the AMM and DMM for energy transport between solids near room temperature.

At moderate cryogenic temperatures and above, R_b is dominated by scattering caused by various sources, such as damage in the dielectric substrates and formation of an imperfect boundary layer near the interface [1]. The properties of the material near the interface could also be widely different from those of the bulk material on either side [4]. All these contribute to R_b, making it larger than that predicted by AMM and DMM. Swartz and Pohl [5] attributed the large value of R_b above 30 K to the formation of an amorphous layer near the interface.

Deviation from the Debye density of states (DOS) at high temperatures also contributes to a difference in R_b, as shown by Phelan [6] for high-temperature superconductors (HTSC) and by Stoner and Maris for FCC materials [7]. But incorporation of a more realistic DOS also falls short in explaining the large values of R_b at high temperatures [5].

From a careful review of the literature on R_b, it seems that scattering near the interface plays a far more dominant role than any other mechanism [5]. Though scattering near the interface has been considered in the past [4,8], these models were either far too complicated or were too simple (i.e., inaccurate) for engineering use. A new model called the scattering-mediated acoustic mismatch model (SMAMM) is developed in this paper, which accurately describes the behavior of R_b at high temperatures and reduces to the AMM at low temperatures, where the AMM is very successful in predicting R_b.

SMAMM is developed by observing the close analogy between radiative and phonon heat transport [9]. The equation of phonon radiative transport (EPRT) and the equation of radiative transport (ERT), as written below for the one-dimensional case are identical, except for the absence of in-scattering, emission and absorption terms in the EPRT [9]:

$$\frac{1}{v}\frac{\partial I}{\partial t}+\mu\frac{\partial I}{\partial x}=\frac{I^0-I}{l}\quad(\text{EPRT}),\tag{1}$$

where v is the speed of phonons, l the mean free path, μ the direction cosine, I the intensity, and I^0 the equilibrium intensity. The form of the ERT is [9]

$$\frac{1}{c}\frac{\partial I}{\partial t}+\mu\frac{\partial I}{\partial x}=\sigma_0 I^0-(\sigma_{\text{abs}}+\sigma_{\text{scatt}})I+\frac{\sigma_{\text{scatt}}}{4\pi}\times\int_{4\pi}\phi(W'\rightarrow W)I'\,dW\quad(\text{ERT}),\tag{2}$$

where c is the speed of light, σ_{abs} and σ_{scatt} the absorption and scattering coefficients, respectively, ϕ the phase function, and W

Contributed by the Heat Transfer Division for publication in the JOURNAL OF HEAT TRANSFER. Manuscript received by the Heat Transfer Division June 1, 1999; revision received, July 12, 2000. Associate Editor: A. Majumdar.

the solid angle. Note that l in the EPRT corresponds to the reciprocal of the extinction coefficient ($\sigma_{\mathrm{abs}}+\sigma_{\mathrm{scatt}}$) in the ERT [9].

It is well recognized that absorption of the EM wave is responsible for a complex refractive index for photons, but to a certain degree the attenuation of light through a slab of particles imbedded in a homogenous medium is also governed by the scattering of light by these particles. Bohren and Huffman [10] have shown that in this kind of a medium the extinction is a sum of absorption and scattering of light by these particles. They also write that even if the particles are non-absorbing, the imaginary part of the refractive index can be non-zero, as shown in the next section. For a collection of such particles, therefore, the concept of an effective complex refractive index is meaningful at least as far as transmission and reflection is concerned.

It is also plausible to consider some inelastic scattering processes, such as Umklapp and Normal scattering, as absorption processes. In these processes two phonons are destroyed to generate another phonon [12]. In metals electron-phonon, normal, and Umklapp scattering mechanisms can also be present. These processes can be thought of as absorption processes in phonon transport.

As the model developed here is closely analogous to radiative transport, a brief review of radiative transport is given in the second section. The third section is devoted to the development of the SMAMM. Finally the SMAMM is used to calculate R_b for two sample interfaces.

2 Extinction of Electromagnetic Waves by a Slab of Particles Embedded in a Homogeneous Medium

Both scattering and absorption affect the transport of electromagnetic (EM) waves across an interface. Scattering and absorption are not mutually independent processes [10]. Refraction of EM waves at an interface is a manifestation of scattering by many molecules that comprise the medium. Because of this reason, all the different models of radiative properties (e.g., Drude and Lorentz models) contain a scattering time in the form of a damping term [9,10]. The effect of both scattering and absorption is to attenuate the incoming wave. Care has to be taken in differentiating the scattering by small particles and other sources in the medium, and the scattering considered in the Lorentz and Drude models.

In an absorbing medium the refractive index (P) is complex and is given by

$$P=p+iq, \tag{3}$$

where p is the real part of P, and q is the complex part, representing attenuation of the wave. Both p and q are related to the complex dielectric constant of the medium. In a perfectly homogeneous medium attenuation is primarily due to absorption and is given by [10,11]

$$I=I_0\exp(-\sigma_{\mathrm{ab}}x), \tag{4}$$

where I_0 is the incident intensity and

$$\sigma_{\mathrm{abs}}=\frac{4\pi q}{\lambda}, \tag{5}$$

where λ is the wavelength of the EM wave. The combined effect of absorption and scattering is called extinction. A good example of extinction is the extinction of EM waves by a collection of small particles in a homogeneous medium. In this case the intensity is given by [10]

$$I=I_0\exp(-\sigma_{\mathrm{ex}}x) \tag{6}$$

where $\sigma_{\mathrm{ext}}=\sigma_{\mathrm{abs}}+\sigma_{\mathrm{scat}}$.

Noting the similarity between a purely absorbing case and a combined scattering and absorbing case, from Eqs. (4) and (6) an effective refractive index, $\tilde{P}$, can be defined and is given by [10]

$$\frac{\tilde{P}}{P}=1+if(\sigma_{\mathrm{scatt}}), \tag{7}$$

where f is a function. The concept of an effective refractive index is very convenient as far as transmission and reflection are concerned. It is this relation which forms the basis for the development of SMAMM. Even if the particles and the medium are nonabsorbing, the imaginary part of $\tilde{P}$ can be nonzero due to scattering.

3 Scattering-Mediated Acoustic Mismatch Model—Formulation

Considering the similarity between the EPRT and ERT discussed in Section 2, the solution of the EPRT at a boundary for a one-dimensional system is given by

$$I=I_0\exp(-x/l), \tag{8}$$

where $1/l$ is the reciprocal of the scattering or extinction coefficients, as the absorption term is absent in EPRT. The effect of the above relation is to dampen the incoming wave or phonon in the medium, as shown in Fig. 1. Medium 1 in Fig. 1 is nonattenuating. It is to be noted that Eq. (8) describes the effect of scattering *within* the medium on the scattering *at* the interface. In the AMM, scattering manifested as specular reflection at the interface is assumed to be independent of the scattering in the bulk of the medium. If the medium is acoustically thin, then l is much larger than the physical thickness of the medium. In such conditions there is hardly any scattering within the medium, which is given by the probabilistic relation $p'=\exp(-x/l)$ [9], where p' is the probability that the particle would travel a distance x without undergoing a collision. A careful comparison shows that this relation is another form of Eq. (8). Therefore, in acoustically thin media it is expected that there is hardly any scattering within the medium. Since l increases with decreasing temperature (T) [12], it is also expected that scattering has hardly any effect on the reflection and transmission of acoustic waves at very low temperatures, and thus the AMM is very accurate in predicting R_b at low temperatures.

The discussion in the preceding paragraph is analogous to the absorption of sound in fluids [13]. Kinsler and Frey [13] discussed the effect of heat conduction on the attenuation of sound. It is to be noted that the relaxation time associated with heat conduction in fluids is nothing but the mean free time of the heat carriers in the fluid [13].

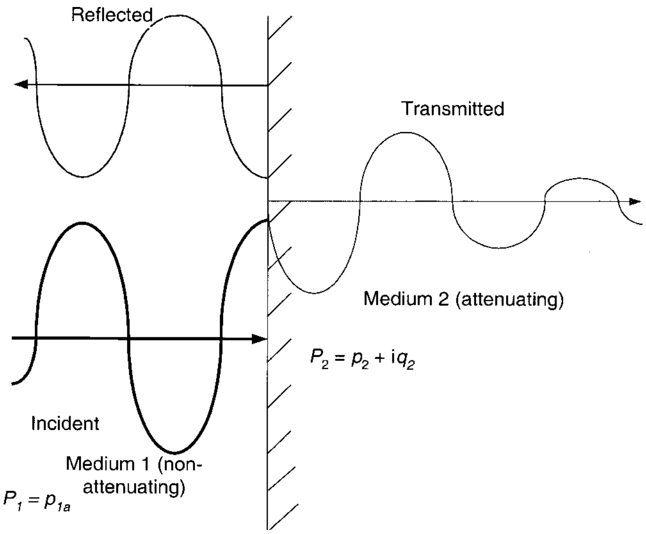

Fig. 1 **Reflection and transmission of a normally incident phonon wave on an attenuating medium**

Before delving into the development of the model some of the key assumptions are described below:

1 Debye DOS is used for the calculation of the energy within the solid.

2 No mode conversion is assumed in this model because the idea is to explore the effect of scattering on R_b. Furthermore, the inclusion of mode conversion, although theoretically straightforward, is mathematically too complex. Therefore only longitudinal vibration is assumed. This was also the assumption by Little [14].

3 Even though mode conversion is neglected, the combined effect of other modes is considered by using the Debye speed for phonons [15].

4 Diffuse scattering at the interface is totally ignored. As discussed earlier the DMM model, based on diffuse scattering at the interface, gives results that are largely indistinguishable from those of the AMM for solid-solid interfaces.

The effect of damping on wave motion is described by the well-known wave equation

$$\frac{d^2y}{dt^2}+\frac{1}{\vartheta}\frac{dy}{dt}=v^2\frac{d^2y}{dx^2}, \tag{9}$$

where ϑ is the damping term, which has units of time. The solution to Eq. (9) can be easily obtained if a wave of the following form is considered

$$y=Y\exp[i(kx-\omega t)], \tag{10}$$

where Y is the amplitude of vibration, k the wave vector and ω the angular frequency. Direct substitution of Eq. (10) in Eq. (9) gives

$$k=\frac{\omega}{v}\left[1+\frac{i}{\vartheta\omega}\right]^{1/2}. \tag{11}$$

The above relation can be separated into real and imaginary parts by the following treatment, which is quite similar to the treatment of EM waves [11]. Let

$$a'+ib'=\left[1+\frac{i}{\vartheta\omega}\right]^{1/2}. \tag{12}$$

Now from Eqs. (11) and (12) a complex speed ($\tilde{v}$) of the wave motion under consideration can be defined as

$$\tilde{v}=\frac{v}{a'+ib'}. \tag{13}$$

Simplification of Eq. (12) leads to

$$a'^2=\frac{1+\sqrt{1+\left(\frac{1}{\vartheta\omega}\right)^2}}{2},\quad b'^2=\frac{-1+\sqrt{1+\left(\frac{1}{\vartheta\omega}\right)^2}}{2}. \tag{14}$$

Using Eqs. (10)–(12) the solution of the damped wave equation is

$$y=Y\exp\left(-\frac{\omega}{v}b'x\right)\exp\left[i\left(\frac{\omega}{v}a'x-\omega t\right)\right]. \tag{15}$$

Therefore, the amplitude of vibration of the damped wave is given by

$$Y_d=Y\exp\left(-\frac{\omega}{v}b'x\right), \tag{16}$$

where Y_d is the damped amplitude. It is well known that I is [11]

$$I\propto Y_d^2\propto Y^2\exp\left(\frac{-2\omega b'}{v}x\right). \tag{17}$$

Comparing the exponential terms in Eqs. (8) and (17) it is easily seen that

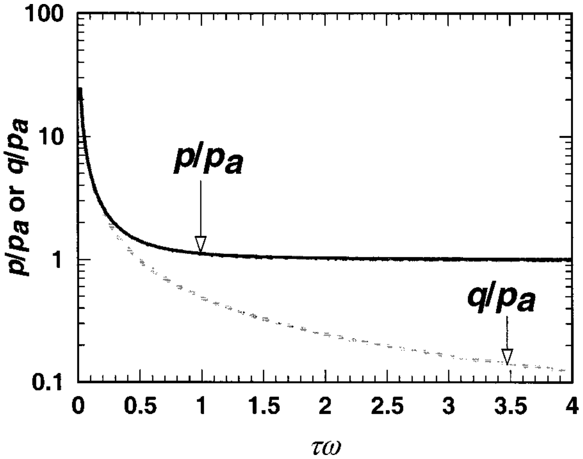

Fig. 2 Real (p) and imaginary (q) parts of the acoustic refractive index, normalized by the AMM refractive index (p_a)

$$b'=\frac{v}{2l\omega}=\frac{1}{2\tau\omega}, \tag{18}$$

where $\tau=l/v$ is the scattering time. This comparison between Eqs. (8) and (17) is applied in radiation as well [11]. With the help of Eqs. (18) and (14) a' can be deduced as

$$a'=\sqrt{1+\left(\frac{1}{2\tau\omega}\right)^2}. \tag{19}$$

The value of ϑ given by Eqs. (18) and (14) is

$$\vartheta=\frac{\tau}{\sqrt{1+\left(\frac{1}{2\tau\omega}\right)^2}}. \tag{20}$$

Thus, the damping time ϑ depends on both scattering time τ and frequency ω.

Now a complex refractive index for the acoustic case can also be defined along the lines of the EM waves. The refractive index of the acoustic wave is complex because of the scattering and is analogous to Eq. (7) for radiation. But note that the refractive index of EM waves can be imaginary even in the absence of scattering [10,16]. Thus for the acoustic case

$$P=\frac{1}{\rho\tilde{v}}=p+iq, \tag{21}$$

where ρ is the mass density and $p=a'/\rho v$, $q=b'/\rho v$. P is just the reciprocal of the acoustic impedance (Z), where $Z=\rho v$ [5]. Since the attenuating term is absent in AMM, for that limiting case P is real and is written as p_a, and is simply given by $p_a=1/\rho v$. The subscript a refers to the properties calculated in AMM. The ratios of p and q with p_a are plotted against $\tau\omega$ in Fig. 2. Some of the key features of Fig. 2 are as follows: (1) both p and q are equal and very large, at low values of $\tau\omega$. This is consistent with the EM wave case, where p and q are equal at long wavelengths or equivalently small ω [11]. This behavior of p and q can also be attributed to the decrease in the scattering time, which results in more attenuation. (2) p approaches p_a and q approaches 0 at large values of $\tau\omega$. The reason for this behavior is that an increasing value of $\tau\omega$ means an increasing scattering time, which results in a large l. Large l means less attenuation and thereby less deviation from AMM.

The reflectance coefficient, r', at the interface between two solids is given by [14,17]

$$r' = \frac{Y_r}{Y_i} = \frac{\left[\dfrac{\cos(\theta_1)}{\rho_1 \tilde{v}_1} - \dfrac{\cos(\theta_2)}{\rho_2 \tilde{v}_2}\right]}{\left[\dfrac{\cos(\theta_1)}{\rho_1 \tilde{v}_1} + \dfrac{\cos(\theta_2)}{\rho_2 \tilde{v}_2}\right]}, \tag{22}$$

where Y_r and Y_i are the reflected and incident amplitudes, respectively, and θ_1 and θ_2 the complex incident and refracted angles in medium 1 and 2, respectively [11]. θ_1 and θ_2 are both real in the AMM limit. Application of Snell's law provides [11,14]

$$\tilde{v}_1 \sin(\theta_2) = \tilde{v}_2 \sin(\theta_1) \tag{23}$$

which reduces to

$$\frac{\cos(\theta_2)}{\tilde{v}_2} = \sqrt{\left(\frac{1}{\tilde{v}_2}\right)^2 - \left(\frac{1}{\tilde{v}_1}\right)^2 \sin^2(\theta_1)}. \tag{24}$$

Using Eq. (13), Eq. (24) can be separated into complex and imaginary parts as shown below

$$A - iB = \frac{\cos(\theta_2)}{\tilde{v}_2} = \sqrt{\frac{(a_2' + ib_2')^2}{v_2^2} - \frac{(a_1' + ib_1')^2}{v_1^2} \sin^2(\theta_1)}. \tag{25}$$

The values of A and B, obtained by a simple mathematical manipulation [11] are

$$2A^2 = \left[\left(\frac{a_2'^2 - b_2'^2}{v_2^2} - \frac{a_1'^2 - b_1'^2}{v_1^2}\sin^2(\theta_1)\right)^2 + 4\left(\frac{a_1' b_1'}{v_1^2}\sin^2(\theta_1) - \frac{a_2' b_2'}{v_2^2}\right)^2\right]^{1/2} + \left(\frac{a_2'^2 - b_2'^2}{v_2^2} - \frac{a_1'^2 - b_1'^2}{v_1^2}\sin^2(\theta_1)\right) \tag{26a}$$

$$2B^2 = \left[\left(\frac{a_2'^2 - b_2'^2}{v_2^2} - \frac{a_1'^2 - b_1'^2}{v_1^2}\sin^2(\theta_1)\right)^2 + 4\left(\frac{a_1' b_1'}{v_1^2}\sin^2(\theta_1) - \frac{a_2' b_2'}{v_2^2}\right)^2\right]^{1/2} - \left(\frac{a_2'^2 - b_2'^2}{v_2^2} - \frac{a_1'^2 - b_1'^2}{v_1^2}\sin^2(\theta_1)\right). \tag{26b}$$

Therefore, r' from Eq. (22) reduces to

$$r' = \frac{\left[\dfrac{\cos(\theta_1)}{\rho_1 v_1} a_1' - \dfrac{A}{\rho_2}\right] + i\left[\dfrac{\cos(\theta_1)}{\rho_1 v_1} a_1' + \dfrac{B}{\rho_2}\right]}{\left[\dfrac{\cos(\theta_1)}{\rho_1 v_1} a_1' + \dfrac{A}{\rho_2}\right] + i\left[\dfrac{\cos(\theta_1)}{\rho_1 v_1} a_1' - \dfrac{B}{\rho_2}\right]}. \tag{27}$$

Now the reflectivity (R') is the product of r' and its complex conjugate, giving

$$R'(\theta_1) = r'\overline{r'} = \frac{\left[\dfrac{\cos(\theta_1)}{\rho_1 v_1} a_1' - \dfrac{A}{\rho_2}\right]^2 + \left[\dfrac{\cos(\theta_1)}{\rho_1 v_1} a_1' + \dfrac{B}{\rho_2}\right]^2}{\left[\dfrac{\cos(\theta_1)}{\rho_1 v_1} a_1' + \dfrac{A}{\rho_2}\right]^2 + \left[\dfrac{\cos(\theta_1)}{\rho_1 v_1} a_1' - \dfrac{B}{\rho_2}\right]^2}. \tag{28}$$

The transmissivity α is given by

$$\alpha(\theta_1) = 1 - R'(\theta_1). \tag{29}$$

Note that α is the equivalent of emissivity in radiation. Just like the normal emissivity in radiation, α for normal incidence is a very valuable parameter in providing physical insight to the behavior at the interface. For normal incidence Eq. (28) reduces to

$$R'_{\text{normal}} = \frac{(p_1 - p_2)^2 + (q_1 - q_2)^2}{(p_1 + p_2)^2 + (q_1 + q_2)^2}. \tag{30}$$

If it is assumed that medium 1 is non-attenuating, the physical basis for which is provided later, then $p_1 = p_{1_a}$ and $q_1 = 0$. With this assumption Eq. (30) reduces to

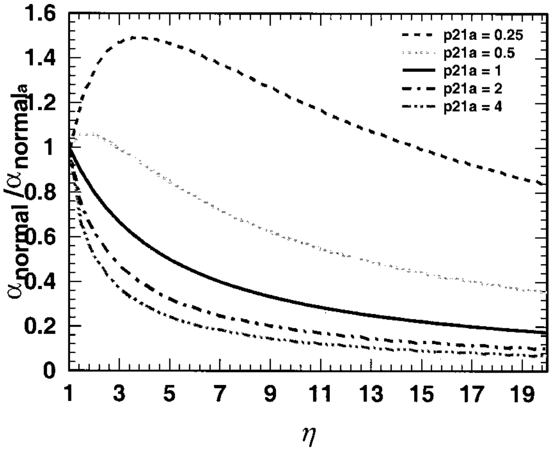

Fig. 3 Ratio of the normal transmissivity calculated from the SMAMM and AMM versus η

$$R'_{\text{normal}} = \frac{(p_{21} - 1)^2 + (q_{21})^2}{(p_{21} + 1)^2 + (q_{21})^2}, \tag{31}$$

where $p_{21} = p_2/p_{1_a}$, and $q_{21} = q_2/p_{1_a}$. With the help of Eqs. (18) and (19) and the definition of p and q the following holds between p and q:

$$q^2 = p^2 - p_a^2. \tag{32}$$

Substitution of Eq. (32) into Eq. (31) results in

$$\alpha_{\text{normal}} = \frac{4p_{21}}{(p_{21} + 1)^2 + (p_{21})^2 - (p_{21_a})^2}, \tag{33}$$

where $p_{21_a} = p_{2_a}/p_{1_a}$. The corresponding α for the AMM case is given by

$$\alpha_{\text{normal}_a} = \frac{4p_{21_a}}{(p_{21_a} + 1)^2}. \tag{34}$$

The ratio of the two α's from Eqs. (33) and (34) is

$$\frac{\alpha_{\text{normal}}}{\alpha_{\text{normal}_a}} = \frac{\eta\left(1 + \dfrac{1}{p_{21_a}}\right)^2}{\left(\eta + \dfrac{1}{p_{21_a}}\right)^2 + \eta^2 - 1}, \tag{35}$$

where $\eta = p_{21}/p_{21_a}$. The ratio of α_{normal} and α_{normal_a} versus η is plotted in Fig. 3. Note that the minimum value of η is 1. For $p_{21_a} > 1$, Fig. 3 shows that α_{normal} is less than α_{normal_a}. Increasing value of η means increasing p_{21} and q_{21}, resulting in more attenuation. Therefore, η is a measure of attenuation, and $\alpha_{\text{normal}}/\alpha_{\text{normal}_a}$ decreases for increasing η. For large values of η, α_{normal} is much less than α_{normal_a}, which would result in an increase in R_b. It is interesting to note that for $p_{21_a} < 1$, α_{normal} reaches a peak and then decreases again. The analogous regime in radiation is called the regime of ''anomalous dispersion'' [10].

α_a for any angle of incidence is written below only in terms of θ_1 [14]

$$\alpha_a(\theta_1) = \frac{4p_{21_a}\cos(\theta_1)\sqrt{1 - \left[\dfrac{v_2}{v_1}\sin(\theta_1)\right]^2}}{\left[\cos(\theta_1) + p_{21_a}\sqrt{1 - \left[\dfrac{v_2}{v_1}\sin(\theta_1)\right]^2}\right]^2}. \tag{36}$$

The evaluation of R_b is now a relatively simple task and the actual derivation is not repeated here as it is available in the literature [14,6]. But there are a few concepts that are only pertinent to this work, such as no mode conversion and the presence of a nonattenuating medium on one side of the interface. If the usual simplification to make the calculation from only one side of the interface, by invoking the 2nd law of thermodynamics, is made then [1,6]

$$\dot{q}=\frac{3}{4\pi^2}\frac{1}{v_1^2}\int_0^{\pi/2}\int_0^{\omega_{d_<}}\hbar\omega^3\left[\frac{1}{\exp\left(\frac{\hbar\omega}{k_bT_2}\right)-1}-\frac{1}{\exp\left(\frac{\hbar\omega}{k_bT_1}\right)-1}\right]\alpha(\theta,\omega)\sin(\theta)\cos(\theta)\,d\omega\,d\theta, \qquad (37)$$

where $\dot{q}$ is the net heat flux across the interface, $\omega_{d_<}$ the smaller Debye frequency among the two media, $\hbar$ Planck's constant, and k_b the Boltzmann constant. Note that α is also a function of ω in the SMAMM, but is independent of ω in the AMM. The calculation of $\dot{q}$ is performed from the side of the nonattenuating medium. This simplifies the analysis because the integration over θ can now be performed without worrying about the critical angle, as the critical angle generally occurs on the side of the attenuating medium. The reason for this is that the material having a higher Debye temperature (θ_d) is the nonattenuating medium because of its larger l [12], and for most pairs of materials used in engineering v is higher for materials having larger θ_d, thereby making the nonattenuating medium independent of the critical angle. This fact about θ_d and v can be verified for the cases considered in Swartz's Ph.D. thesis [1]. For the common dielectric substrates (Al_2O_3, MgO etc.) θ_d is of the order of 1000 K which is generally much higher than that of the film deposited on them.

Since α is also a function of ω, an integrated transmission coefficient [14,18] cannot be directly defined. But following the method used in radiation to obtain total hemispherical properties from the directional spectral properties [11] an integrated transmission coefficient (Γ_{smamm}) for the SMAMM can be defined as

$$\Gamma_{\text{smamm}}=\frac{\displaystyle\int_0^{\pi/2}\int_0^{\omega_{d_<}}\frac{\alpha(\theta,\omega)G(\omega)}{\exp\left(\frac{\hbar\omega}{k_bT}\right)-1}\sin(\theta)\cos(\theta)\,d\omega\,d\theta}{\displaystyle\int_0^{\omega_{d_<}}\frac{G(\omega)}{\exp\left(\frac{\hbar\omega}{k_bT}\right)-1}\,d\omega}, \qquad (38)$$

where $G(\omega)$ is the density of states.

R_b is finally given by

$$R_b=\frac{T_2-T_1}{\dot{q}}=\frac{\Delta T}{\dot{q}}, \qquad (39)$$

where it is assumed that the net heat flux is from medium 2 to medium 1. For calculation of R_b a ΔT of 0.2 K is chosen, and the results are plotted against the substrate temperature (T_1).

4 R_b Calculation for Various Interfaces

Until now the development of the SMAMM is very general in nature, as there have been no assumptions regarding the scattering types and conditions (i.e., the value of τ has not been fixed). Scattering within a solid is a complex phenomenon [12]. Usually different simplifying assumptions are made to understand different properties dependent on the scattering [12,15]. The direct measurement of the scattering time is a monumental task and indirect methods are used to calculate the scattering time. One of the most common methods is to estimate τ from thermal conductivity measurements by using the following kinetic theory expression [19,20]

$$K=\frac{1}{3}Cvl_{\text{eff}}, \qquad (40)$$

where K is the thermal conductivity, l_{eff} the effective mean free path, and C the specific heat per unit volume. l_{eff} is given by Matthiessen's rule [12] and results from a combination of different scattering mechanisms. Some of the common scattering mechanisms are: lattice imperfections, inelastic scattering, and boundary scattering [12,21]. Boundary scattering is basically the reflection at the interface and as already mentioned it is independent of scattering occurring in the bulk at very low temperatures (AMM), and is dependent on the scattering within the medium at high temperatures (SMAMM). There are two types of three-phonon inelastic scattering: the N process and the U process [9,21]. Both of these processes conserve phonon energy before and after the scattering. The N process also conserves momentum and therefore does not pose any resistance to heat flow [12]. Although N processes have been shown to influence the heat flux indirectly, it is usually neglected [9]. At very low temperatures boundary scattering is dominant. At intermediate cryogenic temperatures impurity scattering is important, and as the temperature increases U processes become prominent [9,21]. It is worth mentioning that different temperature regimes are relative and are dependent on θ_d. Room temperature can be considered as very low temperature for diamond, as its θ_d is enormously large [9].

Boundary scattering, which is usually dominant at very low temperatures, affects both K and R_b. It does not affect K as the temperature is increased but R_b is still dependent on the boundary scattering. The effect of bulk scattering on boundary scattering, which increases as the temperature is increased, has mostly been neglected in the past because of two reasons: (1) it doesn't affect K and (2) lack of applications where R_b plays an important role at higher temperatures. But now with the increasing trend towards the miniaturization of devices and the advent of high-temperature superconductors, accurate prediction of R_b is essential [6,22]. The bulk scattering affecting the boundary scattering is basically the scattering occurring very close to the interface. This is because scattering occurring within one mean free path will only affect the boundary scattering. The scattering time near the interface is different from the scattering in the bulk of the medium for the reasons shown later.

Even though impurity scattering is dominant at moderate cryogenic temperatures, only U processes are considered here as the idea is to show the effects of scattering on R_b and to keep the analysis simple. But note that the model is very general in nature and different kinds of scattering can be easily incorporated into the model.

Several expressions for the relaxation times for U processes are available in the literature, but which is correct is still a matter of discussion [19]. The most commonly used expression for the U process relaxation time, τ_u, is [21,9]

$$\tau_u=\bar{D}\frac{T}{\theta_d\omega}\exp\left(\frac{\theta_d}{\varphi T}\right), \qquad (41)$$

where φ is a parameter of the order unity representing the effect of crystal structure, and $\bar{D}$ is a nondimensional parameter, given by [21]

$$\bar{D}=\frac{Mav}{16\pi\gamma^2\hbar}, \qquad (42)$$

where γ is the Grüneisen constant [17], M the atomic mass, and a the lattice spacing. Equation (41) shows that there can be multiple relaxation times because of the dependence on ω. But the phonons of the dominant ω are primarily involved in the thermal transport

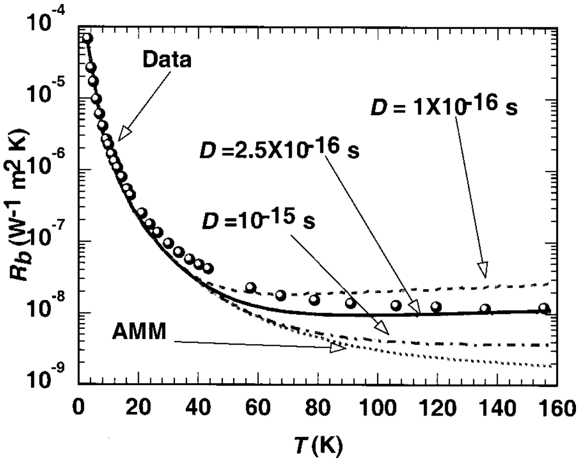

Fig. 4 Comparison of R_b calculated by SMAMM with experimental data [1] for Rh/MgO interface

process, and so ω in Eq. (41) is usually replaced by the dominant phonon frequency, given by $\omega_d = k_b T/\hbar$ [9]. With this Eq. (41) reduces to

$$\tau_u = D \exp\left(\frac{\theta_d}{\varphi T}\right), \tag{43}$$

where

$$D = \frac{Mav}{16\pi k_b \gamma^2 \theta_d}. \tag{44}$$

It is interesting to note that D has the units of time and is generally of the order of pico-seconds or lower, and it is dependent only on the properties of the material. The value of φ is taken as 2 for the present calculations [8,23]. As shown later, R_b is very sensitive to the value of D, and D is used as a fitting parameter for the prediction of R_b.

The first set of calculations is performed for a Rh/Al_2O_3 interface as shown in Fig. 4. The required material properties are listed in Table 1. v is taken as the Debye speed, and the experimental data are taken from Swartz's Ph.D. thesis [1]. Figure 4 shows the general trend that decreasing D, which means an increasing scattering rate because τ_u decreases, increases the value of R_b at higher temperatures compared to that predicted by AMM. Figure 4 also shows that the SMAMM reduces to the AMM at low temperatures because τ_u increases as the temperature is lowered. AMM and SMAMM match very well with the data at low temperatures, showing that neglecting the mode conversion and using the Debye speed is not a bad assumption.

Table 1 Physical properties of the considered materials

Material	v (m s^{-1})	ρ (kg m^{-3})	θ_d (K)	D_0 (s)
Rh[a]	4318	12400	480	2×10^{-13}
Al_2O_3[a]	7144	3970	1042	-
YBCO[b]	3313	6338	410	4.5×10^{-14}
MgO[b]	6667	3576	946	-

[a] Swartz (1987); [b] Phelan (1998)

At high temperatures the exponential term in Eq. (43) is not dominant and is of the order unity, and τ_u is primarily dependent on D, whereas at low temperatures the exponential term is far more dominant. The value of $D = 2.5\times10^{-16}$ s gives the best fit for R_b in Fig. 4. The values of D (D_0) calculated from Eq. (44) are also listed in Table 1. Using the value of D_0 does not predict R_b anywhere close to the data but it does predict R_b very close to that of the AMM. The value of D that provides the best fit to the experimental data is approximately 3 orders of magnitude lower than D_0. Since D is dependent only on the material properties, its value near the interface will be different than that in the bulk, because the properties of the interface material can be different from those of the bulk [4]. Another reason for the very small value of D is that we have completely ignored defect scattering, which can also be prominent at the interface due to substrate damage [5]. As D is the measure of scattering time, its value is further reduced by neglecting defect scattering to match R_b with the experimental data. Although the value of D is an indication of the scattering time, the exact value of scattering time at the temperatures under consideration is an order of magnitude more than the value of D, as seen by Eq. (43) due to the contribution of the exponential term. The value of τ at 100 K for Rh, assuming $D = 2.5\times10^{-16}$ s (Fig. 4), is $\tau \cong 3$ fs.

It is also to be remembered that due to substrate damage, the interface behaves more like an amorphous solid than a crystalline solid [5]. The mean free path of phonons in an amorphous solid is generally much lower than in its crystalline counterpart. In amorphous quartz l is as much as 3 orders of magnitude lower than that in crystalline quartz at moderate cryogenic temperatures [19]. Even though the scattering here is modeled solely as U processes, the scattering time calculated by using the value of τ obtained from the curve fitting is a reflection of the overall scattering time due to all scattering sources. As l or τ for amorphous solids can be more than 2 orders of magnitude less than those for crystalline solids, it is expected that this will be reflected in the value of τ obtained from the R_b experimental data.

The value $\tau \cong 3$ fs is still approximately 5 times lower than the scattering time possible for amorphous solids. This may be a consequence of the fact that at higher temperatures the Debye DOS is not a very good assumption [7]. For a YBCO/MgO interface De Bellis et al. [24] have shown that an R_b prediction using a realistic DOS without considering scattering is approximately 2 times higher than that predicted by AMM or DMM. If a realistic DOS is used in the SMAMM model, τ will increase compared with that calculated by using the Debye model. The various studies in the literature [5] have also indicated the presence of a disordered layer near the interface. It is reasonable to expect that the measured value of R_b also includes the bulk thermal resistance of these layers. Reduced bulk transport in the disordered layer also contributes to the observed R_b [5]. Swartz and Pohl [5] tried to explain the high values of R_b at high temperatures by taking the worst possible thermal conductivity of these disordered layers, but were still unable to match the high values of R_b. If from the measured value of R_b one subtracts out the contribution of the bulk thermal resistance of these layers, and tries to match the remainder with the SMAMM prediction, the calculated value of τ will be closer to 10 fs, as expected for an amorphous solid.

In spite of this approximation in choosing the appropriate value of D to fit through the data, Fig. 4 clearly shows the importance of scattering in the prediction of R_b. Figure 5 shows a second set of calculations performed for a YBCO/MgO interface, selected because of its practical importance [22]. The data are taken from the work of Phelan et al. [25]. Though the experimental data in actuality are those of EBCO and MgO, owing to the similarity in properties they can be used in place of YBCO [25]. Again D is used as a fitting parameter. The value of D chosen to match the data is 4.5×10^{-14} s. For YBCO D_0 is calculated using an effective lattice constant and an average M including all its constituents. The effective lattice constant is given by [26]

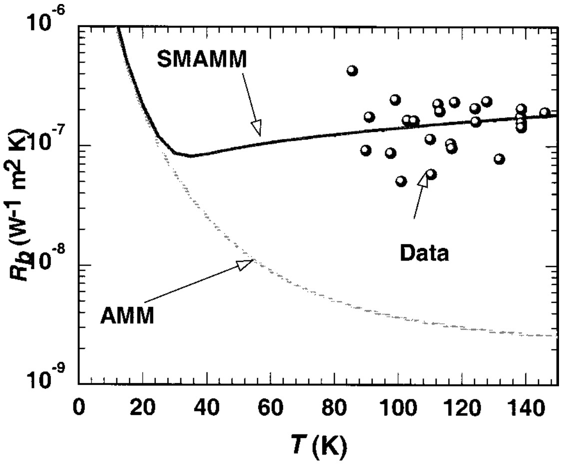

Fig. 5 Comparison of R_b calculated by SMAMM with experimental data for a YBCO/MgO interface [25], where $D = 4.5\times 10^{-17}$ s

$$a = \frac{\pi}{(6\pi^2 n)^{1/3}}, \tag{45}$$

where n is the atomic density per unit volume [27]. Again the value of D chosen to match the data is 3 orders of magnitude less than D_0, but the scattering time in the regime of interest is 1 fs, and some of the reasons for this low value of τ for this interface are the same as those for the Rh/Al_2O_3 interface. Both Figs. 4 and 5 show that with the proper choice of D, SMAMM not only predicts the magnitude but also the general shape of how R_b varies with the temperature T. Both figures also show that increased scattering can lead to an R_b increasing with T.

The discussions in the preceding paragraphs indicate that the exact physical composition and properties of the interface are not known. But SMAMM provides new opportunities to characterize the interface by matching experimental R_b data with calculated values by choosing the proper value of the scattering time. Different models of scattering can easily be incorporated in SMAMM because of its generality. Since the scattering time depends on the physical properties and the microstructure of the solid, the value of scattering time obtained from R_b data and applying SMAMM can be used as a quantitative tool to study the properties near the interface.

5 Conclusion

A new model called the scattering-mediated acoustic mismatch model (SMAMM), which incorporates scattering in the basic acoustic mismatch model (AMM), is developed in this paper. With the help of a fitting parameter the SMAMM is very successful in predicting R_b at high temperatures and reduces to the AMM at low temperatures. The SMAMM can be used to quantify differences in the near interfacial physical properties from those of the bulk material.

Acknowledgments

P.E.P. gratefully acknowledges the support of the National Science Foundation through a CAREER Award (Grant No. CTS-9696003).

Nomenclature

a = lattice constant (Å)
a', b' = defined in Eq. (12)
c = speed of light (m s^{-1})
D = parameter in Umklapp scattering; defined in Eq. (44) (s)
$\overline{D}$ = parameter in Umklapp scattering; defined in Eq. (42)
$\hbar$ = Planck's constant divided by $2\pi = 1.055\times 10^{-34}$ J s
I = intensity (W m^{-2} sterad^{-1})
I^0 = equilibrium intensity (W m^{-2} sterad^{-1})
I_0 = incident intensity (W m^{-2} sterad^{-1})
k = wave vector (m^{-1})
k_b = Boltzmann constant $= 1.3806\times 10^{-23}$ J K^{-1}
l = mean free path (m)
M = average mass of atoms (kg)
n = atomic density (m^{-3})
p' = probability
p = real part of refractive index
P = refractive index
$\tilde{P}$ = effective refractive index
q = complex part of refractive index
$\dot{q}$ = heat flux (W m^{-2})
r' = reflectance coefficient
R' = reflectivity of phonons as defined in Eq. (28)
T = temperature (K)
v = speed of phonons (m s^{-1})
$\tilde{v}$ = complex speed of phonons
W = solid angle (sterad)
Y_d = damped amplitude of vibration (m)
Y_i = incident amplitude (m)
Y_r = reflected amplitude (m)

Greek

σ_{abs} = absorption coefficient (m^{-1})
ϑ = damping coefficient (N m^{-1} s)
φ = defined in Eq. (41)
μ = direction cosine
σ_{ext} = extinction coefficient (m^{-1})
γ = Grüneisen constant
Γ = integrated transmission coefficient in the AMM
ρ = mass density (kg m^{-3})
α = transmission probability of phonons
λ = wavelength (m)
θ = angle of incidence or refraction (rad)
θ_d = Debye temperature (K)
τ = scattering time (s)
ω = phonon angular frequency (rad s^{-1})
ω_d = Debye frequency (rad s^{-1})

Subscripts

a = properties calculated by AMM
smamm = properties calculated by SMAMM
u = Umklapp processes
1, 2 = sides 1 and 2, respectively

References

[1] Swartz, E. T., 1987, ''Solid-Solid Thermal Boundary Resistance,'' Ph.D. thesis, Cornell University, Ithaca, NY.
[2] Cahill, D. G., 1998, ''Heat Transport in Dielectric Thin Films and at Solid-Solid Interfaces,'' in *Microscale Energy Transport*, C. L. Tien, A. Majumdar, and F. M. Gerner, eds., chap. 2, Taylor and Francis, Washington, DC, pp. 95–117.
[3] Goodson, K. E., Ju, Y. S., and Asheghi, M., 1998, ''Thermal Phenomena in Semiconductor Devices and Interconnects,'' in *Microscale Energy Transport*, C. L. Tien, A. Majumdar, and F. M. Gerner, eds., chap. 7, Taylor and Francis, Washington, DC, pp. 229–293.
[4] Kozorezov, A. G., Wigmore, J. K., Erd, C., Peacock, A., and Poelaert, A., 1998, ''Scattering-Mediated Transmission and Reflection of High-Frequency Phonons at a Nonideal Solid-Solid Interface,'' Phys. Rev. B, **57**, No. 13, pp. 7411–7414.
[5] Swartz, E. T., and Pohl, R. O., 1989, ''Thermal Boundary Resistance,'' Rev. Mod. Phys., **61**, No. 3, pp. 605–668.
[6] Phelan, P. E., 1998, ''Application of Diffuse Mismatch Theory to the Prediction of Thermal Boundary Resistance in Thin-Film High-T_c Superconductors,'' J. Heat Transfer, **120**, No. 1, pp. 37–43.
[7] Stoner, R. J., and Maris, H. J., 1993, ''Kapitza Conductance and Heat Flow Between Solids at Temperatures from 50 to 300 K,'' Phys. Rev. B, **48**, No. 22, pp. 16373–16387.
[8] Burkhard, G., Sawaoka, A. B., and Phelan, P. E., 1995, ''The Effect of

Umklapp-Processes on the Heat Transport of Solids: Evaluation of the Thermal Boundary Resistance of Two Joined Solids,'' in *Symposium on Thermal Science and Engineering in Honor of Chancellor Chang-Lin Tien*, R. Buckius et al., eds., University of California, Berkeley, pp. 145–152.

[9] Majumdar, A., 1993, ''Microscale Heat Conduction in Dielectric Thin Films,'' J. Heat Transfer, **115**, No. 1, pp. 7–16.

[10] Bohren, C. F., and Huffman, D. R., 1983, *Absorption and Scattering of Light by Small Particles*, Wiley, New York, pp. 1–81.

[11] Siegel, R., and Howell, J. R., 1992, *Thermal Radiation Heat Transfer*, 3rd Ed., Hemisphere, Washington, pp. 1–150.

[12] Ziman, J. M., 1960, *Electrons and Phonons*, Oxford University Press, pp. 288–333.

[13] Kinsler, L. E., and Frey, A. R., 1967, *Fundamentals of Acoustics*, 2nd Ed., Wiley, New York, pp. 217–246.

[14] Little, W. A., 1959, ''The Transport of Heat Between Dissimilar Solids at Low Temperatures,'' Can. J. Phys., **37**, pp. 334–349.

[15] Ashcroft, N. W., and Mermin, N. D., 1976, *Solid State Physics*, W. B. Saunders, Philadelphia, PA, pp. 415–450.

[16] Majumdar, A., 1998, ''Microscale Energy Transport in Solids,'' in *Microscale Energy Transport*, C. L. Tien, A. Majumdar, and F. M. Gerner, eds., chap. 1., Taylor and Francis, Washington, DC, pp. 3–94.

[17] Elmore, W. C., and Heald, M. A., 1969, *Physics of Waves*, Dover, New York, pp. 1–163.

[18] Cheeke, J. D. N., Ettinger, H., and Hebral, B., 1976, ''Analysis of Heat Transfer Between Solids at Low Temperatures,'' Can. J. Phys., **54**, pp. 1749–1771.

[19] Berman, R., 1979, *Thermal Conduction in Solids*, Oxford University Press, Walton Street, Oxford, pp. 1–114.

[20] MacDonald, W. M., and Anderson, A. C., 1982, ''Illustrative Numerical Comparisons Between Phonon Mean Free Paths and Phonon Thermal Conductivity,'' in *Thermal Conductivity*, J. G. Hust, ed., **17**, pp. 185–193.

[21] Klemens, P. G., 1958, ''Thermal Conductivity and Lattice Vibrational Modes,'' in *Solid State Physics*, F. Seitz and T. Turnbull, eds., Academic Press, New York, **7**, pp. 1–98.

[22] Prasher, R. S., and Phelan, P. E., 1997, ''Review of Thermal Boundary Resistance of High-Temperature Superconductors,'' J. Supercond., **10**, No. 5, pp. 473–484.

[23] Rosenberg, H. M., 1989, *The Solid State*, 3rd Ed., Oxford University Press, New York, pp. 95–105.

[24] De Bellis, L., Phelan, P. E., and Prasher, R. S., 2000, ''Variations of Acoustic and Diffuse Mismatch Models in Predicting Thermal-Boundary Resistance,'' J. Thermophys. Heat Transfer, **14**, No. 2, pp. 144–150.

[25] Phelan, P. E., Song, Y., Nakabeppu, O., Ito, K., Hijikata, K., Ohmori, T., and Torikoshi, K., 1994, ''Film/Substrate Thermal Boundary Resistance for an Er-Ba-Cu-O High-T_c Thin Film,'' J. Heat Transfer, **116**, No. 4, pp. 1038–1041.

[26] Chen, G., 1997, ''Size and Interface Effects on Thermal Conductivity of Superlattices and Periodic Thin-Film Structures,'' J. Heat Transfer, **119**, No. 2, pp. 220–229.

[27] Kittel, C., 1986, *Introduction to Solid State Physics*, Wiley (SEA) PTE LTD, Singapore, pp. 80–124.

Experimental Investigations of Radially Rotating Miniature High-Temperature Heat Pipes

Jian Ling

Yiding Cao

Alex P. Lopez

Department of Mechanical Engineering,
Florida International University,
Miami, FL 33199

A radially rotating miniature high-temperature heat pipe employs centrifugal force to return the condensate in the condenser section to the evaporator section. The heat pipe has a simple structure, very high effective thermal conductance and heat transfer capacity, and can work in hostile high-temperature environments. In this research, a high-speed rotating test apparatus and data acquisition system for radially rotating miniature high-temperature heat pipes are established. Extensive experimental tests on two heat pipes with different dimensions are performed, and various effects of influential parameters on the performance characteristics of the heat pipes are investigated. The ranges of the important parameters covered in the current experiments are: $470 \leqslant \omega^2 \bar{Z} a/g \leqslant 1881$; $47\ \mathrm{W} \leqslant Q \leqslant 325\ \mathrm{W}$; $d_i = 1.5$ *and 2 mm; and* $1.05 \times 10^{-3}\ m^3/s \leqslant W \leqslant 13.4 \times 10^{-3}\ m^3/s$. *The experimental data prove that the radially rotating miniature high-temperature heat pipe has a high effective thermal conductance, which is 60–100 times higher than the thermal conductivity of copper, and a large heat transfer capacity that is more than 300 W. Therefore, the heat pipe appears to be feasible for cooling high-temperature gas turbine components.* [DOI: 10.1115/1.1332777]

Keywords: *Cooling, Heat Transfer, Heat Pipes, High Temperature, Turbines*

Introduction

A radially rotating miniature high-temperature heat pipe, or a radially rotating miniature high-temperature thermosyphon, is an effective heat transfer device which employs the centrifugal force in the heat pipe to return the condensate in the condenser section to the evaporator section, as shown in Fig. 1 [1–4]. Combining the traditional air-cooling technique with radially rotating miniature high-temperature heat pipes for gas turbine blade cooling represents a new cooling method [5]. However, before the heat pipe is employed for the turbine blade cooling, its performance characteristics must be fully understood. Extensive analytical investigations for various rotating heat pipes have been conducted in the past, and analytical solutions for the vapor temperature drop along the heat pipe length, liquid film distribution in the condenser section and heat transfer limitations have been obtained [1,2,6–11]. Experimental investigations have also been conducted for some rotating heat pipes. However, these experiments are limited to axially rotating or revolving heat pipes with a low-temperature working fluid. To the authors' knowledge, no experimental study related to high-temperature heat pipes under a radially rotating condition has been conducted in the past. Also, no attempt has been made in the literature to test miniature rotating heat pipes having a diameter on the order of 1 mm. To prove the performance and reliability of the radially rotating miniature high-temperature heat pipe and provide experimental evidence of the applicability for the turbine blade cooling application, it is necessary to conduct extensive experimental investigations close to turbine blade cooling conditions, which is the objective of this study.

Construction of a High-Speed Rotating Test Apparatus and Fabrication of Radially Rotating Miniature High-Temperature Heat Pipes

A high-speed rotating test apparatus specially built for the experimental investigation is shown in Fig. 2. For this particular apparatus, the major parameters which could be adjusted in the experiment are the revolution of the test apparatus, heat pipe operating temperatures, heat inputs to the evaporator section, and cooling-air flow rate in the condenser section. The vibration of the apparatus should also be controlled to ensure a safe operation. The shaft is driven by a motor [1] having a revolution range up to 3600 rpm. In order to dampen the vibration of the rotor, a flexible coupling is used to connect the shaft with the motor. The springs [3] connecting the rotor and frame would have a significant dampening function when the rotor system has a slight unbalance which causes vibration. As a result, the rotating test apparatus constructed is of certain self-balance capability. Two slip-ring assemblies [7] are mounted on the shaft. One is used to supply the electrical current from the power transformer to the heater that provides the heat input to the heat pipe evaporator, and the other is used to feed the temperature data from the thermocouples mounted on the heat pipe shell to the data acquisition system. The rotor disk of the apparatus consists of an inner cylinder [10] and an outer cylinder [11]. The inner cylinder is mounted on the shaft, and the outer cylinder is in turn fixed on the inner cylinder. The radially rotating miniature high-temperature heat pipe is mounted in the outer cylinder. To balance the rotor system, a counter weight [9] is also mounted in the cylinder opposite the heat pipe. The heater cap [12] connected to the outer cylinder has two functions: one is for the protection of the heater, and the other is for adjusting the cooling-air flow rate over the condenser section through the adjustment of the cooling-air flow window on the heater cap. The flow rate of the cooling air can be calculated through the averaged relative velocity at which the cooling air flows through the window and the area of the window. If the

---

Contributed by the Heat Transfer Division for publication in the JOURNAL OF HEAT TRANSFER. Manuscript received by the Heat Transfer Division June 11, 1999; revision received, September 5, 2000. Associate Editor: T. Avedisian.

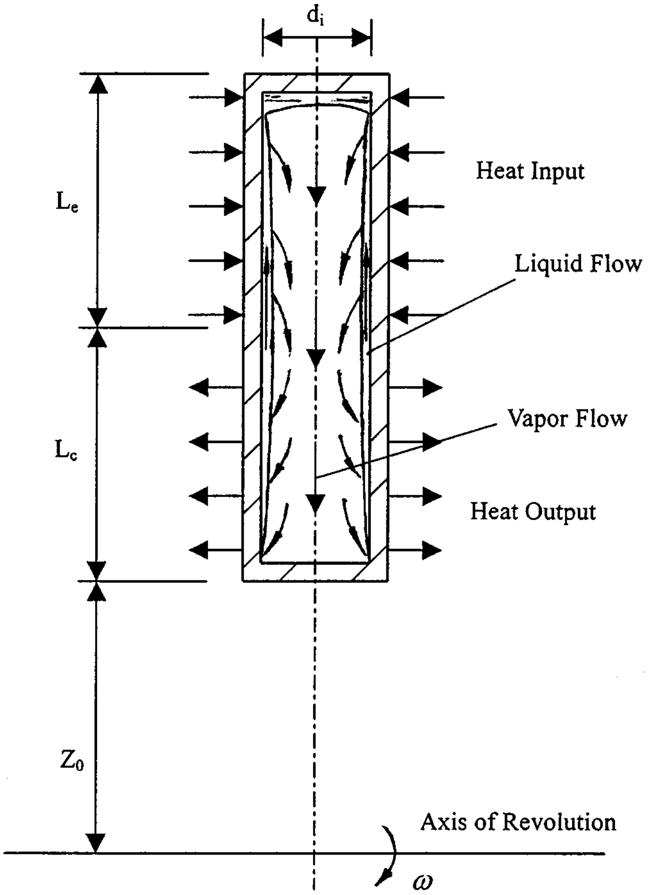

Fig. 1 Schematic of radially rotating heat pipes

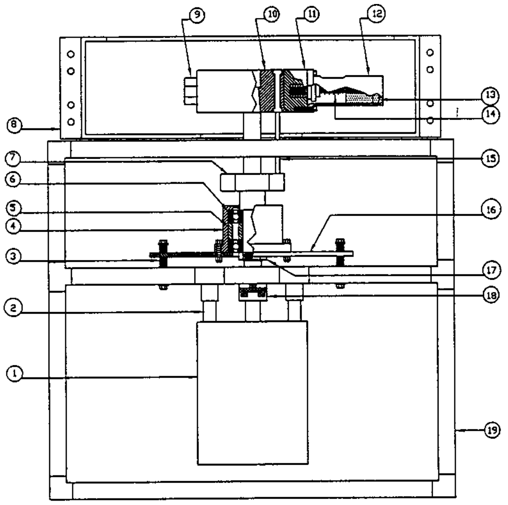

1	Motor	8	Protective Shell	15	Thermocouples
2	Connecting Bar	9	Balancing Weight	16	Bearing Platform
3	Springs	10	Inner Cylinder	17	Bearing Nut
4	Bearing House	11	Outer Cylinder	18	Flexible Coupling
5	Spacer	12	Heater Cap	19	Frame
6	Bearing	13	Heater		
7	Slip Rings	14	Heat Pipe		

Fig. 2 Schematic of the high-speed rotating test apparatus

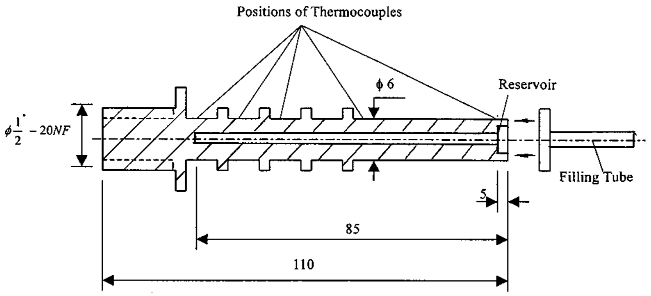

Fig. 3 Schematic of radially rotating miniature heat pipes ($d = 1.5$ and 2 mm)

diameter of the outer cylinder is extended, the rotating radius of the heat pipe could be increased.

In general, gas turbine blades are made of nickel-based alloys. Considering the high costs and difficulty in fabrication of the heat pipe using a nickel-based alloy, the heat pipes tested are high-temperature sodium/stainless steel (Type 304W) heat pipes. Two radially rotating miniature high-temperature heat pipes of 80 mm in length were designed. One has an inner diameter of 1.5 mm and the other 2 mm. The heat pipes designed are shown in Fig. 3. To facilitate sodium charge for the heat pipe, a reservoir with a diameter of 4 mm and length of 5 mm was designed on top of the heat pipe evaporator section. The two heat pipes have the same outer diameter, 6 mm, and the same evaporator and condenser lengths, 40 mm. Four circular fins were manufactured on the outer surface of the condenser section to enhance the convection heat transfer in this region. To install the heat pipe onto the rotating disk, threads were machined at the condenser end so that the heat pipe could be screwed into the outer cylinder of the high-speed rotating test apparatus. The sodium charge for the heat pipes was undertaken by Thermacore, Inc.

For the heat pipe with an inner diameter of 1.5 mm, the sodium charge was approximately 0.06 g, and the sodium charge for the other heat pipe with an inner diameter of 2 mm was approximately 0.08 g.

Five thermocouples of type K were used to measure the heat pipe temperature distribution along the heat pipe length. Two thermocouples were installed at the end cap and the outlet of the evaporator section, respectively, to measure the temperatures in the evaporator section, and the other three thermocouples were mounted in the condenser section to measure the temperature distribution in that section, as shown in Fig. 3.

The heater was mounted on the evaporator sections firmly, and the insulation material of about 16 mm in thickness was clamped between the heater cap and heater to reduce the heat loss from the heater to the surroundings.

Experimental Results and Startup Behavior

According to the analytical investigation on a radially rotating miniature high-temperature heat pipe [12], the temperature distribution along the heat pipe length without an adiabatic section can be expressed by the following relations:

Evaporator Section, $L_c \leqslant z \leqslant L$

$$T_{v,z} = T_{v,e} - \frac{T_v F_v Q_c}{h_{fg} \rho_v \sin\phi} \left\{ L_{\text{eff}} - \left[L - \frac{(L-z)^2}{L-L_c} \right] \right\} - \frac{T_v \omega^2 \sin\phi}{h_{fg}} \left[\left(z_0 + \frac{1}{2} L \right) L - \left(z_0 + \frac{1}{2} z \right) z \right] \quad (1)$$

Condenser Section, $0 \leqslant z \leqslant L_c$

$$T_{v,z}=\begin{cases}\Delta T_{v,z}-\Delta T_{v,L}+T_{v,L_c}-c[\exp(m(2L_c-z))-\exp(mz)] \\ \quad L_{c,n}\leqslant z\leqslant L_c \\ T_s+a-\Delta T_{v,L}+\Delta T_{v,z}+a[\exp(mz)-1] \\ \quad 0\leqslant z\leqslant L_{c,n}\,,\end{cases} \tag{2}$$

where

$$m=\left[\frac{2r_o h_c}{k_p(r_0^2-r_i^2)}\right]^{1/2},$$

$L_{c,n}$ is the condenser length occupied by non-condensable gases, and $\Delta T_{v,z}$ and $\Delta T_{v,L}$ are the temperature drop from $z=0$ to z and the total temperature drop along the entire heat pipe length, respectively, without the diffuse effects of non-condensable gases. The expression for $\Delta T_{v,z}$ is given by the following equation:

$$\Delta T_{v,z}=\begin{cases}\dfrac{T_v F_v Q_c}{2h_{fg}\rho_v L_c \sin\phi}z^2+\dfrac{T_v}{h_{fg}}\left[\omega^2\left(z_0+\dfrac{1}{2}z\sin\phi\right)z\right] & (0\leqslant z\leqslant L_c) \\ \dfrac{T_v F_v Q_c}{2h_{fg}\rho_v \sin\phi}\left[L-\dfrac{(L-z)^2}{L-L_c}\right]+\dfrac{T_v}{h_{fg}}\left[\omega^2\left(z_0+\dfrac{1}{2}z\sin\phi\right)z\right] & (L_c\leqslant z\leqslant L).\end{cases} \tag{3}$$

From these analytical relations, it can be seen that the temperature distribution along the heat pipe length is a function of rotating speed, geometrical size of the heat pipe, working fluid properties, heat input in the evaporator section, cooling condition in the condenser section, and diffuse effects of non-condensable gases. In the experiments that follow, the tilt angle, ϕ, of the heat pipes is fixed at 90 deg. The ranges of the parameters that are covered in experiments (heat inputs, geometric dimensions, flow rates of the cooling air, and the rotating frequencies) are as follows: $47\ W \leqslant Q \leqslant 325\ W$; $d_i=1.5$ and 2 mm; $L=80$ mm; $L_c=L_e=40$ mm; $L_a=0$; $30Hz \leqq f \leqslant 60Hz$; 1.05×10^{-3} m^3/s$\leqslant W \leqslant 13.4\times10^{-3}$ m^3/s; $470 \leqslant \omega^2\bar{Z}a/g \leqslant 1881$.

To illustrate the effectiveness of the heat pipe, Fig. 4 shows the comparisons between the experimental data and closed-form analytical solution along the heat pipe length and the temperature distributions along a heat pipe container (the heat pipe shell without charging any working fluid) with the same flow rate of cooling air, dimensionless centrifugal forces, and geometrical dimensions.

From Fig. 4, it can be seen that the heat transfer capacity of the heat pipe container is very low, which is 47 W for the container with an inner diameter of 2 mm, and 60 W for that of 1.5 mm. The temperature distributions along most of the container length are approximately linear, and the temperature in the portion near the end of the container is close to the temperature of the cooling air. For the heat pipes under the same operating conditions, much more heat can be transferred, which is up to 280 W for the heat pipe with an inner diameter of 2 mm, and 250 W for that of 1.5 mm. If the thermal conductivity of the copper is taken to be 386 W/m-°C, the effective heat conductance of the heat pipes is about 60–100 times higher than the thermal conductivity of copper. This is in turn about 1000–1700 times higher than the conductivity of the stainless steel used as the shell in the current study. These comparisons from Fig. 4 prove that radially rotating miniature high-temperature heat pipes can work very effectively and reliably. Their heat transfer capacities are much higher than any metals available.

It can be seen from the experimental data that the temperature distributions along the evaporator section and most of the condenser section are nearly uniform. It indicates that the heat pipe works perfectly in these sections. However, there exists a large temperature gradient near the end cap of the condenser. This large temperature gradient may be attributable to the non-condensable gases remaining in the heat pipe that were swept to the condenser end cap by the vapor flow. It is believed that during the sodium charging process, the air was not completely driven out of the heat pipe before the sealing of the heat pipe [12].

In addition, the condenser end is mounted onto the outer cylinder of the high-speed rotating test apparatus with a screw thread. A large, extra heat sink is thus formed at the condenser end, and some heat from the condenser end is directly transferred into this heat sink. As a result, the heat pipe temperature near the condenser end is forced to stay at a low level close to the temperature of the outer cylinder. The closed-form analytical solution from Eqs. (1)–(3) gives the temperature distributions along the dimensionless heat pipe length with the diffuse effect of non-condensable gases, but without taking into consideration of the heat sink at the condenser end. Comparing the closed-form analytical solutions with the experimental data in Fig. 4, it is evident

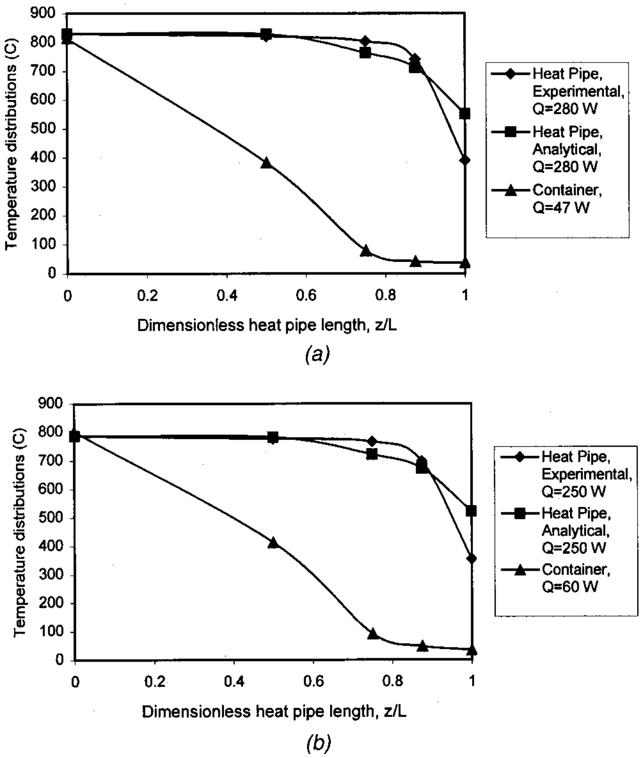

(a)

(b)

Fig. 4 Comparisons of temperature distributions and heat inputs between the experimental data, closed-form analytical solution ($L_{c,n}=4$ mm), and the heat pipe container: (*a*) $\omega^2\bar{Z}_a/g=470$, $d_i=2$ mm, $W=6.7\times10^{-3}$ m^3/s; (*b*) $\omega^2\bar{Z}_a/g=470$, $d_i=1.5$ mm, $W=6.7\times10^{-3}$ m^3/s.

that the closed-form analytical solution from Eqs. (1)–(3) is in good agreement with the experimental results in the entire evaporator section and most of the condenser section. Due to the existence of the heat sink at the condenser end, however, a relatively large deviation from the experimental data occurs close to the condenser end.

Figure 5 illustrates typical temperature distributions of the two heat pipes along the heat pipe length in the process of heat pipe startup. At $t=0$, a heat input of about 176 W was applied suddenly to the heat pipe evaporator section through the heater described earlier. At the initial moments, the temperatures along the heat pipe length were unaffected because of the retardation of the heat transfer from the heater to the heat pipe, as shown in Fig. 5. With an increase in time, the temperatures in the center of the evaporator section rose faster than those near the end cap of the evaporator, and the condenser sections were still at a temperature close to the ambient temperature.

Because the evaporator end has a larger metal mass and holds almost all of the solid sodium, it needs to absorb more heat to raise its temperature. In general, this phenomenon, in which the temperature at the outlet of the evaporator section was higher than that at the end cap of the evaporator, lasted only about 60 s. After that time, the temperature at the end cap of the evaporator rose higher than that at the outlet of the evaporator section, and the temperature in the condenser section increased gradually due to the axial heat conduction along the container wall.

As the temperature in the evaporator section was further increased, the sodium in the evaporator section was vaporized. The generated vapor flowed from the evaporator section to the condenser section, and the heat pipe started to be operational. As a result, the temperatures along the heat pipe length rose quickly. After about 800–1200 s, the temperature distribution along the heat pipe length reached a steady state and the process of the heat pipe startup was completed. Similar to the startup of a high-temperature heat pipe under a non-rotating condition [13], the startup behavior of the current rotating heat pipe is frontal in nature with a sharp drop off in temperature across of vapor front and no pressure recovery in the condenser.

Operating Characteristics of Radially Rotating Miniature High-Temperature Heat Pipes

As mentioned earlier, several parameters would significantly influence the performance of the heat pipe. These parameters and their influence on the heat pipe performance are examined next.

Effect of Heat Inputs. Figure 6 shows the steady-state temperature distributions along the heat pipe length with different heat inputs for both heat pipes. At a low heat input in the evaporator section, most of the condenser section remains inactive with its temperature close to the cooling-air temperature. As the heat input is increased, the active zone expands from the evaporator section into the condenser section towards the condenser end cap. The active length of the condenser at the steady state is determined by the surface area necessary to reject the heat applied in the evaporator section. With a low heat input and a relatively high rotating speed, which would provide a high heat transfer coefficient, only a small portion of the total condenser surface area is needed to reject the applied heat. As a result, most of the con-

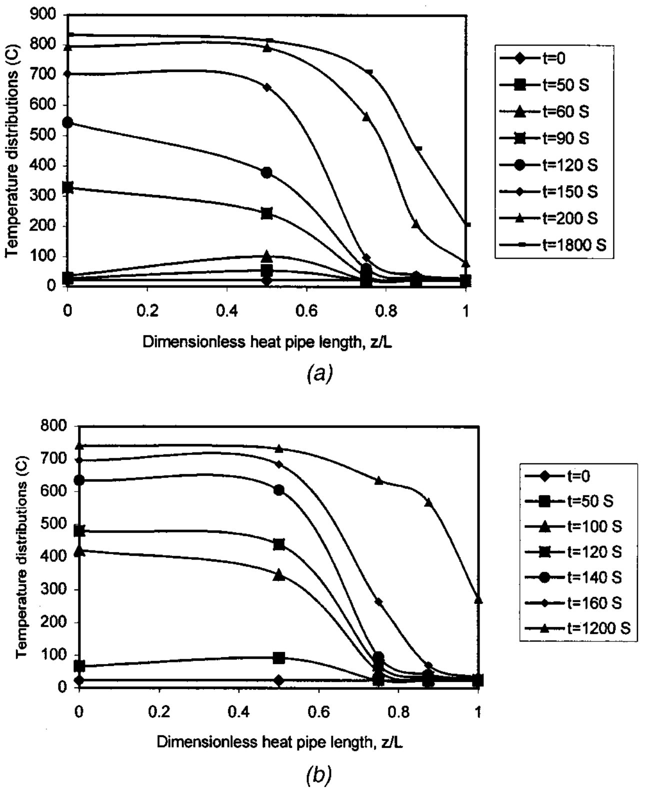

Fig. 5 Temperature distributions along the heat pipe length with the diffuse effects of non-condensable gases during the heat pipe startup process: (*a*) $\omega^2\bar{Z}_a/g=470$, $d_i=1.5$ mm, $Q=176$ W; (*b*) $\omega^2\bar{Z}_a/g=470$, $d_i=2$ mm, $Q=175$ W.

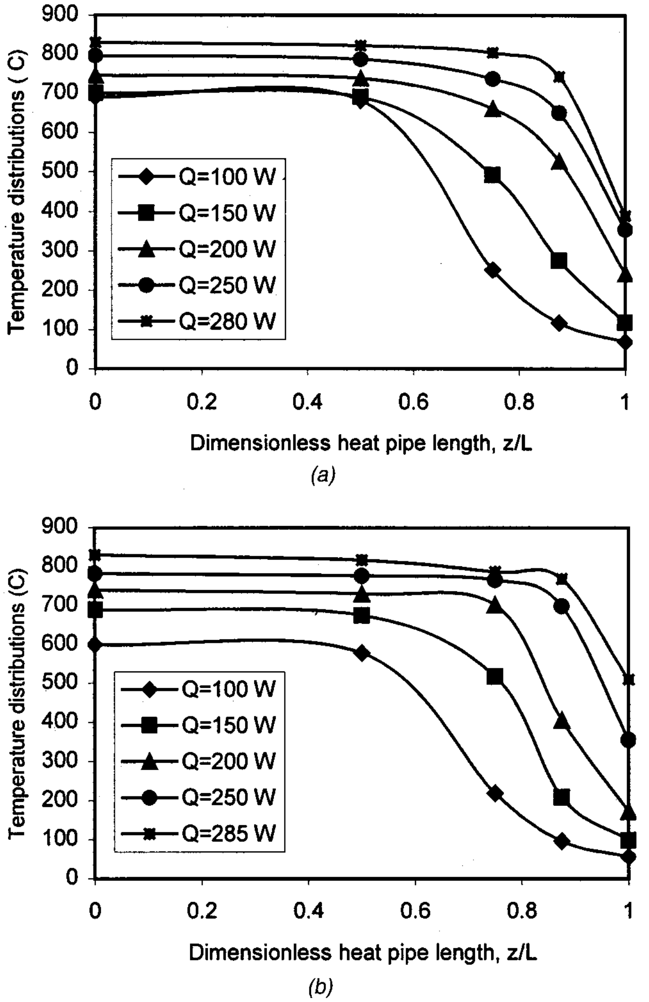

Fig. 6 Temperature distributions along the dimensionless heat pipe length with different heat inputs: (*a*) $\omega^2\bar{Z}_a/g=470$, $d_i=2$ mm, $W=6.7\times10^{-3}$ m^3/s; (*b*) $\omega^2\bar{Z}_a/g=470$, $d_i=1.5$ mm, $W=6.7\times10^{-3}$ m^3/s.

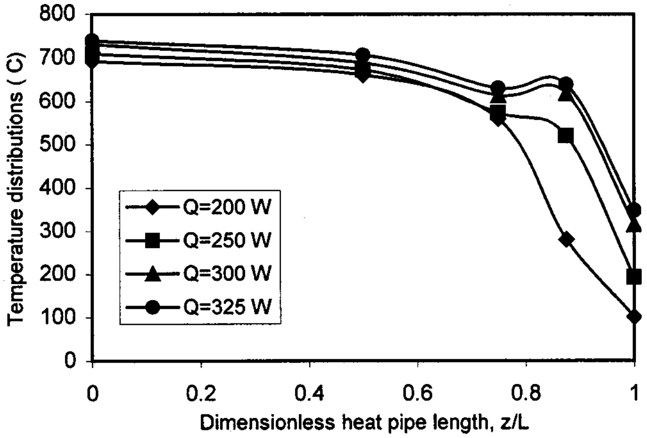

Fig. 7 Temperature distributions along the dimensionless heat pipe length with different rotating frequencies and flow rates of the cooling air ($\omega^2\bar{Z}_a/g=1306$, $d_i=2$ mm, $W=11.2\times10^{-3}$ m^3/s)

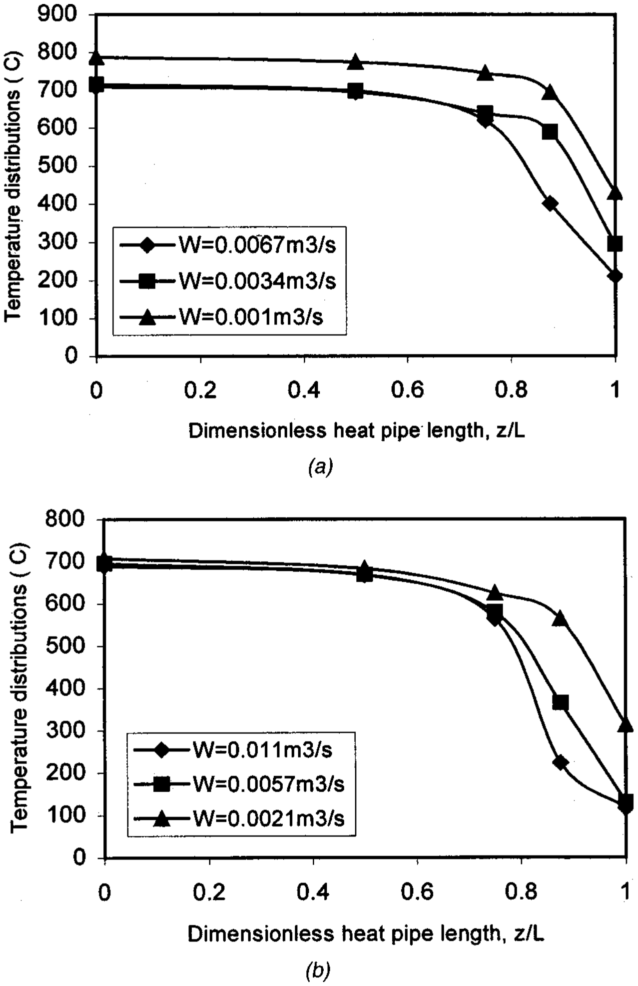

(a)

(b)

Fig. 8 Comparisons of temperature distributions along the dimensionless heat pipe length with different flow rates of the cooling air: (*a*) $\omega^2\bar{Z}_a/g=470$, $d_i=2$ mm, $Q=200$ W; (*b*) $\omega^2\bar{Z}_a/g=1306$, $d_i=2$ mm, $Q=200$ W.

denser would remain inactive at the steady state when the heat input is low. In the current experiment, the inactive part of the condenser may also be attributable to the existence of non-condensable gas remaining in the heat pipe.

When the flow rate of cooling air, dimensionless centrifugal force, and inner diameter of the heat pipe are fixed, the operating temperatures in the evaporator section will be increased with an increase in the heat input, and consequently the temperature along the condenser section will go up, as shown in Fig. 6. Accordingly, the heat transfer characteristics and effective thermal conductance will be improved significantly. When the heat input is further increased and reaches about 300 W for the heat pipe with an inner diameter of 2 mm, as shown in Fig. 7, the temperature distribution stays relatively uniform until reaching the region close to the condenser end. Also, a temperature peak emerges near the condenser end, as shown in Fig. 7. With an increase in the heat input, a large amount of vapor is generated in the evaporator section and the vapor flows with a high speed towards the end of the condenser section. Because of this high speed, the vapor compressibility would take effect, and the vapor flow has reached the choked condition. The vapor continues to expand in the condenser section, which is followed by a pressure recovery. Owing to the effect of non-condensable gases and the heat sink at the condenser end, the temperature at the condenser end is forced to stay at a relative low temperature. As a result, a temperature peak would appear near the end of the condenser section.

Effects of Flow Rates of the Cooling Air. Flow rate of the cooling air in the condenser section has a dominant influence on the operating temperature level of the heat pipe. As the flow rate of the cooling air is increased, the convective heat transfer coefficient at the outer surface of the condenser section is increased. Therefore, the heat transfer capacity at the outer surface of the heat pipe is increased. If the heat input is kept at a constant, as the cooling air flow rate is increased, the operating temperature of the heat pipe will be decreased, the working section of the condenser will be shortened, and the temperature distributions along the condenser section will become less uniform near the condenser end. In this case, when the operating temperature is too low and the heat input is too high, the sonic limit of the heat pipe will be reached.

Figure 8 compares the temperature distributions along the heat pipe length with different cooling-air flow rates when the temperature of the cooling air is kept at 30°C. It can be seen from the figure that, for the same heat input and dimensionless centrifugal force, the temperature along the heat pipe length is increased with a decrease in the flow rate of the cooling air. Due to this increased heat pipe temperature, the vapor pressure is accordingly increased. At the same time, the non-condensable gases in the heat pipe are more likely to be compressed towards the condenser end owing to the increased vapor pressure. As a result, the non-condensable gases would occupy a smaller portion of the condenser section, and the temperature distribution near the condenser end would become more uniform.

Effects of Dimensionless Centrifugal Forces. At a higher revolution or rotating frequency, the dimensionless centrifugal force plays a dominant role in the temperature drop along the heat pipe length. With an increase in the dimensionless centrifugal force, the vapor pressure and temperature drops along the heat pipe length will be increased. Therefore, to some degree, the dimensionless centrifugal force dominates the slope of the temperature distribution and the temperature drop along the heat pipe length.

Although the dimensionless centrifugal force has a similar effect on the total temperature drop along the heat pipe length compared to that of the cooling-air flow rate, the mechanisms that cause the change of the temperature drop are different. As the cooling-air flow rate is increased, the convection on the outer surface of the condenser section will be intensified, the working section of the condenser will be shortened, and the temperature gradient along the condenser length will become steeper. But the slope of the temperature distribution along the evaporator section would remain a constant. On the other hand, when the dimension-

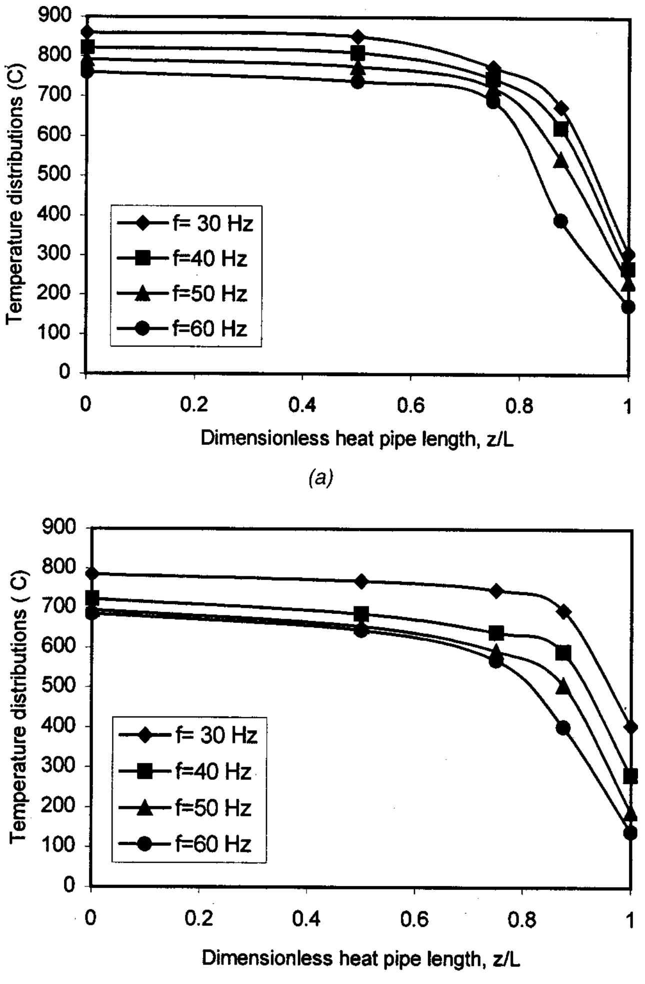

(a)

(b)

Fig. 9 Temperature distributions along the dimensionless heat pipe length with different rotating frequencies: (*a*) $Q=225$ W, $d_i=1.5$ mm; (*b*) $Q=225$ W, $d_i=2$ mm.

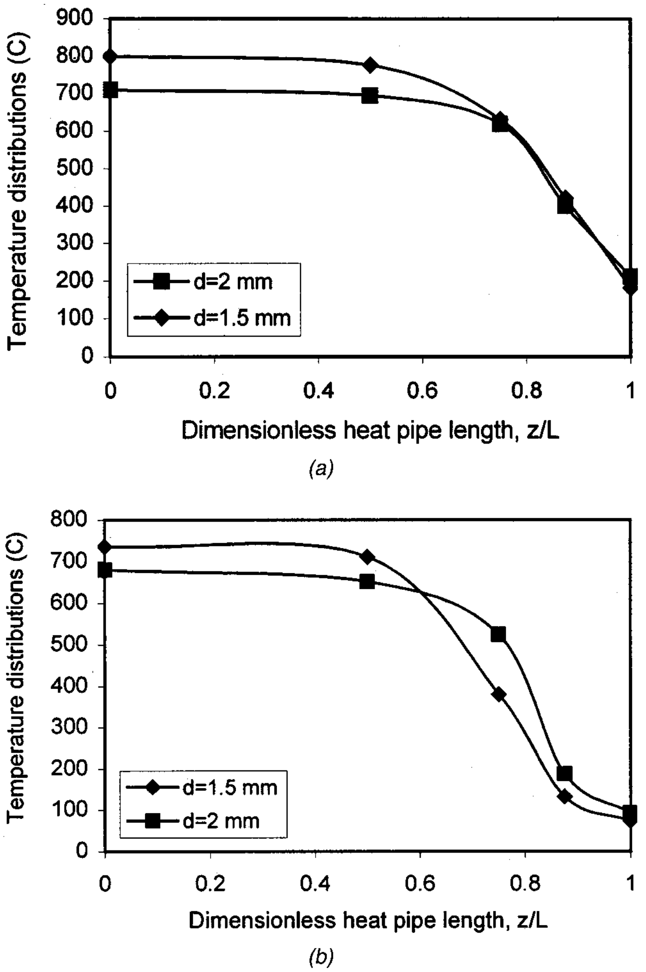

(a)

(b)

Fig. 10 Comparisons of temperature distributions along the dimensionless heat pipe length with different inner diameter: (*a*) $Q=200$ W, $\omega^2\bar{Z}_a/g=470$, $W=6.7\times10^{-3}$ m^3/s; (*b*) $Q=200$ W, $\omega^2\bar{Z}_a/g=1881$, $W=13.4\times10^{-3}$ m^3/s.

less centrifugal force is increased, the temperature drop caused by the vapor centrifugal force will be increased, and the total temperature drop including that in the evaporator section will be increased. Therefore, the analysis here is limited to the slope of temperature distributions along the evaporator section in order to illustrate the effects of dimensionless centrifugal forces.

Figure 9 shows temperature distributions along the heat pipe length at different rotating frequencies. As shown in the figure, at a low rotating frequency, $f=30$ Hz, which corresponds to a dimensionless centrigual force, $\omega^2\overline{Za}/g$, of 470, the slopes of the temperature distributions along the evaporator section are relatively small and temperature distributions in the evaporator section are relatively uniform. When the rotating frequency is increased from $f=30$ Hz to 60 Hz, the slope of the temperature distribution in the evaporator section becomes steeper with an increased temperature drop in the evaporator section.

Effects of Inner Diameters of the Heat Pipes. The inner diameter of a heat pipe determines the cross-section area of vapor flow in the heat pipe. The analytical investigation indicates that for the incompressible flow, the temperature and pressure drops along the heat pipe length are mainly due to the friction and centrifugal forces of the vapor flow if the effect of the noncondensable gases is neglected, as shown in Eq. (3).

The first term on the right hand side of Eq. (3) represents the friction of the vapor flow, and the second term is the centrigual force. The friction of the vapor flow is proportional to F_v. F_v is the frictional coefficient for the vapor flow which is inversely proportional to r_v^4, where r_v is the vapor core radius [4]. For a heat pipe with a larger diameter, the friction is usually small and negligible. But for a miniature heat pipe, F_v in the heat pipe will increase dramatically with a decrease in r_v. As a result, a miniature heat pipe having a smaller inner diameter must be subject to a larger friction of the vapor flow, which results in a larger temperature drop along the heat pipe length. Conversely, for a radially rotating heat pipe having a larger inner diameter, the friction exerted on the vapor flow is smaller.

Figure 10 shows the comparisons of temperature distributions along the heat pipe length for the two heat pipes with inner diameters of 2 mm and 1.5 mm, respectively. It is evident that the temperature drop along the heat pipe with an inner diameter of 1.5 mm is larger than that with an inner diameter of 2 mm when the heat input, dimensionless centrifugal force, and flow rate of cooling air are kept at constants. On the other hand, the operating temperature in the evaporator section of the heat pipe is higher when the inner diameter is smaller. This is because a higher pressure drop is needed to overcome the friction of vapor flow in the heat pipe having a smaller inner diameter. Accordingly, the saturated temperature in the evaporator section of the heat pipe having a smaller inner diameter is higher. This trend would be more evident with a further decrease in the inner diameter of the heat pipe.

Error Analyses of Experimental Measurements

The errors of experimental results include the uncertainties in temperature and heat input measurements. In all experiments, the accuracy of type K thermocouples was 0.5°*C*, the accuracy related to the slip ring which was used to transfer the temperature signals was about 0.5 percent, and the temperature accuracy of the HP34970 Data Acquisition system is about 0.2 percent. In addition, since it was difficult to weld the thermocouples onto the heat pipe shell, a high-temperature chemical cement was used to hold the thermocouples in the small holes drilled in the heat pipe shell. Therefore, it was possible to result in an error in the temperature measurement due to potential contact thermal resistance between the thermocouples and the heat pipe shell. If the error caused by the contact thermal resistance was assumed to be 1 percent, the totally maximum uncertainty in the temperature measurement was about 2 percent.

The flow rate of the cooling air is calculated through the averaged relative velocity of the cooling air and the area of the cooling-air flow window. The totally maximum uncertainty for the flow rate of the cooling air is estimated to be about the 5 percent.

For the measurement of the heat input, the heater in the evaporator section was insulated with an insulation material of 16 mm in thickness. The insulation material was clamped between the heater and the heater cap in order to reduce the heat losses in the evaporator section. It was measured in experiments that the temperature on the outer surface of the heater cap was about 40–45°*C*, which corresponds to a maximum heat loss of about 25 W when the highest temperature in the evaporator section was between 800–850°*C* and the heat input was 250–300W. On the other hand, the maximum fluctuation range of the heat input in experiments was ±2 W, which would result in an error of about 0.8 percent for the heat input. If the accuracy of the wattmeter and slip ring for the heat input was about 1.5 percent, the maximum uncertainty in the heat input was about 10 percent.

Conclusions

Based on the experimental investigations presented in this paper, the following conclusions may be made:

1 The radially rotating miniature heat pipe can work effectively and reliably in the reported laboratory environment, and has a high effective thermal conductance (60–100 times higher than the thermal conductivity of copper).

2 Heat input has a very important influence on the temperature distributions and heat transfer characteristics of the heat pipe. With an increase in the heat input, the temperature level in the condenser sections will go up. Accordingly, the heat transfer characteristics and effective heat conductance of the heat pipe will be improved significantly.

3 The flow rate of the cooling air in the condenser section has a dominant influence on the temperature distribution of the heat pipe. When the flow rate of the cooling air is increased, the heat transfer capacity at the outer surface of the condenser will be increased. As a result, the operating temperature of the heat pipe will be reduced, the working section of the condenser will be shortened, and the temperature distributions near the condenser end will become steeper.

4 The inner diameter of a heat pipe determines the cross-section area of the vapor flow in the heat pipe. The miniature heat pipe with a smaller inner diameter will have a larger temperature drop along the heat pipe than that with a larger inner diameter when the heat input, flow rate of cooling air and dimensionless centrifugal force are kept the same.

Acknowledgments

The authors would like to thank the Air Force Office of Scientific Research for the partial financial support and Dr. James McMichael of AFOSR for his interest in this research project. The authors would also like to thank Thermacore, Inc. for charging the working fluid of the heat pipe.

Nomenclature

a, c = constants
d = heat pipe diameter, m
F_v = frictional coefficient of vapor flow
g = gravitational acceleration, m/s^2
h_c = average heat transfer coefficient in the condenser section, W/m^2-K
h_{fg} = latent heat of vaporization, J/kg
k_p = thermal conductivity of heat pipe wall, W/m-K
L = length of heat pipe, m
m = coefficient, 1/m
Q = heat transfer rate, W
r = heat pipe radius, m
T = temperature, K
W = flow rate of cooling air, kg/m^3
z = axial location of heat pipe, m
z_0 = revolving radius from the heat pipe bottom to the origin of the coordinate system, m
$\overline{Z_a}$ = average revolving radius of the heat pipe, m
ϕ = tilt angle between the heat pipe centerline and the radial line of the rotating axis, degree
ρ = density, kg/m
ω = angular velocity, rad/s

Subscripts

a = adiabatic section
c = condenser
e = evaporator
eff = effective
i = inner
o = outer
s = surrounding
v = vapor phase
z = axial location

References

[1] Cao, Y., Ling, J., and Chang, W. S., 1998, ''Analyses of Liquid and Vapor Flows in a Miniature Radially Rotating Heat Pipe for Turbine Blade Cooling Applications,'' *11th International Heat and Mass Transfer Conference*, South Korea.
[2] Faghri, A., 1995, *Heat Pipe Science and Technology*, Taylor & Francis, Washington, DC.
[3] Dunn, P. D., and Reay, D. A., 1994, *Heat Pipe*, Pergamon, Oxford, New York.
[4] Chi, S. W., 1976, *Heat Pipe Theory and Practice: a Sourcebook*, Hemisphere, New York.
[5] Cao, Y., 1996, ''Rotating Micro/Miniature Heat Pipes for Turbine Blade Cooling Applications,'' *AFOSR Contractor and Grantee Meeting on Turbulence and Internal Flows*, Atlanta, GA.
[6] J., Ling, Cao, Y., and Chang, W. S., 1999, ''Analysis of Radially Rotating High-Temperature Heat Pipes for Turbomachinery Application,'' ASME J. Eng. Gas Turbines Power, **121**, pp. 306–312.
[7] Lin, L., and Faghri, A., 1999, ''Heat Transfer in Micro Region of a Rotating Miniature Heat Pipe,'' Int. J. Heat Mass Transf., **42**, pp. 1363–1369.
[8] Cao, Y., and Chang, W. S., 1997, ''Analyses of Heat Transfer Limitations of Radially Rotating Heat Pipe for Turbomachinery Applications,'' AIAA Paper 97-2542.
[9] Marto, P., 1976, ''Performance Characteristics of Rotating Wickless Heat Pipes,'' *Proc. 2nd Int. Heat Pipe Conf.*, Bologna, pp. 281–291.
[10] Daniels, T., and Al-Jumaily, F., 1975, ''Investigations of the Factors Affecting the Performance of a Rotating Heat Pipe,'' Int. J. Heat Mass Transf., **18**, pp. 961–973.
[11] Gray, V. H., 1969, ''The Rotating Heat Pipe-A Wickless, Hollow Shaft for Transferring Heat Fluxes,'' ASME Paper 69-HT-19.
[12] Ling, J., and Cao, Y., 2000, ''Analytical Investigation of Diffuse Effects of Non-Condensable Gas on Radially Rotating Miniature High-Temperature Heat Pipes,'' Int. J. Heat Mass Transfer, **43**, pp. 3661–3671.
[13] Faghri, A., Buchko, M., and Cao, Y., 1991, ''A Study of High-Temperature Heat Pipes With Multiple Heat Sources and Sinks: Part I—Experimental Methodology and Frozen Startup Profiles,'' ASME J. Heat Transfer, **113**, pp. 1003–1009.

The Effect of Working Fluid Inventory on the Performance of Revolving Helically Grooved Heat Pipes

R. Michael Castle
Graduate Research Assistant

Scott K. Thomas
Associate Professor
Assoc. Mem. ASME

Department of Mechanical
and Materials Engineering,
Wright State University,
Dayton, OH 45435

Kirk L. Yerkes
Research Engineer
Air Force Research Laboratory (PRPG)
Wright-Patterson AFB, OH 45433-7251

The results of a recently completed experimental and analytical study showed that the capillary limit of a helically-grooved heat pipe (HGHP) was increased significantly when the transverse body force field was increased. This was due to the geometry of the helical groove wick structure. The objective of the present research was to experimentally determine the performance of revolving helically-grooved heat pipes when the working fluid inventory was varied. This report describes the measurement of the geometry of the heat pipe wick structure and the construction and testing of a heat pipe filling station. In addition, an extensive analysis of the uncertainty involved in the filling procedure and working fluid inventory has been outlined. Experimental measurements include the maximum heat transport, thermal resistance and evaporative heat transfer coefficient of the revolving helically grooved heat pipe for radial accelerations of $|\vec{a}_r| = 0.0$, *2.0, 4.0, 6.0, 8.0, and 10.0-g and working fluid fills of* $G = 0.5$, *1.0, and 1.5. An existing capillary limit model was updated and comparisons were made to the present experimental data.* [DOI: 10.1115/1.1339982]

Keywords: *Experimental; Heat Transfer; Heat Pipes; Porous Media; Two-Phase*

Introduction

Helically-grooved heat pipes (HGHPs) have potential applications in the thermal management of rotating equipment such as aircraft alternators, large-scale industrial electric motors, and spinning satellites. In two recent studies [1,2], the performance of revolving HGHPs was investigated. It was found that the capillary limit increased with the strength of the acceleration field perpendicular to the heat pipe axis. In order to move HGHPs closer to application, knowledge must be gained concerning the sensitivity of the capillary limit to working fluid fill amount, since variations in the fill amount are inevitable during the manufacture of these devices. Very few studies were available concerning the effect of working fluid fill on the performance of axially grooved heat pipes, but those found have been outlined below. In addition, synopses of the two aforementioned studies on revolving HGHPs have also been provided.

Brennan et al. [3] developed a mathematical model to determine the performance of an axially grooved heat pipe which accounts for liquid recession, liquid-vapor shear interaction and puddle flow in a 1-g acceleration environment. The model considered three distinct flow zones: the grooves unaffected by the puddle, the grooves that emerge from the puddle, and the grooves that are submerged by the puddle. The model for the puddle consisted of satisfying the equation of motion for the puddle and the continuity equation at the puddle-groove interface, and was solved by a fourth-order Runge-Kutta integration method with self-adjusting step sizes. The assumptions made by the model for the puddle were uniform heat addition and removal with a single evaporator and a single condenser section, and one-dimensional laminar flow in the puddle. The transport capability of the grooves unaffected by the puddle and the grooves extending beyond the puddle were approximated by a closed-form solution with laminar liquid and vapor flow. The working fluids used for the experiment were methane, ethane, and ammonia. Brennan et al. [3] stated that the mathematical model agreed well with the experimental data for ideally filled and overfilled heat pipes, but some differences were noted for underfilled heat pipes. In general, it was found for ideally filled heat pipes the predicted transported heat was higher than that measured. Also, this discrepancy was more significant for lower operating temperatures. In addition, it was found during the experiments that the maximum transported heat increased with fill volume.

Vasiliev et al. [4] performed a series of experiments on an aluminum axially grooved heat pipe which was overfilled and ideally filled. The width and height of the grooves were $w = 0.123$ mm and $h = 0.7$ mm, respectively, with an overall heat pipe length of $L_t = 80.0$ cm. The working fluids were acetone and ammonia. Vasiliev et al. showed that the temperature difference from the evaporator to the adiabatic regions increased at a much slower rate with increasing overfills. This was attributed to a thin film of liquid emerging from the overfill pool wetting the upper grooves. Vasiliev et al. stated that this thin film was lifted over the grooves by capillary forces due to microroughness on the groove surface. A mathematical model was developed for low temperature axially grooved heat pipes to estimate heat pipe performance for 0-g and 1-g applications. The mathematical model was a set of boundary-value problems applied to each groove and was solved by a numerical iteration method. The model was based on pressure balance equations and mass continuity written for a single groove. The temperature of the vapor in the adiabatic region was an input parameter, and the vapor pressure gradient was assumed to be one-dimensional. In addition, the liquid-vapor shear stress was assumed to be constant, and the starting liquid film thickness was of the same order of magnitude as the groove microroughness. Very good agreement was reported between the mathematical model and experimental transported heat results for ideally filled and overfilled heat pipes under gravity.

Thomas et al. [2] presented experimental data obtained from a helically grooved copper heat pipe which was tested on a centri-

---

Contributed by the Heat Transfer Division for publication in the JOURNAL OF HEAT TRANSFER. Manuscript received by the Heat Transfer Division April 21, 2000; revision received September 27, 2000. Associate Editor: G. P. Peterson.

fuge table. The heat pipe was bent to match the radius of curvature of the table so that a uniform transverse (perpendicular to the axis of the heat pipe) body force field could be applied along the entire length of the pipe. The steady-state performance of the curved heat pipe was determined by varying the heat input ($Q_{\mathrm{in}}=25$ to 250 W) and centrifuge table velocity (radial acceleration $|\vec{a}_r|=0.01$ to 10-g). It was found that the capillary limit increased by a factor of five when the radial acceleration increased from $|\vec{a}_r|=0.01$ to 6-g due to the geometry of the helical grooves. A model was developed to calculate the capillary limit of each groove in terms of centrifuge table angular velocity, the geometry of the heat pipe and the grooves, and the temperature-dependent working fluid properties. The agreement between the model and the experimental data was satisfactory.

Klasing et al. [1] developed a mathematical model to determine the operating limits of a revolving helically grooved straight heat pipe. The capillary limit calculation required an analysis of the total body force imposed by rotation and gravity on the liquid along the length of the helical grooves. The boiling and entrainment limits were calculated using methods described by Faghri [5]. It was found that the capillary limit increased significantly with rotational speed due to the helical geometry of the heat pipe wick structure. The maximum heat transport was found to be a function of angular velocity and tilt angle from horizontal. In addition, a minimum value of angular velocity was required to obtain the benefits of the helical groove geometry.

The first objective of the present study was to determine the sensitivity of the performance of revolving HGHPs to the working fluid fill amount. This required a precise knowledge of the geometry of the heat pipe and helical grooves. In addition, a precision filling station was constructed and calibrated to determine the uncertainties involved in the filling procedure. The copper-ethanol heat pipe was tested on a centrifuge table at Wright-Patterson AFB (AFRL/PRPG) to determine the capillary limit, thermal resistance and evaporative heat transfer coefficient for fill ratios of $G=0.5$, 1.0, and 1.5, and radial accelerations of $|\vec{a}_r|=0.01$, 2.0, 4.0, 6.0, 8.0, and 10.0-g. The second objective of the present study was to improve the existing analytical capillary limit model developed by Thomas et al. [2] using the above-mentioned geometric measurements and by using improved equations for the working fluid properties.

Determination of Heat Pipe Working Fluid Inventory

The objective of this analysis was to determine the working fluid inventory of a HGHP, which consists of the mass of liquid in the grooves and the mass of vapor in the vapor space. Since the heat pipe is a closed container under saturation conditions, the total mass of working fluid in the heat pipe is given by

$$m_t=m_v+m_l=\frac{V_{\mathrm{vs}}}{v_v}+\frac{GV_{\mathrm{gr}}}{v_l}, \tag{1}$$

where $G=V_l/V_{\mathrm{gr}}$ is the ratio of the volume of liquid to total groove volume. The volume of the vapor space is

$$V_{\mathrm{vs}}=\frac{\pi}{4}D_{\mathrm{vs}}^2L_t+V_{\mathrm{gr}}(1-G). \tag{2}$$

The second term in Eq. (2) accounts for the increase or decrease in the vapor space volume when the parameter G is varied. The total volume of the grooves is

$$V_{\mathrm{gr}}=L_{\mathrm{gr}}N_{\mathrm{gr}}A_{\mathrm{gr}}. \tag{3}$$

A cross-sectional view of a typical helical groove in the experimental test article is shown in Fig. 1. The cross-sectional area of the trapezoidal groove accounts for the differing side angles.

$$A_{\mathrm{gr}}=wh+\frac{1}{2}h^2(\tan\theta_1+\tan\theta_2) \tag{4}$$

The total length of each groove is

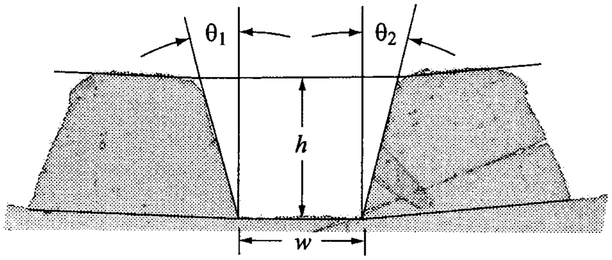

Fig. 1 Helical groove geometry

$$L_{\mathrm{gr}}=L_t\left[\left(\frac{2\pi r_h}{p}\right)^2+1\right]^{1/2}. \tag{5}$$

The radius of the helix is given by

$$r_h=\frac{1}{2}(D_{\mathrm{vs}}+h). \tag{6}$$

The helical pitch is the distance through which the helix makes one revolution around its radius.

$$p=\frac{2\pi(s-s_1)}{(\phi-\phi_1)} \tag{7}$$

The helix angle ϕ corresponds to s, which is the distance traveled along the centerline of the heat pipe.

In order to calculate the working fluid inventory for the HGHP, measurements of the appropriate geometric parameters were made. In addition, an extensive analysis was performed to determine the uncertainties of both the measured and calculated variables used in finding the working fluid inventory.

The physical variables given in Eq. (4) for the cross-sectional area of the grooves have been measured. A sample of the HGHP container was set in an epoxy resin mold, polished, and examined under a microscope with 50× magnification. Computer software was used to make bitmap pictures of ten different grooves and a microscopic calibration scale. These pictures were then analyzed to determine the geometric values shown in Fig. 1. Since the corners at the top of the land between grooves were not well defined, a special procedure was established to determine the geometry of the grooves. First, lines were drawn along the bottom and sides of each groove. Then, a line was drawn across the bottom of the land between grooves, as shown in Fig. 1. This line was then transposed to the top of the land. The intersections between this line and the lines along the sides of the groove were defined as the upper corners of the groove. Note that the two lines along the land tops are at different angles due to the radius of curvature of the heat pipe container. The angles θ_1 and θ_2, and the height and width of the groove h and w were found using a bitmap picture of the microscopic calibration scale as described by Castle [6].

An optical comparator was used to determine the vapor space diameter of the heat pipe container sample. The cross hairs of the optical comparator were carefully aligned with the top of the land between grooves on the left edge of the pipe. The comparator table was then moved until the land tops on the right edge of the pipe were aligned with the cross hairs. The diameter of the heat pipe vapor space was the distance of the table movement.

The helical groove pitch was found using a vertical milling machine and an angular displacement transducer. The heat pipe container material was originally 1 m long. Approximately one-half was used to form the heat pipe, and the other half was used to determine the pitch. The rotation angle $(\phi-\phi_1)$ and the corresponding distance along the centerline of the heat pipe $(s-s_1)$ has been found as shown in Fig. 2(a).

A heat pipe holding device was constructed from two angle aluminum uprights mounted to the table of a vertical milling ma-

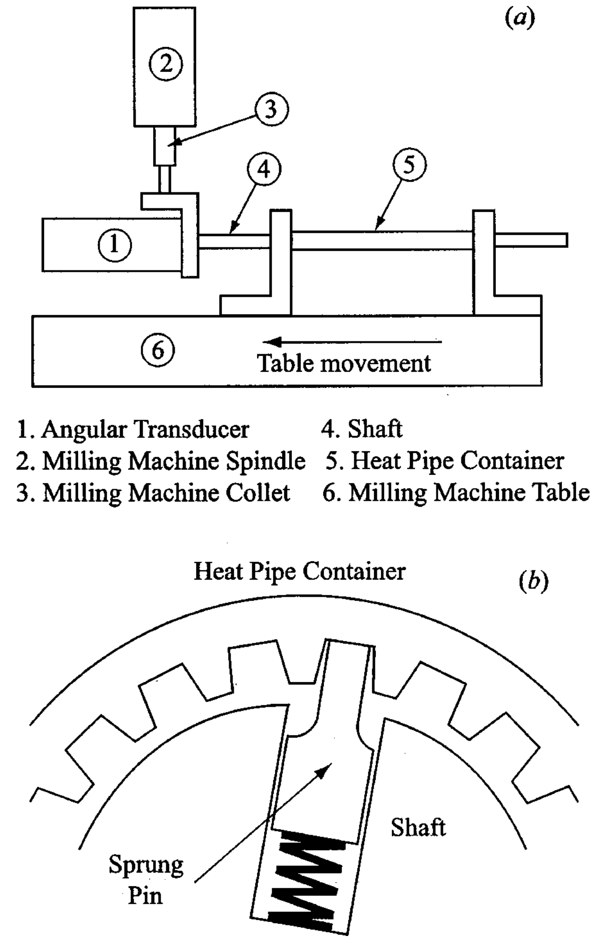

Fig. 2 Schematic of the helical pitch measurement technique: (*a*) major components; (*b*) cross-sectional view of sprung pin engaging a helical groove

chine. Precision alignment blocks were attached to the undersides of the uprights to engage one of the grooves in the milling machine table for improved alignment. Nylon bushings were placed in the uprights to center both the heat pipe container and the shaft, which was concentric with the heat pipe container. A small pin was made from a 1.58 mm (0.0625 in) dowel pin, where one end was ground to 0.26 mm to fit in the base of the helical groove. This sprung pin was set in a hole in the shaft where it engaged one of the grooves, as shown in Fig. 2(*b*). An angular displacement transducer was mounted onto another piece of angle aluminum. A vertical 6.35 mm (0.25 in) dowel pin was placed in the angle aluminum to align with the angular displacement transducer shaft. The dowel pin was held by a collet installed in the milling machine spindle in order to fix the location of the displacement transducer. The shaft of the transducer was linked to the shaft within the heat pipe by three set screws. As the milling machine table moved the pipe over the stationary shaft, the pin followed the helical groove, causing the shaft to rotate. The angular displacement transducer measured this rotation. A multimeter was used to measure the output voltage of the angular displacement transducer. The distance of the table movement was $(s-s_1)$, which was read from the milling machine display unit. The transducer output voltage was measured over 10 cm lengths for ten different groups. Backlash errors were avoided by not reversing the table movement while taking data. The pitch was calculated using Eq. (7) at a point in the center of each 10 cm length. An average of 88 values were used to calculate the helical pitch.

Table 1 The geometric variable values associated with the working fluid inventory

Measured Values	
h	0.03831 ± 0.00076 cm
w	0.03445 ± 0.0010 cm
θ_1	$15.44° \pm 0.91°$
θ_2	$13.80° \pm 0.96°$
D_{vs}	1.359 ± 0.005 cm
L_t	43.8 ± 0.084 cm
Calculated Values	
A_{gr}	$1.703 \times 10^{-3} \pm 6.0 \times 10^{-5}$ cm^2
p	135.8 ± 5.9 cm
r_h	0.6992 ± 0.0025 cm
L_{gr}	43.82 ± 0.84 cm
V_{gr}	3.73 ± 0.13 cm^3

Using the analysis given by Miller [7], the root-sum-square uncertainties for the groove cross-sectional area, helical pitch, helix radius, groove length, groove volume, vapor space volume, and total mass of the working fluid inventory have been calculated. The measured and calculated uncertainties for all geometric variables presented are shown in Table 1.

A literature survey was completed to determine the specific volumes of ethanol vapor and liquid at various saturation temperatures, as shown in Fig. 3. This information was needed to determine the total mass and uncertainty of the working fluid inventory $m_t \pm \Delta m_t$. While existing texts report these properties [5,8–12], it was found that most simply referred to previous sources. Therefore, the data shown in Fig. 3 represent information gathered from primary sources that cannot readily be traced further. In Fig. 3(*a*), the available data for the specific volume of liquid in the range of $T_{sat}=0$ to 100 °C are relatively scattered. Vargaftik [13] stated that the ethanol used was 96 percent pure by volume, with water making up most of the other 4 percent. Ethanol is aggressively hygroscopic, so special procedures are required for further purification as outlined by Timmermans [14] concerning anhydrous ethanol. Since the data by Timmermans [14] and TRC [15] are nearly coincident, it is believed that the data reported by TRC [15] are also for anhydrous ethanol. Dunn and Reay [16] do not provide information concerning purity. Therefore, the Vargaftik [13] data and the Dunn and Reay [16] data have been discarded in Fig. 3(*a*). In Fig. 3(*b*), the deviation of the Dunn and Reay [16] data for the specific volume of vapor is significant. Therefore, the Dunn and Reay [16] data has been discarded in Fig. 3(*b*). Polynomial curve fits from $0 \leq T_{sat} \leq 100$ °C have been obtained for the data shown in Figs. 3(*a*) and 3(*b*) for the specific volumes of liquid and vapor ethanol. These curve fits have been evaluated at room temperature to determine the proper values to be used in the uncertainty analysis, since the heat pipe was filled at room temperature. Information concerning the uncertainty of the original data was not available. Therefore, the uncertainties of these properties have been estimated to be the maximum variance of the data from the curve fits ($\Delta v_l = 3.5 \times 10^{-8}$ m^3/kg, $\Delta v_v = 0.39$ m^3/kg). The specific volumes of liquid and vapor ethanol (m^3/kg) as functions of saturation temperature (°C) are shown below for the range $0 \leq T_{sat} \leq 100$ °C

$$v_l = \exp(a_0 + a_1 T_{sat} + a_2 T_{sat}^2 + a_3 T_{sat}^3 + a_4 T_{sat}^4)/1000 \tag{8}$$

$$v_v = \exp(b_0 + b_1 T_{sat} + b_2 T_{sat}^2 + b_3 T_{sat}^3 + b_4 T_{sat}^4)/1000, \tag{9}$$

where the coefficients are

$$a_0 = 0.2153 \quad b_0 = 10.35$$

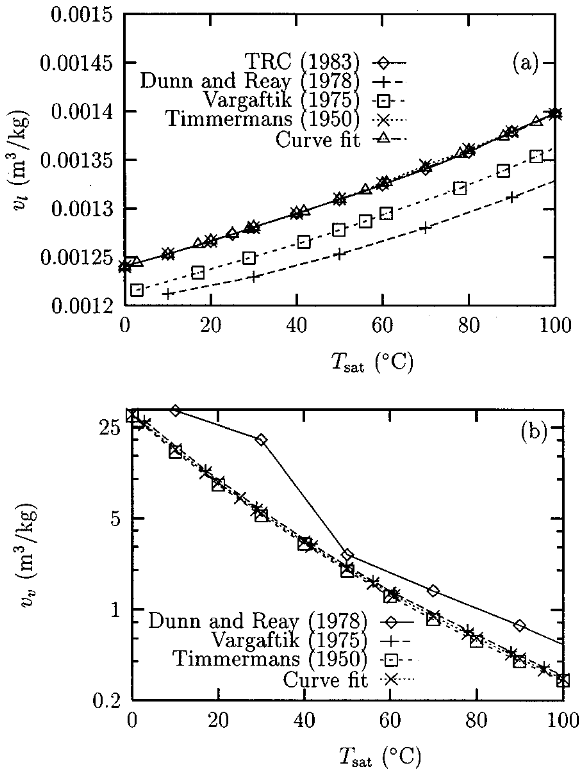

Fig. 3 Specific volume of ethanol versus temperature: (*a*) saturated liquid; (*b*) saturated vapor

Table 2 The calculated total mass of the working fluid inventory

G	m_t (g)	Δm_t (g) Calculated	Δm_d (g) Filling Station
0.5	1.47	± 3.6%	± 5.0%
1.0	2.92	± 3.7%	± 2.9%
1.5	4.38	± 3.6%	± 1.9%

$$a_1 = 1.049\times10^{-3} \quad b_1 = -6.375\times10^{-2}$$

$$a_2 = -1.345\times10^{-8} \quad b_2 = 1.735\times10^{-4}$$

$$a_3 = 2.025\times10^{-8} \quad b_3 = 5.714\times10^{-7}$$

$$a_4 = -5.474\times10^{-11} \quad b_4 = -6.003\times10^{-9}$$

The total mass of the working fluid inventory m_t and the associated uncertainty Δm_t for the range of fill values are given in Table 2.

Heat Pipe Filling Station

A filling station has been constructed which is capable of placing a low-temperature working fluid (i.e., water, ethanol, methanol) into a heat pipe without also introducing ambient air (Fig. 4). The station consisted of a manifold of valves and interconnecting stainless steel tubing, a working fluid reservoir, a dispensing burette, a vacuum pump, and a container of compressed dry nitrogen gas. Previous experience with filling stations showed that long runs of horizontal tubing could cause significant filling errors due to vapor bubbles within the tubing. To address this problem, the manifold was constructed such that the interconnecting tubing runs were very short (on the order of 2 cm). In addition, the tubes which intersect the main vertical tube between valves 2 and 5 (Fig. 4) were offset from each other and ran at a diagonal from the main tube. Again, the purpose of this design was to reduce the possibility of vapor bubbles adhering to the tubing walls, thus causing errors in the fill amount. However, it is likely that some vapor still does adhere to the tubing, so certain procedures were carried out during filling to eject as much vapor as possible. For instance, the 1 psig relief valve over valve 1 was cycled on and off several times. In addition, valves 2 and 5 were cycled on and off while noting the meniscus displacement within the dispensing burette. If the meniscus was displaced more than 0.06 cm^3, vapor was probably trapped within the valve. The valve in question was then cycled until the bubble was ejected.

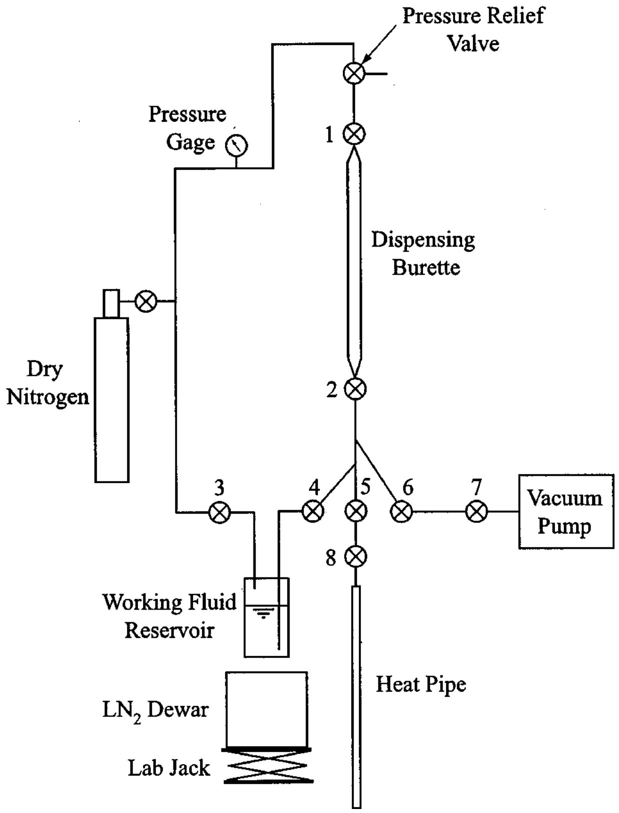

Fig. 4 Schematic of the heat pipe filling station

To fill the heat pipe, the container was first evacuated to a pressure of 10^{-6} Torr using a turbomolecular vacuum pump. The sealed pipe was then connected to the filling station at valve 5. The working fluid was frozen and thawed repeatedly to reduce the amount of dissolved air within the fluid. The entire filling station was then evacuated by a roughing pump, except the working fluid reservoir. After evacuation, the liquid working fluid was drawn up into the dispensing burette and into all interconnecting tubing. After noting the height of the meniscus, the desired amount of working fluid was metered into the heat pipe by carefully opening the heat pipe fill valve 8. The difference in height of the liquid column was related to the dispensed mass of working fluid.

During initial testing of the filling station, it was found that the mass of working fluid dispensed into the heat pipe container was different than what was indicated by the dispensing burette. Therefore, a rigorous calibration of the filling station was undertaken to determine a correlation between the change in volume read by the dispensing burette and the change in mass of a receiving burette attached at valve 5, which was measured using a precision scale. The total uncertainty of the working fluid inventory dispensed by the heat pipe filling station Δm_d is given in Table 2.

Experimental Setup

The purpose of the experiment was to examine the steady-state performance of a helically-grooved copper-ethanol heat pipe under various heat inputs and transverse body force fields using a centrifuge table located at Wright-Patterson AFB (AFRL/PRPG). Specifically, the amount of working fluid was varied ($G=0.5$, 1.0, and 1.5) to determine the effects of under/overfilling on the capillary limit, thermal resistance and evaporative heat transfer coefficient of the HGHP. To ensure uniform radial acceleration fields over the length of the heat pipe, the pipe was bent to match the radius of curvature of the centrifuge table ($R=1.22$ m). Physical information concerning the heat pipe is given in Table 3. It should be noted that the total helix angle was very small: Each groove rotated through an angle of approximately 2.03 rad (116 arc degrees) over the length of the pipe. The heat pipe was mounted to a platform overhanging the edge of the horizontal centrifuge table. This allowed the heat pipe to be positioned such that the radius of curvature was equivalent to the outermost radius of the centrifuge table. Insulative mounting blocks were used to ensure that the heat pipe matched the prescribed radius as closely as possible. The horizontal centrifuge table was driven by a 20-hp dc motor. The acceleration field near the heat pipe was measured by a triaxial accelerometer. The acceleration field at the centerline of the heat pipe radius was calculated from these readings using a coordinate transformation.

A pressure-sensitive nichrome heater tape with an aluminized backing was uniformly wound around the circumference of the evaporator section for heat input. Power was supplied to the heat pipe evaporator section through slip rings. While the current reading could be made directly using a precision ammeter, the voltage across the electric heater had to be measured on the rotating table because of the voltage drop between the control room and the table. Therefore, the voltage at the heater was obtained through the instrumentation slip ring assembly and read by a precision multimeter.

The calorimeter consisted of a length of 1/8 in. OD copper tubing wound tightly around the condenser section. The size of the tubing was chosen to be small to minimize the effects of acceleration on the performance of the calorimeter. Thermal grease was used between the heat pipe and the calorimeter to decrease contact resistance. Type T thermocouples were inserted through brass T-branch connectors into the coolant inlet and exit streams, and a high-resolution digital flow meter was used to measure the mass flow rate of the coolant (50 percent by mass ethylene glycol/water mixture). The mass flow rate was controlled using a high-pressure booster pump, which aided the low-pressure pump in the recirculating chiller. The percentage of ethylene glycol was measured periodically during testing using a precision hydrometer to ensure that the mixture did not change. The temperature of the coolant was maintained at a constant setting by the recirculating chiller. Coolant was delivered to the centrifuge table via a double-pass hydraulic rotary coupling. The mass flow rate was constant for all experiments. Values of the specific heat of ethylene glycol/water mixtures were obtained from ASHRAE [17], which were in terms of percent ethylene glycol by weight and temperature. The average temperature between the calorimeter inlet and outlet was used to evaluate the specific heat. The specific heat did not vary appreciably during testing since it is a weak function of temperature.

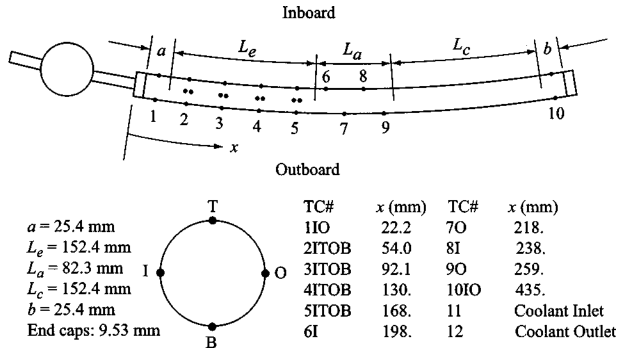

$a=25.4$ mm
$L_e=152.4$ mm
$L_a=82.3$ mm
$L_c=152.4$ mm
$b=25.4$ mm
End caps: 9.53 mm

TC#	x (mm)	TC#	x (mm)
1IO	22.2	7O	218.
2ITOB	54.0	8I	238.
3ITOB	92.1	9O	259.
4ITOB	130.	10IO	435.
5ITOB	168.	11	Coolant Inlet
6I	198.	12	Coolant Outlet

Fig. 5 Thermocouple locations and relevant lengths

Heat pipe temperatures were measured by Type T surface-mount thermocouples, which were held in place using Kapton tape. Mounting locations for the thermocouples are shown in Fig. 5. A short unheated length next to the evaporator end cap was instrumented with thermocouples specifically for accurate thermal resistance measurements. In addition, groups of four thermocouples were arranged around the circumference of the heat pipe at stations in the evaporator section for local heat transfer coefficient information. Temperature signals were conditioned and amplified on the centrifuge table. These signals were transferred off the table through the instrumentation slip ring assembly, which was completely separate from the power slip ring assembly to reduce electronic noise. Conditioning the temperature signals prior to leaving the centrifuge table eliminated difficulties associated with creating additional junctions within the slip ring assembly. Temperature and acceleration signals were collected using a personal computer with data logging software. Since a shortage of thermocouple channels existed on the centrifuge table, a series of three electrical relays were engaged to read one set of thermocouples, and disengaged to read the other set.

Table 3 Helically grooved heat pipe specifications

Working fluid	Ethanol
Working fluid charge	$m_t = 1.47$, 2.92 and 4.38 g
Evaporator length	$L_e = 15.2 \pm 0.16$ cm
Adiabatic length	$L_a = 8.2 \pm 0.16$ cm
Condenser length	$L_c = 15.2 \pm 0.16$ cm
Tube outside diameter	$D_o = 1.588 \pm 0.005$ cm
Tube wall thickness	$t_w = 0.0757$ cm
Radius of curvature	$R = 1.22$ m
Wall/wick materials	Copper
Wick structure	Helical grooves
Number of Grooves	$N_{\mathrm{gr}} = 50$
Heater element	Nichrome heater tape
Fill valve	Nupro B-4HW bellows valve
Calorimeter	1/8 in. OD coiled copper tubing

Table 4 Maximum uncertainties of measured and calculated values

Measured Values	
Coolant mass flow rate	$\Delta \dot{m}_c = \pm\ 0.05$ g/s
Heater voltage	$\Delta \mathrm{V} = \pm\ 0.5$ V
Heater current	$\Delta I = \pm\ 0.1$ A
Radial acceleration	$\Delta a_r = \pm\ 0.1$-g
Calorimeter inlet temperature	$\Delta T_{\mathrm{in}} = \pm\ 0.07$ K
Calorimeter outlet temperature	$\Delta T_{\mathrm{out}} = \pm\ 0.08$ K
Evaporator end cap temperature	$\Delta T_{\mathrm{eec}} = \pm\ 0.09$ K
Condenser end cap temperature	$\Delta T_{\mathrm{cec}} = \pm\ 0.11$ K
Calculated Values	
Heat input	See Fig. 6
Heat transported	$\Delta Q_t = \pm\ 3.2$ W
Thermal resistance	See Fig. 7
Heat transfer coefficient	See Figs. 12 and 13

Since the heat pipe assembly was subjected to air velocities due to the rotation of the table (up to 11 m/s=25 mi/hr), efforts were made to reduce convective heat losses from the exterior of the heat pipe. A thin-walled aluminum box was fabricated to fit around the heat pipe. Ceramic wool insulation was placed inside the box and around the heat pipe through three small doors on the top of the box. This insulation/box arrangement provided an effective barrier to convective losses from the heat pipe to the ambient.

The copper-ethanol HGHP was tested in the following manner. The recirculating chiller was turned on and allowed to reach the setpoint temperature, which was measured at the calorimeter inlet. The centrifuge table was started from the remote control room at a slow constant rotational speed to prevent damage to the power and instrumentation slip rings. In this case, the radial acceleration was less than $|\vec{a}_r|<0.01$-g. In all cases, the centrifuge table rotated in a clockwise direction as seen from above. Power to the heater was applied ($Q_{\rm in}=10\,{\rm W}$) and the heat pipe was allowed to reach a steady-state condition. The power to the heater was then increased to $Q_{\rm in}=20\,{\rm W}$ and again the heat pipe was allowed to reach a steady-state condition. This was repeated until the maximum allowable evaporator temperature was reached ($T_{w,\max}=100\,°{\rm C}$). After all data had been recorded the power to the heater was turned off, and the heat pipe was allowed to cool before shutting down the centrifuge table.

Using the analysis given by Miller [7], the uncertainties for all of the measured and calculated values for the experimental data are presented in Table 4.

Results and Discussion

The objective of this experiment was to determine the steady-state performance of a revolving helically-grooved heat pipe as a function of the working fluid inventory. The heat input, radial acceleration and working fluid fill were varied as follows: $Q_{\rm in}=10$ to 180 W, $|\vec{a}_r|=0.01$ to 10-g, and $G=0.5$, 1.0, and 1.5. Thermocouples on the inboard, outboard, top, and bottom sides of the heat pipe (Fig. 5) were used to determine the axial and circumferential temperature distributions. Typical steady-state temperature distributions for the heat pipe for $G=1.0$ at $|\vec{a}_r|=0.01$-g are shown in Fig. 6. For low power input levels, the temperature distribution was uniform. As the power input increased, the temperatures within the evaporator and the short unheated section adjacent to the evaporator increased significantly, indicating a partial dryout situation. Since the coolant temperature and flow rate were constant for all tests, the adiabatic and condenser temperatures increased slightly with input power. Figure 7 shows the thermal resistance versus transported heat over the en-

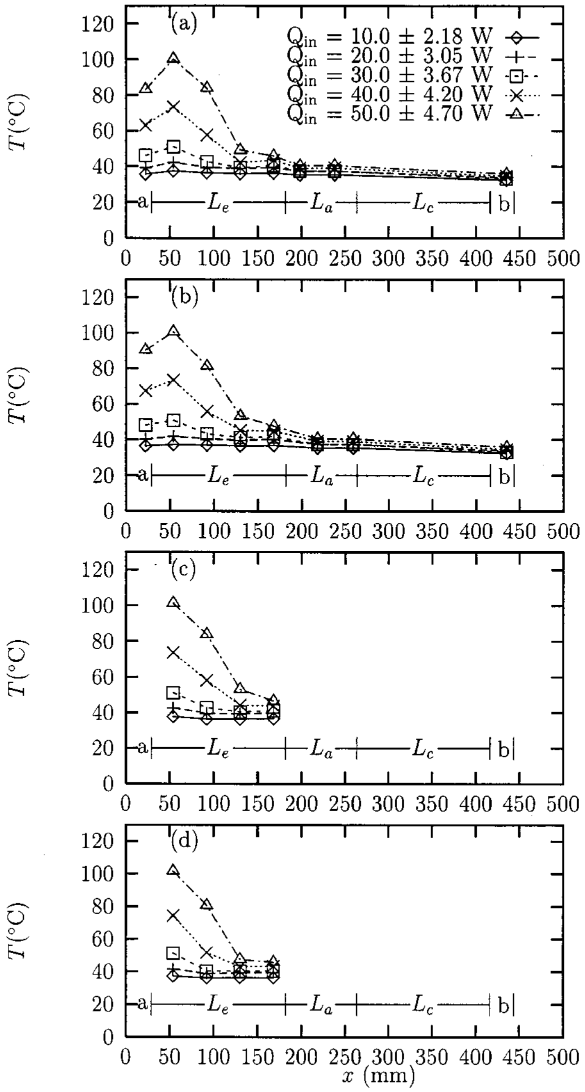

Fig. 6 Steady-state temperature distributions for $|\vec{a}_r|=0.01$-g, $G=1.0$: (*a*) inboard; (*b*) outboard; (*c*) top; and (*d*) bottom

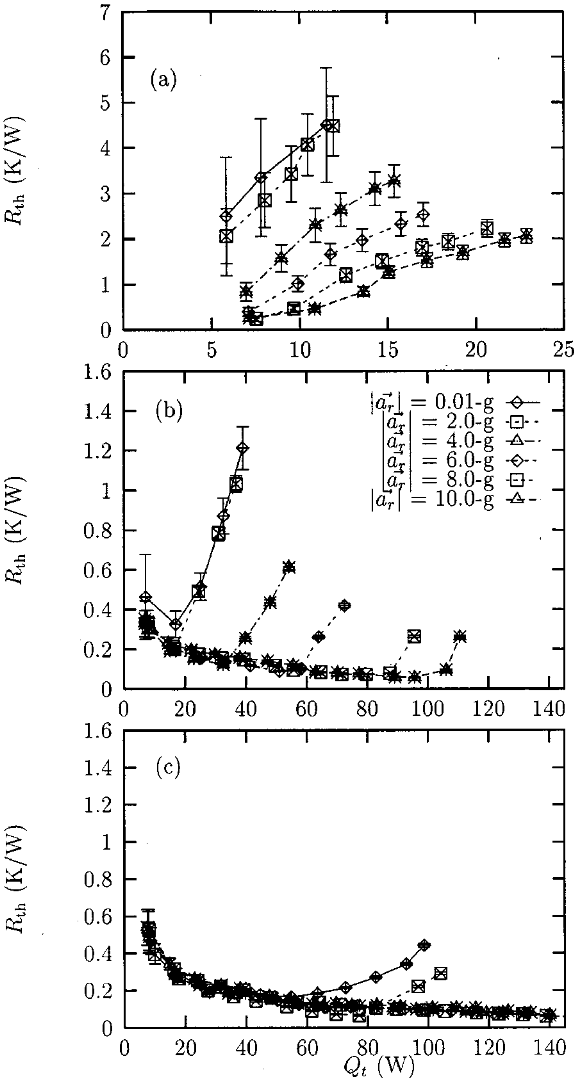

Fig. 7 Thermal resistance versus heat transport: (*a*) $G=0.5$; (*b*) $G=1.0$; and (*c*) $G=1.5$

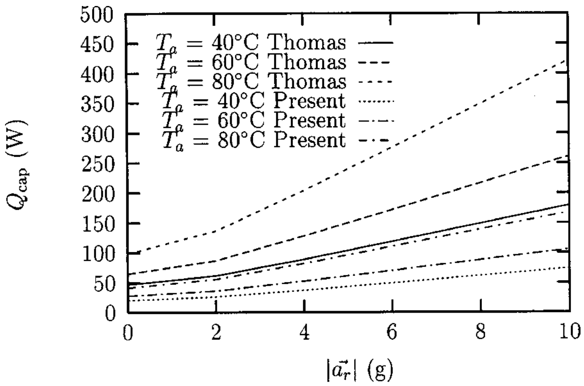

Fig. 8 Capillary limit versus radial acceleration comparison of present model and Thomas et al. [2]

tire range of radial acceleration for each fill level. In Fig. 7(*a*) the thermal resistance was quite high, which indicates that the heat pipe was partially dried out for $G=0.5$, even at the lowest power input levels. However, the thermal resistance decreased significantly as the radial acceleration increased, showing that the capillary pumping ability of the helical grooves increased. For $G=1.0$ and 1.5, the thermal resistance decreased and then increased with transported heat when dryout commenced. The $G=1.5$ fill tests showed dryout occurring only for $|\vec{a}_r|=0.01$ and 2.0-g. Dryout was not reached for $G=1.5$ with $|\vec{a}_r|=4.0$, 6.0, 8.0, and 10.0-g due to reaching the maximum allowable heater temperature. The capillary limit was considered to be reached when the thermal resistance began to increase.

Thomas et al. [2] presented a mathematical model which predicted the capillary limit of a helically-grooved heat pipe subjected to a transverse body force. This model accounted for the geometry of the heat pipe and the grooves (including helix pitch), body force field strength, and temperature-dependent working fluid properties. This model was updated to include the improved measurements of the wick geometry and working fluid properties. Castle [6] provides a detailed comparison of the present model and that given by Thomas et al. [2]. The capillary limit versus radial acceleration is given in Fig. 8 for various working temperatures with the Thomas et al. [2] model and the present model. The capillary limit increased steadily with radial acceleration and working temperature. The present model shows a significantly lower prediction for the capillary limit when compared to the Thomas model due to the improved geometric measurements and working fluid property equations.

Figure 9 shows a comparison of the experimental data and present analytical model for the capillary limit of a revolving helically-grooved heat pipe. In the legend of this figure, No Dryout and Partial Dryout refer to the experimental data. No attempt was made to maintain a constant adiabatic temperature during the experiments. Therefore, the working fluid temperature in the model was set to the adiabatic temperature found experimentally.

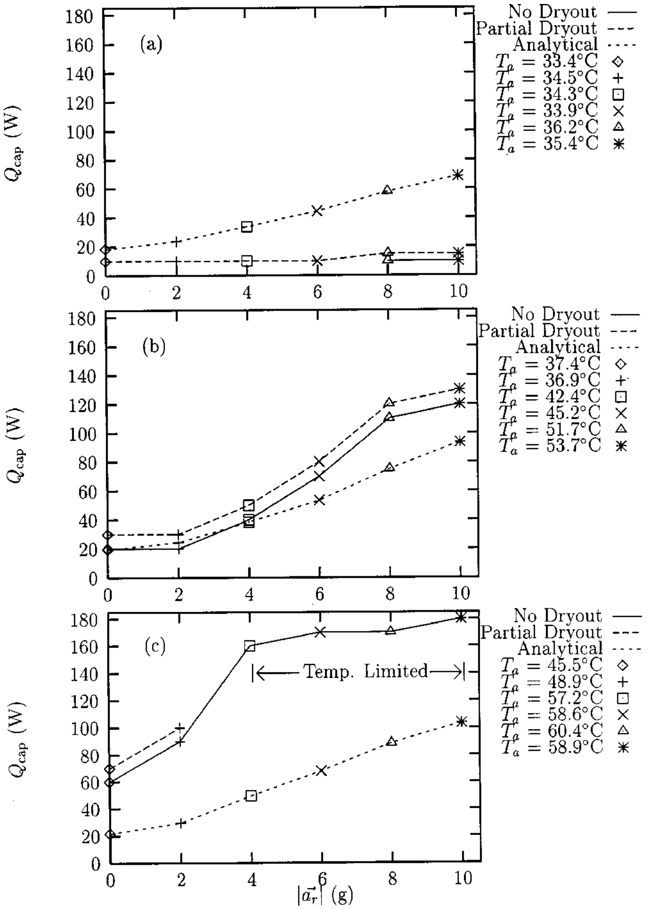

Fig. 9 Comparison of present model and experimental capillary limit data versus radial acceleration: (*a*) $G=0.5$; (*b*) $G=1.0$; and (*c*) $G=1.5$

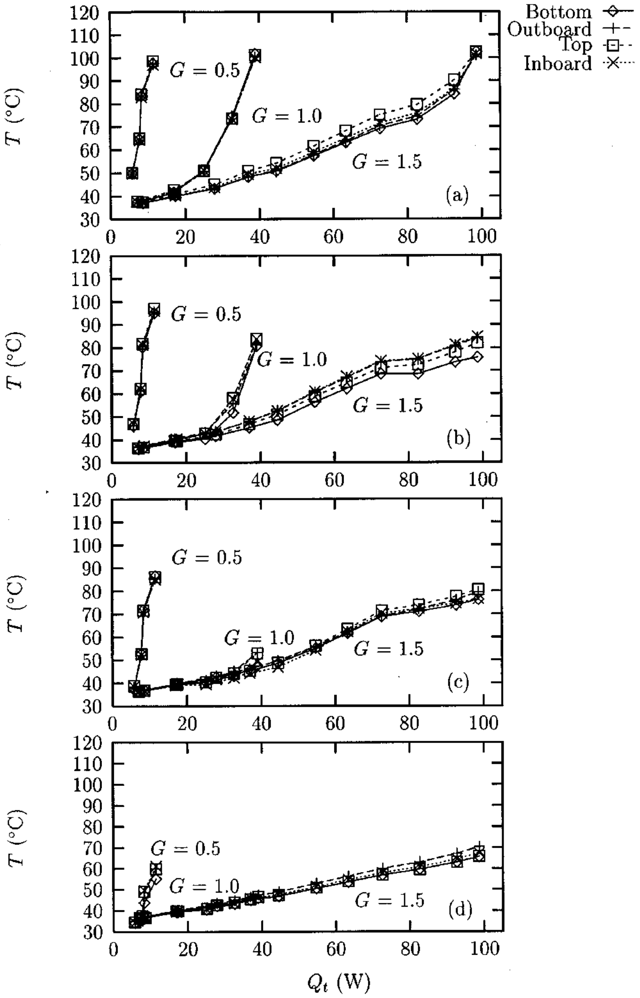

Fig. 10 Temperatures within the evaporator section versus transported heat for $|\vec{a}_r|=0.01$-g: (*a*) $x=54.0$ mm; (*b*) $x=92.1$ mm; (*c*) $x=130$ mm; and (*d*) $x=168$ mm

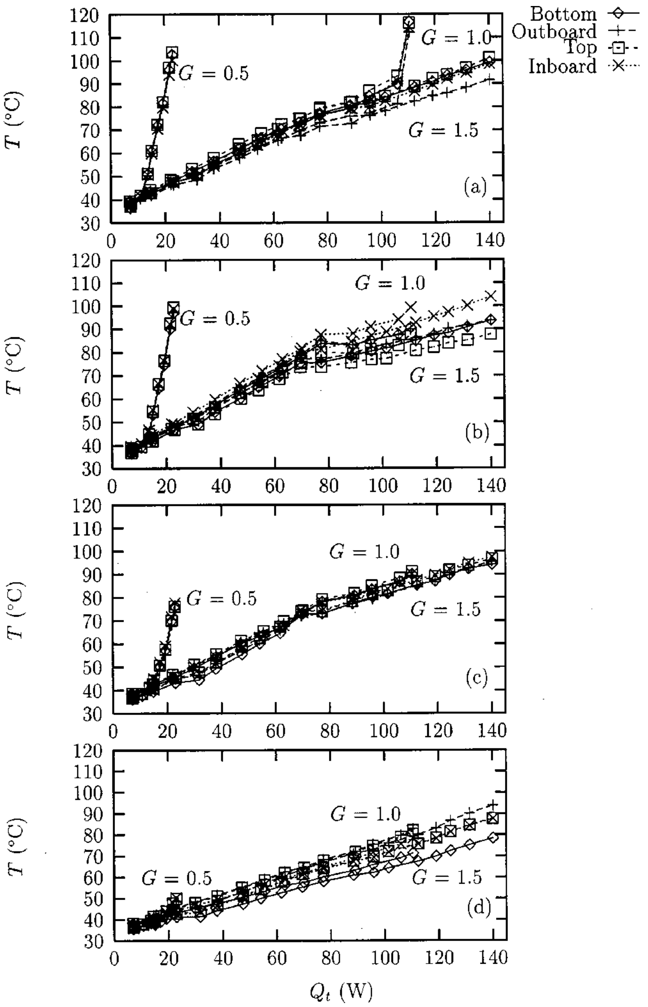

Fig. 11 Temperatures within the evaporator section versus transported heat for $|\vec{a}_r|=10.0$-g: (*a*) $x=54.0$ mm; (*b*) $x=92.1$ mm; (*c*) $x=130$ mm; and (*d*) $x=168$ mm

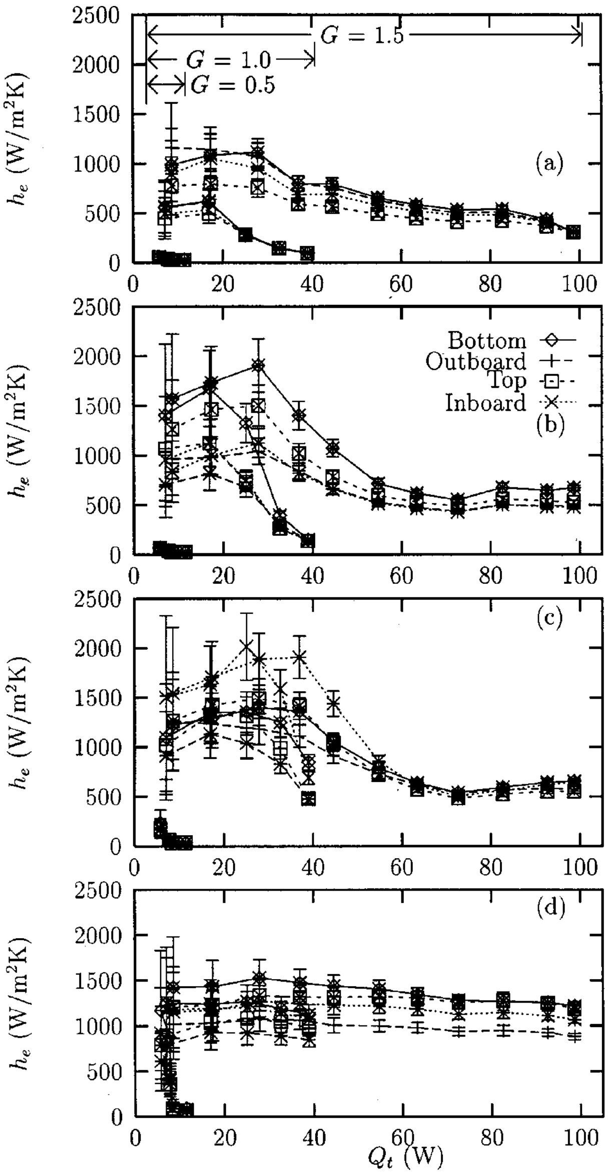

Fig. 12 Heat transfer coefficients within the evaporator section versus transported heat for $|\vec{a}_r|=0.01$-g: (*a*) $x=54.0$ mm; (*b*) $x=92.1$ mm; (*c*) $x=130$ mm; and (*d*) $x=168$ mm

For $G=0.5$, the heat pipe operated successfully only for $|\vec{a}_r|\geqslant 8.0$-g. In Fig. 9(*b*) ($G=1.0$), the capillary limit increased significantly with radial acceleration. With the heat pipe overfilled by 50 percent ($G=1.5$), the capillary limit increased dramatically, showing the effect that overfilling has on performance. The agreement of the analytical model was very good for $G=1.0$ as expected. For $G=0.5$, the model overpredicted the experimental data because it was assumed that the grooves were completely filled. For $G=1.5$, the model underpredicted the data due to the assumption that no liquid communication occurred between the grooves.

Temperatures within the evaporator section are shown in Figs. 10 and 11 for $|\vec{a}_r|=0.01$-g and 10.0-g, respectively. In general, the temperatures within the evaporator increased with transported heat. In addition, the wall temperatures decreased with G for a given heat transport due to the fact that more grooves were active. The temperatures along the length of the evaporator section can be tracked by examining the case for $G=1.0$. Near the evaporator end cap, the temperatures departed those for $G=1.5$ at approximately $Q_t=15$ W (Fig. 10(*a*)). At $x=92.1$ mm (Fig. 10(*b*)), this departure was delayed until approximately $Q_t=25$ W, and at $x=168$ mm (Fig. 10(*d*)), the data for $G=1.0$ and 1.5 were nearly coincident. This behavior shows that the grooves were essentially full near the adiabatic section, and proceeded to dry out closer to the evaporator end cap, as expected. Dryout for the $G=1.5$ case can be seen in Fig. 10(*a*) where the temperatures converged to nearly the same value around the circumference. It should be noted that the temperatures around the circumference were relatively uniform for $|\vec{a}_r|=0.01$-g. Evaporator temperatures for $|\vec{a}_r|=10.0$-g are shown in Fig. 11. In comparison to $|\vec{a}_r|=0.01$-g, the evaporator temperatures were in general lower due to the improved pumping ability of the helical grooves under increased radial acceleration. In addition, the temperatures tended to overlap over a greater range of heat transport values. In contrast to $|\vec{a}_r|=0.01$-g, the evaporator temperature variation was greater around the circumference at higher Q_t, but no pattern was distinguishable in the data.

Local heat transfer coefficient data versus heat transport is shown in Figs. 12 and 13 for $|\vec{a}_r|=0.01$-g and 10.0-g. Overall, the values for h_e were very low for $G=0.5$ due to the fact that most of the grooves were dried out. As the percent fill increased from $G=0.5$ to $G=1.0$, the heat transfer coefficient increased significantly. For $|\vec{a}_r|=0.01$-g (Fig. 12), h_e increased and then decreased with transported heat. This trend was also reported by Vasiliev et al. [4] for an aluminum axially grooved heat pipe with

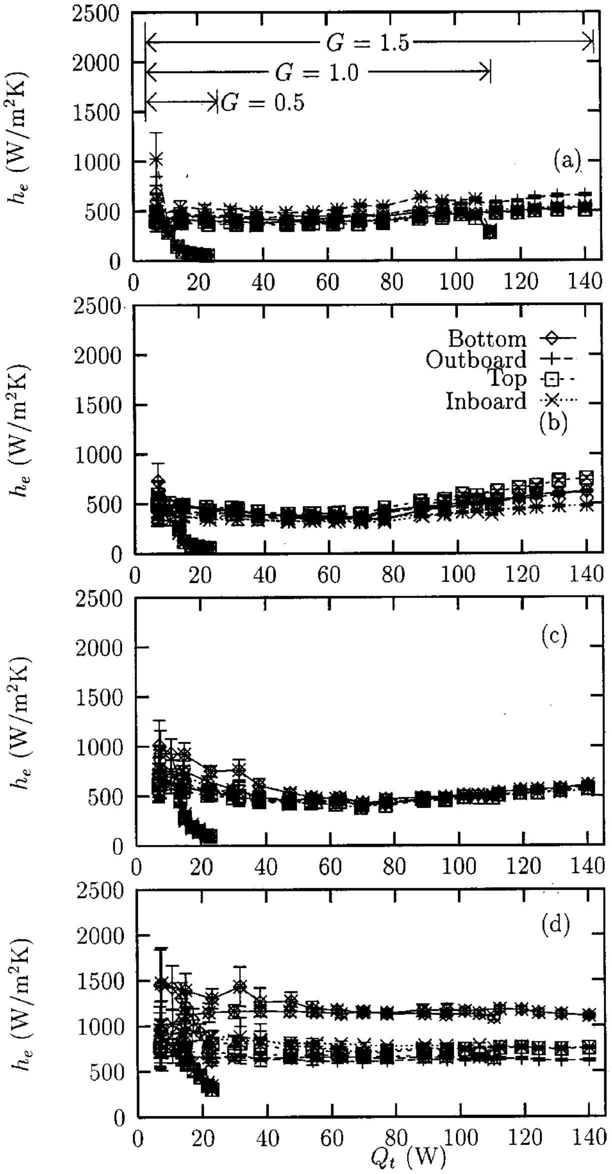

Fig. 13 Heat transfer coefficients within the evaporator section versus transported heat for $|\vec{a}_r|=10.0$-g: (*a*) $x=54.0$ mm; (*b*) $x=92.1$ mm; (*c*) $x=130$ mm; and (*d*) $x=168$ mm

acetone as the working fluid. For $G=1.0$ and 1.5, the heat transfer coefficient near the evaporator end cap (Fig. 12(*a*)) decreased until all of the values around the circumference converged. Closer to the adiabatic section, the heat transfer coefficient values around the circumference had not yet converged, showing these portions to still be active. For $|\vec{a}_r|=10.0$-g (Fig. 13), the values of h_e were significantly more uniform around the circumference and along the axial direction, even during a dryout event ($G=1.0$, Fig. 13(*a*)). In addition, the heat transfer coefficient seems to be more constant with respect to the transported heat compared to $|\vec{a}_r|=0.01$-g.

During the experiments, the heat pipe working temperature was not constant, which resulted in changes in the specific volume of the liquid and vapor of the working fluid. Since the heat pipe was filled at room temperature, it was important to quantify the potential effects of the change in volume of liquid in the grooves with temperature. Figure 14 shows the variation of the percentage of groove volume occupied by liquid G with saturation temperature for the three fill amounts over the range of working temperatures seen in the experiments. The maximum percent difference was 2.7 percent, which was not deemed to be significant.

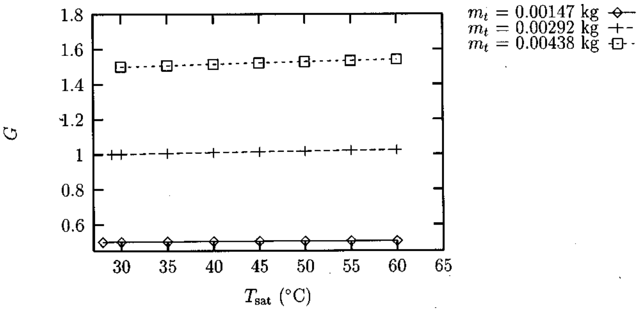

Fig. 14 Ratio of liquid volume to total groove volume versus saturation temperature

Conclusions

The effect of fluid inventory on the steady-state performance of a helically grooved copper-ethanol heat pipe has been examined both experimentally and analytically. It was found that the capillary limit increased and the thermal resistance decreased significantly as the amount of working fluid within the heat pipe increased. In addition, the evaporative heat transfer coefficient was found to be a strong function of the fill amount. The updated analytical model was in very good agreement with the experimental capillary limit results for $G=1.0$. However, the analytical model overpredicted the capillary limit data for $G=0.5$ and underpredicted the data for $G=1.5$.

Acknowledgments

Funding for this project was provided by the Air Force Research Laboratory (PRPG) under Grant F33615-98-1-2844, and by the Ohio Board of Regents. The authors would also like to acknowledge the technical assistance of Mr. Don Reinmuller.

Nomenclature

a = adiabatic length near the evaporator end cap, m
$\vec{a}_r$ = radial acceleration, m/s^2
A_e = surface area in the evaporator section, $\pi r_v^2 L_e$, m^2
A_{gr} = cross-sectional area of a groove, m^2
b = adiabatic length near the condenser end cap, m
D_o = tube outside diameter, m
D_{vs} = diameter of the heat pipe vapor space, m
G = Ratio of liquid volume to total groove volume, V_l/V_{gr}
h = groove height, m
h_e = local heat transfer coefficient in the evaporator section, $Q_t/A_e(T_w-T_a)$, W/m^2-K
I = heater current, A
L_a = adiabatic length, m
L_c = condenser length, m
L_e = evaporator length, m
L_{gr} = helical groove length, m
L_t = total heat pipe length, m
m_d = mass of working fluid dispensed by the filling station, kg
m_l = mass of liquid, kg
m_t = total mass of working fluid inventory, kg
m_v = mass of vapor, kg
$\dot{m}_c$ = coolant mass flow rate, kg/s
N_{gr} = number of grooves
p = helical pitch, m
Q_{cap} = capillary limit, W

Q_{in} = heat input at the evaporator, W

Q_t = heat transported, $\dot{m}_c C_p (T_{\text{out}} - T_{\text{in}})$, W

r_h = radius of the helix, m

r_v = radius of the heat pipe vapor space, m

R = radius of curvature, m

R_{th} = thermal resistance, $(T_{\text{eec}} - T_{\text{cec}})/Q_t$, K/W

s = coordinate along the centerline of the heat pipe, m

t_w = tube wall thickness, m

T_a = adiabatic temperature, K

T_{cec} = condenser end cap temperature, K

T_{eec} = evaporator end cap temperature, K

T_{in} = calorimeter inlet temperature, K

T_{out} = calorimeter outlet temperature, K

T_{sat} = saturation temperature, K

T_w = outer wall temperature, K

v_l, v_v = specific volume of liquid and vapor, m^3/kg

V = heater voltage

V_{gr} = volume of the grooves, m^3

V_{vs} = vapor space volume, m^3

w = width along the bottom of the groove, m

x = distance from the evaporator end cap, m

Δ = uncertainty

θ_1, θ_2 = angles from the sides of the groove to vertical, rad

ϕ = helix angle, rad

Subscripts

cap = capillary

gr = groove

l = liquid

max = maximum

v = vapor

vs = vapor space

References

[1] Klasing, K., Thomas, S., and Yerkes, K., 1999, ''Prediction of the Operating Limits of Revolving Helically Grooved Heat Pipes,'' ASME J. Heat Transfer, **121**, pp. 213–217.

[2] Thomas, S., Klasing, K., and Yerkes, K., 1998, ''The Effects of Transverse Acceleration Induced Body Forces on the Capillary Limit of Helically-Grooved Heat Pipes,'' ASME J. Heat Transfer, **120**, pp. 441–451.

[3] Brennan, P., Kroliczek, E., Jen, H., and McIntosh, R., 1977, ''Axially Grooved Heat Pipes,'' *AIAA 12th Thermophysics Conf.*, Paper No. 77-747.

[4] Vasiliev, L., Grakovich, L., and Khrustalev, D., 1981, ''Low-Temperature Axially Grooved Heat Pipes,'' *Proc. 4th Int. Heat Pipe Conf.*, London, pp. 337–348.

[5] Faghri, A., 1995, *Heat Pipe Science and Technology*, Taylor and Francis, Washington, D.C.

[6] Castle, R., 1999, ''The Effect of Working Fluid Inventory on the Performance of Revolving Helically Grooved Heat Pipes,'' Masters thesis, Wright State University, Dayton, OH.

[7] Miller, R., 1989, *Flow Measurement Engineering Handbook*, 2nd ed., McGraw-Hill, New York.

[8] Peterson, G., 1994, *An Introduction to Heat Pipes: Modeling, Testing, and Applications*, Wiley, New York.

[9] Lide, D., and Kehiaian, H., 1994, *CRC Handbook of Thermophysical and Thermochemical Data*, CRC Press, Boca Raton, FL.

[10] Carey, V., 1992, *Liquid-Vapor Phase-Change Phenomena*, Hemisphere, Washington, D.C.

[11] Schlunder, E., 1983, *Heat Exchanger Design Handbook*, Hemisphere, Washington, D.C.

[12] Ivanovskii, M., Sorokin, V., and Yagodkin, I., 1982, *The Physical Principles of Heat Pipes*, Clarendon, Oxford.

[13] Vargaftik, N., 1975, *Handbook of Physical Properties of Liquids and Gases*, Hemisphere, Washington, D.C.

[14] Timmermans, J., 1950, *Physico-Chemical Constants of Pure Organic Compounds*, Elsevier, New York.

[15] TRC, 1983, *TRC Thermodynamic Tables—Non-Hydrocarbons*, Thermodynamic Research Center: The Texas A & M University System, College Station, TX (loose-leaf data sheets).

[16] Dunn, P., and Reay, D., 1978, *Heat Pipes*, Pergamon, Oxford.

[17] ASHRAE, 1977, *Handbook of Fundamentals*, American Society of Heating, Refrigerating and Air-Conditioning Engineers, Inc., Atlanta, GA.

Sub-Continuum Simulations of Heat Conduction in Silicon-on-Insulator Transistors

Per G. Sverdrup
Department of Mechanical Engineering,
Stanford University,
Stanford, CA 94305

Y. Sungtaek Ju
Associate Mem. ASME
IBM Corporation,
Almaden Research Center

Kenneth E. Goodson
Associate Professor,
Associate Mem. ASME
Department of Mechanical Engineering,
Stanford University,
Stanford, CA 94305

The temperature rise in sub-micrometer silicon devices is predicted at present by solving the heat diffusion equation based on the Fourier law. The accuracy of this approach needs to be carefully examined for semiconductor devices in which the channel length is comparable with or smaller than the phonon mean free path. The phonon mean free path in silicon at room temperature is near 300 nm and exceeds the channel length of contemporary transistors. This work numerically integrates the two-dimensional phonon Boltzmann transport equation (BTE) within the silicon region of a silicon-on-insulator (SOI) transistor. The BTE is solved together with the classical heat diffusion equation in the silicon dioxide layer beneath the transistor. The predicted peak temperature rise is nearly 160 percent larger than a prediction using the heat diffusion equation for the entire domain. The disparity results both from phonon-boundary scattering and from the small dimensions of the region of strongest electron-phonon energy transfer. This work clearly shows the importance of sub-continuum heat conduction in modern transistors and will facilitate the development of simpler calculation strategies, which are appropriate for commercial device simulators. [DOI: 10.1115/1.1337651]

Keywords: Computational; Electronics, Heat Transfer, Numerical Methods, Temperature

1 Introduction

Each successive generation of transistors is scaled to smaller dimensions to improve speed and functionality. This scaling is currently yielding transistors with channels of length near 200 nm. This is comparable to the effective mean free path of phonons, which are quanta of lattice vibrations and dominant heat carriers in silicon, near room temperature [1,2]. The large electric fields near the drain side of transistors create regions of highest electron-phonon energy transfer in a transistor with characteristic dimensions of approximately 100 nm [3,4]. These regions dominate heat generation within the device and decrease in width with device scaling. Silicon-on-insulator (SOI) devices are fabricated in a thin silicon layer that is electrically isolated by a buried oxide layer as shown in Fig. 1(*a*). The isolation provided by the buried oxide reduces the effective electrical capacitance of the channel region and allows for greater transistor speed. However, SOI devices are particularly susceptible to thermal failure because of the low thermal conductivity of the underlying silicon dioxide layer. Cooling is enhanced by lateral thermal conduction in a silicon layer of thickness as low as 50 nm [5]. Because dimensions are comparable with the phonon mean free path, thermal simulations must consider the impact of phonon scattering on material boundaries and the small dimensions of the heated region on the temperature distribution. These sub-continuum thermal conduction phenomena cannot be directly calculated using the heat-conduction equation based on the Fourier law.

Phonon transport in semiconductor devices is modeled at present using diffusion theory based on the Fourier law (e.g., [4,6,7]). However, past work has illustrated the impact of non-local, or sub-continuum, phonon conduction in relatively simple geometries, including thin films, superlattices, and polycrystalline materials [1,8,9]. Sondheimer [10] analytically solved the BTE for electron transport in thin films, yielding a reduced effective electrical conductivity accounting for boundary scattering. This result can also be used to calculate a reduced effective phonon thermal conductivity accounting for interface scattering. This approach does not account for the severe departure from equilibrium in the phonon system that occurs when the phonon mean free path, Λ, is comparable to or exceeds the characteristic heat source dimension [11]. There have been no simulations that resolve non-local phonon transport in practical device geometries.

The present work integrates the two-dimensional BTE to simulate heat transport in a practical silicon-on-insulator (SOI) device geometry schematically drawn in Fig. 1(*b*). This type of device consists of two distinct regions: the silicon device layer and the buried oxide layer in which energy carriers have effective mean free paths of approximately 300 nm [2] and 1 nm, respectively, at room temperature. Although the phonon transport theory and therefore the stated mean free path of 1 nm are not strictly appropriate for amorphous materials (e.g., [12]), the important conclusion gained from this scaling remains valid. The phonon BTE is solved in the silicon layer to accurately model heat transport, but the simpler heat diffusion equation is used in the amorphous buried oxide region because the characteristic lengthscale of conduction is much smaller than the film thickness. The two distinct computational regions are coupled through interface conditions that account for differences in material properties. Predictions are compared to the temperature distribution obtained using the heat diffusion equation with bulk thermal properties in the commercially available semiconductor device simulator, MEDICI [13]. The electrical behavior of the SOI device is simulated in both cases using MEDICI, which solves the Poisson equation together with number conservation equations for electrons and holes. The electrical simulations are used to extract the spatial distribution of heat generation for incorporation into the phonon heat conduction simulations. The goal is to determine the impact of the small dimensions of the heat source and the small film thickness on the temperature distribution within the device. This will help with the interpretation of transistor failure data, e.g., due to electrostatic discharge (ESD) [14]. Furthermore, the simulations developed

---

Contributed by the Heat Transfer Division for publication in the JOURNAL OF HEAT TRANSFER. Manuscript received by the Heat Transfer Division September 23, 1999; revision received June 25, 2000. Associate Editor: A. Majumdar.

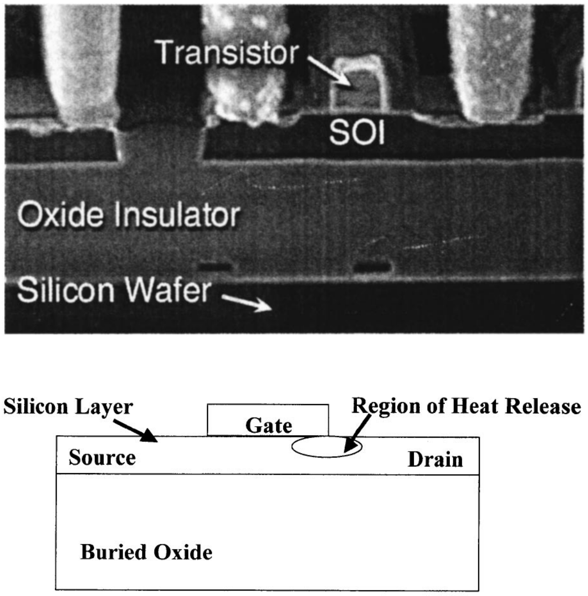

Fig. 1 (*a*) **Scanning electron micrograph of an IBM SOI transistor, which shows the thin silicon device layer separated from the bulk silicon substrate by a buried oxide layer (Courtesy of IBM Corporation); (*b*) schematic representation of a SOI device used in these simulations. The region of heat release corresponds to the region of strong electron-phonon scattering. The simulated device is a NMOS transistor with source/drain doping of arsenic at 1.5e20 cm^{-3}, phosphorous source/drain extensions, and a background boron doping concentration of 1e17 cm^{-3}.**

here will facilitate the development of simpler modeling strategies that can be readily incorporated into MEDICI and similar simulation packages for industrial use.

2 Governing Equations and Solution Approach

This manuscript demonstrates the impact of sub-continuum phonon transport on the temperature distribution in a practical device. The vehicle for demonstrating this is the SOI transistor with channel length of 400 nm shown in Fig. 1(*b*). Because of the computational demands presented by the phonon BTE, this initial study does not bi-directionally couple the electrical and thermal behavior in the device. Electrical transport and the spatial distribution of energy transfer to the phonon system are simulated using the standard industrial approach, which solves the Poisson equation and coupled conservation equations for electrons and holes. The phonon heat conduction simulations solve the BTE in the silicon layer, in which the mean free path is comparable to the layer thickness and the dimensions of the heat source. The continuum heat diffusion equation is solved in the underlying oxide.

2.1 Electrical Transport and Rate of Heat Generation in the Phonon System. The Poisson and electron and hole conservation equations are integrated using a commercial device simulator (MEDICI), which incorporates the distributions of impurities in the device based on a standard processing history. This approach is not the most detailed available for electron transport. More complicated simulations integrate the electron and hole Boltzmann equations [15] or take the hydrodynamic approach [3,16] to model electron energy and momentum transfer. In these simulations, energy transfer from highly energetic electrons, which are accelerated by the electric field in the device, to the heat conducting phonon system is calculated as the dot product of the electric current density and the electric field. This heat generation term is only approximately modeled in this manner in macroscopic devices, and this approach can yield significant errors in sub-micron devices. Due to the ballistic nature of electron transport, the peak in the dot product of current density and electric field profile can be displaced slightly from the peak in the transfer rate of electron energy to phonon energy. This shift in the heat source distribution could be expected to effect the peak temperature and temperature distribution within the device.

However, for two reasons detailed in the following paragraph, the use of the heat generation profile calculated from the dot product of current density and electric field is appropriate for this manuscript. Detailed simulation of hot electron effects in GaAs FET structures using the hydrodynamic electron transport equations [17] and Monte Carlo techniques [18] have demonstrated that the peak in the heat generation profile can be shifted from the peak in the electric field by as much as 100 nm. This work on GaAs found that the displacement of the maximum heating rate from the peak in the electric field is caused by the finite rate at which electrons leaving the high field region emit optical phonons. This shift can be approximated by multiplying the electron velocity (10^5 m/s) with the electron-optical phonon scattering rate, ~1 ps [17], to yield a shift in the heat source of 100 nm. In silicon, the relaxation time for electron-optical phonon scattering is approximately 0.3 ps [19]. The electron drift velocity is approximately 10^5 m/s in the saturation regime in silicon. The product of these two numbers yields $\Lambda_{\text{electron-optical phonon}} \sim 30\,\text{nm}$. This can be compared to the 400 nm channel length of the transistor and the phonon-phonon mean free path for heat transport, which is estimated to be 300 nm at room temperature. Based on this approximate estimate, the shift in the peak of the heated region in the transistors (~30 nm) may be a factor of ten smaller than the channel length (400 nm) and the phonon mean free path (~300 nm). While the impact on the lattice temperature distribution in the device may not be entirely negligible, the effect is indeed anticipated to be small and not expected to significantly alter the basic characteristics (peak and general shape) of the lattice temperature distribution obtained in the analysis.

The displacement of the heat source due to ballistic transport by the electrons is one among many important effects, including recombination of electrical carriers, that are neglected when the heat source is approximated as the dot product of current density and electric field. While the MEDICI simulations do not capture the precise location of the heated region, the magnitude of the heat generation calculated by the dot product of the current density and the electric field is a reasonable approximation to the actual heat generation rate in the steady state [20].

2.2 Phonon BTE in the Silicon Region. The phonon BTE is integrated in the silicon device layer because Λ exceeds the layer thickness and the heat source dimensions. The transient BTE can be written in the relaxation time approximation as

$$\frac{\partial f}{\partial t}+\vec{v}\cdot\nabla f=\frac{f_{\text{eq}}-f}{\tau_{\text{phonon}}}+q_{\text{electron-phonon}}, \tag{1}$$

where $f(x,y,t,\omega\mu,\eta)$ is the number of phonons in a given state described by the spatial coordinates x and y, the time t, the phonon frequency ω, and the direction cosines $\mu=\cos\theta$ and $\eta=\sin\theta\cos\phi$, which project the directions of phonon transport onto the x-y plane using the polar and azimuthal angles, θ and ϕ. In these simulations, the phonon velocity is assumed to be isotropic and is given by v. The first term on the right of Eq. (1) accounts for phonon scattering in the relaxation time approximation using the Planck distribution function,

$$f_{\text{eq}}=\frac{1}{\exp\left(\dfrac{\hbar\omega}{k_bT}\right)-1} \tag{2}$$

and the phonon scattering rate, τ_{phonon}. The mean free path is calculated using

$$\Lambda = v\,\tau_{\text{phonon}}. \tag{3}$$

The second term on the right hand side of Eq. (1) is the heat generation term, which is modeled as the dot product of current density and electric field. The transfer of energy from the electrons to the silicon lattice occurs on a timescale of about 0.3 ps through interactions between electrons and optical phonons [19], while the transport of thermal energy by phonons has an effective relaxation time of approximately 70–80 ps [21], yielding a difference of two orders of magnitude. Consequently, the energy transfer from the electrons to phonons is assumed to occur instantaneously when compared to heat transport time scales. This allows direct incorporation of the heat generation term from the device simulator into the BTE solver without solving coupled phonon and electron equations.

To be rigorous, phonon transport simulations should incorporate the frequency dependence of the phonon mean free path, Λ, and account for interactions between phonons of different frequencies. This requires solution of the BTE for many different frequencies, which has been performed for one-dimensional transport by several authors [9,11,22]. The present study focuses rather on the complexity of two dimensional transport in a practical device structure, and aims to illustrate the key phenomena through calculations neglecting the frequency dependence of phonon properties while capturing the essential heat transport physics. The present calculations are based on a simplified phonon energy transport model [2,21], where phonons are grouped into propagation and reservoir modes based on the dispersion relationships of the phonon modes [23]. The reservoir mode phonons have very small relaxation times or group velocities, and are assumed to remain near equilibrium. The propagation mode accounts for the entire heat transport, and is characterized using a single effective mean free path under the gray medium approximation. The distinction between the two modes is particularly relevant for covalently bonded semiconductors, where neglecting phonon dispersion can lead to significant error in estimating an effective carrier mean free path [24]. Based on the experimentally measured thermal conductivities of silicon films with thickness below 300 nm, Ju and Goodson [2] proposed that the longitudinal acoustic phonons are dominant heat carriers in silicon near room temperature and above. The present study assumes that the longitudinal acoustic phonons constitute the propagation mode, which yields a value for the effective mean free path consistent with the experimental data. The mean free path and phonon scattering rate used in this work are effective values for bulk silicon which account for scattering between all types of phonon modes (propagating-propagating and propagating-reservoir) through Matthiesen's Rule. The effective reduction in thermal conductivity caused by boundary scattering occurs when phonons travel near boundaries, without any additional parameters. The mean free path and relaxation time are extracted from the bulk thermal conductivity using the longitudinal acoustic phonon or propagating mode heat capacity and velocity in the following equation:

$$k = \frac{1}{3} C_{\text{prop}} v_{\text{prop}} \Lambda = \frac{1}{3} C_{\text{prop}} v_{\text{prop}}^2 \tau_{\text{phonon}}. \tag{4}$$

The BTE can be transformed into an equation that describes the phonon energy density by introducing the following quantity [2,21]

$$e'' = \int \hbar\omega [f - f_{\text{eq}}(T_{\text{ref}})] D(\omega)\, d\omega, \tag{5}$$

where e'' is the excess energy of phonons per unit volume and per unit solid angle, $\hbar\omega$ is the phonon energy, $f_{\text{eq}}(T_{\text{ref}})$ is the frequency dependent distribution function at a reference temperature, and $D(\omega)$ is the density of states per unit volume. The transformed BTE becomes

$$\frac{\partial e''}{\partial t} + \vec{v} \cdot \nabla e'' = \frac{e''_{\text{eq}} - e''}{\tau_{\text{phonon}}} + q'_{\text{electron-phonon}} \tag{6}$$

in which the parameters are frequency independent.

The phonon energy per unit volume per unit solid angle, e'', depends on the two dimensional x and y grid location as well as the direction of phonon transport within the sphere of solid angles. For calculations of the heat flux and total energy per unit volume at a given location, the Discrete Ordinates Method (DOM), originally developed for neutron and radiative transport, is used for integration over all solid angles. The solid angle sphere is divided into discrete directions of phonon transport distinguished by sets of μ and η values with weights, w_i, corresponding to solid angle fractions on the unit sphere [25–27]. The weights satisfy

$$\sum_i w_i = 4\pi. \tag{7}$$

This work uses the level symmetric hybrid (LSH) scheme [26] for angular discretization. Level symmetric techniques use the same set of direction cosine values in each coordinate direction ($\mu_1 = \eta_1, \mu_2 = \eta_2, \ldots$). In addition, the directions of phonon transport are chosen such that any particular direction has corresponding directions with 90 deg rotations about any axis ($\mu_n = \eta_n, \mu_n = -\eta_n, -\mu_n = \eta_n, -\mu_n = -\eta_n$). This simplifies the implementation of boundary conditions and removes directional biasing. The LSH method calculates directions and weights based on constraint equations such that moment equations of the phonon intensity are satisfied [26].

In order to obtain the temperature distribution, Eq. (6) is integrated forward in time in each of the discrete directions. The MacCormack time integration method, which is frequently used for solving hyperbolic equations [28], is used for explicit time advancement in order to capture the sharp features associated with the source term and to resolve the wavelike nature of solutions to the BTE. At each time step, e''^{n+1} is calculated from e''^{n} and e''^{n}_{eq}. Then, e''^{n+1}_{eq} is calculated before the solution can proceed. The equilibrium energy per unit volume per unit solid angle, e''_{eq}, is assumed to be the average value of e'' over all solid angles that would be obtained if the phonon system was allowed to relax to a uniform state. The equilibrium value of phonon energy per unit volume per unit solid angle is calculated as shown in Eq. (8).

$$e''_{\text{eq}} = \frac{1}{4\pi} \int_{\Omega = 4\pi} e''\, d\Omega \cong \frac{1}{4\pi} \sum_i e''_i w_i. \tag{8}$$

If the temperatures of the system are large compared to the Debye temperature or if the temperature variations within the system are small, the phonon heat capacity per unit volume, C, can be assumed to be constant. In this case, integration of the equilibrium energy density per unit volume per unit solid angle over all solid angles results in

$$e'_{\text{eq}}(T) = C(T - T_{\text{ref}}). \tag{9}$$

In this study, Eq. (9) is used to set appropriate values for the boundary conditions and to extract the final equilibrium temperature of the system using the frequency averaged heat capacity.

In order to capture the essential physics with the gray medium approximation, the heat capacity of the dominant longitudinal acoustic phonon heat carriers must be properly calculated using the phonon dispersion relation. The temperature dependence of the heat capacity of longitudinal acoustic phonons is evaluated using [21]

$$C = \frac{k_b^4}{2\pi^2 \hbar^2} T^3 \int_0^{\theta_D/T} \frac{1}{\nu_{ph}^2 \nu_{gr}} \frac{x^4 e^x}{(e^x - 1)}\, dx, \tag{10}$$

where θ_D is the Debye temperature for longitudinal acoustic phonons, v_{ph} and v_{gr} are the phase and group velocities of the longitudinal acoustic phonons, respectively, and x is a nondimensional frequency given by $x=(\hbar\omega)/(k_bT)$. Equation (10) is a direct extension of the dispersion model for thermal conduction in silicon developed by Holland [29] who provides the parameters used here.

2.3 Heat Diffusion Equation in the Silicon Dioxide Region The heat diffusion equation is valid in the amorphous buried oxide layer, and is written as

$$\frac{1}{\alpha_t}\frac{\partial T}{\partial t}=\nabla^2 T, \tag{11}$$

where α_t is the thermal diffusivity. Parabolic equations of this type have severe time step restrictions when integrated using explicit methods, resulting in time steps that are much smaller than required for stability by the MacCormack time integration of the BTE. Consequently, the Alternating Direction Implicit scheme [30] is used for time integration of the diffusion equation such that the time step can be made equal to that used for the silicon region.

3 Modeling the Silicon/Oxide Interface

In order to couple the silicon and oxide solution domains, it is necessary to calculate the flux of energy through the interface between the two materials at each point along the interface for every time step. When phonons strike an interface between two dissimilar materials, a fraction of the phonons will be transmitted through the interface with the remainder being reflected. The acoustic mismatch model (AMM) and the diffuse mismatch model (DMM) predict the boundary resistance between dissimilar materials [31,32]. The acoustic mismatch model assumes that all phonons have a specular interaction with the interface. This assumption is appropriate at low temperatures, for which the phonon wavelengths are much larger than the characteristic length scales of the surface roughness (e.g., [33]). For room temperature device operation, the dominant transport phonons have a much shorter wavelength than low temperature phonons, and the diffuse scattering of the DMM is more appropriate. The DMM [32] calculates the phonon transmission probabilities by using the principle of detailed balance and the densities of phonon states in each material. Written in a form appropriate for calculations using a single phonon mode, this yields

$$\alpha_i(\omega)=\frac{\nu_{3-i}^2}{\sum_i \nu_i^{-2}}, \tag{12}$$

where i is the material type (1 or 2) and v is the speed of the phonon. For small temperature differences across the interface, α is frequency independent [33]. Equation (12) does not rigorously account for the dispersion relationships of phonons and is most appropriate for low temperatures. This equation yields values of the transmission coefficient equal to 0.52 from silicon to oxide and 0.48 from oxide to silicon, using phonon velocities equal to 4240 m/s and 4100 m/s for silicon (high temperature longitudinal acoustic phonons) and oxide, respectively [29,34].

Both the DMM and the AMM theories have larger discrepancies with the experimental data near room temperature than at low temperatures. One explanation for this discrepancy is that these theories neglect nonlinear phonon dispersion and the phonon cutoff frequency, ω_d. Lattice vibrations cannot exist with wavelengths smaller than the separation between neighboring atoms, resulting in a phonon frequency, ω_d, above which phonons cannot exist [35]. The cutoff frequency is related to a characteristic temperature known as the Debye temperature, θ_d, by

$$\theta_d=\frac{\hbar\omega_d}{k_b}. \tag{13}$$

If the materials on opposing sides of the interface have different Debye temperatures, the maximum frequency that can be transmitted across the interface is determined by the material with the lower Debye temperature if only elastic scattering events are considered. For the ensemble of phonons at all energy levels, this results in a smaller transmission coefficient than is predicted by the DMM. The Debye temperatures of interest for a SOI device are 570 K [29] and 492 K [34] for silicon (longitudinal acoustic phonons) and amorphous silicon dioxide, respectively. At temperatures significantly below the Debye temperature, phonons are not occupying modes near the cutoff frequency and the DMM is valid. In this case, the device temperature exceeds $0.5\theta_d$ and phonons with frequencies greater than $\omega_{d,oxide}$ cannot transmit between silicon and oxide if only elastic collisions are allowed.

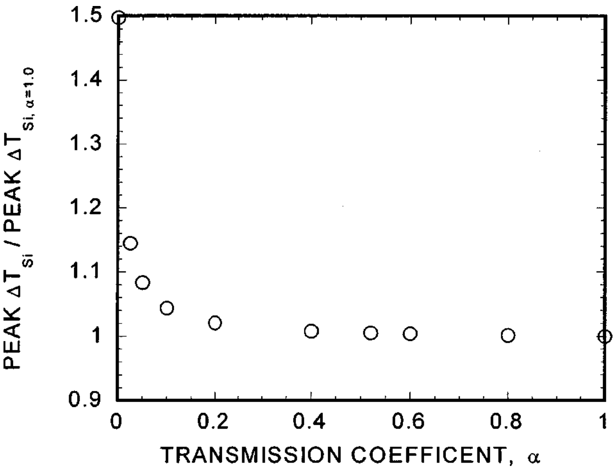

Fig. 2 Impact of the energy transmission coefficient at the silicon/silicon dioxide interface on the peak device temperature rise

In the graybody approximation used here, the effect of the cutoff frequency might be considered by reducing the transmission coefficient for transport from the material with the higher Debye frequency. The reduction would depend on the temperature near the interface because this influences the fraction of phonons above the lower Debye frequency. However, this approach might incur important errors due to inelastic scattering at the interface and nonlinearity in the phonon dispersion relationships near the Brillouin zone edge. For this reason, the present calculations use values of the transmission coefficients calculated using Eq. (12) without modification. In practice for this work, the precise value chosen for the transmission coefficients is not critical. This is shown in Fig. 2, which plots the peak temperature rise for a given transmission coefficient normalized by the peak temperature rise obtained by assuming that all of the incident energy on the silicon/oxide interface can pass through into the oxide ($\alpha=1$). This figure shows that the peak device temperature rise changes by less than two percent resulting from varying the transmission coefficient for materials with similar acoustic properties ($\alpha \sim 0.2-0.8$). The thinness of the silicon layer results in many phonon boundary scattering events at the silicon/oxide interface as the heat is transported along the silicon layer. This means that a large fraction of the heat in the phonon system can pass into the oxide, yielding results insensitive to the transmission coefficient for the geometry and boundary conditions used in this analysis.

The interface condition can now be specified with these coefficients and an energy balance at the interface depicted in Fig. 3. The resulting Eqs. (14) and (15), are listed below.

$$q=G-J=G-(\varepsilon E_b+\rho G) \tag{14}$$

$$J=\varepsilon E_b+\rho G. \tag{15}$$

The parameter q is the flux of energy into the oxide, and G is the irradiation or incident flux on the interface from the silicon side. The radiosity, J, is the flux of energy into the silicon and

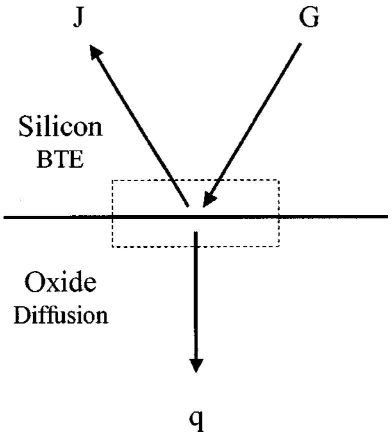

Fig. 3 Energy balance at the silicon/oxide interface

consists of phonon emission at the oxide surface temperature and the fraction of G that is reflected back into the silicon. The quantity E_b is analogous to the blackbody emissive power from radiation theory, but differs slightly due to the complexity of the dispersion relationships of a solid. It can best be defined as the energy flux that would be emitted into a silicon region by a surface maintained at the temperature of the neighboring oxide and is given by

$$E_b=\nu_p\sum_{\eta^+}\eta e''_{\text{eq}}(T^{n+1}_{ox,i})w=\frac{\nu_\rho}{4\pi}C_p(T^{n+1}_{oxi}-T_{\text{ref}})\sum_{\eta^+}\eta w. \tag{16}$$

The parameter α, defined by Eq. (12), is the fraction of G that passes into the oxide, $\rho=1-\alpha$ is the fraction of G reflected back into the silicon, and $\varepsilon=\alpha$ is the emissivity of the interface.

The numerical integration procedure is as follows. First, the solution in the silicon layer is explicitly advanced from time step n to $n+1$, assuming that the entire system is initially in equilibrium at a uniform temperature. This calculation yields the distribution of phonon energy per unit volume and allows for calculation of the irradiation, G, of the interface at each grid point with integration over all solid angles

$$G=\nu\sum_{\eta^-}\eta e''w, \tag{17}$$

where v is the longitudinal acoustic phonon velocity, which is assumed to be a constant. Next, the oxide must be advanced to time $n+1$ using the flux, q, as a boundary condition. The Alternating Direction Implicit method is used for solution of the oxide temperature distribution, and this requires knowledge of the interface flux at time $n+1$ given by

$$q_i=\nu\left(\alpha\sum_{\eta^-}\eta e''w-\varepsilon\sum_{\eta^+}\eta e''_{\text{eq}}(T^{n+1}_{ax,j})w\right), \tag{18}$$

where the diffuse blackbody radiation, E_b, leaving the surface is written in terms of the equilibrium energy per unit volume per unit solid angle at the oxide temperature at the time step $n+1$, ${T_{ox}}^{n+1}$. However, ${T_{ox}}^{n+1}$ is an unknown that is obtained by solution of a system of equations. Iteration must be used with guesses for the oxide temperature in Eq. (18) until the following condition is satisfied:

$$q_i=-k_{ox}\nabla T_{\text{boundary},t=n+1} \tag{19}$$

which states that the flux given by Eq. (18) is equal to the flux given by the diffusion equation in the oxide.

The solution is now updated to the time step $n+1$, and the solution can proceed with another solution of the BTE in the silicon layer. The boundary condition for the BTE at the silicon/oxide interface must be changed to yield the correct energy flux from the boundary, J. This is accomplished by resetting the values of e'' leaving the boundary into the silicon. Diffuse mismatch theory assumes that all scattering events at the boundary are diffuse, resulting in a uniform distribution of phonon intensity over the hemisphere of solid angles leaving the interface. For diffuse scattering, the phonon intensity leaving the surface in each direction is given by

$$I_{\eta^+}=\frac{J}{\pi}, \tag{20}$$

where the intensity is

$$I=ve''. \tag{21}$$

Using these relations, e'' in all directions leaving the interface in the positive direction is

$$e''_{\eta^+}=\frac{1}{\pi}\left(\varepsilon\sum_{\eta^+}\eta e''_{\text{eq}}(T^{n+1}_{ox})w+\rho\sum_{\eta^-}\eta e''w\right). \tag{22}$$

An adiabatic condition is maintained at the top of the silicon device, which yields

$$e''_{\eta^-}=\frac{1}{\pi}\sum_{\eta^+}e''_{\eta^+}w_{\eta^+}\eta. \tag{23}$$

The bottom of the simulation domain is assumed to be at a uniform temperature of 300 K because of the high thermal conductivity silicon substrate that is beneath the silicon dioxide layer. The left and right boundaries are also at a uniform temperature of 300 K at a distance from the heat source of the order of the thermal decay length in the silicon layer. These boundary conditions minimize the impact of the boundaries in the heat source region and effectively illustrate the importance of boundary scattering and small heat source size on the temperature distribution.

4 Numerical Methods and Code Verification

A cartesian grid is used for the discretization of the x-y plane in the silicon and silicon dioxide region. The minimum feature size of the heat generation region is of the order of $0.01\,\mu$m $=10$ nm. This is more than two orders of magnitude smaller than the domain width. Consequently, a non-uniform or stretched grid must be used in order to minimize computation time while accurately modeling the physics in the heat source region. The grid is centered around the peak in the heat generation profile and is increased in size using a geometric series with each consecutive grid spacing increasing by

$$dx_n=dx_{\text{initial}}r^{n-1} \tag{24}$$

in which r is the grid stretching parameter. In these simulations r is 1.04.

This code uses the explicit MacCormack time advancement scheme in order to capture the wave like nature of the solution. The time stepping criterion can be written in the familiar form used for advection type simulations in fluid mechanics

$$v\frac{dt}{dx}=cfl \tag{25}$$

in which v is the carrier velocity, *dx* is the minimum grid size, *dt* is the time step, and *cfl* is a number which relates the grid size and time step. For the BTE, the *cfl* number must be less than 0.5 for numerical stability.

The numerical solution of a transport equation such as the BTE also requires angular discretization within the sphere of solid angles to account for transport out of the two dimensional simulation plane. In these simulations, the S4, S6, and S8 discrete ordinate approximations are used, corresponding to 12, 24, and 40 angular directions, respectively. The run times and relative accu-

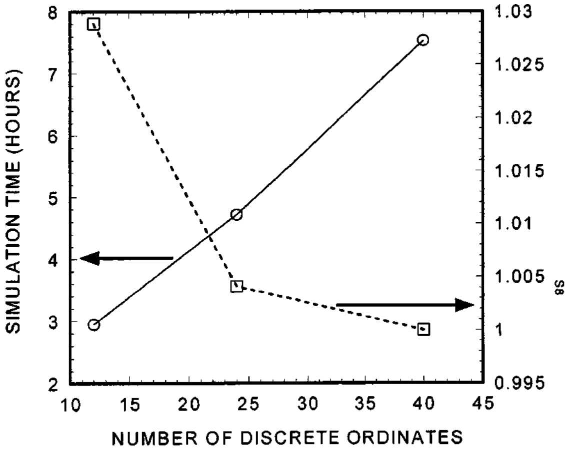

Fig. 4 Numerical characteristics of discrete ordinates approximations

racy are plotted in Fig. 4 and indicate that the S6 approximation is sufficient for reasonable numerical accuracy and run time.

The BTE code was numerically validated at both of its limits: the diffusion limit in which the phonon mean free path, Λ, is much smaller than the domain size and the near ballistic regime in which Λ is greater than the domain size. Excellent agreement is observed between the coupled BTE/diffusion solver and the solution obtained using a diffusion solver throughout the domain. The near ballistic limit can be verified by making comparisons with analytical solutions from radiation theory. Heaslet and Warming [36] calculated the ratio of the heat flux between two parallel plates compared to the heat flux from blackbody emission at the two wall temperatures when the mean free path of the radiation exceeds the plate separation. This is analogous to comparing the heat flux from the BTE to the heat flux from diffusion theory. Excellent agreement is obtained between the BTE code and the analytical solution for all mean free path to film thickness ratios.

5 Results and Discussion

In order to compare the temperature fields predicted by device simulators and the BTE code in a relevant device geometry, a model for a SOI device was generated using the semiconductor process simulator, TSUPREM4 [13]. This simulator models the processing steps required to fabricate transistors, including oxidation, diffusion, etching, and ion implantation. The result is a SOI device structure in which the silicon layer thickness, d_{Si}, is 72 nm, the buried oxide layer thickness, d_{ox}, is 243 nm, and the channel length, L_c, is approximately 400 nm. Each of these dimensions is comparable with the mean free path in silicon, indicating that boundary scattering effects will be important.

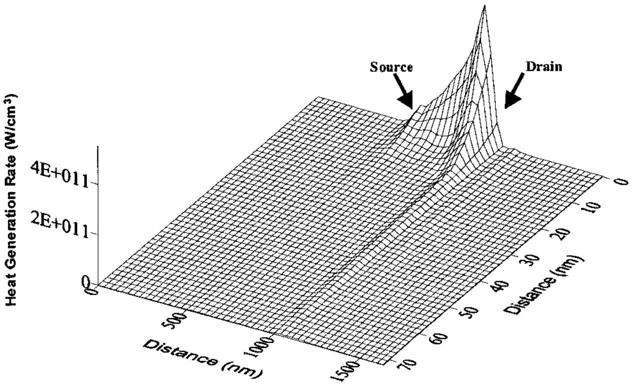

Fig. 5 SOI device heat generation rate caused by strong electron-phonon scattering. This quantity is extracted from an electrical simulation in MEDICI.

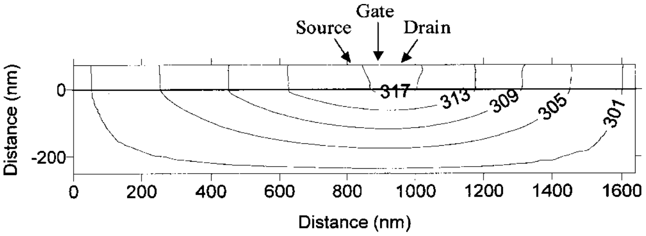

Fig. 6 Temperature contours in a SOI device calculated using the heat diffusion equation and bulk properties in MEDICI

This SOI device structure is then imported into the semiconductor device simulator, MEDICI. This simulator couples electrical transport with the heat equation to model both electrical and thermal characteristics. For this simulation, the gate and drain of the SOI transistor are biased at $V_G=2$ V and $V_D=2$ V, respectively, allowing current to flow through a thin conducting channel between the source and drain of the transistor. The electric field peaks near the drain junction of the device and imparts a large thermal energy to electrons in this region. These hot electrons collide with the lattice through electron-phonon scattering and transfer their energy into the phonon system, which conducts the heat out of the device. In the steady state, the heat generation rate (W/m^3) can be extracted as the dot product of the current density, $J_{current}$, and the electric field, E_{field}

$$q''' = q'_{\text{electron-phonon}} = \vec{J}_{\text{current}} \cdot \vec{E}_{\text{field}}. \tag{26}$$

The extracted heat generation rate is shown in Fig. 5. The heat generation is peaked on the drain side of the transistor. The conducting channel through which the electrical current flows is limited to the first few nanometers of silicon below the gate electrode. Consequently, the region of heat generation is also confined to this region, yielding a localized heat source, which has characteristic dimensions much smaller than the mean free path of phonon energy carriers. The small dimensions of the heat source are expected to increase the temperature rise over that predicted by diffusion theory [11].

Figure 6 plots the temperature contours in the silicon layer and buried oxide layer obtained from the heat diffusion equation and bulk thermal properties in MEDICI. The peak temperature in the device is 317.8 K and is located near the drain junction of the device. The isotherms in the silicon layer are nearly perpendicular to the silicon/oxide interface indicating that the silicon layer is nearly isothermal in the out-of-plane direction and that heat is predominantly transported along the plane of the silicon layer. This is expected because of the relatively large thermal impedance of the buried oxide layer.

The temperature contours within the SOI device from the coupled BTE/heat equation code are presented in Fig. 7. The temperature contours have the same characteristic shape, indicating

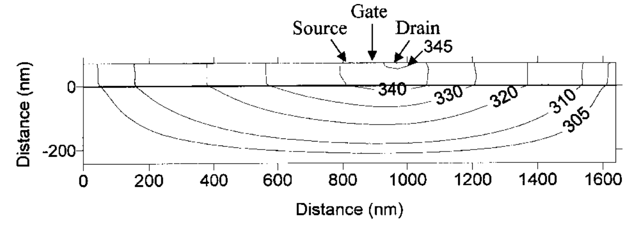

Fig. 7 Temperature contours in a SOI device calculated using the coupled BTE/heat diffusion equation code

that heat is flowing laterally out of the drain junction region. However, the boundary scattering and the effect of a heat source that is smaller than the phonon mean free path result in a peak device temperature of 346.0 K, an increase in the temperature rise of 159 percent over the value predicted by MEDICI. The entire channel region has a significantly higher temperature rise, which will effect electrical transport in the device.

The 317 K temperature contour in the MEDICI solution of Fig. 6 is 0.8 K from the peak temperature in the device and consists of straight lines that extend across the entire silicon layer thickness. In contrast, the 345 K temperature contour in the BTE solution is more curved and does not reach the oxide even though it is 1 K from the peak device temperature. This indicates that there is more temperature uniformity in the vicinity of the heat source region in the diffusion solution as compared to the more localized hot spot of the BTE solution. The increased temperature rise is caused by the fact that the heat source is smaller than the phonon mean free path. This effect is confined to a distance approximately two mean free paths from the edge of the heat source. This can be understood with the help of the survival function from kinetic theory

$$N = N_o \exp\left(-\frac{x}{\Lambda}\right) \tag{27}$$

which states that only a small fraction, N/N_o, of phonons generated in the heated region can traverse a distance much larger than the mean free path without having a collision. This small heat source effect is expected to have a large impact on short time-scale transient temperature rise under brief electrical stressing.

As stated in the introduction, Sondheimer [10] has developed an analytical solution to the BTE that can account for the reduction in thermal conductivity by boundary scattering. This effective thermal conductivity is appropriate for SOI devices because Sondheimer's assumptions for the electrical problem are equivalent to assuming that heat flows only laterally within the silicon layer. The reduced thermal conductivity given by Sondheimer's relation was inserted into MEDICI, and the resulting peak temperature rise was 339.6 K. This temperature is still 16.3 percent smaller than the peak temperature rise calculated using the coupled BTE/diffusion code because it does not account for the small dimension of the heat source.

The solutions from the BTE/diffusion code can also be compared to experimentally measured temperatures in SOI devices in order to explain the observed thermal behavior. Precise comparison of temperature distributions with experimental devices is not possible at present because experimental techniques do not exist for measuring temperature distributions in sub-micron transistors. Average temperature rise in the channel region can be measured and can be used for comparison. Goodson et al. [5] measured the average channel temperature in SOI field-effect transistors using electrical resistance thermometry. The device structure differs from that simulated in this paper; consequently, direct comparisons are not possible for an additional reason not related to experimental methods. The processing conditions and doping profiles used in the study of Goodson et al. [5] are unknown, making it difficult to construct an accurate representation of the device in a process simulator. However, the experimental results for a 78 nm thick silicon layer fall within the temperature rise range observed in this numerical study at the simulated power of 0.6 mW/μm. The study of Goodson et al. [5] yielded temperature rise data that were somewhat larger than their predictions, which were calculated using diffusion theory. This discrepancy could possibly be explained by the phonon non-equilibrium effect examined in this paper and by phonon boundary scattering, but might also result from the uncertainties in the dimensions and impurity concentrations for those devices, which influence predictions. More research needs to examine the phonon non-equilibrium effect in dedicated experimental structures, which resemble transistors and provide the opportunity to diminish the uncertainty in measurements of the temperature rise, the device dimensions, and the impurity concentrations.

6 Summary and Conclusions

This work presents a simulation approach for sub-continuum heat transfer in a SOI device geometry. The simulation couples the phonon BTE and the heat diffusion equation. The solution of the phonon BTE captures the impact of boundary scattering and small dimensions of heat sources on the peak temperature rise in semiconductor devices. The results from the coupled BTE/heat diffusion equation simulation are compared with temperature distributions obtained using the existing heat diffusion capabilities of the commercial device simulator MEDICI. For a SOI device in which the silicon layer thickness, d_{Si}, is 72 nm, the buried oxide layer, d_{ox}, is 243 nm, and the channel length, L_c, is approximately 400 nm, there is a 159 percent discrepancy in the peak steady-state temperature rise in the device between calculations made with the heat diffusion equation and calculations that consider micro-scale heat transfer phenomena. New thermal conductivity models must be developed that can account for both boundary scattering and the small dimensions of the heat source with the diffusion equation. More detailed calculations accounting for the combined behavior of optical, transverse, and longitudinal acoustic phonons can be considered in future work. Optical and high frequency transverse phonons will be grouped into a reservoir or capacitive mode with zero group velocity, and the longitudinal acoustic phonons will be characterized as the propagating mode. Interactions between the two modes will yield solutions appropriate for short transient high current electrical pulses. The solution method developed here for the two-dimensional BTE will be used for studies of the thermal characteristics of short time-scale electrostatic discharge events in which accurate prediction of temperature fields is currently not possible.

Acknowledgments

The authors appreciate technical input and comments from Tristan Burton, Mehdi Asheghi, William King, Robert Jacobs, and Younes Shabany, all from Stanford University. The authors also appreciate financial support from Texas Instruments through a fellowship for Per Sverdrup and from the Semiconductor Research Corporation through contract SJ-461.

Nomenclature

C = volumetric heat capacity, J/m^{3}K
$D(\omega)$ = phonon density of states per unit volume, 1 /m^3
d_{ox} = buried oxide layer thickness, m
d_{sl} = silicon layer thickness, m
E = phonon energy, J
E_b = blackbody energy flux, W/m^2
E_{field} = electric field, V/m
e'' = phonon energy per unit volume per unit solid angle, J/(m^3-sr)
e''_{eq} = equilibrium phonon energy per unit volume per unit solid angle, J/(m^3-sr)
e'_{eq} = equilibrium phonon energy per unit volume, J/m^3
f = phonon distribution function
f_{eq} = equilibrium phonon distribution function, Planck distribution
G = irradiation of silicon/oxide interface from silicon, W/m^2
$\hbar$ = Planck's constant divided by $2\pi = 1.054e^{-34}$ Js
I = phonon intensity, W/m^2
J = flux of energy leaving silicon/oxide interface into silicon, W/m^2
J_{current} = current density, A/m^2

k_b = Boltzmann constant$=1.38e^{-23}$ J/K
k_{ox} = oxide thermal conductivity, W/(m-K)
L_c = transistor channel length, m
N = number of surviving phonons
N_0 = initial number of phonons leaving a point in space
q = energy flux into oxide, W/m^2
q''' = heat generation rate, W/m^3
$q'_{\text{electron-phonon}}$ = source representing electron-phonon scattering, W/m^3
$q_{\text{electron-phonon}}$ = source representing electron-phonon scattering, 1/s
T = temperature, K
T_{ox} = oxide interface temperature, K
T_{ref} = reference temperature, K
t = time, s
V_D = transistor drain voltage, V
V_G = transistor gate voltage, V
v = phonon velocity, m/s
v_{gr} = phonon group velocity, m/s
v_{ph} = phonon phase velocity, m/s
w_i = discrete ordinate weights, steradians
x, y = coordinate, m

Greek Symbols

α = transmission coefficient
α_t = thermal diffusivity, m^2/s
ε = emissivity
Λ = frequency-averaged phonon mean free path, m
μ, η = direction cosine
Ω = solid angle, steradians
ρ = reflectivity
τ_{phonon} = phonon relaxation time
ω_d = phonon cutoff frequency, rad/s

Subscripts

b = blackbody
c = channel
D = transistor drain
d = Debye
eq = equilibrium
G = transistor gate
gr = group
i = index number
o = initial value
ox = oxide
ph = phase
prop = propagating mode
ref = reference value
si = silicon
t = thermal
η^+ = positive y-direction, into silicon
η^- = negative y-direction, into oxide

References

[1] Majumdar, A., 1993, ''Microscale Heat Conduction in Dielectric Thin Films,'' ASME J. Heat Transfer, **115**, pp. 7–16.
[2] Ju, Y. S., and Goodson, K. E., 1999, ''Phonon Scattering in Silicon Films with Thickness of Order 100 nm,'' Appl. Phys. Lett., **74**, pp. 3005–3007.
[3] Lai, J., and Majumdar, A., 1996, ''Concurrent Thermal and Electrical Modeling of Sub-Micrometer Silicon Devices,'' J. Appl. Phys., **79**, pp. 7353–7361.
[4] Raha, P., Ramaswamy, S., and Rosenbaum, E., 1997, ''Heat Flow Analysis for EOS/ESD Protection Device Design in SOI Technology,'' IEEE Trans. Electron Devices, **44**, pp. 464–471.
[5] Goodson, K. E., Flik, M. I., Su, L. T., Antoniadis, D. A., 1995, ''Prediction and Measurement of Temperature Fields in Silicon-on-Insulator Electronic Circuits,'' ASME J. Heat Transfer, **117**, pp. 574–581.
[6] Wolbert, P. B., Wachutka, G. K., Krabbenborg, B. H., and Mouthaan, T. J., 1994, ''Nonisothermal Device Simulation Using the 2-D Numerical Process/Device Simulator TRENDY and Application to SOI-Devices,'' IEEE Trans. Comput.-Aided Des., **13**, pp. 293–302.
[7] Yu, Z., Chen, D., So, L., and Dutton, R. W., 1994, ''PISCES-2ET—Two Dimensional Device Simulation for Silicon and Heterostructures—Device Simulation Manual,'' Stanford University, Stanford, CA.
[8] Chen, G., 1997, ''Size and Interface Effects on Thermal Conductivity of Superlattices and Periodic Thin-Film Structures,'' ASME J. Heat Transfer, **119**, pp. 220–9.
[9] Goodson, K. E., 1996, ''Thermal Conduction in Nonhomogeneous CVD Diamond Layers in Electronic Microstructures,'' ASME J. Heat Transfer, **118**, pp. 279–286
[10] Sondheimer, E. H., 1952, ''The Mean Free Path of Electrons in Metals,'' Adv. Phys., **1**, No. 1
[11] Chen, G., 1996, ''Nonlocal and Nonequilibrium Heat Conduction in the Vicinity of Nanoparticles,'' ASME J. Heat Transfer, **118**, pp. 539–545.
[12] Cahill, D. G., 1997, ''Heat Transport in Dielectric Thin Films and at Solid-Solid Interfaces,'' Microscale Thermophys. Eng., **1**, pp. 85–109.
[13] Avant! Corporation, 1999, *Medici: Two-Dimensional Semiconductor Device Simulation and TSUPREM-4: Two-Dimensional Semiconductor Process Simulation*, Fremont, CA.
[14] Duvvury, C., Amerasekera, A., Joyner, K., Ramaswamy, S., and Young, S., 1996, ''ESD Design For Deep Submicron SOI Technology,'' 1996 Symposium on VLSI Technology, pp. 194–195.
[15] Lundstrom, M., 1998, ''Scattering Theory of Carrier Transport in Semiconductor Devices,'' SISPAD 1998, p. 215–222.
[16] Blotekjaer, K., 1970, ''Transport Equations for Electrons in Two-Valley Semiconductors,'' IEEE Trans. Electron Devices, **ED-17**, No. 1, pp. 38–47.
[17] Buot, F. A., and Sleger, K. J., 1984, ''Numerical Simulation of Hot-Electron Effects on Source-Drain Burnout Characteristics of GaAs Power FETs,'' Solid-State Electron., **27**, No. 12, pp. 1067–1081.
[18] Moglestue, C., Buot, F. A., and Anderson, W. T., 1995, ''Ensemble Monte Carlo Particle Investigation of Hot Electron Induced Source-Drain Burnout Characteristics of GaAs Field Effect Transistors,'' J. Appl. Phys., **78**, No. 4, pp. 2343–2348.
[19] Majumdar, A., 1998, *Microscale Energy Transport*, C.-L. Tien et al., eds., Taylor & Francis, New York.
[20] Wachutka, G. K., 1990, ''Rigorous Thermodynamic Treatment of Heat Generation and Conduction in Semiconductor Device Modeling,'' IEEE Trans. Comput.-Aided Des., **9**, pp. 1141–1149.
[21] Ju, Y. S., 1999, ''Microscale Heat Conduction in Integrated Circuits and their Constituent Thin Films,'' Ph.D. thesis, Stanford University, Stanford, CA.
[22] Joshi, A., and Majumdar, A., 1993, ''Transient Ballistic and Diffusive Phonon Heat Transport in Thin Films,'' J. Appl. Phys., **74**, pp. 31–39.
[23] Armstrong, B., 1981, ''Two-Fluid Theory of Thermal Conductivity of Dielectric Crystals,'' Phys. Rev. B, **23**, No. 2, pp. 883–899.
[24] Ju, Y. S., and Goodson, K. E., 1997, ''Impact of Phonon Dispersion upon the Size Effect on Thermal Conduction along Thin Semiconductor Films,'' *Proc. ASME International Mechanical Engineering Congress and Exposition*, Dallas, TX, **DSC-Vol. 62**, pp. 181–190.
[25] Lewis, E., 1984, *Computational Methods of Neutron Transport*, Wiley, New York.
[26] Fiveland, W. A., 1991, ''The Selection of Discrete Ordinate Quadrature Sets for Anisotropic Scattering,'' *Fundamentals of Radiation Heat Transfer*, HTD-Vol 160, AMSE New York, NY, pp. 89–96.
[27] Siegel, R., and Howell, J., 1992, *Thermal Radiation Heat Transfer*, 3rd ed., Taylor & Francis, Washington, D.C.
[28] Glass, D., Ozisik, M., and McRae, D., 1985, ''On the Numerical Solution of Hyperbolic Heat Conduction,'' Numer. Heat Transfer, **8**, pp. 497–504.
[29] Holland, M. G., 1963, ''Analysis of Lattice Thermal Conductivity,'' Phys. Rev., **132**, pp. 2461–2471.
[30] Kreysig, E., 1993, *Advanced Engineering Mathematics*, 7th ed., Wiley, New York, pp. 1061–1063.
[31] Little, W. A., 1959, ''The Transport of Heat Between Dissimilar Solids at Low Temperatures,'' Can. J. Phys., **37**, pp. 334–349.
[32] Swartz, E. T., and Pohl, R. O., 1989, ''Thermal Boundary Resistance,'' Rev. Mod. Phys., **61**, pp. 605–668.
[33] Phelan, P. E., 1998, ''Application of Diffuse Mismatch Theory to the Prediction of Thermal Boundary Resistance in Thin-Film High-T$_c$ Superconductors,'' ASME J. Heat Transfer, **120**, pp. 37–43.
[34] Stephens, R. B., 1973, ''Low-Temperature Specific Heat and Thermal Conductivity of Noncrystalline Solids,'' Phys. Rev. B, **8**, pp. 2896–2905.
[35] Kittel, C., 1996, *Introduction to Solid State Physics*, Wiley, New York.
[36] Heaslet, M. A., and Warming, R. F., 1965, ''Radiative Transport and Wall Temperature Slip in an Absorbing Planar Medium,'' Int. J. Heat Mass Transf., **8**, pp. 979–984.

Photo-Acoustic Measurement of Thermal Conductivity of Thin Films and Bulk Materials

Xinwei Wang

Hanping Hu[1]

Xianfan Xu

School of Mechanical Engineering,
Purdue University,
West Lafayette, IN 47907

The photoacoustic (PA) technique is one of many techniques for measuring thermal conductivity of thin films. Compared with other techniques for thermal conductivity measurement, the photoacoustic method is relatively simple, yet is able to provide accurate thermal conductivity data for many types of thin films and bulk materials. In this work, the PA measurement in a high frequency range is made possible by a newly developed PA apparatus, which extends the limit of the PA technique. Thermal conductivities of SiO_2 with thicknesses from 0.05 to 0.5 μm on Si wafer, e-beam evaporated thin nickel film on Si wafer, and thermal barrier coatings are obtained. In addition to the commonly used phase shift fitting, which is only appropriate for thermally-thin films, an amplitude fitting method is developed and employed for measuring both thin films and bulk materials with smooth or rough surfaces. Comparing results by amplitude fitting to those obtained by other methods and reference values shows good agreements. Applications and limitations of the photoacoustic technique are discussed. [DOI: 10.1115/1.1337652]

Keywords: *Contact Resistance, Heat Transfer, Measurement Techniques, Thermoacoustics, Thin Films*

I Introduction

Thermal property data are important for any material that experiences heat transfer. The thermal conductivity and diffusivity of thin films are essential for the thin film manufacturing process, as well as for their applications in microelectronic devices. In devices such as radiation detectors, laser diodes, and transistors in electronic circuits, heat accumulated during device operation needs to be rapidly removed, which is greatly affected by their thermal conductivity and diffusivity.

It has been well known that the thermal conductivity of thin films may differ significantly from the bulk value due to the difference in microstructure such as the grain size, amorphousness, and concentration of foreign atoms and defects, which strongly affect the scattering process of the energy carriers. Although theories have been developed to predict the thermal conductivity of thin films, experiments are often needed to determine thermal conductivity of thin films owing to the complexity of the thin film microstructure. Since the microstructures of thin layers depend strongly on fabrication techniques, thermal conductivity measurements must be performed on the same microstructures fabricated with the same processes as those used in real devices for which the thermal conductivity is needed. In the last decade, many techniques have been developed to measure thermophysical properties of thin film materials. Goodson and Flik [1] reviewed techniques for measuring thermal conductivity along and across thin film layers. It is concluded that more detailed uncertainty analysis is required for most of the available techniques. More recently, Mirmira and Fletcher [2] reviewed experimental and analytical techniques for measuring and predicting thermal conductivity of thin films.

Techniques for thermal conductivity measurement can be categorized into contact and non-contact methods. In contact measurements, normally a thin metal film is deposited onto the sample surface that is subsequently patterned into electric circuitry. The temperature response of the sample structure under thermal loading is sensed by the circuit, and related to unknown thermal properties. Methods in this category include the bolometer method [3], 3ω and extended 3ω method [4–6], pulse heating method [7], and micro bridge method [8–10]. Drawbacks of the contact methods are that they are limited to dielectric thin films only, and the sample preparation process is laborious.

The other category of the thermal conductivity measurement technique is the non-contact method. Optical techniques belong to this category, for which the optical response of a probing beam is measured when the sample is subjected to photothermal excitation. The thermal conductivity of the sample can be obtained by measuring the phase shift of the reflected beam due to surface deformation [11], the reflectivity change due to pulse laser heating [10], or deflection of the probing beam due to change of the index of refraction of air near a heated sample [12]. For the reflectance measurement, pico and subpicosecond lasers have been used [13], which make it possible to measure thermal conductivities of thin films as thin as nanometers. In addition to the measurement of thermal properties, the picosecond pulse induced ultrasound was used to simultaneously determine the thickness of the thin film [14].

The photoacoustic (PA) method is a relatively simple, non-contact method for measuring thermal conductivities. However, this method has not received much attention for measuring thermal properties of thin films. For example, there is no discussion of this technique in the review papers mentioned above. In the PA measurement, a heating source, normally a laser beam, is periodically irradiated on the sample surface. The acoustic response of the air above the sample is measured and related to thermal properties of the sample. A review of the PA technique was given by Tam [15]. The PA phenomenon was first explained by Rosencwaig and Gersho [16] as the result of thermal expansion of the gas adjacent to the sample surface. An analytic solution of the PA response of a single layer on a substrate was also given by Rosencwaig and Gersho [16]. Since then, a number of detailed investigations have been performed. Fujii et al. [17] derived an analytical solution of the PA response of two layers of films on a substrate. Baumann and Tilgner [18] developed a model for cases of any number of layers. The constraints of their model are that

---

[1] On leave from the Department of Thermal Science and Energy Engineering, University of Science and Technology of China, China.

Contributed by the Heat Transfer Division for publication in the JOURNAL OF HEAT TRANSFER. Manuscript received by the Heat Transfer Division October 25, 1999; revision received, June 25, 2000. Associate Editor: A. Majumdar.

the laser beam has to be absorbed within the first layer, and no thermal contact resistance is considered. Cole and McGahan [19] provided a solution which can be used for more general PA problems, which considers optical absorption in any layer and contact resistances between layers of a multilayer system. Numerical integration is required to calculate the temperatures in films and in substrate. The PA technique has been used successfully to obtain thermal conductivity of thin films. By fitting amplitude and phase shift of PA signals, Lachaine and Poulet [20] measured the thermal conductivity of 18 μm-thick polyester films. Raman et al. [21] measured the thermal diffusivity by determining the frequency ascertaining whether a layer is thermally thin or thermally thick. By fitting the phase shift of the PA signal, Rohde [22] measured the thermal conductivity of films as thin as 500 nm.

In this work, a PA measurement apparatus is designed for measurements up to a frequency of 20 kHz, higher than the highest frequency used by other investigators (2 kHz). This allows properties of thinner films to be measured. Also an amplitude fitting method is developed to measure bulk materials or films with rough surfaces. The data reduction procedure is based on the recently developed generalized photoacoustic model [23]. By fitting phase shift and amplitude of PA signals, thermal conductivity data of thin SiO_2 films, thin nickel film, thermal barrier coatings, and bulk materials with smooth and rough surface are obtained.

II Theory of the Photoacoustic Method

The sample considered in this work consists of a backing material (0) and N successive layers $(1,2,\cdots,N)$, and is heated by a modulated laser beam with an intensity of $1/2\cdot I_0(1+\cos(\omega t))$. The coordinate x is originated from the surface of the sample and pointing outward. Absorption of the laser beam is allowed in any layer, and in more than one layer. An additional medium $(N+1)$, such as air, is in contact with the surface layer (N). The backing material (0) and the surrounding medium $(N+1)$ are considered to be thermally thick. It has been shown that when the thermal diffusion length in gas is much less than the radius of the sample chamber, the PA signal is independent of the energy distribution of the incident laser beam [24]. Therefore, a one-dimensional model of the PA effect is adequate. The transient temperature field in the multilayer sample and air can be derived by solving a set of one-dimensional heat conduction equations. Details of the derivation process have been described elsewhere [23]. The solution of the complex temperature distribution θ_{N+1} in the air can be expressed as

$$\theta_{N+1}=(1-\rho)\cdot B_{N+1}e^{-\sigma_{N+1}x}e^{j\omega t}, \tag{1}$$

where

$$B_{N+1}=-\frac{[0\ \ 1]\cdot\sum_{m=0}^{N}\left(\prod_{i=0}^{m-1}U_i\right)\cdot V_m\cdot\begin{bmatrix}E_m\\E_{m+1}\end{bmatrix}}{[0\ \ 1]\cdot\left(\prod_{i=0}^{N}U_i\right)\cdot\begin{bmatrix}0\\1\end{bmatrix}}; \tag{2}$$

$$U_i=\frac{1}{2}\begin{bmatrix}u_{11,i} & u_{12,i}\\ u_{21,i} & u_{22,i}\end{bmatrix};\quad V_i=\frac{1}{2}\begin{bmatrix}\nu_{11,i} & \nu_{12,i}\\ \nu_{21,i} & \nu_{22,i}\end{bmatrix}; \tag{3a}$$

$$u_{1n,i}=(1\pm k_{i+1}\sigma_{i+1}/k_i\sigma_i\mp k_{i+1}\times\sigma_{i+1}R_{i,i+1})\cdot\exp(\mp\sigma_{i+1}l_{i+1}),\quad n=1,2; \tag{3b}$$

$$u_{2n,i}=(1\mp k_{i+1}\sigma_{i+1}/k_i\sigma_i\mp k_{i+1}\times\sigma_{i+1}R_{i,i+1})\cdot\exp(\mp\sigma_{i+1}l_{i+1}),\quad n=1,2; \tag{3c}$$

$$\nu_{n1,i}=1\pm\beta_i/\sigma_i,n=1,2; \tag{3d}$$

$$\nu_{n2,i}=(-1\mp k_{i+1}\beta_{i+1}/k_i\sigma_i+k_{i+1}\times\beta_{i+1}R_{i,i+1})\cdot\exp(-\beta_{i+1}l_{i+1}); \tag{3e}$$

$$E_m=\frac{G_m}{\beta_m^2-\sigma_m^2}; \tag{4a}$$

$$G_m=\frac{\beta_m I_0}{2k_m}e^{-\Sigma_{i=m+1}^{N}\beta_i l_i}\ \text{for}\ \ m<N, \tag{4b}$$

$$G_m=\frac{\beta_m I_0}{2k_m}\ \text{for}\ \ m=N,\quad G_m=0,\quad\text{for}\ \ m=N+1.$$

In the above equations, $\sigma_i=(1+j)a_i$ with $j=\sqrt{-1}$ and $a_i=\sqrt{\pi f/\alpha_i}$. α_i is thermal diffusivity of layer i, f is the modulation frequency, k_i is the thermal conductivity of layer i, ρ is surface reflectivity of the sample, β_i is the optical absorption coefficient of layer i, and $R_{i,i+1}$ is thermal contact resistance between layer i and $i+1$. In the calculation, l_{N+1} is taken as 0 and $\Pi_{k=m}^{m-1}U_k$ is taken as $\left[\begin{smallmatrix}1&0\\0&1\end{smallmatrix}\right]$, where m is any integer between 0 and $N+1$.

The temperature in the gas layer is related to the phase shift and the amplitude of the PA signal. According to the generalized PA theory [23], the phase shift of the PA signal is calculated as $Arg(B_{N+1})-\pi/4$, and the amplitude is calculated as $Abs[(1-\rho)\cdot B_{N+1}P_0/\sqrt{2}l_{N+1}a_{N+1}T_0]$, where P_0 and T_0 are the ambient pressure and temperature, respectively.

III Experimental Details

The schematic of the experimental setup is shown in Fig. 1. A diode laser, which operates at a wavelength of 0.8 μm, is used as the heating source. The laser power driver is sinusoidally modulated by the internal function generator of a lock-in amplifier. The output power of the diode laser is around 150 mW at the modulation mode. After being reflected and focused, the laser beam is directed onto the sample mounted at the bottom of the PA cell. During the experiment, the maximum temperature rise at the sample surface is less than 0.5 °C. A condenser microphone, which is built into the PA cell, senses the acoustic signal and transfers it to the lock-in amplifier, where the amplitude and phase of the acoustic signal are measured. A personal computer, which is connected to the GPIB interface of the lock-in amplifier, is used for data acquisition and control of the experiment.

The PA cell used in this experiment is a cylindrical, small volume, resonance-free cell made of highly polished acrylic glass and a sapphire window. Both acrylic glass and sapphire have low reflection and high transmission for the laser beam used, so most of the laser energy reflected from the sample surface transmits out of the cell. At a frequency of 20 kHz, the wavelength of the acoustic wave is about 17.4 mm. In order to avoid resonance occurring in the cell, the characteristic cell size has to be less than 8.7 mm. Therefore, the cell is designed to have an axial bore of 4 mm in diameter and 6 mm high. The side of the bore facing the laser beam is sealed by the sapphire window, and the other side is sealed by the sample with an O-ring. In order to enhance the signal, the microphone is mounted 2 mm away from the inside wall of the cell, which is the smallest distance allowed by the size of the microphone and the cell. On the other hand, the smallest

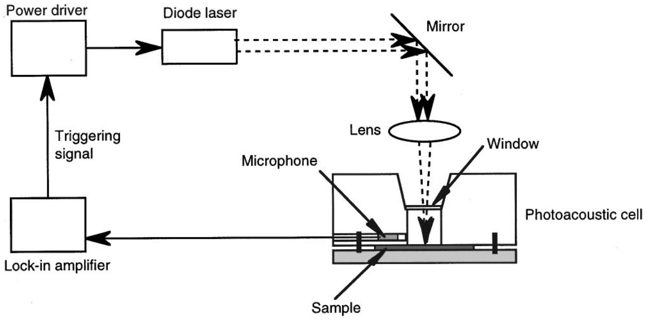

Fig. 1 Schematic diagram of the photoacoustic apparatus

size of the cell is limited by the dimension of the microphone. It is believed that the cell designed in this work is optimized considering both the signal to noise ratio enhancement and resonance suppression.

The PA response is delayed by the time for the acoustic wave to reach the microphone and the electronic circuitry. In order to remove the delay of the PA signal, reference samples of known thermal properties are used for calibration. Two reference samples are measured, one is a 3 mm thick graphite with its surface polished to 50 nm surface finishing, the other is a pure silicon wafer (0.381 mm thick) with a 70 nm thick nickel coating. Because of the small size of the laser beam (1 mm×2 mm), at frequencies lower than 2 kHz, the two-dimensional heat transfer effect could exist, hence, only frequencies from 2 kHz to 20 kHz are used. Within this frequency range, both the polished graphite and the Ni-Si are thick enough to be considered as bulk materials, and the phase shift is −90 deg. For the Ni-Si reference sample, the amplitude of the PA signal only depends on surface reflectivity and thermal properties of the silicon substrate.

After the phase shift of graphite, ϕ'_{graphite}, is obtained, the true phase shift of the sample, ϕ, is calculated as $\phi=\phi'-\phi'_{\text{graphite}}-90$, where ϕ' is the measured phase shift for the sample. The amplitude of the sample signal needs to be normalized with the reference signal since its absolute value is difficult to obtain. The normalized amplitude of the sample, A, is calculated as $A=A'/A'_{\text{Ni-Si}}\cdot A_{\text{Ni-Si}}$, where A' is the measured amplitude, $A'_{\text{Ni-Si}}$ is the measured amplitude for the Ni-Si reference sample, and $A_{\text{Ni-Si}}$ is the amplitude for the Ni-Si sample calculated using Eqs. (1)–(4).

The experimental setup is calibrated before each measurement. At each frequency, the signal is allowed to stabilize first, then data are taken every 8 sec. The phase shift and amplitude data are averaged every 5 min. A computer code determines whether the variation of the average phase shift over the five minutes time span is less than 0.2 deg, and the relative variation of the average amplitude is less than 0.5 percent. Data are stored when the above criterion is reached. In order to determine the drift of the signals with time, the references are also measured after each sample measurement.

A least square fitting procedure is used to determine unknown properties such as thermal conductivity and thermal contact resistance. Trial values of unknown properties are used to calculate the phase shift and the amplitude of the PA signal at each experimental frequency. For each trial value, the sum of the square of the difference between calculated values of phase shift and amplitude, and experimental ones is calculated. The trial values for which the least square is obtained are taken as the property values.

IV Results and Discussion

Thermal conductivities of thin SiO_2 films, nickel film, and thermal barrier coatings are measured. Results of the PA measurements will be first presented. Then, the measurement uncertainty of the PA technique will be discussed.

IV.1 Results of the PA Measurement

SiO_2 Films. Thermal conductivities of four SiO_2 films thermally grown on Si wafer are measured. The thicknesses of the SiO_2 films are 50, 101.9, 201.9 and 484.5 nm. In order to absorb the laser beam, a 70 nm thick nickel film is deposited on top of the SiO_2 layer by e-beam evaporation. The thickness of the nickel film is monitored during the evaporation process. The final film thickness is measured with an accuracy of 0.5 nm.

In Fig. 2, the phase shift as a function of the modulation frequency for the 484.5 nm thick SiO_2 sample is shown. The thermal conductivity of SiO_2 is fitted to be 1.71 W/m·K. Based on the ±0.2 deg uncertainty of the experiment, the uncertainty of thermal conductivity is found to be ±0.08 W/m·K. The fitting lines corresponding to the experimental uncertainty are also shown in Fig. 2. Figure 3 shows thermal conductivities of all the four SiO_2 films. From the figure, it is seen that thermal conductivities of all the SiO_2 films are around 1.66 W/m·K, higher than the thermal conductivity of fused silica (1.4 W/m·K). As shown in Fig. 3, variations of the thermal conductivity with thickness are not evident. This could indicate that the structure of the thermally grown SiO_2 film changes little with thickness.

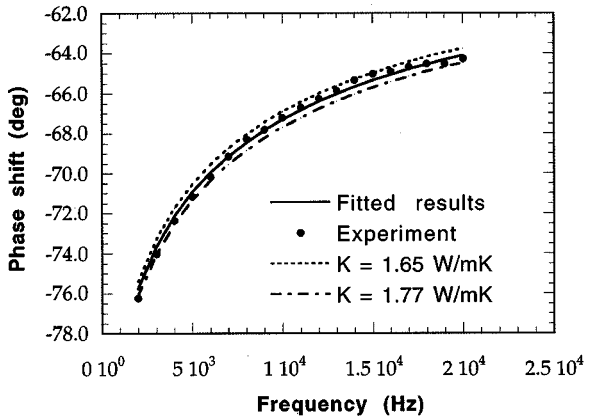

Fig. 2 Phase shift as a function of the modulation frequency of the 70 nm Ni—484.5 nm SiO_2—Si sample

Thermal conductivities of SiO_2 are also obtained by fitting the amplitude of the PA signal. Since the same 70 nm Ni layer is coated on the Ni-Si reference and the samples, reflectivity is expected to be the same, which is verified by measurements. Figure 4 illustrates the normalized amplitude for the 484.5 nm thick SiO_2 sample. The thermal conductivity is found to be 1.47 W/m·K. Based on the ±0.5 percent experimental uncertainty of the measured amplitude of PA signal, the numerical uncertainty analysis shows that the thermal conductivity has an uncertainty of about ±0.1 W/m·K. Thermal conductivity data of SiO_2 with different thicknesses obtained by amplitude fitting are summarized in Fig. 5. From this figure, it seems that thermal conductivity of SiO_2 slightly decreases with the thickness increase, which is not seen in the results obtained from phase shift fitting. However, this trend is not conclusive due to the experimental uncertainties of the measured amplitude of the PA signal. For thinner films, the signal is weaker and less stable, therefore the signal has a larger uncertainty of about ±1.5 percent, which causes a larger uncertainty in the final fitted results. Also when the film thickness is much less than the thermal diffusion length, for the same experimental un-

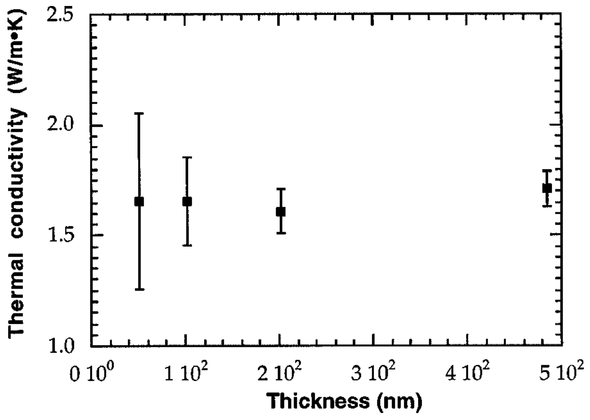

Fig. 3 Thermal conductivity of SiO_2 films obtained by phase shift fitting

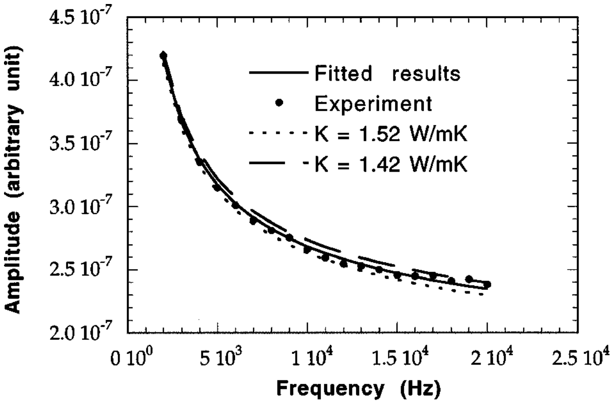

Fig. 4 Normalized amplitude as a function of the modulation frequency of the 70 nm Ni—484.5 nm SiO_2—Si sample

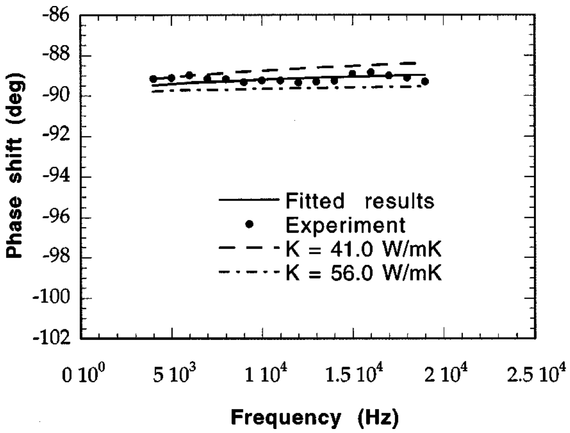

Fig. 6 Phase shift as a function of the modulation frequency of the 999.5 nm Ni—Si sample

certainty, the thinner film will have a larger uncertainty for its fitted thermal conductivity. The measurement sensitivity is discussed in more detail in IV.2.

From Fig. 3 and Fig. 5, it is seen that there is some discrepancy between the thermal conductivity measured by phase shift fitting and amplitude fitting. This discrepancy mostly comes from the uncertainty in the reflectivity measurement, which is required for amplitude fitting, but not for phase shift fitting. If the calculation includes the effect of the uncertainty in the reflectivity measurement, the uncertainty of the thermal conductivity resulted from amplitude fitting will be larger, on the order of 15 percent for the 484.5 nm thick SiO_2 film and 25 percent for the 50 nm-thick SiO_2 film. The thermal conductivity of the SiO_2 film measured in this work is slightly larger than that of fused silica ($k=1.4\,W/m\cdot K$). For thermally grown thin SiO_2 films, measurements using other techniques also showed similar results [7], which were explained as a higher level of crystallinity in SiO_2 thin films than in fused silica.

From both phase shift and amplitude fitting, the thermal contact resistances between the nickel coating and the SiO_2 film, and between the SiO_2 film and the Si wafer, are found to be less than $10^{-8}\,K\cdot m^2/W$. When thermal contact resistances are less than $10^{-8}\,K\cdot m^2/W$, they do not affect the PA signals, and thus can not be determined. Larger thermal contact resistances were found in some other samples [23].

Nickel Film. A thin nickel film is deposited on a pure 0.381 mm thick Si wafer using e-beam evaporation. The thickness of the nickel film is $999.5\pm0.5\,nm$. Reflectivity of the sample is measured to be 0.595. Figures 6 and 7 show the phase shift and the normalized amplitude, respectively. By fitting the phase shift data, the thermal conductivity of the nickel film is found to be 47.5 W/m·K, with an upper limit of 56.0 W/m·K and a lower limit of 41.0 W/m·K. Using amplitude fitting, the thermal conductivity of the nickel film is found to be 35.3 W/m·K. Based on the 1 percent reflectivity measurement error, the thermal conductivity has an upper limit of 54.2 W/m·K and a lower limit of 26.0 W/m·K. Therefore, the thermal conductivity of the nickel film prepared in this work is less than the bulk value of 90.7 W/m·K. The thermal contact resistance between the nickel coating and the Si wafer is also found to be less than $10^{-8}\,K\cdot m^2/W$.

Similar to the measurement of the SiO_2 films, the accuracy of determining thermal conductivity of the Ni film with amplitude fitting is influenced by uncertainties in both the amplitude measurement and the surface reflectivity measurement. Since reflectivity is not needed for phase shift fitting, the thermal conductivity obtained from amplitude fitting has a larger uncertainty range than that obtained from phase shift fitting.

Bulk Materials With Mirror-Like Surface. For bulk materials, the phase shift of the PA signal is −90 deg, no information can be extracted from phase shift fitting. Therefore, only amplitude fitting can be used to obtain thermal conductivity of bulk materials. To demonstrate the PA technique for measuring thermal conductivities of bulk materials, the thermal conductivity of a glass slide is measured. A 70 nm thick nickel coating is deposited onto the glass to absorb the laser beam. Calculations show that this thin nickel layer has no effect on determining the thermal conductivity of glass. The fitting results are shown in Fig. 8. Thermal conduc-

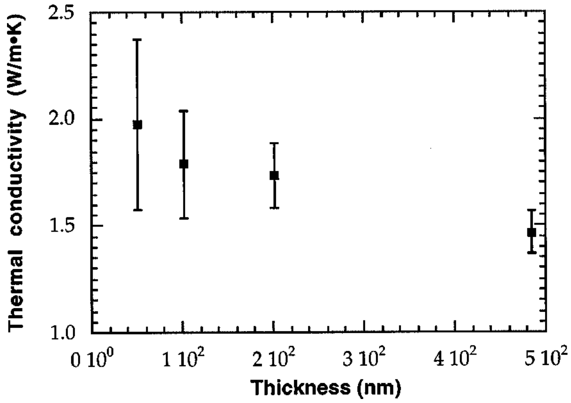

Fig. 5 Thermal conductivity of SiO_2 films obtained by amplitude fitting

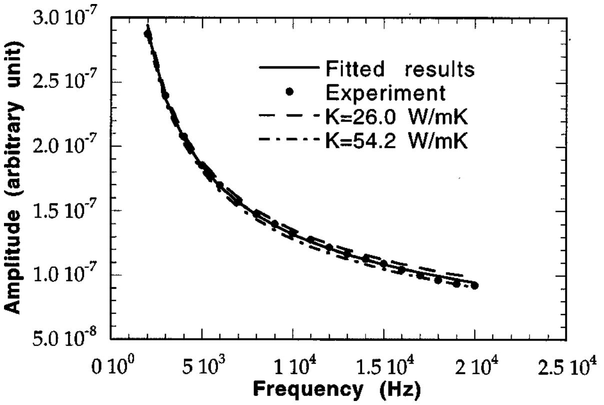

Fig. 7 Normalized amplitude as a function of the modulation frequency of the 999.5 nm Ni—Si sample

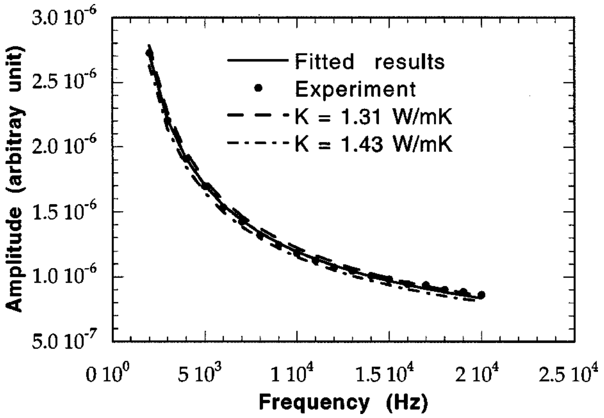

Fig. 8 Normalized amplitude as a function of the modulation frequency of the 70 nm Ni—glass sample

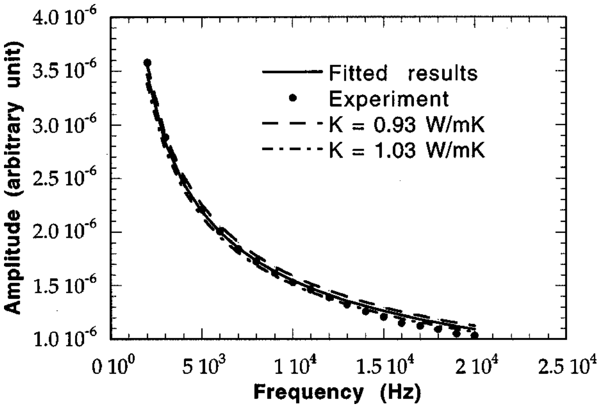

Fig. 10 Normalized amplitude as a function of the modulation frequency of Sample #1787

tivity of glass slide is found to be 1.38 W/m·K, with an upper limit of 1.43 W/m·K and a lower limit of 1.31 W/m·K. This result agrees with the literature value of 1.4 W/m·K [25].

Bulk Materials With Rough Surface. For bulk materials with mirror-like surfaces, measuring surface reflectivity is straightforward. For those with rough surfaces, an ellipsoid is used to measure the diffuse reflectivity. The apparatus is shown in Fig. 9. The sample is placed at one focal point, F1, of the ellipsoid and the detector is placed at the other focal point, F2. The diffusely reflected light from the sample surface is reflected by the inner wall of the ellipsoid and directed to the focal point F2, then is detected by the power meter. In the measurement, the sample is tilted by about 10 deg, so the specular reflection can reach the inner wall of the ellipsoid. Some diffusely reflected light, P_2, will be lost through the open aperture of the ellipsoid. This lost energy is estimated as $P_2 = P_1 * \Omega_2 / \Omega_1$ where P_1 is the energy measured by the detector, Ω_2 is the solid angle of the open aperture with respect to the sample, and Ω_1 is $(2\pi - \Omega_2)$. The variation of the directional reflectivity of the rough sample surface is found to be between 10~15 percent over the surface. Based on this, along with considering the 5 percent measurement error of the power meter, the error for the diffuse reflectivity measurement is estimated to be 10~15 percent.

Thermal conductivities of three thermal barrier coatings and its substrate material, all with rough surfaces are measured. Samples and sample numbers are provided by TPRL.[1] The normalized amplitude as a function of frequency for Sample #1787, which is a 68 μm thick thermal barrier coating on an alloy substrate, is shown in Fig. 10. Thermal conductivity is fitted to be 0.98 ±0.05 W/m·K. The uncertainty of this thermal conductivity value mostly comes from the reflectivity measurement. Surface reflectivity and thermal conductivity values of all the thermal barrier coatings are summarized in Table 1. Sample #1897 is a copper based alloy used as the substrate of the thermal barrier coatings, and Sample #1736 and Sample #1758 are thermal barrier materials prepared by different techniques. The reference values are measured using a laser-flash method at TPRL, with an uncertainty of about ±5 percent. It is seen that the thermal conductivity values obtained from the PA method are in close agreement with the data obtained from the laser-flash method. To reduce the uncertainty of the PA measurement, a more accurate diffuse reflectivity measurement method is required.

IV.2 Discussions. Using phase shift fitting, the photoacoustic technique is most suitable for measuring thin films whose thicknesses, *l*, are on the same order of the thermal diffusion depth, $l_\alpha (= \sqrt{\alpha/\pi f})$. Since the frequency f can be varied in a range, thermal properties of samples within a certain thickness range can be determined accurately. On the other hand, for thin films with thicknesses much less or larger than l_α, the measurement will be less accurate. Based on the results obtained in this work and the uncertainty of the phase shift measurement (±0.2 deg), the numerical uncertainty analysis indicates a ±5 percent uncertainty of the thermal conductivity measurement when l_α / l is around 10 (e.g., the 484.5 nm SiO_2 sample). When l_α / l is around 100, the uncertainty of the thermal conductivity measurement is around ±15 percent (e.g., the 50 nm SiO_2 sample). On the other hand, when the top layer is thick enough that l_α / l is less than 0.15 (e.g., the thermal barrier coatings), the modulated temperature field does not penetrate to the interface of the first two layers, thus, the top layer should be considered as a bulk material. In this case, its thermal conductivity cannot be obtained using phase shift fitting. These uncertainties are summarized in Table 2. Note that the above analysis only applies to the experiment with a ±0.2 deg uncertainty. For an apparatus with a different measurement uncertainty, the uncertainties of the results need to be re-evaluated.

When the thermal conductivity is determined from amplitude fitting, the uncertainty of thermal conductivity is mostly determined by the uncertainty in the surface reflectivity measurement. Based on numerical sensitivity studies, the uncertainty of thermal

---

[1] Thermophysical Properties Research Laboratory Inc., West Lafayette, IN.

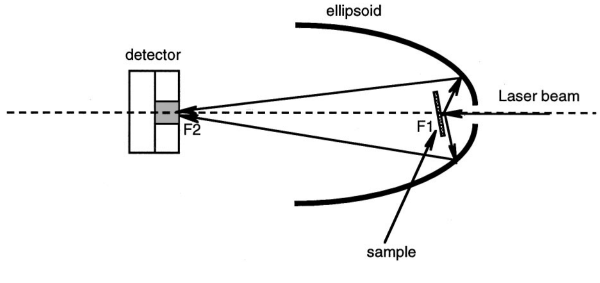

Fig. 9 Schematic diagram of the apparatus for measuring diffuse reflectivity

Table 1 Thermal conductivity of samples from TPRL

Sample index	Surface reflectivity	Thermal conductivity measured by the PA method (W/m·K)	Thermal conductivity measured by the laser flash method (W/m·K)
#1897	0.30 ± 10%	371 ± 32	333 ± 5%
#1736	0.10 ± 15%	0.45 ± 0.02	0.42 ± 5%
#1758	0.35 ± 10%	0.61 ± 0.07	0.66 ± 5%
#1787	0.15 ± 15%	0.98 ± 0.05	0.96 ± 5%

Table 2 Uncertainty of the thermal conductivity measurement (based on ±0.2 deg uncertainty of the measured phase shift, and ±5 percent uncertainty of the measured absorptivity)

l_α / l	Relative uncertainty of the thermal conductivity measurement	Example in this work
< 0.15	± 10% (Amplitude)	Thermal Barrier Coatings
10	± 5% (Phase shift)	484.5 nm SiO_2
100	± 15% (Phase shift)	50 nm SiO_2

conductivity is found to be about twice of that of the absorptivity measurement. Note that in Table 1, the measured surface reflectivity has a large uncertainty, on the order of 10 percent–15 percent. However, the uncertainty in absorptivity is much less, which results in a relatively accurate measurement of thermal conductivity that compares favorably with the results obtained by the laser flash method.

Comparing the PA method (amplitude fitting) with the laser flash method for measuring thermal conductivities of bulk materials, the advantage of the PA method is that it can measure thermal conductivities of coatings that can be treated as bulk materials. On the other hand, the amplitude fitting method has two limitations in comparison with the laser flash method. One is that reflectivity is required for the PA method. The other one is that the PA method works only at the room temperature. Technically, it is possible to develop a high temperature PA apparatus, with the highest temperature limited by the operation temperature of the transducer (normally around a few hundred degrees Celsius). The laser flash method, on the other hand, can measure thermal diffusivities above 1000 °C

Although all the film samples measured in this work do not have significant thermal contact resistance, the current PA apparatus does have the capability of measuring the thermal contact resistance. For example, for a sample of 1.03 μm-thick Ni on glass, the thermal contact resistance between the nickel film and the glass substrate is found to be $5.3 \pm 1.8 \times 10^{-7}$ m^2K/W [23]. For a film with thickness *l* and thermal conductivity *k*, its thermal resistance will be l/k. If the uncertainty of the thermal conductivity measurement is Δk, then the uncertainty in the thermal resistance is $l \cdot \Delta k/k^2$. Therefore, the smallest measurable thermal contact resistance at the interface of that layer is about $l \cdot \Delta k/k^2$, which corresponds to about 10^{-8} m^2K/W for the 484.5 nm SiO_2 film in this work. When the uncertainty in the thermal contact resistance is much larger than the thermal resistance of the film, the thermal contact resistance will play a major role in determining the PA signal. For a layer whose thermal contact resistance has an experimental uncertainty of ΔR, and whose thermal resistance is less than ΔR, the effect of thermal resistance will not be sensed by the experiment. Therefore, the largest measurable thermal conductivity of the layer is $l/\Delta R$.

V Conclusions

This work evaluated the PA technique for measuring thermal conductivities of thin films and bulk materials. In addition to commonly used phase shift fitting, an amplitude fitting method was also employed to determine thermal conductivities of thin films and bulk materials. Thermal conductivities of thin SiO_2 films thermally grown on Si wafer with different thicknesses were measured. It was found that the thermal conductivity of SiO_2 film changed little with thickness. The amplitude fitting method was used successfully to obtain thermal conductivities of bulk materials with smooth or rough surfaces. For bulk materials, thermal conductivity data obtained by the PA method were close to the literature values or the values obtained by the laser flash technique. It was demonstrated that the PA method could be used to determine thermal conductivities of a wide range of materials.

Acknowledgments

Support to this work by the National Science Foundation (CTS-9624890) is acknowledged. The authors would also like to thank Dr. Raymond Taylor of TPRL for providing thermal barrier coating samples, Dr. Magnus Rohde of the Institute of Materials Research at Karlsruhe, Germany for his help in the design of the PA cell, and David A. Willis and Jae Wook Ryu of the School of Mechanical Engineering, Purdue University for e-beam evaporation.

Nomenclature

a = $\sqrt{\pi f/\alpha}$
A = amplitude
B = intermediate coefficient
E, G = intermediate parameter
f = modulation frequency
I = intensity of laser light
j = imaginary unity
k = thermal conductivity
l = thickness
P = laser energy measured by power meter
R = thermal contact resistance
u = element of matrix U
v = element of matrix V
U, V = intermediate coefficient matrix

Greek Symbols

α = thermal diffusivity
β = optical absorption coefficient
ϕ = phase shift
θ = complex temperature
ρ = reflectivity
σ = $(1+j)a$
ω = modulated angular frequency
Ω = solid angle

Subscripts

i = layer i in the multi-layer system

References

[1] Goodson, K. E., and Flik, M. I., 1994, ''Solid Layer Thermal-Conductivity Measurement Techniques,'' Appl. Mech. Rev., **47**, pp. 101–112.
[2] Mirmira, S. R., and Fletcher, L. S., 1998, ''Review of the Thermal Conductivity of Thin Films,'' J. Thermophys. Heat Transfer, **12**, pp. 121–131.
[3] Völklein, F., 1990, ''Thermal Conductivity and Diffusivity of a Thin Film SiO_2-Si_3N_4 Sandwich System,'' Thin Solid Films, **188**, pp. 27–33.
[4] Cahill, D. G., 1990, ''Thermal Conductivity Measurement from 30 to 750 K: the 3ω Method,'' Rev. Sci. Instrum., **61**, pp. 802–808.
[5] Cahill, D. G., and Allen, T. H., 1994, ''Thermal Conductivity of Sputtered and Evaporated SiO_2 and TiO_2 Optical Coatings,'' Appl. Phys. Lett., **65**, pp. 309–311.
[6] Zhou, S. Q., Chen, G., Liu, J. L., Zheng, X. Y, and Wang, K. L., 1998, ''Anisotropic Thermal Conductivity of Si/SiGe Superlattice,'' *Proceedings of the 1998 ASME International Mechanical Engineering Congress and Exposition*, ASME, Fairfield, NJ, **361-4**, pp. 249–254.
[7] Okuda, M., and Ohkubo, S., 1992, ''A Novel Method for Measuring the Thermal Conductivity of Submicrometer Thick Dielectric Films,'' Thin Solid Films, **213**, pp. 176–181.
[8] Zhang, X., and Grigoropoulos, C. P., 1994, ''The Amplitude Technique for Measurement of Free Standing Thin Film Thermal Properties: a Comparison with other Experimental Techniques,'' *Proceedings of the 1994 ASME International Mechanical Engineering Congress and Exposition*, ASME, New York, NY, **293**, pp. 17–24.
[9] Goodson, K. E., Flik, M. I., Su, L. T., and Antoniadis, D. A., 1994, ''Prediction and Measurement of the Thermal Conductivity of Amorphous Dielectric Layers,'' ASME J. Heat Transfer, **116**, pp. 317–324.
[10] Goodson, K. E., Käding, O. W., Rösler, M., and Zachai, R., 1995, ''Experimental Investigation of Thermal Conduction Normal to Diamond-Silicon Boundaries,'' J. Appl. Phys., **77**, pp. 1385–1392.
[11] Wu, Z. L., Reichling, M., Hu, X. Q., Balasubramanian, K., and Guenther, K. H., 1993, ''Absorption and Thermal Conductivity of Oxide Thin Films Measured by Photothermal Displacement and Reflectance Methods,'' Appl. Opt., **32**, pp. 5660–5665.
[12] Machlab, H., McGahan, W. A., and Woollam, J. A., 1992, ''Thermal Diffusivity Measurements by Photothermal Laser Beam Deflection (PTD): Data

Analysis Using the Levenberg-Marquardt Algorithm,'' Thin Solid Films, **215**, pp. 103–107.

[13] Capinski, W. S., and Maris, H. J., 1996, ''Thermal Conductivity of GaAs/AlAs Superlattices,'' Physica B, **219 and 220**, pp. 699–701.

[14] Hostetler, J. L., Smith, A. N., and Norris, P. M., 1997, ''Thin-Film Thermal Conductivity and Thickness Measurements Using Picosecond Ultrasonics,'' Microscale Thermophys. Eng., **1**, pp. 237–244.

[15] Tam, A. C., 1986, ''Applications of Photoacoustic Sensing Techniques,'' Rev. Mod. Phys., **58**, pp. 381–431.

[16] Rosencwaig, A., and Gersho, A., 1976, ''Theory of the Photoacoustic Effect With Solids,'' J. Appl. Phys., **47**, pp. 64–69.

[17] Fujii, Y., Moritani, A., and Nakai, J., 1981, ''Photoacoustic Spectroscopy Theory for Multi-Layered Samples and Interference Effect,'' Jpn. J. Appl. Phys., **20**, pp. 361–367.

[18] Baumann, J., and Tilgner, R., 1985, ''Determining Photothermally the Thickness of a Buried Layer,'' J. Appl. Phys., **58**, pp. 1982–1985.

[19] Cole, K. D., and McGahan, W. A., 1992, ''Theory of Multilayers Heated by Laser Absorption,'' *Proceedings of Winter Annual Meeting of the American Society of Mechanical Engineering*, ASME, New York, NY, **40**, pp. 267–282.

[20] Lachaine, A., and Poulet, P., 1984, ''Photoacoustic Measurement of Thermal Properties of a Thin Polyester Film,'' Appl. Phys. Lett., **45**, pp. 953–954.

[21] Raman, S. S., Nampoori, V. P. N., Vallabhan, C. P. G., Ambadas, G., and Sugunan, S., 1995, ''Photoacoustic Study of the Effect of Degassing Temperature on Thermal Diffusivity of Hydroxyl Loaded Alumina,'' Appl. Phys. Lett., **67**, pp. 2939–2941.

[22] Rohde, M., 1994, ''Photoacoustic Characterization of Thermal Transport Properties in Thin Films and Microstructures,'' Thin Solid Films, **238**, pp. 199–206.

[23] Hu, H., Wang, X., and Xu, X., 1999, ''Generalized Theory of the Photoacoustic Effect with a Multilayer Material,'' J. Appl. Phys., **86**, pp. 3953–3958.

[24] Quimby, R. S., and Yen, W. M., 1980, ''On the Adequacy of One-Dimensional Treatments of the Photoacoustic Effect,'' J. Appl. Phys., **51**, pp. 1252–1253.

[25] Incropera, F. P., and DeWitt, D. P., 1990, *Fundamentals of Heat and Mass Transfer*, 3rd Ed., Wiley, New York, p. A13.

Heat Transfer Regimes and Hysteresis in Porous Media Convection

Peter Vadasz
Professor
Fellow ASME
Department of Mechanical Engineering,
University of Durban-Westville,
Private Bag X54001,
Durban 4000, South Africa

Results of an investigation of different heat transfer regimes in porous media convection are presented by using a truncated Galerkin representation of the governing equations that yields the familiar Lorenz equations for the variation of the amplitude in the time domain. The solution to this system is obtained analytically by using a weak non-linear analysis and computationally by using Adomian's decomposition method. Expressions for the averaged Nusselt number are derived for steady, periodic, as well as weak-turbulent (temporal-chaotic) convection. The phenomenon of Hysteresis in the transition from steady to weak-turbulent convection, and backwards, is particularly investigated, identifying analytically its mechanism, which is confirmed by the computational results. While the post-transient chaotic solution in terms of the dependent variables is very sensitive to the initial conditions, the affinity of the averaged values of these variables to initial conditions is very weak. Therefore, long-term predictability of these averaged variables, and in particular the Nusselt number, becomes possible, a result of substantial practical significance. Actually, the only impact that the transition to chaos causes on the predicted results in terms of the averaged heat flux is a minor loss of accuracy. Therefore, the predictability of the results in the sense of the averaged heat flux is not significantly affected by the transition from steady to weak-turbulent convection. The transition point is shown to be very sensitive to a particular scaling of the equations, which leads the solution to an invariant value of steady-state for sub-transitional conditions, a result that affects the transition point in some cases. [DOI: 10.1115/1.1336505]

Keywords: Weak Turbulence, Hysteresis, Porous Media, Free Convection, Chaos, Lorenz Equations, Heat Flux.

1 Introduction

The wide variety of applications of heat transfer in porous media motivates this study. Examples of such applications are listed in Nield and Bejan [1] and Bejan [2], such as insulation of buildings and equipment, energy storage and recovery, geothermal reservoirs, nuclear waste disposal, chemical reactor engineering, and the storage of heat generating materials such as grain and coal. The latter applications fall into the category of energy self-sufficiency and pollution of the environment. In addition one needs to indicate some geophysical applications, such as ground water flow (where the heat transfer analogy may apply to the mass transfer equations when considering underground water contamination) and the flow of magma in the earth mantle close to the earth crust. In particular, the problem of estimating the heat flux in convective flows in porous media places a special theoretical challenge, as the raw experimental results are very much dispersed over a wide range, beyond the experimental error (see Fig. 6.9 in Nield and Bejan [1]). The reason for this dispersion is associated with a wide variety of possible heat transfer regimes, namely; motionless-conduction, laminar-Darcy, laminar-Forchheimer, weak-turbulent-Darcy (or ''temporal chaotic'') and strong-turbulent (''spatio-temporal-chaotic''). These regimes can occur depending on the combination of appropriate values of Rayleigh, Darcy-Prandtl, and Darcy numbers. The present paper is concerned with the transitions from a motionless-conduction regime to steady laminar-Darcy convection and further to weak-turbulent-Darcy convection. The accurate definitions of each of these regimes can be introduced by considering a fluid layer heated from below and following a procedure of increasing the temperature difference between the bottom and top boundaries. The transition from a motionless-conduction to a steady-convection regime is independent of whether a Darcy or a Forchheimer model is used since this transition is obtained from a linear stability analysis around a motionless solution, hence non-linear effects (such as the Forchheimer terms) vanish. If the porous matrix consists of material that is associated with a very small value of Darcy number ($\mathrm{Da}<10^{-3}$) and the fluid's Prandtl number is of an order of magnitude around $\mathrm{Pr}\sim 10$, then the transition from steady to non-steady convection leads to a weak-turbulent regime. This transition is associated with the loss of stability of the steady convection due to the nonlinear interactions in the energy equation, while the resulting filtration velocity values are still within the Darcy regime.

Vadasz and Olek [3] demonstrated that the transition from steady to chaotic (weak-turbulent) convection in porous media could be recovered from a truncated Galerkin approximation, which yields a system that is equivalent to the familiar Lorenz equations (Lorenz [4] and Sparrow [5]). In particular it was noticed that the transition to chaos when the initial conditions are not too far away from any one of the convective steady state solutions passes through a limit cycle at a particular sub-critical value of Rayleigh number. Here the term ''sub-critical'' is used in the context of the transition from steady convection to a non-periodic state, typically referred to as chaotic. The critical value of the Rayleigh number is the value at which this transition to chaos is predicted by the linear stability analysis of the convective steady state solutions. It is the objective of this paper to investigate the impact of this transition on the heat flux and the corresponding Hysteresis phenomenon linked to the transition from steady convection to chaos and backwards. Vadasz [6] used a weak nonlinear method of solution to this problem, which revealed a mechanism for the Hysteresis phenomenon. The same method is being

---

Contributed by the Heat Transfer Division for publication in the JOURNAL OF HEAT TRANSFER. Manuscript received by the Heat Transfer Division September 13, 1999; revision received, August 17, 2000. Associate Editor: M. Hunt.

used and extended in this paper in conjunction with the computational Adomian decomposition method in order to analyze and investigate the resulting heat flux.

This is accomplished first by using the weak nonlinear results presented by Vadasz [6] in order to evaluate analytically a relationship for the Nusselt number corresponding to the most general post-transient but time dependent conditions. This relationship is expected to break down when transition to chaos occurs. However, the qualitative properties of the derived analytical relationship are shown to be compatible with supercritical conditions and therefore a similar approach was adopted while using a computational method of solution (Adomian's decomposition method) to provide an estimate of the Nusselt number in the weak-turbulent regime. Adomian's decomposition method (Adomian [7,8]) was shown to provide extremely accurate results and in particular its robustness in solving problems that are sensitive to variations in initial conditions was demonstrated by Vadasz and Olek [9].

Nield and Bejan [1] provide an excellent summary of the analytical as well as the experimental work available so far on the estimation of Nusselt number in porous media convection. For example, for values of Rayleigh number slightly beyond the convection threshold a linear relationship between the Nusselt and Rayleigh numbers is suggested in [1] based on Elder [10], which fits well with experimental data. Such a linear relationship can be derived analytically via a weak nonlinear analysis of the problem using an expansion around the convection threshold (see Braester and Vadasz [11], and Vadasz and Braester [12]) and can be expressed in the form

$$\mathrm{Nu}=1+2(R-1), \tag{1}$$

where $R=\mathrm{Ra}/\mathrm{Ra}_{cr}$ is the scaled Rayleigh number and $\mathrm{Ra}_{cr}=4\pi^2$ is the critical value of the Rayleigh number associated with the loss of linear stability of the motionless solution, i.e., on the convection threshold. It is shown in this paper that Eq. (1) represents the first two terms in a Taylor expansion of a more general relationship, that is derived here, and applies to a much wider range of Rayleigh number values.

Bau [13] indicates that, ''*One of the hallmarks of chaotic systems is their sensitivity to initial conditions and small perturbations (noise). . . . Of course, when one is modeling real systems, the initial conditions are not precisely known and all real systems are subject to perturbations and noise. Hence, . . . , no long term prediction of the detailed behavior of a chaotic system is possible. The lack of long-term predictability is a fundamental property of chaotic systems just like the uncertainty principle is a corner stone of quantum mechanics. One of the practical implications is that when one deals with chaotic systems, the availability of large computational resources will not enable one to generate long term predictions*.'' This conclusion is somewhat disappointing as it implies that it is hopeless to attempt modelling real systems within the chaotic regime due to lack of long-term predictability. It is shown in this paper that despite the sensitivity of the post-transient chaotic solution, in terms of its dependent variables, to variations in initial conditions, the dissipative nature of the convective system reduces substantially this sensitivity, when these dependent variables are being averaged over a sufficiently large time range. In this context, Sparrow [5] indicates that in attempting to provide an explanation about the irregularity of the trajectory in the chaotic regime, ''*we know we are seeing a portion of a very high period orbit*.'' If chaotic solutions are a result of a very large period, it implies that by averaging the results over a period smaller than the largest period of the solution, it might compromise the accuracy of the averaging process. This loss of accuracy may be significant, in which case the high sensitivity of the solution to initial conditions applies to the averaged values as well, or this loss of accuracy may be minor, the latter being expected in dissipative systems. Then, despite the sensitivity of the post-transient solution to variations in initial conditions, the corresponding averaged values over a sufficiently large time interval lack this substantial sensitivity. This paper shows that the mean Nusselt number is just an example of such a case. Its affinity to different initial conditions is very weak, and subject to a minor loss of accuracy, one can predict its value even within the weak-turbulent regime, except for some transition regions where the hysteresis phenomenon may substantially affect it. Actually, it will be shown that the only impact that the transition to chaos causes on the predicted results in terms of the averaged heat flux is a minor loss of accuracy. Since chaos is a result of limited and finite accuracy of the solution, one can not expect to obtain results that within the chaotic regime can be reached up to any desired accuracy. This accuracy is limited also by the fact that we have no way to anticipate a finite number of frequencies (and their corresponding periods) over which to integrate the heat flux in order to yield an accurate average Nusselt number. It will be shown that these effects introduce only a minor error in the estimation of the Nusselt number.

2 Problem Formulation and Reduced Set of Equations

A narrow ($W=W_*/H_*\ll 1$) fluid saturated porous layer subject to gravity and heated from below, as presented in Fig. 1, is considered. A Cartesian co-ordinate system is used such that the vertical axis z is collinear with gravity, i.e., $\hat{\mathbf{e}}_g=-\hat{\mathbf{e}}_z$. The time derivative term is not neglected in Darcy's equation, a condition that was well discussed and substantiated by Vadasz and Olek [3,14] and Vadasz [6]. Other than that Darcy's law is assumed to govern the fluid flow, while the Boussinesq approximation is applied for the effects of density variations. Subject to these conditions the following dimensionless set of governing equations is obtained:

$$\nabla\cdot\mathbf{q}=0 \tag{2}$$

$$\left[\frac{1}{\mathrm{Pr}_D}\frac{\partial}{\partial\hat{t}}+1\right]\mathbf{q}=-\nabla p+\mathrm{Ra}T\hat{\mathbf{e}}_z \tag{3}$$

$$\frac{\partial T}{\partial\hat{t}}+\mathbf{q}\cdot\nabla T=\nabla^2 T. \tag{4}$$

The values α_{e*}/H_*M_f, $\mu_*\alpha_{e*}/k_*M_f$, and $\Delta T_c=(T_H-T_C)$ are used to scale the filtration velocity components (u_*,v_*,w_*), pressure (p_*), and temperature variations (T_*-T_C), respectively, where α_{e*} is the effective thermal diffusivity, μ_* is fluid's viscosity, k_* is the permeability of the porous matrix, and M_f is the ratio between the heat capacity of the fluid and the effective heat capacity of the porous domain. The height of the layer H_* was used for scaling the variables x_*, y_*, z_* and H_*^2/α_{e*} for scaling the time t_*. Accordingly, $x=x_*/H_*$, $y=y_*/H_*$ and $z=z_*/H_*$ and $\hat{t}=t_*\alpha_{e*}/H_*^2$. In Eq. (3) Ra is the gravity related Rayleigh number in porous media defined in the form $\mathrm{Ra}=\beta_*\Delta T_c g_* H_* k_* M_f/\alpha_{e*}v_*$. The time derivative term was in-

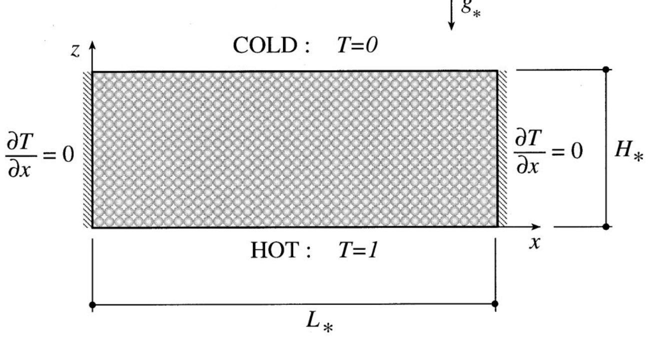

Fig. 1 A fluid saturated porous layer heated from below

cluded in Darcy's Eq. (3), where Pr_D is a dimensionless group (Darcy-Prandtl number) which includes the Prandtl and Darcy numbers as well as the porosity of the porous domain and is defined by $\mathrm{Pr}_D = \phi \mathrm{Pr}/\mathrm{Da}$. Vadasz and Olek [3,14] have shown that when investigating wave phenomena, such as the present case, the time derivative in Eq. (3) needs to be included irrespective of how large the value of Pr_D is. Without including this term the possibility of oscillatory convection is wiped out, and subsequently the transition to turbulence by using the present model becomes impossible. Including the time derivative term in Eq. (3) is equivalent to maintaining the highest derivative in an equation in order to satisfy all boundary (or initial) conditions.

As all the boundaries are rigid the solution must follow the impermeability conditions there, i.e., $\mathbf{q} \cdot \hat{\mathbf{e}}_\mathbf{n} = 0$ on the boundaries, where $\hat{\mathbf{e}}_\mathbf{n}$ is a unit vector normal to the boundary. The temperature boundary conditions are as follows: $T=1$ at $z=0$, $T=0$ at $z=1$ and $\nabla T \cdot \hat{\mathbf{e}}_\mathbf{n} = 0$ on all other walls representing the insulation condition on these walls.

For convective rolls having axes parallel to the shorter dimension (i.e., y) $v=0$, and the governing equations can be presented in terms of a stream function defined by $u = \partial\psi/\partial z$ and $w = -\partial\psi/\partial x$, which upon applying the curl ($\nabla\times$) operator on Eq. (3) yields the following system of partial differential equations from Eqs. (2), (3), and (4):

$$\left[\frac{1}{\mathrm{Pr}_D}\frac{\partial}{\partial \hat{t}} + 1\right]\left[\frac{\partial^2\psi}{\partial x^2} + \frac{\partial^2\psi}{\partial z^2}\right] = -\mathrm{Ra}\frac{\partial T}{\partial x} \tag{5}$$

$$\frac{\partial T}{\partial \hat{t}} + \frac{\partial\psi}{\partial z}\frac{\partial T}{\partial x} - \frac{\partial\psi}{\partial x}\frac{\partial T}{\partial z} = \frac{\partial^2 T}{\partial x^2} + \frac{\partial^2 T}{\partial z^2}, \tag{6}$$

where the boundary conditions for the stream function are $\psi=0$ on all solid boundaries.

The set of partial differential Eqs. (5) and (6) form a nonlinear coupled system, which together with the corresponding boundary conditions accepts a basic motionless conduction solution. To obtain the complete solution to the non-linear coupled system of partial differential Eqs. (5) and (6) we represent the stream function and temperature in the form

$$\psi = -4\tilde{X}\sin\left(\frac{\pi x}{L}\right)\sin(\pi z) \tag{7}$$

$$T = 1 - z + \frac{2\tilde{Y}}{\pi}\cos\left(\frac{\pi x}{L}\right)\sin(\pi z) - \frac{\tilde{Z}}{\pi}\sin(2\pi z). \tag{8}$$

This representation is equivalent to a Galerkin expansion of the solution in both x and z directions, truncated when $i+j=2$, where i is the Galerkin summation index in the x direction and j is the Galerkin summation index in the z direction. Substituting (7) and (8) into the Eqs. (5) and (6), multiplying the equations by the orthogonal eigenfunctions corresponding to (7) and (8) and integrating them over the domain, i.e., $\int_0^L dx \int_0^1 dz(\cdot)$, yields a set of three ordinary differential equations for the time evolution of the amplitudes (see Vadasz and Olek [3,14]).

By using the wave number corresponding to the convection threshold, rescaling the time $\hat{t}$, and introducing the following notation:

$$R = \frac{\mathrm{Ra}}{4\pi^2} \quad \alpha = \frac{\mathrm{Pr}_D}{2\pi^2} \quad t = 2\pi^2\hat{t}, \tag{9}$$

yields the following set of equations

$$\dot{\tilde{X}} = \alpha(R\tilde{Y} - \tilde{X}) \tag{10}$$

$$\dot{\tilde{Y}} = \tilde{X} - \tilde{Y} - \tilde{X}\tilde{Z} \tag{11}$$

$$\dot{\tilde{Z}} = 2(\tilde{X}\tilde{Y} - \tilde{Z}). \tag{12}$$

The fixed points of the system (10)–(12) are obtained by setting the time derivative to be zero, in the form $\tilde{X}_S = \pm(R-1)^{1/2}$, $\tilde{Y}_S = \pm(R-1)^{1/2}/R$ and $\tilde{Z}_S = \pm(R-1)/R$. They represent steady-state solutions consisting of convection cells moving clockwise or counter-clockwise. These fixed points lose stability in the linear sense at a value of $R = R_o = 25$ (for $\alpha=5$ pertaining to the present investigation), at which point a sub-critical Hopf bifurcation occurs (see Vadasz [6], for details). The bifurcation diagram representing the convective fixed points and the unstable bifurcating oscillatory solutions is presented in Fig. 2. A rescaling of the variables with respect to these fixed points in the form

$$X = \frac{\tilde{X}}{\sqrt{(R-1)}} \quad Y = \frac{R\tilde{Y}}{\sqrt{(R-1)}} \quad Z = \frac{R\tilde{Z}}{(R-1)} \tag{13}$$

provides the following set of scaled equations:

$$\dot{X} = \alpha(Y - X) \tag{14}$$

$$\dot{Y} = RX - Y - (R-1)XZ \tag{15}$$

$$\dot{Z} = 2(XY - Z), \tag{16}$$

where the dots ($\dot{}$) denote time derivatives $d(\ )/dt$. Equations (14), (15), and (16) are equivalent to Lorenz equations (Lorenz [4] and Sparrow [5]) although with different coefficients. The demonstration of this equivalence is provided by Vadasz and Olek [3]. Their convective fixed points are $X_S = Y_S = \pm 1$, $Z_S = 1$ for $R > 1$.

It is appropriate at this stage to list all assumptions made in deriving the system of Eqs. (14)–(16) from the original set of partial differential Eqs. (2)–(4), in order to assess the validity and limitations of the present model. There are four inherent assumptions in the derivation of the present model:

1. The spatial convection structure remains unchanged qualitatively, i.e., within the range of Rayleigh number values considered any possible variations in this structure as Ra number varies are small.
2. The wave number variation within the spatial convection structure is small as well.
3. The very truncated Galerkin system might not represent correctly the detailed dynamics within boundary layers that may form at high Ra number values.
4. Temperature or energy equation related turbulence precedes hydrodynamic or momentum related turbulence, i.e., turbulence is created by the nonlinear terms in the energy equation, rather than quadratic drag terms in a Forchheimer formulation of the momentum equation.

Nevertheless, the model is expected to represent qualitatively well the effects related to the overall dynamics of the system. Some wide thermal boundary layers near the top and bottom of the layer can be recovered. However this model excludes the possibility of formation of narrow thermal boundary layers, or of hydrodynamic boundary layers, next to these walls. Note that the formation of hydrodynamic boundary layers near solid walls is not typical for flows in porous media since the non-slip conditions do not apply for the filtration velocity next to these walls. Assumption (4) can be tested *a posteriori* by using a relationship obtained via a scale analysis, between the pore scale Reynolds number and the scaled Rayleigh number in the present model. This relationship yields $\mathrm{Re}_\Delta = \mathrm{Re}\,\mathrm{Da}^{1/2} = 4\pi(R-1)^{1/2}\mathrm{Da}^{1/2}X/(M_f\mathrm{Pr}) = 4\pi(R-1)^{1/2}X\phi/(M_f\mathrm{Pr}_D\mathrm{Da}^{1/2})$. Then by using typical porous media parameter values and typical values of X from the solutions presented by Vadasz [6] and Vadasz and Olek [3] we obtain $\mathrm{Re}_{\Delta\,\max} = 61.56\mathrm{Da}^{1/2}/\mathrm{Pr} = 61.56\phi/(\mathrm{Pr}_D\mathrm{Da}^{1/2})$ for $R \sim 25$. The transition from Darcy to a nonlinear Forchheimer regime in porous media occurs at a pore scale Reynolds number of an order of magnitude of 1. Therefore, for fluid Prandtl numbers around 10 the condition for validity of the Darcy regime is $\mathrm{Da}^{1/2} \ll 1$, which is clearly valid. As the value of the fluid Prandtl number decreases

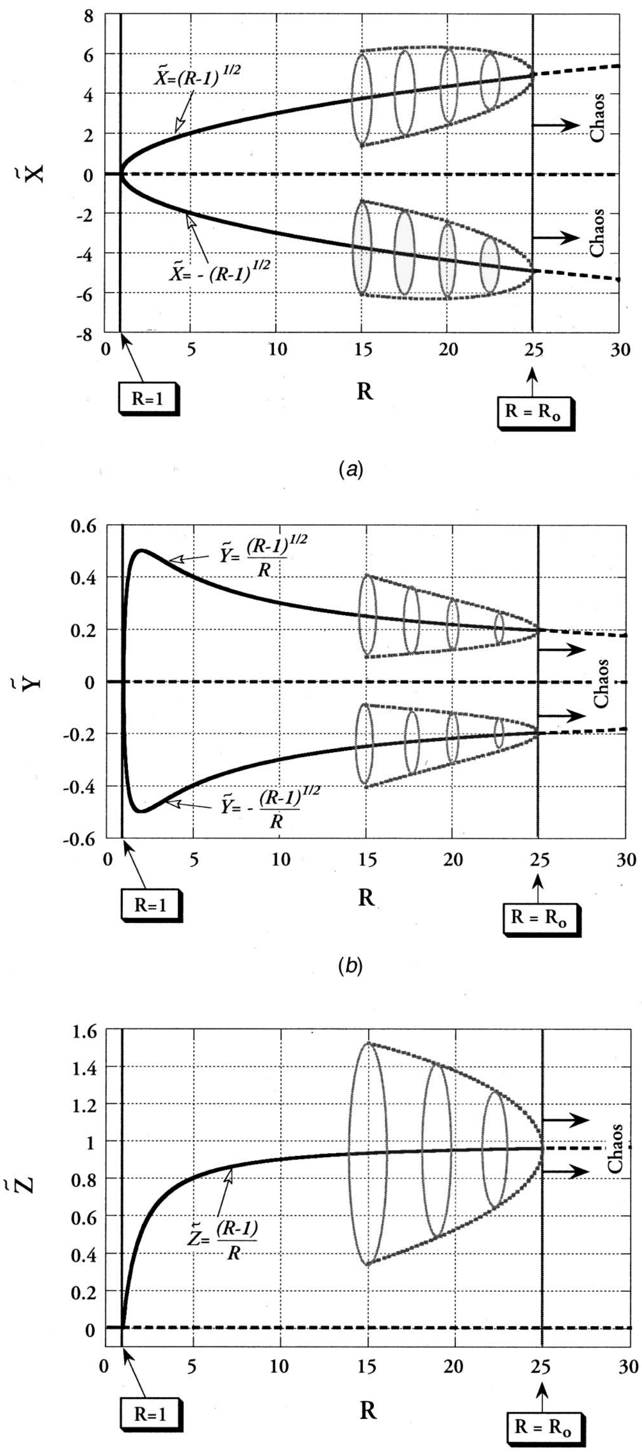

Fig. 2 The bifurcation diagram obtained analytically from Eqs. (10)–(12): (*a*) $\tilde{X}$ versus *R*, (*b*) $\tilde{Y}$ versus *R*, and (*c*) $\tilde{Z}$ versus *R*.

the Darcy regime validity condition may be violated by some combinations of solid-fluid materials forming the porous matrix. In such cases the Darcy regime can not be recovered and the conditions for the validity of assumption (4) might be violated as well.

3 Heat Flux and Nusselt Number

This section is dedicated to the derivation of relationships for the average Nusselt number that are sufficiently general to include post-transient, but time dependent variations of the heat flux. This is accomplished first by using the conservative form of the energy Eq. (4), integrating it over the horizontal plane in order to obtain a spatially averaged Nusselt number, and then substituting the expression from Eq. (8) for the temperature. The definition of the horizontally averaged Nusselt number is given by

$$\overline{\text{Nu}}^h=\frac{1}{LW}\int_0^L dx\int_0^W dy\left[wT-\frac{\partial T}{\partial z}\right]. \tag{17}$$

Averaging horizontally the conservative form of the energy equation and using the boundary conditions on the sidewalls yields

$$\int_0^W dy\int_0^L dx\left[\frac{\partial T}{\partial \hat{t}}+\nabla\cdot(\mathbf{q}T-\nabla T)\right]$$
$$=\int_0^W dy\int_0^L dx\left[\frac{\partial T}{\partial \hat{t}}\right]+\frac{\partial}{\partial z}\int_0^W dy\int_0^L dx\left[wT-\frac{\partial T}{\partial z}\right]=0 \tag{18}$$

and upon introducing Eq. (17) into (18) yields

$$\frac{\partial \overline{T}^h}{\partial \hat{t}}+\frac{\partial \overline{\text{Nu}}^h}{\partial z}=0, \tag{19}$$

where $\overline{(\cdot)}^h=[\int_0^W dy\int_0^L dx(\cdot)]/(WL)$ stands for the horizontal averaging operator. Integrating Eq. (19) in the z-direction and using the boundary condition $w=0$ at $z=0$ yields a relationship for the horizontally averaged Nusselt number in the form

$$\overline{\text{Nu}}^h(\hat{t},z)=-\int_0^z\frac{\partial \overline{T}^h(\hat{t},\zeta)}{\partial \hat{t}}d\zeta-\left(\frac{\partial \overline{T}^h}{\partial z}\right)_{z=0}, \tag{20}$$

where ζ is a dummy integration variable. Substituting now the expression for the temperature from Eq. (8) and using the rescaled variables from Eq. (13) yields

$$\overline{\text{Nu}}^h(\hat{t},z)=1+\frac{2(R-1)}{R}Z+\frac{(R-1)}{R}\dot{Z}[1-\cos(2\pi z)]. \tag{21}$$

An alternative form of Eq. (21) can be obtained by substituting Eq. (16) into (21) to yield

$$\overline{\text{Nu}}^h(\hat{t},z)=1+\frac{2(R-1)}{R}Z+\frac{2(R-1)}{R}(XY-Z)[1-\cos(2\pi z)]. \tag{22}$$

Clearly when the post-transient solution is not time dependent and a steady state is reached, $\dot{Z}=0$ and $Z=Z_S=1$; therefore, Eq. (21) yields

$$\overline{\text{Nu}}^h_{\substack{\text{state}\\\text{steady}}}=3-\frac{2}{R}. \tag{23}$$

A Taylor expansion of Eq. (23) around $R=1$, corresponding to the neighborhood of the convection threshold, produces

$$\overline{\text{Nu}}^h_{\substack{\text{state}\\\text{steady}}}=3-\frac{2}{R}=1+2(R-1)-2(R-1)^2+\ \ldots \tag{24}$$

The first two terms in expansion (24) represent the first order approximation presented in Eq. (1) as obtained via a weak nonlinear solution by using an expansion around $R=1$. Nield and Bejan [1] (based on Elder [10]) suggested a linear approximation as a good curve fitting of the experimental data in the neighborhood of the convection threshold. The present model [Eq. (24)] recovers a linear first order approximation as a particular case of the more general expression for the Nusselt number at steady state, as presented by Eq. (23). However, since we are interested in considering more general time dependent post-transient solutions, the more general equations (21) or (22) need to be used. For the evaluation of the heat flux one is interested in an expression for the Nusselt number which is independent of z. This can be accomplished in two ways. First, one can consider the heat flux into the domain crossing the bottom boundary at $z=0$ or the heat flux from the domain crossing the boundary at $z=1$. They both yield

$$\overline{\mathrm{Nu}}_o^h(\hat{t})=\overline{\mathrm{Nu}}^h(\hat{t},0)=\overline{\mathrm{Nu}}^h(\hat{t})=\overline{\mathrm{Nu}}^h(\hat{t},1)=1+\frac{2(R-1)}{R}Z \tag{25}$$

The second alternative way of obtaining a z-independent Nusselt number is by a vertical averaging of Eq. (21) or (22) to obtain

$$\overline{\mathrm{Nu}}^{hv}(\hat{t})=1+\frac{2(R-1)}{R}Z+\frac{(R-1)}{R}\dot{Z}=1+\frac{2(R-1)}{R}XY, \tag{26}$$

where $\overline{(\cdot)}^{hv}=\int_0^1 dz[\int_0^W dy \int_0^L dx(\cdot)]/(WL)$ represents the overall spatial average operator. While Eqs. (25) and (26) represent equivalent forms for the averaged heat flux they do not in general yield identical values. However, particular cases of interest can be considered when these two different forms of Nusselt number produce identical results. The first particular case of interest is when the solution is periodic with possible multiple harmonics. Then, a time average over the largest period of both Eqs. (25) and (26), while taking into account the property of a periodic solution that $Z(t_o)=Z(t_o+\tau_o)$, where τ_o is the largest period, yields

$$\overline{\mathrm{Nu}}^{hv\tau}=\overline{\mathrm{Nu}}_o^{h\tau}=\overline{\mathrm{Nu}}_1^{h\tau}=1+\frac{2(R-1)}{R}\frac{1}{\tau_o}\int_{t_o}^{(t_o+\tau_o)} Z dt. \tag{27}$$

The major limitation of this representation is the need to evaluate *a priori* all the periods of oscillations (or alternatively the frequencies) in order to identify the largest period. For chaotic solutions, for example, this becomes theoretically impossible because then the largest period is either very large (i.e., beyond the time over which the solution is computed) or does not exist. Nevertheless, for such cases one can adopt an alternative, practical, approach by realising that chaotic solutions are obtained because of the finite (and therefore limited) accuracy of the solution, hence two nearby solutions will diverge. However, this divergence is limited by the dissipative nature of the convection system. Therefore, by taking advantage of this limited divergence one can attempt to integrate the spatially averaged Nusselt number over a very large time range $\tau_1=t_1-t_o$ (starting from arbitrary post-transient values of the solution, at t_o). By separating the constant and time dependent parts of Z in the form $Z=1+Z'(t)$, averaging over the time range τ_1, and looking for the limit as $\tau_1\rightarrow\infty$, yields from Eqs. (25) and (26)

$$\overline{\mathrm{Nu}}_o^{h\infty}=1+\frac{2(R-1)}{R}+\frac{2(R-1)}{R}\lim_{\tau_1\rightarrow\infty}\left[\frac{1}{\tau_1}\int_{t_o}^{\tau_1} Z' dt\right] \tag{28}$$

$$\overline{\mathrm{Nu}}^{hv\infty}=1+\frac{2(R-1)}{R}+\frac{2(R-1)}{R}\lim_{\tau_1\rightarrow\infty}\left[\frac{1}{\tau_1}\int_{t_o}^{t_1} Z' dt\right]$$
$$+\frac{(R-1)}{R}\lim_{\tau_1\rightarrow\infty}\left[\frac{1}{\tau_1}(Z_1-Z_o)\right], \tag{29}$$

where Z_o and Z_1 are the values of Z at $t=t_o$ and $t=t_1$, respectively. The dissipative property of the convection system represented by the Eqs. (14), (15), and (16) imposes the following restrictions on the solution $\lim_{\tau_1\rightarrow\infty}[\int_{t_o}^{t_1} Z' dt]\rightarrow$finite as well as $\lim_{\tau_1\rightarrow\infty}[Z_o]\rightarrow$finite and $\lim_{\tau_1\rightarrow\infty}[Z_1]\rightarrow$finite. This requirement to obtain finite values for the integral and for Z_o and Z_1 as $\tau_1\rightarrow\infty$ causes the limits in Eqs. (28) and (29), which consist of a ratio of a finite value over τ_1, to vanish as $\tau_1\rightarrow\infty$. Then, both Eqs. (28) and (29) yield

$$\overline{\mathrm{Nu}}_o^{h\infty}=\overline{\mathrm{Nu}}^{hv\infty}=1+\frac{2(R-1)}{R}, \tag{30}$$

which is identical to Eq. (23) for the steady state Nusselt number. While the limit as $\tau_1\rightarrow\infty$ has significant theoretical value in providing an upper limit for the heat flux, in real and practical cases its applicability is problematic, especially when chaotic solutions are considered. In such cases evaluating the time average over a large, but finite, post-transient time range can provide an approximation for the heat flux. Because of the finite time range to be used in such a time averaging process the result is expected still to include oscillations, however it is also expected that these oscillations become smaller as the time range used for averaging, τ_1, becomes larger. We will observe this behavior when presenting the computational results. An additional particular point of interest can be observed from Eq. (30) when an upper bound for the heat flux is to be estimated. This can be evaluated using the limit of Eq. (30) for large values of R, i.e., as $R\rightarrow\infty$. For this limit Eq. (30) produces $\overline{\mathrm{Nu}}_{0,\infty}^{h\infty}=\overline{\mathrm{Nu}}_{\infty}^{hv\infty}=\lim_{R\rightarrow\infty}(\overline{\mathrm{Nu}}_{0,\infty}^{h\infty})=\lim_{R\rightarrow\infty}(\overline{\mathrm{Nu}}_{\infty}^{hv\infty})=3$. Therefore, the heat flux over the convective porous layer is limited in the present model by this upper bound value of 3. Higher values can only be obtained by including more modes in the truncated Galerkin representation of the spatial variation of the solution, by allowing the variation of the wave number as the value of R varies, or by considering a Forchheimer model. The latter includes nonlinear interactions in the momentum equation and therefore allowing for the possibility of strong turbulence, which is likely to produce complete time dependent, and three dimensional convection structures. However, this is out of the scope of the present paper.

4 Analytical and Computational Methods of Solution

4.1 The Analytical Solution, Amplitude Equation, and Hysteresis. The analytical solution to the problem is evaluated via a weak nonlinear analysis by using an expansion around the point where the convective stationary solutions lose linear stability. The stationary (fixed) points of the system (14)–(16) are the convective solutions $X_S=Y_S=\pm1$, $Z_S=1$ and the motionless solution $X_S=Y_S=Z_S=0$ (occasionally referred to as the origin). The expansion around the motionless stationary solution yields the familiar results of a pitchfork bifurcation from a motionless state to convection at $R=1$. We expand now the dependent variables around the convection stationary points in the form

$$[X,Y,Z]=[X_S,Y_S,Z_S]+\varepsilon[X_1,Y_1,Z_1]+\varepsilon^2[X_2,Y_2,Z_2]$$
$$+\varepsilon^3[X_3,Y_3,Z_3]+\ \ldots \tag{31}$$

We also expand R in a finite series of the form $R=R_o(1+\varepsilon^2)$ which now defines the small expansion parameter as $\varepsilon^2=(R-R_o)/R_o$, where R_o is the value of R where the stationary convective solutions lose their stability in the linear sense (see Vadasz and Olek [3,14]). Therefore, the present weak nonlinear analysis is expected to be restricted to initial conditions sufficiently close to *any one* of the convective fixed points. Introducing a long time scale $\tau=\varepsilon^2 t$ and replacing the time derivatives in Eqs. (14)–(16) with $d/dt\rightarrow d/dt+\varepsilon^2 d/d\tau$ yields a hierarchy of ordinary differential equations at the different orders. The solutions to order $O(\varepsilon)$ have the following form:

$$X_1=a_1 e^{i\sigma_o t}+a_1^* e^{-i\sigma_o t};\quad Y_1=b_1 e^{i\sigma_o t}+b_1^* e^{-i\sigma_o t};$$
$$Z_1=c_1 e^{i\sigma_o t}+c_1^* e^{-i\sigma_o t}, \tag{32}$$

where the coefficients $a_1(\tau)$, $a_1^*(\tau)$, $b_1(\tau,)$ $b_1^*(\tau)$, $c_1(\tau)$, and $c_1^*(\tau)$ are allowed to vary over the long time scale τ and $\pm i\sigma_o$ are the imaginary parts of the complex eigenvalues corresponding to the linear system at marginal stability (i.e., the real part of the eigenvalues is 0). The details of this solution including relationships between the coefficients are presented by Vadasz [6] and are therefore skipped here. A solvability condition is obtained at order $O(\varepsilon^3)$ in order to prevent terms of the form $e^{i\sigma_o t}$ and $e^{-i\sigma_o t}$ on the right hand side of the $O(\varepsilon^3)$ equations to resonate the homogeneous operator, hence forcing secular solutions of the form $te^{i\sigma_o t}$ and $te^{-i\sigma_o t}$ that are not bounded as $t\to\infty$. Hence, the coefficients of these secular terms must vanish, a requirement which provides a constraint on the amplitudes at order $O(\varepsilon)$ in the form of an amplitude equation

$$\frac{dr}{dt}=\chi[\xi-r^2]r, \tag{33}$$

where the $O(\varepsilon)$ complex amplitude was presented in the form $a=\varepsilon a_1=re^{i\theta}$, $a^*=\varepsilon a_1^*=re^{-i\theta}$ with $aa^*=r^2$, and $\chi=\varphi/\beta$ and $\xi=\varepsilon^2/\varphi=(R-R_o)/R_o\varphi$, where φ and β are parameters that depend on the value of α. For $\alpha=5$, corresponding to a Darcy-Prandtl number of $\Pr_D\cong 98.7$, and consistent with the present study $\varphi=-2.4$, $\beta=0.403226$, and the following critical values apply $R_o=25$ and $\sigma_o=60$. Clearly $\chi<0$ over all the cases to be considered, while $\xi>0$ for $\varepsilon^2<0$ (sub-critical conditions), $\xi<0$ for $\varepsilon^2>0$ (supercritical conditions), and $\xi=0$ for $\varepsilon^2=0$ (critical conditions). The post-transient solution to Eq. (33) yields $r^2=\pm\xi$ which produces a real value of r only for $\varepsilon^2<0$ (because $\varphi<0$ as indicated above). The Hopf bifurcation at $R=R_o=25$ is therefore sub-critical and in order to investigate the breakdown of the periodic solution at $R=R_o=25$ we derive the transient solution of Eq. (33). This transient solution is obtained by direct integration in the form

$$r^2=\frac{\xi}{\left[1-\left(1-\dfrac{\xi}{r_o^2}\right)\exp(-2\xi\chi t)\right]}\quad \text{for}\quad \xi\neq 0\quad (\varepsilon^2\neq 0) \tag{34}$$

$$r^2=\frac{r_o^2}{[1+2r_o^2\chi t]}\quad \text{for}\quad \xi=0\quad (\varepsilon^2=0), \tag{35}$$

where the following initial conditions were introduced: $r=r_o$ at $t=0$.

Clearly, both solutions (34) and (35) are valid at $t=0$ and yield then $r^2=r_o^2$, which can be easily recovered by substituting $t=0$ in Eqs. (34) and (35). Therefore the question which arises is what happens at a later time $t>0$ which causes these solutions to disappear when $\varepsilon^2>0$, (i.e., when $\xi<0$). Vadasz [6] has shown that both solutions (34) and (35) become singular, i.e., their denominator vanishes at a value of t, identified as the critical time, expressed by the equation

$$t_{cr}=\frac{1}{2\chi\xi}\ln\left[1-\frac{\xi}{r_o^2}\right]. \tag{36}$$

The existence of this critical time is linked to a condition for the argument of the $\ln(\cdot)$ function in Eq. (36) to be positive and greater or smaller than 1, depending on whether ξ is negative or positive, respectively. The latter requirement comes to impose a positive value of t_{cr}; otherwise no physical significance can be associated with this critical time. This condition exists only for subcritical values of R, i.e., for $\xi>0$, and is presented in the form $\xi/r_o^2<1$, while for supercritical values of $R(\xi<0)$ the critical time exists unconditionally. The significance of the existence of a critical time when the limit cycle solution diverges is explained in terms of the breakdown of the asymptotic expansion. The latter implicitly assumes (*a*) that the solution is local, around *any one (but only one)* of the fixed points, and (*b*) that the expansion is valid around the critical value of R, i.e., around R_o. The second assumption does not seem to be violated; however, the first assumption is strongly violated by a solution that tends to infinity, starting at sub-critical conditions when $\xi/r_o^2<1$. This condition implies $r_o^2>\xi$, i.e., at a given sub-critical value of R, as long as the initial conditions for r_o^2 are smaller than $\xi(r_o^2<\xi)$ the solution decays, spiralling towards the corresponding fixed point around which we applied the expansion. When the initial conditions satisfy $r_o^2=\xi$ a solitary limit cycle solution around this fixed point exists (the terminology ''solitary limit cycle'' is used to indicate that this limit cycle can be obtained only at $r_o^2=\xi$). As the initial conditions move away from this fixed point and $r_o^2>\xi$, the other fixed point may affect the solution as well. However the asymptotic expansion used does not allow it, and it is because of this reason that the solution diverges, indicating the breakdown of the expansion used, while physically representing the homoclinic explosion. Transforming the condition for this transition to occur, from $r_o^2>\xi$, to the original physical parameters of the system by substituting the definition of ξ and ε^2 one can observe that there is a value of $R\leqslant R_o$, say R_t, beyond which the transition occurs, which can be expressed in the form

$$R_t=R_o(1-|\varphi|r_o^2), \tag{37}$$

where the minus sign and the absolute value of φ appear in order to show explicitly that $\varphi<0$. If $R<R_t$ the solution decays, spiralling towards the corresponding fixed point, and at $R=R_t$ we expect the solitary limit cycle solution. Beyond this transitional value of R, i.e., $R>R_t$, the solution moves away from this fixed point either (*a*) towards the other fixed point, or (*b*) wanders around both fixed points before it stabilises towards one of them, or (*c*) yields a chaotic behavior. The present expansion can not provide an answer to select between these three possibilities. However, it is important to stress that for any initial condition r_o^2, which we choose, we can find a value of $R\leqslant R_o$ which satisfies Eq. (37). At that value of R we expect to obtain a limit cycle solution and beyond it a possible chaotic solution.

Experimental and numerical results of transitions to chaos in the Lorenz system (Wang, Singer, and Bau [15], Yuen and Bau [16], and Sparrow [5]) suggest the existence of a Hysteresis mechanism. The Hysteresis phenomenon is described as follows: when increasing the value of R gradually by approaching R_o from below, the transition to chaos occurs at $R=R_o$, while repeating the same procedure, but approaching R_o from above, the transition from chaos to the stationary solution occurs at a value of $R<R_o$. We provide an explanation of the Hysteresis phenomenon in connection with the transitional value of R which is presented in Eq. (37). Let's imagine a process of approaching R_o from below, say $R<R_t$. This means that the initial conditions lead the solution to one of the convective fixed points, i.e., $r=0$ (the fixed points represent the steady solutions of convective rolls moving clockwise or counter-clockwise). As we gradually increase the value of R by starting the next experiment (or numerical procedure) with initial conditions taken from the post-transient previous solution obtained at the slightly lower value of R, the new initial conditions are very close to the fixed point, i.e., $r_o^2\approx 0$. They are not exactly at the fixed point because the post-transient values of the previous solution are reached asymptotically, and at any finite time there is a slight departure between the solution and the steady state. For numerical solutions this is particularly correct when one solves the system (10)–(12) for the variables $\tilde{X}$, $\tilde{Y}$, $\tilde{Z}$, instead of (14)–(16) for X, Y, Z. The reason for the distinction between the two systems, which are equivalent, is the fact that the fixed points expressed in terms of the former are dependent on the value of R, while the scaling of the latter removes this dependence. As a result the latter system will provide an identical post-transient solution which is independent of R that may converge accurately (within machine precision) to the fixed point, hence preventing the transition to chaos even for values of $R>R_o$. Otherwise, transition to chaos occurs and according to Eq. (37) the corresponding transitional value R_t is very close to R_o. However, when one approaches R_o from above, the initial conditions taken from the previous solution at a value of $R>R_o$ are quite large and far away from the fixed point (because they correspond to a chaotic solution obtained at a higher value of R), i.e., r_o^2 is far away from 0.

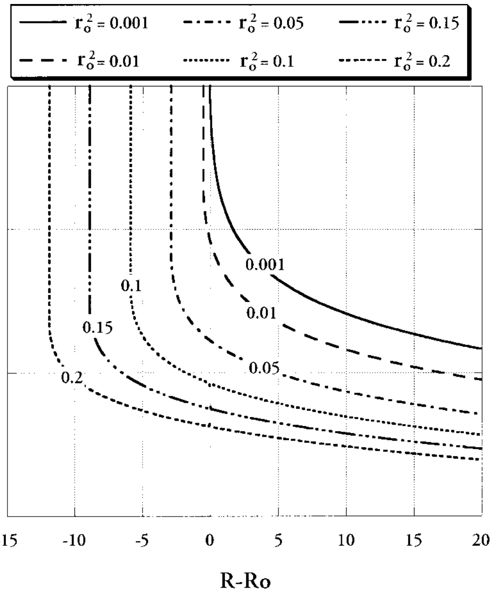

Fig. 3 The critical time as a function of $(R-R_o)$ for six values of initial conditions in terms of r_o^2. The transition from steady convection to chaos (or backwards) is linked to the existence (disappearance) of this critical time, explaining the mechanism for Hysteresis.

Therefore, in such a case it is expected to obtain a chaotic solution for sub-critical values of R until the value of R_t is reached from above, which would be quite far away from R_o, according to Eq. (37). In graphical terms this process can be observed on Fig. 3, where the variation of the explicit critical time is presented as a function of $(R-R_o)$ for different values of r_o^2, by using Eq. (36) and the definitions of ξ and ε^2. The disappearance of the critical time at $R=R_t$ is an indication that the amplitude does not diverge, and therefore a steady convective solution can be obtained. From the figure it is evident that for small values of r_o^2 (e.g., $r_o^2=0.001$), corresponding to the forward transition from steady convection to chaos, the asymptote of t_{cr} (i.e., the point when the critical time disappears) occurs very close to $R=R_o$, while for values of r_o^2 which are not so small, corresponding to the reverse transition from chaos to steady convection, (e.g., $r_o^2=0.2$) the asymptote of t_{cr} occurs at values of $R<R_o$ which are quite far away from R_o. This explains the reason for observing Hysteresis in the transition from steady convection to chaos and backwards, by using initial conditions corresponding to a previous solution at a slightly different value of R.

4.2 The Computational Solution, Adomian's Decomposition Method.

Adomian's decomposition method (Adomian [7,8]) is applied to solve the system of Eqs. (14), (15), and (16). The method provides in principle an analytical solution in the form of an infinite power series for each dependent variable. However, the practical need to evaluate numerical values from the infinite power series, the consequent series truncation, and the practical procedure to accomplish this task transform the otherwise analytical results into a computational solution achieved up to a finite accuracy. This is accomplished by using the decomposition method as an algorithm for the approximation of the dynamical response in a sequence of time intervals $[0,t_1),[t_1,t_2),\ldots,[t_{n-1},t_n)$ such that the solution at t_p is taken as initial condition in the interval $[t_p,t_{p+1})$, which follows. A detailed description of the method of solution is provided by Vadasz and Olek [3,14] and its convergence and accuracy as relevant to the present problem was presented by Vadasz and Olek [9]. The solution to Eqs. (14)–(16) was obtained in the form

$$X_i(t)=\sum_{n=0}^{\infty} c_{i,n}\frac{t^n}{n!} \quad \forall \quad i=1,2,\ldots,m, \tag{40}$$

where

$$c_{i,0}=X_i(0) \quad \forall \quad i=1,2,\ldots,m \tag{41}$$

and the general term for $n\geqslant 1$ is defined through the following recurrence relationship:

$$c_{1,n}=-\alpha(c_{1,(n-1)}-c_{2,(n-1)}) \tag{42a}$$

$$c_{2,n}=Rc_{1,(n-1)}-c_{2,(n-1)}-(R-1)\sum_{k=0}^{n-1}\frac{(n-1)!\,c_{1,k}c_{3,(n-k-1)}}{k!(n-k-1)!} \tag{42b}$$

$$c_{3,n}=-2c_{3,(n-1)}+2\sum_{k=0}^{n-1}\frac{(n-1)!\,c_{1,k}c_{2,(n-k-1)}}{k!(n-k-1)!}. \tag{42c}$$

The advantages of using this method as compared with other, standard and traditional, numerical methods lies predominantly in its robustness and in the fact that it yields an analytical form of the solution to support the computational results. The computations were performed to double precision accuracy on an Apple Power Macintosh G3. In all computations 15 terms in the series and a time interval of $\Delta t=10^{-3}$ were used, and all computations were performed up to post-transient values of $t=t_{\max}=210$, or in cases of particular interest $t=t_{\max}=420$. Subject to these conditions the accuracy of the computational solution reaches saturation at machine precision [9], hence releasing the user from the need to occasionally fine-tune the accuracy of the results.

In order to compare the computational results to the analytical ones obtained in the previous section via the weak nonlinear theory we have to make sure that the initial conditions for the computations are consistent with the initial conditions corresponding to the weak nonlinear solution. It should be pointed out that the set of possible initial conditions in the weak nonlinear solution (34) and (35) is constrained because we did not include the decaying solutions of the form $a_{12}(\tau)\exp(\sigma_3 t)$ (with $\sigma_3<0$ and real) in Eq. (32). Therefore, this constraint, which is equivalent to setting $(a_{12})_{\tau=0}=0$ and $(\theta)_{\tau=0}=0$, is kept valid for all computational results as well. The present weak nonlinear solution provides the following conditions, which are necessary and sufficient to ensure the consistency of the initial conditions between the weak nonlinear and computational solutions

$$X^{(o)}=Y^{(o)}=1+2r_o;$$

$$Z^{(o)}=1+\frac{\sigma_o^2}{\alpha(R_o-1)}[X^{(o)}-1]=1+\frac{2\sigma_o^2}{\alpha(R_o-1)}r_o, \tag{43}$$

where $X^{(o)}$, $Y^{(o)}$, and $Z^{(o)}$ are the initial conditions for X, Y, and Z respectively and r_o is the initial condition for r, as used in the weak nonlinear solution. Furthermore, using Eq. (43) it is noted that $r_o=(X^{(o)}-1)/2=(Y^{(o)}-1)/2$. Clearly this yields negative values of r_o if $X^{(o)}<1$ or $Y^{(o)}<1$. Therefore, we extend the definition of r and allow it to take negative values. This is equivalent to a phase shift in the limit cycle solution of the form $\tilde{\theta}=\theta+\pi$ and can be rigorously justified. For r_o this corresponds to a phase shift $\tilde{\theta}_o=\theta_o+\pi=\pi$, because $\theta_o=(\theta)_{\tau=0}=0$, implicitly in the present case.

5 Results and Discussion

Before presenting the comparison between the computational and weak nonlinear analytical results in terms of the resulting Nusselt number, a brief sequence of computational results are presented in Fig. 4 to demonstrate the transition from steady convection to chaos. These results correspond to initial conditions

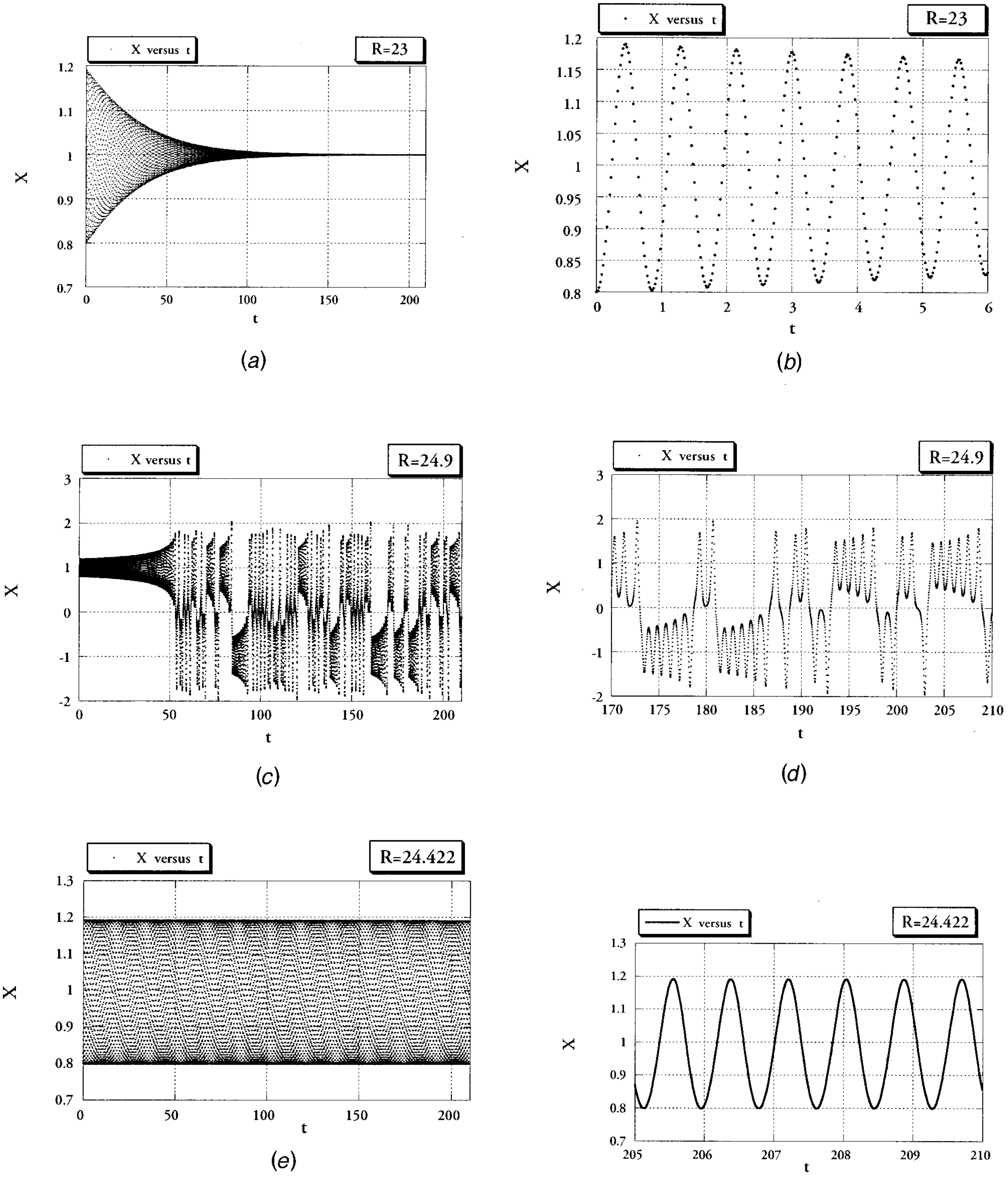

(*a*) (*b*)

(*c*) (*d*)

(*e*) (*f*)

Fig. 4 The computational results for the evolution of $X(t)$ in the time domain for three values of Rayleigh number (in terms of R): (*a*) X as a function of time for $R=23$—the solution stabilizes to the fixed point; (*b*) the inset of Fig. 4(*a*) detailing the oscillatory decay of the solution; (*c*) X as a function of time for $R=24.9$—the solution exhibits chaotic behavior; (*d*) the inset of Fig. 4(*c*) detailing the chaotic solution; (*e*) X as a function of time for $R=24.422$—the solution is periodic; and (*f*) the inset of Fig. 4(e) detailing the periodic solution (data points are connected).

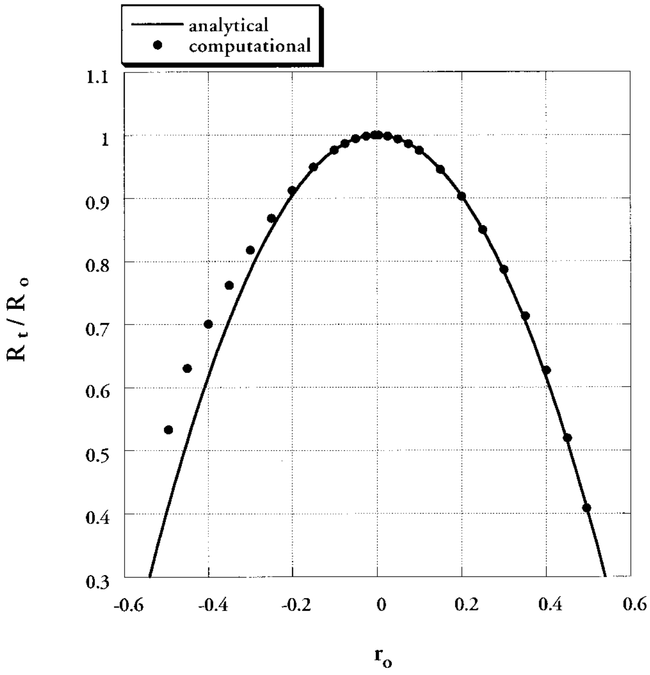

Fig. 5 Transitional sub-critical values of Rayleigh number in terms of R_t/R_o as a function of the initial conditions r_o. A comparison between the weak nonlinear solution (— analytical) and the computational results (● computational).

consistent with $r_o = -0.1$ ($X^{(o)} = Y^{(o)} = 0.8$ and $Z^{(o)} = 0.9$) and are presented at two values of R, the first at $R = 23$ just before the transition to chaos occurs, and the second just after the transition at $R = 24.9 < R_o$ (note that $R_o = 25$). The results for these two values of R in the time domain are presented in Fig. 4 for X as a function of t. The decay of the solution, corresponding to $R = 23$, towards the steady state value of $X = 1$ is clearly identified in Fig. 4(a), and the inset presented in Fig. 4(b) highlights its oscillatory behavior. On the other hand, for $R = 24.9$, Fig. 4(c) shows a typical chaotic result and the inset presented in Fig. 4(d) focuses on the post-transient time domain $170 < t < 210$. It is worth emphasising the fact that the computational results show a transition to chaos at a sub-critical value of R (the critical value is $R_o = 25$). A comparison between Figs. 4(a) and 4(c) at a common transient time domain $0 < t < 50$ shows that the envelope of the function $X(t)$ converges for $R = 23$ (Fig. 4(a)) and diverges for $R = 24.9$ (Fig. 4(c)). This suggests that somewhere in-between $R = 23$ and $R = 24.9$ the envelope of the function $X(t)$ will neither converge nor diverge, producing a typical limit cycle. Looking for this limit cycle provides the result presented in Fig. 4(e), where it is evident that the envelope of the function $X(t)$ does not converge nor diverge, and the inset presented in Fig. 4(f) (where the data points are connected) demonstrates the periodic behavior of the solution. The objective in the presentation of the following results is to demonstrate the appearance of this solitary limit cycle at a particular value of R prior to the transition to chaos and to present the computational values of $R = R_t$ where this transition occurs (the analytical values of R_t where presented in Eq. (37)) for different initial conditions (consistent with the weak nonlinear solution). It should be stressed that this limit cycle was obtained computationally irrespective of whether the initial conditions were consistent with the weak nonlinear solution or not; the consistency is imposed only for quantitative comparison purposes. A comparison between the computational and analytical results regarding the transition value of R as a function of r_o, representing the initial conditions, is presented in Fig. 5. The continuous curve represents the analytical results following Eq. (37) while the dots represent computational results obtained by using initial conditions consistent with their corresponding analytical ones by using the consistency Eq. (43). From the figure it is evident that as long as the initial conditions are not too far away from the convective fixed point, i.e., $|r_o| \ll 1$, the computational and analytical solutions are identical. For values of r_o close to the convective fixed point, i.e., in the neighborhood of $r_o \sim 0$, both solutions overlap. However, as r_o moves away from this neighborhood the weak nonlinear solution loses accuracy and the analytical results for R_t depart from the accurate computational ones. Higher order corrections of this analytical transition value could improve the accuracy of the analytical results, a task that is left for future investigation.

The spatial as well as time average of the Nusselt number was evaluated by using the computational solutions, in order to investigate the impact of these solutions on the heat flux. This was accomplished by evaluating the averaged Nusselt number following the relationship

$$\overline{\mathrm{Nu}}_o^{h\tau_1} = 1 + \frac{2(R-1)}{R}\frac{1}{\tau_1}\int_{t_0}^{t_0+\tau_1} Z\,dt, \qquad (44)$$

which is identical to Eq. (27) with the only exception that τ_1 is not necessarily a period of convection. The lack of knowledge about these periods of oscillations, especially in the chaotic regime, suggests the use of an alternative approach. The value of t_o was taken as any arbitrary post-transient value of time ($t_o = 50$ was found to correspond to this condition), while the time range for the integration was allowed to vary in such a way that one can present the accumulative effect of this time averaging process as $\overline{Nu}_o^{h\tau_1}(\tau_1)$. The result of this procedure for $R = 26$ is presented in Fig. 6, where the initial conditions used for evaluating the solution were $X^{(o)} = Y^{(o)} = Z^{(o)} = 0.9$. It can be observed from Fig. 6(a) that the accumulated effect of this averaging process converges to a very narrow band of variation around an almost constant value for the Nusselt number when the time range is large. From the inset presented in Fig. 6(b) one can estimate the fluctuations around this mean Nusselt number to be about ~0.005 around ~2.619, i.e., approximately 0.2 percent. Such an accuracy in estimating the Nusselt number should be more than sufficient in most engineering applications, and therefore even during the chaotic regime the predictability of the heat flux is not substantially violated by this limited accuracy due to the oscillations of this mean Nusselt number. We can therefore use this procedure and evaluate the Nusselt number over a wide range of values of R. In order to do so we need to take into account the already established fact that in the chaotic regime the results are very sensitive to variations in the initial conditions. While this sensitivity might not affect the mean Nusselt number directly, when using the procedure suggested above, the transitional value of R is significantly affected by the initial conditions as demonstrated above. As a result, the mean Nusselt number around this transitional value of R is expected to be affected significantly. Therefore, the evaluation of this mean Nusselt number was performed for three different cases, as relevant to the impact of the initial conditions on the results. The first case corresponds to *fixed initial conditions* for all values of R considered (the values used correspond to $X^{(o)} = Y^{(o)} = Z^{(o)} = 0.9$), the second case uses the final values of X, Y, and Z obtained at the previous, *slightly smaller*, value of R as initial conditions for the current value of R. This case is referred to as the *''forward moving''* case. The third case is similar to the latter however it differs from it by moving in the opposite R direction, i.e., the values of R decrease and the initial conditions for the solution at the current value of R are taken from the final values of X, Y, and Z obtained at the previous, *slightly larger*, value of R. This case is referred to as the *''backward moving''* case. This procedure was followed for values of R ranging between $1 \le R \le 150$, with a step of $\Delta R = 0.1$. The results are presented in Fig. 7. It is evident from the figure that the transition from steady convection to chaos is associated with a sharp decline in heat flux. This can be linked to the

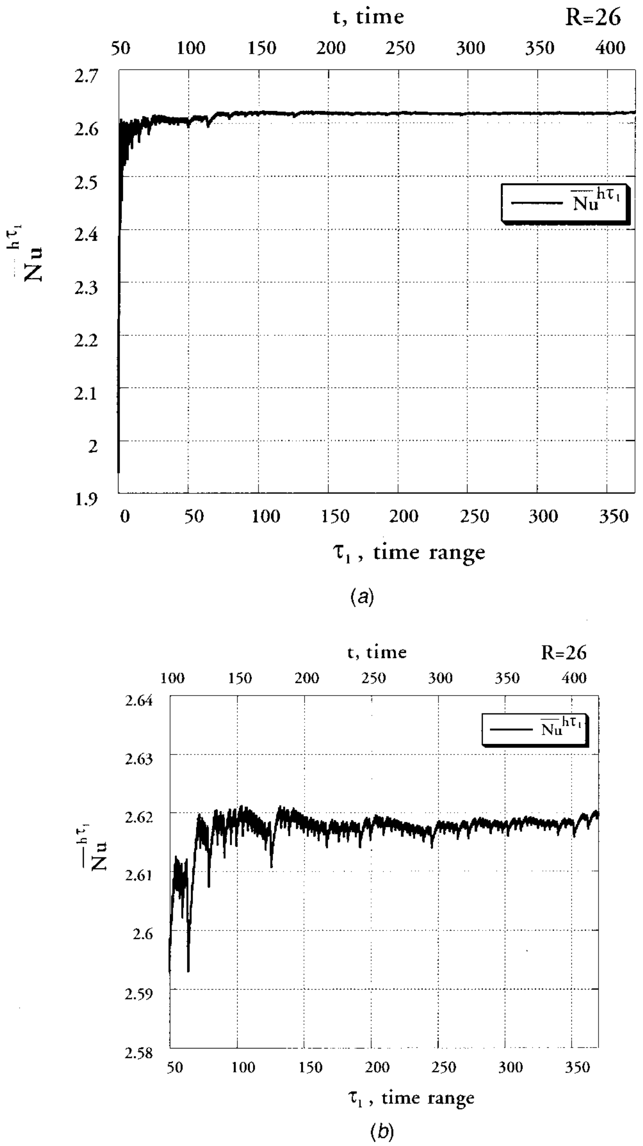

(*a*)

(*b*)

Fig. 6 (*a*) The impact of the accumulated effect of the variation of the mean Nusselt number as a function of the time range of the integration, τ_1; (*b*) the inset of Fig. 6(*a*), highlighting the details of the oscillations.

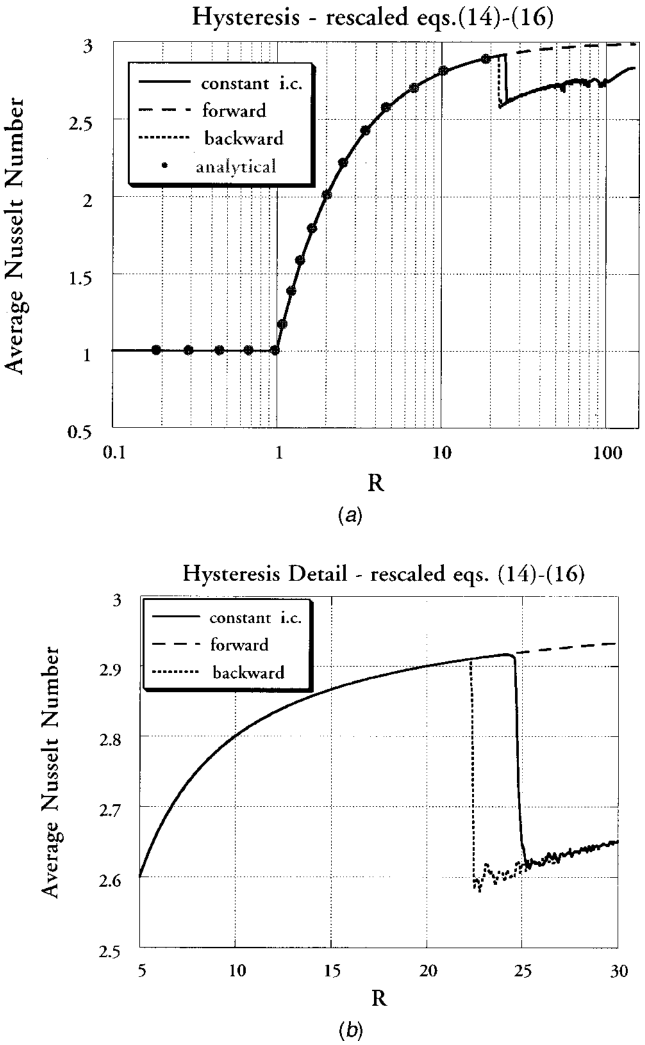

(*a*)

(*b*)

Fig. 7 (a) The variation of the mean Nusselt number as a function of *R* as obtained by solving the system of Eqs. (14)–(16) in terms of the rescaled variables, via constant initial conditions, forward and backward variation of *R*, and compared with the analytical relationship, Eq. (23), for sub-transitional values of *R*; (*b*) the inset of Fig. 7(*a*), highlighting the transition from steady convection to chaos, and the corresponding Hysteresis effect.

solitary limit cycle that appears at this transition, hence the retarding effect that this transition has on the heat flux is due to the oscillatory nature of the transition point, rather than the chaotic (weak-turbulent) nature of the solution beyond this transition point. Furthermore, it is evident that the weak-turbulent regime following the transition point contributes to a recovery from this sharp reduction in heat flux. The retarding effect of oscillatory single frequency convection on the heat flux is well documented in other heat transfer problems. Mladin and Zumbrunnen [17] indicate, for example, that in their investigation of the heat transfer in a pulsating stagnation flow ''both theoretical and experimental results indicate a significant decrease in the (average) Nusselt number with increasing flow pulsation amplitude.'' An additional impressive result evident from Fig. 7 is the effect of Hysteresis linked to the transition from steady to weak-turbulent convection. While the solution corresponding to constant initial conditions experiences the transition (observed by the jump in the value of the mean Nusselt number) at a value of R close to $R=R_o=25$ (actually slightly below it) the transition for the ''backward moving'' case occurs at a value of R substantially below $R_o=25$, as indeed anticipated from the analytical results and the discussion on Hysteresis presented in Section 4.1 and Eq. (37). On the other hand the results pertaining to the ''forward moving'' case do not experience any transition to a weak-turbulent regime over the whole range of R values considered. This apparently surprising result can be explained in terms of the scaling used for the computations. *The system of equations* (14)–(16) *yields a post-transient steady state for* $R<R_t$, *which is independent of* R. Actually they yield accurately $Z=1$ if the post-transient solution is left to be evaluated over a long post-transient time range. By using the ''forward moving'' procedure starting from sub-critical values of R, the solution will eventually converge (after a few values of R) to this accurate (within the machine precision) steady state. Clearly, when the computational procedure starts with initial conditions corresponding to this convective fixed point, which belongs to the stable manifold associated with this fixed point, the solution will remain at the fixed point even at super-critical values of R, because this fixed point is independent of R. It is also a well known experimental result that non-turbulent solutions were recovered in carefully performed experiments in a quiet environ-

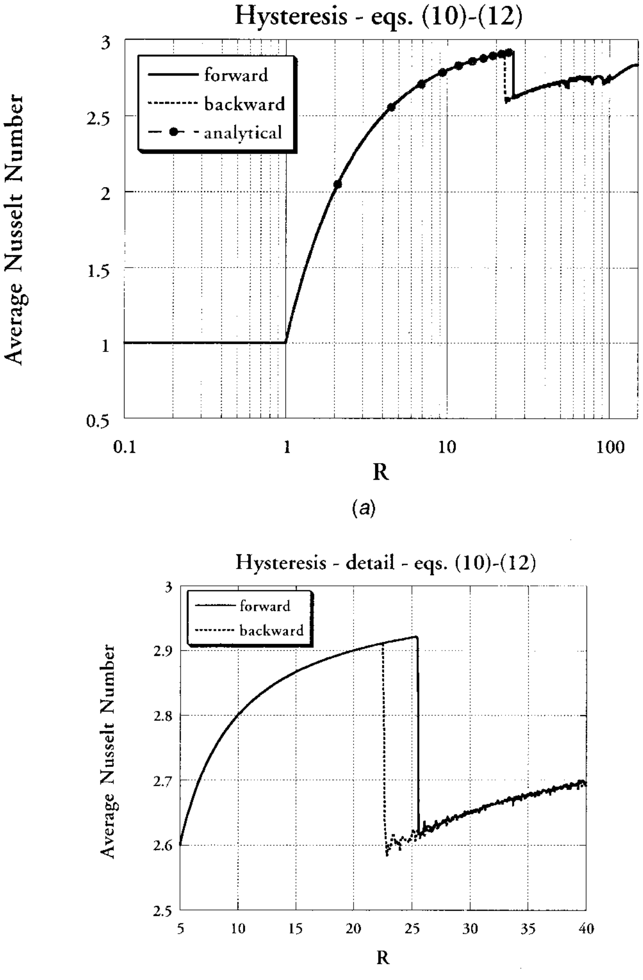

(*a*)

(*b*)

Fig. 8 (*a*) The variation of the mean Nusselt number as a function of *R* as obtained by solving the system of Eqs. (10)–(12), via forward and backward variation of *R*, and compared with the analytical relationship, Eq. (23), for sub-transitional values of *R*; (*b*) the inset of Fig. 8(*a*), highlighting the transition from steady convection to chaos, and the corresponding Hysteresis effect.

ment even for super-critical conditions. A quiet environment in our case is associated with initial conditions of perfect steady state convection and very gradual increase of the value of *R*, pertaining to the ''forward moving'' case. To qualify this explanation that the scaling of the variables prevented the transition to occur in the ''forward moving'' case an additional solution was sought, this time in terms of the pre-scaled variables $\tilde{X}$, $\tilde{Y}$, and $\tilde{Z}$ as represented by Eqs. (10)–(12). *These variables have fixed points (corresponding to the steady state) which depend on the value of R.* Therefore, it is anticipated that the forward moving solution will not be able to converge to an invariant constant value, independent of *R*, and prevent the transition, because the fixed point is a function of *R*. An identical computational procedure was adopted for the solution of the system of Eqs. (10)–(12) producing the results presented in Fig. 8, where the case of fixed initial conditions was omitted because of lack of current interest. It is evident from Fig. 8 that indeed the transition from steady to weak-turbulent convection occurs in the ''forward-moving'' case as well, at a value of *R* very close but slightly higher than $R_o=25$. The transition for the ''backward moving'' case occurs at the same sub-critical value of *R* as in Fig. 7. Therefore, it can be concluded that the scaling of the equations (especially their normalization with respect to their fixed points) may have a substantial impact on the transition from steady to weak-turbulent convection. In both solutions, corresponding to Eqs. (10)–(12) and (14)–(16) presented in Figs. 7 and 8 it is clear that the computational and analytical solutions (Eq. (23)) yield identical results for conditions pertaining to steady state convection. Furthermore, the computational results confirm the analytical upper bound for the average Nusselt number represented by Eq. (30) and in particular the value of $\overline{Nu}_{o,\infty}^{h\infty}=3$ for the limit as $R\rightarrow\infty$.

6 Conclusions

The investigation of heat transfer regimes in a fluid saturated porous layer heated from below was presented by using the weak nonlinear theory and Adomian's decomposition method to provide solutions to a truncated Galerkin representation of the governing equations, which is equivalent to Lorenz equations. Both the analytical and computational results confirmed the transition from steady convection to chaos via a solitary limit cycle at a sub-critical value of the Rayleigh number. The sub-critical transition was explained by investigating the transient amplitude solution obtained via the weak non-linear theory. This investigation reveals analytically the mechanism for the experimentally (or numerically) well known phenomenon of Hysteresis in the transition from steady to weak-turbulent convection. Despite the difficulty to evaluate the averaged heat flux up to any desired accuracy in the weak-turbulent regime, it was demonstrated that the only impact that this regime has on the average heat flux is a minor reduction of accuracy. Hence, in this sense the concept of predictability of the results is not violated. Analytical expressions of upper bounds for the averaged Nusselt number were derived and their comparison with computational results confirms their validity.

Acknowledgment

The author wishes to thank the National Research Foundation (South Africa) for partially supporting this study through the Competitive Industry Research Grant (CIPM-GUN2034039).

Nomenclature

Latin Symbols

Da = Darcy number, defined by k_*/H_*^2
$\hat{\mathbf{e}}_x$ = unit vector in the *x*-direction
$\hat{\mathbf{e}}_y$ = unit vector in the *y*-direction
$\hat{\mathbf{e}}_z$ = unit vector in the *z*-direction
$\hat{\mathbf{e}}_g$ = unit vector in the direction of gravity
$\hat{\mathbf{e}}_n$ = unit vector normal to the boundary, positive outwards
H_* = the height of the layer
H = the front aspect ratio of the porous layer, equals H_*/L_*
k_* = permeability of the porous domain
L_* = the length of the porous layer
L = reciprocal of the front aspect ratio, equals $1/H = L_*/H_*$
Nu = Nusselt number
M_f = a ratio between the heat capacity of the fluid and the effective heat capacity of the porous domain
p = reduced pressure (dimensionless)
Pr_D = Darcy-Prandtl number, equals $\phi\mathrm{Pr}/\mathrm{Da}$
Pr = Prandtl Number, equals v_*/α_{e*}
$\mathbf{q}$ = dimensionless filtration velocity vector, equals $u\hat{\mathbf{e}}_x + v\hat{\mathbf{e}}_y + w\hat{\mathbf{e}}_z$
Ra = porous media gravity related Rayleigh number, equals $\beta_*\Delta T_c g_* H_* k_* M_f/\alpha_{e*}v_*$
Ra_o = critical value of Rayleigh number for the transition from steady convection to chaos
R = scaled Rayleigh number, equals $\mathrm{Ra}/4\pi^2$

R_o = critical value of R for the transition from steady convection to chaos
r = absolute value of the complex amplitude
r_o = initial condition of r
$\hat{t}$ = time
t = rescaled time, Eq. (9)
T = dimensionless temperature, equals $(T_* - T_C)/(T_H - T_C)$
T_C = coldest wall temperature
T_H = hottest wall temperature
u = horizontal x-component of the filtration velocity
v = horizontal y-component of the filtration velocity
w = vertical component of the filtration velocity
W_* = the width of the porous layer
W = the side aspect ratio of the porous layer, equals W_*/H_*
x, y = horizontal length and width co-ordinates
z = vertical co-ordinate
$\tilde{X}, \tilde{Y}, \tilde{Z}$ = pre-scaled amplitudes, Eqs. (7), (8)
X, Y, Z = scaled amplitudes, Eq. (13)

Greek Symbols

α = a parameter related to the time derivative term in Darcy's equation
α_{e*} = effective thermal diffusivity
β_* = thermal expansion coefficient
ε = asymptotic expansion parameter, defined in the text following Eq. (31)
ϕ = porosity
ν_* = fluid's kinematic viscosity
μ_* = fluid's dynamic viscosity
ψ = stream function
ΔT_c = characteristic temperature difference
τ = long time scale
τ_l = large post-transient time range
θ = the phase of the complex amplitude
σ_o = linear frequency

Subscripts

$*$ = dimensional values
c = characteristic values
t = transitional values
cr = critical values

Superscripts

$*$ = complex conjugate

References

[1] Nield, D. A., and Bejan, A., 1999, *Convection in Porous Media*, 2nd ed., Springer Verlag, New York.
[2] Bejan, A., 1995, *Convection Heat Transfer*, 2nd edition, Wiley, New York.
[3] Vadasz, P., and Olek, S., 1999, ''Weak Turbulence and Chaos for Low Prandtl Number Gravity Driven Convection in Porous Media,'' Transport in Porous Media, **37**, pp. 69–91.
[4] Lorenz, E. N., 1963, ''Deterministic Non-Periodic Flows,'' J. Atmos. Sci., **20**, pp. 130–141.
[5] Sparrow, C., 1982, *The Lorenz Equations: Bifurcations, Chaos, and Strange Attractors*, Springer-Verlag, New York.
[6] Vadasz, P., 1999, ''Local and Global Transitions to Chaos and Hysteresis in a Porous Layer Heated from Below,'' Transport in Porous Media, **37**, pp. 213–245.
[7] Adomian, G., 1988, ''A Review of the Decomposition Method in Applied Mathematics,'' J. Math. Anal. Appl., **135**, pp. 501–544.
[8] Adomian, G., 1994, *Solving Frontier Problems in Physics: The Decomposition Method*, Kluwer Academic Publishers, Dordrecht.
[9] Vadasz, P., and Olek, S., 2000, ''Convergence and Accuracy of Adomian's Decomposition Method for the Solution of Lorenz Equations,'' Int. J. Heat Mass Transf., **43**, pp. 1715–1734.
[10] Elder, J. W., 1967, ''Steady Free Convection in a Porous Medium Heated from Below,'' J. Fluid Mech., **27**, pp. 609–623.
[11] Braester, C., and Vadasz, P., 1993, ''The Effect of a Weak Heterogeneity of the Porous Medium on the Natural Convection,'' J. Fluid Mech., **254**, pp. 345–362.
[12] Vadasz, P., and Braester, C., 1992, ''The Effect of Imperfectly Insulated Sidewalls on Natural Convection in Porous Media,'' Acta Mech., **91**, No. 3–4, pp. 215–233.
[13] Bau, H. H., 1994, ''An Engineer's Perspective on Chaos,'' *Chaos in Heat Transfer and Fluid Dynamics*, Arpacci, Hussain, Paollucci and Watts, eds., HTD-Vol. 298, pp. 1–7.
[14] Vadasz, P., and Olek, S., 2000, ''Route to Chaos for Moderate Prandtl Number Convection in a Porous Layer Heated from Below,'' Transport in Porous Media, **41**, pp. 211–239.
[15] Wang, Y., Singer, J., and Bau, H. H., 1992, ''Controlling Chaos in a Thermal Convection Loop,'' J. Fluid Mech., **237**, pp. 479–498.
[16] Yuen, P., and Bau, H. H., 1996, ''Rendering a Subcritical Hopf Bifurcation Supercritical,'' J. Fluid Mech., **317**, pp. 91–109.
[17] Mladin, E. C., and Zumbrunnen, D. A., 1995, ''Dependence of Heat Transfer to a Pulsating Stagnation Flow on Pulse Characteristics,'' J. Thermophys. Heat Transfer, **9**, No. 1, pp. 181–192.

Z. Al-Qodah
Assistant Professor
Department of Chemical Engineering,
Amman College for Engineering Technology,
Al-Balqa' Applied University,
P.O. Box 340558,
Marka, Amman, Jordan
e-mail: zalqodah@hotmail.com

M. Al-Busoul
Assistant Professor
Department of Mechanical Engineering,
Amman College for Engineering Technology,
Al-Balqa' Applied University,
P.O. Box 340558,
Marka, Amman, Jordan

The Effect of Magnetic Field on Local Heat Transfer Coefficient in Fluidized Beds With Immersed Heating Surface

Five different magnetic particles have been used to investigate the effect of a transverse magnetic field on the thermal behavior of a gas fluidized bed, with an immersed heating spherical surface. The effects of gas superficial velocity and magnetic field intensity on the behavior of the temperature distribution and the local heat transfer coefficient at different radial and axial positions in the bed was investigated. In the present study a correlation relating Nusselt number to the magnetic field intensity is proposed.

[DOI: 10.1115/1.1336506]

Keywords: *Fluidized Beds, Magnetic, Magnetohydrodynamics, Thermal, Two-Phase*

1 Introduction

Magnetic stabilization of fluidized beds of magnetically susceptible particles is considered as one of the technologies developed to eliminate the drawbacks of fluidized beds while maintaining their advantages ([1]). It has been shown both experimentally and by modeling that magnetic stabilization of fluidized bed results in an improved fluid-solid contactor that combines the most desirable characteristics of both fluidized and packed beds. The primary advantage of magnetically stabilized beds (MSFBs) is the combination of low-pressure drops of fluidized beds with the bubble-free operation at high gas flow rates of packed bed ([2–5]).

The suppression of the solid phase mixing movements is considered as one of the major consequences of magnetic stabilization of fluidized beds. This effect is expected to represent a considerable drawback of magnetic stabilization if this approach is applied to fluidized beds where temperature control throughout the bed represents a primary requirement, since heat transfer rate in stabilized beds is lower than that of fluidized beds ([6,7]).

Only a few contributions have paid attention to thermal behavior of these magnetically stabilized systems ([8–10]). Lucchesi et al. [8] found in tests of bed-to-wall heat transfer, that the MSFBs performance agreed well with literature values for packed beds of the same superficial velocity. Neff and Rubinsky [9] studied the effect of magnetic stabilization on wall-to-bed heat transfer coefficient and found that each flow regime of the magnetized bed is characterized by a different heat transfer rate. Arnaldos et al. [10] studied the effect of magnetic field stabilization on the temperature distribution for beds with an immersed heating surface under different operating conditions, and proposed a model to calculate the effective thermal conductivity of the bed from experimental data. Recently, Qian and Saxena [11] reported that the heat transfer rates in all flow regimes of the magnetized bed are similar.

In a previous study ([12]) the effect of a transverse magnetic field on the wall-to-bed heat transfer coefficient in gas fluidized bed was investigated. The intent of this study is to characterize the effect of a transverse magnetic field on the local heat transfer coefficient from a spherical immersed heater in various axial and radial locations in a bed of ferromagnetic particles, in connection with bed structure and porosity.

2 Experimental

2.1 Experimental Setup and Materials. A schematic diagram of the experimental setup is shown in Fig. 1. The column is constructed from Plexiglas to facilitate visual observations. The column height is 0.9 m with 0.07 m I.D. At the base of the column, a stainless steel non-magnetic grid of 0.33 mm whole diameter is used to support the solid phase. Below the supporting grid, the gas enters from a calming section filled with polyethylene particles of 3 mm diameter. This section serves to distribute the gas phase uniformly in the bed. The gas is withdrawn from the top of the column using a suction fan. In this way, the gas enters the bed uniformly and at the ambient temperature. The configuration of the magnetic system is described elsewhere ([13,14]). Figure 1 (inset 13) shows the heating system used in the present investigation. It consists of a spherical copper heater of 15 mm o.d., and surface area of $1.768\times10^{-4}\,\mathrm{m}^2$, with an electrical resistance inside it. The electrical power of the heater, *IV*, is constant and is equal to 5W.

The magnetic particles consist of the ferromagnetic magnetite (Fe_3O_4). The magnetic particles were covered by a stable layer of activated carbon or zeolite using epoxy resin as an adhesive in the same manner as described earlier ([12]). The characteristics of the magnetic system and magnetic particles used in this investigation are shown in Tables 1 and 2, respectively.

2.2 Procedure. The mean diameter of the magnetic particles d_p is determined using the following formula proposed by Botterill [15]:

$$d_p=\left[\sum (x_i/d_{pi})\right]^{-1} \tag{1}$$

The initial bed height is 0.10 m. A ruler attached to the column wall is used to measure the bed height. The following equations hold for the initial solid holdup, ε_{so}, solid holdup after bed expansion, ε_s, and the bed porosity, ε, respectively

$$\varepsilon_{so}=(W/\rho_s)/AH_{bo} \tag{2}$$

$$\varepsilon_s=1-(H_{bo}/H_b)\varepsilon_{so} \tag{3}$$

$$\varepsilon=1-\varepsilon_s. \tag{4}$$

Contributed by the Heat Transfer Division for publication in the JOURNAL OF HEAT TRANSFER. Manuscript received by the Heat Transfer Division October 21, 1999; revision received, July 12, 2000. Associate Editor: P. Ayyaswamy.

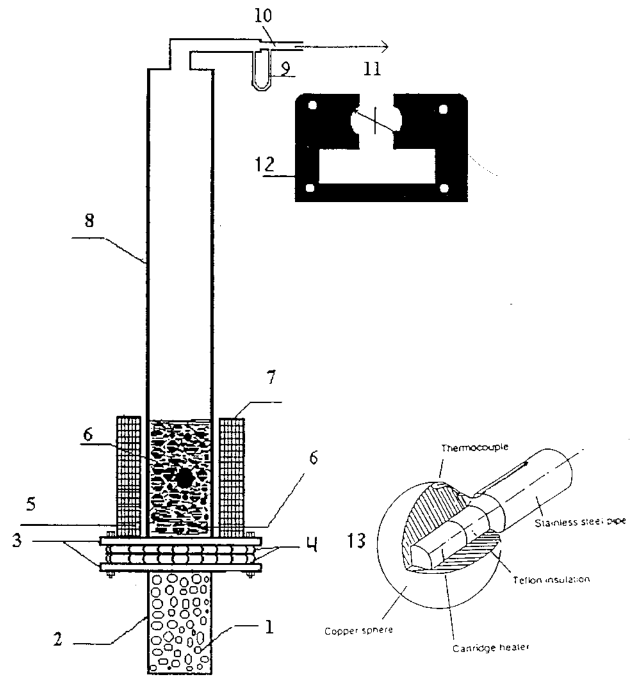

Fig. 1 Schematic of the experimental setup: (1) Gas entrance; (2) Polyethylene particles; (3) Flanges; (4) Supporting grid; (5) Heater; (6) Magnetic particles; (7) Magnetic system; (8) column; (9) Manometer; (10) Orifice; (11) Gas suction; (12) Details of the magnetic sheets; and (13) Details of the heater

The effect of radiation heat transfer in this study is neglected. Temperature is measured with a copper constantan thermocouple. The readout of the temperature device gives directly the difference between the heater and the inlet gas temperature. Gas flow rate was measured using an orifice meter (Armfield, England) located on the line between the suction fan and the top of the column. The magnetic field intensity is measured using Hall probe (Leybolo-Heraeus, Germany).

The local heat transfer coefficient is calculated using the following equation:

$$h_r = Q/[A(T_s - T_b)] = IV/[A(T_s - T_b)] W/m^2.K \tag{5}$$

The heating probe is introduced in the bed at an axial position of 0.06 m above the supporting grid. The radial positions of the heating probe are such that $r/R = (-0.5, -0.3, 0, 0.3, 0.5)$. A copper constantan thermocouple is used to measure the temperature difference between the heater surface temperature and that of the inlet gas.

The bed temperature at radial positions of −3.3, −2.5, −1.5, −0.7, 0.7, 1.5, 2.5 and 3.3 cm from the center is measured, when the heater is located at the center by using a copper constantan thermocouple.

In this study, experiments were conducted in two modes of operation: magnetizing first and magnetizing last mode (Seigell).

3 Results and Discussion

3.1 Effect of Magnetic Field on the Hydrodynamics. It is well known that the application of a magnetic field to a bed of magnetizable particles imposes constraints upon the bed hydrodynamics not experienced in conventional fluidized beds. A magnetic field changes the bed structure and eliminates solid mixing and suppresses bubble formation ([4]). As a consequence, heat transfer behavior and temperature profiles across the bed are affected ([8–10]). In this study the effect of a transverse magnetic field on the bed structure and porosity is investigated, in order to understand the thermal behavior variations in the magnetized bed.

Bed Structure. In magnetically stabilized beds, the stabilized bed regime represents an additional regime to the packed bed and the fluidized bed regimes that are usually found in conventional fluidized beds. This stabilized regime is bounded between two transitional velocities. Beyond the first transitional velocity, which demarcates the stabilized bed regime from the packed bed regime, the pressure drop starts to attain a constant value as the gas velocity increases and while the bed expands with restricted and fixed particles. At the second transitional velocity, the stabilized bed breaks down and unrestricted movement of the bed particles starts. As a result, the definition of U_{mf} in magnetically stabilized beds represents a matter of argument between the researchers who are concerned in this technology. The properties of the bed regimes under the effect of a magnetic field are shown in Table 3.

Bed Porosity. Bed porosity or bed void fraction, ε, is considered as an important parameter affecting the heat transfer rate in fluidized beds. Beyond the minimum fluidization velocity U_{mf}, and as the gas velocity U_g increases, both the bed porosity and the gas turbulence inside it usually increases. As a result the convection heat transfer coefficient h increases. In MSFBs bed, the bed porosity also increases as U_g increases, but the behavior of this increase differs from that in conventional fluidized beds.

Figure 2 illustrates the effect of Re on the porosity of ACM3 bed at magnetic field intensities of 0, 20, and 40 mT. One may find that an initial small expansion occurs in the packed bed di-

Table 1 Summary of the characteristics of the magnetic system

Coil Material	Number of turns	Core Material	Number of sheets	Sheet Thicknes	Inner Diameter	Outer diameter	i_{max}	B_{max}
Copper 0.9mm	1500	Cast Steel	180	0.9mm	200mm	320mm	5 A	200m T

Table 2 Characteristics of the magnetic particles used in this study

Material used to Cover magnetite	ρ_b (kg/m^3)	ρ_s (kg/m^3)	Shape Factor	d_p (mm)	U_{mfo} (m/s)	B_s (m T)	Porosity ε_o (-)	C_p (J/kg)
Activated carbon 1	1360	2305	0.9	0.52	0.39	590	0.41	340
Activated carbon 2	1600	2760	0.9	0.7	0.46	590	0.42	351
Activated carbon 3	1750	3020	0.9	0.9	0.574	590	0.42	362
Activated carbon 4	1905	3230	0.9	1.0	0.690	590	0.41	370
Zeolite	2100	3500	0.8	1.1	0.803	590	0.40	478

Table 3 The main characteristics of MSFBs the flow regimes in magnetizing first mode

Property / Regime	Ranges of gas velocities	Bed state	Pressur Drop	Gas bubbles	Bed Height	Solid mixing
Packed bed	$0 \leq U_g < U_e$	randomly packed	High	none	Constant	none
Stabilized bed	$U_e \leq U_g < U_{mfo}$	Expanded horizontal strings	Low	none	Increases as U_g increases	None but the bed is flowable
Fluidized bed	$U_{mf} \leq U_g < U_{pt}$	strings then particulate fluidization	Low	bubbling then slugging	Increases as U_g increases	slow then intensive

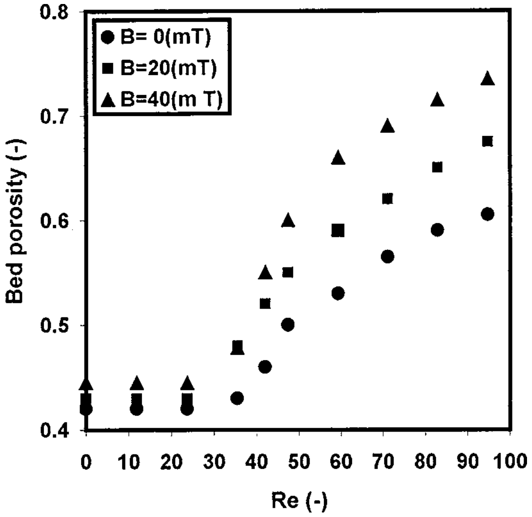

Fig. 2 Effect of Reynolds number on the bed gas holdup for various magnetic field intensities

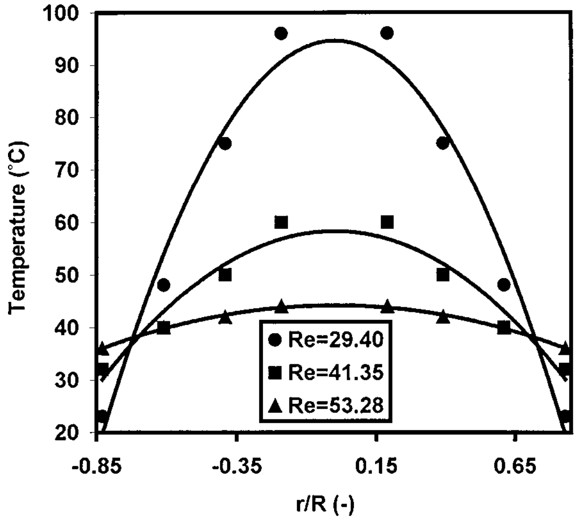

Fig. 3 Temperature profiles in the bed at constant magnetic field intensity and different Reynolds numbers ($B=20$ mT, heater height$=0.12$ m)

rectly after the application of the magnetic field and before starting the gas flow. This initial expansion increases from 0 to 8 percent of the initial porosity as the magnetic field intensity increases from 0 to 40 mT. Its expansion is attributed to the fact that as the bed height is shorter than that of the magnetic system, the field lines tend to stretch up the magnetic particles to cover the whole height of the magnetic system. In the stabilized regime, i.e., $U_e < U_g < U_{mf}$, ε rapidly increases as Reynolds number. For example, at B equal 20 mT, ε increases from 0.435 to 0.51 as Re increases from 0 to 48. Bed porosity at the onset of fluidization increases from 0.42 to 0.71 as the magnetic field intensity increases from 0 to 40 mT. In the fluidized regime, the bed porosity increases as Re increases in the same manner as in conventional fluidized beds.

3.2 Effect of Magnetic Field on Heat Transfer Behavior

Radial Temperature Profile. Figure 3 shows the temperature profiles in a bed of ACM3 particles at constant magnetic field intensity of 20 mT and three different Reynolds numbers of 29.4, 41.31, and 53.28 corresponding to the three subsequent flow regimes: the fixed, the stabilized and fluidized bed, respectively. One finds that as the relative distance r/R increases from 0.2 to 0.94, the measured temperature decreases from 52 to 34.5°C, 45 to 37°C and 43.8 to 40.5°C as the bed passes from the packed through the stabilized to fluidized regime. Although the temperature profile in the stabilized regime is not abrupt as that in the packed regime, it is still steep compared to the relatively flat one in the fluidized regime. This asserts a significant drawback of magnetic stabilization of fluidized beds, as it causes a loss of the isothermicity, which represents one of the major advantages of fluidized beds. These results agree with those of Arnaldos et al. [10].

Variations of Nusselt Number. Figure 4 shows the effect of Reynolds number on Nusselt number for various magnetic field intensities in a bed of ACM3 particles. The heater in this part was located in the center of the column at a 6 cm axial position. It is evident that the heat transfer coefficient increases slowly as the gas velocity increases until the minimum expansion velocity U_e, owing to the slow increase in the turbulence of the flowing gas in the existing packed regime. Beyond U_e, h increases but with relatively high rates, owing to the increase in the convective heat transfer rate in the porous stabilized bed. Beyond U_{mf}, where the fluidized or bubbling regime exists, a sharp increase in the heat transfer coefficient is observed owing to the existence of string like mixing motions and to the increased turbulence in the gas phase. With further increase in the gas velocities, both the gas volume and the intensity of solids mixing increases and as a result the heat transfer coefficient continues to increase but with slow rates.

The radial variation of Nusselt number with magnetic field intensity at a Reynolds number of 51 is shown in Fig. 5. The initial bed height was 15 cm and the particle diameter was 0.52 mm. The heater height from the distributor was 0.12 m. It could be seen in Fig. 5 that for a certain value of B, Nu number increases until it reaches a maximum at the center of the column. For example at B equal 20 mT Nu increase from 9.6 near the wall to about 10.4 at the center. This is attributed to the radial profile in the gas phase. Normally, the gas phase concentration increases from the wall to the center. On the other hand, Nu at the same radial position decreases as B increases. It is evident that at r/R equal 0.39, Nu decreases from 11.8 to 5.3 as B increases from 0 to 40 mT owing to the change of the bed regime from fluidized to frozen state, respectively.

Figure 6 shows the effect of the heater height axial position on

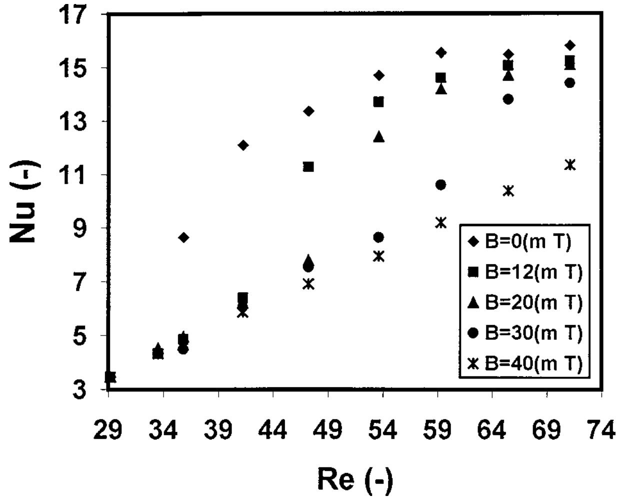

Fig. 4 The effect of Reynolds number on Nusselt number at various magnetic field intensities (Re=65.5, heater height $=0.12$ m, $B=15$ mT)

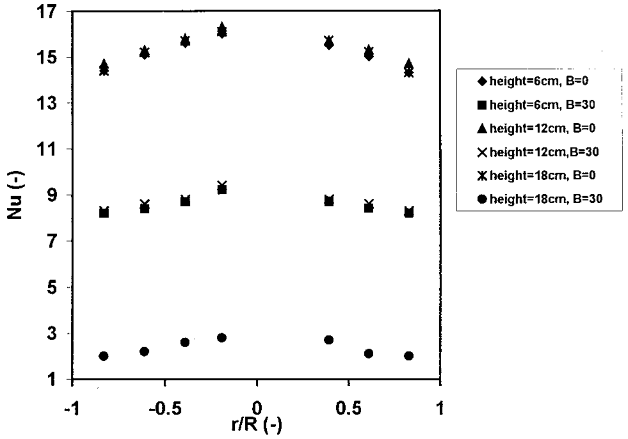

Fig. 5 Effect of the magnetic field intensity on the radial profiles of Nusselt number (Re=52, d_p=0.52 mm, heater height =0.12 m)

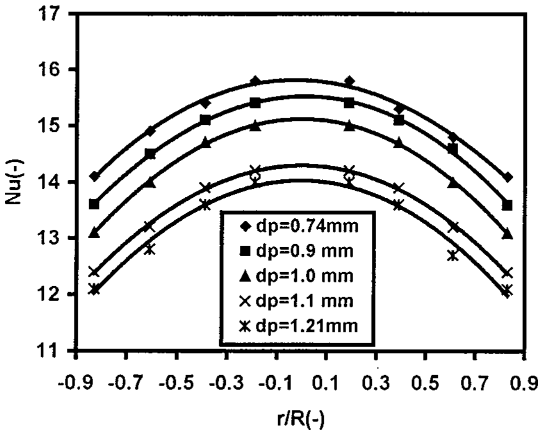

Fig. 7 Effect of particles diameter on Nuselt number at five different radial positions (heater height=0.12 m)

the radial profiles of Nusselt number at two values of B. The initial bed height was 0.13 m and the particle diameter was 0.74 mm. One may find that for a certain radial position and a certain value of B, the changes in Nusselt number are not significant if heater is immersed in the bed. For example, in the absence of a magnetic field i.e., $B=0$ mT, The values of Nu at the same radial position slightly increase as the heater height increases above the distributor. On the other hand, for a heater height of 0.18 m, the stabilized bed height was less than the 0.18 m and the heater was above the bed, i.e., in the air. For this reason Nu values drastically drop to values in the order of 13 percent of those values for an immersed heater.

The effect of the magnetic particle diameter on Nusselt number Nu, at eight radial positions across the bed is shown in Fig. 7. All experiments in this section are conducted at a constant Reynolds number 65.5 and a constant magnetic field intensity of 15 mT. It is evident in Fig. 7 that for a given particle diameter, Nusselt number slightly decreases from 13.8 to 14.9 as the heater position changes from r/R 0.19 to 0.83. This behavior can be attributed to the decrease in the convective heat transfer towards the walls, owing to the existence of radial profile in the gas holdup in fluidized beds. In addition, Fig. 7 illustrates that as the particle diameter increases, Nusselt number decreases, due to the expected decrease in the intensity of solid phase mixing. In addition, the particles of different diameters exist at the same conditions in different flow regimes of different thermal properties. For example, at Re 65.2 and magnetic field intensity of 15 mT, the bed of 0.9 mm particle diameter exists in the particulate fluidized bed regime, while that of 1.1 mm particle diameter exists in the string fluidized bed regime.

Figure 8 shows the variation of Nusselt number with the magnetic field intensity at three different Reynolds numbers 47.3, 59.1, and 71.2 in a bed of ACM3 particles. For a particular Reynolds number, Nusselt number decreases drastically at the onset of stabilization and continues to decrease until the value of B reaches that of the minimum stabilization intensity, B_{fi}. At that point Nu reaches its minimum value. It can be seen that the minimum value of Nu decreases from 11.06 to 7 as Re decreases from 71.2 to 47.3. This behavior can be attributed to the fact that the porosity, and, hence, the gas holdup in the frozen bed increases as the gas velocity increases.

Based on the experimental data, the following empirical equation, which represents the relation between the Nusselt number and Reynolds number was obtained:

$$\mathrm{Nu}=1.04\,\mathrm{Re}^{0.575}(B/B_s)^{-0.092}. \tag{6}$$

The range of parameters in this equation covers Re from 41.5 to 71 and B from 5 to 76 mT. The standard error of estimate is 0.076.

Heat Transfer Coefficient. The effect of magnetic particle diameter on the radial profile of the local heat transfer coefficient, h at various values of B is shown in Fig. 9. The heater height was 0.12 m and Re was 56. It is evident in Fig. 9 that at $B=0$ mT the values of h for the smaller particles, i.e., $d_p=0.52$ mm are higher than those for larger particles. The smaller particles have larger surface area for heat transfer. At a value of $B=25$ mT the values

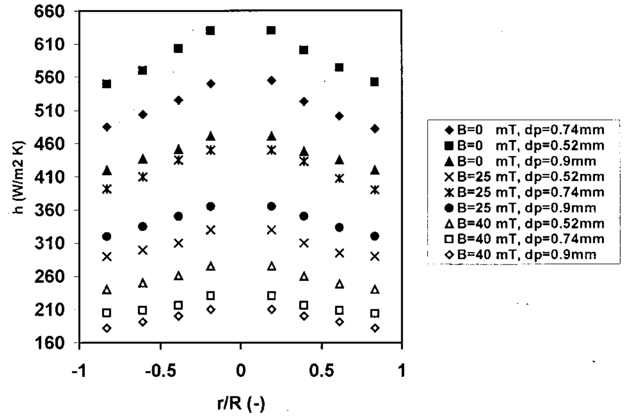

Fig. 6 Effect of heater height on the radial profiles of Nusselt number (Re=52, d_p=0.74 mm, initial bed height=0.13 m)

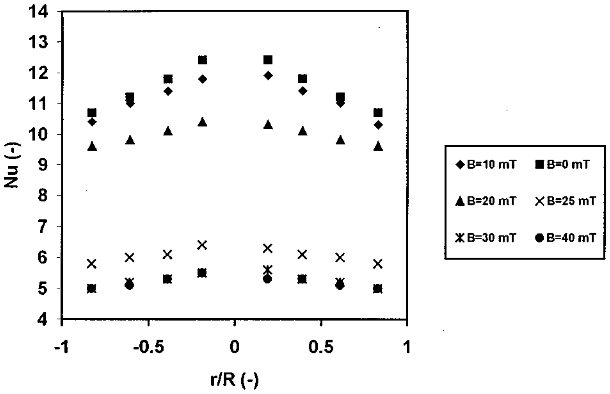

Fig. 8 Variation of Nusselt number with magnetic field intensity at various Reynolds numbers (heater height=0.12 m)

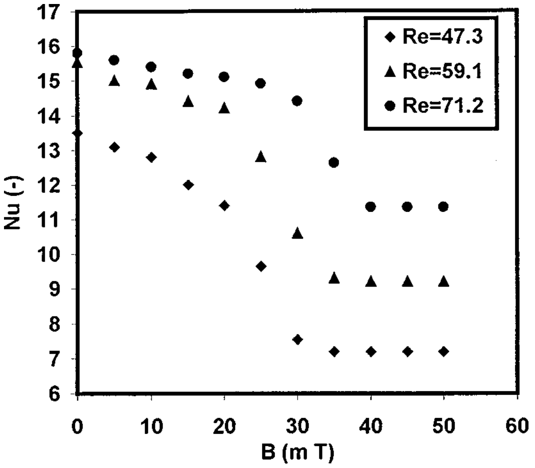

Fig. 9 Effect of particle diameter on the radial profiles of the heat transfer coefficient (Re=56, heater height=0.12 m)

of h for these particles drops drastically as they become stabilized while the larger particles are still fluidized. For example, at a radial position of 0.39, the heat transfer coefficient h, of a 0.52 mm particle drops from 600 to 310 W/m^{2}K as B increases from 0 to 25 mT while it decreases from 448 to 350 W/m^{2}K in the case of 0.9 mm particles. As the magnetic field intensity increases to 40 mT the 0.9 mm particles became stabilized, and h values of the smaller particles became higher again.

Conclusions

The effect of a transverse magnetic field on the temperature distribution and heat transfer coefficient in a bed of ferromagnetic particles has been investigated, in connection with some hydrodynamic parameters such as bed structure and porosity. It was found that as the intensity of the magnetic field increases the temperature variations across the bed increase and the heat transfer coefficient decreases as it impedes the convective mixing of the solid phase. In this study, a correlation that relates Nu number to Re number is proposed. Temperature differences across the bed increase as the magnetic field intensity increases. It was found that the change of the heat transfer coefficient for the smaller particles was sharp compared to that of larger particles as the former particles are more sensitive to the magnetic field intensity. It could be concluded that magnetically stabilized beds offer many advantages in modifying the hydrodynamics of the fluidized bed reactors. But these advantages couldn't compensate for the lack of isothermicity in the bed especially in the case of highly exothermic processes.

Nomenclature

A = surface area of the heater, m^2
ACM3 = activated carbon magnetic particles of $d_p=0.0009$ m
ZM = zeolite magnetic particles of $d_p=0.0011$ m
B = magnetic field intensity, mT
B_{fi} = minimum stabilization intensity, mT
B_{msi} = magnetic intensity above which a frozen bed exists, mT
B_s = saturation magnetic intensity, mT
C_p = specific heat of the magnetic particles, J/g·K
d_p = particle diameter, m
H_b = bed height, m
H_{bo} = initial bed height, m
h_r = local heat transfer coefficient, W/m^2·K
I = current, A
Nu = Nusselt number (hd_p/k)
R = column radius, m
R = radial position, m
Re = Reynolds number (d_pU_g/v)
T_b = bed temperature, K
T_s = heater surface temperature, K
U_e = minimum expansion velocity, m/s
U_g = gas superficial velocity, m/s
U_{mf} = minimum fluidization velocity, m/s
U_{mfo} = minimum fluidization velocity in the absence of magnetic field, m/s
U_t = transitional velocity, m/s
V = voltage, V
W = bed weight, kg
x_i = fraction of particles (−)

Greek Letters

ρ_b = bulk density of the magnetic particles, kg/m^3
ρ_s = molded density of the magnetic particles, kg/m^3
ε = bed porosity
ε_0 = initial bed porosity
ε_s = solid holdup
ε_{so} = initial solid holdup
ν = kinematic viscosity (m^2/s)

References

[1] Liu, Y. A., Hamby, Keith, R., and Colberg, Richard D., 1991, ''Fundamental and Practical Developments of Magnetofluidized Beds, A Review,'' Powder Technol., **64**, pp. 3–41.

[2] Filippov, M. V., 1960, ''The Effect of a Magnetic Field on a Ferromagnetic Particle Suspension Bed,'' Prik. Magnet. Latv. SSR, **12**, pp. 215–220.

[3] Rosensweig, R. E., 1979, ''Fluidization: Hydrodynamic Stabilization with a Magnetic Field,'' Science, **204**, pp. 57–59.

[4] Rosensweig, R. E., 1979, ''Magnetic Stabilization of the State of Uniform Fluidization,'' Ind. Eng. Chem. Fundam., **18**, pp. 260–265.

[5] Penchev, I., and Hristov, J. Y., 1990, ''Fluidization at Beds of Ferro-Magnetic Particles in a Transverse Magnetic Field,'' Powder Technol., **62**, pp. 1–11.

[6] Syutkin, V., and Bologa, M. K., 1976, ''Effect of Magnetic Field in Heat Transfer in Fluidized Bed,'' Electron Obrab. Mater., **67**, pp. 61–67.

[7] Levenspiel, O., and Kamholtz, K., 1981, ''Enhancing the Characteristics of Magnetically Stabilized Beds,'' U.S. Pat. 427, 93.

[8] Luccesi, P. J., Hatch, W. H., Mayer, F. X., and Rosensweig, R. P., 1979, ''Magnetically Stabilized Beds: New Gas-Solids Contacting Technology,'' Proc. 10th World Petroleum Congress, Bacharest, Heyden, Philadelphia, PA, **4**, pp. 419–425.

[9] Neff, J. J., and Rubinsky, B., 1983, ''The Effect of a Magnetic Field on the Heat Transfer Characteristics of an Air-fluidized Bed of Ferromagnetic Particles,'' Int. J. Heat Mass Transf., **26**, pp. 1885–1889.

[10] Arnaldos, J., Lazaro, M., and Casal, J., 1987, ''The Effect of Magnetic Stabilization on the Thermal Behavior of Fluidized Beds,'' Chem. Eng. Sci., **42**, No. 6, pp. 1501–1508.

[11] Qian, R. Z., and Saxena, S. C., 1993, ''Heat Transfer From an Immersed Surface in a Magneto Fluidized Bed,'' Int. Commun. Heat Mass Transfer, **20**, No. 6, pp. 859–869.

[12] Al-Qodah, Z., Ivanova, V., Dobreva, E., Penchev, I., Hristov, J., and Petrov, R., 1991, ''Non-Porous Magnetic Support for Cell Immobilization,'' J. Fer. Bioeng., **71**, pp. 114–117.

[13] Al-Qodah, Z., 2000, ''Hydrodynamic Behavior of Magneto Air-Lift Column in a Transverse Magnetic Field,'' Can. J. Chem. Eng., **78**, No. 3, pp. 458–467.

[14] Al-Qodah, Z., and Al-Hassan, M., 2000, ''Phase Holdup and Gas to Liquid Mass Transfer Coefficient in Magneto G-L-S AirLift Fermenter,'' Chem. Eng. J., **79**, pp. 41–52.

[15] Botterill, J. S. M., 1975, *Fluidized Bed Heat Transfer*, Academic Press, New York.

H. L. Fu[1]

K. C. Leong
e-mail: mkcleong@ntu.edu.sg

X. Y. Huang

C. Y. Liu

School of Mechanical
and Production Engineering,
Nanyang Technological University,
50 Nanyang Avenue, Singapore 639798,
Republic of Singapore

An Experimental Study of Heat Transfer of a Porous Channel Subjected to Oscillating Flow

Experiments have been conducted to study the heat transfer of a porous channel subjected to oscillating flow. The surface temperature distributions for both steady and oscillating flows were measured. The local and length-averaged Nusselt numbers were analyzed. The experimental results revealed that the surface temperature distribution for oscillating flow is more uniform than that for steady flow. Due to the reversing flow direction, there are two thermal entrance regions for oscillating flow. The length-averaged Nusselt number for oscillating flow is higher than that for steady flow. The length-averaged Nusselt number for both steady and oscillating flows increase linearly with a dimensionless grouping parameter $k^*/k_f(D_e/L)^{1/2}Pe^{*1/2}$. The porous channel heat sink subjected to oscillating flow can be considered as an effective method for cooling high-speed electronic devices. [DOI: 10.1115/1.1336510]

Keywords: Cooling, Enhancement, Experimental, Forced Convection, Heat Transfer, Porous Media

1 Introduction

The rapid development in the design of electronic packages for modern high-speed computers has led to the demand for new and reliable methods of chip cooling. As reported by Mahalingam and Berg [1], and Burd [2], the averaged dissipating heat flux can be up to 25 W/cm^2 for high-speed electronic components. However, the conventional natural or forced convection cooling methods are only capable of removing small heat fluxes per unit temperature difference, about 0.001 W/cm^2.°C by natural convection to air, 0.01 W/cm^2.°C by forced convection to air, and 0.1 W/cm^2.°C by forced convection to liquid ([3]). Therefore, it is imperative to look for new methods of cooling the modern high-speed electronic components. One of these methods is to implement a channel filled with high conductivity porous media.

Extensive investigations have been conducted on the flow and heat transfer of a channel filled with porous media. The early works related to heat dissipation are those by Cheng et al. [4], Kaviany [5] and Hunt and Tien [6]. Cheng et al. [4] studied the steady flow forced convection in a packed channel with asymmetric heating. Hunt and Tien [6] studied the heat transfer augmentation in a duct filled with foam material subjected to steady flow. More recently, due to increasing applications in electronic cooling, many researchers have studied the heat transfer enhancement of a channel filled with porous media. Tong et al. [7], Huang and Vafai [8], Hadim and Bethancourt [9], and Sozen [10] numerically studied the heat transfer enhancement of a channel (or duct) filled fully or partially with porous media subjected to steady flow. Fedorov and Viskanta [11] studied the conjugate heat transfer of a porous channel with discrete heat sources numerically. Relatively little experimental work has been performed on electronic cooling with porous channels as heat sinks. Hwang and Chao [12] studied the heat transfer of sintered bronze bead channels with uniform heat flux of up to 3.2 W/cm^2. Local surface temperature distributions and local Nusselt numbers were measured. In the above literature, steady flow through the porous channel was investigated. However, as observed by Hwang and Chao [12], the local temperature of the substrate surface is more important than the averaged surface temperature in the application of electronic cooling. A temperature difference of more than 50°C between the most upstream and the most downstream locations of the channel was measured in the case of $q=3.2\,\mathrm{W/cm^2}$ in their experiments. This indicates that steady flow through a porous channel heat sink still yield a relatively high local surface temperature. In the foregoing review, the research conducted has been on heat transfer of steady flow through a porous channel. Sozen and Vafai [13] conducted a numerical study of compressible flow through a packed bed. The effect of oscillating boundary conditions on the transport phenomena was investigated with the packed wall insulated. Peak et al. [14] experimentally studied pulsating flow through a porous tube. The tube wall was insulated. Transient heat storage characteristics were studied. To the best of the authors' knowledge, there is no previous experimental study of transverse heat transfer of a porous channel subjected to oscillating flow. In the present investigation, a facility was set up to study the heat transfer of a porous channel subjected to both steady and oscillating flows. Local surface temperature distributions were measured. The local Nusselt numbers were calculated. The surface temperature distribution and heat transfer of steady and oscillating flows were analyzed and compared.

2 Experimental Apparatus and Procedure

Test Section and Facility. The schematic diagram of the experimental facility is depicted in Fig. 1(*a*). The facility consists of an oscillating flow generator, a test section, two unheated sections, four coolers and a velocity-measurement section. The oscillating flow generator is a mechanism that generates a sinusoidal oscillating flow. The mechanism consists of a compression cylinder, a piston and a crankshaft with adjustable stroke lengths. The piston was connected to the crankshaft. The crankshaft was driven by a motor to move the piston forward and backward sinusoidally. By adjusting the motor speed and the stroke length, oscillating flows with different amplitudes and frequencies were generated. In the present experiment, oscillating frequencies ranging from 2 to 8 Hz were used. The test section was a well shaped block of porous material. A 1 mm copper plate was attached on the top of the test

---

[1] Currently at Advanced Interconnect Technologies (HK) Ltd., 5/F Southeast Industrial Building, 611-619 Castle Peak Road, Tsuen Wan, Hong Kong.

Contributed by the Heat Transfer Division for publication in the JOURNAL OF HEAT TRANSFER. Manuscript received by the Heat Transfer Division November 15, 1999; revision received, July 12, 2000. Associate Editor: C. Beckermann.

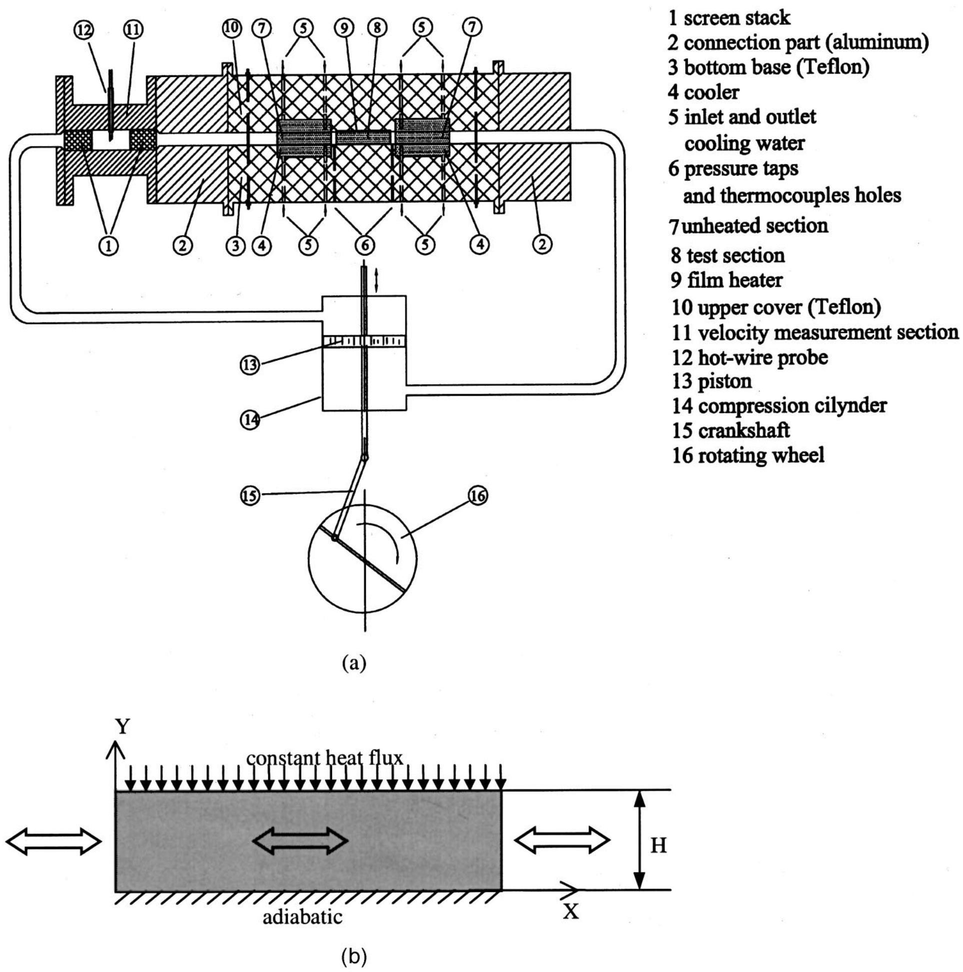

Fig. 1 The schematic of experimental facility and test section: (*a*) experimental setup; (*b*) test section.

section. This copper plate was cut with many narrow slots to minimize the heat conduction along the flow direction. A film heater was firmly mounted on the surface of the copper plate to supply a constant heat flux. By adjusting the supply voltage to the heater, the power input can be adjusted. The two unheated sections are aluminum foam materials with the same dimensions as the test section. They were installed adjacent (but separated) to the two ends of the test section. The two unheated sections built up a nearly uniform velocity profile for flow through the test section. The heat carried by the flow is also transferred to the surface of coolers through the aluminum foam material of the unheated sections. The four coolers are channels filled with aluminum foam materials. Cooling water was forced through the four coolers to remove the heat generated by the film heater. In the present experiment, the oscillating flow amplitude was chosen to be larger than the length of the test section. This ensured that the heated air can be cooled by the coolers adjacent to the test section. As shown in Fig. 1(*a*), the test channel was made of two parts: bottom base and upper cover (Teflon material). In setting up the experimental facility, the width of the teflon channel was carefully machined to be exactly the same width as the test porous block. The thickness of the teflon channel was designed to be 1 mm smaller than that of the test porous block. The bottom base and the upper cover of the teflon channel were combined together by screw bolts with the test porous block, the film heater, the two unheated porous blocks and the four coolers tightly fixed in the channel. This method of assembly ensures the absence of air gaps. The whole section was well insulated. The velocity-measurement section is made from a column of 16 mm diameter. The hot wire sensor was mounted in the center of the two parts packed with 40 mesh woven screen discs. Due to the extremely thin boundary layer of flow through porous media, the velocity measured by this arrangement is approximately the cross-section-averaged velocity through the column. A schematic of the test section is shown in Fig. 1(*b*). The bottom wall of the channel is adiabatic while the upper wall is subjected to a constant heat flux. The porous media in the channel is assumed to have uniform porosity and to be isotropic. Two kinds of foam materials were used: ERG Aluminum foam 40 PPI—pores per linear inch, and ERG Reticulated Vitreous Carbon (RVC) foam 45 PPI, to cover wide range of conductivities. The dimensions of the test section are $50\times50\times10$ mm. Table 1 shows the physical parameters of foam materials. The permeability and

Table 1 Physical parameters of test section materials

Test section material	ERG Al 40 PPI	ERG RVC 45 PPI
Ligament diameter, d_l [m]	1.194×10^{-3}	1.086×10^{-3}
Porosity, ϕ	0.90	0.92
Permeability, K [m^2]	3.36×10^{-8}	2.09×10^{-8}
Inertia coefficient, f	0.09	0.08
Solid phase conductivity, k_s [W/m·K]	170.0	8.37

inertia coefficient constant were determined using a method proposed by Hunt and Tien [6] with the pressure drop and flow velocity data of adiabatic steady flow experiments.

Instrumentation and Experimental Procedure. In the present experiments, the pressure drop across the test section, the temperature along the axial direction as well as at the two exits of the test section and the velocity through the test section were measured. A differential pressure transducer (Validyne DP15) was connected to the two taps along the test section. Seven K-type thermocouples of 45 μm diameter were flushed on the copper plate to measure the surface temperature along the axial direction. The inlet and outlet temperatures were measured by fixing the thermocouples in the gaps between the test section and the unheated sections. The velocity was measured by a hot-wire sensor with an anemometer (TSI IFA 100 and TSI 1210-20w) in the velocity-measurement section. The velocity through the velocity-measurement section was then converted to that through the test section channel. All the signals were connected to a data acquisition system consisting of a 12-bit A/D card (Keithley DAS1402), a computer and a software (TestPoint).

The oscillating flow facility is also capable of performing steady flow experiments. By leaving one end of the test section open to the atmosphere, steady flow, and heat transfer experiments can be conducted with the same test section configuration and sensors. In the steady flow experiments, the main compressed air line was connected to the facility. A valve and a regulator were installed to adjust the flow velocity through the test section. After passing the test section, the coolant air was discharged to the environment. The experiments were performed by increasing the power input while keeping the flow velocity constant. During oscillating flow experiments, cooling water was passed through the four coolers installed at the two ends of the test section to remove the dissipated heat. Frequencies from 2 to 8 Hz and two oscillation amplitudes were tested in the present experiments. The experiments were proceeded by increasing the power input while keeping the oscillating frequency unchanged. To obtain a cyclic steady state, the oscillating velocity, pressure drop, and surface temperature were monitored. Over 80 cycles of data for each case were recorded at sampling rate of 200 Hz or 300 Hz depending on oscillating frequency once the cyclic steady state is reached.

Data Reduction and Uncertainty Analysis. A time-averaging method was used to process steady flow experimental data. 300 data points were used in each case. For electronic cooling applications, time-averaged characteristics are of practical interest instead of instantaneous quantities. Therefore, in the present experiments, experimental data for oscillating flow were reduced by time-averaging 80 completed cycles. To differentiate this process from an arbitrary time-averaging process, we call this kind of time-averaging process *cycle-averaging*. The time-averaged absolute velocity was used to calculate the Reynolds number. In the data reduction process, net heat input to the test section was used. The heat losses through the insulation were measured at different surface temperatures under the condition of no airflow through the test section. The net heat inputs were obtained by subtracting the heat losses from gross heat inputs at the corresponding temperature. Energy balance was checked by calculating the air enthalpy rise along the test section. The error is within 6 percent. Temperature dependent properties of air were used in the data reduction process. Uncertainties were analyzed based on the method described by Taylor [15]. The uncertainties of the measured quantities in the present experiment are assumed to be random with normal distribution. The accuracy of the thermocouple temperature readings is within ±0.1°C. The accuracy of the velocity measured by hot-wire anemometer is ±0.01 m/s. After the time-averaging process (for steady flow) or the cycle-averaging process (for oscillating flow), uncertainties of temperature (°C), velocity and pressure are 3.0 percent, 2.0 percent and 2.0 percent, respectively. The uncertainties of k_f, k_s, v, d_l, D_e, H, and q are estimated to be 1.0, 1.0, 1.0, 1.5, 2.0, 1.0, and 3.0 percent, respectively. Using the root mean square method, the uncertainties of Re_1, and Nu_x are calculated to be 2.7 and 5.7 percent, respectively.

3 Results and Discussions

Heat Transfer of Steady Flow through a Porous Channel. Microelectronics devices may be damaged by excessively high local temperatures. Therefore, the temperature distribution along the flow direction of the test section is of practical interest in design. Figure 2 presents the local surface temperature distribution along the flow direction with the effect of Reynolds number for $q=0.8$, 1.6, 2.4, and 3.2 W/cm^2. The bulk inlet and outlet temperatures of the fluid are distinctly lower than the surface temperature.

The Reynolds number here is defined based on the ligament diameter of the porous foam as

$$\mathrm{Re}_l = U d_l / \nu_f, \tag{1}$$

where U is the Darcy velocity through the test section, d_l is the ligament diameter of the porous foam and v_f is the kinematic viscosity of the fluid.

From Fig. 2, it is obvious that the temperature increases with the increase of dimensionless axial position X/D_e, the decrease in Reynolds number, or the increase in power input. It is seen that the surface temperature approaches a constant value when the flow approaches the thermally developed region. Similar results were also reported by Hwang and Chao [12]. It is shown that higher Reynolds number will produce a more uniform surface temperature distribution. From Figs. 2(*a*) and 2(*b*), it can be seen that using a porous material of lower thermal conductivity will result in a higher surface temperature for the same Reynolds number and power input.

Figure 3 shows the local Nusselt number versus dimensionless axial position for Al 40 PPI and RVC 45 PPI porous foams. The local Nusselt number was calculated by

$$h_x = q/(T_w - T_i) \tag{2}$$

$$\mathrm{Nu}_x = h_x D_e / k_f, \tag{3}$$

where h_x is the local heat transfer coefficient, $D_e = 5H/3$ is the hydraulic diameter of the flow channel, H is the height of the channel, and T_w and T_i are local surface temperature and the inlet bulk temperature, respectively.

The choice of the inlet bulk temperature to calculate the local Nusselt number takes into consideration the thermal potential for heat transfer from the heated surface to the cold fluid (air). In the present study, bulk air temperature inside the porous medium along the test section cannot be easily measured due to the compactness of the porous foams. In Fig. 3, it is seen that the local Nusselt number increases with an increase in Reynolds number. In the thermal entrance region, the local Nusselt number is higher. With increasing axial distance, the Nusselt number for fixed Reynolds number approaches the value for thermally developed flow (minimum constant value). For lower Reynolds number, the variation of local Nusselt number along the axial direction is much smaller than that of larger Reynolds number. This means that the thermal entrance length is shorter for a small Reynolds number than for a large Reynolds number. Obviously, the higher conductivity porous material yields a much higher local Nusselt number than a lower conductivity material.

Figure 4 presents the distribution of local Nusselt number versus Reynolds number at four dimensionless axial locations. The local Nusselt number increases with the increase of Reynolds number and approaches a limiting maximum value. Higher Nusselt numbers in the thermal entrance region are observed. Downstream of the test section at $X/D_e = 2.70$, the local Nusselt number approaches the thermally developed values indicated by the solid lines in the figure. The results reported by Hwang and Chao [12]

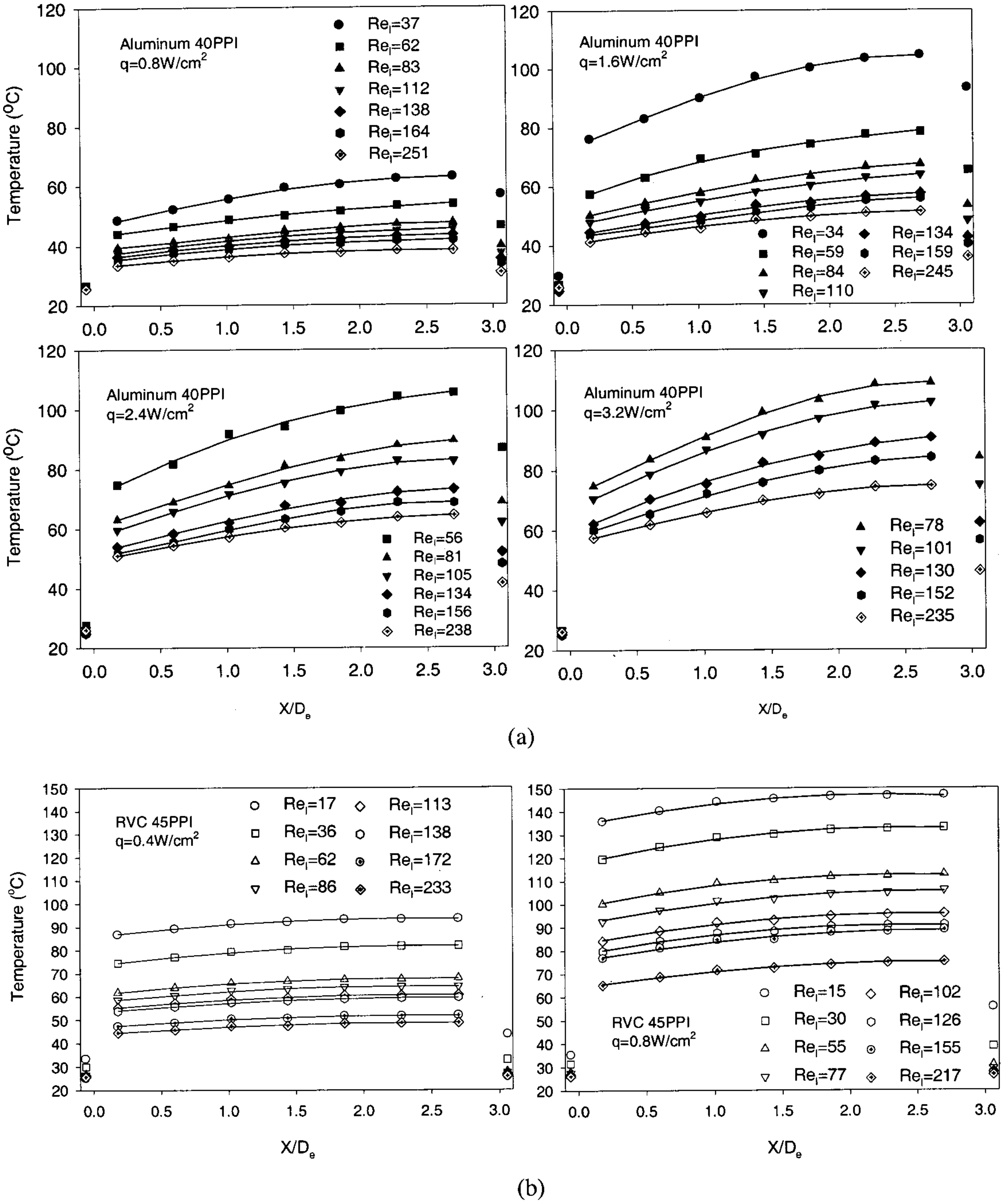

Fig. 2 Surface temperature distribution along the flow direction—steady flow: (*a*) Aluminum 40 PPI; (*b*) RVC 45 PPI.

show the same trend. The present study gives a lower value of local Nusselt number than that of Hwang and Chao's. This is because of the use of bulk inlet temperature rather than the bulk temperature along the test section to calculate the local Nusselt number.

Heat Transfer of Oscillating Flow Through a Porous Channel. Figure 5 shows the cycle-averaged local surface temperature distributions of the test section with the effect of Reynolds number for Al 40 PPI and RVC 45 PPI foam. Once again, we observe that the cycle-averaged local temperature decreases with the increase of Reynolds number but increases with the increase of input heat flux. The surface temperature for RVC foam is much higher than that for Al foam. Due to the reversing flow direction, there are two thermal entrance regions in the test section. The local temperatures near both entrances are lower than that at the center of the test section. The maximum temperature point occurs at the center of the test section. The distribution curves of the local surface temperature are convex with the center of the test section as the symmetric point.

Figure 6 presents a typical variation of the Darcy velocity and pressure drop through the test section. From the figure, it is noted that the measured velocity is always positive (solid line) even though the velocity through the test section is reversing (oscillating). This is because a single wire hot-wire sensor cannot distinguish the direction of the velocity. To obtain a correct velocity direction, the velocity signal was processed by reversing its sign on every other half cycle (dotted line). From the figure, it is seen that the velocity through the test section varies in oscillation style

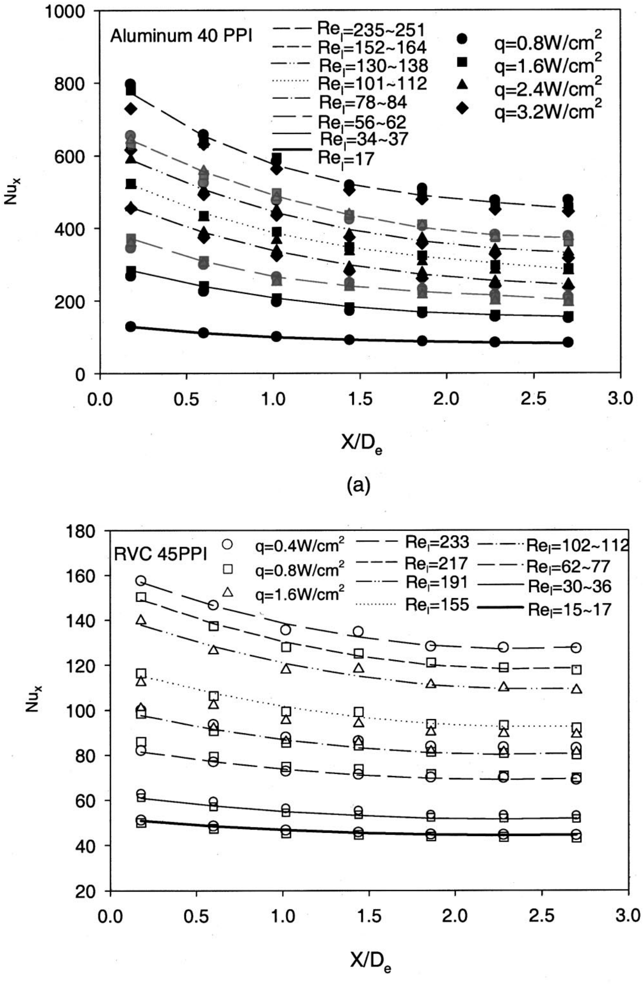

(a)

(b)

Fig. 3 Variation of local Nusselt number along flow direction—steady flow: (*a*) Aluminum 40 PPI; (*b*) RVC 45 PPI.

due to the sinusoidal movement of the piston in the oscillating flow generator. It is also seen that the pressure drop varies almost sinusoidally due to the reversing velocity direction. The maximum pressure drop across the test section is very low for this kind of porous material. This suggests that power required to drive the air through the test section can be very small.

Figure 7 shows the cycle-averaged local Nusselt number versus the dimensionless axial distance with the effect of Reynolds number for oscillating flow. The definition of the Nusselt number is given in Eq. (3). In the calculation, the cycle-averaged absolute velocity was used to calculate Reynolds number. T_w is the cycle-averaged surface temperature while T_i is the cycle-averaged air temperature at left (or right) exit. From the figure, it is seen that there are two thermal entrance regions in the test section. In the thermal entrance region, the cycle-averaged local Nusselt number is higher. The cycle-averaged Nusselt number decreases as X/D_e approaches the center of the test section. As a consequence, the distribution curves of the cycle-averaged local Nusselt number are concave with the center of the test section as symmetric point. The numerical results of oscillating flow through an empty tube by Zhao and Cheng [16] also show the same pattern. It is also seen that the cycle-averaged local Nusselt number increases with the increase of Reynolds number. For higher Reynolds number, the curvature rate is bigger. This implies that the thermal entrance length for higher Reynolds number is longer than that of the lower Reynolds number flow.

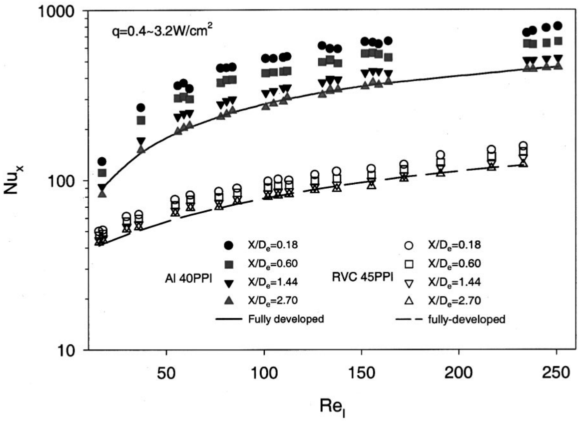

Fig. 4 Effects of Reynolds number on local Nusselt number—steady flow

Figure 8 shows the cycle-averaged local Nusselt number versus Reynolds number for different dimensionless axial distances. The local Nusselt number increases with the increase of the Reynolds number. On closer observation, it is noted that the local Nusselt number reaches the lowest value at the center of the test section ($X/D_e = 1.44$). This reflects the concave shape of local Nusselt number curves. In calculating the cycle-averaged local Nusselt number of oscillating flow, the experimental data covering frequency range from 2 to 8 Hz and two oscillating amplitudes were used. From Figs. 7 and 8, it is seen that the Nusselt number varies very smoothly with the Reynolds number. This means that, after the time-averaging process, the oscillating frequency has no significant effect on cycle-averaged Nusselt number in the frequency range covered by the present experiments.

Comparison of Heat Transfer of Steady and Oscillating Flow through a Porous Channel. In the present study, experiments for steady and oscillating flows were conducted with exactly the same test section and measurement setup. Therefore, the comparison is more convincing.

For steady flow, the surface temperature increases along the flow direction and approaches a constant maximum value when the flow approaches the thermally developed region as seen in Fig. 2. However, for oscillating flow, there are two thermal entrance regions. The surface temperature distribution curves are of convex shape, as seen in Fig. 5. From Figs. 2 and 5, it is observed that the temperature-lift (the temperature difference between the maximum and the minimum temperatures on the heated surface of the test section) for steady flow is 1.5~3.5 times higher than that for oscillating flow. For example, for the case of $q = 2.4\,\mathrm{W/cm}^2$, $\mathrm{Re}_1 = 76$, the surface temperature-lift for oscillating flow is about 8°C, but for the case of $q = 2.4\,\mathrm{W/cm}^2$, $\mathrm{Re}_1 = 81$, the surface temperature-lift for steady flow is about 30°C.

To quantify the temperature distribution uniformity, an index is defined as

$$I_{\mathrm{uni}} = (T_{\max} - T_{\min})/T_{\max}, \tag{4}$$

where $T_{\max}$ and $T_{\min}$ are the maximum and minimum temperatures in Kelvin on the surface of the test section, respectively. The index indicates the ratio of the maximum temperature difference to the maximum local temperature on the surface. When the surface temperature distribution is uniform, the index I_{uni} approaches zero. Figure 9 shows the temperature distribution uniformity for steady and oscillating flows for the aluminum foam test section. It is seen that the temperature uniformity index decreases as Reynolds number increases. The higher flow rate through the porous channel results in more heat removal, thus lowering the global surface temperature level. The index increases with an increase in heat input. From Fig. 9, it is obvious that the temperature distri-

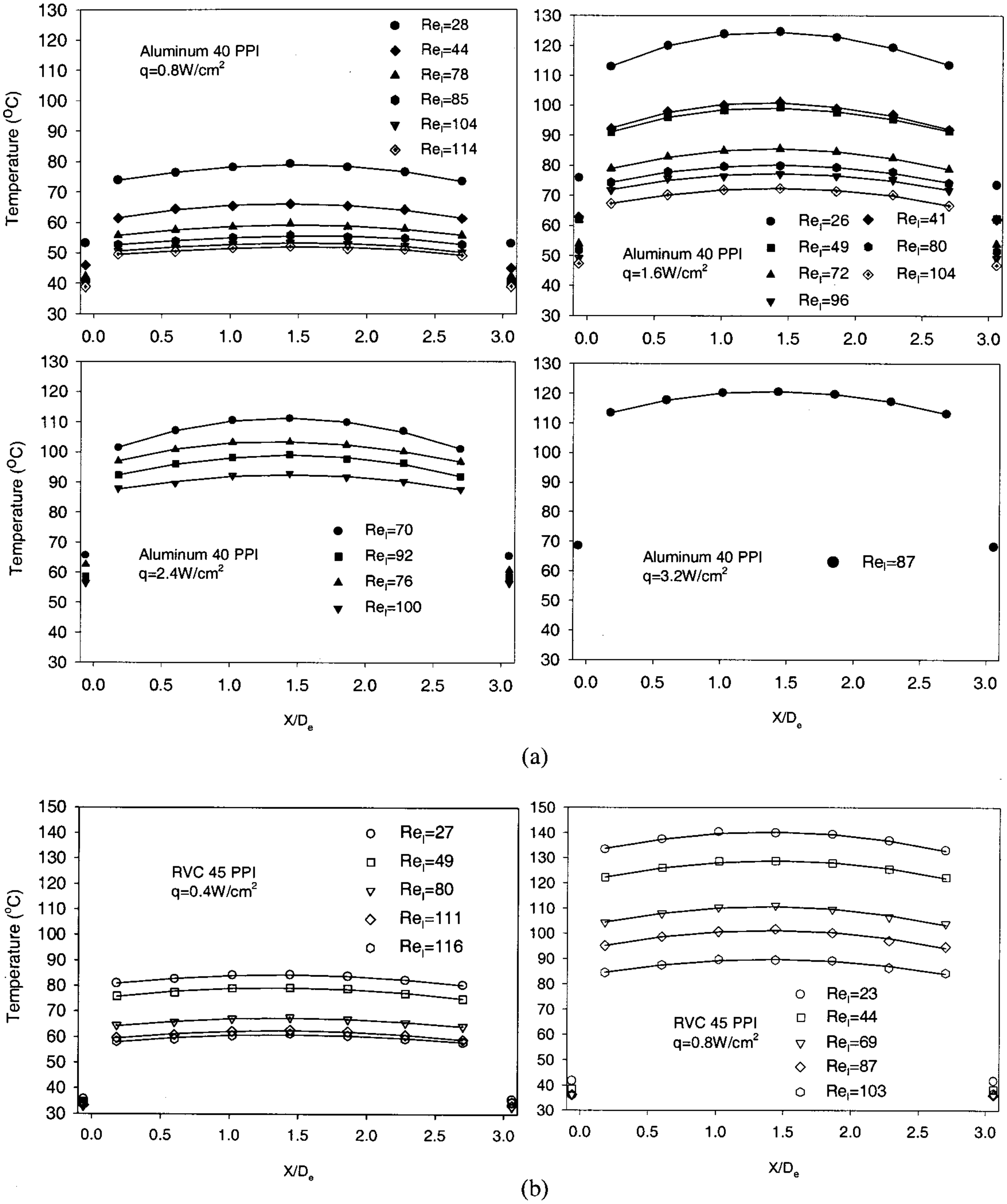

(a)

(b)

Fig. 5 Cycle-averaged surface temperature distribution along axial direction—oscillating flow: (*a*) Aluminum 40 PPI; (*b*) RVC 45 PPI.

bution uniformity index for oscillating flow is much smaller than that for steady flow. This indicates that the surface temperature distribution for oscillating flow is more uniform than that for steady flow.

As seen in Fig. 3, the local Nusselt number decreases along the flow direction for steady flow. As the dimensionless axial increases, the local Nusselt number approaches a minimum constant value (the thermally fully developed region). For oscillating flow (Fig. 7), the local Nusselt number does not decrease monotonically. The local Nusselt number decreases first and then increases after the center point of the test section.

To evaluate the total heat dissipation rate from the electronic devices by a porous channel heat sink subjected to steady or oscillating flow, it is necessary to calculate the averaged Nusselt number for the whole length of the test section. A length-averaged Nusselt number is used. It is defined as the averaged value of the cycle-averaged local Nusselt number along the axial direction. Figure 10 shows the length-averaged Nusselt number for steady and oscillating flows with Reynolds number. It is clear that the length-averaged Nusselt number for oscillating flow is higher than that for steady flow. The larger the Reynolds number, the larger the difference between the length-averaged Nusselt numbers of oscillating and steady flows. For $\mathrm{Re}_1 \approx 114$, the typical length-averaged Nusselt number of oscillating flow is 1.4 times that of steady flow for aluminum foam test section. The higher length-averaged Nusselt number for oscillating flow is due to the higher local Nusselt number in the thermal entrance region. From Fig. 10, it is also noted that the heat transfer enhancement of oscillat-

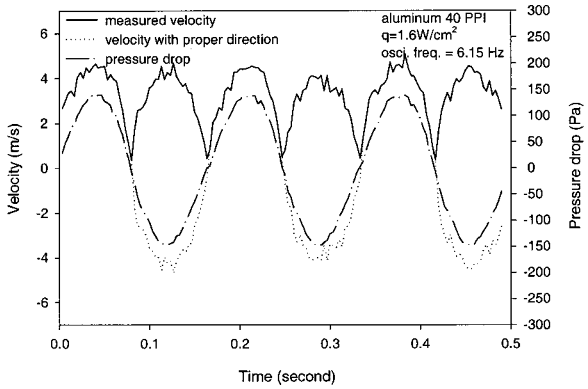

Fig. 6 Typical variations of velocity and pressure drop of oscillating flow through the test section

ing flow for RVC foam is not as significant as that for aluminum foam. This is due to low thermal conductivity of RVC foam.

If the data in Fig. 10 are reduced using the grouping, $k^*/k_f(D_e/L)^{1/2}\,\mathrm{Pe}^{*1/2}$, the data collapse to two lines for steady and oscillating flows, respectively, as shown in Fig. 11. The dependence of this grouping parameter can also be obtained from a scale analysis of the macroscopic governing energy equations of porous media. k^* is the effective conductivity of the porous media, which includes thermal dispersion conductivity due to flow through the tortuous path of porous materials. Pe* is the effective Peclet number. k^* and Pe* are defined as

$$k^* = \phi k_f + (1-\phi)k_s + k_d \tag{5}$$

$$\mathrm{Pe}^* = UD_e/\alpha^*, \alpha^* = k^*/(\rho_f c_{pf}), \tag{6}$$

where k_f and k_s are the conductivity of fluid and solid phases of porous media, respectively, ϕ is the porosity of porous media, α^*

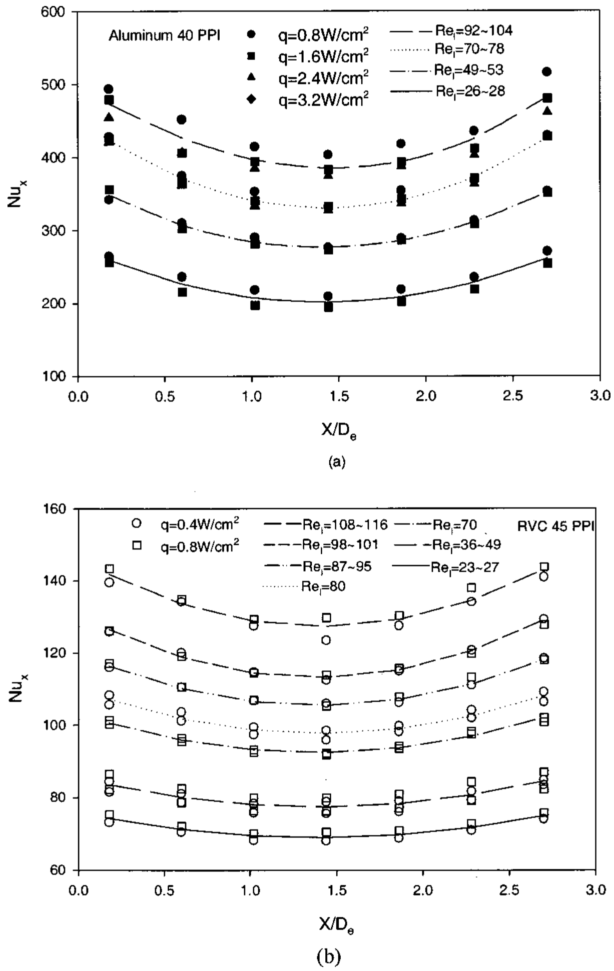

Fig. 7 Variation of local Nusselt number along axial direction—oscillating flow: (*a*) Aluminum 40 PPI; (*b*) RVC 45 PPI.

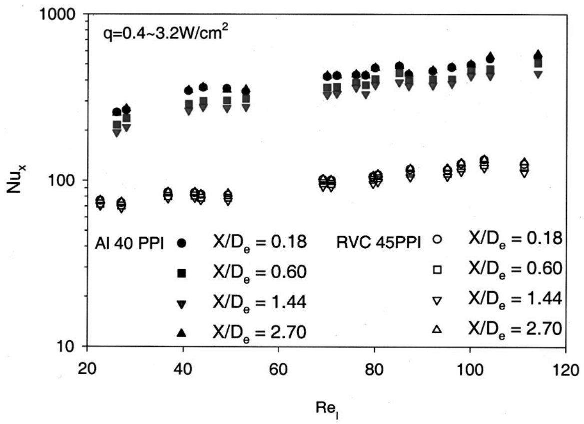

Fig. 8 Effects of Reynolds number on local Nusselt number—oscillating flow

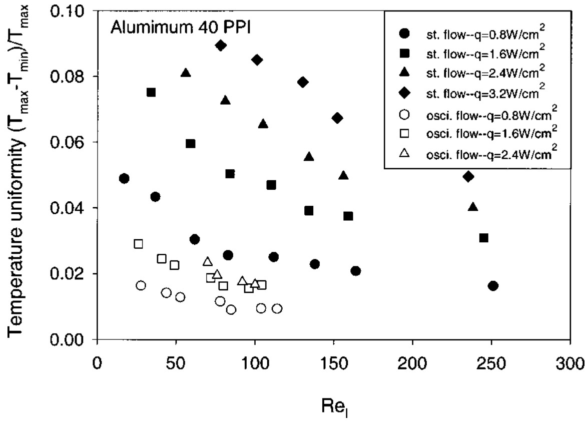

Fig. 9 Temperature uniformity for steady and oscillating flows

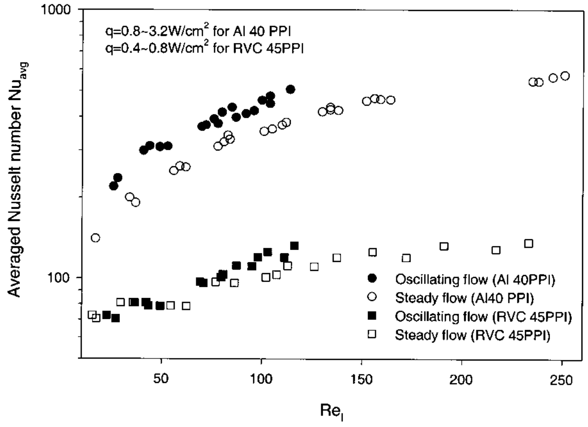

Fig. 10 Comparison of averaged Nusselt number of steady and oscillating flows

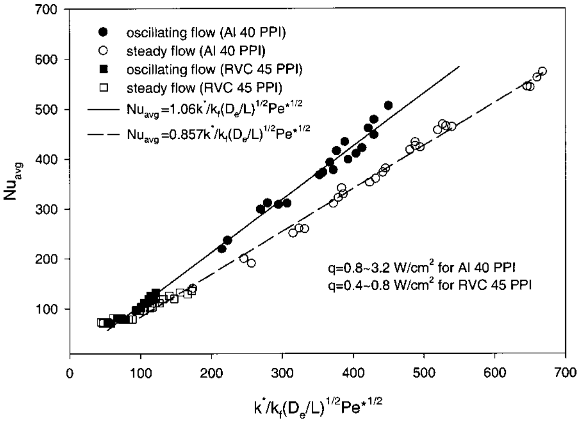

Fig. 11 Length-averaged Nusselt number as a function of parameter $k^*/k_f(D_e/L)^{1/2}\,\mathrm{Pe}^{*1/2}$

is the effective thermal diffusivity of porous media, L is the length of the test section, and k_d is the thermal dispersion conductivity. As proposed by Hunt and Tien [6], thermal dispersion conductivity of porous media can be modeled by

$$k_d=\rho_f c_{pf}\gamma\sqrt{K}U, \tag{7}$$

where γ is the dispersion coefficient taken to be $\gamma=0.025$ in the present study.

From Fig. 11, it is seen that the length-averaged Nusselt number increases linearly with the grouping parameter $k^*/k_f(D_e/L)^{1/2}\,\mathrm{Pe}^{*1/2}$. The slope of the line for oscillating flow is larger than that for steady flow. The larger the grouping parameter, the larger the difference in the length-averaged Nusselt numbers between oscillating and steady flows. A larger grouping parameter implies a higher Reynolds number and higher conductivity ratio k^*/k_f, and, hence, a longer thermal entrance region. The higher local Nusselt number in the thermal entrance region results in a higher length-averaged Nusselt number for oscillating flow. The Nusselt numbers can be correlated empirically with $C=1.06$ and 0.875 for oscillating and steady flows, respectively, with an accuracy of ±13 percent.

$$\mathrm{Nu}_{\mathrm{avg}}=Ck^*/k_f(D_e/L)^{1/2}\,\mathrm{Pe}^{*1/2} \tag{8}$$

For transverse heat transfer of oscillating flow, no experimental data is available in the literature for comparison. Peak et al. [14] presented an experimental study of pulsating flow through an insulated porous tube. No transverse heat transfer results were reported. Figure 12 shows a comparison of our steady flow data with the data reported by Hwang and Chao [12] and Cheng [17]. It should be noted that the bulk inlet temperature was used to calculate local Nusselt number in the present experiments rather than the bulk air temperatures along the test section used by Hwang and Chao [12]. The bulk air temperatures along the test section are unknown in the present experiment. The results are lower than that of Hwang and Chao [12]. The discrepancy may be attributed to the difference in porous material structure.

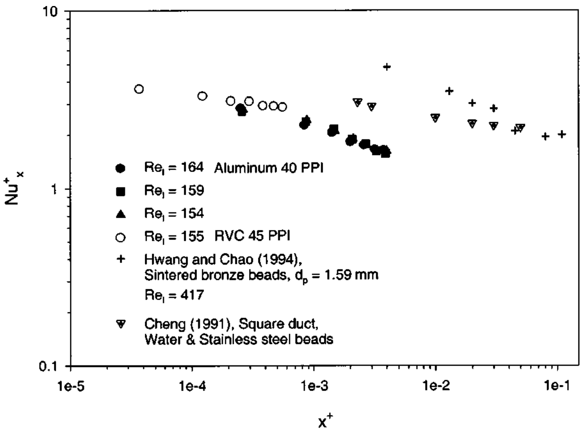

Fig. 12 Comparison of local Nusselt numbers with other experimental data

4 Conclusions

In this study, experiments were conducted to study the heat transfer of a porous channel subjected to both steady and oscillating airflows. The velocity through the porous channel, the pressure-drop across the test section and the temperatures along the hot surface were measured. The following conclusions can be drawn:

1 For steady flow, the local surface temperature increases monotonically as the dimensionless axial direction increases. The local surface temperature distribution for oscillating flow is of a convex shape with a maximum point at the center of the test section. The surface temperature distribution for oscillating flow is more uniform than that for steady flow.

2 For steady flow, the local Nusselt number decreases along the flow direction and approaches the thermally developed value. The cycle-averaged local Nusselt number for oscillating flow, however, decreases first and then increases after the center point of the test section. There are two thermal entrance regions for oscillating flow through a porous channel. Both the local and length-averaged Nusselt numbers increase with an increase in ligament Reynolds number for steady and oscillating flows.

3 The length-averaged Nusselt number for oscillating flow is higher than that for steady flow. The higher length-averaged Nusselt number indicates that the porous channel heat sink subjected to oscillating flow has a higher heat dissipation rate compared to steady flow. The length-averaged Nusselt numbers for both steady and oscillating flows increase linearly with the grouping parameter $k^*/k_f(D_e/L)^{1/2}\,\mathrm{Pe}^{*1/2}$ and can be correlated as $\mathrm{Nu}_{\mathrm{avg}}=Ck^*/k_f(D_e/L)^{1/2}\,\mathrm{Pe}^{*1/2}$ with $C=1.06$ and 0.857 for oscillating flow and steady flow, respectively.

4 The results obtained in the present experiments and the analysis demonstrate that a channel filled with high conductivity porous material subjected to oscillating flow is a new and effective method for cooling electronic devices.

Acknowledgments

The authors gratefully acknowledge the financial support provided under the National Science and Technology Board, Singapore Grant No. JT/ARC 5/96 for the development of the experimental facility described in this paper.

Nomenclature

c_p = specific heat
c_e = equivalent specific heat of porous media$=\phi c_{pf}+(1-\phi)c_{ps}$
D_e = hydraulic diameter of channel$=5H/3$
d_l = ligament diameter of porous material
H = channel height
h_x = local heat transfer coefficient defined in Eq. (2)
I_{uni} = temperature distribution uniformity index defined in Eq. (4)
K = permeability of porous media
k = thermal conductivity
k_d = thermal dispersion conductivity defined in Eq. (7)
k^* = effective thermal conductivity of porous media defined in Eq. (5)

k_e = equivalent thermal conductivity of porous media $= \phi k_f + (1-\phi) k_s$
L = length of porous channel
$\mathrm{Nu}_{\mathrm{avg}}$ = length-averaged Nusselt number
Nu_x = local Nusselt number defined in Eq. (3)
Nu_x^+ = local Nusselt number based on equivalent properties $= h_x D_e / k_e$
Pe^* = effective Peclet number defined in Eq. (6)
Pe^+ = equivalent Peclet numbber $= \rho_e c_e U D_e / k_e$
q = wall heat flux
Re_1 = Reynolds number based on d_l
T = temperature
U = Darcy velocity
X = axial direction
x^+ = inverse Graetz number $= X/(D_e \mathrm{Pe}^+)$
α^* = effective thermal diffusivity defined in Eq. (6)
ϕ = porosity of porous media
γ = thermal dispersion coefficient defined in Eq. (7)
ν_f = kinematic viscosity
ρ = density
ρ_e = equivalent density of porous media $= \phi \rho_f + (1-\phi) \rho_s$

Subscripts

f = quantity based on fluid
s = quantity based on solid
w = quantity based on wall
x = local quantity

References

[1] Mahalingam, M., and Berg, H., 1984, ''Thermal Trend in Component Level Packaging,'' Int. J. Hybrid Microelectron., **7**, pp. 1–9.

[2] Burd, T., 1995, ''CPU Information and System Performance Summary,'' internet site, http://infopad.eecs.berkeley.edu/CIC/summary

[3] Simon, R., 1983, ''Thermal Management of Electronic Packages,'' Solid State Technol., **26**, pp. 131–137.

[4] Cheng, P., Hsu, C. T., and Choudhury, A., 1988, ''Forced Convection in the Entrance Region on a Packed Channel with Asymmetric Heating,'' ASME J. Heat Transfer, **110**, pp. 946–954.

[5] Kaviany, M., 1985, ''Laminar Flow through a Porous Channel Bounded by Isothermal Parallel Plates,'' Int. J. Heat Mass Transf., **28**, pp. 815–858.

[6] Hunt, M. L., and Tien, C. L., 1988, ''Effects of Thermal Dispersion on Forced Convection in Fibrous Media,'' Int. J. Heat Mass Transf., **31**, pp. 301–309.

[7] Tong, T. W., Sharatchandra, M. C., and Gdoura, Z., 1993, ''Using Porous Inserts to Enhance Heat Transfer in Laminar Fully-Developed Flows,'' Int. Commun. Heat Mass Transfer, **20**, pp. 761–770.

[8] Huang, P. C., and Vafai, K., 1994, ''Analysis of Forced Convection Enhancement in a Channel Using Porous Blocks,'' J. Thermophys. Heat Transfer, **8**, pp. 563–573.

[9] Hadim, H. A., and Bethancourt, A., 1995, ''Numerical Study of Forced Convection in a Partially Porous Channel with Discrete Heat Sources,'' ASME J. Electron. Packag., **117**, pp. 46–51.

[10] Sozen, M., 1996, ''Use of Porous Inserts in Heat Transfer Enhancement in Cooling Channels,'' *Proc. ASME Int. Mech. Eng. Congr. & Exhibition*, Atlanta, GA, USA, pp. 1117–1122.

[11] Fedorov, A. G., and Viskanta, R., 1997, ''A Numerical Simulation of Conjugate Heat Transfer in An Electronic Package Formed by Embedded Discrete Sources in Contact with a Porous Heat Sink,'' ASME J. Electron. Packag., **119**, pp. 8–16.

[12] Hwang, G., and Chao, C., 1994, ''Heat Transfer Measurement and Analysis for Sintered Porous Channels,'' ASME J. Heat Transfer, **116**, pp. 456–464.

[13] Sozen, M., and Vafai, K., 1991, ''Analysis of Oscillating Compressible Flow Through a Packed Bed,'' Int. J. Heat Fluid Flow, **12**, pp. 130–136.

[14] Peak, J. W., Kang, B. H., and Hyun, J. M., 1999, ''Transient Cool-Down of a Porous Medium in Pulsating Flow,'' Int. J. Heat Mass Transf., **42**, pp. 3523–3527.

[15] Taylor, J. R., 1982, *An Introduction to Error Analysis—Study of Uncertainty in Physical Measurements*, Oxford University Press.

[16] Zhao, T., and Cheng, P., 1995, ''A Numerical Solution of Laminar Forced Convection in a Heated Pipe Subjected to a Reciprocating Flow,'' Int. J. Heat Mass Transf., **38**, pp. 3011–3022.

[17] Cheng, C. J., 1991, ''Heat Transfer Experiment and Flow Visualization of Non-Darcian Mixed Convection in Horizontal Square Packed-Sphere Channels,'' Master's thesis, National Central University, Taiwan (cited by Hwang and Chao [12]).

Transient Elastic Thermal Stress Development During Laser Scribing of Ceramics

Michael F. Modest

Thomas M. Mallison

Department of Mechanical Engineering,
The Pennsylvania State University,
University Park, PA 16802

Lsaers are emerging as a valuable tool for shaping and cutting hard and brittle ceramics. Unfortunately, the large, concentrated heat flux rates that allow the laser to efficiently cut and shape the ceramic also result in large localized thermal stresses in a small heat-affected zone. These notable thermal stresses can lead to micro-cracks, a decrease in strength and fatigue life, and possibly catastrophic failure. In order to assess where, when, and what stresses occur during laser scribing, an elastic stress model has been incorporated into a three-dimensional scribing and cutting code. First, the code predicts the temporal temperature fields and the receding surface of the ceramic. Then, using the scribed geometry and temperature field, the elastic stress fields are calculated as they develop and decay during the laser scribing process. The analysis allows the prediction of stresses during continuous wave and pulsed laser operation, a variety of cutting speeds and directions, and various shapes and types of ceramic material. The results of the analysis show substantial tensile stresses develop over a thick layer below and parallel to the surface, which may be the cause of experimentally observed subsurface cracks.

[DOI: 10.1115/1.1332779]

Keywords: *Ceramics, Computational, Heat Transfer, Laser, Stress*

Introduction

Various types of ceramics appear to be excellent candidates for high-temperature, high-load applications due to their high-temperature strength, oxidation resistance, and thermal shock resistance. However, because ceramics are so brittle, they are susceptible to cracking during machining and are extremely hard to fabricate and machine into delicate or complex parts. Most ceramics can be efficiently scribed or cut with a laser, although many aspects of this process are still poorly understood. During laser machining of ceramics, laser irradiation produces thermal stresses that often result in micro-cracks and even catastrophic failure; in all cases laser processing severely reduces the bending strength of the ceramic [1–3].

Most analytical investigations of thermal stresses have been limited to thermoelastic bodies using one-dimensional analysis or commercial finite element programs. Hasselman et al. [4–6] subjected a one-dimensional slab to external radiation to investigate the transient thermal stress field. They found the largest tensile stresses occurred in slabs of medium optical thickness ($\kappa H \sim 3$ to 5 with κ being the absorption coefficient of the ceramic). Bradley [7] performed a similar analysis for an opaque slab using a procedure to describe the total strain energy at fracture due to the thermal stresses.

Sumi et al. [8] used an analytical/numerical solution for transient stresses for a simplified three-dimensional problem. They described a local square surface heat source moving in the *x*-direction across an infinite flat plate in the *x*-*y*-plane. The results were a largely compressive stress field with some small tensile stresses. However, the tensile stresses did appear near the edge of the heat source. Ferrari and Harding [9] used a one-dimensional, ceramic-coated sphere to simulate the residual thermal stress field. They observed moderate compressive stresses in the radial direction, and large tensile stresses in the transverse direction.

Gross et al. [10] investigated crack formation in thin silicon wafers during drilling with CO_2 and Nd-YAG lasers. They developed a simple one-dimensional model incorporating compressive plastic deformation to predict the thermal stresses. The model predicted that, during cooldown, the residual circumferential stresses are in tension in the deformation zone and are in compression outside the deformation zone. The model also predicted the radial thermal stresses are tensile everywhere with a maximum at the deformed zone boundary. Experimentally, they observed radial cracks that extended to the deformed zone boundary and circumferential cracks that followed the zone boundary. Both types of cracks confirmed qualitatively the nature of the theoretically predicted stress.

Modest [11] also developed a two-dimensional, axisymmetric model for laser drilling of ceramics. The model was able to handle CW and pulsed laser operation and elastic as well as viscoelastic stress calculations. He noted that during drilling, substantial hoop and normal tensile stresses develop over a thick layer below and parallel to the surface. These stresses could result in experimentally observed subsurface cracks in the same region. He also found that viscoelastic effects were mostly limited to an extremely thin layer near the ablation front. There the ceramic had softened, relaxing the compressive stresses during heating and causing strong tensile stresses during cooling.

In the present paper our three-dimensional laser machining code has been augmented by an elastic stress model, to predict thermal stresses as they develop during CW and pulsed laser scribing of ceramics. It should be realized at this point that mechanical properties of ceramics at high temperatures (near the ablation/decomposition point) are not very well known, let alone their fatigue and fracture behavior at such temperatures. However, Modest [11] has shown that non-elastic behavior is limited to a very thin surface layer. Thus, the objective of the present paper is two fold: (1) to predict, at least on a semi-quantitative level, when and where destructive tensile stresses occur during laser machining, and (2) to provide a tool for the engineer to minimize such stresses by varying laser parameters.

Theoretical Background

Modest [12] used several assumptions in order to obtain a realistic, yet mathematically simple description of the laser scribing

---

Contributed by the Heat Transfer Division for publication in the JOURNAL OF HEAT TRANSFER. Manuscript received by the Heat Transfer Division December 7, 1999; revision received, September 11, 2000. Associate Editor: D. Poulikakos.

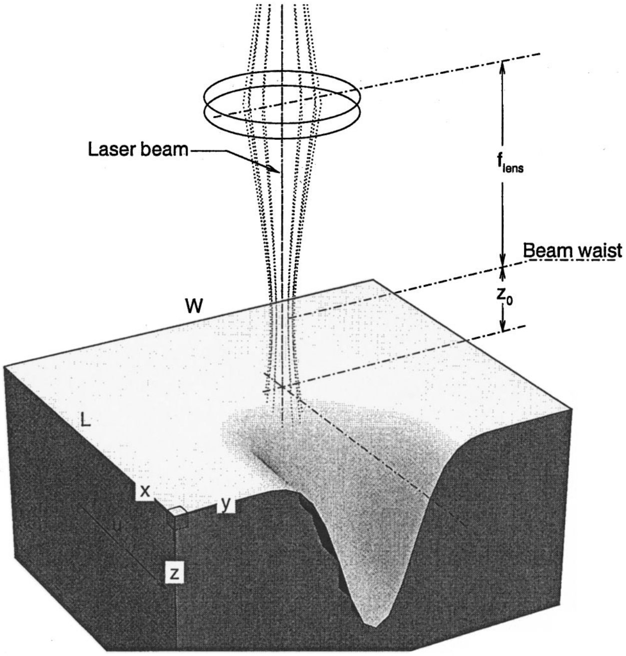

Fig. 1 Laser scribing setup and coordinate system

process. Although the heat transfer code allows for many scenarios, the following assumptions will be used in the present stress model:

1. The solid is isotropic, has constant density, and is opaque, i.e., the laser beam does not penetrate appreciably into the solid.
2. The solid moves with constant velocity.
3. Change of phase from solid to vapor occurs in a single step with a rate governed by a single Arrhenius relation.
4. The evaporated material does not interfere with the incoming laser beam (or is removed by an external gas jet).
5. The heat transfer properties are temperature independent.
6. Heat losses by convection and re-radiation are small compared to conduction.
7. Multiple reflections of laser radiation within the groove are neglected, restricting the model to shallow holes, holes with steep sidewalls, or material with high absorptivity.
8. Heat transfer is unaffected by thermal expansion (always true for opaque ceramics as shown by an order of magnitude analysis).

In addition the following assumptions are made for the stress calculations:

1. The mechanical properties, such as the modulus of elasticity, are temperature independent.
2. Displacements are small quantities that vary over the entire volume. Large displacements, such as buckling of thin plates are not allowed.
3. No external forces are applied to the solid. Stresses occur only due to thermal expansion or contraction.
4. Inertia effects are negligible during stress development (always true of opaque ceramics, but may break down for semitransparent ceramics subjected to ns laser pulsing).

Heat Transfer. The heat transfer model developed by Roy and Modest [13] is summarized here. The transient conduction equation for a solid workpiece of dimensions $L \times W \times H$, irradiated by a Gaussian laser beam moving into the positive x-direciton with constant velocity u, may be expressed in terms of temperature as (see Fig. 1):

$$\rho c_p \frac{\partial T}{\partial \bar{t}} = \nabla \cdot (k \nabla T) \tag{1}$$

subject to the boundary conditions

$$\bar{x}=0 \ : \ T \to T_\infty \qquad \bar{x}=L \ : \ T \to T_\infty \tag{2a}$$

$$\bar{y}=0 \ : \ T \to T_\infty \qquad \bar{y}=W \ : \ T \to T_\infty \tag{2b}$$

$$\bar{z}=0 \ : \ -\hat{\mathbf{n}} \cdot (k \nabla T) + v_n \rho \Delta h_{\mathrm{re}} = \alpha_{\mathrm{abs}} \mathbf{F} \cdot \hat{\mathbf{n}} \simeq \alpha_{\mathrm{abs}} F_0(\bar{t}) e^{-2[(\bar{x}-u\bar{t})^2+\bar{y}^2]/w_0^2} \tag{2c}$$

$$\bar{z}=H \ : \ \frac{\partial T}{\partial \bar{z}} = 0, \tag{2d}$$

and appropriate initial conditions such as

$$\bar{t}=0 \ : \ T(\bar{x},\bar{y},\bar{z},0) = T_\infty \tag{3}$$

$$\bar{s}(\bar{x},\bar{y},\bar{z},0) = \bar{s}_0(\bar{x},\bar{y},\bar{z}), \tag{4}$$

where ρ, c_p, k, and α_{abs} are the density, specific heat, thermal conductivity, and the material's absorptance, respectively; $\bar{x}$, $\bar{y}$, and $\bar{z}$ are the Cartesian coordinates and $\bar{s}$ is the local depth of groove under the laser (i.e., the $\bar{z}$-coordiante of the top surface); $\hat{\mathbf{n}}$ is the unit vector normal to the surface pointing into the solid; v_n is the local surface recession velocity (normal to the surface) during scribing, and $\mathbf{F}$ is the irradiation intensity distribution. For a focussed laser beam the intensity is a relatively involved expression, depending on the local surface coordinates $\bar{x}, \bar{y}$, as well as the local groove depth, $\bar{z}=\bar{s}$ [12]; we give here only an approximate expression valid in the vicinity of the lens' focal point ($z=0$), in which $F_0(\bar{t})$ is the (time-varying) laser intensity at the center of the laser beam, Eq. (2c). The overbar quantities distinguish the present dimensional quantities from the nondimensional quantities below. The boundary conditions are sufficient to solve Eq. (1) for the temperature distribution, if the shape of the groove is known. The previous work assumes that ablation/decomposition of the solid material is governed by a simple equation of the Arrhenius type. This relation gives the rate of mass loss per unit area as

$$\dot{m}'' = \rho v_n = \rho C_1 e^{-E_h/\bar{R}T}, \tag{5}$$

where E_h is the decomposition energy, $\bar{R}$ is the universal gas constant, and C_1 is the preexponential factor that depends on the type of ablation.

The governing equations and boundary conditions are nondimensionalized using the beam radius at the focal point, w_0, and the ablation temperature of the material, T_{re},

$$x = \frac{\bar{x}}{w_0} \quad y = \frac{\bar{y}}{w_0} \quad z = \frac{\bar{z}}{w_0} \tag{6a}$$

$$t = \frac{k\bar{t}}{\rho c_p w_0^2} \quad s = \frac{\bar{s}}{w_0} \quad \theta = \frac{T - T_\infty}{T_{\mathrm{re}} - T_\infty}. \tag{6b}$$

This leads to two basic non-dimensional parameters governing the laser/material interaction

$$N_k = \frac{k(T_{\mathrm{re}} - T_\infty)}{F_0 w_0}, \quad \mathrm{Ste} = \frac{\Delta h_{\mathrm{re}}}{c_p(T_{\mathrm{re}} - T_\infty)}, \quad U = \frac{u w_0}{(k/\rho c_p)}. \tag{7}$$

Boundary-fitted coordinates are employed for the numerical solution. A detailed discussion can be found in Roy and Modest [13].

Thermal Stresses. The extreme temperature gradients that occur during laser machining result in large, localized thermal expansion. This thermal expansion, in turn, causes large thermal stresses in the ceramic. While under most conditions ceramics may be considered elastic, during laser machining there will be a thin zone near the receding surface where significant creep may occur. Theoretically, stress distributions for the shapes and temperature distributions obtained from the heat transfer code can be determined using a commercial finite-element package. However, the extreme temperature gradients normal to the top surface encountered during laser machining necessitate extreme aspect ratios for the finite volumes (up to 1000:1 and more), which precludes the use of such commercial finite-element codes. In the present first attempt to quantify the thermal stresses during laser scribing, the influence of the thin creep zone near the top surface will be neglected, since its contribution to the overall stress field is expected to be small [11].

Under the conditions given by the heat transfer portion, the stress distribution is solved using the following sets of equations. The first set is the non-dimensional governing equation for the entire stress distribution $\underline{\underline{\sigma}}$ of the part,

$$\nabla\cdot\underline{\underline{\sigma}}=0 \tag{8}$$

or expanding Eq. (8) into the three following equations:

$$\frac{\partial\sigma_{xx}}{\partial x}+\frac{\partial\tau_{xy}}{\partial y}+\frac{\partial\tau_{xz}}{\partial z}=0 \tag{9a}$$

$$\frac{\partial\tau_{xy}}{\partial x}+\frac{\partial\sigma_{yy}}{\partial y}+\frac{\partial\tau_{yz}}{\partial z}=0 \tag{9b}$$

$$\frac{\partial\tau_{xz}}{\partial x}+\frac{\partial\tau_{yz}}{\partial y}+\frac{\partial\sigma_{zz}}{\partial z}=0. \tag{9c}$$

The second set are the constitutive equations, in nondimensional form, relating stress and strain $\underline{\underline{\epsilon}}$, and strain and displacement $\underline{u}$ for an elastic body, as given by Boley and Weiner [14]:

$$\sigma_{ij}=\epsilon_{ij}+\delta_{ij}[a\epsilon-(a+1)\theta];\qquad \epsilon_{ij}=\frac{1}{2}\left(\frac{\partial u_i}{\partial x_j}+\frac{\partial u_j}{\partial x_i}\right), \tag{10}$$

where $\sigma_{11}=\sigma_{xx}$, $\sigma_{12}=\tau_{xy}$, $\epsilon_{11}=\epsilon_{xx}$, $\epsilon_{12}=\epsilon_{xy}$, etc., $\epsilon=1/3(\epsilon_{xx}+\epsilon_{yy}+\epsilon_{zz})$ and the following non-dimensional quantities are defined as

$$\underline{\underline{\sigma}}=\frac{\overline{\underline{\underline{\sigma}}}}{2\mu\alpha(T_{\mathrm{re}}-T_\infty)};\qquad \underline{\underline{\epsilon}}=\frac{\overline{\underline{\underline{\epsilon}}}}{\alpha(T_{\mathrm{re}}-T_\infty)} \tag{11a}$$

$$\underline{u}=\frac{\overline{\underline{u}}}{w_0\alpha(T_{\mathrm{re}}-T_\infty)};\qquad a=\frac{3\nu}{(1-2\nu)}, \tag{11b}$$

where μ is Lamé's elastic constant ($=G$, the shear modulus), ν is Poisson's ratio, and α is the coefficient of linear expansion.

Expanding and inserting the relationships from Eq. (10) produces the equations for the stress components in terms of the displacements:

$$\sigma_{xx}=\frac{a}{3}\left(\frac{\partial u}{\partial x}+\frac{\partial v}{\partial y}+\frac{\partial w}{\partial z}\right)+\frac{\partial u}{\partial x}-(a+1)\theta \tag{12}$$

$$\sigma_{yy}=\frac{a}{3}\left(\frac{\partial u}{\partial x}+\frac{\partial v}{\partial y}+\frac{\partial w}{\partial z}\right)+\frac{\partial v}{\partial y}-(a+1)\theta \tag{13}$$

$$\sigma_{zz}=\frac{a}{3}\left(\frac{\partial u}{\partial x}+\frac{\partial v}{\partial y}+\frac{\partial w}{\partial z}\right)+\frac{\partial w}{\partial z}-(a+1)\theta \tag{14}$$

$$\tau_{xy}=\tau_{yx}=\frac{1}{2}\left(\frac{\partial u}{\partial y}+\frac{\partial v}{\partial x}\right) \tag{15}$$

$$\tau_{xz}=\tau_{zx}=\frac{1}{2}\left(\frac{\partial u}{\partial z}+\frac{\partial w}{\partial x}\right) \tag{16}$$

$$\tau_{yz}=\tau_{zy}=\frac{1}{2}\left(\frac{\partial v}{\partial z}+\frac{\partial w}{\partial y}\right). \tag{17}$$

The governing equation, Eq. (8), is an elliptic vector equation requiring three boundary conditions at each surface point. The surfaces perpendicular to the laser beam ($z=s$ and $z=H$) have a no-traction boundary condition,

$$\underline{\underline{\sigma}}\cdot\hat{\mathbf{n}}=0, \tag{18}$$

and the side surfaces parallel to the laser beam ($x=0$, $y=0$, $x=L$, and $y=W$) have either no traction or clamped boundary conditions. If the heat-affected zone of an actual workpiece is confined to a small internal area, it is reasonable to confine the calculations to a smaller piece containing the heat-affected zone, together with a clamped boundary condition. On the other hand, for operations where the laser is near the edge of the part or where significant temperature gradients remain at the edge of the part, the no-traction boundary condition must be invoked on that boundary. For the present research all operations are assumed to take place on a small heat-affected zone in the middle of a large part.

Inserting Eqs. (12)–(17) into Eq. (9) and applying the boundary conditions, Eq. (18), gives a set of equations in terms of displacements, from which the stress distribution of the entire part can be determined. This final set of three equations in three unknowns contains partial derivatives of the displacement vector that must be solved numerically. The numerical solution follows the approach of the ablation code as given by Roy and Modest [13]. From this previous work the temperature field, and equally important, the shape of the part, are known. The stress code will use the temperature field and the shape of the part as inputs. After a coordinate transformation from physical to computational coordinates, as outlined by Thompson et al. [15], and finite differencing, the code solves the displacement field using an over-relaxation scheme with a block-tridiagonal solver. Special consideration must be given at the no-traction boundaries because of the out-of-plane derivatives. The internal node equations and the no-traction boundary condition equations are combined to remove the desired out-of-plane derivatives using integration over half-nodes adjacent to the surface. After long and tedious manipulations (not shown), the result is a set of three equations for each of the $N_\xi\times N_\eta\times N_\zeta$ nodes that forms the overall grid (cutting through is not allowed for the present stress calculations). The final nineteen point stencil is of the following form:

$$\begin{aligned}\underline{\underline{p}}_{ijk}\underline{\phi}_{i,j,k}={}&\underline{\underline{n}}_{ijk}\underline{\phi}_{i,j+1,k}+\underline{\underline{s}}_{ijk}\underline{\phi}_{i,j-1,k}+\underline{\underline{e}}_{ijk}\underline{\phi}_{i+1,j,k}+\underline{\underline{w}}_{ijk}\underline{\phi}_{i-1,jk}\\&+\underline{\underline{t}}_{ijk}\underline{\phi}_{i,j,k+1}+\underline{\underline{b}}_{ijk}\underline{\phi}_{i,j,k-1}+\underline{\underline{ne}}_{ijk}(\underline{\phi}_{i+1,j+1,k}\\&+\underline{\phi}_{i-1,j-1,k}-\underline{\phi}_{i+1,j-1,k}-\underline{\phi}_{i-1,j+1,k})\\&+\underline{\underline{te}}_{ijk}(\underline{\phi}_{i+1,j,k+1}+\underline{\phi}_{i-1,j,k-1}-\underline{\phi}_{i+1,j,k-1}\\&-\underline{\phi}_{i-1,j,k+1})+\underline{\underline{tn}}_{ijk}(\underline{\phi}_{i,j+1,k+1}+\underline{\phi}_{i,j-1,k-1}\\&-\underline{\phi}_{i,j+1,k-1}-\underline{\phi}_{i,j-1,k+1})+\underline{R}_{ijk}.\end{aligned} \tag{19}$$

Equations (19) are a system of linear equations in the form $\underline{\underline{A}}\,\underline{\phi}=\underline{R}$, where $\underline{\underline{A}}$ is a coefficient matrix, whose overall dimension is determined by the number of nodes and where each individual component is a 3×3 matrix (for example $\underline{\underline{p}}_{ijk}$). The solution vector, $\underline{\phi}$, is the displacement vector, and the right-hand-side vector, $\underline{R}$, contains the temperature gradients at the interior nodes and temperatures at the boundary nodes. Once the displacement field is known the strain and stress fields are easily obtained using Eq. (10) and Eqs. (12)–(17). Finally, the principal stresses are the eigenvalues for the stress matrix, sorted by magnitude, at each node.

Numerical Uncertainty. All results were obtained with an *x-y-z* unequally-spaced nodal system of $93\times44\times51$ nodes. Results are, of course, affected by nodal numbers and also by their (unequal) spacing (especially near the surface in the *z*-direction, where the nodes open up rapidly across the thin heat-affected zone). Using a 64×32×31 nodal system resulted in different groove depths of up to 1 percent of maximum, temperatures of up to 0.1 percent of maximum, while stresses deviated also by about 1 percent of their respective (tensile or compressive) maxima, with up to about 5 percent deviation for intermediate values.

Results and Discussion

The principal aim of the present study was to develop a tool, which—at least on a qualitative level—can predict what kind of thermal stresses occur during laser machining of ceramics that cause a decrease in strength and fatigue life, and *when* and *where* they occur. At this point we know too little about temperature dependence of elastic material properties, and even less about ceramics' non-elastic material behavior. However, a previous study on drilling showed that non-elastic deformations are confined to a very thin surface layer, causing no appreciable change in the overall stress field [11]. Only a few typical scenarios are presented here to show, qualitatively, how damaging tensile stresses occur during laser scribing of ceramics. These scenarios include scribing operations for a CW laser and a conventionally-pulsed laser, with pulse duration on the order of hundreds of microseconds. The simulated material is silicon carbide because of its wide range of applications. The pertinent material properties for silicon carbide at 1500°C are given in Table 1. All these material properties are assumed to be temperature independent.

The laser simulated is a typical CO_2 laser (such as the one in our laboratory), with a beam radius of $w_0 = 170\ \mu$m and absorbed laser power of $\alpha_{\text{abs}} P = 600$ W. The speed of the laser for all of the scribing operations is 10 cm/sec. The simulated silicon carbide workpiece has non-dimensional dimensions of 12×12×5 (or 2 mm×2 mm×0.85 mm). As previously mentioned, actual workpieces tend to have much larger length and width dimensions, although stresses decay rapidly beyond the heat-affected zone. Thus, smaller dimensioned workpieces, clamped on all sides, have essentially the same distributions, but the stress distributions can be calculated on a smaller piece much more rapidly.

The first simulation is a drilling operation with a CW laser to allow comparison with our previous two-dimensional model [11], and to highlight the differences between drilling and scribing. This is followed by a CW scribing operation starting the laser in the pre-drilled hole to investigate the development of the stress distributions. Finally, CW and pulsed laser operations are compared for a pure scribing operation.

The principle stresses are sorted by magnitude and the results shown are the maximum principal stress, which generally consist of stresses in the direction normal to the top surface, and the intermediate principal stress that generally consists of stresses in the radial and hoop directions. The smallest principal stress is always compressive and, thus, uninteresting and is not shown.

Table 1 Properties of silicon carbide

Thermal		Mechanical	
T_{re}	3000 K	ρ	3185 kg/m^3
c_p	1359 J/(kg K)	ν	0.17
k_h	17.3 W/(m K)	α	4.02×10^{-6}/K
Δh_{re}	12.1 MJ/kg	μ	175 GPa
α_{abs}	0.9		
Ste	3.3		

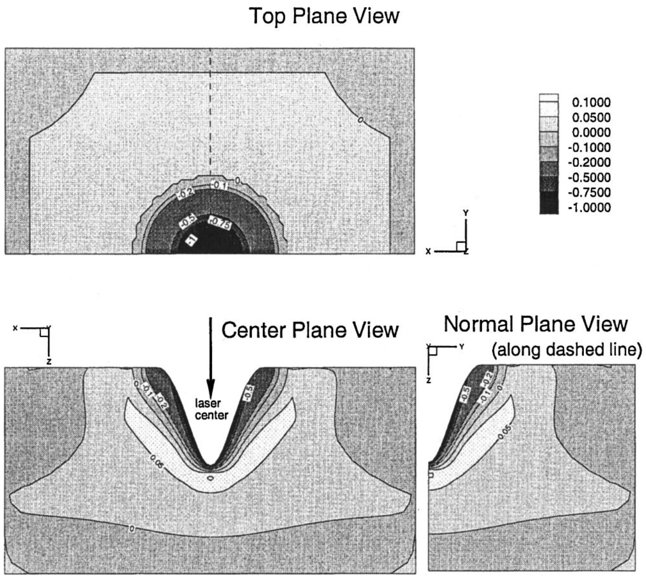

Fig. 2 Intermediate principal stress distribution during CW CO_2 laser drilling; time=1.8 ms

Figures 2 and 3 show the half-views of the principal stresses for laser drilling lasting 1.8 ms. The stresses are symmetric about the *x* and *y*-axes, with the laser positioned over the center of the workpiece. Figure 2 shows the intermediate principal stress distribution, composed primarily of hoop stresses in the heat-affected zone and radial stresses elsewhere, with a large tension sheet above 0.05 (190 MPa) in a region just outside the heat-affected zone. There are large compressive stresses directly under the laser, limited to a thin layer near the surface, and a small spot with strong tension (above 0.1 or 400 MPa, inside the material directly under the laser center). Figure 3 shows the maximum principal stresses whose directions are primarily normal to the top surface. The only exception is the lobe of maximum principal stress extending from the interior tensile region to the top surface, as shown in the normal and center plane views of Fig. 3. In this tensile region the maximum principal stress is in the radial direction. The maximum tension is 0.11 (440 MPa) in a ring approximately 0.17 mm below the top surface, just outside the heat-affected zone.

Figure 4 gives the maximum principal stress distributions for laser scribing starting in a previously drilled hole and shows the stress field skewing and shifting to the region in front of the laser. Lasing conditions are identical to the drilling case, except that the laser starts moving after $t = 1.8$ ms (i.e., the time in Figs. 2 and 3),

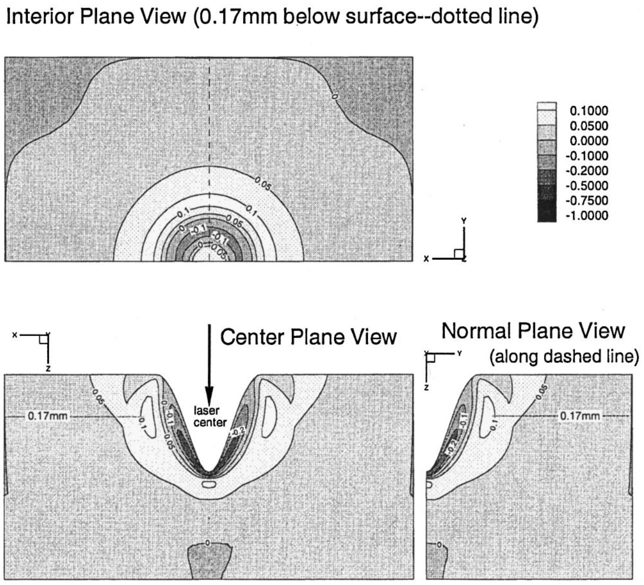

Fig. 3 Maximum principal stress distribution during CW CO_2 laser drilling; time=1.8 ms

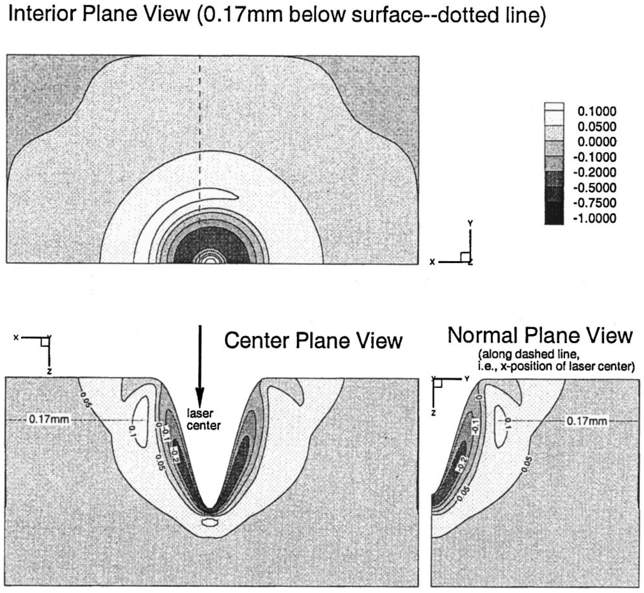

Fig. 4 Maximum principal stress distribution during CW CO_2 laser scribing commencing after drilling for 1.8 ms; time=2.5 ms

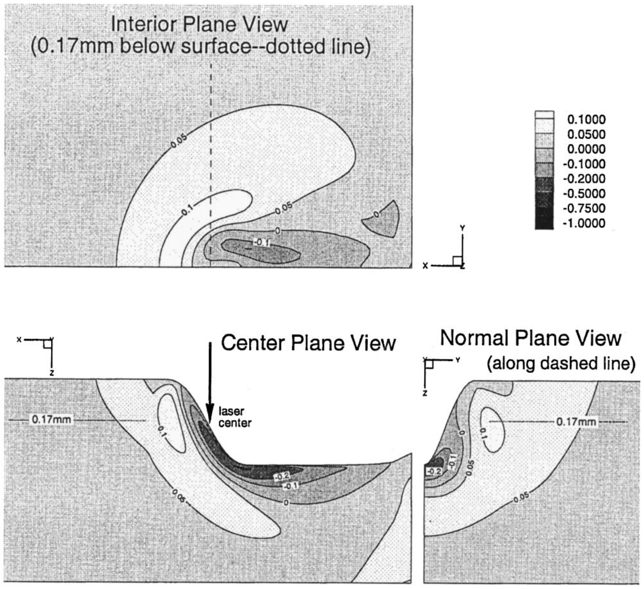

Fig. 6 Maixmum principal stress distribution during CW CO_2 laser scribing; time=3.5 ms

with a velocity of 10 cm/sec in the positive x-direction. The intermediate principal stresses are very similar to those for pure drilling (Fig. 2), and are not shown here. The maximum principal tensile stress (shown in Fig. 4) moves toward the region in front of the laser and increases to 115 (440 MPa), with its direction being normal to the top surface. This tension region is now in the shape of a moon crescent, with less tension behind the laser. The shift in the stress fields is due to the fact that the hot region behind the moving laser is spreading and becoming larger than in front of the laser. This again causes sharper temperature gradients (and, thus, larger stresses) ahead of the laser than in the cool-down zone behind it.

For the pure scribing case (with the laser scanning onto the workpiece from outside) three of the side surfaces have been assumed clamped, while the no-traction boundary condition was applied at $x=0$ where the laser scans onto the surface. For pure scribing the shifting and twisting of the stress fields is more dramatic. As shown in Fig. 5 for CW laser scribing, the subsurface tensile region has completely shifted to the front and the sides of the laser. Additionally, there is a region of tension forming close to the top surface near the edge of the groove behind the laser. This is due to the region behind the laser expanding outward faster, causing the material to tear near the edge of the groove. Again, the intermediate principal stresses are primarily hoop stresses in the heat-affected zone and radial stresses outside the heat-affected zone. The dramatic shift in the stress fields is also visible in Fig. 6, which shows the maximum principal stresses are primarily in the direction normal to the top surface, with a lobe of radial stresses extending from the interior tension region to the top surface of the laser. For the pure scribing case there is no subsurface tensile region behind the laser as there was in the drilling and pre-drilling cases. Figure 6 also shows increased tension in the

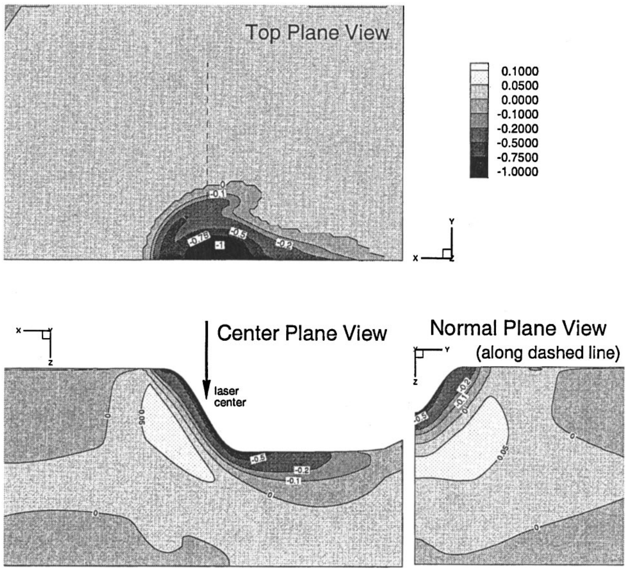

Fig. 5 Intermediate principal stress distribution during CW CO_2 laser scribing; time=2.5 ms

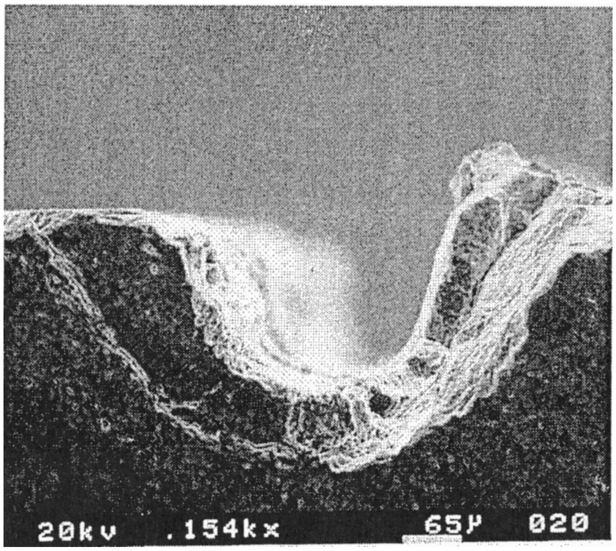

Fig. 7 SEM cross-section of CW CO_2 laser scribed of α-SiC (power $P=600$ W, laser scan velocity=5 cm/s)

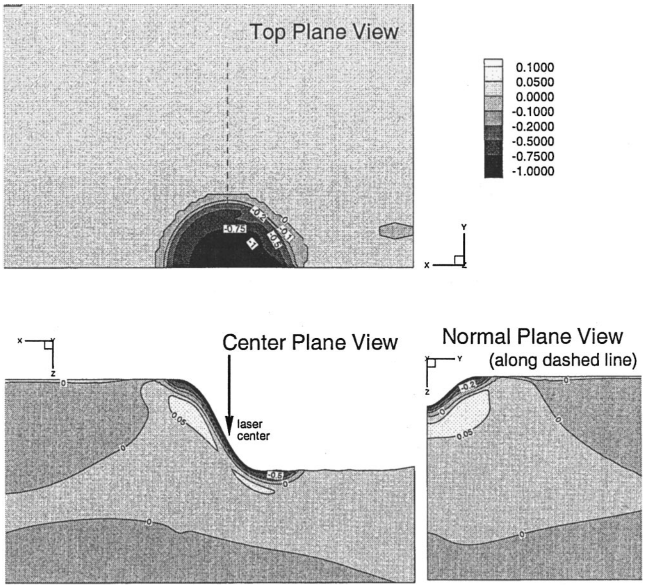

Fig. 8 Intermediate principal stress distribution during pulsed CO_2 laser scribing; time=2.2 ms

maximum principal stresses in front of the laser, at 0.17 mm below the top surface, with a maximum value of 0.126 (480 MPa). On a qualitative level the results explain beautifully the damage we have routinely observed when scribing α-SiC with our CW CO_2 laser (see, e.g., Fig. 7, which shows α-SiC scribed at 5 cm/sec and CW power of 600 W; this particular photo was chosen because it displays much stronger than average thermal stress damage).

There is a substantial difference in the temperature profiles between a pulsed laser and a continuous wave laser. The heat-affected zone for the pulsed laser scribing case is consistently shallower than for the CW case. Even for a laser with a relatively long pulse duration ($\sim$1 ms), the groove becomes much deeper since there are much lower conduction losses into the material. In general, temperature gradients during pulsed laser operation are much larger, and because they occur over such a short depth, the stress fields are more concentrated. In our sample calculations, average absorbed laser power is again 600 W with a duty cycle of 25 percent (on-time is 25 percent of total pulse time). The total duration of the operation is such that the total amount of energy released into the part is the same as for the CW laser scribing case shown in Figs. 5 and 6.

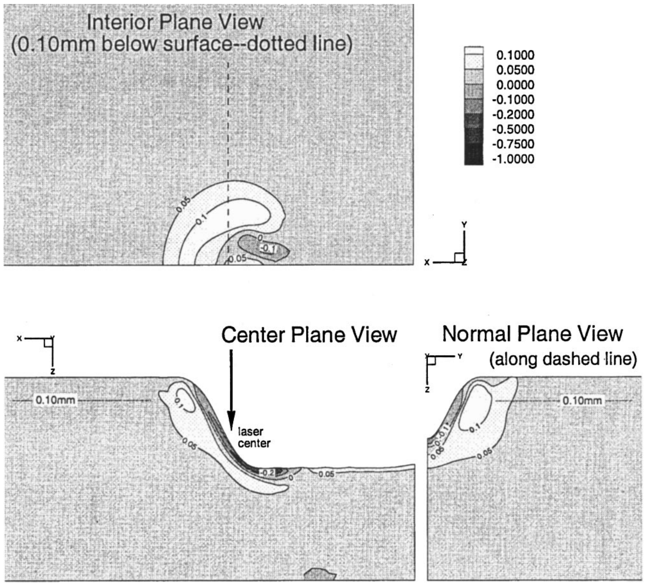

Fig. 9 Maximum principle stress distribution during pulsed CO_2 laser scribing; time=2.2 ms

Figure 8 shows the combination of hoop and radial principal stresses for the pulsed laser scribing case as they exist at the end of a pulse (i.e., just before the laser shuts off). It is seen that the stress field, compression as well as tension, are thinner in depth, and smaller in area, with a much shorter cool-down tail, essentially following the trends of the much thinner and smaller (in area) heat-affected zone during pulsed scribing. Surprisingly, pulsing has little effect on the magnitude of hoop and radial stresses. The maximum normal principal stress, shown in Fig. 9, is higher for the pulsed laser scribing operation, the maximum value being 0.178 (675 MPa) located to the side of the laser, while in the CW case the maximum tension was in front of the laser.

Conclusions

To investigate the stress distributions during CW and pulsed laser scribing of ceramics, an elastic stress model has been incorporated into our three-dimensional machining code. Simulations have been performed on thin wafers of silicon carbide to observe the development of the stress distributions. Because of simplifying assumptions, such as constant properties and elastic behavior, results obtained are only semi-quantitative but serve to illuminate the damaging thermal stresses as they develop during laser scribing. The stress fields for the scribing operations are nonsymmetric and shift to the region in front of the laser as compared to the drilling operation. For the simulated CW conditions, the maximum principal stress was found to be 480 MPa in a direction normal to the surface and located in front of the laser just outside the heat-affected zone. The maximum principal stress shows, on a qualitative level, the damage observed during experimental laser scribing. The intermediate principal stress consists of compressive hoop stresses in the heat-affected zone and smaller tensile radial stresses outside the heat-affected zone. For CW and pulsed scribing a region of tensile stresses forms below the surface near the edge of the groove to the side and behind the laser. For pulsed laser scribing, stress fields are considerably more compact but, with the exception of normal tensile stresses, not greatly increased. The maximum principal stress for pulsed laser scribing is again normal to the surface, but located to the side of the laser with a value of 675 MPa for the conditions simulated here.

Acknowledgments

Support by the National Science Foundation through Grant no. CMS-9634744 is gratefully acknowledged.

Nomenclature

a = stress constant, Eq. (11*b*)
c_p = specific heat of ceramic, [J/(kg K)]
C_1 = preexponential factor for the ablation process, [m/s]
E = modulus of elasticity, [Pa]
E_h = decomposion energy, [J/kmol]
Δh_{re} = ablation enthalpy, [J/kg]
$\mathbf{F}$ = laser irradiation flux, [W/m^2]
F_0 = laser irradiation flux at center of beam, [W/m^2]
k = thermal conductivity, [W/(mK)]
L,W,H = length, width, and thicknesses of ceramic workpiece, [m]
$\hat{\mathbf{n}}$ = unit surface normal pointing into workpiece,
N_k = Conduction-to-laser power parameter, Eq. (7)
$\bar{R}$ = universal gas constant, [J/(kmol K)]
$s,\bar{s}$ = (nondimensional) hole depth, Eq. (6*b*) [m]

Ste = Stefan number, Eq. (7)
$t,\bar{t}$ = (nondimensional) time, Eq. (6*b*), [s]
T = temperature, [K]
$\underline{u},\bar{\underline{u}}$ = (nondimensional) displacement vector, Eq. (11*b*), [m]
$u,v,\bar{w}$ = displacements in *x*, *y*, and *z* directions, respectively
U,u = (nondimensional) laser scanning speed, Eq. (2*c*), [m/s]
v_n = local surface recession speed, [m/s]
w_0 = focal radius of laser beam, [m]
$x,y,z,$ $\bar{x},\bar{y},z$ = (nondimensional) Cartesian coordinates, Eq. (6*b*), [m]
α = coefficient of thermal expansion, $[\mathrm{K}^{-1}]$
α_{abs} = laser absorptance, $[-]$
$\underline{\underline{\delta}}$ = identity tensor
$\underline{\underline{\epsilon}},\bar{\underline{\underline{\epsilon}}}$ = (nondimensional) strain tensor, Eq. (11*b*), $[-]$
ϵ = Average of trace for the strain tensor, Eq. (10)
κ = absorption coefficient of ceramic, $[\mathrm{cm}^{-1}]$
μ = Lamé elastic constant ($=G$, the shear modulus), [Pa]
ν = Poisson's ratio, $[-]$
ρ = density of ceramic, $[\mathrm{kg/m}^3]$
$\underline{\underline{\sigma}},\bar{\underline{\underline{\sigma}}}$ = (nondimensional) stress tensor, Eq. (11*b*), [Pa]
ξ,η,ζ = computational coordinates,
θ = nondimensional temperature, Eq. (6*b*),

Subscripts

∞ = at ambient, or at far-away conditions
re = at removal temperature
x = *x*-component
y = *y*-component
z = *z*-component

Superscripts

$-$ = dimensional quantity

References

[1] Copley, S. W., Wallace, R. J., and Bass, M., 1983, ''Laser Shaping of Materials,'' in *Lasers in Materials Processing*, E. A. Metzbower, ed., American Society for Metals, Metals Park, OH.

[2] Yamamoto, J., and Yamamoto, Y., 1987, ''Laser Machining of Silicon Nitride,'' in *International Conference on Laser Advanced Materials Processing—Science and Applications,* Osaka, Japan, High Temperature Society of Japan, Japan Laser Processing Society, pp. 297–302.

[3] DeBastiani, D., Modest, M. F., and Stubican, V. S., 1990, ''Mechanisms of Reactions During CO_2-Laser Processing of Silicon Carbide,'' J. Am. Ceram. Soc., **73**, No. 7, pp. 1947–1952.

[4] Hasselman, D. P. H., Thomas, J. R., Kamat, M. P., and Satyamurthy, K., 1980, ''Thermal Stress Analysis of Partially Absorbing Brittle Ceramics Subjected to Symmetric Radiation Heating,'' J. Am. Ceram. Soc., **63**, No. 1–2, pp. 21–25.

[5] Thomas, J. R., Singh, J. P., and Hasselman, D. P. H., 1981, ''Analysis of Thermal Stress Resistance of Partially Absorbing Ceramic Plate Subjected to Asymmetric Radiation: I—Convective Cooling at Rear Surface,'' J. Am. Ceram. Soc., **64**, No. 3, pp. 163–173.

[6] Singh, J. P., Sumi, N., Thomas, J. R., and Hasselman, D. P. H., 1981, ''Analysis of Thermal Stress Resistance of Partially Absorbing Ceramic Plate Subjected to Asymmetric Radiation: II—Convective Cooling at Front Surface,'' J. Am. Ceram. Soc., **64**, pp. 169–173.

[7] Bradley, F., 1988, ''Thermoelastic Analysis of Radiation-Heating Thermal Shock,'' High Temp. Technol., **6**, No. 2, pp. 63–72.

[8] Sumi, N., Hetnarski, R. B., and Noda, N., 1987, ''Transient Thermal Stresses Due to a Local Source of Heat Moving Over the Surface of an Infinite Elastic Slab,'' J. Thermal Stresses, **10**, pp. 83–96.

[9] Ferrari, M., and Harding, J. H., 1992, ''Thermal Stress Field in Plasma-Sprayed Ceramic Coatings,'' J. Energy Resour. Technol., **114**, pp. 105–109.

[10] Gross, T. S., Hening, S. D., and Watt, D. W., 1991, ''Crack Formation During Laser Cutting of Silicon,'' J. Appl. Phys., **69**, No. 2, pp. 983–989.

[11] Modest, M. F., 1998, ''Transient Elastic and Viscoelastic Thermal Stresses During Laser Drilling of Ceramics,'' ASME J. Heat Transfer, **120**, pp. 892–898.

[12] Modest, M. F., 1996, ''Three-Dimensional, Transient Model for Laser Machining of Ablating/Decomposing Materials,'' Int. J. Heat Mass Transf., **39**, No. 2, pp. 221–234.

[13] Roy, S., and Modest, M. F., 1993, ''CW Laser Machining of Hard Ceramics: Part I—Effects of Three-Dimensional Conduction and Variable Properties and Various Laser Parameters,'' Int. J. Heat Mass Transf., **36**, No. 14, pp. 3515–3528.

[14] Boley, B. A., and Weiner, J. H., 1960, *Theory of Thermal Stresses,* Wiley, New York.

[15] Thompson, J. F., Warsi, Z. U. A., and Mastin, C. W., 1985, *Numerical Grid Generation, Foundations and Applications,* North-Holland, New York.

Experimental Investigation of Heat Dispersion Due to Impregnation of Viscous Fluids in Heated Fibrous Porous During Composites Processing

Kuang-Ting Hsiao

Hans Laudorn

Suresh G. Advani

Mechanical Engineering Department,
University of Delaware,
Newark, DE 19716

Resin Transfer Molding (RTM) is a composite manufacturing process in which a fibrous preform is placed in a closed mold and a viscous resin is injected into the mold to fill the empty spaces between the stationary network of fibers. The fiber preform and the mold are usually hot and transfer the heat to the moving resin. In this paper, we carried out an experimental investigation to validate the importance of heat dispersion in RTM and the local thermal equilibrium assumption during the non-isothermal mold filling process. In addition, we have developed an expression for the temperature boundary condition at the moving flow front for this moving boundary mold filling process based on volume averaging method and verified it with experiments. The heat dispersion was found to vary linearly with Peclet number and contributed significantly to the temperature distribution in RTM. Using order of magnitude analysis, it was clearly shown that the local thermal equilibrium is a reasonable assumption to model RTM processes and was verified with experimental results. Finally, as many fiber preforms consist of two scales of pore sizes, it is pointed out that further research is necessary in characterization and prediction of heat dispersion in dual scale porous media. [DOI: 10.1115/1.1338131]

Keywords: Composites, Heat Transfer, Manufacturing, Moving Boundaries, Packed Beds, Porous Media, Thermal

Introduction

A composite is a combination of two or more materials that can inherently furnish desirable characteristics, which the component materials cannot provide separately. Several manufacturing techniques exist for making composites. The Resin Transfer Molding (RTM) is one of the widely used techniques. In this process, a fiber preform is placed and compacted (which anchors the preform firmly) in a closed mold. The mold and the stationary preform may be heated. A resin is injected into the mold to fill the empty space between the fibers. The resin cross-links and solidifies and then the mold is opened and the part is de-molded. This study will focus on experimental investigation of the role of heat dispersion in fibrous porous media when describing heat transfer in processes such as RTM where a fibrous preform is placed in a closed mold and a viscous resin is injected to saturate the fibrous porous media. In almost all advanced resin systems, the mold is heated to a higher temperature before the resin is injected into the mold to saturate the porous preform. Heat diffuses to the resin from the mold wall and the fibrous porous preform to the resin during mold filling. This approach is widely used in practice to trigger and expedite the curing cycle as well as to reduce the resin viscosity during filling. It is important to predict the transient heating of the resin as it flows inside the mold because the heat will trigger chemical reactions in the resin which will cross-link the resin molecules around a critical temperature increasing the resin viscosity rapidly. This will arrest the impregnation process and leave empty spaces between the fibers called ''dry spots'' or voids that are detrimental to the properties of the composite part. Hence, it is important that the resin saturates the preform completely before this critical temperature is reached.

In this non-isothermal mold filling process, the heat conduction and heat convection play an important role. The heat transfer phenomenon in a porous medium is more involved as the microscopic heat convection and conduction are enhanced due to the porous structure of the preform. One approach to model the heat transfer process is to zoom into a unit cell of the porous medium and find the volume-averaged thermal properties of the unit cell. By assembling these volume-averaged thermal properties, the volume-averaged energy equation is obtained with the volume-averaged temperature as the governing variable. During the volume-averaging operation, the contribution from the microscopic heat conductivity is lumped into an ''effective thermal conductivity'' term. The deviation between the total microscopic heat convection and the volume-averaged heat convection is represented by and called as the ''heat dispersion'' term.

In this paper, the values for the ''effective thermal conductivity'' and ''heat dispersion'' terms are primarily evaluated by performing controlled experiments. We first qualitatively characterize the importance of heat dispersion in RTM by repeating the non-isothermal mold filling process with identical Darcy velocity and porosity (identical Peclet number) by changing only the fiber orientation of a unidirectional fiber preform. The temperature along the flow direction of the resin was recorded during the mold filling process for the case when the fibers were parallel to the flow and for the case when the fibers were perpendicular to the flow direction. Different temperature distributions confirmed for the first time that the differences were definitely due to the different degrees of ''heat dispersion'' during flow. The dispersion characteristics were distinctly different for the two cases due to different microscopic heat convection pattern invoked by the fiber orientation architecture. Hence, for the first time, the importance of heat dispersion was systematically evaluated and validated in the RTM process.

The generalized volume-averaged energy equation [1] is used

Contributed by the Heat Transfer Division for publication in the JOURNAL OF HEAT TRANSFER. Manuscript received by the Heat Transfer Division January 6, 1999; revision received, July 20, 2000. Associate Editor: S. Sadhal.

to model this non-isothermal mold filling process. One important feature of this energy equation is the ease with which one can perform an energy balance in a moving observation frame, which is pertinent in RTM, at the moving flow front as the resin saturates the porous preform. This energy balance at the moving flow front boundary in the porous medium was derived for the first time and shown to be consistent with experimental measurements. Another important feature of the energy equation is that it can also capture the local thermal non-equilibrium phenomena with one lumped temperature instead of using fluid temperature and solid temperature separately as in the two-phase model [2]. Hence, we conducted experiments to evaluate the contribution of local thermal non-equilibrium phenomenon in RTM as the thermocouples can only measure a temperature value that will represent the ''lumped temperature'' in the generalized energy equation.

Scaling analysis of the energy equation for RTM was conducted to explore the conditions when a quasi-steady state solution will be valid. Experiments were conducted under those conditions to verify the analytical steady state solution for temperature. A transient numerical solution was developed and compared with the experimental results in the transient zone. It was found that the experimental results, the analytical solution and the numerical solution could be made to agree by selecting the right dispersion coefficient and effective thermal conductivity value. The experimental data and the order of magnitude analysis suggest that the use of local thermal equilibrium in RTM is justifiable at low Peclet number. The experimental results for a woven preform highlight the deviation of the experimental measurements from the predictions due to the presence of dual porosity scale in such fibrous porous media. This suggests that one may have to resort to advanced homogenization techniques to find the temperatures in such non-isothermal processes.

Previous Work

Previous non-isothermal studies [3–6] for liquid composites processing assumed that heat dispersion could be neglected. Tucker and Dessenberger [7] showed that heat dispersion is important in typical RTM process by conducting a non-dimensional analysis. Dessenberger and Tucker [8] conducted experiments by using random preforms and compared the data with numerical results with and without heat dispersion. They used the local thermal equilibrium model, which assumes that the fiber tows and resin system reach the same temperature instantaneously on contact, in their study. The comparison showed that heat dispersion through the thickness made a significant contribution to the temperature distribution of the fibrous porous media during mold filling and therefore should not be ignored in non-isothermal simulations. However, they did not compare different architectures in their experiments neither did they measure the temperature of the resin without the preform in the mold. Hence, their conclusion was based solely on the fact that they needed a dispersion coefficient in their theoretical predictions to match their experimental results. Also the boundary condition at the moving flow front applied by them was incorrect and could have influenced their theoretical solution. Hence, we wanted to carry out a systematic study to exhibit the significance of heat dispersion in RTM as some researchers [8,9] recommended that heat dispersion be considered in the non-isothermal modeling of the RTM filling process while others have ignored it [3–6]. Another unresolved issue was the validity of using local thermal equilibrium assumption in such a manufacturing process [9,10]. These researchers resorted to use of the two-phase model to predict the fluid temperature and the solid temperature. However, it is impossible to distinguish which temperature is measured by the thermocouple and hence it is not easy to compare the predictions with experimental results. Also, the two-phase model needs many volume-averaged thermal coefficients as input before it can be applied effectively. The experimental measurement of those coefficients are very difficult to achieve and not very reliable [2]. In addition, the two-phase model is computationally inefficient and expensive, as one has to solve a coupled set of governing equations for the average fluid and solid temperatures in this model. For lack of a criterion as to when the local thermal non-equilibrium effect is significant, the decision to either include it or ignore it has been left to the convenience of the researcher. In fact, in RTM all researchers assume local thermal equilibrium without justifying it. Hence, a need for an evaluation criterion.

In the following sections, we will describe the carefully designed experiments to systematically study the role of heat dispersion in RTM. We will also evaluate the local thermal equilibrium assumption in RTM process by using an order of magnitude analysis and validate it with experimental results.

Experimental Investigation

The experimental system was constructed to be able to control the resin injection rate and the mold temperature separately and accurately. First, an existing injection system that produced a constant flow rate for the lab-scale RTM process was calibrated. Next, aluminum was chosen as the mold material and a heat exchanger was designed and manufactured within the mold plates to optimize the control of the mold surface temperature. Water, the coolant, was circulated through the small ducts inside the mold walls. Two plate-heaters were used to heat the circulating coolant. The resulting mold allows the circulating coolant to pass through the small ducts inside the mold walls at a flow rate of 6.3 liters/s and could maintain the mold surface temperature to within 1C.

Fourteen thermocouples (K-type, 0.4 mm in diameter, error in $\pm 1.1K$ or 0.4 percent) were arranged perpendicular to the flow direction to minimize disturbances. Seven thermocouples on the mold walls were attached to the aluminum surface. The remaining seven thermocouples were located along the mid-plane of the mold cavity and were supported by Kevlar fibers stretched between the sides of the spacer plate. The distance between the thermocouples in the flow direction was 5.08 cm. The entry region before the fluid came in contact with the fiber preform allowed the flow to be developed and was 10.16 cm (4 in.) in length. The width of the mold cavity was 24.77 cm (9 3/4 in.). The length of

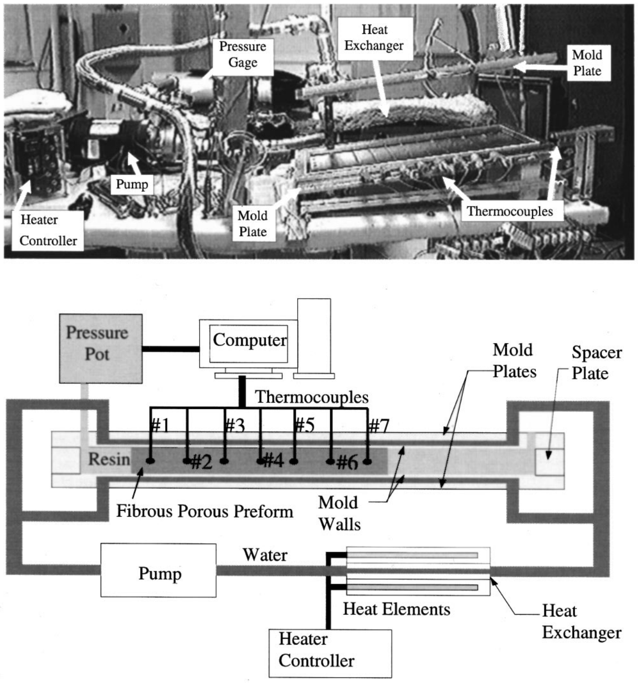

Fig. 1 Experimental setup of the mold (photograph and schematic)

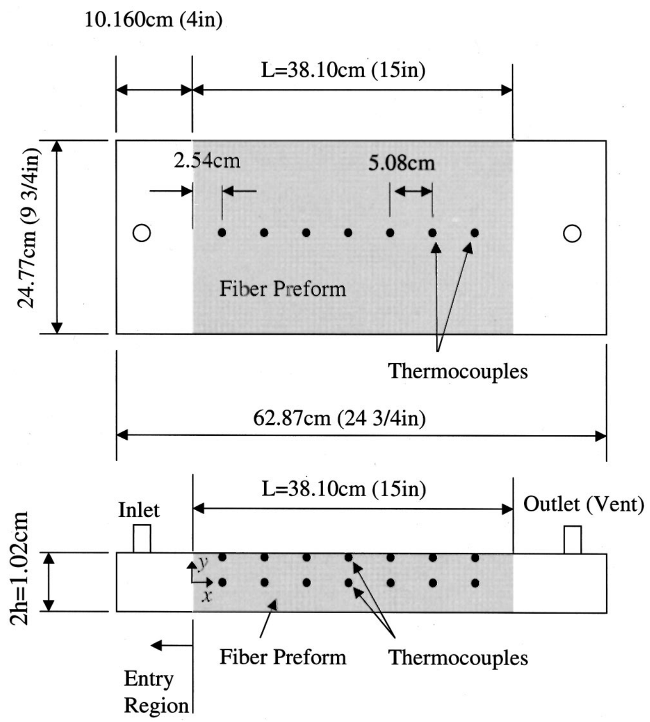

Fig. 2 Dimensions of the mold cavity and the locations of thermocouples

the mold cavity was 62.87 cm (24 3/4 in.). Finally, a composite specimen was made to insure a uniform and accurate measurement of the cavity thickness that was measured to be 1.02 cm. The experimental configuration is shown in Fig. 1. The dimensions of the mold cavity are shown in Fig. 2.

Experiments were performed using a non-curing fluid to avoid complications caused by exothermic reactions that actual resin systems undergo. The fluid used was a mixture of 2/3 Glycerin and 1/3 Ethylene Glycol. This combination provides a viscosity similar to typical resin systems, 200–220 centipoise at room temperature. In addition, the thermophysical properties of the fluid were also very similar and known. Experiments were first completed in a mold made of Plexiglas to ensure and observe the uniform Darcy velocity during the injection. During the actual experimentation, which used the aluminum mold, race-tracking [11] was avoided by monitoring the outlet port as well as inspecting that the preform was saturated fully, immediately after the experiment was completed. Preforms were weighed to calculate accurate volume fractions and a constant flow rate for the fluid was maintained for each experiment performed.

Table 1 Experiments

No.	Preform	T_{inflow} (°C)	T_{wall} (°C)	Fiber volume fraction %	Darcy velocity $\langle u \rangle_x$
1	Uni-directional fiberglass roving (Flow perpendicular to fiber tows)	24	60	23	0.462
2	Uni-directional fiberglass roving (Flow parallel to fiber tows)	24	60	23	0.460
3	Carbon biweave	24	60	43	0.122
4	Carbon biweave	24	60	43	0.192
5	Carbon biweave	25	60	43	0.239
6	Carbon biweave	25	60	43	0.292
7	Carbon biweave	24	60	43	0.341
8	Random fiberglass	24	60	22	0.204
9	Random fiberglass	22	60	22	0.368
10	Random fiberglass	24	60	22	0.582
11	Random fiberglass	22	60	22	0.734
12	Random fiberglass	24	60	22	0.826
13	Random fiberglass	24	60	15	0.884

Table 2 Material thermal properties

Material	ρ $\left(\frac{\text{kg}}{\text{m}^3}\right)$	C_p $\left(\frac{\text{J}}{\text{kg}\cdot{}^\circ\text{C}}\right)$	k $\left(\frac{\text{W}}{\text{m}\cdot{}^\circ\text{K}}\right)$	$d_p(m)$
Carbon fiber	1180	712	7.8	8.0×10^{-6}
E-Glass fibers	2560	670	0.417	1.4×10^{-4}
1/3 ethylene glycol + 2/3 glycerin	1202	2500	0.276	-

Tables 1 and 2 list the experiments and the thermal material properties. The principal purpose of experiments 1 and 2 was to evaluate the existence of heat dispersion in RTM by directly comparing the influence of the fiber architecture on the transient temperature history. In experiment 1, the resin was injected at the constant rate through a line gate into the mold containing unidirectional preform (in which the fibers are all aligned along one direction) creating a one-dimensional flow perpendicular to the fiber direction. Experiment 2 was repeated with identical flow parameters with identical unidirectional preform with the fibers oriented along the flow direction. The hypothesis we wanted to systematically test was whether the temperature history was influenced by the microscopic heat convection, which depends on the fiber orientation. That is, when the flow is along the fiber direction, the fluid motion at the scale of the fiber diameters or fiber tows and therefore the microconvection will be distinctly different as compared to when the fibers are perpendicular to the flow direction. One would expect, the bulk flow will be disturbed more when the fibers are perpendicular to the flow direction invoking a higher degree of microconvection. As in the generalized volume-averaged energy equation, microconvection is expressed as dispersion, one would expect a higher dispersion coefficient for the case of flow across the fibers. The comparison of the measured temperatures at the seven locations during experiments 1 and 2 are shown in Fig. 3. The differences in the temperature history for the same flow parameters, initial and boundary conditions for the resin and mold temperatures with identical fiber volume fractions clearly underline the significance of heat dispersion in RTM at least qualitatively. Experiment 1 due to higher degree of microconvection causes higher degree of dispersion and hence records higher temperatures, which supports our hypothesis. Note that the above experiments were repeated and the same results were observed. This is the first time that the relation of heat dispersion with fiber preform architecture is systematically depicted. Experiments 3–7 were performed to screen the suitable model of the effective thermal conductivity for both glass and carbon preforms from several candidates, since the carbon has much higher thermal conductivity than the fiberglass and the fluid. Experiments 8–12 were performed to explore the dependence of thermal dispersion on the mean velocity (or the Peclet number) of the resin. Experiments 12 and 13 have the same flow front velocity ($u_{\text{front}}=\langle u_f\rangle^f=\langle u\rangle/\varepsilon_f$) but different fiber volume fraction, ε_s (which is equal to unity minus the resin volume fraction, $1-\varepsilon_f$). This provided us with an opportunity to explore the influence of fiber volume fraction as well.

Approach for Temperature Predictions

(a) Governing Equations. We focus on one-dimensional flow, which creates two-dimensional heat transfer as the heat can convect along the flow direction and conduct in both the flow and thickness direction. The x-direction is denoted as the Darcy flow direction and the y-direction is the direction along the thickness. The fluid phase which is the resin system is denoted by "f" and the solid phase which is the fibrous porous preform is denoted by "s." The geometry of the fibrous porous unit cell is symmetric with respect to its own x-axis and has its principal permeability directions aligned with the x and y-directions. For this case, the

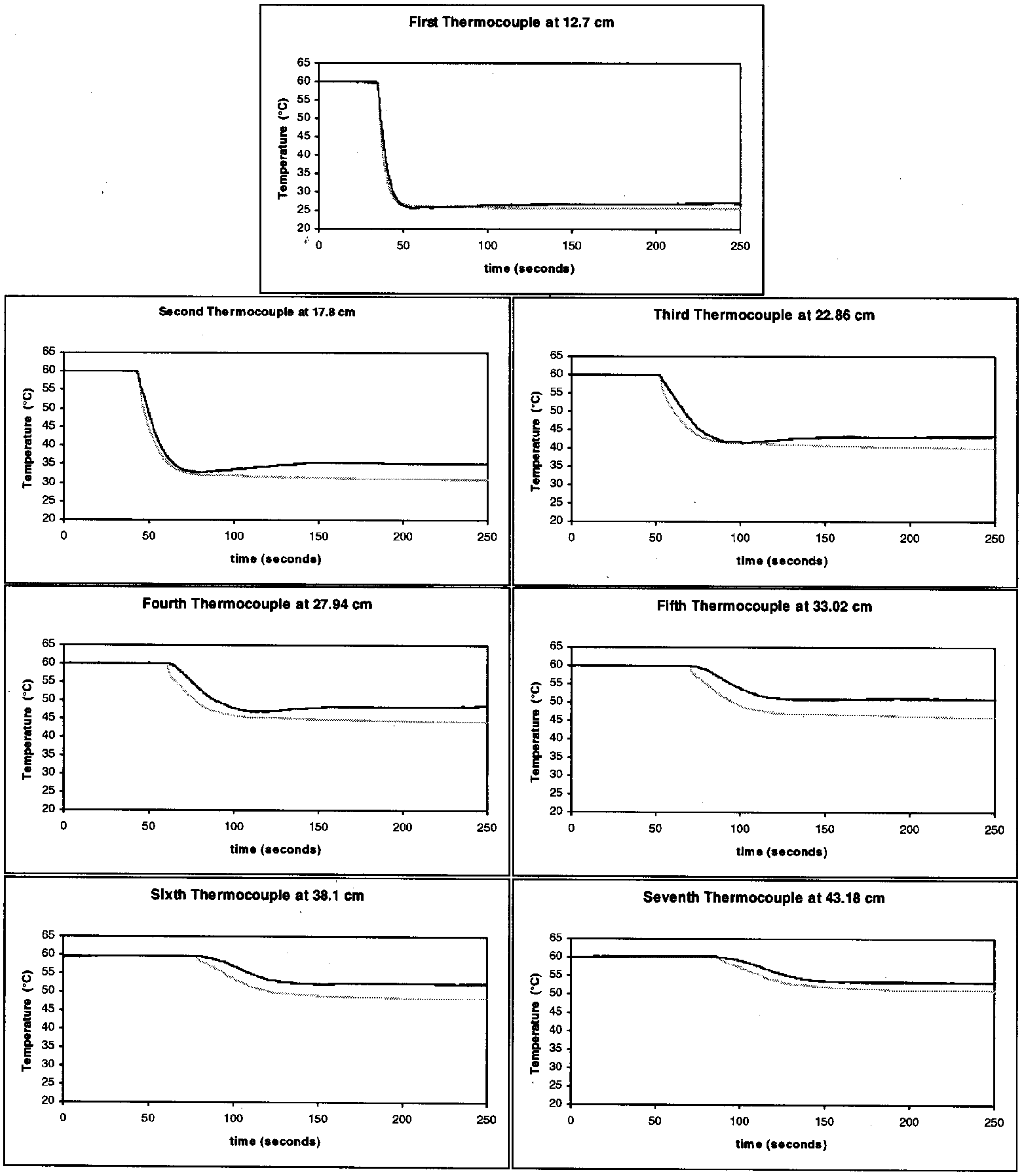

Fig. 3 Comparison of the experimental temperature histories of the uni-directional fiberglass roving; Experiments 1 (black lines): the fiber-roving orientated perpendicular to the flow direction. Experiment 2 (gray lines): the fiber-roving orientated along the flow direction. The thermocouples locate along the mid-plane of the mold cavity as shown in Fig. 1 and Fig. 2.

generalized volume-averaged energy equation [1], which does not assume local thermal equilibrium between the solid and the fluid, in the stationary observation frame can be rewritten as

$$c_{hcx}\frac{\partial}{\partial t}\frac{\partial\langle T\rangle}{\partial x}+\{(\rho c_p)_s\varepsilon_s+(\rho c_p)_f\varepsilon_f\}\frac{\partial\langle T\rangle}{\partial t}+(\rho c_p)_f\langle u\rangle_x\frac{\partial\langle T\rangle}{\partial x}$$
$$=\left\{K_{xx}\frac{\partial^2\langle T\rangle}{\partial x^2}+K_{yy}\frac{\partial^2\langle T\rangle}{\partial y^2}\right\}+k_{2dx}\frac{\partial}{\partial x}\left(\frac{\partial^2\langle T\rangle}{\partial x^2}+\frac{\partial^2\langle T\rangle}{\partial y^2}\right)+\langle\dot{s}\rangle \tag{1}$$

and the volume-averaged heat flux can be expressed as

$$\langle\dot{\mathbf{q}}_{\text{total}}\rangle=\left\{[(\rho c_p)_s\langle u_s\rangle_x+(\rho c_p)_f\langle u_f\rangle_x]\langle T\rangle-K_{xx}\frac{\partial\langle T\rangle}{\partial x}\right.$$
$$\left.-k_{2dx}\frac{\partial^2\langle T\rangle}{\partial x^2}\right\}\mathbf{e}_x+\left\{[(\rho c_p)_s\langle u_s\rangle_y+(\rho c_p)_f\langle u_f\rangle_y]\langle T\rangle\right.$$
$$\left.-K_{yy}\frac{\partial\langle T\rangle}{\partial y}-k_{2dx}\frac{\partial^2\langle T\rangle}{\partial x\partial y}\right\}\mathbf{e}_y, \tag{2}$$

where $\langle *\rangle:=(\frac{1}{V})\int_v * dV$ is the volume average operator. Heat capacity and volume fraction are denoted as (ρc_p) and ε respectively. Temperature and velocity are denoted as ''T'' and ''u,'' respectively. To capture the local non-equilibrium effect, two terms are introduced in this generalized model. First, to compensate for the energy storage, the heat capacity correction, $c_{hcx} = \Sigma_{i=s,f}(\rho c_p)_i\langle b_{x_i}\rangle$, is added. Note that the b-vector maps the deviation between the microscopic temperature and the local volume-averaged temperature onto the gradient of local volume-average temperature and is defined as $T_i = \langle T\rangle + \mathbf{b}_i \cdot \nabla\langle T\rangle$. The other additional term is the thermal diffusive correction vector, $k_{2dx} = \Sigma_{i=s,f} k_i \langle b_{xi}\rangle$, which captures the heat conduction deviations due to the local thermal non-equilibrium. The principal components of the total effective thermal conductivity tensor for this two dimensional heat transfer case can be expressed as

$$\begin{gathered} K_{xx} = k_{exx} + K_{Dxx} - \langle u\rangle_x c_{hcx} \\ K_{yy} = k_{eyy} + K_{Dyy}, \end{gathered} \tag{3}$$

whereas the effective thermal conductivity tensor contributed due to micro-conduction is defined as

$$\mathbf{k}_e = \sum_{i=s,f} k_i\left(\varepsilon_i \mathbf{I} + \frac{1}{V}\int_{S_i} \mathbf{n}\mathbf{b}_i dS\right). \tag{4}$$

Note that "S_i" is the interface between the solid phase and the fluid phase. In this paper, for sake of simplicity, we assume $k_{exx} \approx k_{eyy} = k_e$. The heat dispersion tensor is given as

$$\mathbf{K}_D = \sum_{i=s,f} -\frac{(\rho c_p)_i}{V}\int_{V_i} (\mathbf{u}_i - \langle \mathbf{u}\rangle)\mathbf{b}_i dV. \tag{5}$$

The heat dispersion accounts for and lumps together the enhanced heat transfer due to microscopic temperature and velocity deviations from their volume-averaged values. Note that the K_{xx} value is frame dependent since the volume-averaged velocity $\langle u\rangle_x$ is frame dependent. Because all other components of K_{xx} are frame independent, Eq. (3) will be very useful to find the value of c_{hcx}, and, hence, can be used to calculate the temperature difference between the fluid phase and the solid phase.

The mold in composites processing such as RTM is usually very thin and long, and the characteristic length along the x-direction, x_c, is usually about two to three orders of magnitude more than the thickness. Hence, we assume that the contribution of k_{2dx} can be neglected for such processes as compared with the contributions from K_{xx} and K_{yy}.

The boundary conditions for the wall and inflow are Dirichlet's boundary conditions, i.e.,

$$\langle T\rangle = T_{\text{wall}} \quad \text{at top and bottom of the mold} \tag{6}$$

$$\langle T\rangle = T_{\text{inflow}} \quad \text{at inflow.} \tag{7}$$

The flow front velocity relative to the fiber preform is

$$\mathbf{u}_{\text{front}} = \langle \mathbf{u}_f\rangle^f = \frac{\langle u\rangle_x}{\varepsilon_f}\mathbf{e}_x. \tag{8}$$

(b) Temperature Boundary Condition at the Moving Flow Front. An energy balance approach is used at the moving flow front. To describe the heat balance at the flow front, it is imperative to use the moving observation frame attached to the flow front. Hence, the dry preform enters the flow front at a relative velocity, $-\mathbf{u}_{\text{front}}$. The dry preform is preheated to the initial temperature of the wall $T_0 = T_{\text{wall}}$. The volume averaged heat flux balance can be written as

$$\overbrace{(\rho c_p)_s\varepsilon_s T_0\left(-\frac{\langle u\rangle_x}{\varepsilon_f}\right)}^{\text{On the Dry Side of the Flow Front}}$$
$$= \underbrace{[(\rho c_p)_s\langle u_s\rangle_x + (\rho c_p)_f\langle u_f\rangle_x]_{\underline{\underline{\text{rel. to front}}}}\langle T\rangle - K_{xx\,\underline{\underline{\text{rel. to front}}}}\frac{\partial\langle T\rangle}{\partial x}}_{\text{On the Saturated Side of the Flow Front}}, \tag{9}$$

where $T_0 = T_{\text{wall}}$ and $\varepsilon_s + \varepsilon_f = 1$. As $\langle u_f\rangle_{x_{\underline{\underline{\text{rel. to front}}}}} = 0$ and $\langle u_s\rangle_{x_{\underline{\underline{\text{rel. to front}}}}} = -\varepsilon_s/\varepsilon_f\langle u\rangle_x$ in the frame attached to the moving front, the energy balance simplifies to

$$(\rho c_p)_s\varepsilon_s\left(-\frac{\langle u\rangle_x}{\varepsilon_f}\right)(T_0 - \langle T\rangle) = -K_{xx,\underline{\underline{\text{rel. to front}}}}\frac{\partial\langle T\rangle}{\iota x}, \tag{10}$$

where

$$\begin{aligned} K_{xx\,\underline{\underline{\text{rel. to front}}}} &= k_{exx} + K_{Dxx} - \langle u\rangle_{x\,\underline{\underline{\text{rel. to front}}}} c_{hcx} \\ &= k_{exx} + K_{Dxx} - \frac{\varepsilon_f - 1}{\varepsilon_f}\langle u\rangle_x c_{hcx}. \end{aligned} \tag{11}$$

This boundary condition is usually absent in flow through porous media in which one does not encounter a moving flow front boundary. However, it is important to consider such a moving boundary in manufacturing process as it does influence the temperature downstream.

(c) Dimensionless Form of the Governing Equation With Boundary Conditions. The governing equations in dimensionless form can be expressed as

$$\begin{aligned} &\frac{c_{hcx}}{(\rho c_p)_f U t_c}\frac{\partial}{\partial t'}\frac{\partial T'}{\partial x'} + \frac{\lfloor(\rho c_p)_s\varepsilon_s + (\rho c_p)_f\varepsilon_f\rfloor x_c}{(\rho c_p)_f U t_c}\frac{\partial T'}{\partial t'} + u_x'\frac{\partial T'}{\partial x'} \\ &\quad = \left\{\frac{K_{xx}}{(\rho c_p)_f U x_c}\frac{\partial^2 T'}{\partial x'^2} + \frac{K_{yy}x_c}{(\rho c_p)_f U y_c^2}\frac{\partial^2 T'}{\partial y'^2}\right\} + \frac{\langle \dot{s}\rangle x_c}{(\rho c_p)_f U\Delta T} \end{aligned} \tag{12}$$

with boundary conditions

$$T' = 1 \qquad \text{at the mold walls}$$

$$T' = 0 \qquad \text{at inflow}$$

$$1 - T' = \frac{K_{xx\,\underline{\underline{\text{rel. to front}}}}\varepsilon_f}{(\rho c_p)_s\varepsilon_s x_c U u_x'}\frac{\partial T'}{\partial x'} \quad \text{at the flow front,} \tag{13}$$

where the dimensionless variables are defined as

$$\begin{gathered} T' = \frac{T - T_{\text{inflow}}}{\Delta T} = \frac{T - T_{\text{inflow}}}{T_{\text{wall}} - T_{\text{inflow}}} \\ u_x' = \langle u\rangle_x/U \\ x' = x/x_c \end{gathered} \tag{14}$$

$$y' = y/y_c = y/h$$

$$t' = t/t_c\,.$$

Here the thickness of the mold cavity is $2h$. The characteristic velocity U is assigned to be the Darcy velocity. Note that as uniform Darcy velocity in the thickness direction is equivalent to plug flow and hence the dimensionless velocity in the x direction is unity, i.e., $u'_x = 1$. The characteristic length x_c and the characteristic time t_c will be discussed later.

(d) Analytical Solution for the Quasi-Steady State Case. We define $Pe := (\rho c_p)_f \langle u \rangle d_p / 2k_f$. Here d_p is the diameter of the solid particles (either fiber or fiber-tow). If a low Peclet number is assumed, we can neglect the complex effects due to the inclusion of K_{xx}, c_{hcx}, k_{2dx} for a thin mold cavity and we assume presence of no heat source. The volume-averaged energy Eq. (12) for the quasi-steady state simplifies to

$$u'_x \frac{\partial T'}{\partial x'} = \frac{x_c K_{yy}}{h^2 (\rho c_p)_f U} \frac{\partial^2 T'}{\partial y'^2}, \quad 0 < x' < \infty, \quad -1 < y' < 1. \tag{15}$$

The velocity profile is assumed to be uniform (one-dimensional flow) and hence $u'_x = 1$. The boundary conditions are constant inflow temperature and constant wall temperature. Note that the flow front boundary condition is not required and does not appear in the steady state problem. The analytical solution is:

$$T' = 1 - \frac{4}{\pi} \sum_{n=0}^{\infty} \frac{(-1)^n}{2n+1} \cos\left[(2n+1) \frac{\pi}{2} y' \right] \times \exp\left[-\left(n + \frac{1}{2} \right)^2 \pi^2 x^* \right], \tag{16}$$

where $x^* = x'(x_c K_{yy} / h^2 (\rho c_p)_f U)$. This solution can be used to find optimal K_{yy} to numerically fit the temperature field with the measured experimental data. Once we know K_{yy} and the value of effective thermal conductivity (k_{eyy}), the difference between the two is due to heat dispersion (K_{Dyy}).

This analytical solution can also be used to determine the characteristic length along the x-direction in this problem. If we assume the characteristic length to correspond to the 99 percent temperature drop along the centerline ($y' = 0$), one can write and solve the following equation to find x_c:

$$0.01 = \frac{4}{\pi} \sum_{n=0}^{\infty} \frac{(-1)^n}{2n+1} \exp\left[-\left(n + \frac{1}{2} \right)^2 \pi^2 x'_c \right]. \tag{17}$$

This allows one to solve for x_c^* and hence x_c. The characteristic thickness in the y-direction is $y_c = h$. One can now compare the magnitude of conduction effects in Eq. (12) to formulate a criterion for neglecting x-direction conduction in the quasi-steady state case as

$$\frac{K_{yy}}{K_{xx}} \left(\frac{x_c}{h} \right)^2 \gg 1. \tag{18}$$

The quasi-steady state assumption is justifiable if the magnitudes of the two transient terms in Eq. (12) are much less than the convection term and the conduction term in y-direction. Hence, to obtain a quasi-steady state the following two conditions should be met:

$$t \gg \mathrm{MAX}\left(\frac{((\rho c_p)_s \varepsilon_s + (\rho c_p)_f \varepsilon_f) h^2}{K_{yy}}, \frac{((\rho c_p)_s \varepsilon_s + (\rho c_p)_f \varepsilon_f) x_c}{(\rho c_p)_f U} \right) \tag{19}$$

and

$$t \gg \mathrm{MAX}\left(\frac{c_{hcx}}{(\rho c_p)_f U}, \frac{c_{hcx} h^2}{K_{yy} x_c} \right). \tag{20}$$

(e) Numerical Approach for the Transient Temperature Predictions. A fully implicit finite difference scheme is employed to solve Eq. (1) with the transient term. We assume that k_{2dx} term can be neglected. An upwind scheme is used for computing all $\partial \langle T \rangle / \partial x$ terms in the energy equation and boundary conditions. A central differential scheme is used to compute $\partial^2 \langle T \rangle / \partial x^2$ and $\partial^2 \langle T \rangle / \partial y^2$. It is assumed that the fluid's velocity is uniform throughout the thickness, thus producing a plug profile. Therefore, the mesh is fixed with a plug-shaped numerical flow front. The incremental length corresponds to the user-specified Darcy velocity, porosity, and total filling time. An iterative solver with a floating relaxation factor executes the fully implicit scheme. We verified the accuracy of our numerical code by comparing its steady state predictions with the analytical solution.

To solve for the transient problem, we need to input the values of K_{xx} and c_{hcx} in addition to the value of K_{yy}, which is used from the quasi-steady state solution. Unlike the value of K_{yy} can be fitted from the experimental results, to find the values for K_{xx} and c_{hcx} is not straightforward. However, it is possible that K_{xx} and c_{hcx} are negligible under some constraints. One can use order of magnitude analysis to find the conditions under which we can neglect the influence of K_{xx} and c_{hcx} in the transient problem. K_{xx} was found to be negligible as stated in Eq. (18). Next, we turn to the flow front boundary conditions, Eq. (13). In most of the experimental data, we found that this temperature drop was insignificant, i.e., $0 \leqslant 1 - T' \ll 1$, at flow front boundary. Previous researchers [12,13] explained such a phenomenon as a thermal wave traveling behind the flow front boundary at its initial temperature, T_0. Combining the experimental observation with Eq. (13), we obtain

$$0 \leqslant \frac{K_{xx\,\underline{\underline{\text{rel. to front}}}}}{(\rho c_p)_s x_c U} \frac{\varepsilon_f}{1 - \varepsilon_f} \ll 1. \tag{21}$$

This equation can be used to determine the order of magnitude of $K_{xx\,\underline{\underline{\text{rel. to front}}}}$. If we know the order of magnitude of both $K_{xx\,\underline{\underline{\text{rel. to front}}}}$ and K_{xx}, which can be found from some previous reports [14,15], we can determine the order of magnitude of c_{hcx} as

$$c_{hcx} = -\frac{\varepsilon_f (K_{xx} - K_{xx\,\underline{\underline{\text{rel. to front}}}})}{\langle u \rangle_x}$$

$$\Rightarrow O\{c_{hcx}\} = O\left\{ -\frac{\varepsilon_f (K_{xx} - K_{xx\,\underline{\underline{\text{rel. to front}}}})}{\langle u \rangle_x} \right\}. \tag{22}$$

By comparing the magnitude of the transient terms in the energy equation, Eq. (12), we find the transient effect of c_{hcx} can be neglected if

$$|c_{hcx}| \ll |(\rho c_p)_s \varepsilon_s + (\rho c_p)_f \varepsilon_f| x_c\,. \tag{23}$$

Results and Discussions

We had investigated two types of fiber preforms, the random fiber preform and the woven preforms. The random fiber preform is representative of isotropic porous media and woven or stitched preform exhibits dual scale porous media. In woven or stitched preforms, such as the unidirectional fiberglass and the carbon biweave, the dual scale is created because the spaces between the fiber tows is an order of magnitude larger than the spaces between individual fibers in a fiber tow.

(a) The Significance of Heat Dispersion in RTM. As the theory is strictly valid for single scale porous media and since the fiber-tow does not completely saturate when the resin flow front reaches the fiber-tow [16], for the unidirectional fiberglass and the carbon biweave cases, we only performed the quasi-steady state analysis to quantify the importance of heat dispersion.

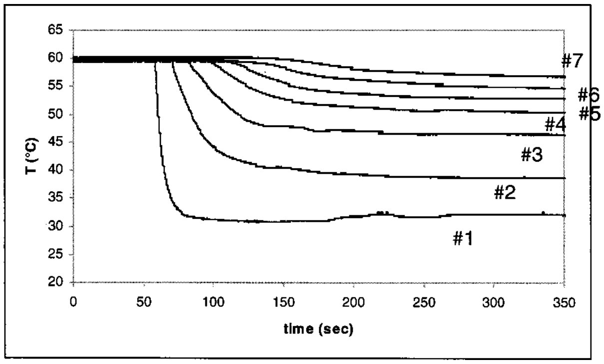

Fig. 4 Centerline temperature history for carbon biweave (Experiment 5) at the seven locations as shown in Fig. 1 and Fig. 2

Figure 3 presents the effect of fiber orientation on the temperature history for the unidirectional preform. It is clear from the figure that there is over 10 to 40 percent difference in the temperature due to the change in the fiber orientation direction by 90 deg to the flow direction with all other parameters being the same. By using the quasi-steady state analytical solution we can find the K_{yy} values that best match the quasi-steady state temperature distribution along the midplane in the flow direction. We found that $K_{yy} = 0.882\,\mathrm{W/m\cdot K} = 3.20 k_f$ (3.2 times the thermal conductivity of the fibers) for the fiber-tow perpendicular to the flow direction and $K_{yy} = 0.737\,\mathrm{W/m\cdot K} = 2.67 k_f$ for the fiber-tow orientated along the flow direction. The differences in both the temperature history and the K_{yy} values (about $0.53 k_f$) show that heat dispersion effect is significant and is influenced by the changes in the microstructure of the porous media.

Figure 4 shows the typical temperature history along the fluid flow direction when a carbon biweave preform is used as the fibrous porous media. The carbon biweave preform has the fiber-tows orientated in both along and perpendicular to the flow direction alternatively. One can observe similar temperature behavior as observed for unidirectional fibers, however with some subtle differences. Figure 5 shows the values of K_{yy} used to match the experimental data is linear with Peclet number (or Darcy velocity) in our experiments. The diameter of carbon fiber is about 8 μm. Recalling from Eqs. (3–5), the micro-velocity deviation $\mathbf{u}_i - \langle \mathbf{u} \rangle$ linearly increases with Darcy velocity for laminar flow and hence the linearity of K_{yy} with Peclet number. Table 3 compares the various models used for predicting k_e, the effective thermal conductivity of the fluid saturated porous medium. Because of $k_e \leqslant K_{yy}$, we found that Chang's model [17] and the series arrangement model provided a better match with experimental results. In practice, it will be of interest to examine the necessity of considering the K_{Dyy} in the temperature prediction. Figure 6 shows it is necessary to include the heat dispersion effect (K_{Dyy}) in the quasi-steady state temperature prediction in order to match the quasi-steady state experimental results.

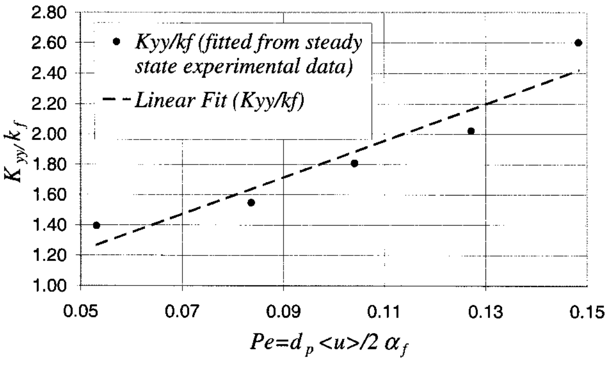

Fig. 5 K_{yy} versus the Peclet number for the experiments using carbon biweave preform with fiber volume fraction of 43 percent

Table 3 Comparison of various predictions [15] of k_e for carbon biweave

Model	Formula	$k_e (W/m\cdot K)$	k_e/k_f
Parallel arrangement	$k_e = k_f \varepsilon_f + k_s \varepsilon_s$	3.59	13.01
Series arrangement	$k_e = \dfrac{k_f k_s}{k_f \varepsilon_s + k_s \varepsilon_f}$	0.47	1.71
Geometric mean	$k_e = (k_f)^{\varepsilon_f} (k_s)^{\varepsilon_s}$	1.17	4.24
Homogenization of diffusion equation in a two-dimensional periodic unit cell (by Chang[17])	$\dfrac{k_e}{k_f} = \dfrac{(2-\varepsilon_f) k_s/k_f + 1}{2 - \varepsilon_f + k_s/k_f}$	0.39	1.40
Note: For the carbon biweave experiments, we have $0.385 \le K_{yy} \le 0.718\,(W/m-K)$, i.e., $1.39 \le K_{yy}/k_f \le 2.60$			

In summary, from this set of steady state analysis and experiments, we verified and validated the significance of heat dispersion K_{Dyy} in RTM. In addition, we presented a way to calculate the value for K_{yy} and hence K_{Dyy}. K_{Dyy} was found to be linear with Peclet number. After comparing several models for k_e, we found that Chang's model [17] and the series arrangement model agreed well with our experimental results.

(b) Local Thermal Equilibrium Assumption. For the random fiberglass, both the quasi-steady state and transient state analysis will be performed since it is composed of single-scale fibrous porous media, instead of dual-scale fibrous porous media (e.g., fiber-tow), and does saturate immediately.

To analyze the random fiberglass experimental data, we start with the quasi-steady state data. Using the analytical solution, we first find the value of K_{yy} that matches the temperature predictions with the measured temperatures from the experiments. As expected, we find that it is proportional to Peclet number as shown in Fig. 7. We find that the dispersion coefficient varies from $0.98 \leqslant K_{Dyy}/k_f \leqslant 2.36$ if we assume $k_e \cong 0.29\,\mathrm{W/m\cdot K} = 1.05 k_f$ by using Chang's model [17]. The diameter of the fiberglass is 0.14 mm which gives the range of Peclet number to be $1.54 \leqslant Pe := 0.5 \cdot d_p \langle u \rangle / \alpha_f \leqslant 6.28$. Our results are very similar to Koch and Brady's prediction [14], although their porous media consisted of random arrangement of spheres. Koch and Brady predicted $0.30 \leqslant K_{Dyy}/k_f \leqslant 1.24$ and $1.70 \leqslant K_{Dxx}/k_f \leqslant 14.20$ for the corresponding Peclet number range. As our K_{Dyy} value was close to their K_{Dyy}, we assume their prediction range of K_{Dxx}/k_f as the starting initial guess values for us to perform the transient state analysis. Use of different K_{Dxx} values into the numerical solution, had almost no significant effect on the temperature history. This can be explained by conducting an order of magnitude analysis of the energy equations. For example, for $Pe = 6.28$, i.e. $\langle u \rangle_x = 0.826\,\mathrm{cm/sec}$, we calculated $x_c = 1.429\,\mathrm{m}$ from Eq. (17). And note that $y_c = h = 0.0102/2 = 0.0051\,\mathrm{m}$. Using the above values into Eq. (18), we get

$$\frac{K_{yy}}{K_{xx}} \left(\frac{x_c}{h} \right)^2 \approx \frac{2.36 + 1.05}{14.20 + 1.05} \left(\frac{1.429}{0.0051} \right)^2 = 17594.19 \gg 1. \qquad (24)$$

This implies K_{xx} has no significance in the energy equation, Eq. (1), for RTM type of porous media processes in which the in-plane direction is much longer than the thickness direction. We

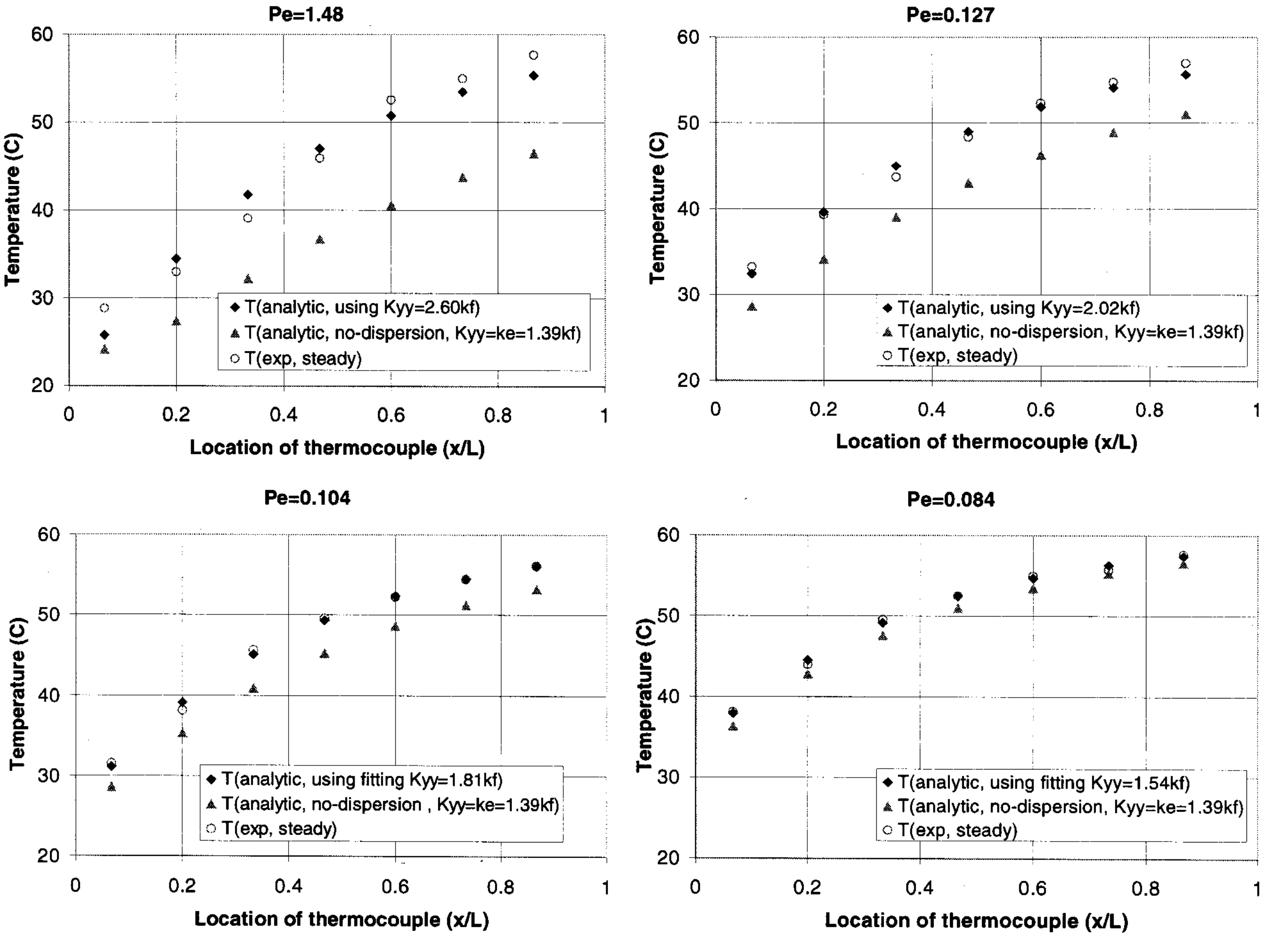

Fig. 6 The significance of heat dispersion for the steady state temperature predictions for four different Peclet numbers. The dependence of K_{yy} on Peclet number must be considered to match the experimental data from the carbon biweave cases.

observed no significant temperature drop at the flow front from the experimental data. Hence, the condition stated in Eq. (21) must be satisfied hence reduces to

$$0 \leqslant K_{xx\,\underline{\underline{\text{rel. to front}}}} \ll 5710.25. \tag{25}$$

We then estimated the order of magnitude of c_{hcx} by using Eq. (22) and obtain

$$-1.44\times 10^3 \leqslant O\{c_{hcx}\} \ll 5.38\times 10^5. \tag{26}$$

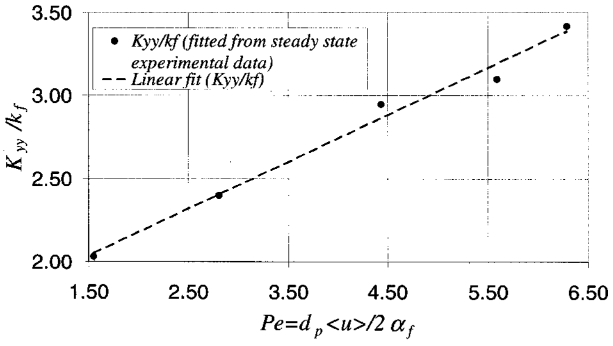

Fig. 7 K_{yy} versus Peclet number for the experiments using the random fiberglass preform with fiber volume fraction of 22 percent.

Since we have $\langle b_{sx}\rangle = -\langle b_{fx}\rangle \geqslant 0$ and $(\rho c_p)_s < (\rho c_p)_f$ for this case, we can tighten the bounds by further restricting $c_{hcx} \leqslant 0$ and $K_{xx_{\overline{\underline{\text{rel. to front}}}}} \leqslant K_{xx}$. Substituting the order of magnitude of c_{hcx} into Eq. (23), we have

$$\underbrace{O\{|c_{hcx}|\}}_{\leqslant 1.44\times 10^3} \ll \underbrace{((\rho c_p)_s\varepsilon_s + (\rho c_p)_f\varepsilon_f)x_c}_{3.88\times 10^6} \tag{27}$$

Equation (27) clearly implies that the transient term of c_{hcx} can be neglected in the energy equation, Eq. (1), while comparing its order of magnitude to the macroscopic transient term, i.e., the transient term with $(\rho c_p)_s\varepsilon_s + (\rho c_p)_f\varepsilon_f$. Hence, for this case, from Eq. (24) and Eq. (27) we conclude that the effects of K_{xx} and c_{hcx} can be neglected for both the quasi-steady state and the transient state analysis. The most significant thermal coefficient that needs to be determined is K_{yy}, which can be easily found by matching the temperature profiles from the as mentioned quasi-steady state analytical solution with the experimental data. Applying the fitted K_{yy} value in the numerical solution, a good agreement between the predicted temperature history and experimental data as shown in Fig. 8 which suggests that at low Peclet number, local thermal equilibrium assumption is a justifiable one. Thus, one can use the order of magnitude analysis as shown above to evaluate the local thermal equilibrium assumption.

(c) Influence of Fiber Volume Fraction. In experiments 12 and 13, we use random fiberglass to make a study of the effect

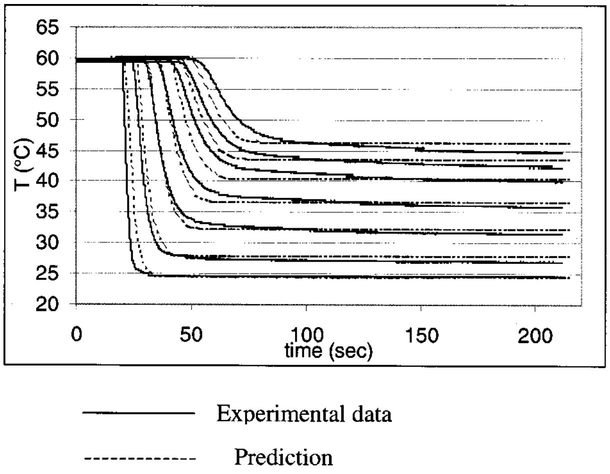

Fig. 8 The centerline temperature history at seven locations as shown in Fig. 1 and Fig. 2; random fiberglass, $\varepsilon_S = 22$ percent, $\langle u\rangle_x = 0.826$ cm/sec, Pe$= d_p\langle u\rangle/2\alpha_f = 6.28$, $K_{yy} = 0.94$ W/m·$K = 3.41k_f$

of porosity, or fiber volume fraction. We find that K_{yy} increases from $3.11k_f$ (0.858 W/m-K) to $3.42k_f$ (0.943 W/m-K) while the porosity decreases from 0.85 to 0.78. Note that we are using the same flow front velocity (fluid phase average velocity) of 1 cm/sec for the two experiments. If we use Chang's model [17] to approximate k_e, it increases from $1.08k_f$ (0.297 W/m-K) to $1.11k_f$ (0.307 W/m-K) as the porosity decreases from 0.85 to 0.78. Since $K_{yy} = k_{eyy} + K_{Dyy}$, hence K_{Dyy} increases from $2.03k_f$ (0.561 W/m-K) to $2.30k_f$ (0.636 W/m-K) as the porosity decreases from 0.85 to 0.78. The rate of increase in K_{Dyy} is much higher than the rate of increase in k_e for the porosity change from 0.85 to 0.78. The heat dispersion enhances because the microscopic velocity increases and microscopic flow path becomes more tortuous when the porosity decreases.

Summary

The heat dispersion for a viscous fluid saturating a heated fibrous porous medium is an important phenomenon in composites manufacturing process such as RTM. Because the mold thickness of such flow domains is much less than its in-plane dimension, the through thickness dispersion K_{Dyy} has a strong effect on the non-isothermal RTM process. Lab-scale experiments were conducted in which temperatures were measured at seven different locations in the flow direction during mold filling. Three different types of fibrous porous media were used in the carefully designed experiments. From the experimental data, we can distinguish a quasi-steady state region and a transient region. We presented a method to characterize dispersion coefficient by finding the K_{yy} value by matching the analytical solution for the quasi-steady state region with the experimental data. By using order of magnitude analysis, we found that we can neglect the effects of total effective thermal conductivity in the flow direction (K_{xx}) and justify local thermal equilibrium assumption in the lab-scale RTM cases. We also presented a method to conduct energy balance at the moving flow front for such moving boundary problems. The most significant influence is the total effective thermal conduction in the thickness direction (K_{yy}) which includes strong dispersion effect (K_{Dyy}). The K_{Dyy} and K_{yy} were found to be linear with Peclet number and increase as the porosity decreases. The dual-scale fibrous porous preform such as biweave and unidirectional preforms were observed to have a different pattern in temperature history due to their partial saturation at the flow front [16]. Further non-isothermal study of using such dual-scale fibrous porous preform in RTM should be explored and will prove useful in industrial-scale RTM processes.

Acknowledgment

For this research, we acknowledge the financial support provided by the National Science Foundation (Grant DMI9713521), the Office of Naval Research (Grant N00014-97-C-0415), the manufacturing expertise provided by High Industries and assistance given by Simon Bickerton.

Nomenclature

$\mathbf{b}$ = closure vector function (m)
$\mathbf{c}_{hc}$ = thermal capacity correction vector (J/m^2-K)
c_p = specific heat (J/kg-K)
d_p = particle diameter (m)
$\mathbf{e}$ = unit vector
h = thickness of mold cavity (m)
$\mathbf{I}$ = identity tensor
k_f = thermal conductivity of the fluid (W/m-K)
$\mathbf{k}_e$ = effective thermal conductivity of the fluid saturated porous media (W/m-K)
$\mathbf{k}_{2d}$ = thermal diffusive correction vector (W/K)
$\mathbf{K}$ = total effective thermal conductivity tensor (W/m-K)
$\mathbf{K}_D$ = effective thermal conductivity for dispersion effect (W/m-K)
L = length of the fiber preform (m)
$\mathbf{n}$ = normal vector
Pe = Peclet number
$\dot{\mathbf{q}}$ = heat flux vector (W/m^2)
S = surface (m^2)
$\dot{s}$ = heat source (W/m^3)
t = time (sec)
t_c = characteristic time (sec)
T = temperature (K)
T_0 = initial temperature (K)
U = magnitude of Darcy velocity (m/sec)
$\mathbf{u}$ = velocity vector (m/sec)
V = representative volume (m^3)
x, y, z = Cartesian coordinates
x_c, y_c = characteristic length (m)

Greek

ΔT = temperature difference (K)
α = thermal diffusivity (m^2/s)
ε = volume fraction
ρ = density (kg/m^3)

Subscripts

f = fluid phase
i = material index
s = solid phase

Superscripts

f = fluid phase
i = material index
s = solid phase
$'$ = non-dimensional index

Others

$\langle\,\rangle$ = local volume-averaging operator

References

[1] Hsiao, K.-T., and Advani, S. G., 1999, ''A Theory to Describe Heat Transfer During Laminar Incompressible Flow of a Fluid in Periodic Porous Media,'' Phys. Fluids, **11**, No. 7, pp. 1738–1748.
[2] Quintard, M., Kaviany, M., and Whitaker, S., 1997, ''Two-Medium Treatment of Heat Transfer in Porous Media: Numerical Results for Effective Properties,'' Adv. Water Resour., **20**, pp. 77–94.
[3] Bruschke, M. V., and Advani, S. G., 1994, ''A Numerical Approach to Model Non-Isothermal, Viscous flow with Free Surfaces Through Fibrous Media,'' Int. J. Numer. Methods Fluids, **19**, pp. 575–603.
[4] Liu, B., and Advani, S. G., 1995, ''Operator Splitting Scheme for 3-D Temperature Solution Based on 2-D Flow Approximation,'' Computational Mechanics, **38**, pp. 74–82.

[5] Lee, L. J., Young, W. B., and Lin, R. J., 1994, ''Mold Filling and Cure Modeling of RTM and SRIM Processes,'' Composite Structures, **27**, No. 1–2, pp. 109–120.

[6] Gao, D. M., Trochu, F., and Gauvin, R., 1995, ''Heat Transfer Analysis of Non-Isothermal Resin Transfer Molding by the Finite Element Method,'' Mater. Manuf. Processes, **10**, No. 1, pp. 57–64.

[7] Tucker III, C. L., and Dessenberger, R. B., 1994, ''Chapter 8th, Governing Equations for Flow and Heat Transfer in Stationary Fiber Beds,'' in *Flow and Rheology in Polymer Composites Manufacturing*, S. G. Advani, ed., Elsevier Science, New York.

[8] Dessenberger, R. B., and Tucker III, C. L., 1995, ''Thermal Dispersion in Resin Transfer Molding,'' Polym. Compos., **16**, No. 9, pp. 495–506.

[9] Chiu, H.-T., Chen S.-C., and Lee, L. J., 1997, ''Analysis of Heat Transfer and Resin Reaction in Liquid Composite Molding,'' ANTEC, pp. 2424–2429.

[10] Lin, R., Lee, L. J., and Liou, M., 1991, ''Non-Isothermal Mold Filling and Curing Simulation in Thin Cavities with Preplaced Fiber Mats,'' Int. Polym. Process., **6**, pp. 356–369.

[11] Bickerton, S., and Advani, S. G., 1999, ''Characterization of Racetracking in Liquid Composite Molding Process,'' Composites Science and Technology, **59**, pp. 2215–2229.

[12] Tucker III, C. L., 1996, ''Heat Transfer and Reaction Issues in Liquid Composite Molding,'' Polym. Compos., **17**, No. 1, pp. 60–72.

[13] Mal, O., Couniot, A., and Dupret, F., 1998, ''Non-Isothermal Simulation of the Resin Transfer Moulding Process,'' Composites Part A, **29A**, pp. 189–198.

[14] Koch, D. L., and Brady, J. F., 1985, ''Dispersion in Fixed Beds,'' J. Fluid Mech., **154**, pp. 399–427.

[15] Kaviany, M. V., 1995, *Principles of Heat Transfer in Porous Media*, 2nd ed., Springer-Verlag, New York, pp. 157–258.

[16] Pillai, K. M., and Advani, S. G., 1998, ''Numerical Simulation of Unsaturated Flow in Woven or Stitched Fiber Mats in Resin Transfer Molding,'' Polym. Compos., **19**, No. 1, pp. 71–80.

[17] Chang, H.-C., 1982, ''Multi-Scale Analysis of Effective Transport in Periodic Heterogeneous Media,'' Chem. Eng. Commun., **15**, pp. 83–91.

I. Ahmed
Assistant Professor,
Department of Mechanical Engineering,
Wichita State University,
1845 Fairmount,
Wichita, KS 67260-0133
e-mail: iahmed@me.twsu.edu

T. L. Bergman
Professor and Head
Fellow ASME
Department of Mechanical Engineering,
The University of Connecticut,
191 Auditorium Road,
Storrs, CT 06269-3139
e-mail: tberg@engr.uconn.edu

Simulation of Thermal Plasma Spraying of Partially Molten Ceramics: Effect of Carrier Gas on Particle Deposition and Phase Change Phenomena

A three-dimensional simulation of the thermal plasma spraying process is reported. In particular, the effect of the radial injection of a carrier gas is taken into account for a dilute spray. The thermal history of powder particles of different sizes is predicted. It is shown that introduction of a carrier gas can lead to a significant modification of the plasma jet, and can have an effect on the thermal histories of the injected particles. The study is motivated by the processing of non-traditional materials, specifically nanostructured ceramics. [DOI: 10.1115/1.1338117]

Introduction

Thermal spraying is a major materials processing operation used to achieve improved surface properties. Applications are found in the power, aviation, automotive, marine, and biomedical industries [1–7]. Pawlowski [8] provides a comprehensive review of the various techniques used in applying thermally sprayed coatings, including the typical ranges of corresponding processing parameters. The atmospheric plasma spray (APS), which is one of the most common techniques, has been studied with various levels of sophistication [9,10].

A recent innovation in plasma sprayed coatings is the introduction of nanostructured materials which are expected to provide enhanced insulation capability, wear and corrosion resistance, and surface finishes [11,12]. Some preliminary diagnostics of the sprayed particles and predictions of nanostructure retention in coatings have been reported [13,14]. Spraying nanostructured materials presents an added level of complexity relative to the use of conventional powder because complete melting (which is desirable when spraying conventional material) is to be avoided if some nanostructure is to be retained in the coating. On the other hand, at least some melting may be desirable in order to provide a mechanism for the sprayed material to adhere to the substrate. Of course, partial melting may be achieved by (*a*) melting some of the particles entirely (while the rest remain unmolten), (*b*) partially melting all the particles that are sprayed, or (*c*) some combination of the two. In any case, an improved understanding of the melting and possible resolidification phenomena of the particles and their dependence upon conditions within the plasma jet is needed for identifying key factors that influence the final coating characteristics.

Since partial melting is desirable, it is probable that the appropriate operating conditions for spraying nanostructured material will be different than those used to spray conventional material. Narrower processing windows may emerge, and a higher level of process control may be needed. With lower temperature particles (relative to conventionally sprayed material), physical phenomena that are normally important (such as vaporization) may not occur. On the other hand, effects that are usually deemed to be unimportant (such as cooling of the plasma jet by the gas that carries the particles to the jet or three-dimensionality within the jet) may play a more significant role. With spraying partially-molten materials as the motivation, the objective of this study is to predict partial particle melting and possible resolidification phenomena of powders as they are sprayed using a conventional plasma setup. The effect of the carrier gas on the plasma jet is accounted for. The results reported here are relevant to dilute sprays; here, dilute sprays are those in which the cooling and redirection of the plasma gases by the particles themselves is neglected.

Problem Description. The plasma torch, the injection port, and a substrate are shown schematically in Fig. 1. In plasma sprays, gas temperatures typically exceed 10,000 K and particle velocities are on the order of 100 m/s. The micron-sized particles that are injected into the plasma usually melt within a few ms prior to deposition on the substrate. Experimental observation of the process is difficult because of the extreme conditions. An efficient method to investigate melting (and possible resolidification) within the sprayed particles is via simulation.

In APS, the particles are delivered to the plasma in a stream of carrier gas. Radial injection of the carrier gas has been neglected in nearly all of the simulations reported in the literature. Although some attempts have been made to justify neglecting the carrier gas, it is usually the case that the gas is not accounted for because with radial injection the flow field is fully three-dimensional, and the descriptive equations become elliptic in form. In turn, the computational expense associated with investigating carrier gas

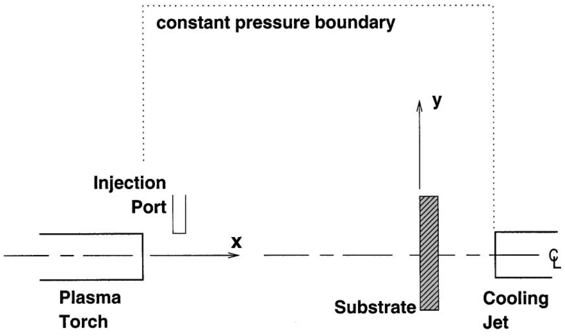

Fig. 1 A schematic representation of the thermal plasma spraying system along with the injection port and substrate

---

Contributed by the Heat Transfer Division for publication in the JOURNAL OF HEAT TRANSFER. Manuscript received by the Heat Transfer Division February 17, 2000; revision received September 27, 2000. Associate Editor: D. A. Kaminski.

effects can become prohibitively large. It appears that only a recent computational effort [10] has addressed the issue of carrier gas injection, but to a limited extent.

In this study, a three-dimensional plasma jet issuing into an ambient, quiescent atmosphere is modeled as a non-reacting, turbulent mixture of Ar-H_2 with temperature-dependent thermophysical properties. Powder particles are introduced into the jet radially (along with the carrier gas; Ar at room temperature). The particles are entrained into and heated by the plasma. A low (relative to conventional processing) power operating condition is considered, since low temperatures are desired relative to the spraying of conventional powder.

The orifice of the torch is 8 mm in diameter, and the injection port for the carrier gas and particles (located 5.5 mm from the torch orifice and 5 mm off-axis) has a hydraulic diameter of 1.9 mm. These dimensions are typical of production hardware [13]. The substrate is a 3 mm thick, 50 mm diameter disk located coaxially with the torch at a distance of $L_{\mathrm{stdf}}=100\,\mathrm{mm}$. The boundary of the computational domain is cylindrical, and coaxial with the plasma torch. The radius of the domain is 50 mm, and the domain extends beyond the substrate disk for an additional 20 mm in the x-direction. A cooling jet is located behind the substrate in order to constrain its temperature to realistic levels. Back cooling is often employed in practice.

The torch operating conditions are fixed. These are: an average torch exit velocity and temperature of $V_j=300\,\mathrm{m/s}$ and $T_j=12{,}000\,\mathrm{K}$, respectively. (Note that the jet velocity is low relative to standard conditions because of the lower power level assumed.) Plasma torches are characterized by a high degree of intermittent arcing, which can induce high levels of instability within the plasma itself. The species composition is taken to be 80 percent–20 percent Ar-H_2 by volume (The resulting plasma gas mass flow rate is $\sim 0.5\times 10^{-3}$ kg/s). The back cooling jet is of air, issuing at 10 m/s and 300 K from an 8 mm round exit. The remaining computational boundaries are specified to be at a constant pressure; in the case of entrainment of ambient air, the conditions are set at room temperature.

The carrier gas is argon, introduced into the injection port at 300 K. The carrier gas injection velocities (at the exit of the injection port) are varied from $V_{cg}=0$ to 15 m/s. Although nanostructured material (zirconia) may have different thermophysical properties relative to bulk material, the sprayed powder properties are specified to be that of bulk zirconia ($k=2.4\,\mathrm{W/m\text{-}K}$, $c=620\,\mathrm{J/kg\text{-}K}$, $\rho=5700\,\mathrm{kg/m^3}$, $\Delta h_{1s}=700\,000\,\mathrm{J/kg}$, $T_{1s}=2\,980\,\mathrm{K}$, [15,16]) due to lack of information. The particle injection velocity is radially inward and is fixed at $V_p=5$ m/s. Typically, particle injection velocities have been measured to be within approximately ± 20 percent of the mean value [17]. The particles are injected at $T_p=300\,\mathrm{K}$. Note that differences between V_{cg} and V_p are commonplace and have been discussed elsewhere [18,19] and the conditions specified here (except for the low V_{cg} cases) are realistic. All dimensions, and process as well as carrier gases used here are typical of APS technology. Again, the power assumed here is relatively low in order to avoid complete melting of the powder. Although particle injection velocities have been related to carrier gas velocities in some studies [20–23] the relationships are typically hardware-specific and so are not used here.

Modeling

The assumptions associated with the plasma are (*a*) the gaseous species behave as ideal gases at atmospheric pressure; (*b*) no plasma ionization or chemical reaction takes place; (*c*) the system is in steady state, with time-averaged turbulent fluctuations taken into account, and (*d*) the plasma components are in local thermodynamic equilibrium. In addition, the plasma is modeled as a turbulent free jet composed of a high temperature mixture of Ar-H_2 issuing into ambient air. The transport properties for plasma (Ar and H_2), carrier gas (Ar), and air are calculated based on the Chapman-Enskog theory. Numerical values reported by Boulos et al. [24] are used here. Mixture transport properties are calculated with Wilke's formula [24].

Because of their anticipated small effect in influencing the sprayed particles, and the expense of including them in a fully elliptic three-dimensional simulation, chemical reactions within the plasma are not modeled here. It is estimated that the reactions would contribute to less than 10 percent of the particle heating. It is noted that a higher level of uncertainty is associated with values of the transport properties [24]. Neglecting chemical reactions for plasma jet simulation has been adopted in a number of recent works [22,25,26].

The equations solved for the gases are conservation of mass, momentum, enthalpy, radiative energy, species (Ar, H_2, and air), and turbulence kinetic energy as well as its dissipation:

$$\nabla\cdot(\rho\mathbf{V})=0 \tag{1}$$

$$\nabla\cdot(\rho VV)=-\nabla(p)+\nabla\cdot(\tau_{\mathrm{eff}}) \tag{2}$$

$$\nabla\cdot(\rho hV)=\nabla\cdot((k_{\mathrm{eff}})\nabla(T))-\nabla\cdot\mathbf{q}_r \tag{3}$$

$$-\nabla\cdot(\mathbf{q}_r)=-4\int\alpha_\lambda e_{\lambda b}(\lambda,T)d\lambda+\int\int\alpha_\lambda i_\lambda(\lambda,\omega)d\omega d\lambda \tag{4}$$

$$\nabla\cdot(\rho m_i\mathbf{V})=\nabla\cdot(\rho(D_{\mathrm{eff}})\nabla(m_i)) \tag{5}$$

$$\nabla\cdot(\rho k\mathbf{V})=\nabla\cdot((\alpha_k\mu_{\mathrm{eff}})\nabla(k))+\mu_tS^2-\rho\varepsilon \tag{6}$$

$$\nabla\cdot(\rho\varepsilon\mathbf{V})=\nabla\cdot((\alpha_\varepsilon\mu_{\mathrm{eff}})\nabla(\varepsilon))+C_{1\varepsilon}\mu_tS^2\varepsilon/k-C_{2\varepsilon}\rho\varepsilon^2/k-R \tag{7}$$

In the above, τ_{eff} is the stress tensor [27] with the molecular viscosity replaced by the effective viscosity, $\mu_{\mathrm{eff}}=\mu+\mu_t$. The turbulent viscosity μ_t, the inverse Prandtl numbers α_k and α_ε, the effective thermal conductivity and species diffusivity, and the quantities C_μ and R are determined through the RNG extension [28] of the k-ε turbulence model [29]. $C_{1\varepsilon}$ and $C_{2\varepsilon}$ have the values 1.42 and 1.68, respectively. Also, $S=\sqrt{S_{ij}S_{ij}}$, where $S_{ij}=(\partial U_j/\partial x_i+\partial U_i/\partial x_j)/2$ is the mean-rate-of-strain tensor. Note that the effective transport properties are dominated by the turbulent field. The radiative flux (Eqs. 3 and 4) is determined by balancing the local emission and local absorption of thermal radiation. Here, $e_{\lambda b}$ is the spectral blackbody emissive power, i_λ is the spectral radiative intensity and α_λ is the spectral absorptivity of the gases [30]. The radiative transfer Eq. (4) is modeled with the P_l approximation for diffuse radiation, yielding $-\nabla\cdot(\mathbf{q}_r)=-4\kappa\sigma T^4+\kappa G$, where $\kappa=\kappa(T)$ is the Planck mean absorption coefficient, and G is the incident radiation. Data for κ is obtained from Menart et al. [31].

The boundary conditions are based on the physical configurations described in Fig. 1. In brief, flat profiles for plasma jet exit conditions are used in terms of velocity (300 m/s) and temperature (12,000 K). The turbulence intensity ($I=u'/u$, u' being the RMS of the fluctuating component) is specified along with the length scale (l) set to the torch exit diameter of 8 mm (hence, at torch exit, $k=3/2u'^2$, $\varepsilon=C_\mu^{3/4}k^{3/2}/l$). The influence of the DC arc fluctuations, which are originally driven by random arc initiation and extinction between the cathode and the anode, is not a truly turbulence phenomenon. However, because of the lack of understanding of the detailed arc physics, this fluctuation is accounted for by specifying a high level of turbulence at the jet exit, with $I=20$ percent [32]. For the cooling jet (which merely constrains the substrate to reasonable temperatures), constant velocity (10 m/s) and temperature (300 K) profiles are assumed with no turbulence intensity. For the regions of the boundary where gases flow out, zero-gradient conditions are imposed for all quantities. Parts of the boundaries at $x=0$ and $x=120$ mm are held at zero velocity and temperatures of $700\,\mathrm{K}$ $(x=0)$ and $300\,\mathrm{K}$ $(x=120\,\mathrm{mm})$ in order to account for the finite wall thicknesses of the plasma and cooling jet ports. The wall of the injection port is assumed to be constructed of non thermally-conducting material. The substrate is stainless steel with $k=25.4$ W/m-K (at 1 000 K, [33]) while the radiative surroundings are at 300 K.

Once the steady state flow field is calculated, the particle trajectories are predicted using a Lagrangian scheme. The viscous force acting upon the particle, as well as the particle heating rates are calculated on the bases of Stokes' law and Ranz-Marshall correlations. The descriptive equations for the particles (correction factors for the correlations, boundary conditions as well as heat transfer, melting and resolidification within the particles) are identical to those of Wan et al. [[23], Eqs. 1–18] and will not be repeated here. The only exception is that material vaporization is neglected since the partially molten particles experience relatively low maximum temperatures. The discrete random walk model that is used to predict particle trajectories within the highly turbulent jet has been documented [34] along with the numerical scheme for tracking the solid-liquid interface within each particle.

The fluid dynamics of the plasma jet, the carrier gas, and the ambient air is predicted using a finite volume method [35]. The computational grid is polar cylindrical, with the radius of the outer boundary at 50 mm. The mesh is more refined near the axis (in the radial direction), as well as near the jet exit (in the axial direction). The angular resolution is uniform. The grid used to make the predictions reported here has a resolution of 20(axial) $\times$24(radial)$\times$32(angular) cells in the region between the injection port and the substrate. A grid dependence study was made by comparing the peak gas temperatures at $x=18$, 27, 37, 48, 58, 67, and 76 mm on the plane of injection as obtained by using different grids. Specifically, a finer mesh ($40\times24\times32$) and a coarser grid ($10\times12\times32$) were considered. Using the finer mesh as the standard, the coarsest mesh produced a maximum local error of 28 percent [error$=|T-T_{\text{fine-mesh}}|/(T_{\text{fine-mesh}}-300)$] (with the errors increasing in the coolest regions of the domain), the medium resolution grid had a maximum local error of 6 percent. Comparisons were also made for the mean trajectories of the particles. Because the particles traverse the gases from the injection point to the substrate (with local overpredictions of heat transfer rates offsetting local underpredictions), particle deposition locations and temperatures at the substrate were within 2 percent when comparisons for the medium grid and the finest grid were made. Because the trajectory and state of the sprayed material is of primary concern here, the intermediate resolution grid was used to generate the results reported here.

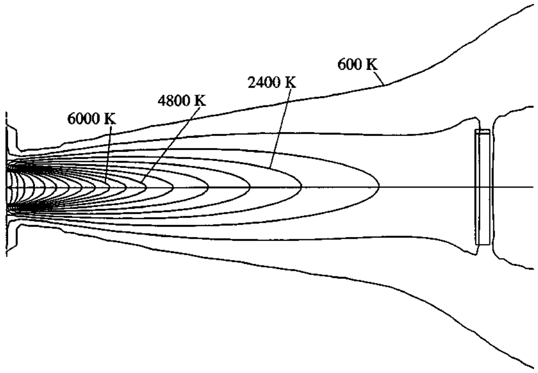

Fig. 2 Temperature distributions for the plasma jet without carrier gas injection (side view)

The grid resolution requirements in the region between the jet exit and the injection port was also examined by comparing the axial temperature variations, and with errors less than 0.5 percent between resolutions of 5 and 10 cells, the coarser resolution was chosen for all subsequent calculations. A comparison of measured and predicted centerline temperature distributions is presented in the Appendix.

Results

Plasma Jet. The predicted plasma jet temperature distribution ($V_{cg}=0$ m/s) is shown in Fig. 2. This result is presented as a reference for comparing the plasma temperatures when carrier gas is introduced. Although this prediction is obtained with a fully three-dimensional model, the jet structure is axisymmetric.

The plasma jet exit is at the left. As evident from the isotherms, the potential core found in typical free jets is absent. This is attributed to the high turbulence in the jet which also loses energy rapidly via thermal emission. Two nonzero carrier gas exit velocities, $V_{cg}=5$ m/s and 15 m/s, were considered (Fig. 3). Note that temperature contours on two perpendicular planes are shown, the vertical plane passes through the injection port and the axis of the plasma torch-substrate assembly (Figs. 3(a) and 3(c)). With the introduction of carrier gas, the loss of symmetry in the vertical

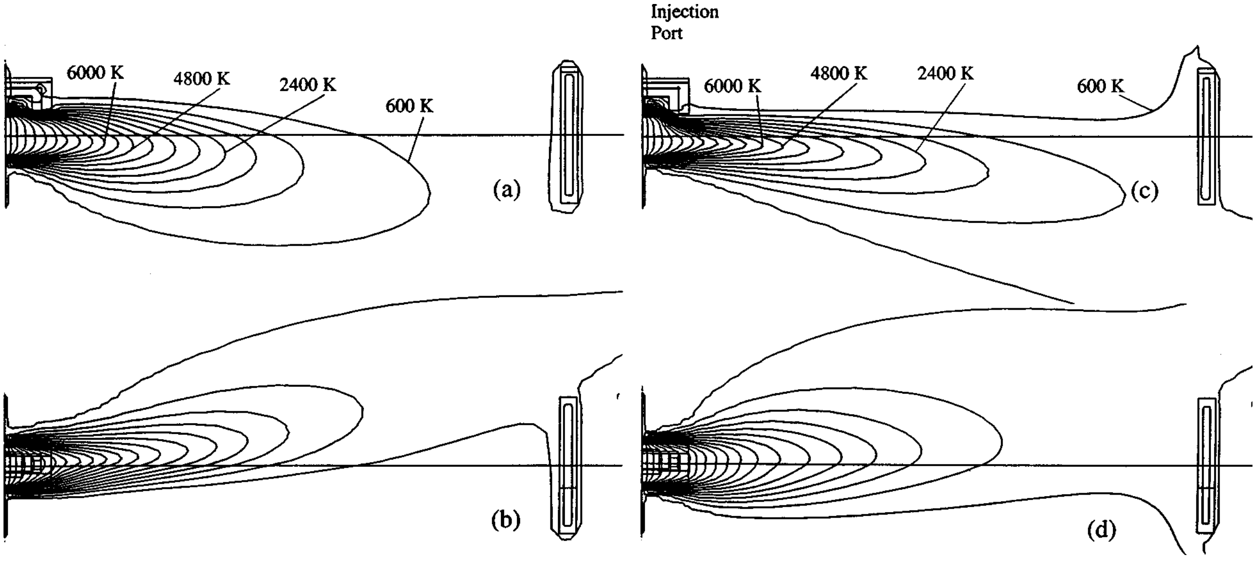

Fig. 3 Temperature distributions for the plasma jet with carrier gas injection (a) side view (b) top view with $V_{cg}=5$ m/s; (c) side view; and (d) top view with $V_{cg}=15$ m/s.

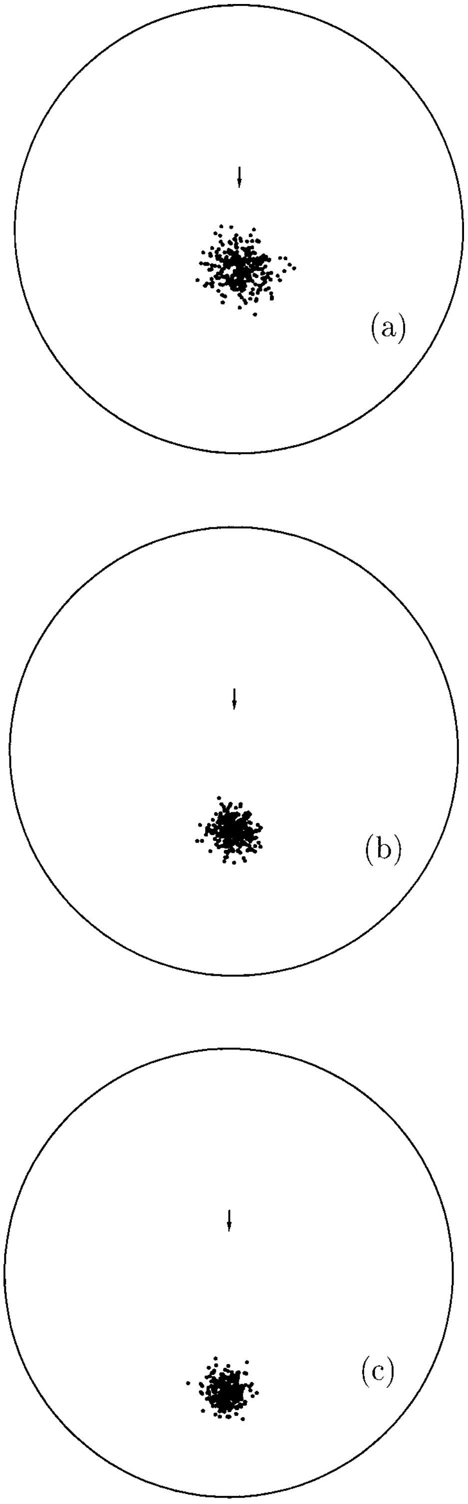

Fig. 4 Deposition locations for (*a*) 30 μm, (*b*) 50 μm, and (*c*) 70 μm particles with no carrier gas injection

plane is expected since the momentum of the carrier gas pushes the plasma jet downward. However, loss of symmetry about the horizontal plane of injection is also observed (Figs. 3(*b*) and 3(*d*)). Lateral asymmetry is especially pronounced for the $V_{cg}=5$ m/s case. Lateral deflection of the plasma jet has been mentioned briefly in other computational studies [10] and, as will become evident, can lead to a pronounced re-direction of the injected particles (also see [25]). Experimental collection of sprayed particles downstream of the plasma torch has also revealed a modest degree of lateral offset with respect to the plane of injection [36].

Particle History: Base Case. In the base case, the particles are introduced into the jet radially at 5 m/s, at a location 5 mm from the torch axis and 5.5 mm from the torch exit. As with nearly all the previous simulations of this process, no carrier gas is included. The instantaneous liquid fraction of the particles, f_L, was tracked, along with the evolution of each particle's f_{RN}. Here, f_{RN} is the fraction of material that has never been molten; for nanostructured particles, f_{RN} is an indirect measure of retained nanostructure. A particle that completely melts and subsequently completely resolidifies would be characterized by $f_L=0$ and $f_{RN}=0$.

Particles of three sizes (30, 50, and 70 μm diameter; typical size of both conventional and nanostructured particles) were numerically injected into the plasma jet, with 900 particles in each size group. The deposition locations for 300 of each of the size groups (900 particle deposition locations are not shown for clarity) are reported in Fig. 4. (In Figs. 4, 8, and 11, the arrow tip indicates the location of the outlet of the injection port.)

As expected, the 30 μm particles are scattered most severely by the turbulence within the jet (Fig. 4(*a*)). Also as expected, the center of the deposition cloud is closer to the center of the substrate, relative to the center of the deposition cloud associated with the larger particles (Figs. 4(*b*) and 4(*c*)). The 30 μm particles melt completely.

The 70 μm particles never melt (even partially), and are deposited furthest from the torch axis, and with the least degree of scatter (Fig. 4(*c*)). This is expected since all the particles issue from the injection port at the same velocity, and the larger particles have a greater initial momentum. The 70 μm particles pass through the core of the jet faster than do the smaller ones, thus minimizing their exposure to high temperature plasma conditions.

The 50 μm particles exhibit a rich history in terms of melting and resolidification phenomena. Most of these particles experience partial melting. Furthermore, once out of the hot plasma flame, some particles undergo resolidification which initiates at their exposed surface. The melting and resolidification phenomena are illustrated in Fig. 5 for a 50 μm particle that follows the mean trajectory of the 900 particles. As the particle enters the plasma, it is heated and the solid-liquid interface (shown as a continuous vertical line) moves inward until the particle reaches $x=40$ mm. At this point, it begins to resolidify at the surface as it enters the lower temperature plasma field (Fig. 2). A second solid-liquid interface appears and moves inward. Because the secondary phase change holds the inner regions of the particle at a nearly isothermal state, the primary interface remains stationary for the remainder of the trajectory. Presumably, an intermediate shell of molten material is trapped between the core (that has never melted) and an outer solid crust (which has lost its nanostructure). The mechanisms associated with the ''splatting'' phenomena of such a particle would be extremely complex and may, in turn, determine the properties of the coating [37].

The variations of f_L and f_{RN} of all 900 (50 μm) particles were recorded, and are presented in Fig. 6. Note that individual data points correspond with specific particles, while the dashed and solid lines represent the mean behavior for the 900 particles. Although individual particles may exhibit significantly different degrees of melting, the maximum average f_L is attained at $x=40$ mm, beyond which point the average f_{RN} remains nearly constant (since the resolidification phenomena of Fig. 5 does not return the material to a nanostructured state).

The local normalized mass flux as well as the average state of the particles (at the substrate) is reported in Fig. 7. As expected, most of the particle flux (largest f_m) occurs at the horizontal center of the substrate (Fig. 7(*a*)). The average state of the particles (calculated within 20 spatial bins located along the horizontal and vertical directions from the center of the substrate) also displays symmetry about the horizontal center of the substrate. As ex-

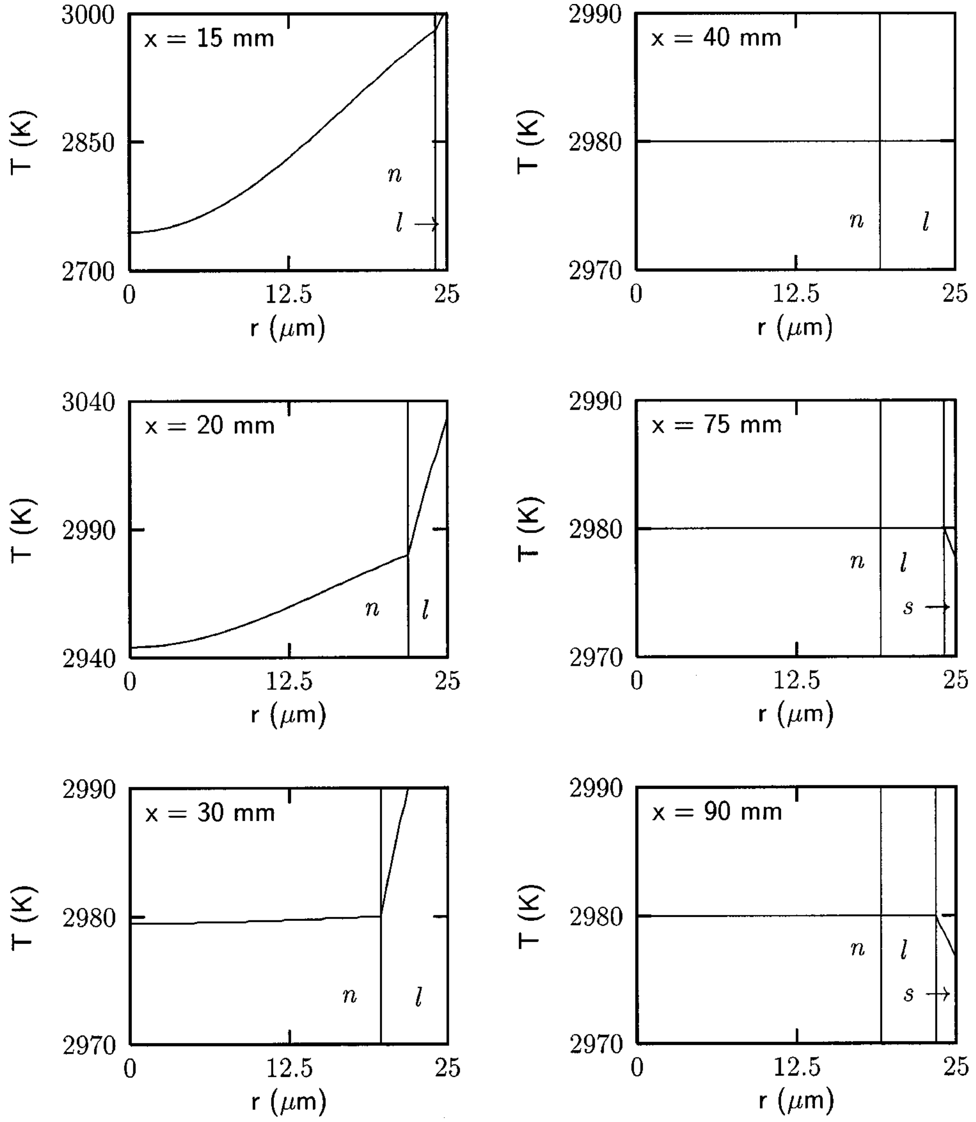

Fig. 5 Phase change inside a 50 μm particle (no carrier gas). The vertical lines mark the solid-liquid interface with *n* being nanostructured material, *l* being molten material, and *s* being resolidified material.

pected, the normalized mass flux in the y direction (Fig. 7(*b*)) is displaced downward from the center of the substrate. Retained nanostructure is locally minimum near the center of the particle cloud since particles at small y rapidly pass through the peak plasma temperatures of Fig. 2, while particles at relatively large (slightly negative) y are not heated as extensively as those near the center of the cloud.

High Carrier Gas Flow Case. Here, the more realistic scenario of a non-zero carrier gas exit velocity ($V_{cg} = 15$ m/s) is considered. The particle injection velocity is retained at 5 m/s.

As carrier gas is included in the simulation, additional mixing between the two gas streams leads to a higher degree of turbulence. In turn, the deposition locations for the three sizes of particles are spread, and are presented in Fig. 8. Compared with the ideal case of Fig. 4, the deposition footprint is much larger, and the particles are carried further downward from the torch axis by the carrier gas momentum. A significant portion of the larger (50 and 70 μm) particles misses the substrate (Figs. 8(*b*) and 8(*c*)). Symmetry of the deposition footprint about the vertical plane is retained. Similar trends have been observed by Vardelle et al. [10].

Phase Change of 50 μm Particles. As before, the 30 μm particles melt completely, although by the time they reach the substrate, some of them are partially resolidified with a molten inner core. The 70 μm particles never melt and arrive at the substrate with $f_{RN} = 1$. The 50 μm particles are partially molten. The variation of f_L and f_{RN} of the 50 μm particles is shown in Fig. 9. Compared with the results of Fig. 6, less melting occurs overall, and more nanostructure is retained, as expected since the carrier gas cools the plasma jet. Note that although a high degree of dispersion occurs in terms of the particle deposition locations (Fig. 8), a similar high degree of dispersion is not evident in the f_L and f_{RN} values associated with the individual particles.

The spatial distribution of f_m and f_{RN} is shown in Fig. 10. As expected from the deposition locations of Fig. 8, the distribution of f_m is nearly symmetric about the plane of injection in the x-direction (Fig. 10(*a*)). However, the thermal asymmetry of Figs. 3(*c*) and 3(*d*) leads to a distinct asymmetry of f_{RN} with more retained nanostructure in the particles that traverse the low temperature regions of the plasma jet. The presence of the carrier gas leads to very different y distributions of f_m and f_{RN} relative to the base case of Fig. 7. Near symmetry in the local mass flux is

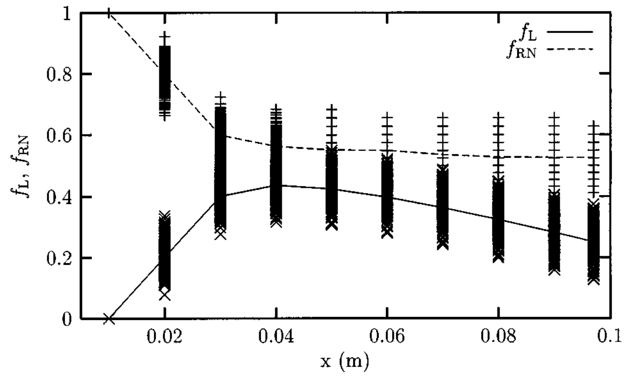

Fig. 6 Evolution of f_L and f_{RN} for 50 μm particles with no carrier gas injection

retained, but the carrier gas momentum pushes more particles through the hot core of the plasma near the injection port, ultimately leading to relatively high values of f_{RN} at small y.

Low Carrier Gas Flow Case. The deposition locations for the $V_{cg}=5$ m/s case are presented in Fig. 11. Now, the particle trajectories have become significantly affected by the carrier gas, with lateral deflections *increased* relative to the high V_{cg} case and vertical deflections *decreased* relative to the high V_{cg} case. This result is unexpected and remarkable, and is indicative of the highly nonlinear nature of the problem. Presumably, a carrier gas injection-to-plasma gas flow rate ratio exists for which the lateral deflection of the particles is maximized. The size of the deposition footprint is intermediate to those of the $V_{cg}=15$ m/s and $V_{cg}=0$ cases, as expected.

Phase Change of 50 μm Particles. As before, the 50 μm particles are partially molten when they arrive at the substrate with the average degree of melting intermediate to that of the previous cases (Fig. 12). However, the degree of scatter in the f_L (or f_{RN}) variation along the x-axis is larger than the $V_{cg}=15$ m/s case. Again, all the 30 μm particles are completely molten whereas none of the 70 μm particles melts prior to deposition. The spatial distribution of the average f_m and f_{RN} is reported in Fig. 13. Obviously, more particles are found to the left of the centerline than to the right. The asymmetry of the problem that is

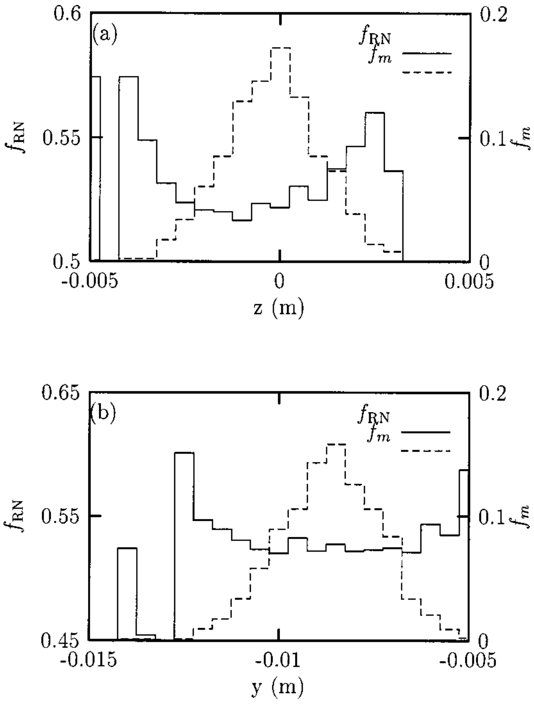

Fig. 7 Average f_{RN} and f_m for particles deposited at different (*a*) horizontal and (*b*) vertical distances from the centerline (no carrier gas)

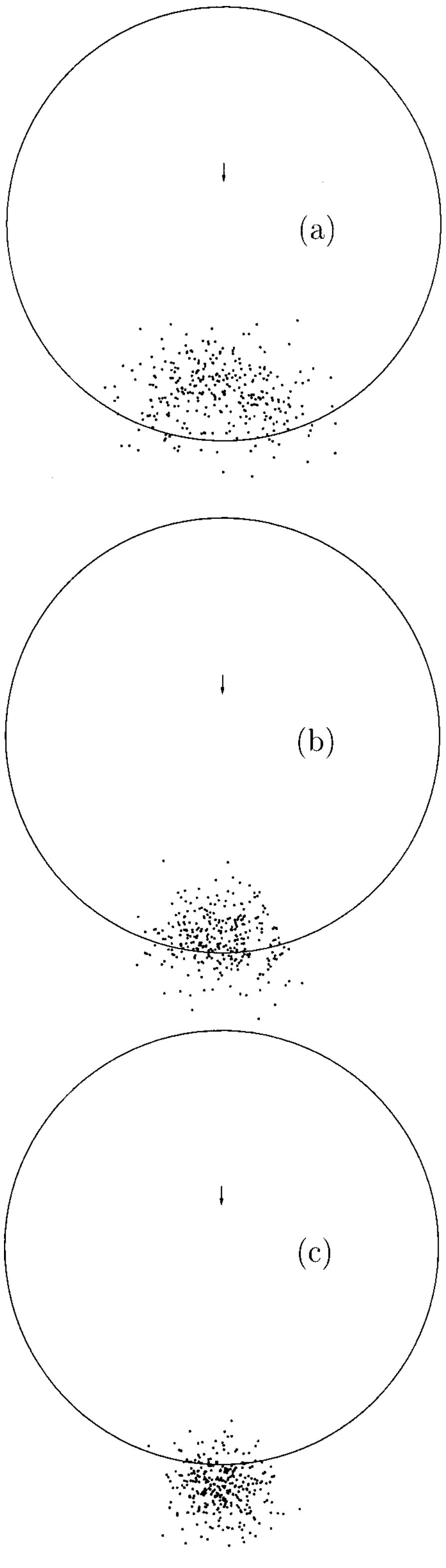

Fig. 8 Deposition locations for (*a*) 30 μm, (*b*) 50 μm, and (*c*) 70 μm particles with $V_{cg}=15$ m/s

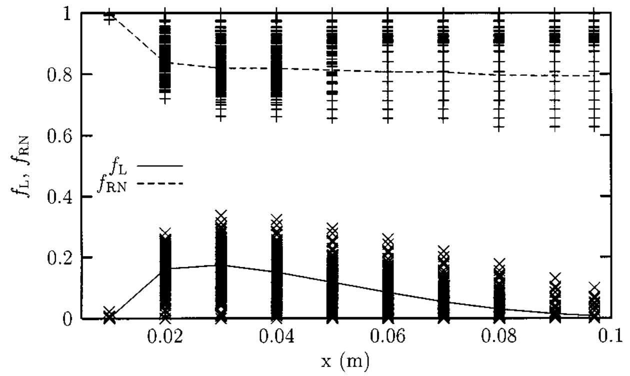

Fig. 9 Evolution of f_L and f_{RN} for 50 μm particles with $V_{cg}=15$ m/s

induced by carrier gas injection leads to asymmetry in terms of the nanostructure distribution of the particle cloud.

Summary, Conclusions, and Recommendations

This study has involved the three-dimensional, elliptic simulation of APS with carrier gas injection. The study was motivated by the desire to identify new processing parameters relevant to the delivery of partially-molten nanostructured powder to the substrate.

The main contribution of this study is the development of a comprehensive model which predicts fully three-dimensional behavior of a plasma spray with carrier gas injection. The effects of the three dimensionality upon powder particle melting and resolidification are accounted for. For the conditions considered here, it is clear that carrier gas injection plays a major role in determining the trajectory and dispersion of the sprayed particles. However, the influence of carrier gas injection on the nanostructure and liquid fraction of the average particle, is deemed to be minor (although noticeable) relative to the sensitivity of the particle's state upon the particle's size. Considerable asymmetry of the particle's state about the plane of injection is induced by the carrier gas under certain operating conditions. This asymmetry may be significant, and might be exploited to, for example, deposit functionally graded coatings [38]. The microstructure of such coatings might be significantly altered by minor modifications in the process such as, for example, sweeping the plasma torch in a vertical

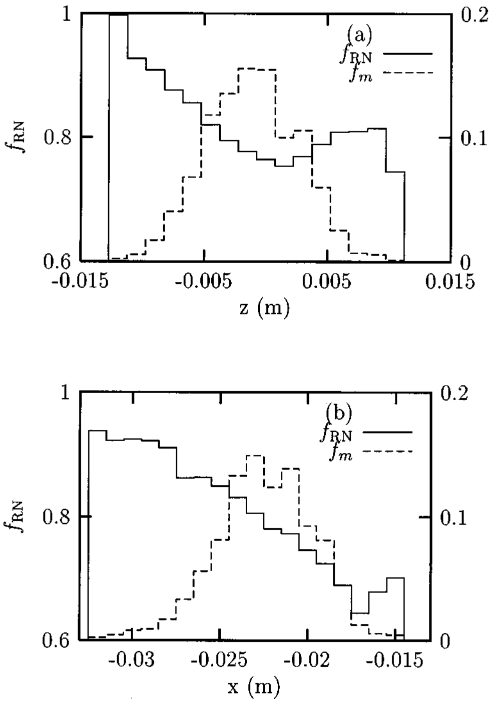

Fig. 10 Average f_{RN} and f_m for particles deposited at different (*a*) horizontal and (*b*) vertical distances from the centerline ($V_{cg}=15$ m/s)

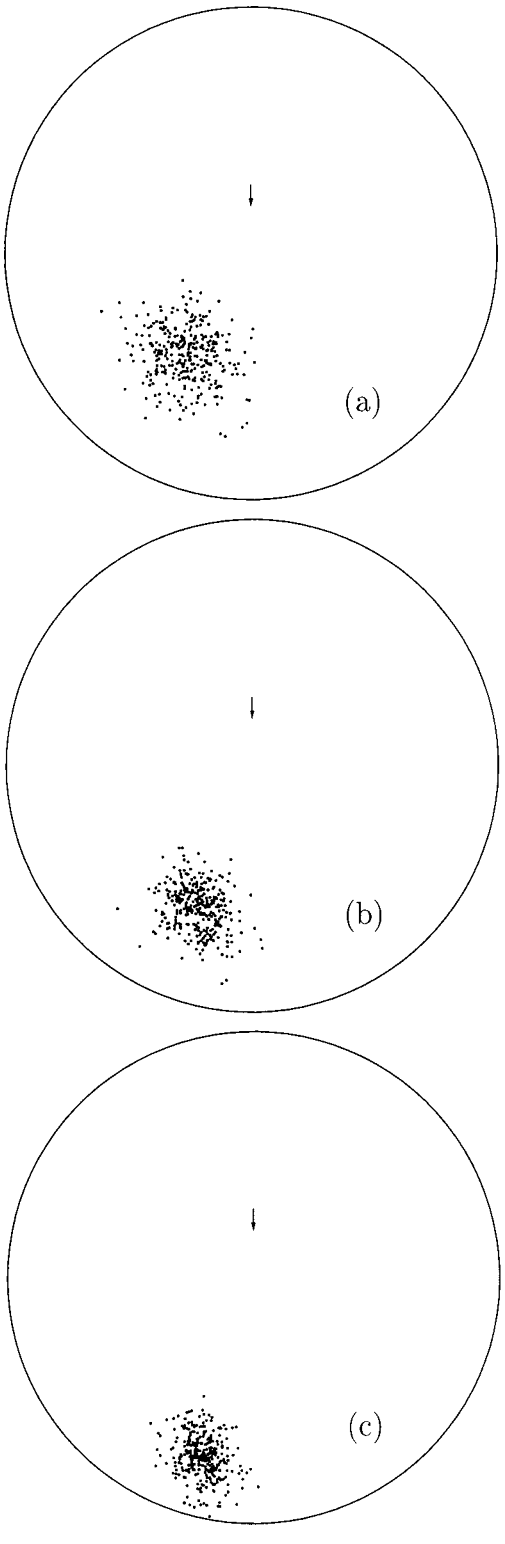

Fig. 11 Deposition locations for (*a*) 30 μm, (*b*) 50 μm, and (*c*) 70 μm particles with $V_{cg}=5$ m/s

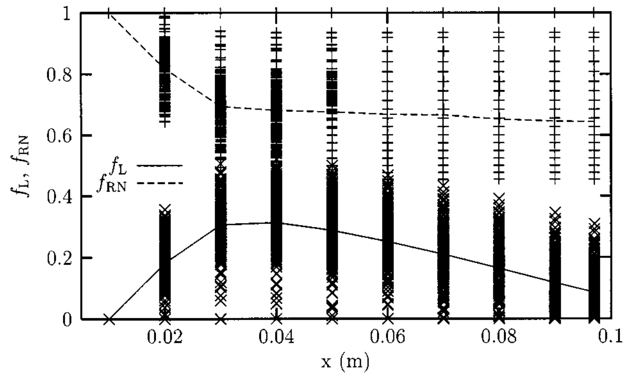

Fig. 12 Evolution of f_L and f_{RN} for 50 μm particles with V_{cg} =5 m/s

direction as opposed to a horizontal direction during spraying. The efficiency with which novel (and expensive) materials may be applied to a substrate will also depend strongly on the size distribution of the powder and processing conditions, and may depend upon the sweep direction of the plasma torch.

Obviously, inclusion of plasma chemistry will alter the quantitative results reported here. However, inclusion of detailed chemistry in the model is not expected to impact the ability of the carrier gas to redirect the plasma, change the particle trajectories, affect the particles' state, or induce variations in the particle's state about the center plane of the plasma torch. Inclusion of particle loading effects (momentum and heat transfer coupling between the particles and gases) will lead to quenching of the gases (and cooler particle temperatures) but, as with plasma chemistry, is not expected to change the general conclusions drawn here.

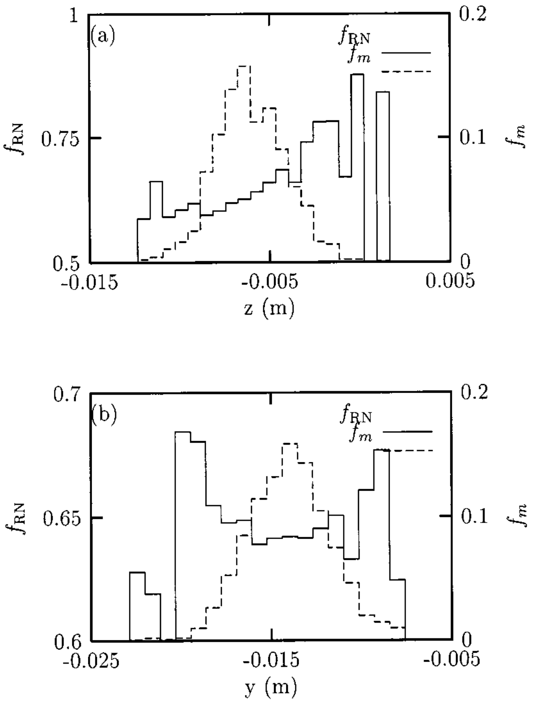

Fig. 13 Average f_{RN} and f_m for particles deposited at different (*a*) horizontal and (*b*) vertical distances from the centerline (V_{cg}=5 m/s)

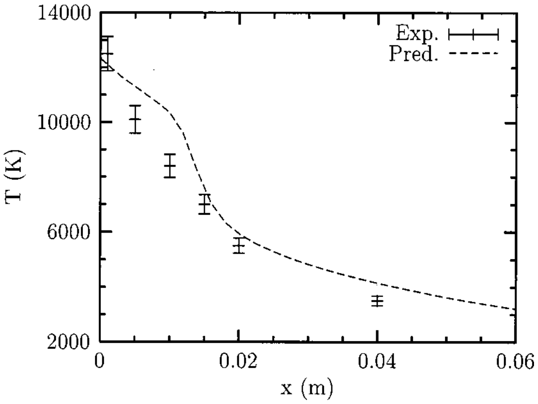

Fig. 14 Comparison of predicted and measured centerline temperatures

Appendix

A comparison of predictions with experimental data has been made. Actual plasma torch (Metco 9MB equipped with a GH nozzle) operating conditions (14.4 kW electrical input power, with 0.787×10^{-3} kg/s of 80:20 Ar-H_2) yielded T_j = 12 000 K (measured) and V_j = 600 m/s (calculated, assuming ideal gas). These values were used in the model in order to compare measurements with the predictions. Experimental measurement of the plasma temperature distribution was made using optical diagnostic methods by Semenov and Cetegen [39]. The axial variation in centerline temperatures is presented in Fig. 14, and the agreement between measurement and prediction is reasonably good. Differences near the exit (x = 0.01 m) are attributed to uncertainties in the plasma properties used in the simulation. A comparison between measurements and predictions with carrier gas injection is difficult because the data analysis technique employed (Abel's inversion of spectroscopic information) is based upon the assumption of axisymmetric plasma jet structure.

Acknowledgments

The work reported here has been funded by the US Office of Naval Research (Grant No. N00014-0843). The authors are grateful for helpful discussions with Professor B. M. Cetegen and Mr. S. Y. Semenov of the University of Connecticut.

Nomenclature

m_i = mass fraction of the specie i
f_L = fraction of molten material in a particle
f_m = fraction of total powder sprayed
f_{RN} = minimum unmelted fraction of material in a particle
k = kinetic energy of turbulence, m^2/s^2
L_{stdf} = torch to target stand-off distance, m
$\mathbf{q}_r$ = radiative flux, W/m^2
V = velocity, m/s
x = horizontal coordinate, along torch centerline, origin at torch exit
y = vertical coordinate, origin at torch axis
z = horizontal coordinate, perpendicular to x-direction (on substrate)
ε = turbulent kinetic energy dissipation rate, m^2/s^3

Subscripts

cg = carrier gas
eff = effective value
j = plasma jet exit conditions
p = particle conditions

References

[1] Nelson, W. A., and Orenstein, R. M., 1997, ''TBC Experience in Land-Based Turbines,'' Journal of Thermal Spray Technology, **6**, pp. 176–180.

[2] Parker, D. S., 1995, ''Practical Application of HVOF Thermal Spray Technology for Navy Jet Engine Overhaul & Repair,'' Plating & Surface Finishing, **82**, pp. 20–23.

[3] Popoola, O. O., Zaluzec, M. J., and McCune, R. C., 1998, ''Novel Powertrain Applications of Thermal Spray Coatings,'' Surf. Eng., **14**, pp. 107–112.

[4] Wuest, G., Barbezat, G., and Keller, S., 1997, ''The Key Advantages of the Plasma-Powder Spray Process for the Thermal Spray Coating of Cylinder Bores in Automotive Industry,'' *Applications for Aluminum in Vehicle Design*, R. A. Borgeson et al., eds., SAE, Warrendale, PA, Special Publications, Vol. 1251, pp. 33–43.

[5] Seitzman, L. E., 1995, ''An Overview of Advanced Surface Engineering Technologies for Protection against Wear,'' *Advances in Coatings Technologies for Corrosion and Wear Resistant Coatings*, A. R. Srivastava et al., eds., TMS, Warrendale, PA, pp. 13–25.

[6] Jones, R. L., 1997, ''Some Aspects of the Hot Corrosion of Thermal Barrier Coatings,'' Journal of Thermal Spray Technology, **6**, pp. 77–84.

[7] Gross, K. A., and Berndt, C. C., 1998, ''Thermal Processing of Hydroxyapatite for Coating Production,'' J. Biomed. Mater. Res., **39**, pp. 580–587.

[8] Pawlowski, L., 1995, *The Science and Engineering of Thermal Spray Coatings*, Wiley, New York.

[9] Ramshaw, J. D., and Chang, C. H., 1992, ''Computational Fluid Dynamics Modeling of Multicomponent Thermal Plasmas,'' Plasma Chem. Plasma Process., **12**, pp. 299–325.

[10] Vardelle, A., Fauchais, P., Dussoubs, B., and Themelis, N. J., 1998, ''Heat Generation and Particle Injection in a Thermal Plasma Torch,'' Plasma Chem. Plasma Process., **18**, pp. 551–574.

[11] Kear, B. H., and Strutt, P. R., 1995, ''Chemical Processing and Applications for Nanostructured Materials,'' Nanostruct. Mater., **6**, pp. 227–236.

[12] Gell, M., 1995, ''The Potential for Nanostructured Materials in Gas Turbine Engines,'' Nanostruct. Mater., **6**, pp. 997–1000.

[13] Cetegen, B. M., and Yu, W., 1999, ''In-Situ Particle Temperature, Velocity and Size Measurements in DC Arc Plasma Thermal Sprays,'' Journal of Thermal Spray Technology, **8**, pp. 57–67.

[14] Ahmed, I., and Bergman, T. L., 1999, ''Thermal Modeling of Plasma Spray Deposition of Nanostructured Ceramics,'' Journal of Thermal Spray Technology, **8**, pp. 315–322.

[15] Ganz, B., Koch, R., Krebs, W., and Wittig, S., 1998, ''Spectral Emissivity Measurements of Thermal Barrier Coatings,'' *Proceedings, 7th AIAA/ASME Joint Thermophysics and Heat Transfer Conference*, Part 1 (of 4), B. F. Armaly et al., eds., ASME, New York, **HTD 357-1**, pp. 291–296.

[16] Hasselman, D. P. H., Johnson, L. F., Bensten, L. D., Syed, R., Lee, H. L., and Swain, M. V., 1987, ''Thermal Diffusivity and Conductivity of Dense Polycrystalline ZrO_2 Ceramics: A Survey,'' Am. Ceram. Soc. Bull., **66**, pp. 799–806.

[17] Williamson, R. L., Fincke, J. R., and Chang, C. H., 2000, ''A Computational Examination of the Sources of Statistical Variance in Particle Parameters During Thermal Plasma Spraying,'' Plasma Chem. Plasma Process., in press.

[18] Houben, J. M., 1976, ''Some Remarks on Plasma Spraying Powder Injection Techniques,'' *Proceedings, 8th International Thermal Spraying Conference*, American Welding Society, Miami Beach, Florida, pp. 68–77.

[19] Pawlowski, L., 1980, ''Optimization of Arc Plasma Spraying Parameters,'' Surfacing Journal, **11**, pp. 8–16.

[20] Zhuang, W. H., Gray, D., Etemadi, K., and Beneson, D. M., 1996, ''Study of Deposition Offset in Plasma Spray of Zirconia,'' Plasma Chem. Plasma Process., **16S**, pp. 127S–139S.

[21] Choi, B. L., and Hong, S. H., 1997, ''Theoretical Investigations on Sprayed Particle-Plasma Interactions to Optimize Processing Parameters in D.C. Thermal Plasma Spraying,'' Mater. Manuf. Processes, **12**, pp. 309–328.

[22] Lugscheider, E., Ladru, F., Eritt, U., Landes, K., Reusch, A., and Mayr, W., 1997, ''Process Modeling and Control of Atmospheric Plasma Spraying of Alumina Coatings,'' *Proceedings, 4th International Thermal Plasma Processes Conference*, P. Fauchais, ed., Begell House, New York, pp. 761–769.

[23] Wan, Y. P., Prasad, V., Wang, G.-X., Sampath, S., and Fincke, J., 1999, ''Modeling of Powder Particle Heating, Melting, Resolidification, and Evaporation in Plasma Spraying Processes,'' ASME J. Heat Transfer **121**, pp. 691–699.

[24] Boulos, M., Fauchais, P., and Pfender, E., 1994, *Thermal Plasmas*, Vol. 1, Plenum Press, New York.

[25] Dussoubs, B., Vardelle, A., and Fauchais, P., 1997, ''Modeling of a Plasma Spray System,'' Progress in Plasma Processing of Materials, 1997, *Proceedings, 4th International Thermal Plasma Processes Conference*, Athens, Greece, July, 1996, P. Fauchais, ed., Begell House, New York, pp. 861–869.

[26] Kang, K. D., and Hong, S. H., 1999, ''Numerical Analysis of Shroud Gas Effects on Air Entrainment into Thermal Plasma Jet in Ambient Atmosphere of Normal Pressure,'' J. Appl. Phys., **85**, pp. 6373–6380.

[27] Panton, R. L., 1984, *Incompressible Flow*, Wiley Interscience, New York, p. 748.

[28] Yakhot, V., and Orszag, S. A., 1986, ''Renormalization Group Analysis of Turbulence: I—Basic Theory,'' J. Sci. Comput., **1**, pp. 3–51.

[29] Launder, B. E., and Spalding, B., 1972, *Mathematical Models of Turbulence*, Academic Press, New York.

[30] Modest, M. F., 1993, *Radiative Heat Transfer*, McGraw Hill, New York.

[31] Menart, J., Heberlein, J., and Pfender, E., 1996, ''Theoretical Radiative Emission Results for Argon/Copper Thermal Plasmas,'' Plasma Chem. Plasma Process., **16S**, pp. 245S–265S.

[32] Planche, M. P., Coudert, J. F., and Fauchais, P., 1998, ''Velocity Measurements for Arc Jets Produced by a DC Plasma Spray Torch,'' Plasma Chem. Plasma Process., **18**, pp. 263–282.

[33] Incropera, F. P., and DeWitt, D. P., 1996, *Fundamentals of Heat and Mass Transfer*, Wiley, New York.

[34] Ahmed, I., and Bergman, T. L., 2000, ''Three-Dimensional Simulation of Thermal Spraying of Partially Molten Ceramic Agglomerates,'' Journal of Thermal Spray Technology, **9**, pp. 240–249.

[35] Patankar, S. V., 1980, *Numerical Heat Transfer and Fluid Flow*, Hemisphere, Washington, D.C.

[36] Semenov, S. Y., 1999, private communication, University of Connecticut, Storrs, CT.

[37] Bianchi, L., Leger, A. C., Vardelle, M., Vardelle, A., and Fauchais, P., 1997, ''Splat Formation and Cooling of Plasma-Sprayed Zirconia,'' Thin Solid Films, **305**, pp. 35–47.

[38] Smith, R. W., and Knight, R., 1996, ''Thermal Spraying II: Recent Advances in Thermal Spray Forming,'' JOM, **48**, pp. 16–19.

[39] Semenov, S. Y., and Cetegen, B. M., 2000, ''Spectroscopic Temperature Measurements in DC-Arc Plasma Jets Utilized in Thermal Spray Processing of Materials,'' submitted to the Journal of Thermal Spray Technology.